frontiers
RESEARCH TOPICS

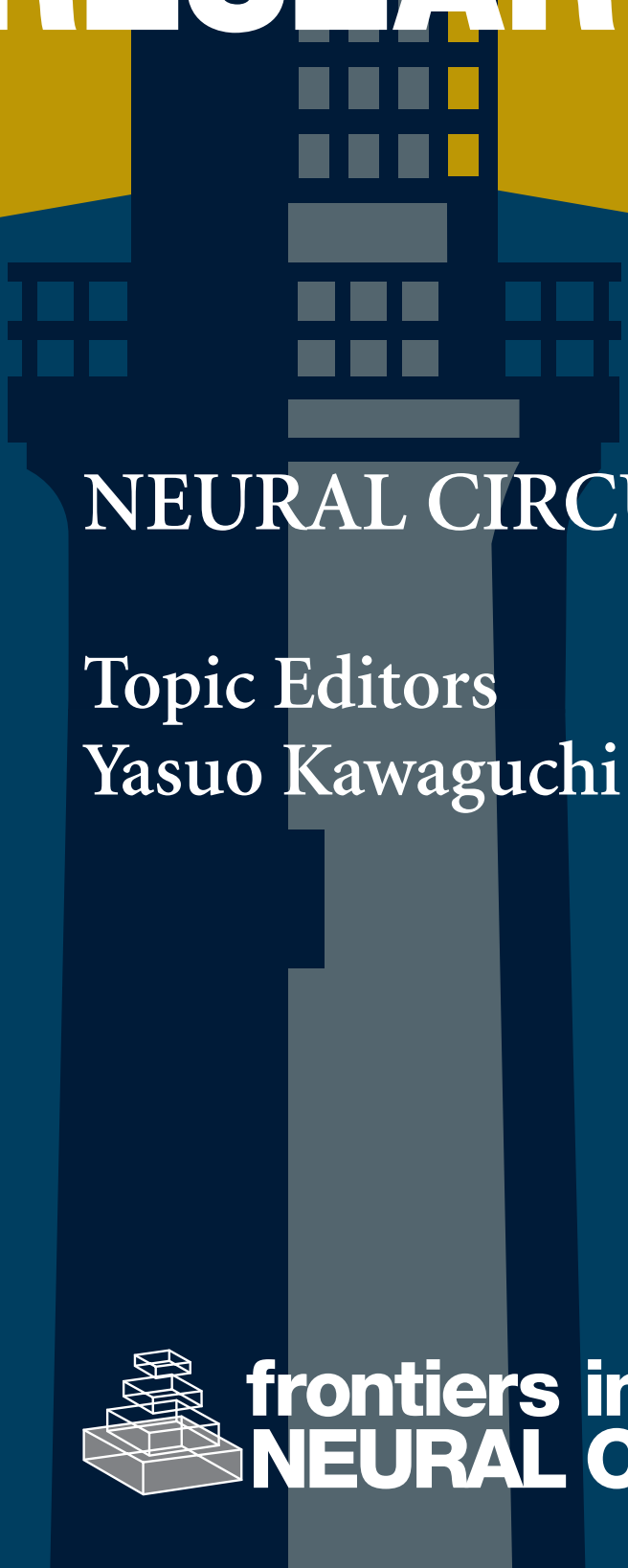

NEURAL CIRCUITS: JAPAN

Topic Editors
Yasuo Kawaguchi and Masanobu Kano

frontiers in
NEURAL CIRCUITS

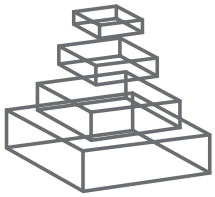

frontiers

Cover image provided by Ibbl sarl, Lausanne CH

ISSN 1664-8714
ISBN 978-2-88919-437-7
DOI 10.3389/978-2-88919-437-7

ABOUT FRONTIERS

Frontiers is more than just an open-access publisher of scholarly articles: it is a pioneering approach to the world of academia, radically improving the way scholarly research is managed. The grand vision of Frontiers is a world where all people have an equal opportunity to seek, share and generate knowledge. Frontiers provides immediate and permanent online open access to all its publications, but this alone is not enough to realize our grand goals.

FRONTIERS JOURNAL SERIES

The Frontiers Journal Series is a multi-tier and interdisciplinary set of open-access, online journals, promising a paradigm shift from the current review, selection and dissemination processes in academic publishing.
All Frontiers journals are driven by researchers for researchers; therefore, they constitute a service to the scholarly community. At the same time, the Frontiers Journal Series operates on a revolutionary invention, the tiered publishing system, initially addressing specific communities of scholars, and gradually climbing up to broader public understanding, thus serving the interests of the lay society, too.

DEDICATION TO QUALITY

Each Frontiers article is a landmark of the highest quality, thanks to genuinely collaborative interactions between authors and review editors, who include some of the world's best academicians. Research must be certified by peers before entering a stream of knowledge that may eventually reach the public - and shape society; therefore, Frontiers only applies the most rigorous and unbiased reviews.
Frontiers revolutionizes research publishing by freely delivering the most outstanding research, evaluated with no bias from both the academic and social point of view.
By applying the most advanced information technologies, Frontiers is catapulting scholarly publishing into a new generation.

WHAT ARE FRONTIERS RESEARCH TOPICS?

Frontiers Research Topics are very popular trademarks of the Frontiers Journals Series: they are collections of at least ten articles, all centered on a particular subject. With their unique mix of varied contributions from Original Research to Review Articles, Frontiers Research Topics unify the most influential researchers, the latest key findings and historical advances in a hot research area!
Find out more on how to host your own Frontiers Research Topic or contribute to one as an author by contacting the Frontiers Editorial Office: researchtopics@frontiersin.org

NEURAL CIRCUITS: JAPAN

Topic Editors:
Yasuo Kawaguchi, Division of Cerebral Circuitry, National Institute for Physiological Sciences, Okazaki, Japan
Masanobu Kano, Department of Neurophysiology, Graduate School of Medicine, The University of Tokyo, Tokyo, Japan

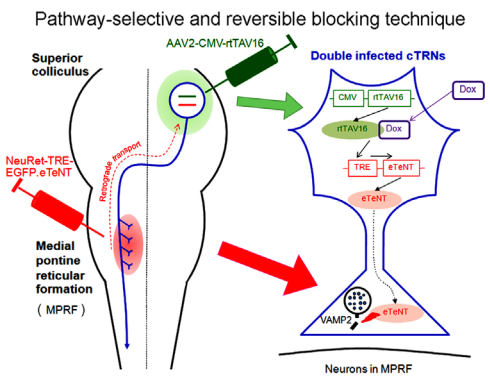

Diagram for the pathway-selective and reversible blockade by double injection of the viral vectors. The interaction of NeuRet-TRE-EGFP.eTeNT injected into the medial pontine reticular formation, and AAV2-CMV-rtTAV16 injected into the superior colliculus, selectively blocks the tectoreticular neurons (cTRNs).

This Frontiers Research Topic on 'Neural Circuits: Japan' explores the diversity of neural circuit research occurring across Japan by innovative researchers using cutting-edge approaches. This issue has brought together papers revealing the development, structure, and physiology of neuronal circuits involved in sensory perception, sleep and wakefulness, behavioral selection, and motor command generation in a range of species from the nematode to the primate. Like the USA and Europe, Japan is now making a strong effort to elucidate neural circuit function in diverse organisms by taking advantages of optogenetics and innovative approaches for gene manipulation, traditional physiological and anatomical approaches, and neural pathway-selective inactivation techniques that have recently been developed in Japan.

Table of Contents

frontiers in
NEURAL CIRCUITS

EDITORIAL
published: 10 November 2014
doi: 10.3389/fncir.2014.00135

Neural circuits: Japan

Yasuo Kawaguchi[1]* and Masanobu Kano[2]*

[1] *Division of Cerebral Circuitry, National Institute for Physiological Sciences, Okazaki, Japan*
[2] *Department of Neurophysiology, Graduate School of Medicine, The University of Tokyo, Tokyo, Japan*
**Correspondence: yasuo@nips.ac.jp; mkano-tky@m.u-tokyo.ac.jp*

Edited and reviewed by:
Takao K. Hensch, Harvard University, USA

Keywords: neocortex, hippocampus, olfactory bulb, basal ganglia, hypothalamus, cerebellum, Drosophila, *C. elegans*

This Frontiers Research Topic on "Neural Circuits: Japan" explores the diversity of innovative neural circuit research occurring across Japan. This issue brings together papers revealing the development, structure, and physiology of neuronal circuits involved in sensory perception, sleep and wakefulness, behavioral selection, and motor command generation in a range of species, from nematode to primate.

One area of interest includes cerebellar local and efferent circuits, as well as mechanisms underlying synaptic plasticity in Purkinje cells, which have been a focus of intensive investigation by many Japanese researchers. Long-term depression at connections between parallel fibers and Purkinje cells is thought to play a critical role in motor learning. In mice without Cbln1, delay eye blink conditioning, as well as LTD at the parallel fiber to Purkinje cell synapse, were impaired, even as previously formed conditioning responses were retained, suggesting a necessity for LTD selectively in conditioning formation (Emi et al., 2013). The cerebellar cortex is composed of functionally different microzones. Investigation of microzonal organization in glutamate receptor δ2 knockout mice revealed that proper innervation by individual climbing fibers is necessary for functional microzone formation (Hashizume et al., 2013). In dystonia, the cerebellum as well as the basal ganglia may be involved in its pathogenesis. Deletion of type 1 inositol 1,4,5-trisphosphate receptors in the cerebellum induced dystonic movements and abnormal movement-coupled firing in Purkinje cells, while inactivation of the inferior olive suppressed abnormal movements. These results suggest the involvement of the olivo-cerebellar pathway in dystonia (Hisatsune et al., 2013).

For analysis of synaptic plasticity in the cerebral cortex, diverse imaging techniques and optical probes have been used. Among them, Förster resonance energy transfer (FRET), combined with newly developed probes, will greatly contribute to our understanding of synaptic plasticity mechanisms at the molecular level (Ueda et al., 2013). During normal formation of cortical circuits, axons and dendrites need to generate boutons and spines at proper locations, respectively. In the cerebral cortex, collateralization of thalamocortical fibers depends on concentrations of brain-derived neurotrophic factor (BDNF), and this BDNF-dependent collateralization was absent after suppression of synaptic vesicle recycling (Granseth et al., 2013). In hippocampal CA3 neurons, application of corticosterone increased the density of dendritic thorny excrescences in pyramidal cells for short time. Similarly, acute stress increases the connectional strength of dentate gyrus to CA3 synapses (Yoshiya et al., 2013). Neocortical pyramidal cells are composed of multiple subtypes that differ in their subcortical projection targets. The subtype composition of layer 5 pyramidal cells connecting cortical areas is also variable, and depends on the target area (Ueta et al., 2013). These observations suggest that cortical neurons are selectively connected according to their individual identities. Further, the temporal pattern of spike discharges may reflect the connectional selectivity of cortical neurons. Large scale activity recordings in the CA3 region of the hippocampus have revealed that temporal firing sequences among a given group of pyramidal cells are repeated among spontaneous spikes of hippocampal neurons *ex vivo* (Matsumoto et al., 2013).

Compared to projections from the retina to primary visual cortex (V1), connections between higher visual centers are less understood. In mice, axons from V1 respond differently to visual input depending on their projection to higher visual areas (Matsui and Ohki, 2013). These results suggest that different V1 cells with distinct visual responses project to different higher visual areas. In *Drosophila*, analysis of visual stimuli-dependent behaviors revealed visual response differences among higher visual centers (Otsuna et al., 2014). On the other hand, in the olfactory system, newly generated neurons are continually integrated into neuronal circuits, and the survival of new neurons is dependent on sleep following food consumption. The olfactory bulb and cortex are suitable for the analysis of sleep-dependent plastic mechanisms in the brain (Yamaguchi et al., 2013).

To understand the switching mechanism between sleep and wakefulness, it is necessary to understand the synaptic interactions between hypothalamic nuclei participating this process. Optogenetic analysis has revealed inhibitory connections from GABAergic cells in the preoptic area to Orexin cells in the lateral hypothalamic area (Saito et al., 2013). The planning and execution of behavior require computation in the basal ganglia and frontal cortex, as well as cortical output to the spinal cord. Conventional electrophysiological and anatomical methods have proven insufficient to clarify these complex circuits. On the other hand, the combined use of local transfection and retrograde transport of viruses were able to block synaptic outputs in the crossed tecto-reticular pathway to suppress motor function (Sooksawate et al., 2013). The combination of retrogradely-transported virus and immunotoxins have also successfully blocked synaptic transmission from motor-related cortical areas to the subthalamic nucleus (Takada

et al., 2013). Pathway-selective inhibition using retrogradely-transported viruses will continue to be a critical tool for elucidating the functions of individual projection systems. The connection loops formed by the basal ganglia and frontal cortex participate in selection of proper movements depending on sensory information. The globus pallidus and frontal areas, such as the dorsal premotor cortex, the dorsolateral prefrontal cortex, and the ventrolateral prefrontal cortex, participate in setting behavioral goals according to cues in the external environment (Hoshi, 2013).

On the other hand, *C. elegans* is an excellent model organism for circuit function analysis because its neuronal organization has been well-characterized, and diverse genetic manipulations are easily achievable. Using *C. elegans*, Japanese researchers have made significant contributions to the understanding of neural circuit that generate behaviors in response to sensory information such as odor and temperature (Sasakura et al., 2013). Thus, as in the USA and Europe, researchers in Japan are now focusing efforts to elucidate the function of neural circuits in diverse organisms by taking advantage of optogenetics, genetic manipulations, and traditional physiological and anatomical approaches, as well as neural pathway-selective inactivation techniques that have recently been developed in Japan.

REFERENCES

Emi, K., Kakegawa, W., Miura, E., Ito-Ishida, A., Kohda, K., and Yuzaki, M. (2013). Reevaluation of the role of parallel fiber synapses in delay eyeblink conditioning in mice using Cbln1 as a tool. *Front. Neural Circuits* 7:180. doi: 10.3389/fncir.2013.00180

Granseth, B., Fukushima, Y., Sugo, N., Lagnado, L., and Yamamoto, N. (2013). Regulation of thalamocortical axon branching by BDNF and synaptic vesicle cycling. *Front. Neural Circuits* 7:202. doi: 10.3389/fncir.2013.00202

Hashizume, M., Miyazaki, T., Sakimura, K., Watanabe, M., Kitamura, K., and Kano, M. (2013). Disruption of cerebellar microzonal organization in GluD2 (GluRδ2) knockout mouse. *Front. Neural Circuits* 7:130. doi: 10.3389/fncir.2013.00130

Hisatsune, C., Miyamoto, H., Hirono, M., Yamaguchi, N., Sugawara, T., Ogawa, N., et al. (2013). IP_3R1 deficiency in the cerebellum/brainstem causes basal ganglia-independent dystonia by triggering tonic Purkinje cell firings in mice. *Front. Neural Circuits* 7:156. doi: 10.3389/fncir.2013.00156

Hoshi, E. (2013). Cortico-basal ganglia networks subserving goal-directed behavior mediated by conditional visuo-goal association. *Front. Neural Circuits* 7:158. doi: 10.3389/fncir.2013.00158

Matsui, T., and Ohki, K. (2013). Target dependence of orientation and direction selectivity of corticocortical projection neurons in the mouse V1. *Front. Neural Circuits* 7:143. doi: 10.3389/fncir.2013.00143

Matsumoto, K., Ishikawa, T., Matsuki, N., and Ikegaya, Y. (2013). Multineuronal spike sequences repeat with millisecond precision. *Front. Neural Circuits* 7:112. doi: 10.3389/fncir.2013.00112

Otsuna, H., Shinomiya, K., and Ito, K. (2014). Parallel neural pathways in higher visual centers of the *Drosophila* brain that mediate wavelength-specific behavior. *Front. Neural Circuits* 8:8. doi: 10.3389/fncir.2014.00008

Saito, Y., Tsujino, N., Hasegawa, E., Akashi, K., Abe, M., Mieda, M., et al. (2013). GABAergic neurons in the preoptic area send direct inhibitory projections to orexin neurons. *Front. Neural Circuits* 7:192. doi: 10.3389/fncir.2013.00192

Sasakura, H., Tsukada, Y., Takagi, S., and Mori, I. (2013). Japanese studies on neural circuits and behavior of *Caenorhabditis elegans*. *Front. Neural Circuits* 7:187. doi: 10.3389/fncir.2013.00187

Sooksawate, T., Isa, K., Matsui, R., Kato, S., Kinoshita, M., Kobayashi, K., et al. (2013). Viral vector-mediated selective and reversible blockade of the pathway for visual orienting in mice. *Front. Neural Circuits* 7:162. doi: 10.3389/fncir.2013.00162

Takada, M., Inoue, K., Koketsu, D., Kato, S., Kobayashi, K., and Nambu, A. (2013). Elucidating information processing in primate basal ganglia circuitry: a novel technique for pathway-selective ablation mediated by immunotoxin. *Front. Neural Circuits* 7:140. doi: 10.3389/fncir.2013.00140

Ueda, Y., Kwok, S., and Hayashi, Y. (2013). Application of FRET probes in the analysis of neuronal plasticity. *Front. Neural Circuits* 7:163. doi: 10.3389/fncir.2013.00163

Ueta, Y., Hirai, Y., Otsuka, T., and Kawaguchi, Y. (2013). Direction- and distance-dependent interareal connectivity of pyramidal cell subpopulations in the rat frontal cortex. *Front. Neural Circuits* 7:164. doi: 10.3389/fncir.2013.00164

Yamaguchi, M., Manabe, H., Murata, K., and Mori, K. (2013). Reorganization of neuronal circuits of the central olfactory system during postprandial sleep. *Front. Neural Circuits* 7:132. doi: 10.3389/fncir.2013.00132

Yoshiya, M., Komatsuzaki, Y., Ikeda, M., Hojo, Y., Mukai, H., Hatanaka, Y., et al. (2013). Corticosterone rapidly increases thorns of CA3 neurons via synaptic/extranuclear glucocorticoid receptor in rat hippocampus. *Front. Neural Circuits* 7:191. doi: 10.3389/fncir.2013.00191

Conflict of Interest Statement: The authors declare that the research was conducted in the absence of any commercial or financial relationships that could be construed as a potential conflict of interest.

Received: 24 September 2014; accepted: 24 October 2014; published online: 10 November 2014.

Citation: Kawaguchi Y and Kano M (2014) Neural circuits: Japan. Front. Neural Circuits ***8****:135. doi: 10.3389/fncir.2014.00135*

This article was submitted to the journal Frontiers in Neural Circuits.

frontiers in
NEURAL CIRCUITS

REVIEW ARTICLE
published: 14 August 2013
doi: 10.3389/fncir.2013.00132

Reorganization of neuronal circuits of the central olfactory system during postprandial sleep

Masahiro Yamaguchi*[1,2]*, *Hiroyuki Manabe*[1,2], *Koshi Murata*[1,2] and *Kensaku Mori*[1,2]

[1] *Department of Physiology, Graduate School of Medicine, The University of Tokyo, Tokyo, Japan*
[2] *Japan Science and Technology Agency, CREST, Tokyo, Japan*

Edited by:
Yasuo Kawaguchi, National Institute for Physiological Sciences, Japan

Reviewed by:
Donald A. Wilson, New York University School of Medicine, USA
Itaru Imayoshi, Institute for Virus Research, Kyoto University, Japan

***Correspondence:**
Masahiro Yamaguchi and Kensaku Mori, Department of Physiology, Graduate School of Medicine, The University of Tokyo, 7-3-1 Hongo, Bunkyo-ku, Tokyo, 113-0033, Japan
e-mail: yamaguti@m.u-tokyo.ac.jp; moriken@m.u-tokyo.ac.jp

Plastic changes in neuronal circuits often occur in association with specific behavioral states. In this review, we focus on an emerging view that neuronal circuits in the olfactory system are reorganized along the wake-sleep cycle. Olfaction is crucial to sustaining the animals' life, and odor-guided behaviors have to be newly acquired or updated to successfully cope with a changing odor world. It is therefore likely that neuronal circuits in the olfactory system are highly plastic and undergo repeated reorganization in daily life. A remarkably plastic feature of the olfactory system is that newly generated neurons are continually integrated into neuronal circuits of the olfactory bulb (OB) throughout life. New neurons in the OB undergo an extensive selection process, during which many are eliminated by apoptosis for the fine tuning of neuronal circuits. The life and death decision of new neurons occurs extensively during a short time window of sleep after food consumption (postprandial sleep), a typical daily olfactory behavior. We review recent studies that explain how olfactory information is transferred between the OB and the olfactory cortex (OC) along the course of the wake-sleep cycle. Olfactory sensory input is effectively transferred from the OB to the OC during waking, while synchronized top-down inputs from the OC to the OB are promoted during the slow-wave sleep. We discuss possible neuronal circuit mechanisms for the selection of new neurons in the OB, which involves the encoding of olfactory sensory inputs and memory trace formation during waking and internally generated activities in the OC and OB during subsequent sleep. The plastic changes in the OB and OC are well coordinated along the course of olfactory behavior during wakefulness and postbehavioral rest and sleep. We therefore propose that the olfactory system provides an excellent model in which to understand behavioral state-dependent plastic mechanisms of the neuronal circuits in the brain.

Keywords: olfactory bulb, olfactory cortex, adult neurogenesis, cell elimination, behavioral state, slow-wave sleep, sharp waves, sensory experience

INTRODUCTION

We sleep every night after experiencing a variety of events and happenings during the day. Recent studies on neuronal activities during sleep have begun to elucidate the adaptive value of postbehavioral sleep. For example, accumulating evidence has shown that the hippocampus and neocortex actively undertake the reorganization of their neural circuitry during postbehavioral sleep (Buzsaki, 1989; Diekelmann and Born, 2010). In the rodent hippocampus, synchronized activities of CA1 pyramidal cells occur in association with sharp wave (SPW)/ripple events during postbehavioral rest and sleep periods (Buzsaki, 1989). These self-organized activities during rest and sleep represent the replay of place cell activities in the CA1 region based on memory traces stored in the CA3–CA1 regions of the hippocampus during the preceding behavioral stage (Wilson and McNaughton, 1994; Lee and Wilson, 2002; Foster and Wilson, 2006). The SPW/ripple-associated replay activities of hippocampal neurons are thought to play an important role in spatial and episodic memory consolidation and concomitant reorganization of neuronal circuitry not only in the hippocampus but also in the neocortex, the target of hippocampal SPW/ripple activities (Buzsaki, 1989; Hasselmo, 1999).

Recent studies have shown that neuronal circuitries in the central olfactory system are reorganized during postbehavioral rest and sleep (Yokoyama et al., 2011). Here, we review accumulating evidence that support the idea that neuronal circuitries of the olfactory cortex (OC) and olfactory bulb (OB) undergo substantial reorganization during the rest and sleep periods subsequent to eating. In particular, we focus on the reorganization of the OB circuitry that involves incorporation or elimination of newly generated adult-born neurons into or from the preexisting neuronal circuitry in the OB.

Neuronal circuitry in the rodent central olfactory system mediates a vast variety of odor-guided behavioral responses, including approaching behaviors to the odor of foods or to the odor (or pheromone) of partners, and flight behaviors to predator odors (Doty, 1986). Although innately determined neuronal circuits mediate some of the basic odor-induced behaviors, including freezing response to the fox odor trimethylthiazoline (TMT) (Morrow et al., 2000; Kobayakawa et al., 2007), a majority of

odor-guided behaviors are heavily dependent on previous experience of the odor and memory of the odor objects or odor environments. It is therefore likely that neuronal circuits in the central olfactory system are highly plastic, and reorganized on a daily basis according to the experiences of odor-guided behaviors and their consequences with the aim of improving behavioral responses to the ever-changing external odor world. It is also likely that a culminating feature of the high plasticity of the olfactory neuronal circuitry is that new neurons are continually integrated into the circuitry throughout life (Lledo et al., 2006).

Because knowledge of structure is prerequisite to an understanding of function (Crick and Koch, 2005), we first summarize the structural features of neuronal circuits in the olfactory system. We then discuss the life and death decision of adult-born new neurons along the course of the wake-sleep cycle and possible underlying mechanisms. The olfactory system consists of two parallel olfactory pathways, the main olfactory system and accessory olfactory system; in this review we focus on the main olfactory system.

NEURONAL CIRCUITRY OF THE MAIN OLFACTORY SYSTEM

Olfaction is mediated by odor molecules, small volatile compounds with a molecular weight of around 25–300 daltons. To enable reception of a huge variety of odor molecules, the rodent olfactory system has developed ∼1,000 types of odorant receptors (ORs), each encoded by distinct gene (Buck and Axel, 1991). ORs are G-protein-coupled seven-transmembrane proteins expressed on the cilial surface membrane of olfactory sensory neurons (OSNs) in the olfactory epithelium (OE). Individual ORs respond to a range of odor molecules that share specific molecular features (Malnic et al., 1999). Individual odor molecules bind to and are received by a specific combination of ORs.

Individual OSNs in the OE express a single type of OR (called "one cell-one receptor rule") (Chess et al., 1994). Each OSN projects a single axon to a single glomerulus at the surface of the OB, the first relay center in the central olfactory system (**Figure 1**). Each OB contains about 1,800 glomeruli in mice. OSNs expressing a given OR project and converge their axons to a few topographically fixed glomeruli ("glomerular convergence rule"). Because of this axonal convergence of OSNs, individual glomeruli represent a single type of OR ("one glomerulus-one receptor rule"). Accordingly, the spatial arrangement of glomeruli in the OB can be viewed as a sensory map which represents numerous types of ORs (Mori et al., 2006; Mori and Sakano, 2011). It should be noted that OSNs are continuously turning over. Despite this, however, the "one glomerulus-one receptor rule" is maintained throughout life in rodents (Gogos et al., 2000).

Within glomeruli, OSN axons form excitatory synaptic connections on primary dendrites of mitral and tufted cells, the glutamatergic projection neurons in the OB (**Figure 1C**) (Mori, 1987; Shepherd et al., 2004). Each mitral/tufted cell projects a single primary dendrite to a single glomerulus, and thus each glomerulus and its associated mitral and tufted cells form a structural and functional module which represents a single OR. Cell bodies of mitral cells are aligned in the mitral cell layer (MCL), while those of tufted cells distribute in the external plexiform layer (EPL) (**Figures 1B,C**). A single glomerulus is estimated to receive primary dendrites from several tens of mitral and tufted cells (Allison and Warwick, 1949).

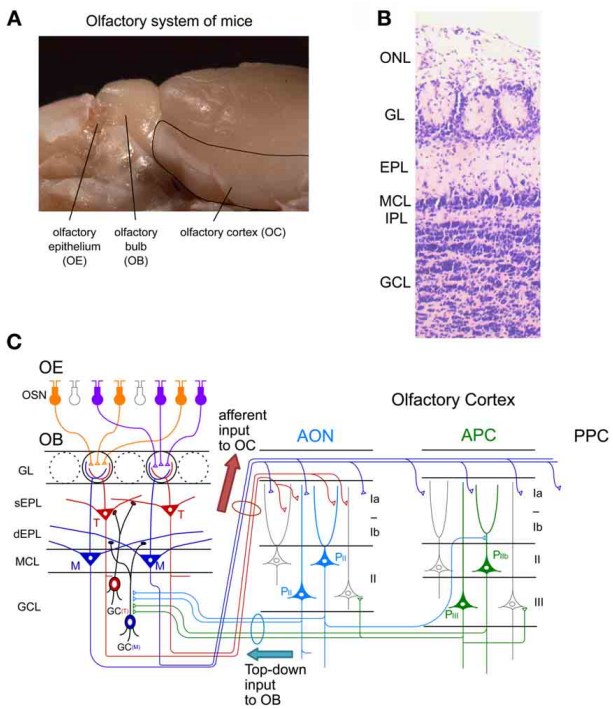

FIGURE 1 | Neuronal circuit of the olfactory system. (A) A picture of the mouse olfactory system. The olfactory epithelium (OE), olfactory bulb (OB), and olfactory cortex (OC) are shown. **(B)** Layer structure of the OB. A nissl-stained coronal section is shown. ONL, olfactory nerve layer; GL, glomerular layer; EPL, external plexiform layer; MCL, mitral cell layer; IPL, internal plexiform layer; GCL, granule cell layer. **(C)** Schematic diagram of the neuronal circuit of the olfactory system. Connectivity of olfactory sensory neurons (OSNs) in the OE, projection neurons and local interneurons in the OB, and pyramidal cells in the anterior olfactory nucleus (AON) and anterior piriform cortex (APC) are shown. sEPL, superficial EPL; dEPL, deep EPL; M, mitral cell; T, tufted cell; GC(T), tufted cell-targeted GC; GC(M), mitral cell-targeted GC; P_{II}, pyramidal cell in layer II of the AON; P_{IIb}, pyramidal cell in layer IIb of the APC; P_{III}, pyramidal cell in layer III of the APC; PPC, posterior piriform cortex.

Mitral and tufted cells project their axons to the OC and make excitatory synapses with apical dendrites of pyramidal cells in the OC (**Figure 1C**). The OC is divided into several areas (Neville and Haberly, 2004). The largest of these is the piriform cortex, which is further subdivided into the anterior piriform cortex (APC) and posterior piriform cortex (PPC). In addition, the OC includes small areas of the olfactory peduncle (anterior olfactory nucleus (AON), tenia tecta and dorsal peduncular cortex), olfactory tubercle, cortical amygdaloid nuclei, lateral entorhinal cortex, and agranular insula.

Tufted cells project axons to focal targets within the rostral areas, including the AON, tenia tecta, rostrolateral part of the olfactory tubercle, and rostroventral part of the APC (Nagayama et al., 2010; Igarashi et al., 2012). In striking contrast, individual mitral cells project axons in a dispersed manner to nearly

all areas of the OC (Nagayama et al., 2010; Ghosh et al., 2011; Sosulski et al., 2011; Igarashi et al., 2012). While mitral cells send signals directly to the piriform cortex, signals conveyed by tufted cells are relayed via pyramidal cells in the olfactory peduncle areas (e.g., AON) and then sent to the piriform cortex via Ib association fibers of pyramidal cells in the olfactory peduncle areas.

Each area of the OC has a pyramidal cell-based cortical structure with three distinct layers (**Figure 1C**). Pyramidal cells in layer IIb and III of the OC extend apical dendrites superficially into layer I and receive glutamatergic excitatory synaptic inputs from mitral/tufted cell axons (in layer Ia). Pyramidal cells give rise to association fibers that terminate in layers Ib, II and III of the same or other areas of the OC. The OC pyramidal cells send axons within the OC and outside the OC, including to the ventral agranular insular cortex, orbitofrontal cortex, amygdaloid complex, thalamus and hypothalamus (Shipley and Ennis, 1996). In addition, pyramidal cells in the AON and APC project axon collaterals massively back to the OB. The top-down centrifugal axons of the pyramidal cells distribute mostly to the GCL of the OB and terminate on inhibitory interneurons such as GCs and short axon cells (Luskin and Price, 1983; Boyd et al., 2012; Markopoulos et al., 2012).

The local neuronal circuitry in the OB is unique among cortical regions in that inhibitory interneurons outnumber excitatory projection neurons. The two most abundant populations of local interneurons in the OB are granule cells (GCs) and periglomerular cells (PGCs) (Mori, 1987; Shepherd et al., 2004). Both GCs and PGCs are continually generated even in adulthood. The number of GCs is about one order larger than that of PGCs. The total number of GCs in the adult rat OB is calculated to be around ten million, which is two orders of magnitude larger than that of mitral/tufted cells (Kaplan et al., 1985; Parrish-Aungst et al., 2007). GCs are axonless inhibitory interneurons. They have soma in the granule cell layer (GCL), and extend apical dendrites into the EPL and basal dendrites within the GCL (**Figures 1B,C**). Apical dendrites of GCs form dendrodendritic reciprocal synapses with lateral dendrites of mitral/tufted cells in the EPL. The dendrodendritic reciprocal synapse consists of a mitral/tufted-to-granule glutamatergic excitatory synapse and a granule-to-mitral/tufted GABAergic inhibitory synapse. A given GC makes such dendrodendritic reciprocal synapses with sister mitral/tufted cells belonging to the same glomerulus and with mitral/tufted cells belonging to different glomeruli, thereby modulating OB output through the synchronization and lateral inhibition of mitral/tufted cells (Yokoi et al., 1995; Kashiwadani et al., 1999).

A subset of GCs preferentially forms dendrodendritic synapses with mitral cells (mitral cell-targeted GCs) in the deep sublamina of the EPL (**Figure 1C**). Another subset of GCs preferentially forms dendrodendritic synapses with tufted cells (tufted cell-targeted GCs) in the superficial EPL. Soma of mitral cell-targeted GCs tend to distribute to the deep portion of the GCL while those of tufted cell-targeted GCs distribute to the MCL and superficial portion of the GCL.

Another type of major interneuron in the OB, PGCs, have soma in the glomerular layer (GL), and typically extend dendrites into a single glomerulus. Within the glomerulus, PGC dendrites receive excitatory inputs from the OSNs and mitral/tufted cell primary dendrites, and send output via dendrodendritic inhibitory synapses to mitral/tufted cell primary dendrites (Shepherd et al., 2004). PGCs modulate the activity of mitral/tufted cells belonging to the same glomerulus and those belonging to different glomeruli. Thus, these two types of OB local interneurons substantially modulate responses of mitral/tufted cells to olfactory sensory input. The OB also contains other types of inhibitory neurons called short axon cells, whose function has attracted recent interest but remains largely unknown (Schneider and Macrides, 1978; Eyre et al., 2008; Arenkiel et al., 2011; Boyd et al., 2012; Deshpande et al., 2013).

REMARKABLE PLASTICITY IN THE OLFACTORY SYSTEM: ADULT NEUROGENESIS

The two major types of inhibitory interneuron in the OB, GCs and PGCs, are continually generated in the adult brain (Lledo et al., 2006). Precursors of these inhibitory interneurons are produced in the subventricular zone (SVZ) of the lateral ventricle (**Figure 2A**), to which ganglionic eminence- and neocortex-derived embryonic precursors for interneurons

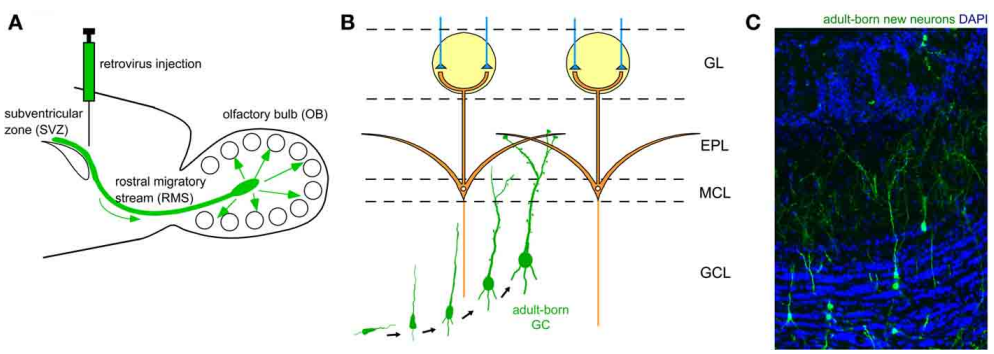

FIGURE 2 | Adult neurogenesis in the OB. (A) Neuronal precursors are generated in the subventricular zone (SVZ) around the lateral ventricle and migrate to the OB via a specific route called the rostral migratory stream (RMS). **(B)** In the OB, neuronal precursors differentiate into GCs. Their apical dendrites form synaptic contacts with lateral dendrites of mitral cells. **(C)** Adult-born GCs are visualized by retrovirus-mediated GFP expression (green). GFP-expressing retrovirus was injected in the SVZ and the OB was analyzed 28 days after the injection. Blue, nuclear staining with DAPI.

immigrate (Young et al., 2007). The newly generated neuronal precursors migrate along a specific route called the rostral migratory stream (RMS) to the OB (**Figure 2A**), where they mature to become GCs and PGCs (**Figures 2B,C**). While the production of mitral/tufted cells is limited only during the mid- to late embryonic period (Hinds, 1968; Bayer, 1983), GCs and PGCs are generated extensively during the late embryonic and early neonatal periods, with substantial production continuing in adulthood. The number of adult-born OB interneurons is very large. In rodents, at least several tens of thousands of neurons enter the OB each day (Alvarez-Buylla et al., 2001; Winner et al., 2002; Lledo et al., 2006), corresponding to roughly one percent of the total number of OB interneurons. Thus, a simple calculation suggests that adult-born interneurons will outnumber preexisting interneurons within 100 days. Although the exact percentage of adult-born interneurons in the entire interneuron population has been unclear, recent advances in molecular and developmental biology provide an estimated figure (Lagace et al., 2007; Ninkovic et al., 2007; Imayoshi et al., 2008). One report indicates that roughly 70% of GCs in the adult OB are adult-born (Imayoshi et al., 2008), suggesting that odor information processing in the adult OB is heavily dependent on adult-born GCs.

An outstanding feature of adult neurogenesis is that new neurons are synaptically integrated into preexisting neuronal circuits. Similar to embryonic- and neonatal-born GCs, adult-born GCs receive glutamatergic synaptic contact from the same two major sources, namely mitral/tufted cells via dendrodendritic synapses in the EPL and pyramidal cells in the OC via axodendritic synapses in the GCL (**Figure 1C**). Such synaptic incorporation of adult-born GCs occurs roughly within a month after their generation (Petreanu and Alvarez-Buylla, 2002; Carleton et al., 2003; Whitman and Greer, 2007; Kelsch et al., 2008, 2010; Katagiri et al., 2011). Axodendritic synaptic contacts from axons of OC pyramidal cells occurs earlier, at around day 14. Synaptic contacts from mitral/tufted cell dendrites become apparent later, at around day 21, and by day 28, all synaptic structures become indistinguishable from those of preexisting mature GCs. Both types of glutamatergic synapse appear to be crucial to the proper selection of new GCs for incorporation or elimination.

ADULT-BORN GCs ARE UNDER A SELECTION PROCESS, AND EITHER INCORPORATED INTO OR ELIMINATED FROM THE NEURONAL CIRCUITRY

Although a majority of adult-born GCs initially enter into the bulbar circuitry by forming immature synaptic contacts, many of these GCs are eliminated during maturation. Under normal conditions only half of new GCs succeed in living longer than one month after generation, while the other half are eliminated by apoptosis (Petreanu and Alvarez-Buylla, 2002; Winner et al., 2002; Yamaguchi and Mori, 2005). Initial excess neurogenesis and subsequent apoptotic elimination occur in both embryonic and adult neurogenesis. This selection process during embryonic development is crucial to ensuring that the neuronal circuitry has been appropriately tuned to the provision of proper information processing (Buss et al., 2006). This process also appears crucial for adult neurogenesis. When apoptotic elimination of adult-born neurons is suppressed by a caspase inhibitor, odor discrimination ability is disturbed (Mouret et al., 2009), presumably because of the presence of inappropriately incorporated adult-born GCs. However, the cellular and molecular mechanisms by which adult-born GCs are selected to survive or die is not well understood.

Survival and death of adult-born GCs depends on olfactory sensory experience. An increased survival rate of adult-born GCs was observed in those mice that were repeatedly exposed to novel odors (odor-enriched environment) (Rochefort et al., 2002). Conversely, the survival rate of adult-born GCs was decreased in anosmic mice lacking a cyclic nucleotide-gated channel in OSNs (Petreanu and Alvarez-Buylla, 2002) and in the ipsilateral OB of mice with unilateral sensory input deprivation (Corotto et al., 1994; Saghatelyan et al., 2005; Yamaguchi and Mori, 2005; Mandairon et al., 2006). GC elimination appears to be driven by an apoptotic pathway. Olfactory sensory deprivation by nostril occlusion remarkably increased apoptotic GCs, as immunohistochemically detected by the activation of caspase-3 (**Figures 3A,B**) (Yamaguchi and Mori, 2005).

Sensory experience-dependent plastic change in the developing central nervous system occurs during specific time windows, called critical periods. For example, ocular dominance plasticity

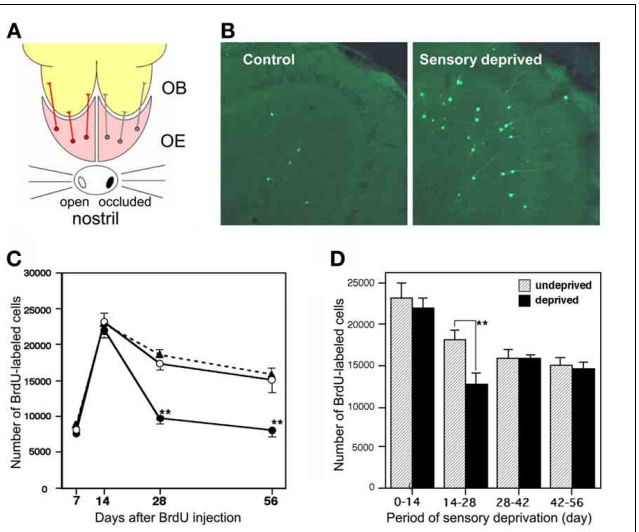

FIGURE 3 | Sensory experience-dependent life and death decision of adult-born GCs. (A) Deprivation of olfactory sensory input by single-nostril occlusion. Olfactory sensory input is conducted from an open nostril (left) to the same side of the OE and OB, while input is not conducted to the occluded side (right) of the OE and OB. **(B)** Caspase-3-activated apoptotic GCs in the OB (green). Compared to the control (sensory input-intact) OB, a large number of apoptotic GCs are seen in the sensory-deprived OB. **(C)** Number of BrdU-labeled new GCs at various periods after labeling in the control OB (black triangles), sensory input-intact OB of mice under unilateral sensory deprivation (open circles), and sensory input-deprived OB (closed circles). Sensory deprivation remarkably decreased the number of new GCs during days 14–28 after labeling. **(D)** Effect of sensory deprivation for 14 days at various periods after BrdU labeling on the survival of BrdU-labeled new GCs. Sensory deprivation during day 14–28 decreased survival, while deprivation before or after this period showed no significant effect on survival. Modified from Yamaguchi and Mori (2005).

in the primary visual cortex occurs selectively during the critical period after birth (Hensch, 2005). We examined whether there is a critical period for adult-born GCs during which their survival and death is strongly influenced by olfactory sensory experience. Newly generated GCs in adult mice were labeled by systemic BrdU injection, and the mice were then deprived of olfactory sensory input by nostril occlusion at various time periods after labeling. The results showed that sensory deprivation during days 14–28 after GC generation greatly reduced the survival of GCs, whereas deprivation before or after this period had no significant effect (**Figures 3C,D**) (Yamaguchi and Mori, 2005). Consistent with this observation, most apoptotic GCs showing caspase-3 activation were aged 14–28 days. These observations indicate that the sensory experience-dependent life and death decision of new GCs occurs during a critical time window at days 14–28 after their generation.

Importantly, this time window corresponds to the period when adult-born GCs make and maturate synaptic contacts with preexisting neurons (Petreanu and Alvarez-Buylla, 2002; Carleton et al., 2003; Whitman and Greer, 2007; Kelsch et al., 2008, 2010; Katagiri et al., 2011), suggesting that synaptic input plays a crucial role in the selection of adult-born GCs. Morphological examination of adult-born GCs in anosmic mice showed that young GCs destined for later elimination had already developed many synaptic structures in the EPL (Petreanu and Alvarez-Buylla, 2002). Thus, the basic strategy for GC selection appears to be that most new GCs temporally establish immature synaptic contacts with preexisting neurons before their life or death decision is made. Subsequent to the formation of immature synapses, they may undergo a "quality check" by the activity of the synapses they have made with preexisting neurons. Some are successfully incorporated for long-term function while others are eliminated by apoptosis. Although apoptotic cells are found throughout the neurogenic routes in the SVZ, RMS and OB (Biebl et al., 2000; Mandairon et al., 2003), close to 80% of apoptotic cells are found within the OB (Biebl et al., 2000). This observation further supports the notion that selection of adult-born GCs is primarily conducted at their final destination, namely neuronal circuits in the OB, where their usability might be determined by interaction with preexisting neuronal circuits.

SELECTION OF ADULT-BORN GCs DURING A BEHAVIORAL STATE-DEPENDENT TIME WINDOW

Neuronal plasticity is tightly linked to the behavioral state of animals. A conspicuous alteration in behavioral state is the wake-sleep cycle. Neuronal plasticity is well organized along the wake-sleep cycle and sleep plays a critical role in the long-lasting neuronal plasticity that accompanies memory consolidation (Buzsaki, 1989; Diekelmann and Born, 2010).

Temporal incorporation and later elimination of newly generated GCs in the OB are accompanied by substantial structural reorganization of the neuronal circuitry. Because olfactory sensory experience determines the magnitude of the elimination and survival of new GCs (Corotto et al., 1994; Petreanu and Alvarez-Buylla, 2002; Rochefort et al., 2002; Saghatelyan et al., 2005; Yamaguchi and Mori, 2005; Mandairon et al., 2006), we hypothesized that structural reorganization of the OB circuitry occurs during the time course of olfactory sensory experience followed by sleep. To examine the time course of this reorganization, we thus looked for typical and appropriate behaviors of rodents that included olfactory experience and sleep.

Finding and eating foods are typical daily olfactory behaviors (Doty, 1986). Olfactory memory of a food encoded during the search and eating plays a key role in subsequent odor cue-based decision making as to the whether the animal will eat or reject the food. We therefore selected feeding behavior and subsequent sleep as a candidate behavioral sequence which accompanies structural reorganization of the OB circuitry, including the elimination of newly generated GCs.

Under *ad libitum* feeding conditions, mice show sporadic eating behavior which is unsuitable for experimental analysis. We therefore controlled feeding behavior using a restricted feeding paradigm. Food pellets were available only during a fixed 4-h time window (11:00–15:00) (**Figure 4A**). After habituation to this schedule for 9 days, all mice showed extensive eating behavior followed by postprandial (after-meal) behaviors such as grooming, resting and sleeping. During the first hour of food availability (11:00–12:00), mice were mostly devoted to consuming behavior, namely food eating and water drinking. In this eating period, no increase in apoptotic GCs was observed

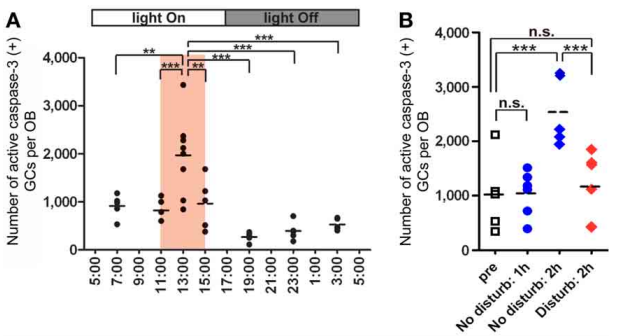

FIGURE 4 | GC elimination is promoted during the postprandial period. **(A)** Apoptotic GCs increase during the feeding and postprandial periods. Mice were under restricted feeding in which food is supplied for only 4 h (11:00–15:00; an orange bar) per day. On day 10 of restricted feeding, mice were analyzed at various circadian time points for caspase-3-activated apoptotic GCs in the OB. Each dot represents the number of caspase-3-activated GCs in one animal (average of left and right OBs), and bars indicate the average number at respective time points. **(B)** Postprandial behaviors including sleep are crucial to the increase in GC elimination. After food delivery, mice were allowed to behave freely (blue) for 1 or 2 h and then analyzed for caspase-3-activated apoptotic GCs. At 1 h after food presentation (No disturb: 1h), the number of apoptotic GCs was not increased compared to just before food delivery (pre). In contrast, at 2 h after food presentation (No disturb: 2 h), the apoptotic GC number was considerably increased. When postprandial behaviors including rest, grooming and sleep were disturbed during the postprandial period (between 1 and 2 h after food delivery) (red, Disturb: 2 h), the apoptotic GC number was significantly suppressed. In **(A)** and **(B)**, each dot represents the number of caspase-3-activated GCs in one animal (average of left and right OBs), and bars indicate the average number at respective time points. **, $p < 0.01$; ***, $p < 0.001$; n.s., not significant; One-Way ANOVA with *post-hoc* Bonferroni test. Modified from Yokoyama et al. (2011) with permission.

(**Figure 4B**). During the subsequent hour (12:00–13:00), mice appeared to be satiated with food, and instead showed grooming, resting and sleeping. Surprisingly, the number of apoptotic GCs increased ∼2-fold during this time window of postprandial behaviors (**Figure 4**). Most of the apoptotic GCs were newly generated GCs aged 14–28 days after generation, which corresponded to the critical period for the sensory experience-dependent survival and death decision. Perturbation of these postprandial behaviors by gently touching the mouse's body remarkably suppressed the GC apoptosis, suggesting the importance of these postprandial behaviors to the increased GC elimination.

Sleep is the most characteristic behavior during the postprandial period and includes various stages (light sleep, slow-wave sleep and REM sleep). We then asked during which sleep stage does the increase in the number of apoptotic GCs occur. To address this question, we examined the correlation between the length of each sleep stage and the magnitude of the GC apoptosis (**Figure 5**). Mice showed several tens of minutes of slow-wave sleep during the first one hour of the postprandial period, and the length of the slow-wave sleep roughly correlated with the number of apoptotic GCs in the OB (**Figure 5**, middle). In contrast, REM sleep was rarely observed during this period, and the length of REM sleep when it did occur showed no significant correlation with the magnitude of GC apoptosis (**Figure 5**, right). These observations suggest that postprandial slow-wave sleep plays an important role in promoting GC elimination. It should be emphasized that the length of slow-wave sleep during the first one hour of the postprandial period is only 10–30 min in total, indicating that short time periods of slow-wave sleep in the range of a "nap" can nevertheless strongly promote GC elimination.

Does the increase in GC apoptosis occur during all sleep episodes or only during postprandial sleep? Of course, food-restricted mice sleep not only during the feeding time but also without preceding feeding. We observed that GC apoptosis did not increase during sleep periods outside the feeding time (Yokoyama et al., 2011). Thus, the increased GC apoptosis is dependent not on the sleep alone, but on the combination of feeding and subsequent sleep episodes.

OLFACTORY SENSORY EXPERIENCE INFLUENCES THE EXTENT OF GC ELIMINATION DURING THE POSTPRANDIAL PERIOD

The above findings indicate that the survival and death of adult-born GCs are regulated by olfactory sensory experience. We then asked whether olfactory sensory experience influences the extent of GC elimination during the postprandial period. Mice received unilateral sensory deprivation by chronic occlusion of one nostril, and were then subjected to restricted feeding. As expected, the number of apoptotic GCs increased dramatically in the sensory-deprived OB during the postprandial period, at about 7-fold larger than that in the sensory input-intact OB of the same mice (**Figure 6**, 13:00). Intriguingly, the number of apoptotic GCs just before feeding time (11:00) was comparable to that in the control OB without sensory deprivation. Moreover, the number of apoptotic GCs at any period outside the feeding time did not differ from that in the OB without sensory deprivation, in spite of the fact that sensory deprivation was continuously maintained by chronic occlusion of the nostril. These results indicate that (1) olfactory sensory experience influences the extent of GC elimination during the postprandial period, and that (2) the increase in GC apoptosis in the sensory-deprived OB is restricted to a specific time window of feeding and subsequent sleep period in food-restricted mice. The sensory experience-dependent life and death decision of new GCs does not appear to be a "passive" phenomenon which is present at any behavioral period, but rather an "active" phenomenon which is tightly regulated by the sequence of olfactory sensory experience during feeding followed by postprandial sleep.

TWO-STAGE MODEL FOR SENSORY EXPERIENCE-DEPENDENT GC SELECTION

The majority of apoptotic GCs observed during postprandial sleep were newly generated GCs aged days 14–28 after generation, the period in which new GCs establish extensive synaptic contacts with preexisting neuronal circuitry in

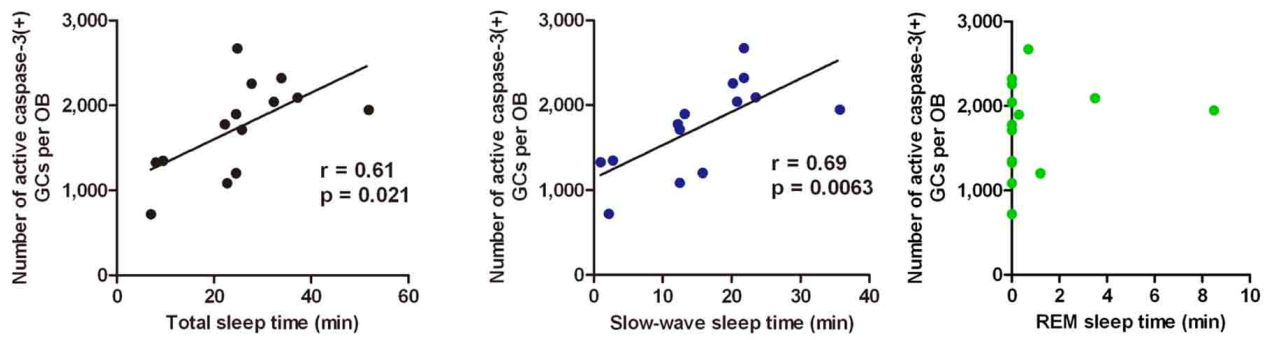

FIGURE 5 | GC elimination correlates with the occurrence of postprandial slow-wave sleep. Behavioral state of mice during the first hour of the postprandial period is classified into waking, and the light sleep, slow-wave sleep, and REM sleep states according to neocortical EEG, neck muscle EMG and behavior. Correlation of the number of caspase-3-activated GCs with the total time length of sleep (left), slow-wave sleep (middle), and REM sleep (right) during the first hour of the postprandial period were examined. Each dot represents the data from one animal. Regression line, Pearson's *r*-value and *p*-value are indicated (left, middle). Modified from Yokoyama et al. (2011) with permission.

the OB. These observations led us to propose a "two-stage model" for the sensory experience-dependent selection of new GCs, in which the two stages represent olfactory sensory experience during food search and eating (sensory experience-stage) followed by postprandial sleep (sleep-stage) (**Figure 7**).

During the waking period when mice show food-searching and eating behaviors, one subset of newly generated adult-born GCs receives olfactory sensory inputs mainly via dendrodendritic synapses from mitral/tufted cells in the EPL, while the remaining subset does not (**Figure 7**, left). We assume that new GCs that are activated by the olfactory sensory inputs receive a kind of synaptic tagging that works as a substrate for subsequent plastic change (Frey and Morris, 1997; Redondo and Morris, 2011). These GCs may be "tagged" in the dendrodendritic synapses or the cells themselves, while other GCs that are not activated by olfactory sensory input remain "non-tagged." Alternatively, new GCs might instead receive a "survival tag" when they receive strong synaptic input during the experience of salient olfactory-guided behaviors. New GCs that were not activated might receive a "death tag." It is also possible that top-down axodendritic synapses from the OC pyramidal cells to new GCs are tagged by olfactory sensory experience, although whether and how a subset of new GCs receives olfactory sensory

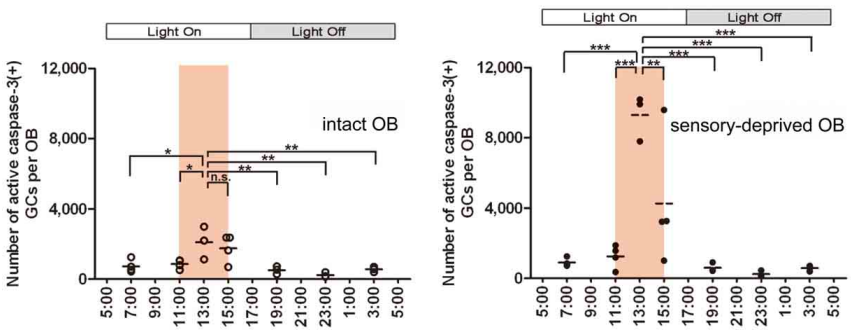

FIGURE 6 | Olfactory sensory experience influences the magnitude of GC apoptosis during the postprandial period. In food-restricted mice (food delivery at 11:00–15:00; orange bars), olfactory sensory input was deprived unilaterally by chronic occlusion of one nostril. The number of caspase-3-activated apoptotic GCs was examined at various circadian time points in the sensory input-intact (left) and sensory input-deprived (right) OB. The number of apoptotic GCs increased dramatically in the sensory-deprived OB during the postprandial period (13:00) compared to the sensory input-intact OB. The apoptotic GC numbers just before the feeding time (11:00) and at any time period outside the feeding time were comparable between sensory-deprived and sensory input-intact OB. Each dot represents the number of caspase-3-activated GCs in one animal. Bars represent the average. *, $p < 0.05$; **, $p < 0.01$; ***, $p < 0.001$; n.s., not significant; One-Way ANOVA with *post-hoc* Bonferroni test. Modified from Yokoyama et al. (2011) with permission.

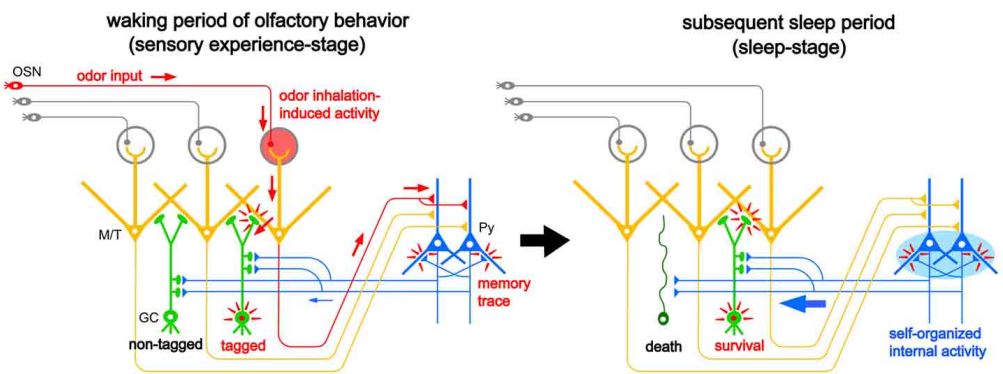

FIGURE 7 | "Two-stage model" for behavioral state-dependent GC elimination. Adult-born GCs (green) make dendrodendritic reciprocal synapses with mitral/tufted cells (yellow, M/T) and receive top-down synaptic contacts from pyramidal cells in the OC (blue, Py). **Left panel**, during the waking period of olfactory behavior (sensory experience-stage), local sensory input from the OSNs (red arrows) activates a subset of mitral/tufted cells. Activated mitral/tufted cells activate a subset of adult-born GCs. The activated GCs might deposit "sensory experience-dependent tags" in the dendrodendritic reciprocal synapses or the cells themselves (red marks). Other adult-born GCs lacking activation by sensory experience are left "non-tagged." Activated mitral/tufted cells further activate pyramidal cells in the OC. The memory trace of the odor experience is deposited in the association fiber synapses among pyramidal cells in the OC (red marks). **Right panel**, during the subsequent sleep period (sleep-stage), association fiber synapses among pyramidal cells in the OC are reactivated and induce synchronized firing of the pyramidal cells. This self-organized internal activity of OC pyramidal cells (a blue oval) is transferred to the adult-born GCs as synchronized top-down synaptic inputs (a thick blue arrow). The synchronized top-down synaptic inputs may contribute to the putative "reorganizing signal" that promotes GC elimination during the postbehavioral sleep period. Adult-born GCs which are tagged by sensory experience during the preceding waking period survive while adult-born GCs which are not tagged are eliminated by the "reorganizing signal."

experience-dependent top-down inputs is totally unknown at present.

Importantly, although differential tagging of new GCs might occur during feeding behavior, the life and death decision of GCs is not made during feeding. During the subsequent postprandial period, food-searching and eating behaviors are overtaken by postprandial behaviors, including sleeping, and the increased GC apoptosis occurs during this period. We thus hypothesized that some sort of "reorganizing signal" enters the OB during the postprandial period and promotes GC selection according to the presence or absence or type of tag that the GCs received during the preceding waking period. Adult-born GCs "survival-tagged" by sensory experience might be selected to survive by this "reorganizing signal," whereas other "non-tagged" or "death-tagged" adult-born GCs might be eliminated by it (**Figure 7**, right). Thus, the fate of individual adult-born GCs might be determined by the interplay between tagging, reflecting the memory trace of sensory experience during the waking period, and the reorganizing signal that enters the OB during the subsequent sleep period. This idea of a two-stage model of GC elimination is based on the two-stage model of memory formation and consolidation in the hippocampus, which proposes that sensory input induces memory trace formation during awake learning experience and that replay of the experience occurs for neuronal circuit reorganization during subsequent sleep or rest (Buzsaki, 1989; Diekelmann and Born, 2010).

Enhanced GC elimination during the postprandial period also resembles homeostatic synaptic downscaling during sleep (Tononi and Cirelli, 2006). It has been shown in the rodent neocortex and hippocampus that behavioral state modulates synaptic strength. Synapses become potentiated and contain more synaptic proteins and AMPA receptors after waking, while they are globally depressed (downscaled) during sleep (Vyazovskiy et al., 2008; Maret et al., 2011). In the fly brain also, synaptic size or number increases during wakefulness and decreases after sleep (Bushey et al., 2011). Importantly, sleep deprivation inhibits the synaptic homeostasis.

It is not clear whether behavioral states modulate the strength of dendrodendritic synapses on new GCs in the EPL and the top-down centrifugal fiber synapses on new GCs in the GCL. Based on the finding that GC elimination is enhanced during postprandial sleep, we speculate that the strength of these synapses on new GCs is under the modulation of behavioral state. One possibility is that new GCs lacking a net increase in total synaptic strength during feeding behavior might be eliminated by apoptosis during subsequent sleep. Sensory experience-dependent elimination of adult-born GCs during the postprandial period downscales the GC number. Because a large number of adult-born GCs are recruited in the OB every day, elimination of adult-born GCs is necessary to maintaining the overall number of GCs in the entire OB within an appropriate range. This downscaling may increase the ratio of useful vs. useless GCs, thereby improving the signal-to-noise ratio for olfactory information processing, and may make room for a successive cohort of new GCs to be integrated in preparation for the next round of new olfactory experience.

BEHAVIORAL STATE-DEPENDENT SIGNAL FLOW IN THE OLFACTORY SYSTEM: INTERACTION BETWEEN THE OB AND THE OC

To investigate neural circuit mechanisms in the life and death decision of new GCs during the sequence of eating and subsequent rest/sleep, we need to understand how the central olfactory system works not only in encoding olfactory memory of food during the waking period but also in stabilizing the resulting memory traces during the subsequent rest/sleep period.

During the waking period, odor inhalation induces spike responses of mitral/tufted cells in the OB. These activated mitral/tufted cells then activate GCs via mitral/tufted-to-granule dendrodendritic excitatory synapses in the EPL (**Figure 10**, upper). Mitral/tufted cells also activate pyramidal cells of the AON and APC via axons that terminate in layer Ia. Activated pyramidal cells of the AON send signals via Ib associational fibers to APC pyramidal cells. During waking states, therefore, odor information is conveyed by pathways consisting of OSNs-mitral/tufted cells-pyramidal cells in the AON and APC (**Figure 10**, upper). During the slow-wave sleep state, however, the OC is isolated from the external odor world by sensory gating mechanisms that diminish signal transmission from the OB to the OC (**Figure 10**, lower) (Murakami et al., 2005; Manabe et al., unpublished). The mechanism of this behavioral state-dependent olfactory sensory gating is not yet understood.

What types of neural activity occur in the isolated OC during sleep? Local field potential (LFP) recording in the deep layer (layer III) of the APC during the slow-wave sleep state in freely-behaving rats revealed that the APC generates repetitive sharp negative potentials that resemble hippocampal SPWs in shape and duration (∼100 ms) (**Figure 8A**) (Manabe et al., 2011). These sharp waves were observed in wide areas of the APC and AON and are called "olfactory cortex sharp waves" (OC-SPWs). OC-SPWs are associated with synchronized spike discharges of numerous neurons in the APC and AON (**Figure 8A**).

As described in the Introduction, hippocampal SPWs are thought to play an important role in memory consolidation and concomitant reorganization of the neuronal circuitry in the hippocampus and neocortex. In analogy with the function of hippocampal SPWs, we speculate that OC-SPWs might be involved in the olfactory memory consolidation and reorganization of neuronal circuitry in the central olfactory system.

Table 1 summarizes a comparison of the properties of hippocampal SPWs and OC-SPWs. Hippocampal SPWs are a self-organized activity originating in recurrent excitatory synaptic connections among CA3 pyramidal cells (Csicsvari et al., 2000). Transient memory traces of experienced episodes are thought to be deposited in the recurrent excitatory synaptic connections. Similarly, OC-SPWs are generated by pyramidal cells of the piriform cortex and also by neurons in the endopiriform nucleus, which is located just deep to the piriform cortex. The recurrent excitatory synaptic connections among piriform cortex pyramidal cells are thought to be involved in the generation of OC-SPWs. Current source density analysis of OC-SPWs in the APC during slow-wave sleep revealed the existence of a dense current sink in layers II and III, which are deep layers in which association fibers of APC pyramidal cells form excitatory synaptic connections on

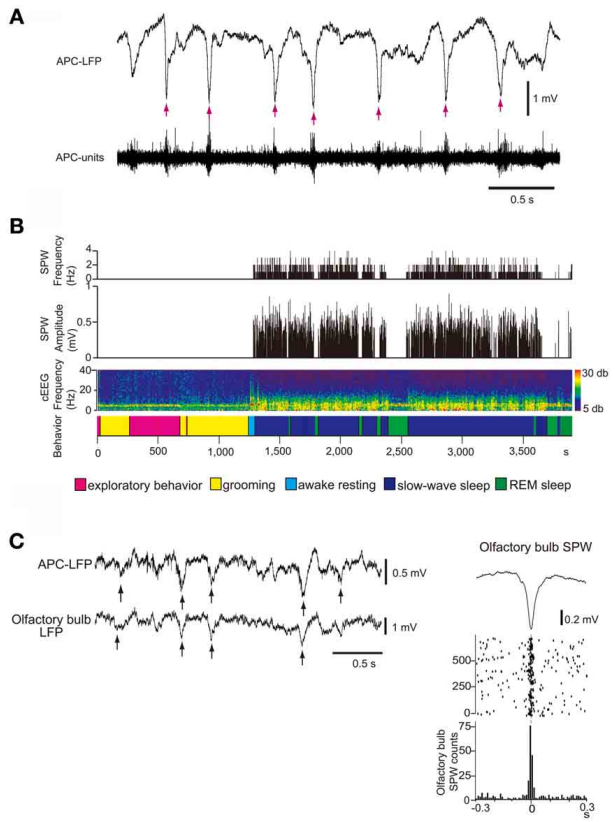

FIGURE 8 | SPW generation in the OC and its transmission to the OB during slow-wave sleep. (A) The occurrence of OC-SPWs is associated with synchronized spike discharges of APC neurons. Simultaneous recordings of local field potentials in layer III (APC-LFP) and multiunit spike activity (APC-units) of the APC during slow-wave sleep of freely-behaving rats. OC-SPWs are indicated by red arrows. **(B)** OC-SPWs occur repeatedly during slow-wave sleep. The frequency and amplitude of OC-SPWs (top two histograms), neocortical EEG pattern (cEEG, shown by a spectrogram), and behavioral states (bottom bar). The spectrogram of the neocortical EEG chronologically represents the intensity of power (shown by color, right inset) at each frequency. The x-axis indicates time and the y-axis indicates frequency. In the bottom bar, different behavioral states are shown by distinct colors as indicated. OC-SPWs occur repeatedly during slow-wave sleep, while they are suppressed during waking and REM sleep. **(C)** OC-SPW activity is transferred to the OB as synchronized top-down inputs. Left, simultaneous recording of LFP in layer III of the APC (APC-LFP) and LFP in GCL of the OB (olfactory bulb-LFP). Arrows indicate SPWs. Right, averaged time course of olfactory bulb SPWs (top trace), and the raster plot (middle traces) and event-correlation histogram (bottom trace) of the nadir of olfactory bulb SPWs in reference to the nadir of OC-SPWs are shown. Time 0 indicates the time of nadir of OC-SPWs. Modified from Manabe et al. (2011).

Table 1 | Comparison between hippocampal sharp waves and olfactory cortex sharp waves.

	Hippocampal-SPWs	Olfactory cortex (OC)-SPWs
Origin	CA3 pyramidal cells (recurrent excitation path)	Piriform cortex pyramidal cells Endopiriform nucleus (recurrent excitation path)
Synchronization	CA1 pyramical cells	Piriform cortex pyramical cells
Replay/ reactivation	Place cell activity during exploratory behavior	Not known
Target	Hippocampus, Subiculum, Entorhinal cortex, Neocortex	Piriform cortex, Olfactory bulb, Orbitofrontal cortex, Cortical amygdaloid nuclei, Olfactory tubercle
Behavioral states	Awake resting Slow-wave sleep	Slow-wave sleep
Possible function	Consolicdation of spatial and episodic memory	Not known
Abnormal activity	Hippocampal epilepsy	The area tempestas

dendritic spines of APC pyramidal cells (**Figure 9**) (Neville and Haberly, 2004; Manabe et al., 2011). Memory traces of olfactory images of objects are thought to be encoded in plastic changes occurring in the recurrent association fiber synapses among pyramidal cells of the OC (Haberly, 2001; Neville and Haberly, 2004; Wilson, 2010; Wilson and Sullivan, 2011).

While hippocampal SPWs are associated with synchronized discharges of CA1 pyramidal cells, OC-SPWs accompany synchronized discharges of piriform cortex pyramidal cells. Replay of CA1 place cell ensemble activity occurs during the short time window of individual hippocampal SPWs. However, it is not known whether replay or reactivation of OC ensemble activity occurs during OC-SPWs. Hippocampal SPWs travel from the CA1 region, through the subiculum, entorhinal cortex and up to the wide areas of the neocortex. Similarly, OC-SPWs travel to all parts of the piriform cortex, AON, OB, cortical amygdaloid nuclei, olfactory tubercle and orbitofrontal cortex.

Both hippocampal SPWs and OC-SPWs occur in a behavioral state-dependent manner. They are absent during awake exploratory behavior and REM sleep. Hippocampal SPWs occur selectively during slow-wave sleep, awake resting and consuming behavior. OC-SPWs occur during slow-wave sleep, and SPW-like potentials are present in the APC during postprandial rest (**Figure 8B**) ((Manabe et al., 2011); Komano-Inoue et al., unpublished).

Given that a large population of pyramidal cells in the AON and APC send massive top-down centrifugal fibers to GCs in the OB (Luskin and Price, 1983), the OC-SPW-associated synchronized discharges of numerous AON and APC neurons would likely cause massive synchronous excitatory synaptic inputs to GCs. Indeed, simultaneous recording of LFP in the ipsilateral APC layer III and OB GCL showed that SPW-like potentials in the OB occurred in close temporal proximity to OC-SPWs (**Figure 8C**). Synchronous discharge of APC neurons occurs repeatedly during slow-wave sleep and causes repeated strong and synchronized synaptic excitation of GCs in the OB (**Figure 10**, lower).

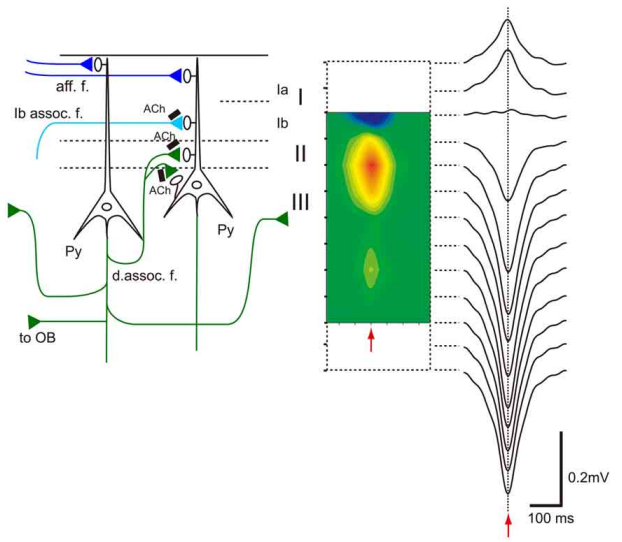

FIGURE 9 | Association fiber excitatory synapses on OC pyramidal cells participate in the generation of OC-SPWs. Left, schematic diagram illustrating mitral cell axon (afferent fiber) excitatory synapses that terminate in layer Ia (aff. f.; dark blue lines), association fiber excitatory synapses from pyramidal cells of the AON that terminate in layer Ib (Ib assoc. f.; a light blue line), and deep recurrent association fiber (d. assoc. f.; green) excitatory synapses of APC pyramidal cells on APC pyramidal cells that terminate in layer II and III. Association fiber terminals are under the control of cholinergic presynaptic inhibition (black bars with Ach). Top-down projection from the APC pyramidal cells to the OB is also shown. Right, current source density analysis of averaged OC-SPWs in a rat under urethane anesthesia. The depth profile of averaged OC-SPW potentials is shown. Pseudo-color representation of current sink (red) and current source (blue) is also shown. Red arrows indicate the nadir of OC-SPW. OC-SPWs generate a large current sink in layer II and the adjacent superficial part of layer III. Modified from Manabe et al. (2011).

OC-SPWs occur in the absence of olfactory sensory inputs, suggesting that they are a self-organized activity originating in the piriform cortex. During awake states, recurrent association fiber synapses on APC pyramidal cells are presynaptically inhibited by tonic cholinergic tone (Hasselmo and Bower, 1992). During slow-wave sleep, however, reduced cholinergic tone liberates the recurrent association fiber from this cholinergic suppression to promote the generation of highly synchronized discharges of pyramidal cells and OC-SPWs (**Figures 9**, **10**).

POSSIBLE MECHANISMS UNDERLYING THE BEHAVIORAL STATE-DEPENDENT SELECTION OF ADULT-BORN GCs

The finding of increased GC death during postprandial sleep raises a number of interesting questions. One major question is what kind of signals new GCs receive during the sequence of eating behavior and postprandial sleep. A second is how these signals relate to the life and death decision of new GCs during sleep. One possible scenarios is that (1) new GCs receive odor-induced signals from mitral and tufted cells during eating, but repetitively receive OC-SPW-associated synchronized top-down inputs from the OC during subsequent sleep; and that (2) the synchronized top-down inputs are crucial in promoting GC elimination (**Figures 7**, **10**, **11**).

In this scenario, olfactory sensory input is transmitted from mitral/tufted cells to new GCs via the dendrodendritic synapses in the EPL. Some GCs might be "tagged" by the synaptic inputs while others are left "non-tagged." In spite of the tagging, the life and death decision of new GCs is not conducted during waking states. Rather, only during the subsequent sleep period do OC neurons generate memory trace-based synchronized activity (OC-SPWs) and send synchronized top-down inputs to new GCs. This signal may trigger mechanisms that eliminate "non-tagged" GCs while promoting long-lasting incorporation of "tagged" GCs.

We are currently examining this hypothesis, and have observed that pharmacological suppression of the synchronized top-down inputs during the postprandial period in freely-behaving mice inhibits the increased GC apoptosis (Komano-Inoue et al., unpublished observation). This observation favors the notion that the major contributor to the putative "reorganizing signal" that promotes GC elimination during the postprandial period is the synchronized top-down input from the OC to the OB (**Figures 7**, **10**, **11**).

Enhanced GC death occurs during postprandial sleep but not during sleep without preceding eating. In contrast, OC-SPW-associated synchronized top-down inputs to GCs always occur during slow-wave sleep regardless of the presence or absence of preceding eating. Thus, the synchronized top-down inputs from the OC alone may not be sufficient to trigger GC elimination. Deposition of putative tag signals during preceding waking may be prerequisite, and the life and death decision of new GCs might be determined after collation of the top-down reorganization signal with the putative deposited tag signals. Further, other behavioral state-dependent signals such as neuromodulatory and hormonal signals might also be involved in triggering GC elimination.

A key question yet to be answered is how neuromodulatory inputs to the OB influence GC elimination during postprandial sleep. The OB is targeted by subcortical neuromodulatory systems (Shipley and Ennis, 1996) that include cholinergic input from the horizontal limb of the diagonal band of Broca, noradrenergic input from the locus ceruleus, and serotonergic input from the raphe nuclei (**Figure 11**). Olfactory sensory experience during feeding and mating strongly increase noradrenergic signals (Brennan et al., 1990; Wellman, 2000). In addition, a variety of olfactory learning depends on neuromodulatory signals to the OB. Blockade of noradrenergic (Sullivan et al., 1989; Veyrac et al., 2009) or cholinergic signals (Devore et al., 2012) in the OB perturbs olfactory learning.

Female mice form olfactory recognition memory to male mouse pheromones at mating. The memory trace for this is deposited as the plastic change in the dendrodendritic reciprocal synapses between mitral cells and GCs in the accessory OB (Kaba and Nakanishi, 1995). The mating-induced increase in noradrenalin reduces granule-to-mitral dendrodendritic inhibitory synaptic transmission and induces olfactory memory of male pheromones. It is possible that an increase in neuromodulatory tone during olfactory learning may be important to the formation of memory traces in the dendrodendritic synapses, which can be used later in the life and death decision of new GCs. In the main

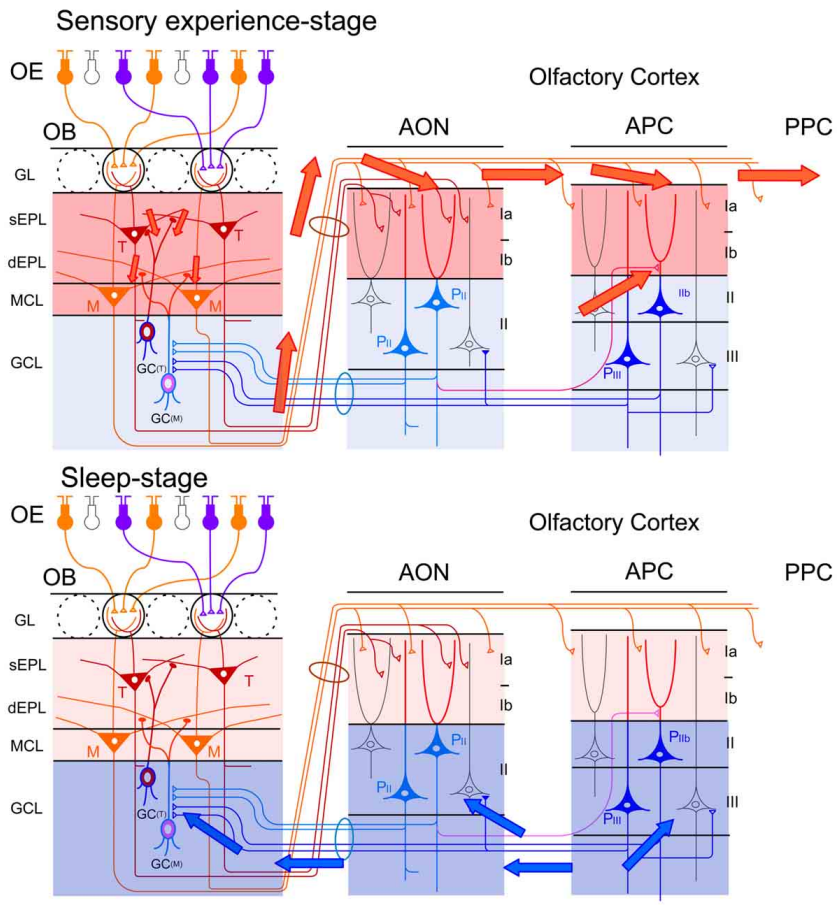

FIGURE 10 | Behavioral state-dependent signal flow between the OB and OC. Upper panel, during the waking period (sensory experience-stage), information about the external odor world is efficiently transferred from mitral (M) and tufted (T) cells in the OB to pyramidal cells (P) in the AON, APC and PPC (red arrows). Olfactory sensory inputs from the OE to the OB activate synapses in the sEPL, dEPL and MCL of the OB. Outputs from mitral and tufted cells in the OB to the OC activate synapses in the layer Ia of the AON and APC. Activated pyramidal cells in the AON activate synapses in the layer Ib of the APC via their association fibers (a red line in the deep layer). Layers with activated synapses are highlighted with red. Synaptic inputs of recurrent association fibers to pyramidal cells are reduced by cholinergic presynaptic suppression. **Lower panel**, during the slow-wave sleep period (sleep-stage), afferent fiber inputs to the OC are blocked by behavioral state-dependent sensory gating. In contrast, synaptic inputs of recurrent association fibers to pyramidal cells in layer II and III of the olfactory cortex are released from cholinergic presynaptic inhibition and internally generate synchronized spike discharges of pyramidal cells in the AON, APC and PPC. The synchronized spike discharges of pyramidal cells in the OC travel back to GCs in the GCL of the OB as synchronized top-down synaptic inputs (blue arrows). Layers with activated synapses are highlighted with blue.

OB, noradrenergic fibers from the locus ceruleus are distributed predominantly in the GCL (McLean et al., 1989), and GCs express several subtypes of adrenergic receptors (McCune et al., 1993; Nai et al., 2010).

Cholinergic fibers primarily innervate the GL and GCL in the OB (Kasa et al., 1995), and GCs express several subtypes of cholinergic receptors (Le Jeune et al., 1995). During the waking period, enhanced cholinergic tone reduces granule-to-mitral dendrodendritic synaptic transmission by a presynaptic inhibition mechanism (Tsuno et al., 2008). The top-down synaptic inputs from the OC to GCs are also reduced during the waking period, presumably by cholinergic presynaptic inhibition (Manabe et al., 2011). In the absence of cholinergic tone during slow-wave sleep, both the granule-to-mitral synaptic transmission and top-down synaptic inputs are enhanced as a result of the release from cholinergic presynaptic inhibition. These results suggest the involvement of a behavioral state-dependent change in neuromodulatory inputs in the regulation of GC death during postprandial sleep. In fact, the effects of systemic modulation of noradrenergic or cholinergic signals on the survival of new GCs have been well documented (Cooper-Kuhn et al., 2004; Kaneko et al., 2006; Veyrac et al., 2009; Moreno et al., 2012). We thus assume that the integration of odor-induced glutamatergic signals that occur during odor experiences, synchronized top-down glutamatergic inputs during sleep, and behavioral state-dependent changes in neuromodulatory signals is the key mechanism for sensory experience-dependent and behavioral state-dependent GC selection (**Figure 11**). Further study is necessary to examine how the neuromodulatory signals contribute to the life and death decision of new GCs.

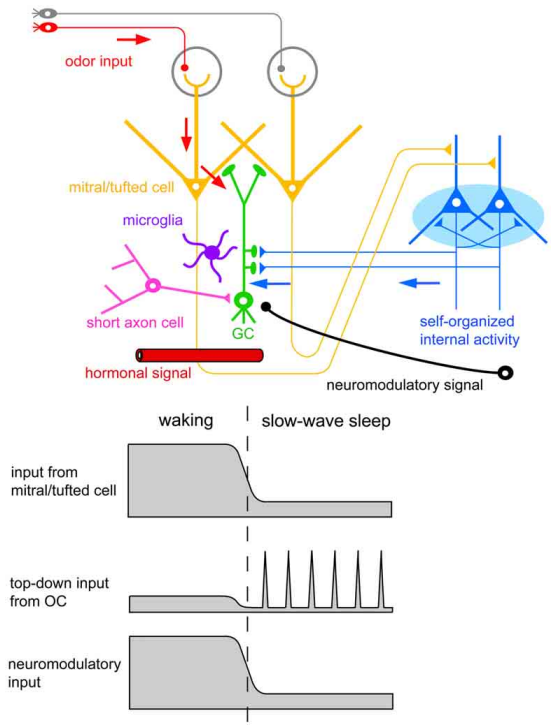

FIGURE 11 | Possible contributors to the behavioral state-dependent life and death decision of adult-born GCs. Adult-born GCs receive excitatory synaptic inputs from mitral/tufted cells via dendrodendritic synapses (red arrows). These inputs represent olfactory sensory inputs and are strongly activated during waking olfactory behavior. Adult-born GCs also receive excitatory synaptic inputs from pyramidal cells in the OC via axodendritic synapses (blue arrows). These inputs represent self-organized internal activity of OC pyramidal cells and are strongly activated during the subsequent slow-wave sleep period. Adult-born GCs receive neuromodulatory signals including noradrenergic, cholinergic, and serotonergic inputs. These neuromodulatory inputs are elevated during waking olfactory behavior and suppressed during the subsequent slow-wave sleep period. Behavioral state-dependent hormonal signals may be also involved in the life and death decision of adult-born GCs. Deep short axon cells in the OB form GABAergic synapses onto adult-born GCs. Top-down inputs from OC pyramidal cells may induce inhibitory synaptic inputs on adult-born GCs via the activation of deep short axon cells. Resident microglia in the OB play a crucial role in sensory experience-dependent GC elimination. Behavioral state-dependent life and death decision of adult-born GCs may operate with the cooperation of these signal systems and cell types.

Hormonal signals also depend on behavioral state and substantially influence olfactory neurogenesis (**Figure 11**). An increase in prolactin secretion by sexual and social behaviors promotes cell proliferation in the SVZ (Shingo et al., 2003; Mak et al., 2007; Mak and Weiss, 2010). Food restriction and food intake recruit a variety of stress- and energy status-related hormonal signals (Dallman et al., 1993; Gao and Horvath, 2007). Stress-induced glucocorticoid decreases cell proliferation in the SVZ (Lau et al., 2007). Although little is known at present, the life and death decision of new GCs might be regulated by a behavioral state-dependent change in hormonal signals.

Other potential contributors to the life and death decision of new GCs are deep short-axon cells and microglia in the OB (**Figure 11**). In addition to glutamatergic inputs, new GCs receive GABAergic synaptic inputs from deep short-axon cells in the OB (Arenkiel et al., 2011; Deshpande et al., 2013). Because deep short-axon cells receive direct top-down synaptic inputs from the OC (Boyd et al., 2012), the top-down inputs may activate inhibitory synaptic inputs onto new GCs via deep short-axon cells, in addition to direct excitatory synaptic inputs. Microglial cells are present at high density in the OB and contribute to GC elimination. Activation of microglial cells is crucial to the enhanced GC elimination by sensory deprivation (Lazarini et al., 2012). An understanding of how these signal systems and cell types work together in promoting the behavioral state-dependent life and death decision of new GCs is therefore important.

SIGNIFICANCE OF BEHAVIORAL STATE-DEPENDENT SELECTION OF ADULT-BORN GCs

Why is GC death enhanced during sleep? Cell death is an irreversible process: once the apoptotic machinery is initiated, the cell is destined to be eliminated from the circuit. This suggests that the cell death process of new GCs occurs under strict regulation during slow-wave sleep, unperturbed by unpredictable olfactory sensory inputs. Furthermore, if elimination or incorporation of new neurons were to occur during awake behavior states, this would cause severe disturbance in odor information processing. Therefore, neuronal circuits in the olfactory system require that the processing of external odor information and reorganization of connectivity occur during different time windows. These ideas are in accord with the notion that the brain requires separate time windows (awake and sleep periods) for the active processing of external sensory information and the structural reorganization of its neuronal circuitry.

Refinement of OB circuits by the elimination of "non-tagged" or "death-tagged" GCs during sleep may increase the signal-to-noise ratio for odor information processing, as proposed for synaptic downscaling during sleep (Tononi and Cirelli, 2006). When animals wake up, their odor information processing ability might be improved such that odor-cued behaviors can be more efficiently executed. In addition, elimination of GCs may make room for the integration of successive cohorts of new GCs during subsequent wake-sleep cycles. We observed that enhanced elimination of preexisting GCs in a local area of the OB by local injection of immunotoxin facilitates the incorporation of newly generated GCs in the local OB area (Murata et al., 2011). This observation supports the idea that elimination of less useful GCs during sleep would facilitate the incorporation of new useful GCs during subsequent wake-sleep cycles. By using and repeating the wake-sleep cycle as a single unit for olfactory experience-based circuit reorganization, the olfactory neuronal circuit may be continually remodeled to meet the ever-changing odor circumstances.

It has been demonstrated that odor learning, but not simple odor experience, is important for the survival of new GCs (Alonso et al., 2006; Mouret et al., 2008, 2009; Sultan et al., 2010). We speculate that food finding and eating periods provide rich opportunity for odor-food association learning with the animal's decision making to eat or reject the encountered food. This notion is in agreement with the observation that the life and

death decision of new GCs is promoted during postprandial sleep but not during sleep without preceding eating. Beside the odor-food association learning during the eating period, mice and rats show olfactory learning in a variety of occasions, including mating, encountering danger (odor-danger association learning), and social behaviors (Keverne, 2004; Sanchez-Andrade and Kendrick, 2009; Landers and Sullivan, 2012). It would be interesting to examine which types of olfactory learning induce enhanced GC death during postbehavioral sleep.

COORDINATION OF PLASTIC CHANGE IN THE OB, OC AND OTHER BRAIN REGIONS

Odor learning-induced plastic changes occur not only in the OB, but widely in the central olfactory system. For example, major plastic changes associated with olfactory memory are considered to occur in association fiber synapses of pyramidal cells in the piriform cortex. The association fiber synapses are active in odor information processing during waking, causing odor-induced activation of targeted pyramidal cells in the piriform cortex (Poo and Isaacson, 2011). Association fiber synapses are highly plastic. They exhibit NMDA-dependent long-term potentiation (LTP) *in vitro* (Kanter and Haberly, 1990; Poo and Isaacson, 2007), and synaptic transmission of association fibers is enhanced by associative odor learning in rats (Saar et al., 2002). We speculate that deposited memory traces in the association fiber synapses might be consolidated by the reactivation of synaptic connections during the subsequent sleep period, whose activity is represented as OC-SPWs. In fact, firing activity of piriform cortical neurons during the slow-wave state is influenced by odor stimulation during the preceding fast-wave state (Wilson, 2010).

Because OC-SPW-associated activity during slow-wave sleep presumably depends on the plastic changes in association fiber synapses, top-down inputs from the OC to the OB reflect olfactory memory information stored during the awake behavior period. An intriguing possibility is that the top-down synaptic inputs are not random but rather targeted to a selective population of GCs. Only the targeted GCs might be plastically modulated by the top-down inputs. Furthermore, the synaptic efficacy of the top-down inputs onto GCs is plastic. LTP can be induced in the top-down synapses both *in vitro* (Gao and Strowbridge, 2009; Nissant et al., 2009) and *in vivo* (Manabe et al., 2011). Thus, plastic changes in connectivity may occur widely in a coordinated manner across the entire neuronal circuitry of the OB and OC.

The neuronal circuitry of the OB and OC functions within a large network of the central nervous system. The OC has massive reciprocal connections with the amygdaloid complex and orbitofrontal cortex (Shipley and Ennis, 1996). During odor-guided behaviors, odor information is transferred from the OB to these regions via the OC. During slow-wave sleep periods, generation of OC-SPWs is under the control of slow-wave activity in the orbitofrontal cortex (Onisawa et al., unpublished). Thus, plastic change in the OC circuitry during sleep may be coordinated with the plasticity in the orbitofrontal cortex. In this context, the top-down inputs from the OC to the OB would reflect the coordinated activity of the OC and orbitofrontal cortex.

CONCLUSION

Neuronal circuits in the olfactory system require highly plastic properties to acquire new odor-guided behaviors in response to the changing external odor world, and adult-born GCs in the OB provide remarkable plasticity to the neuronal circuit. The survival rate of adult-born GCs is influenced by olfactory sensory experience. The sensory experience-dependent life and death decision of new GCs occurs extensively during the 2–4 weeks after GC generation, and during this period new GCs make synaptic contacts with the preexisting neuronal circuit. At this critical period new GCs receive olfactory sensory inputs from mitral/tufted cells in the OB and top-down inputs from pyramidal cells in the OC. Further, the life and death decision of new GCs occurs in a behavioral state-dependent manner. Elimination of new GCs occurs extensively in the sequence of feeding behavior and postprandial slow-wave sleep. During waking, olfactory sensory information is efficiently transmitted from the OB to the OC. During slow-wave sleep, in contrast, signal transmission from the OB to the OC diminishes, and deep-association fiber-mediated synchronous firing of OC pyramidal cells occurs, which causes synchronous top-down inputs from the OC to the OB. In addition, GCs are targeted by neuromodulatory systems whose activities considerably change along the course of the wake-sleep cycle. These observations suggest the hypothesis that the key mechanism for sensory experience-dependent and behavioral state-dependent GC selection is integration across the distinct time windows of odor-induced glutamatergic input signals during odor experiences, synchronized top-down glutamatergic inputs during sleep, and behavioral state-dependent changes in neuromodulatory signals. On this basis, the GC selection process represents the coordination of a variety of activities of wide brain areas across different behavioral states. New GCs in the olfactory neuronal circuit might provide a good platform to understanding how neuronal circuits are plastically modulated in order to change animal behavioral outputs in response to the ever-changing external world.

ACKNOWLEDGMENTS

This work was supported by a Grant-in-Aid for Scientific Research from JSPS (Masahiro Yamaguchi and Kensaku Mori), a Grant-in-Aid for Young Scientists (B) from MEXT (Hiroyuki Manabe), and a Grant-in-Aid for JSPS Fellows (Koshi Murata).

REFERENCES

Allison, A. C., and Warwick, R. T. (1949). Quantitative observations on the olfactory system of the rabbit. *Brain* 72, 186–197. doi: 10.1093/brain/72.2.186

Alonso, M., Viollet, C., Gabellec, M. M., Meas-Yedid, V., Olivo-Marin, J. C., and Lledo, P. M. (2006). Olfactory discrimination learning increases the survival of adult-born neurons in the olfactory bulb. *J. Neurosci.* 26, 10508–10513. doi: 10.1523/JNEUROSCI.2633-06.2006

Alvarez-Buylla, A., Garcia-Verdugo, J., and Tramontin, A. D. (2001). A unified hypothesis on the lineage of neuroal stem cells. *Nat. Rev. Neurosci.* 2, 287–293. doi: 10.1038/35067582

Arenkiel, B. R., Hasegawa, H., Yi, J. J., Larsen, R. S., Wallace, M. L., Philpot, B. D., et al. (2011). Activity-induced remodeling of olfactory bulb microcircuits revealed by monosynaptic tracing. *PLoS ONE* 6:e29423. doi: 10.1371/journal.pone.0029423

Bayer, S. A. (1983). 3H-thymidine-radiographic studies of neurogenesis in the rat olfactory bulb. *Exp. Brain Res.* 50, 329–340.

Biebl, M., Cooper, C. M., Winkler, J., and Kuhn, H. G. (2000). Analysis of neurogenesis and programmed cell death reveals a self-renewing capacity in the adult rat brain. *Neurosci. Lett.* 291, 17–20. doi: 10.1016/S0304-3940(00)01368-9

Boyd, A. M., Sturgill, J. F., Poo, C., and Isaacson, J. S. (2012). Cortical feedback control of olfactory bulb circuits. *Neuron* 76, 1161–1174. doi: 10.1016/j.neuron.2012.10.020

Brennan, P., Kaba, H., and Keverne, E. B. (1990). Olfactory recognition: a simple memory system. *Science* 250, 1223–1226. doi: 10.1126/science.2147078

Buck, L., and Axel, R. (1991). A novel multigene family may encode odorant receptors: a molecular basis for odor recognition. *Cell* 65, 175–187. doi: 10.1016/0092-8674(91)90418-X

Bushey, D., Tononi, G., and Cirelli, C. (2011). Sleep and synaptic homeostasis: structural evidence in drosophila. *Science* 332, 1676–1581. doi: 10.1126/science.1202839

Buss, R. R., Sun, W., and Oppenheim, R. W. (2006). Adaptive roles of programmed cell death during nervous system development. *Annu. Rev. Neurosci.* 29, 1–35. doi: 10.1146/annurev.neuro.29.051605.112800

Buzsaki, G. (1989). Two-stage model of memory trace formation: a role for "noisy" brain states. *Neuroscience* 31, 551–570. doi: 10.1016/0306-4522(89)90423-5

Carleton, A., Petreanu, L. T., Lansford, R., Alvarez-Buylla, A., and Lledo, P. M. (2003). Becoming a new neuron in the adult olfactory bulb. *Nat. Neurosci.* 6, 507–518.

Chess, A., Simon, I., Cedar, H., and Axel, R. (1994). Allelic inactivation regulates olfactory gene expression. *Cell* 78, 823–834. doi: 10.1016/S0092-8674(94)90562-2

Cooper-Kuhn, C. M., Winkler, J., and Kuhn, H. G. (2004). Decreased neurogenesis after cholinergic forebrain lesion in the adult rat. *J. Neurosci. Res.* 77, 155–165. doi: 10.1002/jnr.20116

Corotto, F., Henegar, J., and Maruniak, J. (1994). Odor deprivation leads to reduced neurogenesis and reduced neuronal survival in the olfactory bulb of the adult mouse. *Neuroscience* 61, 739–744. doi: 10.1016/0306-4522(94)90397-2

Crick, F. C., and Koch, C. (2005). What is the function of the claustrum? *Philos. Trans. R. Soc. Lond. B Biol. Sci.* 360, 1271–1279. doi: 10.1098/rstb.2005.1661

Csicsvari, J., Hirase, H., Mamiya, A., and Buzsaki, G. (2000). Ensemble patterns of hippocampal CA3-CA1 neurons during sharp wave-associated population events. *Neuron* 28, 585–594. doi: 10.1016/S0896-6273(00)00135-5

Dallman, M. F., Strack, A. M., Akana, S. F., Bradbury, M. J., Hanson, E. S., Scribner, K. A., et al. (1993). Feast and famine: critical role of glucocorticoids with insulin in daily energy flow. *Front. Neuroendocrin.* 14, 303–347. doi: 10.1006/frne.1993.1010

Deshpande, A., Bergami, M., Ghanem, A., Conzelmann, K. K., Lepier, A., Götz, M., et al. (2013). Retrograde monosynaptic tracing reveals the temporal evolution of inputs onto new neurons in the adult dentate gyrus and olfactory bulb. *Proc. Natl. Acad. Sci. U.S.A.* 110, E1152–E1161. doi: 10.1073/pnas.1218991110

Devore, S., Manella, L. C., and Linster, C. (2012). Blocking muscarinic receptors in the olfactory bulb impairs performance on an olfactory short-term memory task. *Front. Behav. Neurosci.* 6:59. doi: 10.3389/fnbeh.2012.00059

Diekelmann, S., and Born, J. (2010). The memory function of sleep. *Nat. Rev. Neurosci.* 11, 114–126.

Doty, R. L. (1986). Odor-guided behavior in mammals. *Experientia* 42, 257–271. doi: 10.1007/BF01942506

Eyre, M. D., Antal, M., and Nusser, Z. (2008). Distinct deep short-axon cell subtypes of the main olfactory bulb provide novel intrabulbar and extrabulbar GABAergic connections. *J. Neurosci.* 28, 8217–8229. doi: 10.1523/JNEUROSCI.2490-08.2008

Foster, D. J., and Wilson, M. A. (2006). Reverse replay of behavioural sequences in hippocampal place cells during the awake state. *Nature* 440, 680–683. doi: 10.1038/nature04587

Frey, U., and Morris, R. G. M. (1997). Synaptic tagging and long-term potentiation. *Nature* 385, 533–536. doi: 10.1038/385533a0

Gao, Q., and Horvath, T. L. (2007). Neurobiology of feeding and energy expenditure. *Annu. Rev. Neurosci.* 30, 367–398. doi: 10.1146/annurev.neuro.30.051606.094324

Gao, Y., and Strowbridge, W. (2009). Long-term plasticity of excitatory inputs to granule cells in the rat olfactory bulb. *Nat. Neurosci.* 12, 731–733. doi: 10.1038/nn.2319

Ghosh, S., Larson, S. D., Hefzi, H., Marnoy, Z., Cutforth, T., Dokka, K., et al. (2011). Sensory maps in the olfactory cortex defined by long-range viral tracing of single neurons. *Nature* 472, 217–220. doi: 10.1038/nature09945

Gogos, J. A., Osborne, J., Nemes, A., Mendelsohn, M., and Axel, R. (2000). Genetic ablation and restoration of the olfactory topographic map. *Cell* 103, 609–620. doi: 10.1016/S0092-8674(00)00164-1

Haberly, L. B. (2001). Parallel-distributed processing in olfactory cortex: new insights from morphological and physiological analysis of neuronal circuitry. *Chem. Senses* 26, 551–576. doi: 10.1093/chemse/26.5.551

Hasselmo, M. E. (1999). Neuromodulation: acetylcholine and memory consolidation. *Trends Cogn. Sci.* 3, 351–359. doi: 10.1016/S1364-6613(99)01365-0

Hasselmo, M. E., and Bower, J. M. (1992). Cholinergic suppression specific to intrinsic not afferent fiber synapses in rat piriform (olfactory) cortex. *J. Neurophysiol.* 67, 1222–1229.

Hensch, T. K. (2005). Critical period plasticity in local cortical circuits. *Nat. Rev. Neurosci.* 6, 877–888. doi: 10.1038/nrn1787

Hinds, J. W. (1968). Autoradiographic study of histogenesis in the mouse olfactory bulb. I. Time of origin of neurons and neuroglia. *J. Comp. Neurol.* 134, 287–304. doi: 10.1002/cne.901340304

Igarashi, K. M., Ieki, N., An, M., Yamaguchi, Y., Nagayama, S., Kobayakawa, K., et al. (2012). Parallel mitral and tufted cell pathways route distinct odor information to different targets in the olfactory cortex. *J. Neurosci.* 32, 7970–7985. doi: 10.1523/JNEUROSCI.0154-12.2012

Imayoshi, I., Sakamoto, M., Ohtsuka, T., Takao, K., Miyakawa, T., Yamaguchi, M., et al. (2008). Roles of continuous neurogenesis in the structural and functional integrity of the adult forebrain. *Nat. Neurosci.* 11, 1153–1161. doi: 10.1038/nn.2185

Kaba, H., and Nakanishi, S. (1995). Synaptic mechanisms of olfactory recognition memory. *Rev. Neurosci.* 6, 125–141. doi: 10.1515/REVNEURO.1995.6.2.125

Kaneko, N., Okano, H., and Sawamoto, K. (2006). Role of cholinergic system in regulating survival of newborn neurons in the adult mouse dentate gyrus and olfactory bulb. *Genes Cells* 11, 1145–1159. doi: 10.1111/j.1365-2443.2006.01010.x

Kanter, E. D., and Haberly, L. B. (1990). NMDA-dependent induction of long-term potentiation in afferent and association fiber systems of piriform cortex *in vitro*. *Brain Res.* 525, 175–179. doi: 10.1016/0006-8993(90)91337-G

Kaplan, M. S., McNelly, N. A., and Hinds, J. W. (1985). Population dynamics of adult-formed granule neurons of the rat olfactory bulb. *J. Comp. Neurol.* 239, 117–125. doi: 10.1002/cne.902390110

Kasa, P., Hlavati, I., Dobo, E., Wolff, A., Joo, F., and Wolff, J. R. (1995). Synaptic and non-synaptic cholinergic innervation of the various types of neurons in the main olfactory bulb of adult rat: immunocytochemistry of choline acethyltransferase. *Neuroscience* 67, 667–677. doi: 10.1016/0306-4522(95)00031-D

Kashiwadani, H., Sasaki, Y. F., Uchida, N., and Mori, K. (1999). Synchronized oscillatory discharges of mitral/tufted cells with different molecular receptive ranges in the rabbit olfactory bulb. *J. Neurophysiol.* 82, 1786–1792.

Katagiri, H., Pallotto, M., Nissant, A., Murray, K., Sassoè-Pognetto, M., and Lledo, P. M. (2011). Dynamic development of the first synapse impinging on adult-born neurons in the olfactory bulb circuit. *Neural Syst. Circuits* 1:6. doi: 10.1186/2042-1001-1-6

Kelsch, W., Lin, C. W., and Lois, C. (2008). Sequential development of synapses in dendritic domains during adult neurogenesis. *Proc. Natl. Acad. Sci. U.S.A.* 105, 16803–16808. doi: 10.1073/pnas.0807970105

Kelsch, W., Sim, S., and Lois, C. (2010). Watching synaptogenesis in the adult brain. *Annu. Rev. Neurosci.* 33, 131–149. doi: 10.1146/annurev-neuro-060909-153252

Keverne, E. B. (2004). Importance of olfactory and vomeronasal systems for male sexual function. *Physiol. Behav.* 83, 177–187.

Kobayakawa, K., Kobayakawa, R., Matsumoto, H., Oka, Y., Imai, T., Ikawa, M., et al. (2007). Innate versus learned odour processing in the mouse olfactory bulb. *Nature* 450, 503–508. doi: 10.1038/nature06281

Lagace, D. C., Whitman, M. C., Nooman, M. A., Ables, J. L., DeCarolis, N. A., Arguella, A. A., et al. (2007). Dynamic contribution of nestin-expressing stem cells to adult neurogenesis. *J. Neurosci.* 27, 12623–12629. doi: 10.1523/JNEUROSCI.3812-07.2007

Landers, M. S., and Sullivan, R. M. (2012). The development and neurobiology of infant attachment and fear. *Dev. Neurosci.* 34, 101–114. doi: 10.1159/000336732

Lau, W. M., Qiu, G., Helmeste, D. M., Lee, T. M., Tang, S. W., So, K. F., et al. (2007). Corticosteroid decreases subventricular zone cell proliferation, which could

be reversed by paroxetine. *Restor. Neurol. Neurosci.* 25, 17–23.

Lazarini, F., Gabellec, M. M., Torquet, N., and Lledo, P. M. (2012). Early activation of microglia triggers long-lasting impairment of adult neurogenesis in the olfactory bulb. *J. Neurosci.* 32, 3652–3664. doi: 10.1523/JNEUROSCI.6394-11.2012

Lee, A. K., and Wilson, M. A. (2002). Memory of sequential experience in the hippocampus during slow wave sleep. *Neuron* 36, 1183–1194. doi: 10.1016/S0896-6273(02)01096-6

Le Jeune, H., Aubert, I., Jourdan, F., and Quirion, R. (1995). Comparative laminar distribution of various autoradiographic cholinergic markers in adult rat main olfactory bulb. *J. Chem. Neuroanat.* 9, 99–112. doi: 10.1016/0891-0618(95)00070-N

Lledo, P. M., Alonso, M., and Grubb, M. S. (2006). Adult neurogenesis and functional plasticity in neuronal circuits. *Nat. Rev. Neurosci.* 7, 179–193. doi: 10.1038/nrn1867

Luskin, M. B., and Price, J. L. (1983). The topographic organization of associational fibers of the olfactory system in the rat, including centrifugal fibers to the olfactory bulb. *J. Comp. Neurol.* 216, 264–291. doi: 10.1002/cne.902160305

Mak, G. K., Enwere, E. K., Gregg, C., Pakarainen, T., Poutanen, M., Huhtaniemi, I., et al. (2007). Male pheromone-stimulated neurogenesis in the adult female brain: possible role in mating behavior. *Nat. Neurosci.* 10, 1003–1011. doi: 10.1038/nn1928

Mak, G. K., and Weiss, S. (2010). Paternal recognition of adult offspring mediated by newly generated CNS neurons. *Nat. Neurosci.* 13, 753–758. doi: 10.1038/nn.2550

Malnic, B., Hirono, J., Sato, T., and Buck, L. B. (1999). Combinatorial receptor codes for odors. *Cell* 96, 713–723. doi: 10.1016/S0092-8674(00)80581-4

Manabe, H., Kusumoto-Yoshida, I., Ota, M., and Mori, K. (2011). Olfactory cortex generates synchronized top-down inputs to the olfactory bulb during slow-wave sleep. *J. Neurosci.* 31, 8123–8133. doi: 10.1523/JNEUROSCI.6578-10.2011

Mandairon, N., Jourdan, F., and Didier, A. (2003). Deprivation of sensory inputs to the olfactory bulb upregulates cell death and proliferation in the subventricular zone of adult mice. *Neuroscience* 119, 507–516. doi: 10.1016/S0306-4522(03)00172-6

Mandairon, N., Sacquet, J., Jourdan, F., and Didier, A. (2006). Long-term fate and distribution of newborn cells in the adult mouse olfactory bulb: influences of olfactory deprivation. *Neuroscience* 141, 443–451. doi: 10.1016/j.neuroscience.2006.03.066

Maret, S., Faraguna, U., Nelson, A. B., Cirelli, C., and Tononi, G. (2011). Sleep and waking modulate spine turnover in the adolescent mouse cortex. *Nat. Neurosci.* 14, 1418–1420. doi: 10.1038/nn.2934

Markopoulos, F., Rokni, D., Gire, D. H., and Murthy, V. N. (2012). Functional properties of cortical feedback projections to the olfactory bulb. *Neuron* 76, 1175–1188. doi: 10.1016/j.neuron.2012.10.028

McCune, S. K., Voigt, M. M., and Hill, J. M. (1993). Expression of multiple alpha adrenergic receptor subtype messenger RNAs in the adult rat brain. *Neuroscience* 57, 143–151. doi: 10.1016/0306-4522(93)90116-W

McLean, J. H., Shipley, M. T., Nickell, W. T., Aston-Jones, G., and Reyher, C. K. H. (1989). Chemoanatomical organization of the noradrenergic input from locus coeruleus to the olfactory bulb of the adult rat. *J. Comp. Neurol.* 285, 339–349. doi: 10.1002/cne.902850305

Moreno, M. M., Bath, K., Kuczewski, N., Sacquet, J., Didier, A., and Mandairon, N. (2012). Action of the noradrenergic system on adult-born cells is required for olfactory learning in mice. *J. Neurosci.* 32, 3748–3758. doi: 10.1523/JNEUROSCI.6335-11.2012

Moreno, M. M., Linster, C., Escanilla, O., Sacquet, J., Didier, A., and Mandairon, N. (2009). Olfactory perceptual learning requires adult neurogenesis. *Proc. Natl. Acad. Sci. U.S.A.* 106, 17980–17985. doi: 10.1073/pnas.0907063106

Mori, K. (1987). Membrane and synaptic properties of identified neurons in the olfactory bulb. *Prog. Neurobiol.* 29, 275–320. doi: 10.1016/0301-0082(87)90024-4

Mori, K., and Sakano, H. (2011). How is the olfactory map formed and interpreted in the mammalian brain? *Annu. Rev. Neurosci.* 34, 467–499. doi: 10.1146/annurev-neuro-112210-112917

Mori, K., Takahashi, Y. K., Igarashi, K. M., and Yamaguchi, M. (2006). Maps of odorant molecular features in the mammalian olfactory bulb. *Physiol. Rev.* 86, 409–433. doi: 10.1152/physrev.00021.2005

Morrow, B. A., Redmond, A. J., Roth, R. H., and Elsworth, J. D. (2000). The predator odor, TMT, displays a unique, stress-like pattern of dopaminergic and endocrinological activation in the rat. *Brain Res.* 864, 146–151. doi: 10.1016/S0006-8993(00)02174-0

Mouret, A., Gheusi, G., Gabellec, M. M., de Chaumont, F., Olivo-Martin, J. C., and Lledo, P. M. (2008). Learning and survival of newly generated neurons: when time matters. *J. Neurosci.* 28, 11511–11516. doi: 10.1523/JNEUROSCI.2954-08.2008

Mouret, A., Lepousez, G., Gras, J., Gabellec, M. M., and Lledo, P. M. (2009). Turnover of newborn olfactory bulb neurons optimizes olfaction. *J. Neurosci.* 29, 12302–12314. doi: 10.1523/JNEUROSCI.3383-09.2009

Murakami, M., Kashiwadani, H., Kirino, Y., and Mori, K. (2005). State-dependent sensory gating in olfactory cortex. *Neuron* 46, 285–296. doi: 10.1016/j.neuron.2005.02.025

Murata, K., Imai, M., Nakanishi, S., Watanabe, D., Pastan, I., Kobayashi, K., et al. (2011). Compensation of depleted neuronal subsets by new neurons in a local area of the adult olfactory bulb. *J. Neurosci.* 31, 10540–10557. doi: 10.1523/JNEUROSCI.1285-11.2011

Nagayama, S., Enerva, A., Fletcher, M. L., Masurkar, A. V., Igarashi, K. M., Mori, K., et al. (2010). Differential axonal projection of mitral and tufted cells in the mouse main olfactory system. *Front. Neural Circuits* 4:120. doi: 10.3389/fncir.2010.00120

Nai, Q., Dong, H. W., Linster, C., and Ennis, M. (2010). Activation of alpha1 and alpha2 noradrenergic receptors exert opposing effects on excitability of main olfactory bulb granule cells. *Neuroscience* 169, 882–892. doi: 10.1016/j.neuroscience.2010.05.010

Neville, K. R., and Haberly, L. B. (2004). "Olfactory cortex," in *The Synaptic Organization of the Brain, 5th Edn.,* ed G. Shepherd (New York, NY: Oxford UP), 415–454. doi: 10.1093/acprof:oso/9780195159561.003.0010

Ninkovic, J., Mori, T., and Gotz, M. (2007). Distinct modes of neuron addition in adult mouse neurogenesis. *J. Neurosci.* 27, 10906–10911. doi: 10.1523/JNEUROSCI.2572-07.2007

Nissant, A., Bardy, C., Katagiri, H., Murray, K., and Lledo, P. M. (2009). Adult neurogenesis promotes synaptic plasticity in the olfactory bulb. *Nat. Neurosci.* 12, 728–730. doi: 10.1038/nn.2298

Parrish-Aungst, S., Shipley, M. T., Erdelyi, F., Szabo, G., and Puche, A. C. (2007). Quantitative analysis of neuronal diversity in the mouse olfactory bulb. *J. Comp. Neurol.* 501, 825–836. doi: 10.1002/cne.21205

Petreanu, L., and Alvarez-Buylla, A. (2002). Maturation and death of adult-born olfactory bulb granule neurons: role of olfaction. *J. Neurosci.* 22, 6106–6113.

Poo, C., and Isaacson, J. S. (2007). An early critical period for long-term plasticity and structural modification of sensory synapses in olfactory cortex. *J. Neurosci.* 27, 7553–7558. doi: 10.1523/JNEUROSCI.1786-07.2007

Poo, C., and Isaacson, J. S. (2011). A major role for intracortical circuits in the strength and tuning of odor-evoked excitation in olfactory cortex. *Neuron* 72, 41–48. doi: 10.1016/j.neuron.2011.08.015

Redondo, R. L., and Morris, R. G. (2011). Making memories last: the synaptic tagging and capture hypothesis. *Nat. Rev. Neurosci.* 12, 17–30. doi: 10.1038/nrn2963

Rochefort, C., Gheusi, G., Vincent, J., and Lledo, P. M. (2002). Enriched odor exposure increases the number of newborn neurons in the adult olfactory bulb and improves odor memory. *J. Neurosci.* 22, 2679–2689.

Saar, D., Grossman, Y., and Barkai, E. (2002). Learning-induced enhancement of postsynaptic potentials in pyramidal neurons. *J. Neurophysiol.* 87, 2358–2363.

Saghatelyan, A., Roux, P., Migliore, M., Rochefort, C., Desmaisons, D., Charneau, P., et al. (2005). Activity-dependent adjustments of the inhibitory network in the olfactory bulb following early postnatal deprivation. *Neuron* 46, 103–116. doi: 10.1016/j.neuron.2005.02.016

Sanchez-Andrade, G., and Kendrick, K. M. (2009). The main olfactory system and social learning in mammals. *Behav. Brain Res.* 200, 323–335. doi: 10.1016/j.bbr.2008.12.021

Schneider, S. P., and Macrides, F. (1978). Laminar distributions of interneurons in the main olfactory bulb of the adult hamster. *Brain Res. Bull.* 3, 73–82. doi: 10.1016/0361-9230(78)90063-1

Shepherd, G. M., Chen, W., and Greer, C. (2004). "Olfactory bulb," in *The Synaptic Organization of the Brain, 5th Edn.,* ed G. Shepherd (New York, NY: Oxford University Press), 165–216. doi: 10.1093/acprof:oso/9780195159561.003.0005

Shingo, T., Gregg, C., Enwere, E., Fujikawa, H., Hassam, R., Geary, C., et al. (2003). Pregnancy-stimulated neurogenesis in the adult female forebrain mediated by

prolactin. *Science* 299, 117–120. doi: 10.1126/science.1076647

Shipley, M. T., and Ennis, M. (1996). Functional organization of olfactory system. *J. Neurobiol.* 30, 123–176.

Sosulski, D. L., Bloom, M. L., Cutforth, T., Axel, R., and Datta, S. R. (2011). Distinct representations of olfactory information in different cortical centres. *Nature* 472, 213–216. doi: 10.1038/nature09868

Sullivan, R. M., Wilson, D. A., and Leon, M. (1989). Norepinephrine and learning-induced plasticity in infant rat olfactory system. *J. Neurosci.* 9, 3998–4006.

Sultan, S., Mandairon, N., Kermen, F., Garcia, S., Sacquet, J., and Didier, A. (2010). Learning-dependent neurogenesis in the olfactory bulb determines long-term olfactory memory. *FASEB J.* 24, 2355–2363. doi: 10.1096/fj.09-151456

Tononi, G., and Cirelli, C. (2006). Sleep function and synaptic homeostasis. *Sleep Med. Rev.* 10, 49–62. doi: 10.1016/j.smrv.2005.05.002

Tsuno, Y., Kashiwadani, H., and Mori, K. (2008). Behavioral state regulation of dendrodendritic synaptic inhibition in the olfactory bulb. *J. Neurosci.* 28, 9227–9238. doi: 10.1523/JNEUROSCI.1576-08.2008

Veyrac, A., Sacquet, J., Nguyen, V., Marien, M., Jourdan, F., and Didier, A. (2009). Novelty determines the effects of olfactory enrichment on memory and neurogenesis through noradrenergic mechanisms. *Neuropsychopharmacology* 34, 786–795. doi: 10.1038/npp.2008.191

Vyazovskiy, V. V., Cirelli, C., Pfister-Genskow, M., Faraguna, U., and Tononi, G. (2008). Molecular and electrophysiological evidence for net synaptic potentiation in wake and depression in sleep. *Nat. Neurosci.* 11, 200–208. doi: 10.1038/nn2035

Wellman, P. J. (2000). Norepinephrine and the control of food intake. *Nutrition* 16, 837–842. doi: 10.1016/S0899-9007(00)00415-9

Whitman, M. C., and Greer, C. A. (2007). Synaptic integration of adult-generated olfactory bulb granule cells: basal axodendritic centrifugal input precedes apical dendrodendritic local circuits. *J. Neurosci.* 27, 9951–9961. doi: 10.1523/JNEUROSCI.1633-07.2007

Wilson, D. A. (2010). Single-unit activity in piriform cortex during slow-wave state is shaped by recent odor experience. *J. Neurosci.* 30, 1760–1765. doi: 10.1523/JNEUROSCI.5636-09.2010

Wilson, D. A., and Sullivan, R. M. (2011). Cortical processing of odor objects. *Neuron* 72, 506–519. doi: 10.1016/j.neuron.2011.10.027

Wilson, M. A., and McNaughton, B. L. (1994). Reactivation of hippocampal ensemble memories during sleep. *Science* 265, 676–679. doi: 10.1126/science.8036517

Winner, B., Cooper-Kuhn, C. M., Aigner, R., Winkler, J., and Kuhn, H. G. (2002). Long-term survival and cell death of newly generated neurons in the adult rat olfactory bulb. *Eur. J. Neurosci.* 16, 1681–1689. doi: 10.1046/j.1460-9568.2002.02238.x

Yamaguchi, M., and Mori, K. (2005). Critical period for sensory experience-dependent survival of newly generated granule cells in the adult mouse olfactory bulb. *Proc. Natl. Acad. Sci. U.S.A.* 102, 9697–9702. doi: 10.1073/pnas.0406082102

Yokoi, M., Mori, K., and Nakanishi, S. (1995). Refinement of odor molecule tuning by dendrodendritic synaptic inhibition in the olfactory bulb. *Proc. Natl. Acad. Sci. U.S.A.* 92, 3371–3375. doi: 10.1073/pnas.92.8.3371

Yokoyama, T. K., Mochimaru, D., Murata, K., Manabe, H., Kobayakawa, K., Kobayakawa, R., et al. (2011). Elimination of adult-born neurons in the olfactory bulb is promoted during the postprandial period. *Neuron* 71, 883–897. doi: 10.1016/j.neuron.2011.05.046

Young, K. M., Fogarty, M., Kessaris, N., and Richardson, W. D. (2007). Subventricular zone stem cells are heterogeneous with respect to their embryonic origins and neurogenic fates in the adult olfactory bulb. *J. Neurosci.* 27, 8286–8296. doi: 10.1523/JNEUROSCI.0476-07.2007

Conflict of Interest Statement: The authors declare that the research was conducted in the absence of any commercial or financial relationships that could be construed as a potential conflict of interest.

Received: 02 July 2013; accepted: 26 July 2013; published online: 14 August 2013.
Citation: Yamaguchi M, Manabe H, Murata K and Mori K (2013) Reorganization of neuronal circuits of the central olfactory system during post-prandial sleep. Front. Neural Circuits 7:132. doi: 10.3389/fncir.2013.00132

frontiers in
NEURAL CIRCUITS

REVIEW ARTICLE
published: 10 October 2013
doi: 10.3389/fncir.2013.00163

Application of FRET probes in the analysis of neuronal plasticity

Yoshibumi Ueda[1†], Showming Kwok[2] and Yasunori Hayashi[1,3]*

[1] *Brain Science Institute, RIKEN, Wako, Saitama, Japan*
[2] *Department of Brain and Cognitive Sciences, The Picower Institute for Learning and Memory, Massachusetts Institute of Technology, Cambridge, MA, USA*
[3] *Brain Science Institute, Saitama University, Saitama, Japan*

Edited by:
Masanobu Kano, The University of Tokyo, Japan

Reviewed by:
Akihiro Yamanaka, Nagoya University, Japan
Michiyuki Matsuda, Kyoto University, Japan

***Correspondence:**
Yasunori Hayashi, Brain Science Institute, RIKEN, 2-1 Hirosawa, Wako, Saitama, 351-0198, Japan
e-mail: yhayashi@brain.riken.jp; yhayashi-tky@umin.ac.jp

[†]***Present address:***
Yoshibumi Ueda, Department of Hematology and Immunology, Kanazawa Medical University, Kahoku, Ishikawa, Japan

Breakthroughs in imaging techniques and optical probes in recent years have revolutionized the field of life sciences in ways that traditional methods could never match. The spatial and temporal regulation of molecular events can now be studied with great precision. There have been several key discoveries that have made this possible. Since green fluorescent protein (GFP) was cloned in 1992, it has become the dominant tracer of proteins in living cells. Then the evolution of color variants of GFP opened the door to the application of Förster resonance energy transfer (FRET), which is now widely recognized as a powerful tool to study complicated signal transduction events and interactions between molecules. Employment of fluorescent lifetime imaging microscopy (FLIM) allows the precise detection of FRET in small subcellular structures such as dendritic spines. In this review, we provide an overview of the basic and practical aspects of FRET imaging and discuss how different FRET probes have revealed insights into the molecular mechanisms of synaptic plasticity and enabled visualization of neuronal network activity both *in vitro* and *in vivo*.

Keywords: optical probes, synaptic plasticity, Förster resonance energy transfer, fluorescence lifetime imaging microscopy

INTRODUCTION

The brain is a highly interconnected functional network comprised of billions of neurons that communicate with each other at synapses. Throughout life, the neuronal connectivity that subserves brain function is modified and refined in an activity-dependent manner, a phenomenon termed neuronal plasticity. Plasticity mechanisms can influence neuronal function and structure through modifications at the level of synapses, dendrites and axons (Citri and Malenka, 2008; Holtmaat and Svoboda, 2009).

Different forms of plasticity are tightly regulated by a complex network of signal transduction cascades, which are the results of protein-protein interaction, posttranslational modification, subcellular translocation of proteins, protein synthesis, etc. Therefore, the temporal and spatial precision of these events is critical to support proper brain function in the developing and mature brain. The development of probes that offer spatiotemporal detection of these cellular events is vital to our ability to examine these important molecular mechanisms in biological systems. For this purpose, optical microscopic imaging enables complex and varied neuronal signals to be captured with high temporal and spatial resolution from live biological samples.

Technological advances in the past two decades have made a significant contribution to our ability to extend fluorescent imaging techniques beyond that of simple morphological analysis. One of the key developments is Förster resonance energy transfer (FRET). First reported by Förster (1946), the technique describes how energy from a "donor" fluorophore can excite an "acceptor" fluorophore, resulting in light emission from the latter. The efficiency of FRET depends on two main factors, the distance between the two fluorophores and their relative orientation. This feature enables the change in distance and angle between two fluorophores to be calculated, leading Lubert Stryer to call FRET a "molecular ruler" (Stryer, 1978). Using this property of FRET, various optical probes have been designed to detect aspects of different cellular functions *in vitro* and *in vivo*.

The sensitivity and compatibility of FRET imaging with live imaging are critical for analyzing the molecular mechanisms of neuronal circuit plasticity. In particular, much progress has been made in recent years regarding the analysis of synaptic plasticity of excitatory synapses in excitatory neurons, which are typically formed on dendritic spines (Hayashi and Majewska, 2005; Bosch and Hayashi, 2012). FRET imaging is now being applied *in vivo* and offers a unique opportunity to study how and when neurons or synapses change and which signaling events contribute to such changes in response to stimuli in the intact brain.

In this article, we will provide an overview of the basic and practical aspects of FRET imaging, summarize currently available FRET-based probes and then discuss how these probes advanced our understanding of the molecular mechanisms underlying neuronal plasticity, mainly hippocampal long-term potentiation (LTP).

MONITORING *in situ* BIOCHEMICAL PROCESSES USING FRET-BASED PROBES

In 1991, Tsien's group made the first attempt to image live cellular functions using FRET (Adams et al., 1991; Zhang et al., 2002).

They attempted to visualize the intracellular dynamics of adenosine 3′, 5′- cyclic monophosphate (cAMP) by designing a probe based on cAMP-dependent protein kinase, in which the regulatory and catalytic subunits were labeled with fluorescein and rhodamine, respectively. Upon binding of cAMP, the regulatory subunit dissociates from the catalytic subunit, thereby eliminating FRET.

Subsequently, they also reported a voltage sensing FRET probe utilizing fluorescein-labeled lectin as a donor and oxonol, an anionic fluorescent compound, as an acceptor in living cells (Gonzalez and Tsien, 1995). At resting membrane potential, both dyes are localized on the outer leaflet of the plasma membrane and FRET occurs. Upon depolarization, negatively charged oxonol translocates to the inner leaflet of the plasma membrane and increases the distance from the donor, leading to a reduction in the efficiency of FRET.

However, FRET approaches using small molecular weight fluorescent compounds are technically demanding. For example, generation of the cAMP probe requires the cumbersome process of protein purification, *in vitro* chemical coupling with dyes and introduction into cells. The success of the oxonol-based probe largely owed to the identification of oxonol as a fluorescent molecule that travels across the plasma membrane upon a change in membrane voltage.

The emergence of genetically encoded FRET probes in the late 1990s dramatically changed the situation. This largely owes to the development and expansion of green fluorescent protein (GFP) and its color variants (Shaner et al., 2005). In a landmark study of genetically encoded FRET probes, Miyawaki et al. developed the first GFP-based calcium indicator, cameleon using cyan fluorescent protein (CFP) as a donor and yellow fluorescent protein (YFP) as an acceptor (Miyawaki et al., 1997). Cameleon consists of a calmodulin (CaM) protein fused with a M13 sequence (a 26-residue CaM binding peptide from myosin light-chain kinase), flanked by CFP and YFP. The gly-gly motif between CaM and the M13 peptide gives this probe its conformational flexibility. In the absence of calcium, CaM and the M13 sequence do not interact with each other. However, in the presence of calcium, they form a complex, which shortens the distance between the donor and acceptor fluorophores, allowing FRET to occur. Using this probe, they observed calcium dynamics in living cells and demonstrated the potential of FRET for the analysis of neuronal circuit dynamics. Since then, probes for other molecules such as cAMP, guanosine 3′, 5′- cyclic monophosphate (cGMP), and Cl^-, small GTP-binding protein (small G-protein), phosphoinositide and signaling events e.g., phosphorylation have been developed (**Table 1**).

Compared to small molecular weight fluorescent molecule-based FRET probes, genetically encoded FRET probes offer a number of advantages. They can be constructed easily with standard molecular biological techniques, thus making probe design simple and flexible. They can be expressed in cells by simply introducing vector DNA into neurons without protein purification and chemical labeling. Use of an appropriate DNA transduction method or a promoter to express the probe allow cell-type specific labeling. Due to these technical advantages, the genetically-encoded FRET probes are now widely used standard tools in biological systems.

STRATEGIES OF PROBE DESIGN

Multiple genetically-encoded FRET probes have been developed for use in neuronal and non-neuronal cells. These probes can be classified into several categories depending on the approach used to detect different types of biological phenomena (**Table 1**, **Figure 1**).

Cleavage-based approach

The first reported GFP-based probe detecting Factor Xa activity employed the cleavage-based approach (**Figure 1A**) (Mitra et al., 1996). In this type of probe, a protease cleavage sequence was flanked by donor and acceptor fluorophores. Under basal conditions, FRET occurs between the fluorophores. However, cleavage of the target sequence causes a resultant separation of donor and acceptor molecules, leading to a decrease in FRET efficiency. The same approach was used to study other proteases including caspases (Xu et al., 1998; Onuki et al., 2002; Li et al., 2006; Joseph et al., 2011). One thing to note when using this type of probe is that the protease cleavage is irreversible. Therefore, it is not suitable for detecting a protease with high basal activity. Also, the measurement cannot be repeated multiple times as the uncleaved fraction decreases and the cleaved fraction accumulates over time.

Intermolecular FRET approach

The interaction between proteins can be monitored by intermolecular FRET, where one party of the protein complex is tagged by a donor and the other by an acceptor (**Figure 1B**). The interaction can be a heteromer of two different proteins or a homomer of the same protein. Application of this approach includes, small G-protein activity (Yasuda et al., 2006), 3-phosphoinositide-dependent protein kinase 1 (PDK)-Akt (Calleja et al., 2007), phosphatase and tensin homolog deleted from chromosome 10 (PTEN)-myosin V (van Diepen et al., 2009), and protein-tyrosine phosphatase 1B (PTP1B)-receptor tyrosine kinases (RTKs) (Haj et al., 2002) interaction (**Table 1**). A variant of this approach is homomultimer FRET where a monomer in a polymeric protein complex is labeled with both donor and acceptor molecules (**Figure 1C**), which allows the polymerization status of the protein to be monitored. This was employed to detect actin polymerization/depolymerization (Okamoto et al., 2004).

The quantitative aspect of FRET is difficult to control in intermolecular FRET (when compared with intramolecular FRET) because the expression level of donor and acceptor molecules often varies amongst cells. In contrast, in an intramolecular FRET probe, the donor and acceptor are on the same molecule and thus, the ratio of the donor to acceptor is always constant. Also, endogenous proteins may participate in forming protein complexes and this can decrease intermolecular FRET efficiency. Therefore, with intermolecular FRET, the efficiency must be measured as an average of multiples cells or compared before and after a treatment (e.g., induction of synaptic plasticity) in the same cell. In practice, a donor which does not interact with an acceptor increases the background of the measurement, whereas excess levels of

Table 1 | A list of genetically encoded FRET probes.

Classification	Target	Name of probe	Year	Probe design	References
Small molecule	Calcium	Cameleon	1997	3-2	Miyawaki et al., 1997
Small molecule	Cyclic guanosine monophosphate (cGMP)	CGY, Cygnet, pGES-DE2, cGi	2000, 2001, 2006, 2013	3-1	Sato et al., 2000; Honda et al., 2001; Nikolaev et al., 2006; Thunemann et al., 2013
Small molecule	Cyclic adenosine monophosphate (cAMP)	Epac	2000, 2004	2, 3-1	Zaccolo and Pozzan, 2002; Nikolaev et al., 2004
Small molecule	Inositol trisphosphate (IP_3)	LIBRA, Fretino, FIRE	2004, 2005, 2006	3-1	Tanimura et al., 2004; Sato et al., 2005a; Matsu-ura et al., 2006
Small molecule	Nitric oxide (NO)	NOA-1, Piccell	2005, 2006	3-1	Sato et al., 2005b, 2006b
Small molecule	Adenosine triphosphate (ATP)	A Team 1.03-nD/nA	2012	3-1	Imamura et al., 2009
Small molecule	Estrogen	SCCoR	2004	3-3	Awais et al., 2004
Small molecule	Androgen	Ficaro	2006	3-3	Awais et al., 2006
Small molecule	Glucocorticoid receptor ligands	GLUCOCOR	2007	3-3	Nishi et al., 2004; Awais et al., 2007a
Small molecule	Neurotrophic factor	ECaus	2008	3-3	Nakajima et al., 2008
Small molecule	Nuclear receptor	conpro	2007	3-2	Awais et al., 2007b
Small molecule	O-N-acetylglucosamine (O-GlcNAc)		2006	3-3	Carrillo et al., 2006
Small molecule	Vitamin A (Retinoic acid)	GEPRAS	2013	3-1	Shimozono et al., 2013
Small molecule	Molybdate	MolyProbe	2013	3-1	Nakanishi et al., 2013
Small molecule	Glutamate	FLIPE	2005	3-1	Okumoto et al., 2005
Small molecule	Zn^{2+}	eCALWY-1	2009	2	Vinkenborg et al., 2009
Small molecule	Cl^-	Clomeleon	2000	other	Kuner and Augustine, 2000
Small molecule	pH	GFpH, YFpH	2001	other	Awaji et al., 2001
Small molecule	Glucose	FLIPglu	2003	3-1	Fehr et al., 2003
Small molecule	Maltose	FLIPmal	2002	3-1	Fehr et al., 2002
Small molecule	Ribose	FLIPrib	2003	3-1	Lager et al., 2003
Kinase	Calcium/Calmodulin-dependent protein kinase II (CaMKII)	Camui α, green-Camui α, Camk2a reporter	2005, 2009, 2011, 2013	3-1	Takao et al., 2005; Lee et al., 2009; Piljic et al., 2011; Fujii et al., 2013
Kinase	Src	Srcus	2001, 2005, 2007	3-3	Ting et al., 2001; Wang et al., 2005; Hitosugi et al., 2007
Kinase	Protein kinase C (PKC)	CKAR, CY-PKCdelta	2003, 2005	3-3, 3-1	Violin et al., 2003; Braun et al., 2005
Kinase	Protein kinase D (PKD)	DKAR	2007	3-3	Kunkel et al., 2007
Kinase	Protein kinase A (PKA)	ART, AKAR	2000, 2001	3-3	Nagai et al., 2000; Zhang et al., 2001
Kinase	Abl	Picchu	2001	3-3	Ting et al., 2001
Kinase	Bcr-Abl	Bcr-Abl activity sensor	2010	3-3	Tunceroglu et al., 2010
Kinase	c-Raf	Prin-cRaf	2005	3-1	Terai and Matsuda, 2005
Kinase	PAK1	Pakabi	2009	3-1	Parrini et al., 2009
Kinase	B-raf	Prin-Braf	2006	3-1	Terai and Matsuda, 2006
Kinase	ZAP-70	ROZA	2008	3-3	Randriamampita et al., 2008
Kinase	Akt	Aktus, BKAR, Akind	2003, 2005, 2007	3-3	Sasaki et al., 2003; Kunkel et al., 2005; Calleja et al., 2007
Kinase	ERK	Miu2, Erkus, EKAR	2006, 2007, 2008	3-1, 3-3, 3-3	Fujioka et al., 2006; Sato et al., 2007; Harvey et al., 2008a

(Continued)

Table 1 | Continued

Classification	Target	Name of probe	Year	Probe design	References
Kinase	Insulin receptor	Phocus	2002	3-3	Sato et al., 2002
Kinase	Epidermal Growth factor receptor (EGFR)		2001	3-3	Ting et al., 2001
Kinase	Ataxia telangiectasia mutated (ATM)		2007	3-3	Johnson et al., 2007
Kinase	Aurora B kinase		2008	3-3	Fuller et al., 2008
Kinase	Cyclin B1-CDK1		2010	3-3	Gavet and Pines, 2010
Kinase	Myosine light chain kinase	MLCK-FIP	2002	3-1	Chew et al., 2002
Kinase	JNK	JNKAR1, JUNKAR1EV	2010, 2011	3-3	Fosbrink et al., 2010; Komatsu et al., 2011
Kinase	RSK	Eevee-RSK	2011	3-3	Komatsu et al., 2011
Kinase	S6K	Eevee-S6K	2011	3-3	Komatsu et al., 2011
Kinase	Focal Adhesion Kinase (FAK)	CYFAK413, FERM-sensor	2008, 2009	2, 3-1	Cai et al., 2008; Papusheva et al., 2009
Kinase	PLK1		2008	3-3	Macurek et al., 2008
Kinase	SAP3K		2009	3-3	Tomida et al., 2009
Kinase	DAPK1	DAPK1(334)-F40	2011	3-1	Piljic et al., 2011
Phosphatase	Calcineurin	CaNAR1	2008, 2013	3-1	Newman and Zhang, 2008; Fujii et al., 2013
Small G-protein	Ras	Raichu-Ras, Fras	2001, 2006	3-2, 2	Yasuda et al., 2006; Mochizuki et al., 2001
Small G-protein	Rap	Raichu-Rap	2001	3-2	Mochizuki et al., 2001
Small G-protein	Rac	Raichu-Rac1	2004	3-2	Aoki et al., 2004
Small G-protein	Rab5	Raichu-Rab5	2008	3-2	Kitano et al., 2008
Small G-protein	Rho	Raichu-RhoA	2003, 2011	3-2, 2	Yoshizaki et al., 2003; Murakoshi et al., 2011
Small G-protein	Cdc42	Raichu-cdc42	2004, 2011	3-2, 2	Aoki et al., 2004; Murakoshi et al., 2011
Small G-protein	Ral	Raichu-Ral	2004	3-3	Takaya et al., 2004
Small G-protein	TC10	Raichu-TC10	2006	3-2	Kawase et al., 2006
Signal transduction	RCC1 (GEF of Ran)	CFP-RCC1-YFP	2008	3-1	Hao and Macara, 2008
Signal transduction	CrkII phosphorylation	Picchu	2001	3-1	Kurokawa et al., 2001
Signal transduction	N-WASP	Stinger	2004	3-1	Lorenz et al., 2004; Ward et al., 2004
Signal transduction	Adrenergic receptor	α_{2A}AR-cam	2003	3-1	Vilardaga et al., 2003
Signal transduction	Parathyroid hormone receptor	PTHR-cam	2003	3-1	Vilardaga et al., 2003
Signal transduction	Plasma membrane Calcium pump	BFP-PMCA-GFP	2007	3-1	Corradi and Adamo, 2007
Acetylation	Histone acetylation	Histac	2004, 2009	3-3	Lin et al., 2004; Sasaki et al., 2009
Lipid	Phosphatidylinositol (3,4,5)-trisphosphate (PIP3)	FIlip, FLIMPA	2003, 2013	3-4	Sato et al., 2003; Ueda and Hayashi, 2013
Lipid	Phosphatidylinositol (4,5)-bisphosphate (PIP2)	Pippi-PI(4,5)P_2	2008	3-4	Nishioka et al., 2008
Lipid	Phosphatidylinositol (3,4)-bisphosphate (PI(3,4)P2)	Pippi-PI(3,4)P_2	2008	3-4	Nishioka et al., 2008
Lipid	Phosphatidylinositol 4-phosphate (PI4P)	Pippi-PI(4)P	2008	3-4	Nishioka et al., 2008
Lipid	Phosphatidic acid	Pii	2010	3-4	Nishioka et al., 2010
Lipid	Diacylglycerol (DAG)	Daglas, DIGDA	2006, 2008	3-4	Sato et al., 2006a; Nishioka et al., 2008
Protein interaction	Actin		2004, 2008	2	Okamoto et al., 2004; Murakoshi et al., 2008
Protein interaction	PDK1-Akt interaction		2007	2	Calleja et al., 2007

(Continued)

Table 1 | Continued

Classification	Target	Name of probe	Year	Probe design	References
Protein interaction	Protein tyrosine phosphatase 1B-receptor tyrosine kinases (PTP 1B-RTKs) interaction		2002	2	Haj et al., 2002
Protein interaction	Breast cancer resistance protein/ATP-binding cassette sub-family G member (BCRP/ABCG)		2010	2	Ni et al., 2010
Protein interaction	Cofilin-actin interaction		2008	2	Homma et al., 2008
Protein interaction	PTEN-Myosin V interaction		2009	2	van Diepen et al., 2009
Protease	Caspase-3	EGFP-DEVD-EBFP	1998	1	Xu et al., 1998
Protease	Caspase-8	CFP-c3-YFP-c6-mRFP	2002	1	Onuki et al., 2002
Protease	Caspase-9	SCAT9	2011	1	Joseph et al., 2011
Protease	Caspase-7	VDEVDc	2006	1	Li et al., 2006
Protease	Matrix Metalloproteinase (MMP)	YFP-MSS-CFP^{display}, MTI-MMP-FRET biosensor	2007, 2008	1	Yang et al., 2007; Ouyang et al., 2008
Protease	Protease activity (Factor Xa)		1996	1	Mitra et al., 1996
Protease	Calpain activity	pYSCS	2000	1	Vanderklish et al., 2000
Protease	Presenilin	GFP-PSI-RFP	2009	3-1	Uemura et al., 2009
Other	Strain sensor	stFRET	2008	3-1	Meng et al., 2008
Other	Membrane potential	VSFP, Mermaid, ArcLight, VSFP-Butterfly	2001, 2008, 2012, 2013	3-1	Sakai et al., 2001; Tsutsui et al., 2008; Jin et al., 2012; Akemann et al., 2013
Other	Myosin II	GSldCB	1998, 2006	3-1	Suzuki et al., 1998; Zeng et al., 2006
Other	HIV Rev protein	YRGnC-11ad	2005	3-1	Endoh et al., 2005
Other	Redox	Redoxfluor, Gaskins	2010, 2011	3-1	Yano et al., 2010; Kolossov et al., 2011

The numbers in the Probe Design column correspond to the section number in the "Strategies of probe design" chapter of the main text. Names of probes are shown. See the webpage by Dr. Michiyuki Matsuda http://www.lif.kyoto-u.ac.jp/labs/fret/e-phogemon/unifret.htm for updated information.

acceptor molecules usually does not cause a problem (Okamoto and Hayashi, 2006). Therefore, whenever possible, excess acceptor molecules should be used.

Intramolecular FRET approach

This approach detects the conformational change of the probe via a change in the distance and angle of donor and acceptor proteins located on the same molecule. Because both fluorophores are on the same molecule, complications such as the differential redistribution of the donor and acceptor proteins and heterogeneity in the expression level of donor and acceptor among cells can be eliminated. Using this approach, many different probes have been generated to enable the detection of covalent modifications of proteins, membrane voltage, small biological molecules, and signal transduction (**Table 1**). One can design a probe to detect conformational change that is intrinsic to the protein of interest or design a fusion protein that changes its conformation upon the occurrence of a specified biological event. Advantage of intramolecular FRET is relative ease of constructing probe which shows FRET. But it is sometimes difficult to find right position of the fluorophore so that external stimuli change the FRET efficiency.

Intrinsic conformation change of protein. If a protein of interest changes its conformation by activation/inactivation, one can design a probe to detect the conformational change as a way of monitoring the activity level (**Figure 1D**). This may be accomplished by flanking the protein with a donor and an acceptor or inserting one or both of the fluorophore(s) between the domains. This approach has been successfully employed for Ca^{2+}/CaM-dependent protein kinase II (CaMKII) (Takao et al., 2005; Kwok et al., 2008; Fujii et al., 2013), calcineurin (Fujii et al., 2013), c-raf (Terai and Matsuda, 2005), p21 protein-activated kinase 1 (PAK1) (Parrini et al., 2009), B-raf (Terai and Matsuda, 2006), regulator of chromosome condensation 1 (RCC1) (Hao and Macara, 2008), vitamin A receptor (Shimozono et al., 2013) and to monitor changes in membrane potential (Tsutsui et al., 2008; Akemann et al., 2012). X-ray crystal structure is a useful guide to identify locations on a protein where the donor and acceptor pair can be placed.

Conformation change induced by a specific protein interaction. Activation or inactivation of a protein can trigger an interaction with a specific target protein. By using such an interaction, one can design a FRET probe to detect the activation of a protein

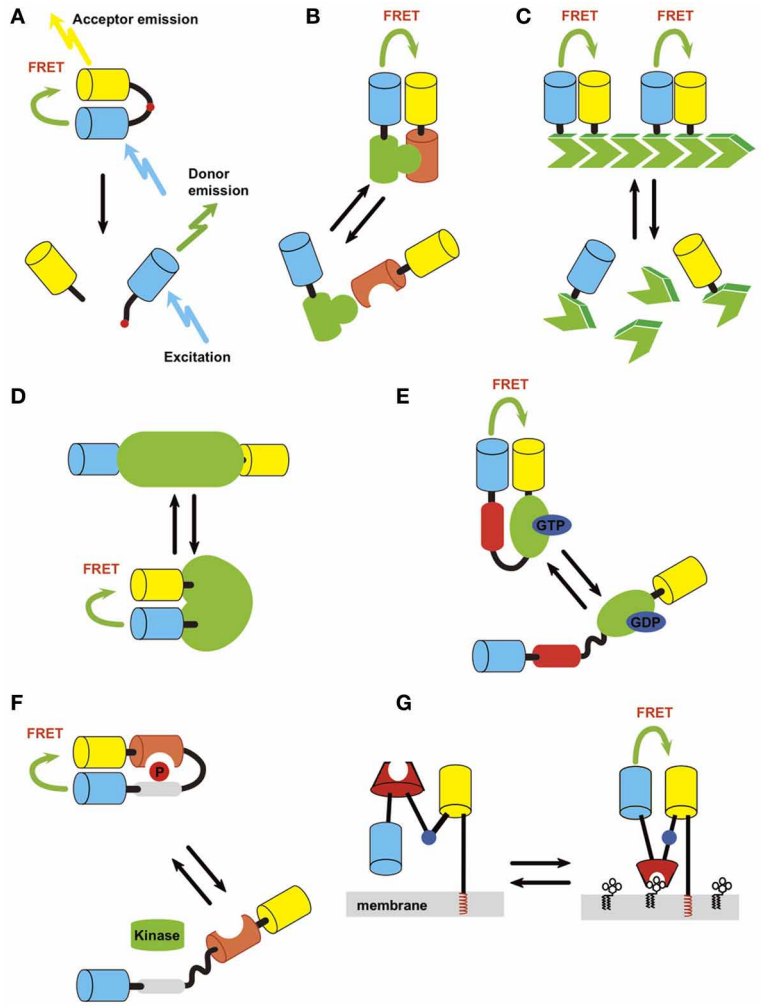

FIGURE 1 | Strategies of probe design. Light blue, donor; yellow, acceptor. **(A)** Protease. **(B)** Intermolecular protein interaction. **(C)** Polymerization status. **(D)** Intrinsic conformation change of protein, which can be used to detect activation of a protein if it accompanies conformation change of the structure. **(E)** Conformation change of fusion protein induced by activation/inactivation. An example of detection of small GTPase activation (green) by small GTPase binding protein (red) is shown. **(F)** Conformation change of fusion protein induced by covalent modification/inactivation. Here an example of detection of kinase activity by substrate sequence (gray) and phosphoprotein binding domain (orange) is depicted. **(G)** Small molecule on membrane lipid.

(**Figure 1E**). The cameleon probe mentioned above falls into this category. Another example is the Raichu series of probes that were developed to observe the activity of small G-proteins (Mochizuki et al., 2001). The basic structure of Raichu probes is comprised of four modules; a donor, an acceptor, a G-protein, and a G-protein-binding domain from its binding partner (**Figure 1E**). The inactive GDP-bound form does not interact with each other the G-protein-binding domain. Upon binding with GTP, the G-protein and G-protein-binding domain interact with each other to bring the two fluorophores into close proximity, thereby leading to FRET. This probe design strategy has been applied to Ras, Rho family protein, and other small G-proteins (Hao and Macara, 2008; Kiyokawa et al., 2011).

Conformation change induced by a covalent modification of protein. This type of probe consists of a donor and an acceptor, which flank a substrate domain that can be covalently modified by the protein of interest and a protein domain that specifically recognizes the covalently modified protein (**Figure 1F**). When the protein is covalently modified, it binds to the adjacent recognition domain, leading to a conformational change in the entire molecule, resulting in a change in FRET. By making use of specific kinase substrate and phosphor-protein recognition domains, this strategy has been applied to the design of FRET sensors for kinases and phosphatases including PKA (Zhang et al., 2001), C (Violin et al., 2003), and D (Kunkel et al., 2007), Akt (Sasaki et al., 2003), and Src (Ting et al., 2001). It should be noted that this type of probe actually detects a temporal integration of both kinase and phosphatase activity. Also, there may be kinases or phosphatases other than the target protein, which also phosphorylate or dephosphorylate the probe.

Small molecules on membranes. Using a similar strategy, small molecules on membranes can also be measured (**Figure 1G**). In this case, one of the fluorophores is tethered to the membrane through rigid α-helical linkers whereas the other fluorophore retains its flexibility via a gly-gly hinge. A specific lipid-binding domain is inserted in-between. When a small molecule binding domain interacts with its target of interest, a conformational change occurs through the hinge, resulting in an increase in FRET efficiency. This strategy has mainly been used to design probes for lipid second messengers such as phosphatidylinositol 3,4-bisphosphate ($PI(3,4)P_2$), phosphatidylinositol 4,5-bisphosphate ($PI(4,5)P_2$), phosphatidylinositol 3,4,5-trisphosphate (PIP_3), phosphatidylinositol 4-monophosphate (PI(4)P), and diacylglycerol (DAG) (Sato et al., 2003, 2006a; Nishioka et al., 2008; Ueda and Hayashi, 2013).

DETECTION OF FRET

Several imaging methods for FRET detection are used in typical biological laboratory settings (Miyawaki, 2003; Yasuda, 2006, 2012).

Ratiometric FRET detection

In ratiometric FRET detection, the acceptor and donor images are acquired separately and the ratio of fluorescent intensity between the two images is subsequently calculated. When FRET occurs, the acceptor/donor ratio increases. Because any fluorescent microscopy (e. g., wide field, confocal, two-photon) can be used for this measurement, ratiometric FRET measurement is often used, though it is not best for several reasons. When performing this type of imaging, maximum care must be taken to minimize spectral bleed-through, to properly subtract background and to take into account the fluorophore relocalization. These factors make imaging in small structures particularly challenging. For example, CFP, a donor fluorophore that is often paired with YFP as an acceptor, can bleed into the YFP channel, thereby decreasing the signal/noise ratio. Hence to minimize bleed-through, a suitable band-pass filter should be used, even if the overall brightness of the signal is compromised. Also, background subtraction has to be performed with great care, as a subtle change in background can have a significant effect on the signal ratio. The issue of probe relocalization should also be carefully considered. This may be particularly problematic when measuring intermolecular FRET between two different molecules, which may differentially relocalize during neuronal plasticity. For example, if donor moves while the acceptor does not, it will cause an apparent change in fluorescent ratio without an actual change in protein interaction. This situation can be circumvented by using a probe with intramolecular FRET, where both donor and acceptor are on the same molecule or intermolecular FRET between homomers, where both are expected to move in parallel (Ni and Zhang, 2010). It is also possible to mathematically correct the FRET by separately measuring the amount of local acceptor. But in such cases, it is better to employ fluorescent life-time imaging microscopy, which relies only on donor fluorescence (see below).

Acceptor bleaching

When the acceptor is photobleached with an appropriate wavelength, the donor fluorescence is dequenched and increased. This maneuver, called acceptor bleaching, gives a quantitative reading of FRET as it depends only on the donor fluorescence intensity. Excitation light wavelength, intensity, and duration must be carefully chosen to photobleach only the acceptor fluorophore. The photobleaching of the donor fluorophore will underestimate the FRET. This can be done by simply illuminating the donor protein without an acceptor and making sure that donor fluorescence does not photobleach. It should be noted that the photobleaching of an acceptor is irreversible and therefore, acceptor photobleaching is a terminal experiment where only a single, specific and accurate static measure of FRET efficiency is needed (Miyawaki, 2003). Obviously, for this reason, acceptor bleaching is not compatible with time-lapse imaging.

Fluorescent lifetime imaging

The third approach to quantifying FRET relies on a parameter of fluorescence, called fluorescence lifetime (Yasuda, 2006). When a fluorescent molecule is excited, it emits fluorescence in a decaying manner from the time of activation, typically in exponential fashion. When FRET occurs, the donor fluoresecence lifetime is shortened. Because fluorescence lifetime is unaffected under a wide range of concentrations and does not depend on acceptor fluorescence, it is less prone to artifact caused by a change in the local concentration of donor and acceptor, which is especially important in heterooligomer FRET. In contrast, ratiometric measurement can show a pseudopositive signal caused by bleed-through between fluorescence channels, which can be an issue when measuring FRET from a structure where protein composition can change. Therefore, fluorescence lifetime imaging microscopy (FLIM) is the ideal choice for FRET detection.

There are largely two different methods of FLIM, time and frequency domain measurements (Yasuda, 2006). The time domain measures the fluorescence decay after a brief ($<$ picoseconds) excitation pulse, while frequency domain measures lifetime by modulating the excitation light intensity and the detector gain differently (heterodyning) at high frequency (Yasuda, 2006). Both imaging systems are costly because FLIM requires a dedicated light-source and time-resolved detection. However, if one already has a two-photon microscope, adding components onto the existing system is straightforward. Current systems allow the detection of FRET signals at second order time resolution from single dendritic spines (Murakoshi et al., 2011), which is still slower than the ratiometric imaging that can go to video rate.

For the time domain measurement, time correlated single photon counting is currently widely used. This method measures the time elapses between an excitation pulse and an emitted single photon, which is binned into a histogram. The data will then be fitted to exponential curve (Yasuda, 2006). When two states are expected, such as in the case where both bound and unbound FRET pair coexist, it is possible to do double exponential fitting to obtain the ratio of two components (Yasuda, 2006). However, whether fitting double exponential is appropriate or not to a given FRET pair should be carefully considered based on the protein structure. For example, if donor forms a homodimer, it is enough

to complicate the situation. When endogenous counterpart exists, often the case in a cell, the dimer can be either between two exogenous donor molecules or between one donor and one endogenous counterpart, in addition to the dimer made of two endogenous molecules. As a result, the acceptor interacts with either two, one or zero fluorescent molecules. Mathematically, it is possible to perform triple (or more) exponential fitting. However, such measurement requires (1) bright sample, (2) capability of hardware that captures high photon counts over a large number of pixels rapidly, and (3) ease of sophisticated data analysis. Cellular autofluorescence also complicates the analysis (Colyer et al., 2012). To circumvent this, one can calculate average lifetime of the photons, which theoretically gives lifetime in single exponential. This will not give absolute proportion of component showing FRET but by comparing the average lifetime over time, will give sufficient information even from a noisy decay curve not suitable for fitting (Lee et al., 2009; Murakoshi et al., 2011).

Another issue of the time domain measurement is the "dead zone" of the sampling. For example, in a system set up on a Ti-sapphire laser based two-photon microscope, the repetition rate of the laser is at 80 MHz or every 12.5 ns. There is always a dead zone of sampling between each cycle, where the acquisition system must reset for the next cycle. Given that many fluorescent proteins have lifetime of 2–5 ns range, the dead zone can limit the effective range of fitting and underestimate especially the component with longer lifetime. Recent studies that introduced widefield photon-counting detector and phasor analysis might provide a new approach to perform FLIM experiments, alleviating these shortfalls (Kwok et al., 2008; Colyer et al., 2012).

CHOICE OF FLUORESCENCE PROTEINS

To effectively measure the change in the distance and angle between two fluorophores in a FRET construct, it is critical to start with a suitable pair of fluorescent molecules with efficient FRET. The efficiency of FRET (E) depends on several parameters characteristic to each pair of fluorescent proteins. Förster distance (R_0), the distance at which the energy transfer efficiency is 50%, depends on the overlap of donor emission and acceptor excitation (J), quantum yield of the donor (Q_0), and acceptor molar extinction coefficient (ε_A). As the values for J, Q_0, and ε_A increase, so does the value of R_0, which in turn produces a larger E value. So far, CFP (or an improved version such as Cerulean or K26R/N164H mutant of ECFP) and YFP (such as Venus) is the most commonly for ratiometric FRET measurements. A CFP-YFP pair gives a R_0 of 4.8–5.2 nm, depending on the variants used (Rizzo et al., 2006; Kwok et al., 2008; Lam et al., 2012). Recently, it was reported that the Clover and mRuby2 offers Förster radius of 6.3 nm and is currently considered to be the best FRET pair available to date (Lam et al., 2012).

For FLIM, enhanced GFP (EGFP) is often used as a donor, and paired with either monomeric red fluorescent protein (mRFP) or mCherry as an acceptor. The acceptor brightness is not an issue in FLIM as it relies solely on the donor fluorescence measurement. Therefore, non-fluorescent, quencher proteins such as REACh (Ganesan et al., 2006), darkVenus (Kwok et al., 2008), and super REACh (Lee et al., 2009) may also be used as acceptors to donor EGFP. Ideally, the donor should show a single lifetime with FLIM, which is the case for EGFP. The original enhanced CFP (ECFP) is not optimal as it shows two lifetime components, in addition to its relatively weak fluorescence. Cerulean and mTurquoise2 are both brighter and have mono exponential decay, therefore, can be used when the cyan range is needed (Rizzo et al., 2004; Goedhart et al., 2012).

EGFP has a weak tendency to dimerize (Zacharias et al., 2002), which can lead to issues with protein aggregation, depending on the protein it is fused with (Lantsman and Tombes, 2005). Therefore, monomerized versions of EGFP, such as the A206K mutant (the amino acid numbering is based on wild type GFP) is preferred for FRET experiments as it will reduce any pseudopositive FRET signal caused by non-specific aggregation. However, in certain cases, such as in cleavage-based protease sensors, the dimerization of donor and acceptor molecules can be beneficial to increase the difference in FRET efficiency before and after cleavage. In fact, a random mutagenesis study to enhance FRET efficiency of caspase probe lead to the identification of a CyPet-YPet pair (Nguyen and Daugherty, 2005), which was subsequently shown to form a dimer between donor and acceptor (Ohashi et al., 2007). For comprehensive review on fluorescence proteins, please refer to Shaner et al. (2005) and Newman et al. (2011).

APPLICATION OF FRET PROBES TO STUDY NEURONAL CIRCUIT DYNAMICS

Numbers of FRET probes have been developed and tested in various cell types. Here we list some of the recent research accomplishments using FRET probes in neuronal circuits. See **Table 1** for an extended list of various FRET probes.

Ca^{2+}

Intracellular Ca^{2+} plays an important role in regulating various cellular functions such as signaling, gene regulation, cell death, and survival. Under basal conditions, the intracellular Ca^{2+} concentration is maintained at low levels by various Ca^{2+}-extrusion and sequestration mechanisms. Upon neuronal activation, local intracellular Ca^{2+} concentration increases through influx from the extracellular fluid or efflux from the intracellular pool (Hayashi and Majewska, 2005). Different sources of Ca^{2+} can have distinct kinetics, subcellular localization and functions. Therefore, it is not very surprising that a Ca^{2+}-sensing FRET probe was one of the first genetically encoded FRET sensors ever made (Miyawaki et al., 1997). A popular use of this type of probe is to detect neuronal circuit activity through a detection of action potentials as Ca^{2+} influx into cells via voltage dependent Ca^{2+} channels. The activity of hundreds of neurons can be simultaneously monitored (Wallace et al., 2008).

Since Miyawaki et al. characterized cameleon, the first Ca^{2+} sensing FRET probe, various probes with different affinities to Ca^{2+} have been reported (Miyawaki, 2005). Cameleon was expanded into the yellow cameleon series, which had greater sensitivity to Ca^{2+} and better signal/noise ratio (Nagai et al., 2004; Horikawa et al., 2010). Griesbeck et al. utilized troponin C and I to generate the Tn series Ca^{2+} sensor protein (Heim and Griesbeck, 2004). Cameleon has been mainly applied to zebrafish (Mizuno et al., 2013) and *C. elegans* (Haspel et al., 2010). Recently

YC-Nano 140, new version of cameleon, was expressed to barrel cortex of mice using adeno-associated virus vector and showed different responses between two groups of neurons which are projected to different regions in neocortex (Chen et al., 2013).

Using a separate approach not involving FRET for its principle mode of detection, Nakai et al. generated G-CaMP (Nakai et al., 2001). G-CaMP was engineered to express CaM and a M13 peptide inserted in the β-barrel wall of GFP, which ultimately distorts its overall structure of GFP and quenches its fluorescence. An increase in Ca^{2+} concentration induces CaM and M13 peptide to interact, which then leads to a conformation change in the β-barrel. This in turn changes the protonation status of the fluorophore and dequenches the fluorescence. A related Ca^{2+} sensor termed pericam also utilizes a similar strategy (Nagai et al., 2001). Recently, B-GECO and R-GECO, a blue and red version of G-CaMP were developed to allow the simultaneous detection of calcium in more than one subcellular compartments or cell types (Zhao et al., 2011). With improvements in the sensitivity of probes and detection methods, it is now possible to visualize the Ca^{2+}-influx in single dendritic spines evoked by unitary excitatory postsynaptic potential (epsp) (Ohkura et al., 2012). Currently G-CaMP is becoming the first choice for Ca^{2+} imaging, especially *in vivo* because it is convenient to detect the Ca^{2+} responses with one channel. However, a recent report comparing the sensitivity between G-CaMP3 and YCs in Purkinje cells of acute cerebellar slice from mice (Yamada et al., 2011) showed that YC exhibited better response than G-CaMP3, indicating that optimal probes need to be carefully chosen in a given brain region of interest.

A CaMKII activity sensor, Camui

CaMKII is a member of the serine/threonine protein kinase family that is highly expressed in the brain, especially at the postsynaptic density (PSD) of excitatory synapses (Kennedy et al., 1983; Chen et al., 2005). CaMKII has been highly implicated in both induction and maintenance of functional and structural LTP (Lisman et al., 2002; Matsuzaki et al., 2004). The activation of CaMKII precedes the structural enlargement of stimulated spines, suggesting that CaMKII is a molecular trigger of downstream processes that lead to structural changes. In addition, the CaMKII has structural role at the synapse through its capacity to bundle F-actin (Okamoto et al., 2007, 2009).

Under basal conditions, CaMKII is kept inactive by intrasubunit steric block of the substrate-binding site (S site) in the kinase domain by a pseudosubstrate region within the autoinhibitory domain (Lisman et al., 2002). Binding of Ca^{2+}/CaM to the regulatory domain (adjacent to the autoinhibitory domain) alters its conformation and disrupts the inhibitory interaction at the S site. This disruption releases the kinase domain from autoinhibition and allows it to rapidly self-phosphorylate threonine 286 (T286) of CaMKII, as well as other substrates. CaMKII autophosphorylation at T286 prevents the autoinhibitory domain from binding with the T site of the catalytic domain and from blocking the kinase activity, thereby allowing the kinase to retain substantial activity even in the absence of Ca^{2+}. Thus, this holoenzyme remains active for a prolonged period of time, significantly outlasting that of a Ca^{2+} spike. Based on these observations, CaMKII was proposed as a memory molecule, which can be used to store long term information after a synapse undergoes LTP (Lisman et al., 2002).

However, direct demonstration of the persistent activation of CaMKII after the induction of LTP was lacking because of a deficiency in effective methods to detect the spatial and temporal activation of CaMKII at the single spine level. To circumvent this, a FRET probe, Camui, was engineered by employing the intramolecular FRET approach to detect the conformational change associated with CaMKII activation by fusing donor and acceptor fluorophores to both termini of CaMKII (Takao et al., 2005; Kwok et al., 2008). Camui shows FRET in its basal inactive state. Addition of ATP, CaM, and Ca^{2+} leads to a rapid and persistent decrease in FRET. The conformational change due to binding of Ca^{2+}/CaM and autophosphorylation is accountable for the change in FRET. This persistent, Ca^{2+}-independent change in FRET is absent when ATP is omitted or when a kinase dead mutant is used. Furthermore, a phosphoblocking mutant (T286A) stops the persistent change in FRET, whereas a phosphomimicking mutant (T286D) shows decreased FRET without Ca^{2+} stimulation. Hence, Camui detects the collective activation of CaMKII by the binding of Ca^{2+}/CaM and the autophosphorylation at T286. Using a FLIM version of Camui, green-Camuiα, Lee et al. discovered that CaMKII activity is only transient (<2 min) after the induction of structural LTP (sLTP) even though CaMKII activation is required for sustaining structural synaptic plasticity. This is much shorter than what had been believed (Lee et al., 2009).

We investigated the spatial and temporal regulation of CaMKII in rapid ocular dominance (OD) plasticity in layer II/III of ferret visual cortex *in vivo*, a paradigmatic model for studying the role of sensory experience in shaping cortical neural circuits (Mower et al., 2011). By taking advantage of the superficial location of layer II/III pyramidal neurons for optical detection of Camui signals (**Figure 2A**), we found that brief monocular deprivation (MD, 4 h) leads to activation of CaMKII at most synapses in the deprived eye domains (**Figure 2B**). However, a change in CaMKII activity was not observed in the spines located in binocular and non-deprived eye domains following the same visual manipulation. Four hours of MD also lead to the elimination of a small fraction of spines in the deprived eye domain, whose basal CaMKII activity was lower than the average CaMKII activity in the same cortical site. The spines that persisted after MD had either high basal CaMKII activity or increased activity. Therefore, the emerging picture of the role of CaMKII activity *in vivo* is that (1) the eliminated spines have low CaMKII activity (although not all spines with low activity are removed) and (2) high CaMKII activity might have a protective role for spines and these preserved spines could potentially serve as a substrate for the reorganization of intracortical presynaptic partners.

At first, this result is seemingly at odds with the study by Lee et al., where they observed a transient activation of CaMKII by LTP induction with glutamate uncaging. However, this result most likely reflects the ability of CaMKII to respond to different neuronal activity patterns (De Koninck and Schulman, 1998; Fujii et al., 2013). In the study by Lee et al. (2009),

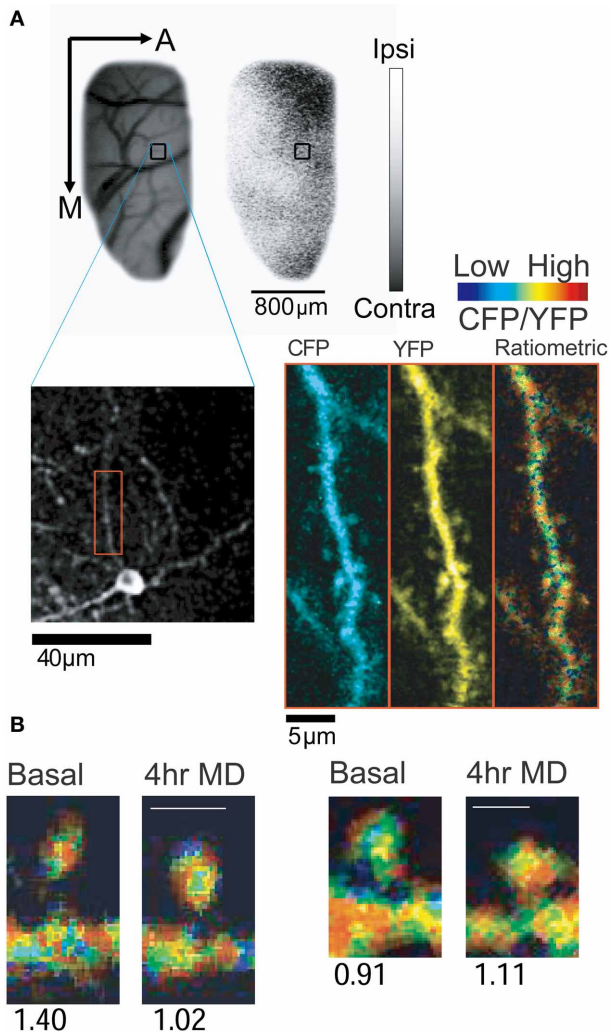

FIGURE 2 | *In vivo* imaging of CaMKII activity using Camui. (A) Expression of Camui in ferret visual cortex allowed for visualization of CaMKII activity in dendrites and spines of a neuron in a specific ocular dominance (OD) domain. Blood vessel and OD maps were acquired using intrinsic signal optical imaging (*Upper panel*: A, anterior; M, medial). Gray scale indicates ocular dominance index (white, ipsilateral eye dominated; black, contralateral eye dominated). Blood vessels map and the low magnification two-photon microscopic image were cross referenced to identify the two-photon images (*Lower panel*) in a given OD map. A dendritic segment (red box) is magnified (*Right*) and displayed as channel separated images (CFP and YFP) as well as a ratiometric image in intensity-modulated display mode, indicating the CFP/YFP ratio. Warm hue represents high CaMKII activity. **(B)** Sample images of spines with decreased (left) or increased (right) CaMKII activity after 4 h of monocular deprivation. Numbers below the images indicate the normalized CFP/YFP ratio, a measurement of FRET signal. From Mower et al. (2011).

CaMKII is activated by local *N*-methyl-D-aspartate type glutamate receptor (NMDA-R) activation. However, in the visual cortex, it likely detects an integration of complex local and global activity patterns that encompass both Hebbian and homeostatic mechanisms. Further studies are required to fully elucidate the role of CaMKII in synaptic plasticity both *in vitro* and *in vivo*.

Small G-protein

Small G-protein family, including Ras, Rho, Ran, Rab, Sar/Arf subfamilies, is a large group of signaling molecules that control various cellular functions (Saneyoshi and Hayashi, 2012). The activity of small G-protein is controlled by intrinsic GTPase activity and by the type of guanine nucleotide it is bound with. GTP-bound form consists active form, which is converted into GDP-bound form by the GTPase activity. The cycle between GDP-bound inactive and GTP-bound active forms is regulated by three classes of proteins, guanine nucleotide exchange factors (GEFs), GTPase-activating proteins (GAPs), and guanine nucleotide dissociation inhibitors (GDIs) (Saneyoshi and Hayashi, 2012). GEFs exchange GDP bound on a small G-protein with GTP, which leads to an activation of signaling activity of the small G-protein. The GTP-bound forms of G-protein lapse into inactive forms when GAP induces activation of GTPase activity that converts the bound GTP to GDP. GDI removes GDP-bound inactive forms of G-proteins from cell membranes and therefore maintains them in inactive forms.

Two family member of Ras family, Ras itself and Rap are implicated in synaptic plasticity. Zhu et al. showed that Ras relays the NMDA-R and CaMKII signaling that drives synaptic delivery of α-amino-3-hydroxy-5-methyl-4-isoxazolepropionic acid type glutamate receptors (AMPA-Rs) during LTP (Zhu et al., 2002). In contrast, Rap mediates NMDA-R-dependent removal of synaptic AMPA-Rs that occurs during LTD. Thus, Ras and Rap serve as independent regulators for potentiating and depressing central synapses. Ras is also implicated in spine formation. The expression of a constitutively active Ras in neocortex neurons lead to an increase in spine density (Gartner et al., 2005). Conversely, a loss of SynGAP, a Ras-GAP that expresses specifically in the brain, leads to an increase in spine formation and enlargement of spine size (Vazquez et al., 2004).

In order to elucidate the Ras activity during LTP in the spines of hippocampal neurons, Yasuda et al. designed an intermolecular FLIM-based probe to detect Ras activity, in which momomeric EGFP was tagged to the N-terminus of Ras, and two momomeric RFPs were attached to the N- and C-termini of the Ras binding domain (RBD) of Raf (Yasuda et al., 2006). When Ras at the plasma membrane is activated, RBD is recruited to the membrane and binds to Ras, resulting in an increase in FRET. Using this probe, they investigated the activity of G-proteins in single dendritic spines in CA1 pyramidal neurons during sLTP. After the induction of sLTP, Ras was activated, which was then maintained for 30 min (Yasuda et al., 2006). Interestingly, the Ras signaling is not restricted to spines but spreads over 10 μm into dendritic shafts and eventually reaches neighboring spines, which can subsequently undergo sLTP with only weak stimulation (a stimulation that would normally induce only temporary potentiation) (Harvey et al., 2008b). These data suggest that the spread of Ras-dependent signaling is necessary for the local regulation of the LTP induction threshold.

Rho family G-proteins, including ras homolog family member (Rho), ras-related C3 botulinum toxin substrate (Rac), and cell division control protein 42 homolog (Cdc42), are small GTP binding proteins that control the actin cytoskeleton (Komatsu et al., 2011; Saneyoshi and Hayashi, 2012). Because actin is the

major cytoskeletal protein in dendritic spines, the role of the Rho family G-proteins on the maintenance and rearrangement of spine morphology has been investigated (Saneyoshi and Hayashi, 2012). The expression of a constitutively active form of Rac1 in hippocampal pyramidal neurons leads to an increase in the number (Tashiro et al., 2000), length and width of spines (Zhang and Macara, 2006), while a dominant negative had the opposite effect (Nakayama et al., 2000; Zhang and Macara, 2006; Impey et al., 2010). In contrast, a constitutively active form of RhoA reduces the density of spines (Tashiro et al., 2000; Impey et al., 2010) and causes a simplification of dendritic branch pattern (Nakayama et al., 2000). Inhibition of RhoA activity leads to an increase in the number of spines in some neurons (Tashiro et al., 2000; Impey et al., 2010). Cdc42 is also implicated in spine morphogenesis (Tashiro et al., 2000; Irie and Yamaguchi, 2002).

Murakoshi also applied the same Ras probe design strategy to construct probes for Rho family protein (Murakoshi et al., 2011). The temporal and spatial extent of activity spreading over the dendritic shaft was investigated (Murakoshi et al., 2011). Activity of both RhoA and Cdc42 was maintained for up to 30 min, which is consistent with the observation that the filamentous (F-) actin/globular (G-) actin equilibrium moves toward F-actin after LTP induction (Okamoto et al., 2004, see below). RhoA spreads with a length constant of 4.5 μm along the dendrite. On the other hand, Cdc42 activity was restricted only in the stimulated spine, whose length constant is 1.9 μm.

Phosphatidylinositol 3,4,5-Trisphosphate (PIP_3)

PIP_3 is a phosphoinositide that plays an important role in a variety of cellular functions. PIP_3 is produced from phosphatidylinositol 4,5-bisphosphate (PIP_2) by phosphoinositide 3-kinase (PI3K) in response to hormone and neurotransmitter while PTEN converts PIP_3 back to PIP_2. In hippocampal pyramidal neurons, PIP_3 is crucial for maintaining AMPA-R clustering during LTP (Arendt et al., 2010). PIP_3 also regulates neuronal polarity, dendritic arborization, and nerve growth factor-induced axonal filopodia formation (Jaworski et al., 2005; Ketschek and Gallo, 2010). In order to exert these functions, local PIP_3 accumulation leads to the recruitment of effector proteins such as Akt (Thomas et al., 2001), WASP family Verprolin-homologous protein (WAVE) (Oikawa et al., 2004) and GEF of small G proteins to specific subcellular compartments (Han et al., 1998; Shinohara et al., 2002; Innocenti et al., 2003).

In order to investigate PIP_3 function and regulation in spines, we developed a FLIM-based PIP_3 FRET probe, FLIMPA3, by concatenating a donor, a specific PIP_3-binding domain, flexible di-glycine hinge, and an acceptor tethered to the membranes through rigid α-helical linkers (Sato et al., 2003; Murakoshi et al., 2008; Ueda and Hayashi, 2013) (**Figure 1G**). When FLIMPA3 was expressed in hippocampal CA1 pyramidal neurons, we found that PIP_3 showed greater accumulation in spines than in dendritic shafts under basal conditions (Ueda and Hayashi, 2013). PI3K inhibitor treatment decreased PIP_3 accumulation in spines, indicating that PIP_3 accumulation is largely due to basal PI3K activity in spines. This result is consistent with a previous report in which PI3K is ubiquitously localized in neuronal cells, but only becomes active after AMPA-R binding (Man et al., 2003). During sLTP, PIP_3 in spines was reduced. Application of a PTEN inhibitor did not significantly change the reduction in PIP_3. Additionally, the reduction of PIP_3 after sLTP was highly correlated with PIP_3 enrichment before sLTP induction. Therefore, the reduction in PIP_3 during sLTP is likely to be due to the addition of membrane from the dendritic shaft. Interestingly, whilst PIP_3 globally decreases in spines during sLTP, we observed a specific accumulation of PIP_3 in spinules, filopodia-like protrusions found on spines. When PIP_3 in spinules was blocked by a PI3K inhibitor that reduces PIP_3 levels, the number of spinules after sLTP were diminished, indicating that PIP_3 in spinules regulates spinule formation.

Electron microscopic studies found that spinules could be trans-synaptically endocytosed by presynaptic terminals as separate vesicles from the postsynaptic side (Spacek and Harris, 2004). Therefore, the trans-endocytosis of spinules may serve as a mechanism for retrograde signaling or may aid postsynaptic membrane remodeling by removing excess membrane (Spacek and Harris, 2004). Accumulated PIP_3 in spinules that traffic to the presynaptic side may act as a retrograde signal or contribute to the formation of new synapses with functional presynaptic boutons.

Extracellular Signal-regulated Kinase (ERK)

ERK is a serine/threonine protein kinase that belongs to the mitogen-activated protein kinase (MAPK) family, which plays important roles in a variety of cellular functions such as cell differentiation, proliferation, and survival (Chang and Karin, 2001). In neuronal circuits, ERK is involved in a wide range of functions including the regulation of dendritic protein synthesis (Impey et al., 1998a,b; Roberson et al., 1999; Davis et al., 2000; Patterson et al., 2001; Waltereit et al., 2001), morphological changes in dendritic spines (Wu et al., 2001; Goldin and Segal, 2003) and hippocampal LTP and memory formation *in vivo* (Giovannini et al., 2001). Abnormal ERK signaling is associated with mental retardation (Costa et al., 2002).

In order to obtain information about the spatiotemporal dynamics of ERK activity in neuronal cells, several FRET-based probes have been developed. Miu2 detects the conformational change of ERK activation by flanking ERK with CFP and YFP (Fujioka et al., 2006). Erkus is based on the detection of substrate protein phosphorylation (Sato et al., 2007) (**Figure 1F**). The ERK substrate sequence was obtained from EGFR and fused to the phospho-binding domain from FHA2 by a flexible peptide linker. The D domain, a sequence that selectively binds to ERK was attached to increase the specificity and efficiency of phosphorylation. This fusion protein was flanked by CFP and YFP. When phospho-substrate peptide is phosphorylated by active ERK, the phosphoprotein-binding domain interacts with the phospho-substrate peptide, leading to a change in overall conformation, which can be detected by a change in FRET efficiency. EKAR uses a similar approach but with a different substrate and a phosphoprotein-binding domain (Harvey et al., 2008a).

Using EKAR in hippocampal pyramidal neurons, Harvey et al. observed ERK activity induced by back-propagating action potentials (Harvey et al., 2008a). Stimulated bursts of action potentials caused global Ca^{2+} influx through voltage-gated Ca^{2+} channels, leading to Ras activation, an upstream molecule of

ERK (Yasuda et al., 2006; Harvey et al., 2008b). After stimulation, ERK activity reached a peak by around 5 min, then gradually decreased, and finally returned to basal levels by 30 min. The time course of ERK activation was longer than that of Ras, consistent with the idea that ERK is the downstream effector of Ras. They also investigated ERK activity in the somatic cytoplasm and nucleus of neuronal cells. After theta-burst stimulation, ERK activity in both regions was up-regulated in a parallel manner, indicating that global Ca^{2+} influx through VGCCs can diffuse rapidly between these two compartments (Harvey et al., 2008a).

Chloride sensor

Cl^- ion regulates neuronal properties such as intracellular pH, cell volume, and fluid secretion (Duran et al., 2010). More importantly, Cl^- is a major carrier of electrical current in inhibitory synaptic transmission mediated by GABA and glycine receptors. The basal level of intracellular chloride ions (Cl^-) is maintained by a number of mechanisms including chloride transporter system that consist of Na^+-Cl^-, Na^+-K^+-$2Cl^-$, and K^+-Cl^- transporters, and the activation of tonic GABA receptors, calcium-activated Cl^- channels, cAMP-activated Cl^- channels, cell-volume regulated anion channels, and transporters localized within subcellular organelles (Duran et al., 2010). Since all these factors sum up to determine the intracellular Cl^- concentration, it is of a great interest to visualize the dynamics of intracellular Cl^-.

The chloride sensor, Clomeleon, consists of CFP, a flexible peptide linker, and a Cl^- sensitive YFP (with S65G, S72A, K79R, T203Y, H231L mutations) (Kuner and Augustine, 2000). YFP intensity is quenched in the presence of Cl^-, thereby changing FRET efficiency in a Cl^- concentration-dependent manner. Using this probe, in hippocampal dissociated cultures of neurons and glial cells, the developmental time course of Cl^- concentration was investigated (Kuner and Augustine, 2000). While the Cl^- concentration in glia cells was low throughout embryonic and postnatal stages, the concentration in neurons was higher at embryonic stages, and then decreased during postnatal development, consistent with the observation that activation of GABA receptors in immature neurons leads to neuronal excitation rather than inhibition (Kuner and Augustine, 2000). Using this probe, it was also possible to observe Cl^- influx through GABA receptors in hippocampal CA1 pyramidal neurons following interneuron stimulation (Berglund et al., 2006). However, at this point, the sensitivity of the Cl^- sensor is not as good as to visualize Cl^- influx induced by unitary inhibitory postsynaptic current (ipsc). This would require further elaboration of the probe.

Actin

Actin is the major cytoskeletal protein in dendritic spines (Matus, 2005; Okamoto et al., 2009). It exists in equilibrium between two forms, globular (G-actin) and filamentous actin (F-actin) (Okamoto et al., 2009; Saneyoshi and Hayashi, 2012). Actin has a rapid turnover time within the dendritic spine. An experiment using fluorescence recovery after photobleaching (FRAP) of GFP-fused actin revealed that over 85% of actin in dendritic spines is dynamically turning over, with an average time constant of 44 s (Star et al., 2002). This dynamic turnover is the underlying molecular basis of motility and morphological changes of spines (Okamoto et al., 2004, 2009; Matus, 2005; Honkura et al., 2008).

As in non-neuronal cells, F-actin in dendritic spines undergoes a unique directional treadmilling as revealed with experiments using a photoactivatable (PA)-GFP-actin or a photoconvertable fluorescent protein (Honkura et al., 2008; Frost et al., 2010). G-actin is added to the barbed end of F-actin at the periphery of dendritic spines and at the base of the dendritic spine, F-actin is continuously disassembled to G-actin at the pointed end of actin. Taken together, there is an overall directional movement of F-actin from the periphery toward the spine base (Honkura et al., 2008; Frost et al., 2010). Another way to look at this is to divide the actin population into different pools. The first pool of F-actin, found at the periphery, has a relatively high turnover of about 40 s (Honkura et al., 2008). The second pool is the population that resides at the base of spines, with a turnover time of 17 min (Honkura et al., 2008). These two pools are relatively static and help to maintain the overall spine shape and size. In addition, there is a third pool that appears after LTP induction (Honkura et al., 2008). The turnover time of this pool is 2–15 min and it spreads all over the spine. This pool is required to maintain dendritic spine enlargement upon sLTP induction. If this pool extrudes into the dendritic shafts then sLTP was not maintained.

Actin exists in equilibrium between F-actin/G-actin but it was not known how the F-actin/ G-actin equilibrium changes during synaptic plasticity. This is because the dendritic spine is too small and does not show discrete F-actin structure that is observable with light microscopy. To circumvent this, an intermolecular FRET approach was used to monitor the F-actin/ G-actin equilibrium (Okamoto et al., 2004). The distance between actin monomers in F-actin is 55 Å, which is within the appropriate range to be detected with FRET. Actin was tagged with CFP and YFP as a donor and an acceptor, respectively. Using this approach, Okamoto et al. observed actin dynamics in hippocampal CA1 pyramidal neuronal cells during bidirectional plasticity (Okamoto et al., 2004). Upon tetanic stimulation, the equilibrium of F-actin/G-actin shifted toward F-actin, which was accompanied by spine enlargement (**Figure 3**). In contrast, prolonged low-frequency stimulation, typically inducing LTD, lead to spine shrinkage and actin depolymerization. This evidence suggests that the equilibrium of F-actin/ G-actin regulates bidirectional structural plasticity.

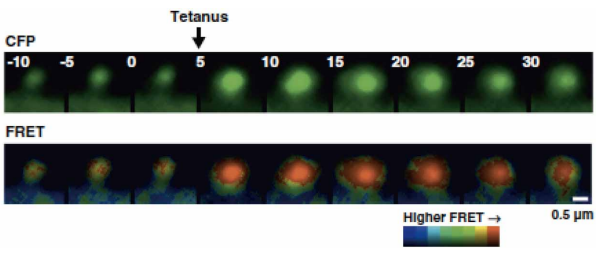

FIGURE 3 | Dendritic spine expressing actin FRET probe. Single dendritic spine that was subjected to local tetanic stimulation is accompanied by the enlargement of spine and actin polymerization. From Okamoto et al. (2004).

Voltage sensors

Electrophysiological recordings are considered to be the "gold standard" technique for measuring neuronal membrane potentials. However, several drawbacks to this method exist, such as the invasive nature of the technique and limitations in the number of neurons that can be measured simultaneously. To circumvent these issues, small molecular weight voltage-sensitive fluorescent dyes have been used with some success. The main disadvantage of using small molecular weight voltage-sensitive fluorescent dyes is the lack of cell-type specificity, because the dyes are generally bogus loaded and taken up by cells in a non-specific manner. It is also important to note that the dyes can diminish over time or cause toxicity. Therefore, these dyes are mostly suited for use in acute experiments.

Genetically-encoded membrane potential sensors, VSFP2 (Sakai et al., 2001) and Mermaid (Tsutsui et al., 2008), allow us to visualize the membrane voltage of a large number of individual neurons with high temporal resolution. Both probes are based on a membrane embedded phosphatase that senses voltage, Ci-VSP, a protein derived from tunicate, *Ciona intestinalis*. Ci-VSP is composed of a voltage-sensor domain (VSD) and phosphatase domain (Murata et al., 2005). The phosphatase domain on the C-terminus was replaced with a fluorophore pair fused in tandem. Membrane depolarization causes a conformational change in the overall structure, leading to a decrease in the distance between fluorophores, and ultimately a change in FRET efficiency. In cultured cortical neurons expressing Mermaid, a stimulated burst (30 pulses at 100 Hz) of spikes could be observed (Tsutsui et al., 2008). Recently, VSFP-butterfly and ArcLight were developed, where the acceptor was moved from the C-terminus to the N-terminus (Akemann et al., 2012, 2013; Jin et al., 2012). VSFP-butterfly has been used to visualize changes in membrane voltage elicited by the stimulation of a single whisker in layer 2/3 pyramidal neurons in the mouse barrel cortex (Akemann et al., 2012). The authors also succeeded in visualizing spontaneous slow brain oscillations traveling over the somatosensory cortex (Akemann et al., 2012).

CONCLUDING REMARKS

In 1990s, the readout of synaptic plasticity was mostly limited to the size of electrical response of synapse. The data were analyzed by applying to mathematical model of synaptic transmission established from studies on neuromuscular junction, which later turned out to be not compatible to the central synapse and caused a huge confusion in the field. The title of a review written by Sanes and Lichtman "Can molecules explain long-term potentiation?" (Sanes and Lichtman, 1999), well represents the sentiment around that time on the never-ending debate on the mechanism of LTP. Fortunately, the recent introduction of technologies to optically measure the activity of molecules involved in synaptic plasticity has drastically changed the field and successfully clarified a number of points that remained unsolved before and provided new concepts of synaptic plasticity.

In the quest to understand the molecular mechanisms underpinning neuronal circuit plasticity, FRET has played a critical role in revealing important insights into the spatiotemporal dynamics of the key players. However, limiting its further application, it has been empirically known that it is difficult to establish transgenic mice expressing FRET probes (Hara et al., 2004). This may be due to the repeat of very similar DNA sequence (CFP and YFP) within transgene (Kamioka et al., 2012). It is also possible that probe proteins work as a gain-of-function mutant that hampers the function of endogenous proteins (Hara et al., 2004). Nonetheless, number of transgenic animals expressing FRET probes has been increasing (Hara et al., 2004; Berglund et al., 2006; Zhang et al., 2010; Yamaguchi et al., 2011; Kamioka et al., 2012; Wang et al., 2012; Thunemann et al., 2013). Additional difficulty lies in the detection of FRET, especially in the *in vivo* preparation. In practice, the animal's heartbeat and breathing introduce not only the movement of the cells during imaging but also the hemodynamic noise and therefore changes the absorbance in the optical path of the excitation and emission of fluorescence (Akemann et al., 2012). This will affect the accuracy of FRET data acquisition. With continued technological advances, it will be possible to apply FRET to increasingly complex preparations, even *in vivo,* to fully understand the complicated neuronal signaling processes that occur in the ever-changing brain.

AUTHOR CONTRIBUTIONS

Yoshibumi Ueda, Showming Kwok, and Yasunori Hayashi jointly wrote the manuscript.

ACKNOWLEDGMENTS

We thank Takeo Saneyoshi, Akihiro Goto, Ryan A. Colyer, and Lily Yu for comments on the manuscript. This work was supported by RIKEN, NIH grant R01DA17310, Grant-in-Aid for Scientific Research (A) and Grant-in-Aid for Scientific Research on Innovative Area "Foundation of Synapse and Neurocircuit Pathology" from the Ministry of Education, Culture, Sports, Science and Technology of Japan (Yasunori Hayashi).

REFERENCES

Adams, S. R., Harootunian, A. T., Buechler, Y. J., Taylor, S. S., and Tsien, R. Y. (1991). Fluorescence ratio imaging of cyclic AMP in single cells. *Nature* 349, 694–697. doi: 10.1038/349694a0

Akemann, W., Mutoh, H., Perron, A., Park, Y. K., Iwamoto, Y., and Knöpfel, T. (2012). Imaging neural circuit dynamics with a voltage-sensitive fluorescent protein. *J. Neurophysiol.* 108, 2323–2337. doi: 10.1152/jn.00452.2012

Akemann, W., Sasaki, M., Mutoh, H., Imamura, T., Honkura, N., and Knopfel, T. (2013). Two-photon voltage imaging using a genetically encoded voltage indicator. *Sci. Rep.* 3, 2231. doi: 10.1038/srep02231

Aoki, K., Nakamura, T., and Matsuda, M. (2004). Spatio-temporal regulation of Rac1 and Cdc42 activity during nerve growth factor-induced neurite outgrowth in PC12 cells. *J. Biol. Chem.* 279, 713–719. doi: 10.1074/jbc.M306382200

Arendt, K. L., Royo, M., Fernandez-Monreal, M., Knafo, S., Petrok, C. N., Martens, J. R., et al. (2010). PIP3 controls synaptic function by maintaining AMPA receptor clustering at the postsynaptic membrane. *Nat. Neurosci.* 13, 36–44. doi: 10.1038/nn.2462

Awais, M., Sato, M., Lee, X., and Umezawa, Y. (2006). A fluorescent indicator to visualize activities of the androgen receptor ligands in single living cells. *Angew. Chem.*

Int. Ed. Engl. 45, 2707–2712. doi: 10.1002/anie.200503185

Awais, M., Sato, M., Sasaki, K., and Umezawa, Y. (2004). A genetically encoded fluorescent indicator capable of discriminating estrogen agonists from antagonists in living cells. *Anal. Chem.* 76, 2181–2186. doi: 10.1021/ac030410g

Awais, M., Sato, M., and Umezawa, Y. (2007a). Optical probes to identify the glucocorticoid receptor ligands in living cells. *Steroids* 72, 949–954. doi: 10.1016/j.steroids.2007.08.006

Awais, M., Sato, M., and Umezawa, Y. (2007b). Imaging of selective nuclear receptor modulator-induced conformational changes in the nuclear receptor to allow interaction with coactivator and corepressor proteins in living cells. *Chembiochem* 8, 737–743. doi: 10.1002/cbic.200700001

Awaji, T., Hirasawa, A., Shirakawa, H., Tsujimoto, G., and Miyazaki, S. (2001). Novel green fluorescent protein-based ratiometric indicators for monitoring pH in defined intracellular microdomains. *Biochem. Biophys. Res. Commun.* 289, 457–462. doi: 10.1006/bbrc.2001.6004

Berglund, K., Schleich, W., Krieger, P., Loo, L. S., Wang, D., Cant, N. B., et al. (2006). Imaging synaptic inhibition in transgenic mice expressing the chloride indicator, Clomeleon. *Brain Cell Biol.* 35, 207–228. doi: 10.1007/s11068-008-9019-6

Bosch, M., and Hayashi, Y. (2012). Structural plasticity of dendritic spines. *Curr. Opin. Neurobiol.* 22, 383–388. doi: 10.1016/j.conb.2011.09.002

Braun, D. C., Garfield, S. H., and Blumberg, P. M. (2005). Analysis by fluorescence resonance energy transfer of the interaction between ligands and protein kinase Cdelta in the intact cell. *J. Biol. Chem.* 280, 8164–8171. doi: 10.1074/jbc.M413896200

Cai, X., Lietha, D., Ceccarelli, D. F., Karginov, A. V., Rajfur, Z., Jacobson, K., et al. (2008). Spatial and temporal regulation of focal adhesion kinase activity in living cells. *Mol. Cell. Biol.* 28, 201–214. doi: 10.1128/MCB.01324-07

Calleja, V., Alcor, D., Laguerre, M., Park, J., Vojnovic, B., Hemmings, B. A., et al. (2007). Intramolecular and intermolecular interactions of protein kinase B define its activation *in vivo*. *PLoS Biol.* 5:e95. doi: 10.1371/journal.pbio.0050095

Carrillo, L. D., Krishnamoorthy, L., and Mahal, L. K. (2006). A cellular FRET-based sensor for beta-O-GlcNAc, a dynamic carbohydrate modification involved in signaling. *J. Am. Chem. Soc.* 128, 14768–14769. doi: 10.1021/ja065835+

Chang, L., and Karin, M. (2001). Mammalian MAP kinase signalling cascades. *Nature* 410, 37–40. doi: 10.1038/35065000

Chen, J. L., Carta, S., Soldado-Magraner, J., Schneider, B. L., and Helmchen, F. (2013). Behaviour-dependent recruitment of long-range projection neurons in somatosensory cortex. *Nature* 499, 336–340. doi: 10.1038/nature12236

Chen, X., Vinade, L., Leapman, R. D., Petersen, J. D., Nakagawa, T., Phillips, T. M., et al. (2005). Mass of the postsynaptic density and enumeration of three key molecules. *Proc. Natl. Acad. Sci. U.S.A.* 102, 11551–11556. doi: 10.1073/pnas.0505359102

Chew, T. L., Wolf, W. A., Gallagher, P. J., Matsumura, F., and Chisholm, R. L. (2002). A fluorescent resonant energy transfer-based biosensor reveals transient and regional myosin light chain kinase activation in lamella and cleavage furrows. *J. Cell Biol.* 156 543–553. doi: 10.1083/jcb.200110161

Citri, A., and Malenka, R. C. (2008). Synaptic plasticity: multiple forms, functions, and mechanisms. *Neuropsychopharmacology* 33, 18–41. doi: 10.1038/sj.npp.1301559

Colyer, R. A., Siegmund, O. H., Tremsin, A. S., Vallerga, J. V., Weiss, S., and Michalet, X. (2012). Phasor imaging with a wide-field photon-counting detector. *J. Biomed. Opt.* 17, 016008. doi: 10.1117/1.JBO.17.1.016008

Corradi, G. R., and Adamo, H. P. (2007). Intramolecular fluorescence resonance energy transfer between fused autofluorescent proteins reveals rearrangements of the N- and C-terminal segments of the plasma membrane Ca2+ pump involved in the activation. *J. Biol. Chem.* 282, 35440–35448. doi: 10.1074/jbc.M703377200

Costa, R. M., Federov, N. B., Kogan, J. H., Murphy, G. G., Stern, J., Ohno, M., et al. (2002). Mechanism for the learning deficits in a mouse model of neurofibromatosis type 1. *Nature* 415, 526–530. doi: 10.1038/nature711

Davis, S., Vanhoutte, P., Pages, C., Caboche, J., and Laroche, S. (2000). The MAPK/ERK cascade targets both Elk-1 and cAMP response element-binding protein to control long-term potentiation-dependent gene expression in the dentate gyrus *in vivo*. *J. Neurosci.* 20, 4563–4572.

De Koninck, P., and Schulman, H. (1998). Sensitivity of CaM kinase II to the frequency of Ca^{2+} oscillations. *Science* 279, 227–230. doi: 10.1126/science.279.5348.227

Duran, C., Thompson, C. H., Xiao, Q., and Hartzell, H. C. (2010). Chloride channels: often enigmatic, rarely predictable. *Annu. Rev. Physiol.* 72, 95–121. doi: 10.1146/annurev-physiol-021909-135811

Endoh, T., Funabashi, H., Mie, M., and Kobatake, E. (2005). Method for detection of specific nucleic acids by recombinant protein with fluorescent resonance energy transfer. *Anal. Chem.* 77, 4308–4314. doi: 10.1021/ac048491j

Fehr, M., Frommer, W. B., and Lalonde, S. (2002). Visualization of maltose uptake in living yeast cells by fluorescent nanosensors. *Proc. Natl. Acad. Sci. U.S.A.* 99, 9846–9851. doi: 10.1073/pnas.142089199

Fehr, M., Lalonde, S., Lager, I., Wolff, M. W., and Frommer, W. B. (2003). *In vivo* imaging of the dynamics of glucose uptake in the cytosol of COS-7 cells by fluorescent nanosensors. *J. Biol. Chem.* 278, 19127–19133. doi: 10.1074/jbc.M301333200

Förster, T. (1946). Energiewanderung und Fluoreszenz. *Naturbreakwissenschaften* 33, 166–175. doi: 10.1007/BF00585226

Fosbrink, M., Aye-Han, N. N., Cheong, R., Levchenko, A., and Zhang, J. (2010). Visualization of JNK activity dynamics with a genetically encoded fluorescent biosensor. *Proc. Natl. Acad. Sci. U.S.A.* 107, 5459–5464. doi: 10.1073/pnas.0909671107

Frost, N. A., Shroff, H., Kong, H., Betzig, E., and Blanpied, T. A. (2010). Single-molecule discrimination of discrete perisynaptic and distributed sites of actin filament assembly within dendritic spines. *Neuron* 67, 86–99. doi: 10.1016/j.neuron.2010.05.026

Fujii, H., Inoue, M., Okuno, H., Sano, Y., Takemoto-Kimura, S., Kitamura, K., et al. (2013). Nonlinear decoding and asymmetric representation of neuronal input information by CaMKIIα and calcineurin. *Cell Rep.* 3, 978–987. doi: 10.1016/j.celrep.2013.03.033

Fujioka, A., Terai, K., Itoh, R. E., Aoki, K., Nakamura, T., Kuroda, S., et al. (2006). Dynamics of the Ras/ERK MAPK cascade as monitored by fluorescent probes. *J. Biol. Chem.* 281, 8917–8926. doi: 10.1074/jbc.M509344200

Fuller, B. G., Lampson, M. A., Foley, E. A., Rosasco-Nitcher, S., Le, K. V., Tobelmann, P., et al. (2008). Midzone activation of aurora B in anaphase produces an intracellular phosphorylation gradient. *Nature* 453, 1132–1136. doi: 10.1038/nature06923

Ganesan, S., Ameer-Beg, S. M., Ng, T. T., Vojnovic, B., and Wouters, F. S. (2006). A dark yellow fluorescent protein (YFP)-based resonance energy-accepting chromoprotein (REACh) for Förster resonance energy transfer with GFP. *Proc. Natl. Acad. Sci. U.S.A.* 103, 4089–4094. doi: 10.1073/pnas.0509922103

Gartner, U., Alpar, A., Behrbohm, J., Heumann, R., and Arendt, T. (2005). Enhanced Ras activity promotes spine formation in synRas mice neocortex. *Neuroreport* 16, 149–152. doi: 10.1097/00001756-200502080-00016

Gavet, O., and Pines, J. (2010). Progressive activation of CyclinB1-Cdk1 coordinates entry to mitosis. *Dev. Cell* 18, 533–543. doi: 10.1016/j.devcel.2010.02.013

Giovannini, M. G., Blitzer, R. D., Wong, T., Asoma, K., Tsokas, P., Morrison, J. H., et al. (2001). Mitogen-activated protein kinase regulates early phosphorylation and delayed expression of Ca^{2+}/calmodulin-dependent protein kinase II in long-term potentiation. *J. Neurosci.* 21, 7053–7062.

Goedhart, J., von Stetten, D., Noirclerc-Savoye, M., Lelimousin, M., Joosen, L., Hink, M. A., et al. (2012). Structure-guided evolution of cyan fluorescent proteins towards a quantum yield of 93%. *Nat. Commun.* 3, 751. doi: 10.1038/ncomms1738

Goldin, M., and Segal, M. (2003). Protein kinase C and ERK involvement in dendritic spine plasticity in cultured rodent hippocampal neurons. *Eur. J. Neurosci.* 17, 2529–2539. doi: 10.1046/j.1460-9568.2003.02694.x

Gonzalez, J. E., and Tsien, R. Y. (1995). Voltage sensing by fluorescence resonance energy transfer in single cells. *Biophys. J.* 69, 1272–1280. doi: 10.1016/S0006-3495(95)80029-9

Haj, F. G., Verveer, P. J., Squire, A., Neel, B. G., and Bastiaens, P. I. (2002). Imaging sites of receptor dephosphorylation by PTP1B on the surface of the endoplasmic reticulum. *Science* 295, 1708–1711. doi: 10.1126/science.1067566

Han, J., Luby-Phelps, K., Das, B., Shu, X., Xia, Y., Mosteller, R. D., et al. (1998). Role of substrates

and products of PI 3-kinase in regulating activation of Rac-related guanosine triphosphatases by Vav. *Science* 279, 558–560. doi: 10.1126/science.279.5350.558

Hao, Y., and Macara, I. G. (2008). Regulation of chromatin binding by a conformational switch in the tail of the Ran exchange factor RCC1. *J. Cell Biol.* 182, 827–836. doi: 10.1083/jcb.200803110

Hara, M., Bindokas, V., Lopez, J. P., Kaihara, K., Landa, L. R. Jr., Harbeck, M., et al. (2004). Imaging endoplasmic reticulum calcium with a fluorescent biosensor in transgenic mice. *Am. J. Physiol. Cell Physiol.* 287, C932–C938. doi: 10.1152/ajpcell.00151.2004

Harvey, C. D., Ehrhardt, A. G., Cellurale, C., Zhong, H., Yasuda, R., Davis, R. J., et al. (2008a). A genetically encoded fluorescent sensor of ERK activity. *Proc. Natl. Acad. Sci. U.S.A.* 105, 19264–19269. doi: 10.1073/pnas.0804598105

Harvey, C. D., Yasuda, R., Zhong, H., and Svoboda, K. (2008b). The spread of Ras activity triggered by activation of a single dendritic spine. *Science* 321, 136–140. doi: 10.1126/science.1159675

Haspel, G., O'Donovan, M. J., and Hart, A. C. (2010). Motoneurons dedicated to either forward or backward locomotion in the nematode *Caenorhabditis elegans*. *J. Neurosci.* 30, 11151–11156. doi: 10.1523/JNEUROSCI.2244-10.2010

Hayashi, Y., and Majewska, A. K. (2005). Dendritic spine geometry: functional implication and regulation. *Neuron* 46, 529–532. doi: 10.1016/j.neuron.2005.05.006

Heim, N., and Griesbeck, O. (2004). Genetically encoded indicators of cellular calcium dynamics based on troponin C and green fluorescent protein. *J. Biol. Chem.* 279, 14280–14286. doi: 10.1074/jbc.M312751200

Hitosugi, T., Sasaki, K., Sato, M., Suzuki, Y., and Umezawa, Y. (2007). Epidermal growth factor directs sex-specific steroid signaling through Src activation. *J. Biol. Chem.* 282, 10697–10706. doi: 10.1074/jbc.M610444200

Holtmaat, A., and Svoboda, K. (2009). Experience-dependent structural synaptic plasticity in the mammalian brain. *Nat. Rev. Neurosci.* 10, 647–658. doi: 10.1038/nrn2699

Homma, K., Niino, Y., Hotta, K., and Oka, K. (2008). Ca^{2+} influx through P2X receptors induces actin cytoskeleton reorganization by the formation of cofilin rods in neurites. *Mol. Cell. Neurosci.* 37, 261–270. doi: 10.1016/j.mcn.2007.10.001

Honda, A., Adams, S. R., Sawyer, C. L., Lev-Ram, V., Tsien, R. Y., and Dostmann, W. R. (2001). Spatiotemporal dynamics of guanosine 3', 5'-cyclic monophosphate revealed by a genetically encoded, fluorescent indicator. *Proc. Natl. Acad. Sci. U.S.A.* 98, 2437–2442. doi: 10.1073/pnas.051631298

Honkura, N., Matsuzaki, M., Noguchi, J., Ellis-Davies, G. C., and Kasai, H. (2008). The subspine organization of actin fibers regulates the structure and plasticity of dendritic spines. *Neuron* 57, 719–729. doi: 10.1016/j.neuron.2008.01.013

Horikawa, K., Yamada, Y., Matsuda, T., Kobayashi, K., Hashimoto, M., Matsu-ura, T., et al. (2010). Spontaneous network activity visualized by ultrasensitive Ca(2+) indicators, yellow cameleon-nano. *Nat. Methods* 7, 729–732. doi: 10.1038/nmeth.1488

Imamura, H., Nhat, K. P., Togawa, H., Saito, K., Iino, R., Kato-Yamada, Y., et al. (2009). Visualization of ATP levels inside single living cells with fluorescence resonance energy transfer-based genetically encoded indicators. *Proc. Natl. Acad. Sci. U.S.A.* 106, 15651–15656. doi: 10.1073/pnas.0904764106

Impey, S., Davare, M., Lesiak, A., Fortin, D., Ando, H., Varlamova, O., et al. (2010). An activity-induced microRNA controls dendritic spine formation by regulating Rac1-PAK signaling. *Mol. Cell. Neurosci.* 43, 146–156. doi: 10.1016/j.mcn.2009.10.005

Impey, S., Obrietan, K., Wong, S. T., Poser, S., Yano, S., Wayman, G., et al. (1998a). Cross talk between ERK and PKA is required for Ca^{2+} stimulation of CREB-dependent transcription and ERK nuclear translocation. *Neuron* 21, 869–883. doi: 10.1016/S0896-6273(00)80602-9

Impey, S., Smith, D. M., Obrietan, K., Donahue, R., Wade, C., and Storm, D. R. (1998b). Stimulation of cAMP response element (CRE)-mediated transcription during contextual learning. *Nat. Neurosci.* 1, 595–601.

Innocenti, M., Frittoli, E., Ponzanelli, I., Falck, J. R., Brachmann, S. M., Di Fiore, P. P., et al. (2003). Phosphoinositide 3-kinase activates Rac by entering in a complex with Eps8, Abi1, and Sos-1. *J. Cell Biol.* 160, 17–23. doi: 10.1083/jcb.200206079

Irie, F., and Yamaguchi, Y. (2002). EphB receptors regulate dendritic spine development via intersectin, Cdc42 and N-WASP. *Nat. Neurosci.* 5, 1117–1118. doi: 10.1038/nn964

Jaworski, J., Spangler, S., Seeburg, D. P., Hoogenraad, C. C., and Sheng, M. (2005). Control of dendritic arborization by the phosphoinositide-3′-kinase-Akt-mammalian target of rapamycin pathway. *J. Neurosci.* 25, 11300–11312. doi: 10.1523/JNEUROSCI.2270-05.2005

Jin, L., Han, Z., Platisa, J., Wooltorton, J. R., Cohen, L. B., and Pieribone, V. A. (2012). Single action potentials and subthreshold electrical events imaged in neurons with a fluorescent protein voltage probe. *Neuron* 75, 779–785. doi: 10.1016/j.neuron.2012.06.040

Johnson, S. A., You, Z., and Hunter, T. (2007). Monitoring ATM kinase activity in living cells. *DNA Repair (Amst.)* 6, 1277–1284. doi: 10.1016/j.dnarep.2007.02.025

Joseph, J., Seervi, M., Sobhan, P. K., and Retnabai, S. T. (2011). High throughput ratio imaging to profile caspase activity: potential application in multiparameter high content apoptosis analysis and drug screening. *PLoS ONE* 6:e20114. doi: 10.1371/journal.pone.0020114

Kamioka, Y., Sumiyama, K., Mizuno, R., Sakai, Y., Hirata, E., Kiyokawa, E., et al. (2012). Live imaging of protein kinase activities in transgenic mice expressing FRET biosensors. *Cell Struct. Funct.* 37, 65–73. doi: 10.1247/csf.11045

Kawase, K., Nakamura, T., Takaya, A., Aoki, K., Namikawa, K., Kiyama, H., et al. (2006). GTP hydrolysis by the Rho family GTPase TC10 promotes exocytic vesicle fusion. *Dev. Cell* 11, 411–421. doi: 10.1016/j.devcel.2006.07.008

Kennedy, M. B., Bennett, M. K., and Erondu, N. E. (1983). Biochemical and immunochemical evidence that the "major postsynaptic density protein" is a subunit of a calmodulin-dependent protein kinase. *Proc. Natl. Acad. Sci. U.S.A.* 80, 7357–7361. doi: 10.1073/pnas.80.23.7357

Ketschek, A., and Gallo, G. (2010). Nerve growth factor induces axonal filopodia through localized microdomains of phosphoinositide 3-kinase activity that drive the formation of cytoskeletal precursors to filopodia. *J. Neurosci.* 30, 12185–12197. doi: 10.1523/JNEUROSCI.1740-10.2010

Kitano, M., Nakaya, M., Nakamura, T., Nagata, S., and Matsuda, M. (2008). Imaging of Rab5 activity identifies essential regulators for phagosome maturation. *Nature* 453, 241–245. doi: 10.1038/nature06857

Kiyokawa, E., Aoki, K., Nakamura, T., and Matsuda, M. (2011). Spatiotemporal regulation of small GTPases as revealed by probes based on the principle of forster resonance energy transfer (FRET): implications for signaling and pharmacology. *Annu. Rev. Pharmacol. Toxicol.* 51, 337–358. doi: 10.1146/annurev-pharmtox-010510-100234

Kolossov, V. L., Spring, B. Q., Clegg, R. M., Henry, J. J., Sokolowski, A., Kenis, P. J., et al. (2011). Development of a high-dynamic range, GFP-based FRET probe sensitive to oxidative microenvironments. *Exp. Biol. Med. (Maywood)* 236, 681–691. doi: 10.1258/ebm.2011.011009

Komatsu, N., Aoki, K., Yamada, M., Yukinaga, H., Fujita, Y., Kamioka, Y., et al. (2011). Development of an optimized backbone of FRET biosensors for kinases and GTPases. *Mol. Biol. Cell* 22, 4647–4656. doi: 10.1091/mbc.E11-01-0072

Kuner, T., and Augustine, G. J. (2000). A genetically encoded ratiometric indicator for chloride: capturing chloride transients in cultured hippocampal neurons. *Neuron* 27, 447–459. doi: 10.1016/S0896-6273(00)00056-8

Kunkel, M. T., Ni, Q., Tsien, R. Y., Zhang, J., and Newton, A. C. (2005). Spatio-temporal dynamics of protein kinase B/Akt signaling revealed by a genetically encoded fluorescent reporter. *J. Biol. Chem.* 280, 5581–5587. doi: 10.1074/jbc.M411534200

Kunkel, M. T., Toker, A., Tsien, R. Y., and Newton, A. C. (2007). Calcium-dependent regulation of protein kinase D revealed by a genetically encoded kinase activity reporter. *J. Biol. Chem.* 282, 6733–6742. doi: 10.1074/jbc.M608086200

Kurokawa, K., Mochizuki, N., Ohba, Y., Mizuno, H., Miyawaki, A., and Matsuda, M. (2001). A pair of fluorescent resonance energy transfer-based probes for tyrosine phosphorylation of the CrkII adaptor protein *in vivo*. *J. Biol. Chem.* 276, 31305–31310. doi: 10.1074/jbc.M104341200

Kwok, S., Lee, C., Sanchez, S. A., Hazlett, T. L., Gratton, E., and Hayashi, Y. (2008). Genetically encoded probe for fluorescence lifetime imaging of CaMKII activity. *Biochem. Biophys. Res. Commun.* 369, 519–525. doi: 10.1016/j.bbrc.2008.02.070

Lager, I., Fehr, M., Frommer, W. B., and Lalonde, S. (2003). Development of a fluorescent nanosensor for ribose. *FEBS Lett.* 553, 85–89. doi: 10.1016/S0014-5793(03)00976-1

Lam, A. J., St-Pierre, F., Gong, Y., Marshall, J. D., Cranfill, P. J., Baird, M. A., et al. (2012). Improving FRET dynamic range with bright green and red fluorescent proteins. *Nat. Methods* 9, 1005–1012. doi: 10.1038/nmeth.2171

Lantsman, K., and Tombes, R. M. (2005). CaMK-II oligomerization potential determined using CFP/YFP FRET. *Biochim. Biophys. Acta* 1746, 45–54. doi: 10.1016/j.bbamcr.2005.08.005

Lee, S. J., Escobedo-Lozoya, Y., Szatmari, E. M., and Yasuda, R. (2009). Activation of CaMKII in single dendritic spines during long-term potentiation. *Nature* 458, 299–304. doi: 10.1038/nature07842

Li, I. T., Chiang, J. J., and Truong, K. (2006). FRET evidence that an isoform of caspase-7 binds but does not cleave its substrate. *Conf. Proc. IEEE Eng. Med. Biol. Soc.* 1, 531–534. doi: 10.1109/IEMBS.2006.260832

Lin, C. W., Jao, C. Y., and Ting, A. Y. (2004). Genetically encoded fluorescent reporters of histone methylation in living cells. *J. Am. Chem. Soc.* 126, 5982–5983. doi: 10.1021/ja038854h

Lisman, J., Schulman, H., and Cline, H. (2002). The molecular basis of CaMKII function in synaptic and behavioural memory. *Nat. Rev. Neurosci.* 3, 175–190. doi: 10.1038/nrn753

Lorenz, M., Yamaguchi, H., Wang, Y., Singer, R. H., and Condeelis, J. (2004). Imaging sites of N-wasp activity in lamellipodia and invadopodia of carcinoma cells. *Curr. Biol.* 14, 697–703. doi: 10.1016/j.cub.2004.04.008

Macurek, L., Lindqvist, A., Lim, D., Lampson, M. A., Klompmaker, R., Freire, R., et al. (2008). Polo-like kinase-1 is activated by aurora A to promote checkpoint recovery. *Nature* 455, 119–123. doi: 10.1038/nature07185

Man, H. Y., Wang, Q., Lu, W. Y., Ju, W., Ahmadian, G., Liu, L., et al. (2003). Activation of PI3-kinase is required for AMPA receptor insertion during LTP of mEPSCs in cultured hippocampal neurons. *Neuron* 38, 611–624. doi: 10.1016/S0896-6273(03)00228-9

Matsu-ura, T., Michikawa, T., Inoue, T., Miyawaki, A., Yoshida, M., and Mikoshiba, K. (2006). Cytosolic inositol 1 4, 5-trisphosphate dynamics during intracellular calcium oscillations in living cells. *J. Cell Biol.* 173, 755–765. doi: 10.1083/jcb.200512141

Matsuzaki, M., Honkura, N., Ellis-Davies, G. C., and Kasai, H. (2004). Structural basis of long-term potentiation in single dendritic spines. *Nature* 429, 761–766. doi: 10.1038/nature02617

Matus, A. (2005). Growth of dendritic spines: a continuing story. *Curr. Opin. Neurobiol.* 15, 67–72. doi: 10.1016/j.conb.2005.01.015

Meng, F., Suchyna, T. M., and Sachs, F. (2008). A fluorescence energy transfer-based mechanical stress sensor for specific proteins *in situ*. *FEBS J.* 275, 3072–3087. doi: 10.1111/j.1742-4658.2008.06461.x

Mitra, R. D., Silva, C. M., and Youvan, D. C. (1996). Fluorescence resonance energy transfer between blue-emitting and red-shifted excitation derivatives of the green fluorescent protein. *Gene* 173, 13–17. doi: 10.1016/0378-1119(95)00768-7

Miyawaki, A. (2003). Visualization of the spatial and temporal dynamics of intracellular signaling. *Dev. Cell* 4, 295–305. doi: 10.1016/S1534-5807(03)00060-1

Miyawaki, A. (2005). Innovations in the imaging of brain functions using fluorescent proteins. *Neuron* 48, 189–199. doi: 10.1016/j.neuron.2005.10.003

Miyawaki, A., Llopis, J., Heim, R., McCaffery, J. M., Adams, J. A., Ikura, M., et al. (1997). Fluorescent indicators for Ca^{2+} based on green fluorescent proteins and calmodulin. *Nature* 388, 882–887. doi: 10.1038/42264

Mizuno, H., Sassa, T., Higashijima, S. I., Okamoto, H., and Miyawaki, A. (2013). Transgenic zebrafish for ratiometric imaging of cytosolic and mitochondrial Ca response in teleost embryo. *Cell Calcium* 54, 236–245. doi: 10.1016/j.ceca.2013.06.007

Mochizuki, N., Yamashita, S., Kurokawa, K., Ohba, Y., Nagai, T., Miyawaki, A., et al. (2001). Spatio-temporal images of growth-factor-induced activation of Ras and Rap1. *Nature* 411, 1065–1068. doi: 10.1038/35082594

Mower, A. F., Kwok, S., Yu, H., Majewska, A. K., Okamoto, K., Hayashi, Y., et al. (2011). Experience-dependent regulation of CaMKII activity within single visual cortex synapses *in vivo*. *Proc. Natl. Acad. Sci. U.S.A.* 108, 21241–21246. doi: 10.1073/pnas.1108261109

Murakoshi, H., Lee, S. J., and Yasuda, R. (2008). Highly sensitive and quantitative FRET-FLIM imaging in single dendritic spines using improved non-radiative YFP. *Brain Cell Biol.* 36, 31–42. doi: 10.1007/s11068-008-9024-9

Murakoshi, H., Wang, H., and Yasuda, R. (2011). Local, persistent activation of Rho GTPases during plasticity of single dendritic spines. *Nature* 472, 100–104. doi: 10.1038/nature09823

Murata, Y., Iwasaki, H., Sasaki, M., Inaba, K., and Okamura, Y. (2005). Phosphoinositide phosphatase activity coupled to an intrinsic voltage sensor. *Nature* 435, 1239–1243. doi: 10.1038/nature03650

Nagai, T., Sawano, A., Park, E. S., and Miyawaki, A. (2001). Circularly permuted green fluorescent proteins engineered to sense Ca^{2+}. *Proc. Natl. Acad. Sci. U.S.A.* 98, 3197–3202. doi: 10.1073/pnas.051636098

Nagai, T., Yamada, S., Tominaga, T., Ichikawa, M., and Miyawaki, A. (2004). Expanded dynamic range of fluorescent indicators for Ca^{2+} by circularly permuted yellow fluorescent proteins. *Proc. Natl. Acad. Sci. U.S.A.* 101, 10554–10559. doi: 10.1073/pnas.0400417101

Nagai, Y., Miyazaki, M., Aoki, R., Zama, T., Inouye, S., Hirose, K., et al. (2000). A fluorescent indicator for visualizing cAMP-induced phosphorylation *in vivo*. *Nat. Biotechnol.* 18, 313–316. doi: 10.1038/73767

Nakai, J., Ohkura, M., and Imoto, K. (2001). A high signal-to-noise Ca^{2+} probe composed of a single green fluorescent protein. *Nat. Biotechnol.* 19, 137–141. doi: 10.1038/84397

Nakajima, T., Sato, M., Akaza, N., and Umezawa, Y. (2008). Cell-based fluorescent indicator to visualize brain-derived neurotrophic factor secreted from living neurons. *ACS Chem. Biol.* 3, 352–358. doi: 10.1021/cb800052v

Nakanishi, Y., Iida, S., Ueoka-Nakanishi, H., Niimi, T., Tomioka, R., and Maeshima, M. (2013). Exploring dynamics of molybdate in living animal cells by a genetically encoded FRET nanosensor. *PLoS ONE* 8:e58175. doi: 10.1371/journal.pone.0058175

Nakayama, A. Y., Harms, M. B., and Luo, L. (2000). Small GTPases Rac and Rho in the maintenance of dendritic spines and branches in hippocampal pyramidal neurons. *J. Neurosci.* 20, 5329–5338.

Newman, R. H., Fosbrink, M. D., and Zhang, J. (2011). Genetically encodable fluorescent biosensors for tracking signaling dynamics in living cells. *Chem. Rev.* 111, 3614–3666. doi: 10.1021/cr100002u

Newman, R. H., and Zhang, J. (2008). Visualization of phosphatase activity in living cells with a FRET-based calcineurin activity sensor. *Mol. Biosyst.* 4, 496–501. doi: 10.1039/b720034j

Nguyen, A. W., and Daugherty, P. S. (2005). Evolutionary optimization of fluorescent proteins for intracellular FRET. *Nat. Biotechnol.* 23, 355–360. doi: 10.1038/nbt1066

Ni, Q., and Zhang, J. (2010). Dynamic visualization of cellular signaling. *Adv. Biochem. Eng. Biotechnol.* 119, 79–97. doi: 10.1007/10_2008_48

Ni, Z., Mark, M. E., Cai, X., and Mao, Q. (2010). Fluorescence resonance energy transfer (FRET) analysis demonstrates dimer/oligomer formation of the human breast cancer resistance protein (BCRP/ABCG2) in intact cells. *Int. J. Biochem. Mol. Biol.* 1, 1–11.

Nikolaev, V. O., Bunemann, M., Hein, L., Hannawacker, A., and Lohse, M. J. (2004). Novel single chain cAMP sensors for receptor-induced signal propagation. *J. Biol. Chem.* 279, 37215–37218. doi: 10.1074/jbc.C400302200

Nikolaev, V. O., Gambaryan, S., and Lohse, M. J. (2006). Fluorescent sensors for rapid monitoring of intracellular cGMP. *Nat. Methods* 3, 23–25. doi: 10.1038/nmeth816

Nishi, M., Tanaka, M., Matsuda, K., Sunaguchi, M., and Kawata, M. (2004). Visualization of glucocorticoid receptor and mineralocorticoid receptor interactions in living cells with GFP-based fluorescence resonance energy transfer. *J. Neurosci.* 24, 4918–4927. doi: 10.1523/JNEUROSCI.5495-03.2004

Nishioka, T., Aoki, K., Hikake, K., Yoshizaki, H., Kiyokawa, E., and Matsuda, M. (2008). Rapid turnover rate of phosphoinositides at the front of migrating MDCK cells. *Mol. Biol. Cell* 19, 4213–4223. doi: 10.1091/mbc.E08-03-0315

Nishioka, T., Frohman, M. A., Matsuda, M., and Kiyokawa, E. (2010). Heterogeneity of phosphatidic acid levels and distribution at the plasma membrane in living cells as visualized by a Foster resonance energy transfer (FRET) biosensor. *J. Biol. Chem.* 285, 35979–35987. doi: 10.1074/jbc.M110.153007

Ohashi, T., Galiacy, S. D., Briscoe, G., and Erickson, H. P. (2007). An experimental study of GFP-based FRET, with application to intrinsically unstructured proteins. *Protein Sci.* 16, 1429–1438. doi: 10.1110/ps.072845607

Ohkura, M., Sasaki, T., Sadakari, J., Gengyo-Ando, K., Kagawa-Nagamura, Y., Kobayashi, C., et al. (2012). Genetically encoded green fluorescent Ca^{2+} indicators with improved detectability for neuronal Ca^{2+} signals. *PLoS ONE* 7:e51286. doi: 10.1371/journal.pone.0051286

Oikawa, T., Yamaguchi, H., Itoh, T., Kato, M., Ijuin, T., Yamazaki, D., et al. (2004). PtdIns(3 4, 5)P3 binding is necessary for WAVE2-induced formation of lamellipodia. *Nat. Cell Biol.* 6, 420–426. doi: 10.1038/ncb1125

Okamoto, K., Bosch, M., and Hayashi, Y. (2009). The roles of CaMKII and F-actin in the structural plasticity of dendritic spines: a potential molecular identity of a synaptic tag? *Physiology (Bethesda)* 24, 357–366. doi: 10.1152/physiol.00029.2009

Okamoto, K., and Hayashi, Y. (2006). Visualization of F-actin and G-actin equilibrium using fluorescence resonance energy transfer (FRET) in cultured cells and neurons in slices. *Nat. Protoc.* 1, 911–919. doi: 10.1038/nprot.2006.122

Okamoto, K., Nagai, T., Miyawaki, A., and Hayashi, Y. (2004). Rapid and persistent modulation of actin dynamics regulates postsynaptic reorganization underlying bidirectional plasticity. *Nat. Neurosci.* 7, 1104–1112. doi: 10.1038/nn1311

Okamoto, K., Narayanan, R., Lee, S. H., Murata, K., and Hayashi, Y. (2007). The role of CaMKII as an F-actin-bundling protein crucial for maintenance of dendritic spine structure. *Proc. Natl. Acad. Sci. U.S.A.* 104, 6418–6423. doi: 10.1073/pnas.0701656104

Okumoto, S., Looger, L. L., Micheva, K. D., Reimer, R. J., Smith, S. J., and Frommer, W. B. (2005). Detection of glutamate release from neurons by genetically encoded surface-displayed FRET nanosensors. *Proc. Natl. Acad. Sci. U.S.A.* 102, 8740–8745. doi: 10.1073/pnas.0503274102

Onuki, R., Nagasaki, A., Kawasaki, H., Baba, T., Uyeda, T. Q., and Taira, K. (2002). Confirmation by FRET in individual living cells of the absence of significant amyloid beta -mediated caspase 8 activation. *Proc. Natl. Acad. Sci. U.S.A.* 99, 14716–14721. doi: 10.1073/pnas.232177599

Ouyang, M., Lu, S., Li, X. Y., Xu, J., Seong, J., Giepmans, B. N., et al. (2008). Visualization of polarized membrane type 1 matrix metalloproteinase activity in live cells by fluorescence resonance energy transfer imaging. *J. Biol. Chem.* 283, 17740–17748. doi: 10.1074/jbc.M709872200

Papusheva, E., Mello de Queiroz, F., Dalous, J., Han, Y., Esposito, A., Jares-Erijmanxa, E. A., et al. (2009). Dynamic conformational changes in the FERM domain of FAK are involved in focal-adhesion behavior during cell spreading and motility. *J. Cell. Sci.* 122, 656–666. doi: 10.1242/jcs.028738

Parrini, M. C., Camonis, J., Matsuda, M., and de Gunzburg, J. (2009). Dissecting activation of the PAK1 kinase at protrusions in living cells. *J. Biol. Chem.* 284, 24133–24143. doi: 10.1074/jbc.M109.015271

Patterson, S. L., Pittenger, C., Morozov, A., Martin, K. C., Scanlin, H., Drake, C., et al. (2001). Some forms of cAMP-mediated long-lasting potentiation are associated with release of BDNF and nuclear translocation of phospho-MAP kinase. *Neuron* 32, 123–140. doi: 10.1016/S0896-6273(01)00443-3

Piljic, A., de Diego, I., Wilmanns, M., and Schultz, C. (2011). Rapid development of genetically encoded FRET reporters. *ACS Chem. Biol.* 6, 685–691. doi: 10.1021/cb100402n

Randriamampita, C., Mouchacca, P., Malissen, B., Marguet, D., Trautmann, A., and Lellouch, A. C. (2008). A novel ZAP-70 dependent FRET based biosensor reveals kinase activity at both the immunological synapse and the antisynapse. *PLoS ONE* 3:e1521. doi: 10.1371/journal.pone.0001521

Rizzo, M. A., Springer, G., Segawa, K., Zipfel, W. R., and Piston, D. W. (2006). Optimization of pairings and detection conditions for measurement of FRET between cyan and yellow fluorescent proteins. *Microsc. Microanal.* 12, 238–254. doi: 10.1017/S1431927606060235

Rizzo, M. A., Springer, G. H., Granada, B., and Piston, D. W. (2004). An improved cyan fluorescent protein variant useful for FRET. *Nat. Biotechnol.* 22, 445–449. doi: 10.1038/nbt945

Roberson, E. D., English, J. D., Adams, J. P., Selcher, J. C., Kondratick, C., and Sweatt, J. D. (1999). The mitogen-activated protein kinase cascade couples PKA and PKC to cAMP response element binding protein phosphorylation in area CA1 of hippocampus. *J. Neurosci.* 19, 4337–4348.

Sakai, R., Repunte-Canonigo, V., Raj, C. D., and Knöpfel, T. (2001). Design and characterization of a DNA-encoded, voltage-sensitive fluorescent protein. *Eur. J. Neurosci.* 13, 2314–2318. doi: 10.1046/j.0953-816x.2001.01617.x

Sanes, J. R., and Lichtman, J. W. (1999). Can molecules explain long-term potentiation? *Nat. Neurosci.* 2, 597–604. doi: 10.1038/10154

Saneyoshi, T., and Hayashi, Y. (2012). The Ca^{2+} and Rho GTPase signaling pathways underlying activity-dependent actin remodeling at dendritic spines. *Cytoskeleton (Hoboken)* 69, 545–554. doi: 10.1002/cm.21037

Sasaki, K., Ito, T., Nishino, N., Khochbin, S., and Yoshida, M. (2009). Real-time imaging of histone H4 hyperacetylation in living cells. *Proc. Natl. Acad. Sci. U.S.A.* 106, 16257–16262. doi: 10.1073/pnas.0902150106

Sasaki, K., Sato, M., and Umezawa, Y. (2003). Fluorescent indicators for Akt/protein kinase B and dynamics of Akt activity visualized in living cells. *J. Biol. Chem.* 278, 30945–30951. doi: 10.1074/jbc.M212167200

Sato, M., Hida, N., Ozawa, T., and Umezawa, Y. (2000). Fluorescent indicators for cyclic GMP based on cyclic GMP-dependent protein kinase Ialpha and green fluorescent proteins. *Anal. Chem.* 72, 5918–5924. doi: 10.1021/ac0006167

Sato, M., Kawai, Y., and Umezawa, Y. (2007). Genetically encoded fluorescent indicators to visualize protein phosphorylation by extracellular signal-regulated kinase in single living cells. *Anal. Chem.* 79, 2570–2575. doi: 10.1021/ac062171d

Sato, M., Ozawa, T., Inukai, K., Asano, T., and Umezawa, Y. (2002). Fluorescent indicators for imaging protein phosphorylation in single living cells. *Nat. Biotechnol.* 20, 287–294. doi: 10.1038/nbt0302-287

Sato, M., Ueda, Y., Shibuya, M., and Umezawa, Y. (2005a). Locating inositol 1 4, 5-trisphosphate in the nucleus and neuronal dendrites with genetically encoded fluorescent indicators. *Anal. Chem.* 77, 4751–4758. doi: 10.1021/ac040195j

Sato, M., Hida, N., and Umezawa, Y. (2005b). Imaging the nanomolar range of nitric oxide with an amplifier-coupled fluorescent indicator in living cells. *Proc. Natl. Acad. Sci. U.S.A.* 102, 14515–14520. doi: 10.1073/pnas.0505136102

Sato, M., Ueda, Y., Takagi, T., and Umezawa, Y. (2003). Production of PtdInsP3 at endomembranes is triggered by receptor endocytosis. *Nat. Cell Biol.* 5, 1016–1022. doi: 10.1038/ncb1054

Sato, M., Ueda, Y., and Umezawa, Y. (2006a). Imaging diacylglycerol dynamics at organelle membranes. *Nat. Methods* 3, 797–799. doi: 10.1038/nmeth930

Sato, M., Nakajima, T., Goto, M., and Umezawa, Y. (2006b). Cell-based indicator to visualize picomolar dynamics of nitric oxide release from living cells. *Anal. Chem.* 78, 8175–8182. doi: 10.1021/ac061791b

Shaner, N. C., Steinbach, P. A., and Tsien, R. Y. (2005). A guide to choosing fluorescent proteins. *Nat. Methods* 2, 905–909. doi: 10.1038/nmeth819

Shimozono, S., Iimura, T., Kitaguchi, T., Higashijima, S., and Miyawaki, A. (2013). Visualization of an endogenous retinoic acid gradient across embryonic development. *Nature* 496, 363–366. doi: 10.1038/nature12037

Shinohara, M., Terada, Y., Iwamatsu, A., Shinohara, A., Mochizuki, N., Higuchi, M., et al. (2002). SWAP-70 is a guanine-nucleotide-exchange factor that mediates signalling of membrane ruffling. *Nature* 416, 759–763. doi: 10.1038/416759a

Spacek, J., and Harris, K. M. (2004). Trans-endocytosis via spinules in adult rat hippocampus. *J. Neurosci.* 24, 4233–4241. doi: 10.1523/JNEUROSCI.0287-04.2004

Star, E. N., Kwiatkowski, D. J., and Murthy, V. N. (2002). Rapid turnover of actin in dendritic spines and its regulation by activity. *Nat. Neurosci.* 5, 239–246. doi: 10.1038/nn811

Stryer, L. (1978). Fluorescence energy transfer as a spectroscopic ruler. *Annu. Rev. Biochem.* 47, 819–846. doi: 10.1146/annurev.bi.47.070178.004131

Suzuki, Y., Yasunaga, T., Ohkura, R., Wakabayashi, T., and Sutoh, K. (1998). Swing of the lever arm of a myosin motor at the isomerization and phosphate-release steps. *Nature* 396, 380–383. doi: 10.1038/24640

Takao, K., Okamoto, K., Nakagawa, T., Neve, R. L., Nagai, T., Miyawaki, A., et al. (2005). Visualization of synaptic Ca^{2+} /calmodulin-dependent protein kinase II activity in living neurons. *J. Neurosci.* 25, 3107–3112. doi: 10.1523/JNEUROSCI.0085-05.2005

Takaya, A., Ohba, Y., Kurokawa, K., and Matsuda, M. (2004). RalA activation at nascent lamellipodia of epidermal growth factor-stimulated Cos7 cells and migrating Madin-Darby canine kidney cells. *Mol. Biol. Cell* 15, 2549–2557. doi: 10.1091/mbc.E03-11-0857

Tanimura, A., Nezu, A., Morita, T., Turner, R. J., and Tojyo, Y. (2004).

Fluorescent biosensor for quantitative real-time measurements of inositol 1 4, 5-trisphosphate in single living cells. *J. Biol. Chem.* 279, 38095–38098. doi: 10.1074/jbc.C400312200

Tashiro, A., Minden, A., and Yuste, R. (2000). Regulation of dendritic spine morphology by the rho family of small GTPases: antagonistic roles of Rac and Rho. *Cereb. Cortex* 10, 927–938. doi: 10.1093/cercor/10.10.927

Terai, K., and Matsuda, M. (2005). Ras binding opens c-Raf to expose the docking site for mitogen-activated protein kinase kinase. *EMBO Rep.* 6, 251–255. doi: 10.1038/sj.embor.7400349

Terai, K., and Matsuda, M. (2006). The amino-terminal B-Raf-specific region mediates calcium-dependent homo- and hetero-dimerization of Raf. *EMBO J.* 25, 3556–3564. doi: 10.1038/sj.emboj.7601241

Thomas, C. C., Dowler, S., Deak, M., Alessi, D. R., and van Aalten, D. M. (2001). Crystal structure of the phosphatidylinositol 3, 4-bisphosphate-binding pleckstrin homology (PH) domain of tandem PH-domain-containing protein 1 (TAPP1): molecular basis of lipid specificity. *Biochem. J.* 358, 287–294. doi: 10.1042/0264-6021:3580287

Thunemann, M., Wen, L., Hillenbrand, M., Vachaviolos, A., Feil, S., Ott, T., et al. (2013). Transgenic Mice for cGMP Imaging. *Circ. Res.* 113, 365–371. doi: 10.1161/CIRCRESAHA.113.301063

Ting, A. Y., Kain, K. H., Klemke, R. L., and Tsien, R. Y. (2001). Genetically encoded fluorescent reporters of protein tyrosine kinase activities in living cells. *Proc. Natl. Acad. Sci. U.S.A.* 98, 15003–15008. doi: 10.1073/pnas.211564598

Tomida, T., Takekawa, M., O'Grady, P., and Saito, H. (2009). Stimulus-specific distinctions in spatial and temporal dynamics of stress-activated protein kinase kinase kinases revealed by a fluorescence resonance energy transfer biosensor. *Mol. Cell. Biol.* 29, 6117–6127. doi: 10.1128/MCB.00571-09

Tsutsui, H., Karasawa, S., Okamura, Y., and Miyawaki, A. (2008). Improving membrane voltage measurements using FRET with new fluorescent proteins. *Nat. Methods* 5, 683–685. doi: 10.1038/nmeth.1235

Tunceroglu, A., Matsuda, M., and Birge, R. B. (2010). Real-time fluorescent resonance energy transfer analysis to monitor drug resistance in chronic myelogenous leukemia. *Mol. Cancer Ther.* 9, 3065–3073. doi: 10.1158/1535-7163.MCT-10-0623

Ueda, Y., and Hayashi, Y. (2013). PIP_3 regulates spinule formation in dendritic spines during structural long-term potentiation. *J. Neurosci.* 33, 11040–11047. doi: 10.1523/JNEUROSCI.3122-12.2013

Uemura, K., Lill, C. M., Li, X., Peters, J. A., Ivanov, A., Fan, Z., et al. (2009). Allosteric modulation of PS1/gamma-secretase conformation correlates with amyloid beta(42/40) ratio. *PLoS ONE* 4:e7893. doi: 10.1371/journal.pone.0007893

Vanderklish, P. W., Krushel, L. A., Holst, B. H., Gally, J. A., Crossin, K. L., and Edelman, G. M. (2000). Marking synaptic activity in dendritic spines with a calpain substrate exhibiting fluorescence resonance energy transfer. *Proc. Natl. Acad. Sci. U.S.A.* 97, 2253–2258. doi: 10.1073/pnas.040565597

van Diepen, M. T., Parsons, M., Downes, C. P., Leslie, N. R., Hindges, R., and Eickholt, B. J. (2009). MyosinV controls PTEN function and neuronal cell size. *Nat. Cell Biol.* 11, 1191–1196. doi: 10.1038/ncb1961

Vazquez, L. E., Chen, H. J., Sokolova, I., Knuesel, I., and Kennedy, M. B. (2004). SynGAP regulates spine formation. *J. Neurosci.* 24, 8862–8872. doi: 10.1523/JNEUROSCI.3213-04.2004

Vilardaga, J. P., Bunemann, M., Krasel, C., Castro, M., and Lohse, M. J. (2003). Measurement of the millisecond activation switch of G protein-coupled receptors in living cells. *Nat. Biotechnol.* 21, 807–812. doi: 10.1038/nbt838

Vinkenborg, J. L., Nicolson, T. J., Bellomo, E. A., Koay, M. S., Rutter, G. A., and Merkx, M. (2009). Genetically encoded FRET sensors to monitor intracellular Zn^{2+} homeostasis. *Nat. Methods* 6, 737–740. doi: 10.1038/nmeth.1368

Violin, J. D., Zhang, J., Tsien, R. Y., and Newton, A. C. (2003). A genetically encoded fluorescent reporter reveals oscillatory phosphorylation by protein kinase C. *J. Cell Biol.* 161, 899–909. doi: 10.1083/jcb.200302125

Wallace, D. J., Meyer zum Alten Borgloh, S., Astori, S., Yang, Y., Bausen, M., Kugler, S., et al. (2008). Single-spike detection *in vitro* and *in vivo* with a genetic Ca2+ sensor. *Nat. Methods* 5, 797–804. doi: 10.1038/nmeth.1242

Waltereit, R., Dammermann, B., Wulff, P., Scafidi, J., Staubli, U., Kauselmann, G., et al. (2001). Arg3.1/Arc mRNA induction by Ca^{2+} and cAMP requires protein kinase A and mitogen-activated protein kinase/extracellular regulated kinase activation. *J. Neurosci.* 21, 5484–5493.

Wang, D., McMahon, S., Zhang, Z., and Jackson, M. B. (2012). Hybrid voltage sensor imaging of electrical activity from neurons in hippocampal slices from transgenic mice. *J. Neurophysiol.* 108, 3147–3160. doi: 10.1152/jn.00722.2012

Wang, Y., Botvinick, E. L., Zhao, Y., Berns, M. W., Usami, S., Tsien, R. Y., et al. (2005). Visualizing the mechanical activation of Src. *Nature* 434, 1040–1045. doi: 10.1038/nature03469

Ward, M. E., Wu, J. Y., and Rao, Y. (2004). Visualization of spatially and temporally regulated N-WASP activity during cytoskeletal reorganization in living cells. *Proc. Natl. Acad. Sci. U.S.A.* 101, 970–974. doi: 10.1073/pnas.0306258101

Wu, G. Y., Deisseroth, K., and Tsien, R. W. (2001). Spaced stimuli stabilize MAPK pathway activation and its effects on dendritic morphology. *Nat. Neurosci.* 4, 151–158. doi: 10.1038/83976

Xu, X., Gerard, A. L., Huang, B. C., Anderson, D. C., Payan, D. G., and Luo, Y. (1998). Detection of programmed cell death using fluorescence energy transfer. *Nucleic Acids Res.* 26, 2034–2035. doi: 10.1093/nar/26.8.2034

Yamada, Y., Michikawa, T., Hashimoto, M., Horikawa, K., Nagai, T., Miyawaki, A., et al. (2011). Quantitative comparison of genetically encoded Ca indicators in cortical pyramidal cells and cerebellar Purkinje cells. *Front. Cell. Neurosci.* 5:18. doi: 10.3389/fncel.2011.00018

Yamaguchi, Y., Shinotsuka, N., Nonomura, K., Takemoto, K., Kuida, K., Yosida, H., et al. (2011). Live imaging of apoptosis in a novel transgenic mouse highlights its role in neural tube closure. *J. Cell Biol.* 195, 1047–1060. doi: 10.1083/jcb.201104057

Yang, J., Zhang, Z., Lin, J., Lu, J., Liu, B. F., Zeng, S., et al. (2007). Detection of MMP activity in living cells by a genetically encoded surface-displayed FRET sensor. *Biochim. Biophys. Acta* 1773, 400–407. doi: 10.1016/j.bbamcr.2006.11.002

Yano, T., Oku, M., Akeyama, N., Itoyama, A., Yurimoto, H., Kuge, S., et al. (2010). A novel fluorescent sensor protein for visualization of redox states in the cytoplasm and in peroxisomes. *Mol. Cell. Biol.* 30 3758–3766. doi: 10.1128/MCB.00121-10

Yasuda, R. (2006). Imaging spatiotemporal dynamics of neuronal signaling using fluorescence resonance energy transfer and fluorescence lifetime imaging microscopy. *Curr. Opin. Neurobiol.* 16, 551–561. doi: 10.1016/j.conb.2006.08.012

Yasuda, R. (2012). Studying signal transduction in single dendritic spines. *Cold Spring Harb. Perspect. Biol.* 4, 005611. doi: 10.1101/cshperspect.a005611

Yasuda, R., Harvey, C. D., Zhong, H., Sobczyk, A., van Aelst, L., and Svoboda, K. (2006). Supersensitive Ras activation in dendrites and spines revealed by two-photon fluorescence lifetime imaging. *Nat. Neurosci.* 9, 283–291. doi: 10.1038/nn1635

Yoshizaki, H., Ohba, Y., Kurokawa, K., Itoh, R. E., Nakamura, T., Mochizuki, N., et al. (2003). Activity of Rho-family GTPases during cell division as visualized with FRET-based probes. *J. Cell Biol.* 162, 223–232. doi: 10.1083/jcb.200212049

Zaccolo, M., and Pozzan, T. (2002). Discrete microdomains with high concentration of cAMP in stimulated rat neonatal cardiac myocytes. *Science* 295, 1711–1715. doi: 10.1126/science.1069982

Zacharias, D. A., Violin, J. D., Newton, A. C., and Tsien, R. Y. (2002). Partitioning of lipid-modified monomeric GFPs into membrane microdomains of live cells. *Science* 296, 913–916. doi: 10.1126/science.1068539

Zeng, W., Seward, H. E., Malnasi-Csizmadia, A., Wakelin, S., Woolley, R. J., Cheema, G. S., et al. (2006). Resonance energy transfer between green fluorescent protein variants: complexities revealed with myosin fusion proteins. *Biochemistry* 45, 10482–10491. doi: 10.1021/bi060943u

Zhang, H., and Macara, I. G. (2006). The polarity protein PAR-3 and TIAM1 cooperate in dendritic spine morphogenesis. *Nat. Cell Biol.* 8, 227–237. doi: 10.1038/ncb1368

Zhang, J., Campbell, R. E., Ting, A. Y., and Tsien, R. Y. (2002). Creating new fluorescent probes for cell biology. *Nat. Rev. Mol. Cell Biol.* 3, 906–918. doi: 10.1038/nrm976

Zhang, J., Chen, L., Raina, H., Blaustein, M. P., and Wier, W.

G. (2010). *In vivo* assessment of artery smooth muscle [Ca2+]i and MLCK activation in FRET-based biosensor mice. *Am. J. Physiol. Heart Circ. Physiol.* 299, H946–H956. doi: 10.1152/ajpheart.00359.2010

Zhang, J., Ma, Y., Taylor, S. S., and Tsien, R. Y. (2001). Genetically encoded reporters of protein kinase A activity reveal impact of substrate tethering. *Proc. Natl. Acad. Sci. U.S.A.* 98, 14997–15002. doi: 10.1073/pnas.211566798

Zhao, Y., Araki, S., Wu, J., Teramoto, T., Chang, Y. F., Nakano, M., et al. (2011). An expanded palette of genetically encoded Ca^{2+} indicators. *Science* 333, 1888–1891. doi: 10.1126/science.1208592

Zhu, J. J., Qin, Y., Zhao, M., Van Aelst, L., and Malinow, R. (2002). Ras and Rap control AMPA receptor trafficking during synaptic plasticity. *Cell* 110, 443–455. doi: 10.1016/S0092-8674(02)00897-8

Conflict of Interest Statement: Yasunori Hayashi is partly supported by Takeda Pharmaceuticals Co. Ltd. and Fujitsu Laboratories. The other authors declare that the research was conducted in the absence of any commercial or financial relationships that could be construed as a potential conflict of interest.

Received: 30 July 2013; accepted: 23 September 2013; published online: 10 October 2013.

Citation: Ueda Y, Kwok S and Hayashi Y (2013) Application of FRET probes in the analysis of neuronal plasticity. Front. Neural Circuits ***7****:163. doi: 10.3389/fncir. 2013.00163*

This article was submitted to the journal Frontiers in Neural Circuits.

frontiers in
NEURAL CIRCUITS

REVIEW ARTICLE
published: 28 November 2013
doi: 10.3389/fncir.2013.00187

Japanese studies on neural circuits and behavior of *Caenorhabditis elegans*

Hiroyuki Sasakura[1], Yuki Tsukada[1], Shin Takagi[2]* and Ikue Mori[1]*

[1] *Laboratory of Molecular Neurobiology, Division of Biological Science, Nagoya University, Nagoya, Japan*
[2] *Laboratory of Brain Function and Structure, Division of Biological Science, Nagoya University, Nagoya, Japan*

Edited by:
Masanobu Kano, The University of Tokyo, Japan

Reviewed by:
William Schafer, Medical Research Council Laboratory of Molecular Biology, UK
Takeshi Ishihara, Kyushu University, Japan

****Correspondence:***
Ikue Mori, Laboratory of Molecular Neurobiology, Division of Biological Science, Nagoya University, Furou-cho, Chikusa-ku, Nagoya 464-8602, Japan
e-mail: m46920a@nucc.cc.nagoya-u.ac.jp;
Shin Takagi, Laboratory of Brain Function and Structure, Division of Biological Science, Nagoya University, Furou-cho, Chikusa-ku, Nagoya 464-8602, Japan
e-mail: i45116a@nucc.cc.nagoya-u.ac.jp

The nematode *Caenorhabditis elegans* is an ideal organism for studying neural plasticity and animal behaviors. A total of 302 neurons of a *C. elegans* hermaphrodite have been classified into 118 neuronal groups. This simple neural circuit provides a solid basis for understanding the mechanisms of the brains of higher animals, including humans. Recent studies that employ modern imaging and manipulation techniques enable researchers to study the dynamic properties of nervous systems with great precision. Behavioral and molecular genetic analyses of this tiny animal have contributed greatly to the advancement of neural circuit research. Here, we will review the recent studies on the neural circuits of *C. elegans* that have been conducted in Japan. Several laboratories have established unique and clever methods to study the underlying neuronal substrates of behavioral regulation in *C. elegans*. The technological advances applied to studies of *C. elegans* have allowed new approaches for the studies of complex neural systems. Through reviewing the studies on the neuronal circuits of *C. elegans* in Japan, we will analyze and discuss the directions of neural circuit studies.

Keywords: *C. elegans*, neural circuits, learning and memory, plastic behavior, behavioral genetics, studies on Japan

THE NERVOUS SYSTEM OF *C. elegans*

Understanding the mechanisms underlying neural operation and processing is a major goal in neuroscience. One approach is to study a simple neural circuit, in which neurons and neural pathways can be identified and diagrammed for analysis. Another approach is the application of molecular genetic techniques to reveal the molecular components that govern the neural functions and clarify the site of action of molecules in brain (Brenner, 1974; Quinn et al., 1974).

The soil nematode *Caenorhabditis elegans* is an ideal organism for studying neural circuits and related behavior, since it completely fulfills the above-mentioned criteria. The nervous system of *C. elegans* consists of only 302 neurons and the entire neuronal system of *C. elegans* is composed of approximately 5,000 synapses and 600 gap junctions, as revealed by electron microscopic analysis (Brenner, 1974; Ward et al., 1975; Ware et al., 1975; Sulston et al., 1983; White et al., 1986). Major neurotransmitters in mammals such as glutamate, acetylcholine, GABA, and monoamines all occur in the nervous system of *C. elegans* (Jorgensen, 2005; Brockie and Maricq, 2006; Chase and Koelle, 2007; Rand, 2007; Li and Kim, 2008). In addition, homologs of genes important for neural development and function in mammals are found in the *C. elegans* genome, suggesting that findings on the *C. elegans* nervous system will be useful for understanding the human brain (Bargmann, 1998; C. elegans Sequencing Consortium, 1998; Hobert, 2005). Furthermore, calcium imaging and optogenetics have been effectively applied to the *C. elegans* nervous system, yielding valuable information about dynamics of neurons and circuit in living animals (Schafer, 2005, 2006; Kerr, 2006; Han and Boyden, 2007; Zhang et al., 2007; Tian et al., 2009; Xu and Kim, 2011).

Caenorhabditis elegans exhibits a rich repertoire of behaviors that are important for its survival and reproduction (**Figure 1**). Several studies have shown that *C. elegans* is not only capable of non-associative learning and short-term memory, but also capable of associative learning and long-term memory (Bargmann and Kaplan, 1998; Chalfie and Jorgensen, 1998; Rankin, 2002; Hobert, 2003; de Bono and Maricq, 2005; Giles et al., 2006; Giles and Rankin, 2009; Hart and Chao, 2010; Sasakura and Mori, 2013).

On the occasion of the Frontiers in Neural Circuits special issue on Japanese studies of neural circuits, we will describe the contributions of Japanese studies on *C. elegans* to the understanding of the neuronal bases of behavior. As mentioned above, molecules and neural signaling that underlie the plastic behavior of *C. elegans* are homologous to those found in mammals. Thus, the highly accurate genetic, neuronal, and behavioral studies on the *C. elegans* nervous system give great insights into our own nervous systems.

REGULATION OF NEURAL CIRCUITS GOVERNING PLASTIC BEHAVIORS

ENHANCEMENT OF ODOR RESPONSE ASSOCIATIVE LEARNING

Learning and memory are the fundamental neural processes in any animal, and the understanding of them is one of the

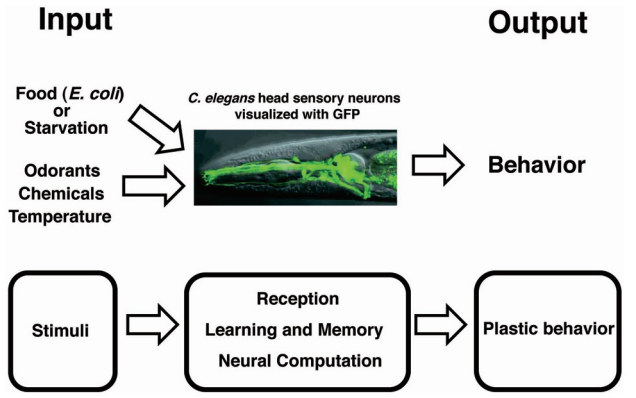

FIGURE 1 | Conceptual scheme for plastic behavior.

most challenging fields in science (Kandel, 2001). *C. elegans* exhibits several behaviors that reflect two forms of learning: non-associative learning and associative learning (Bargmann and Kaplan, 1998; Chalfie and Jorgensen, 1998; Rankin, 2002; Hobert, 2003; de Bono and Maricq, 2005; Giles et al., 2006; Giles and Rankin, 2009; Hart and Chao, 2010; Sasakura and Mori, 2013). Non-associative learning is defined as a change in responses to a stimulus without association with a positive or negative reinforcement. In contrast, associative learning is defined as the process by which an association occurs between two different stimuli. *C. elegans* eats bacteria as a food source (Brenner, 1974; Avery and You, 2012). Food is the fundamental environmental cue for *C. elegans* and profoundly influences several of its behaviors. Dynamic changes in behaviors related to food are thought to be a behavioral strategy critical for acquiring food that may be scarce in nature. *C. elegans* associates food with several environmental stimuli, enabling worm researchers to study associative learning.

Butanone and benzaldehyde are attractive odorants that are sensed by AWC olfactory neurons (Bargmann et al., 1993; Bargmann, 2006). Torayama et al. (2007) established a novel assay system whereby associative learning between an attractive odorant and food can be observed. They found that pre-exposure to butanone in the presence of food induces increased attraction toward butanone (**Figure 2**). Pre-exposure to butanone with food did not change the degree of chemotaxis to benzaldehyde, suggesting that this enhancement of chemotaxis was odorant-specific. The enhancement of chemotaxis to butanone did not require serotonin, which is responsible for food signaling, despite the essential role of food during the conditioning.

The forward genetic screen technique was used to isolate 10 mutants that showed limited butanone-enhanced chemotaxis. Of these, two mutants were further investigated and were found to show almost normal chemotaxis and adaptation to butanone, suggesting that the association between food and butanone is specifically impaired (**Figure 2B**). The first mutant, *olrn-1*, had a mutation in the gene encoding a novel transmembrane protein. Interestingly, *olrn-1* expression was strictly required in AWC neurons for the proper butanone enhancement. The left and right AWC neurons develop distinct sensory properties through an unusual stochastic lateral signaling interaction (Troemel et al., 1999; Wes and Bargmann, 2001). The best example of such regulation is the G-protein-coupled receptor STR-2, the expression of which is stochastically confined to either the left or right AWC neurons, resulting in the asymmetric expression of STR-2. The expression of STR-2 "on" cells is defined as AWC^{ON}, and that of STR-2 "off" cells is defined as AWC^{OFF}. AWC^{ON} and AWC^{OFF} express the different types of chemosensory receptors, thereby contributing to the sensation of different types of odors (Troemel et al., 1999; Wes and Bargmann, 2001). Notably, *olrn-1* mutants were defective in the asymmetry of AWC left and right cell fate and showed two AWC^{OFF} phenotypes, which suggests that the existence of AWC^{ON} is required for butanone enhancement (Bauer Huang et al., 2007; Torayama et al., 2007). Consistent with this hypothesis, another $2AWC^{OFF}$ mutant, *daf-11*, and the ablation of AWC^{ON} by a laser beam both caused the abnormal butanone enhancement.

Interestingly, $2AWC^{ON}$ mutants conversely showed defective butanone adaptation, in which animals pre-exposed to butanone showed an impaired chemotactic response to butanone, suggesting the importance of AWC^{OFF} for sensory adaptation. The asymmetric cell fate of AWC^{ON} and AWC^{OFF} is important not only for generating the diversity of sensation by expressing the different

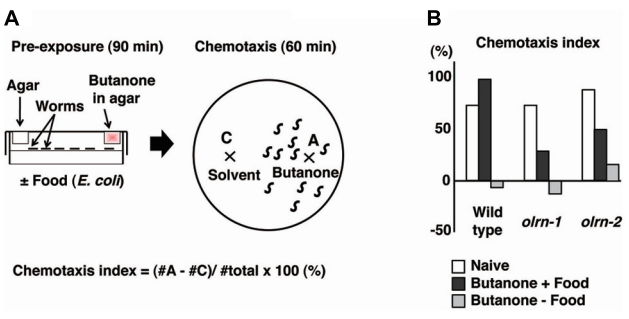

FIGURE 2 | The association of butanone and food to enhance chemotaxis to butanone (Torayama et al., 2007). (A) Scheme for experiments. **(B)** Chemotaxis index of *olrn-1* and *olrn-2* mutants after butanone is associated with or without food.

types of receptors, but also for generating the opposite types of plastic behaviors.

The second gene analyzed was *olrn-2*, which is identical to *bbs-8*, one of the Bardet–Biedl syndrome (BBS) genes (Torayama et al., 2007). BBS is a human genetic disorder that exhibits pleiotropic abnormalities, such as retinal dystrophy, polydactyly, renal malformation, and learning disabilities. Several BBS gene products are reported to be associated with ciliary biogenesis and functions (Ansley et al., 2003). The *C. elegans* genome contains at least eight homologs of human BBS genes designated as *bbs-1* to *-8*. They are all expressed exclusively in ciliated sensory neurons (Ansley et al., 2003). Indeed, *bbs-8/olrn-2* mutants showed structural defects in sensory cilia (Blacque et al., 2004). The expression pattern of STR-2 was normal in *bbs-8/olrn-2* mutants. Torayama et al. (2007) examined the dozens of *C. elegans* mutants defective in cilia structures and found that only *bbs* mutants showed abnormal butanone enhancement, although other cilia-defective mutants showed normal butanone enhancement, despite the fact that the chemotaxis to the butanone itself is impaired in these mutants. Torayama et al. (2007) revealed that butanone enhancement is specifically impaired in *bbs* genes, but the reason for this is unclear. Finding the reason for this may aid the understanding of BBS since BBS is known to cause learning disabilities.

FORGETTING OF ODORANT MEMORY

Forgetting is the process of eliminating unnecessary or excessive information in the brain, enabling animals to obtain new information from their continuously changing environment. Despite the importance of forgetting, the neural and molecular bases of forgetting are almost unknown.

Olfactory adaptation is the plastic behavior in which animals pre-exposed to an odor in the absence of food show decreased response to the odor compared with naive animals. *C. elegans* shows attractive responses and adaptation to odorants sensed by two pairs of olfactory neurons, the AWA neurons and the AWC neurons (Colbert and Bargmann, 1995, Bargmann and Mori, 1997). Inoue et al. (2013) used the recovery from olfactory adaptation against AWA-sensed diacetyl as a behavioral paradigm for forgetting and found that the TIR-1/JNK-1 pathway regulates forgetting (**Figure 3**). *C. elegans* animals grown with food were exposed to diacetyl in foodless conditions for 1.5 h. Then, the animals were re-grown on food-rich plate for a certain period of time before a chemotaxis assay was performed (**Figure 3A**). Wild type animals pre-exposed to diacetyl for 1.5 h recovered normal chemotaxis to diacetyl within 4 h of exposure to food. In contrast, *tir-1* mutants isolated by forward genetics screen showed long-lasting adaptation: they gradually recovered the chemotaxis to diacetyl over about 25 h (**Figure 3B**). Calcium imaging revealed that the AWA response to diacetyl was suppressed during the adaptation period and recovered after 4 h in wild type animals, whereas the AWA response to diacetyl was still suppressed after 4 h in *tir-1* mutants. The sensory perception and the adaption to diacetyl were normal in *tir-1* mutants, suggesting that *tir-1* mutants are defective specifically in the process of forgetting. Notably, *tir-1* encodes a Toll/interleukin-1-resistance domain protein that is homologous to the mammalian adaptor protein SARM, which is known to be expressed in the brain.

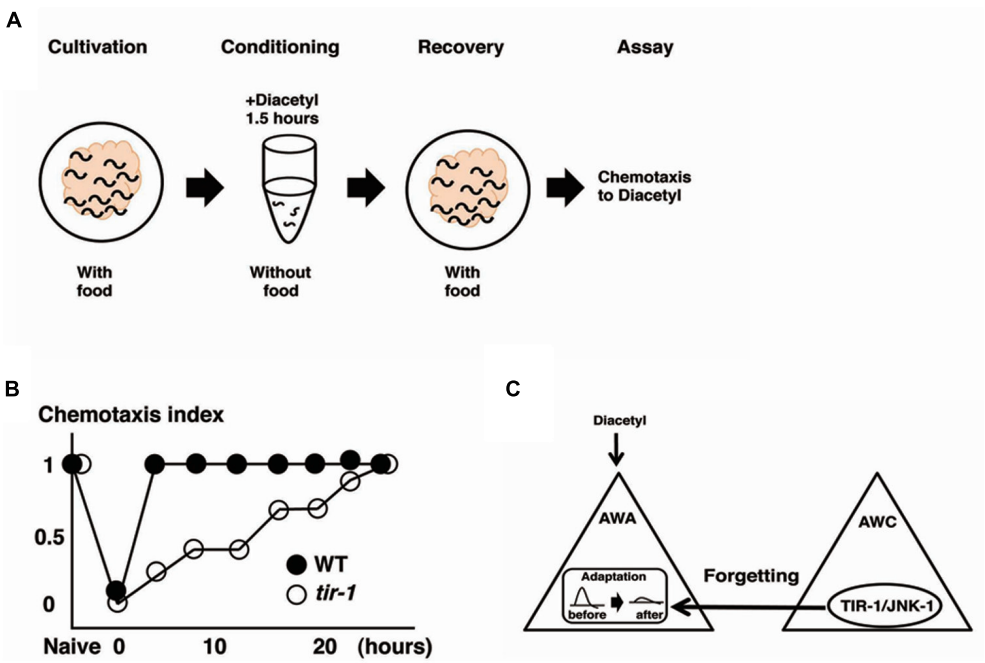

FIGURE 3 | The forgetting of adaptation to diacetyl is regulated through a TIR-1/JNK-1 pathway (Inoue et al., 2013). (A) Scheme for experiments. **(B)** Retention curves of adaptation to diacetyl in wild type animals and *tir-1* mutants. **(C)** A model for the regulation of forgetting of olfactory adaptation to diacetyl. The TIR-1/JNK-1 pathway in AWC neurons regulates the forgetting process of adaptation in AWA neurons.

In *C. elegans*, the TIR-1-mediated p38 mitogen-activated protein kinase (MAPK) pathway is known to regulate the asymmetric cell fate decision of AWC neurons. It also regulates the innate immune response. The UNC-43(CAMKII)-TIR-1-NSY-1(MAPKKK)-SEK-1 (MAPKK) pathway is required for the determination of AWC cell fate, whereas the TIR-1-NSY-1-SEK-1-PMK-1 (MAPK) pathway is required for the innate immune response (Troemel et al., 1999; Sagasti et al., 2001; Wes and Bargmann, 2001; Tanaka-Hino et al., 2002; Chuang and Bargmann, 2005; Shivers et al., 2009). Inoue et al. (2013) tested whether these molecular components were also involved in the forgetting process and found that *unc-43*, *nsy-1*, and *sek-1* mutants exhibited the similar forgetting defects to *tir-1* mutants, but *pmk-1* showed the normal phenotype. JNK-1 and PMK-1 are both MAPKs known to be phosphorylated by SEK-1 (MAPKK). The *jnk-1* mutants displayed forgetting defects, thus, the process of forgetting diacetyl is regulated through the TIR-1/JNK-1 pathway, which is partly overlapping but distinct from the pathways for AWC-asymmetric cell fate and the innate immune response. The TIR-1/JNK-1 pathway is critical for the forgetting process of AWC-sensed odor and of salt chemotaxis learning, suggesting the general role of the TIR-1/JNK-1 pathway in forgetting.

The neurons responsible for the process of forgetting diacetyl have been identified. Expression of *tir-1* cDNA into *tir-1* mutants under the AWA-specific promoter did not rescue the phenotype, but under the AWC-specific promoter rescued the defects. Expression of *sek-1* cDNA into *sek-1* mutants under the AWC-specific promoter also rescued the forgetting defects. Likewise, the expression of the dominant negative forms of *sek-1* and *jnk-1* only in the AWC neurons mimicked the forgetting-defective phenotype. These results suggest that the TIR-1/JNK-1 pathway in AWC neurons is sufficient and necessary for the forgetting process. Two pieces of evidence support the notion that the AWC cell itself plays an important role in the forgetting process of AWA neurons. First, *ceh-36* mutants, in which functional AWC neurons are undifferentiated because of developmental errors, exhibited forgetting defects (Lanjuin et al., 2003). Second, silencing of AWC neural activity by expressing the gain-of-function form of the UNC-103 potassium channel in AWC neurons induced the forgetting defects (Gruninger et al., 2008). The break of AWC-asymmetric cell fate mediated by the TIR-1/NSY-1 pathway is unrelated to the forgetting defects for the following reasons: *nsy-4* mutants, in which the asymmetry of AWC neurons is impaired, exhibited normal forgetting (Vanhoven et al., 2006); and *tir-1(gk264)* mutants, a special allele of the *tir-1* gene that retains AWC asymmetry, also exhibited forgetting defects. AWC neurons are critical for forgetting the adaptive process of AWA-sensed odor, and the TIR-1/JNK-1 pathway in the AWC neurons is essential for the forgetting process (**Figure 3C**).

The next question is how AWC neurons, apparently having no relation to diacetyl sensation, affect the forgetting events in AWA neurons. No neural connections have been reported between AWA and AWC neurons (White et al., 1986), so the information flow from AWC to AWA neurons cannot be explained by neural wiring. The secretion of some molecules by AWC neurons may play an important role for the regulation of forgetting events in AWA neurons. PKC-1, a novel protein kinase C-epsilon/eta is thought to regulate the synaptic release of neuropeptides and gain-of-function of PKC-1 is thought to activate the neuropeptide release at synapses (Okochi et al., 2005; Sieburth et al., 2007; Adachi et al., 2010). Expression of the gain-of-function form of *pkc-1* in AWC neurons rescued the forgetting defects in *tir-1* mutants, although it does not affect the chemotaxis and adaptation to diacetyl, suggesting that the TIR-1/JNK-1 pathway regulates neurosecretion from AWC neurons. Reciprocally, the expression of TetX (tetanus toxin light chain), an inhibitor of synaptic transmission in AWC neurons, caused wild type animals to exhibit the forgetting defects. Thus, AWC neurons may send a forgetting-accelerating signal to AWA neurons through secretion molecules. What induces AWC neurons to release the forgetting signal? The sensory perception of AWC neurons is not involved in forgetting, because *tax-4* mutants defective in AWC sensory signaling showed normal forgetting behavior (Komatsu et al., 1996). In contrast, whether animals were well fed or starved would be critical for AWC neurons to send forgetting signal to AWA neurons. Food signals could be captured in the synaptic region of the AWC axon to modulate TIR-1/JNK-1 signaling, thereby regulating the release of forgetting molecules. Consistent with this hypothesis, TIR-1 is localized at synapses (Chuang and Bargmann, 2005).

Inoue et al. (2013) clarified the existence of forgetting signals and showed that forgetting is not the passive decay of memory, but rather an active process. This study also revealed the hierarchical regulation of forgetting at molecular, cellular, and circuit levels. Further identifications of molecular components involved in forgetting, such as peptides and receptors, and the elucidation of neural regulation will help us understand the nature of forgetting.

ENHANCEMENT OF REPULSIVE RESPONSE TO HARMFUL STIMULI THROUGH NON-ASSOCIATIVE LEARNING

In adaptation and habituation, which are classified as non-associative learning, sensory experiences weaken responses to stimuli. The opposite form of neural plasticity is also known, in which sensory responses are enhanced and animals overreact to previously experienced stimuli. The enhancement of sensory responses is critical for animals to escape from harmful environments. Well-known examples are the sensitization of mammalian peripheral pain sensations and the defensive responses in leeches and *Aplysia* (Hawkins et al., 1993; Sahley, 1995; Millan, 1999). Although addictive rather than defensive, drug addiction is another example of the enhancement of neural responses.

An experimental system to explore the molecular and neural bases for sensory enhancement was established in *C. elegans* (Kimura et al., 2010). *C. elegans* shows avoidance behavior in response to the volatile odorant 2-nonanone, which is sensed mainly by AWB olfactory neurons (Troemel et al., 1997). Exposure to 2-nonanone for 1 h induced animals to move further away from the odor source than naive animals, and the enhancement of this escape response lasted at least 1 h (**Figure 4**). The enhancement of the touch response in *C. elegans* has also been reported, yet the molecular and neural bases for this are unknown (Rankin et al., 1990). The enhancement of 2-nonanone

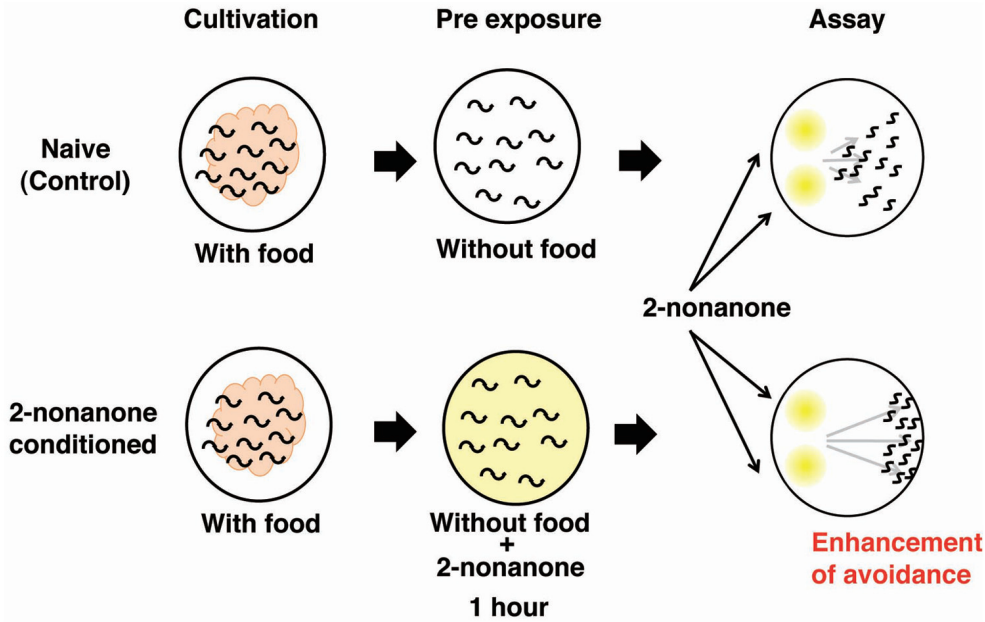

FIGURE 4 | The enhancement of avoidance behavior after the exposure to 2-nonanone (Kimura et al., 2004). Scheme for experiments and the image for results.

avoidance was not influenced by feeding state, hinting at the non-associative nature of this plasticity. Molecular genetic analysis revealed that dopamine signaling is involved in the enhancement of 2-nonanone avoidance. Notably, *dop-3* mutants lacking the D2-like dopamine receptor and dopamine biosynthesis-impaired mutants did not exhibit enhanced avoidance. In addition, the application of haloperidol, a D2-specific antagonist known as an antipsychotic drug, to wild type animals suppressed enhanced avoidance. The DOP-3 functioning neurons were investigated through cell-specific rescue experiments and a single pair of interneurons, known as RIC neurons, was identified as the site of dopamine action. The RIC neurons are known to be octopaminergic and it has been suggested that *dop-3* activity in the RIC neurons suppresses octopamine release (Suo et al., 2009). It has also been reported that RIC neurons form synaptic connections mainly with AVA neurons, which are involved in locomotion. Thus, dopamine signaling in RIC neurons may control the release of octopamine and/or the activity of AVA neurons. A video-based tracking system revealed the effect of 2-nonanone enhancement on escape behavior: the migration velocity remained constant, but the time taken to initiate escape behavior increased, as did the time taken to change the direction of movement. This technique, combined with the recently developed optogenetic system that enables researchers to control the neural activity of living animals during escape behavior, has shed light on the molecular and neural basis for sensory enhancement in *C. elegans* (Kawazoe et al., 2012).

ASSOCIATIVE LEARNING BETWEEN ODORANT AND pH

Caenorhabditis elegans is able to sense environmental pH. Murayama et al. (2013) showed that a transmembrane receptor-type guanylyl cyclase GCY-14 may be the alkaline receptor in the ASEL gustatory neuron. Since food is a strong unconditional stimulus (US) in any conditioning paradigm, the behavioral protocol that avoids using food as US was established. Amano and Maruyama (2011) recently combined two defined chemical cues to analyze associative learning in *C. elegans*. They conditioned worms with 1-propanol as a conditioned stimulus (CS) and acidic pH as an US, and then conducted spaced training and massed training. Spaced training consists of repeated trials with an inter-trial interval (ITI), whereas massed training consists of repeated trials without an ITI. The memory after the spaced training was retained for 24 h, whereas the memory after the massed training lasted only 3 h. Consistent with the theory for touch response (Giles et al., 2006; Giles and Rankin, 2009), *C. elegans* likely processes both long- and short-term memories. Amano and Maruyama (2011) reported that the mutants defective in *nmr-1* encoding of an NMDA receptor subunit fail to form both long- and short-term memories, while mutations in *crh-1* encoding the CREB (cAMP-responsive element binding protein) transcriptional factor only affect long-term memory.

NEURAL INTEGRATION OF TWO TYPES OF INFORMATION AND DECISION ON BEHAVIORAL CHOICE: A MODEL SYSTEM FOR DECISION-MAKING

Decision-making is the cognitive process by which animals select one action among several different choices. In order to study behavioral decision from two conflicting choices and the integration of two different sensory cues, an interaction assay system was developed (Ishihara et al., 2002). Diacetyl is an attractive odor sensed by AWA olfactory neurons and Cu^{2+} ion is aversive metal

sensed by ASH and ADL sensory neurons (Bargmann et al., 1993; Sambongi et al., 2000). The attractive odor, diacetyl, is applied to one side of the assay plate, *C. elegans* animals are placed on the other side of the plate, and a Cu^{2+} barrier is established on the midline of the plate (**Figure 5A**). When *C. elegans* encounters the Cu^{2+} barrier during their migration toward diacetyl, the balance between concentrations of diacetyl and Cu^{2+} regulates the behavioral decision whether they go straight toward diacetyl or withdraw (**Figure 5B**).

The *hen-1* gene, which encodes a secretory protein with an LDL (low-density lipoprotein) receptor motif, regulates sensory integration and decision-making. In the interaction assay, Ishihara et al. (2002) found that *hen-1* mutants showed a weaker tendency to cross the Cu^{2+} barrier when approaching the attractive odorant diacetyl. Since *hen-1* mutants show a normal attractive response to diacetyl and aversion from the Cu^{2+} ion, the HEN-1 protein likely plays a role in decision-making in behavioral choice (**Figure 5B**). The cell non-autonomous function of the HEN-1 protein suggests that HEN-1 acts as a secreted molecule. Secretion of HEN-1 from AIY interneurons is crucial because *ttx-3* mutants (Hobert et al., 1997), which are defective in AIY cell fate, showed a similar phenotype to *hen-1* mutants.

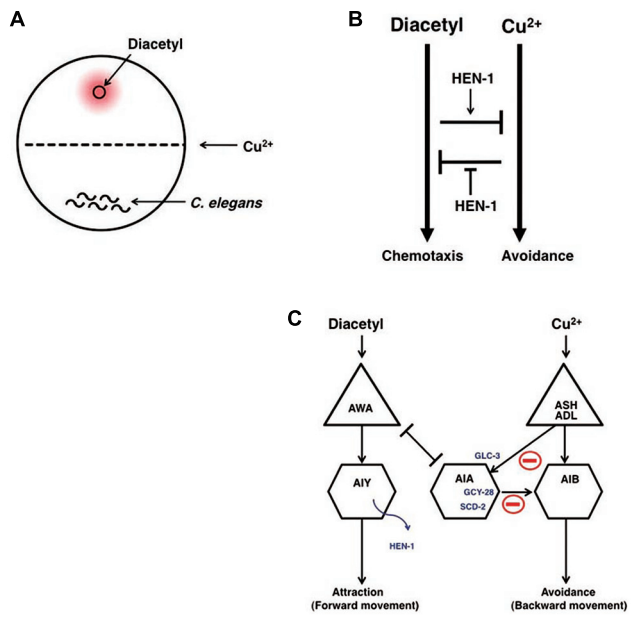

FIGURE 5 | Neural integration of two different types of information and decision on behavioral choice (Ishihara et al., 2002; Shinkai et al., 2011). (A) The assay system of interaction assay. **(B)** The reciprocal inhibition model of the attractive signaling to diacetyl and the avoidance signaling to Cu^{2+}. **(C)** A neural circuit model of the interaction of two sensory signals and decision-making. The activity of AIA interneurons is regulated by the balance between excitatory inputs from AWA through the gap junction and inhibitory inputs from ASH and ADL neurons through the glutamate-gated chloride channel GLC-3. Activated AIA interneurons would increase the relative strength of the signals for diacetyl by inhibiting the signals for Cu^{2+}. GCY-28 and SCD-2 may enhance the inhibitory synaptic outputs from AIA neurons. HEN-1, a secretory protein released from AIY neurons, may act on the receptor SCD-2. The details of the mechanism of HEN-1 action are not yet fully understood.

The jeb protein in *Drosophila* is homologous to HEN-1 and has been reported to regulate the development of visceral mesodermal cells via the tyrosine kinase receptor Dalk (Weiss et al., 2001). SCD-2 is the sole *C. elegans* homolog of Dalk. The phenotype of *scd-2* mutants is almost the same as that of *hen-1* mutants, and *scd-2;hen-1* double mutants behave like both single mutants (Shinkai et al., 2011). These results suggest that *scd-2* and *hen-1* act via the same genetic pathway and support the idea that SCD-2 is a receptor of HEN-1. Forward genetic analysis identified the *gcy-28* gene as a key regulator for interaction behavior. GCY-28 is a membrane-bound guanylyl cyclase that produces cGMP (Tsunozaki et al., 2008; Shinkai et al., 2011). It was found that *gcy-28* was expressed broadly in neurons, however, the expression of *gcy-28.d*, one of the splicing isoforms, was expressed specifically in a pair of AIA interneurons. AIA interneurons were identified as the key neurons for the interaction behavior both through cell-specific rescue experiments and genetic cell-ablation experiments. The defects in *gcy-28* mutants were restored only when *gcy-28* cDNA was expressed in AIA neurons. Likewise, the genetic ablation of AIA neurons in wild type animals induced similar phenotypes to the *gcy-28* mutants. CNG-1 was identified as a cyclic nucleotide-gated channel (Cho et al., 2005) that functions downstream of GCY-28 in AIA neurons. Molecular genetic analysis suggested that the GCY-28/CNG-1 pathway is parallel to the HEN-1/SCD-2 pathway. The site of action of SCD-2 was also shown to be AIA neurons. Hence, both the GCY-28/CNG-1 and HEN-1/SCD-2 pathways are needed in AIA interneurons to act as integrators of conflicting sensory cues (**Figure 5C**).

The next question is how AIA neurons integrate sensory cues and make behavioral decisions. AWA olfactory neurons that are activated by diacetyl make gap junctions with AIA neurons, suggesting that AIA neurons can also be activated by diacetyl. However, ASH/ADL sensory neurons that are activated by Cu^{2+} form synapses with AIA neurons. ASH neurons are known to be glutamatergic, and the glutamate-gated chloride channel GLC-3 is known to be functional in AIA neurons (Chalasani et al., 2007). Interestingly, *glc-3* mutants crossed the Cu^{2+} barrier more frequently than did wild type animals and this phenotype was rescued by expressing *glc-3* cDNA in AIA neurons. These results suggest that ASH neurons activated by Cu^{2+} inhibit AIA neurons through the glutamate-gated chloride channel. The activity of AIA neurons is regulated in opposing fashion through AWA and ASH neurons: AWA neurons activate AIA neuron activity, whereas ASH neurons inhibit AIA neuron activity. The balanced regulation of AIA neuron activity may be important for behavioral decisions (**Figure 5C**). Although AIA neurons send synaptic outputs to many neurons, a major synaptic target of AIA neurons are AIB interneurons that are known to regulate a reversal of movement: removal of an odor sensed by AWC neurons activates AIB neurons to produce a reversal behavior, which reorients the animals to the odor source (de Bono and Maricq, 2005; Gray et al., 2005; Chalasani et al., 2007). In contrast, the application of an odor sensed by AWC neurons activates AIY neurons to induce forward movement that contributes to direct the animals straight to the odor source. Thus, AIA neurons and AIB interneurons have opposite effects on behaviors, hinting that AIA neurons activate inhibitory synapses on

AIB neurons. Inhibitory connectivity from AIA to AIB neurons is also hinted by the laser ablation studies (Wakabayashi et al., 2004).

AIB interneurons receive synaptic inputs from ASH and ADL neurons, both of which sense aversive stimuli, including Cu^{2+}. AIB may play a critical role in aversion behavior: ASH and ADL neurons activated by aversive stimuli convey the information to AIB neurons, and the activated AIB neurons induce reversal behavior, thereby enabling the animal to successfully escape from the aversive stimuli in the integration assay. Consequent activation of AIA interneurons that are connected via gap junctions to the activated AWA olfactory neurons may inhibit AIB neuronal activity, thereby preventing an aversive response to the Cu^{2+} barrier and accelerating migration toward diacetyl over the Cu^{2+} barrier. Consistent with this, activation of synaptic transmission of AIA neurons through AIA-specific expression of the gain-of-function form of *pkc-1* encoding nPKC-epsilon/eta (Okochi et al., 2005; Sieburth et al., 2007; Adachi et al., 2010) caused *gcy-28* mutants to cross over Cu^{2+} barrier. As discussed later, AIA neurons are important for associative learning (Tomioka et al., 2006), indicating that AIA neurons may function as controllers of neural plasticity (**Figures 5C** and **7C**). Further analysis, such as clarification of the physiological properties of AIA neurons, identification and analysis of other molecules, and clarification of the relationship between these molecules will shed light on the decision-making process at the molecular and circuit levels.

ALTERATION TO ODORANT PREFERENCE INFLUENCED BY POPULATION DENSITY OF ANIMALS

Caenorhabditis elegans strains isolated from natural environments all over the world are categorized based on behavioral properties into two group: social and solitary strains. Social strains show the aggregation of animals on the boundary of food where oxygen concentration is low. The standard laboratory strain of *C. elegans* is the Bristol type, which was isolated in England and exhibits the solitary phenotype (Brenner, 1974; de Bono and Bargmann, 1998; Gray et al., 2004; de Bono and Maricq, 2005). Social and solitary behaviors are regulated by FMRFamide-related neuropeptides and homologs of the neuropeptide Y receptor (de Bono and Bargmann, 1998; Rogers et al., 2003). It is important to consider the behavior of animals not only as individuals, but as populations.

As mentioned in the previous section, *C. elegans* stops approaching otherwise attractive odors and disperse from them after exposure to the odor in the absence of food (Colbert and Bargmann, 1995; Nuttley et al., 2002; Hirotsu and Iino, 2005). The density of animals has a large influence on this olfactory plasticity: animals grown in dense conditions exhibit a stronger tendency toward dispersion than the animals grown at a low density (Bowler and Benton, 2005). The interpretation of this phenomenon is that the association between the absence of food and an odorant helps animals to escape from foodless environments and motivates animals to explore new food sources. The high density of animals enhances the tendency toward dispersion and the tendency to explore new environments, because the animal judges that there is little hope of getting food due to the severe competition between individuals (Yamada et al., 2010).

Caenorhabditis elegans recognizes the density of animals through a crude pheromone sensed by chemosensory neurons, including ASI neurons (Hu, 2007). When the crude pheromone was applied to *C. elegans*, the expression of SNET-1, a homolog of the *Aplysia* L11 peptide, was downregulated in ASI neurons. Yamada et al. (2010) found that SNET-1 is a signaling molecule that conveys the density of animals to the nervous system to regulate plastic behavior. The loss-of-function mutation of the *snet-1* gene mimicked high-density conditions and caused the enhancement of dispersion behavior after associative learning between the absence of food and benzaldehyde (**Figure 6**). On the other hand, the overexpression of *snet-1* weakened the tendency toward dispersion. The *nep-2* gene encoding the extracellular peptidase neprilysin was identified as the negative regulator that controls the activity of SNET-1. In *nep-2* mutants, the degradation of SNET-1 peptide is inhibited and the accumulated SNET-1 suppressed dispersion behavior. Taken together, the information on population density is transmitted through external pheromone and endogenous peptide signaling, thereby assuring behavioral plasticity that may be important for the survival of species (**Figure 6**; Yamada et al., 2010).

ASSOCIATIVE LEARNING BETWEEN SALT AND FOOD

Caenorhabditis elegans displays chemotaxis to salt that is mediated mainly by ASE chemosensory neurons (Bargmann, 2006). A gene expression analysis of guanylyl cyclases suggested that ASEL and ASER neurons were different cells: *gcy-6* is expressed almost exclusively in ASEL, whereas *gcy-5* is expressed in ASER (Yu et al., 1997). The transcriptional control of left and right asymmetry has been examined in detail (Hobert et al., 2002; Ortiz et al., 2009). Laser ablation experiments have shown that left and right ASE neurons indeed sense different ions: ASEL senses Na^+ and ASER senses Cl^- (Pierce-Shimomura et al., 2001). The physiological properties of ASE neurons were analyzed with electrophysiology and Ca^{2+} imaging. Whole-cell patch clumping of ASER neurons showed that ASER neurons are electrically isopotent, do not generate Na^+ action potential, and are highly sensitivity to input currents over a wide voltage range (Goodman et al., 1998). Ca^{2+} imaging using a genetically encoded calcium indicator (GECI) showed that ASEL neurons responded to the addition of salt, whereas ASER neurons responded to the removal of salt (Suzuki et al., 2008).

Caenorhabditis elegans subjected to prolonged exposure to salt under starvation conditions induced a dramatic reduction and negative chemotaxis to salt, suggesting that associative learning occurs between starvation and salt (termed "salt learning"; **Figure 7A**; Saeki et al., 2001; Hukema et al., 2006). Tomioka et al. (2006) showed that 10 min of starvation was enough to induce associative learning and that this learning lasted for approximately 1 h. Molecules involved in salt learning have been investigated. Hukema et al. (2006, 2008) showed that the G-protein, Ca^{2+}, and cGMP pathways were involved in salt learning. Tomioka et al. (2006) revealed that the insulin-like signaling pathway played a critical role in salt learning (**Figures 7A,B**). The insulin-like signaling pathway is well known to regulate dauer formation (an arrested developmental variant) and aging in *C. elegans* (Hu, 2007). Mutants of *ins-1*, *daf-2*, *age-1*, *pdk-1*, and *akt-1*, which encode the homologs of insulin, insulin/IGF-1 receptor,

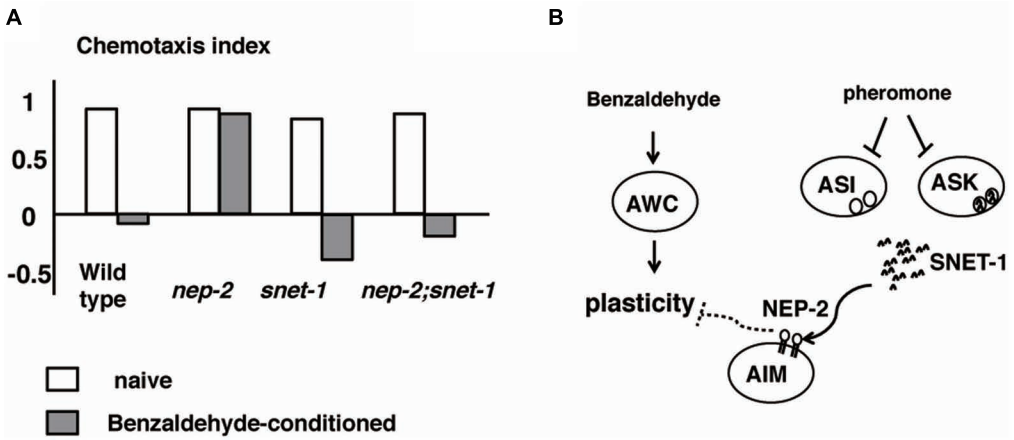

FIGURE 6 | Alteration to odorant preference influenced by population density of animals (Yamada et al., 2010). (A) Olfactory plasticity of *nep-2, snet-1, nep-2:snet-1* mutants. The *nep-2* mutants exhibited defective olfactory plasticity. The abnormality olfactory plasticity of *nep-2* mutants is suppressed by the mutation in the *snet-1* gene. **(B)**. Proposed model of the alteration of olfactory plasticity induced by crude pheromone. SNET-1 is a peptide that inhibits olfactory plasticity. NEP-2 is an extracellular peptidase homologous to neprilysin. The environmental crude pheromone suppresses the expression of SNET-1, thereby facilitating the animals' olfactory plasticity and ability to move away from the odor source. SNET-1 is accumulated in *nep-2* mutants causing the loss of olfactory plasticity and the migration to the odor source.

PI3-kinase, phosphoinositide-dependent kinase, and Akt/PKB, respectively, showed severe defects in salt learning. INS-1 was secreted from AIA interneurons and localized to the synaptic regions of AIA neurons, which are connected to ASER neurons. Tomioka et al. (2006) showed that the DAF-2/PI3 kinase pathway in ASER neurons was required for salt learning. Their proposed model holds that INS-1-mediated feedback signaling acts on the salt receptor neuron ASER and activates the PI3 kinase pathway that may suppresses the synaptic releases from ASER neurons, thereby inhibiting the chemotaxis to NaCl (**Figure 7C**).

Suppression of synaptic release was supported by the finding that the activity of AIB neurons, one of the downstream interneurons of ASER neurons, is downregulated after salt learning (Oda et al., 2011). The molecular mechanism for synaptic transmission of ASER neurons has been partially elucidated. The expression of gain-of-function form of EGL-30/Gq, as well as gain-of-function form of PKC-1/nPKC in ASER neurons of wild type animals suppressed salt learning. In addition, PMA (phorbol myristate acetate), which is an analog of DAG and an activator of the PKC pathway, also suppressed salt learning. It is likely that the Gq/DAG/nPKC pathway promotes a subset of molecular activity that underlies the synaptic transmission of ASER neurons. The elucidation of the relationship between the Gq/DAG/nPKC pathway and the PI3 kinase pathway must be clarified in the future (Adachi et al., 2010).

Ikeda et al. (2008) screened mutants defective in salt learning and isolated *casy-1*. CASY-1 is a transmembrane protein carrying two tandem cadherin domains and an LG/LNS domain in the ectodomain. CASY-1 is an ortholog of calsyntenins (alcadeins) that is reported to be involved in episodic memory performance in humans (Ikeda et al., 2008; Hoerndli et al., 2009). The *casy-1* promoter::*gpf* was expressed broadly in neurons including ASE. The expression of *casy-1* solely in ASER neurons is sufficient to rescue the learning defects. In contrast, the defects were not rescued by expression in other neurons. These results indicate that CASY-1 plays a role in ASER neurons in salt learning. Ikeda et al. (2008) further showed that the ectodomain released through cleavage of CASY-1 is critical for salt learning (**Figure 7C**).

CIRCUIT REGULATION OF ASSOCIATIVE LEARNING BETWEEN TEMPERATURE AND FOOD: A PROPOSED ANALOGY TO HUMAN BRAIN OPERATION

Caenorhabditis elegans associates past growth temperature with food. In its natural habitat, *C. elegans* likely adapts to the fluctuating temperatures in soil in order to stay near food sources. We can observe this behavior as thermotaxis in the laboratory (Hedgecock and Russell, 1975; Mori et al., 2007; Kimata et al., 2012; Sasakura and Mori, 2013). After animals were grown with food at a certain temperature ranging from 15 to 25°C and placed on an agar surface with a temperature gradient, they migrate toward the past growth temperature and move isothermally near that temperature (**Figures 8A–C**). Growth temperature-shift experiments indicated that the acquisition of a new temperature memory requires 2–4 h. Dynamic alternation of temperature preference is also induced by starvation. Growth without food at a certain temperature for several hours induces animals to disperse or avoid the past growth temperature (**Figures 8B,C**).

The simple neural circuit involved in thermotaxis is the perfect subject for the study of the functional connectome. In *C. elegans*, the environmental temperature is sensed by AFD and AWC sensory neurons, and then thermal signals are transmitted to the downstream interneurons AIY, AIZ, and RIA. The AIY-mediated neural pathway is responsible for thermophilic movement, whereas the AIZ-mediated neural pathway is responsible for cryophilic movement. The counterbalanced regulation of the activities of AIY and AIZ neurons is thought to be essential for thermotaxis. The

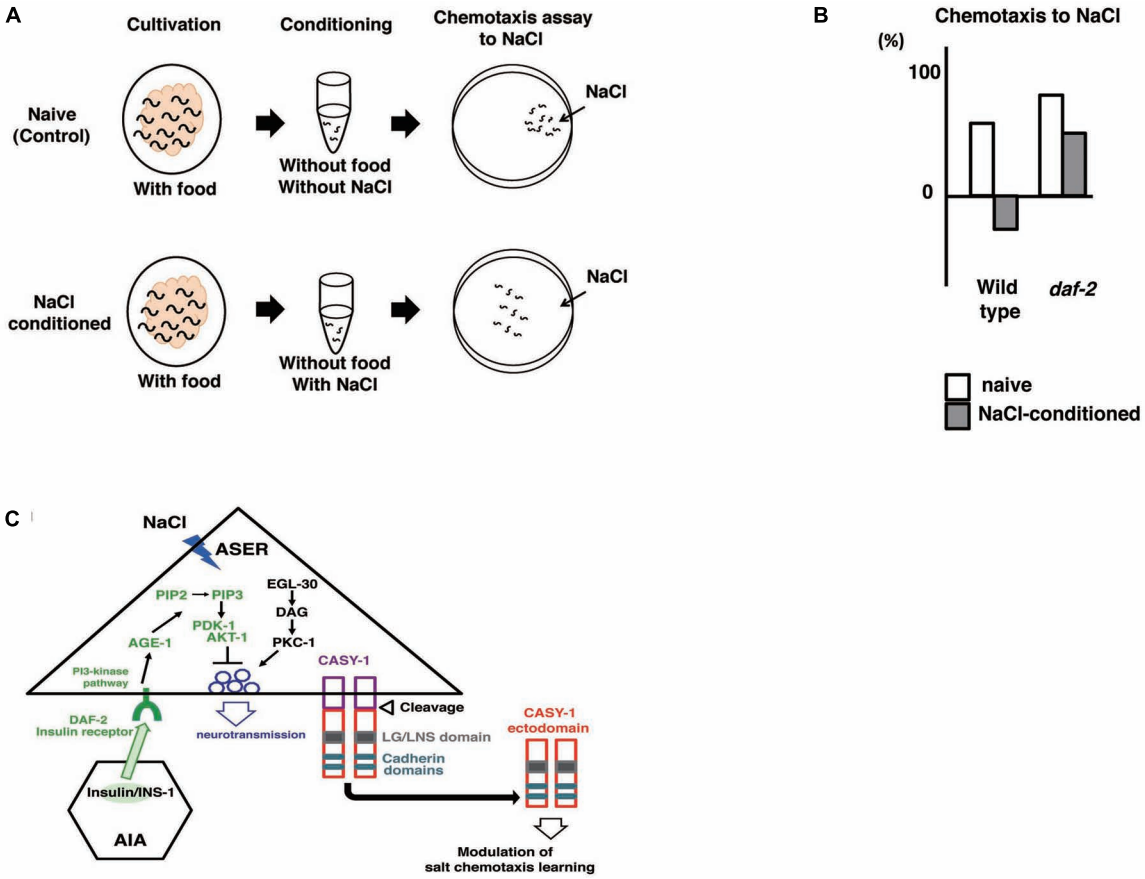

FIGURE 7 | Associative learning between salt and food (Saeki et al., 2001; Tomioka et al., 2006; Ikeda et al., 2008). (A) Scheme for experiments. **(B)** The *daf-2* mutants are defective in salt learning. **(C)** Proposed model for the regulation of salt learning. Insulin-like peptide INS-1 is secreted from AIA interneurons and the insulin-like signaling pathway is activated in the ASER neuron through the insulin receptor DAF-2. DAF-2 activates PI3 kinase AGE-1 that converts PIP2 to PIP3, which leads to activation of the downstream signal components Ser/Thr kinases PDK-1 and AKT-1. Then, the activation of this pathway negatively regulates neuronal activity of the ASER neuron, thereby generating plasticity in salt chemotaxis. EGL-30/Gq, DAG, and PKC-1/nPKC pathway in the ASER neuron may positively regulate the synaptic transmission antagonize to PI3 kinase pathway. Calsyntenins expressed in the ASER neuron is cleaved and the ectodomain is released. Released ectodomain acts on either the ASER neuron itself or others to modulate salt chemotaxis learning.

RIA interneurons integrate signals from both upstream interneurons AIY and AIZ neurons. Consequently, the outcome of neural computations in the core thermotaxis circuit regulates the body wall muscles, thereby controlling the worm's ultimate behavior (**Figure 8D**).

In addition to their thermosensory function, AFD neurons also serve as a temperature memory device. The memory function of AFD neurons was revealed by Ca^{2+} imaging, where the response of AFD neurons to warming corresponded to their past growth temperature (Kimura et al., 2004; Clark et al., 2006; Mori et al., 2007; Kimata et al., 2012; Sasakura and Mori, 2013). The CREB is a transcriptional factor that regulates neural plasticity from invertebrates to mammals. Nishida et al. (2011) showed that the mutants in *crh-1* gene encoding a *C. elegans* homolog of CREB showed abnormal thermotaxis and the expression of *crh-1* cDNA only in AFD neurons almost completely reversed the defects. CREB function in AFD may be required for temperature memory or the presynaptic plasticity.

Kodama et al. (2006) showed by Ca^{2+} imaging that food or starvation signals did not affect AFD neuronal response to temperature. These results imply that food or starvation signals influence the neural activity of interneurons in the circuit, thereby generating plastic behaviors. Molecular genetic analysis has identified the several molecules critical for the associative learning between food and temperature. The *aho-2* mutation, isolated in a forward genetic screen, was identical to the *ins-1* mutation, suggesting the general role of insulin in learning (Kodama et al., 2006; Tomioka et al., 2006). INS-1 acts in a cell non-autonomous fashion in interneurons required for thermotaxis. INS-1 antagonizes the DAF-2/insulin receptor and the AGE-1/PI3 kinase pathway. The behavioral defects of *age-1* mutants were rescued by expressing the *age-1* gene in any of three interneurons, AIY, AIZ, and RIA, all of which are component interneurons in the thermotaxis circuit. Thus, INS-1 acts on the interneurons to change the dynamics of the neural circuit. These results are in contrast to salt learning, in which

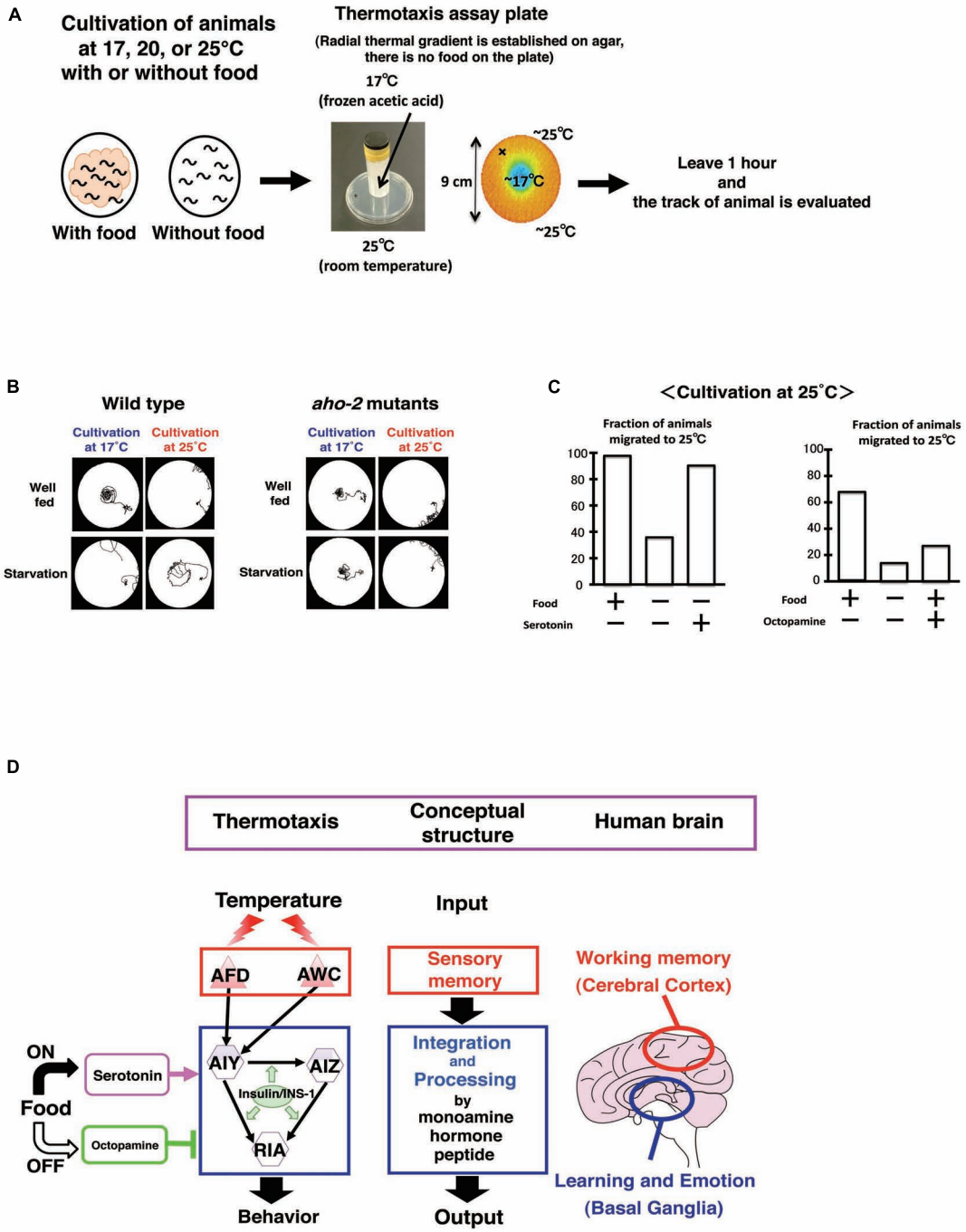

FIGURE 8 | Circuit regulation of associative learning between temperature and food (Hedgecock and Russell, 1975; Mori and Ohshima, 1995; Mohri et al., 2005; Kodama et al., 2006; Sasakura and Mori, 2013). **(A)** Assay system and scheme for experiments. **(B)** Thermotaxis of wild type animals and *aho-2/ins-1* mutants. Wild type animals cultivated with food at 17 or 25°C migrate to the past growth temperature on a radial thermal gradient plate. In contrast, wild type animals cultivated without food (starvation conditions) diffuse and avoid the growth temperature area. The *aho-2/ins-1* mutants exhibited normal thermotaxis when grown with food, but exhibited abnormal thermotaxis when grown without food. Despite the starvation conditions, *aho-2/ins-1* mutants migrate to the past growth temperature. **(C)** Exogenous serotonin mimics the well-fed state and octopamine mimics the starvation state in thermotaxis. *C. elegans* grown at 25°C without food but with serotonin behaves like well-fed animals, whereas *C. elegans* grown with food but with octopamine behaves like starved animals. **(D)** Proposed analogy between the thermotaxis neural circuit in *C. elegans* and the human brain. Neural operation logic in *C. elegans* thermotaxis is analogous to that in the human brain. Stored thermal information in AFD neurons is transmitted to the thermotaxis core interneurons AIY, AIZ, and RIA. Thermal information and food state are integrated and processed in those interneurons by monoamines and insulin to generate output behavior. In the human brain, working memory is coded in the cerebral cortex, and the coded information is conveyed to the basal ganglia, where learning and emotion proceed with modulation through monoamines. We propose here a functional analogy between the simple neural circuit in *C. elegans* thermotaxis and the functionally layered structure of the human brain.

INS-1 acts on the salt-sensing neuron ASER (Tomioka et al., 2006).

An ortholog of the human calcineurin alpha subunit TAX-6 is required in two pairs of interneurons, AIZ and RIA, for the associative learning between food and temperature (Kuhara and Mori, 2006). A novel type of hydrolase AHO-3 is important for this learning (Nishio et al., 2012). The expression of FAM108B1, which is a human homolog of AHO-3 and strongly expressed in the human brain, restored the defects of *aho-3* mutants. ABHD6, another protein related to AHO-3, was reported to be involved in endocannabinoid signaling in mouse neural culture cells (Marrs et al., 2010). Hence, endocannabinoid signaling could be involved in the associative learning between food and temperature.

Exogenous serotonin mimics the presence of food, whereas exogenous octopamine mimics the absence of food in many aspects of *C. elegans* behavior, such as locomotion, pharyngeal pumping, and egg laying (Horvitz et al., 1982; Sawin et al., 2000; Chase and Koelle, 2007). Mohri et al. (2005) found that the application of serotonin to food-deprived animals induces thermotaxis to a memorized temperature, while the application of octopamine to well-fed animals suppresses thermotaxis to a memorized temperature (**Figure 8C**). These results suggest that the balanced regulation through these two monoamines in interneurons is a key process for thermotactic plasticity. It is intriguing to ask how the antagonistic behavioral regulation through serotonin and octopamine is related to the antagonistic neural regulation between AIY and AIZ neurons (Mori and Ohshima, 1995). It is also important to uncover the relationship between insulin signaling and monoamine signaling. A recent unexpected finding is that temperature information sensed by non-neuronal tissues such as intestines and body wall muscles through the heat shock transcriptional factor-1 (HSF-1) feeds back to the core thermosensory circuit and regulates the activity of AFD neurons via estrogen signaling (Sugi et al., 2011).

We propose that the neural circuit for thermotactic plasticity is amazingly similar to two functional parts of the human brain: the cerebral cortex and basal ganglia (**Figure 8D**; Sasakura and Mori, 2013). The cerebral cortex encodes the working memory that is required for the temporal storage of information. The basal ganglia play an important role in learning, emotion, and motivation. In the neural circuits for themotaxis, temperature information stored in the sensory neurons AFD and probably AWC, is transmitted to the interneurons, AIY, AIZ, and RIA, where the temperature information is associated with feeding and/or starvation signals to generate associative learning. Thus, the sensory neurons AFD and probably AWC, working as a memory storage device, are equivalent to the cerebral cortex, while the three interneurons AIY, AIZ, and RIA, which play a part in learning and likely receive neuromodulatory monoamines according to feeding states, are equivalent to the basal ganglia (**Figure 8D**).

There is mounting evidence to support the notion that the *C. elegans* nervous system has many physiological similarities to the human brain. Serotonin and dopamine signaling regulates the motivational behavior in locomotion in *C. elegans* (Sawin et al., 2000). The serotonin reuptake inhibitor fluoxetine (Prozac) is able to change locomotion behavior in *C. elegans* (Choy and Thomas, 1999; Ranganathan et al., 2000, 2001). Catecholamine modulates the sensory stimulus from environmental food to determine whether *C. elegans* remains in the vicinity of food (Bendesky et al., 2011). Vasopressin/oxytocin signaling, which regulates water balance, reproduction, and social behavior in mammals, is critical for gustatory associative learning and reproductive behaviors (Beets et al., 2012; Garrison et al., 2012). Sleep-like behavior and EGF signaling, which are important for the day–night cycle behavior in mice, is also critical for *C. elegans* rest-taking behavior (Van Buskirk and Sternberg, 2007; Raizen et al., 2008).

The *C. elegans* genome contains nearly the same suit of neuronal genes as humans: transcriptional factors, components of synapses, gap junctions, neurotransmitters, neuromodulators, receptors, ion channels, and so on (Bargmann, 1998; C. elegans Sequencing Consortium, 1998; Hobert, 2005; Jorgensen, 2005; Brockie and Maricq, 2006; Chase and Koelle, 2007; Rand, 2007; Li and Kim, 2008). Their genome-level similarity suggests that the neural bases underlying behavior are indeed similar. In addition, recent work on connectivity patterns in the male *C. elegans* nervous system tells us that principles of the *C. elegans* neural network are also similar to those of the human brain (Jarrell et al., 2012). Given that neural plasticity is necessary for survival of the animal from an early stage of evolution, the principles of neural function that underlie behaviors may be conserved between *C. elegans* and humans.

DISSECTION OF INFORMATION FLOW AND PROCESSING IN NEURAL CIRCUITS THROUGH ADVANCED TECHNOLOGY: IMAGING, OPTOGENETICS, AND TRACKING SYSTEMS

MONITORING NEURAL ACTIVITIES

Monitoring intercellular activity is important for understanding the mechanism of neural circuits. The first GECI, called cameleon, was invented in 1997 by Miyawaki et al. (1997). Deployment of GECIs in biological sciences, particularly in neurosciences, has accelerated the development of various GECIs (Nakai et al., 2001; Tian et al., 2009; Zhao et al., 2011; Akerboom et al., 2012; Chen et al., 2013). Attempts to develop new and modified GECIs have greatly promoted studies of neural circuits as well. Calcium imaging techniques are powerful tools, because calcium signals transduce a variety of information in tissues and organelles. Other monitoring techniques also have the potential to enable the observation of different types of intercellular events. Tomida et al. (2012) monitored activity of MAPK in the salt-sensing sensory neuron ASER in living worms. Using a Förster resonance energy transfer (FRET)-based probe, they showed that MAPK activity corresponded to salt stimulus depending on its given patterns of repetitive salt pulses. Comparison between the time course of MAPK and Ca^{2+} activities showed that MAPK activity is related to the non-linear response of Ca^{2+} to the given salt patterns. These results shed light on the modulation mechanisms of signal transduction inside cells that respond to the environmental signals.

For the purpose of monitoring neural activity, neuroscientists require good voltage-sensitive fluorescence sensors. Although voltage-sensitive dyes have certain advantages such as to allow direct monitoring of the signals of neural activity, recording both synaptic input and action potential output, and comparing the

acquired data with electrophysiological results, their low signal-to-noise ratio limits their practical use. *In vivo* electrical recording using genetically encoded voltage indicators (GEVI) is a particularly challenging problem. Using the voltage-sensitive fluorescent protein VSFP 2.42 (Akemann et al., 2010), activity of AIY interneuron was explored by Shidara et al. (2013). They reported different dynamics of the neurite and the soma in response to given odorant stimuli. Since some interneurons, such as RIA and AIY, show compartmental activity of calcium dynamics (Clark et al., 2006; Hendricks et al., 2012), different types of imaging probes are necessary to address whether different locations in neurons have different functions.

BEHAVIORAL ANALYSIS WITH AUTOMATED TRACKING SYSTEMS

Behavior is the eventual output of neural circuits. Behavioral analysis therefore clarifies the meanings and functions of each neural mechanism. To perform behavioral analysis, automated data acquisition and computational methods are useful to increase throughput of tedious experiments and to exclude the subjectivity of experimenters. In fact, computational methods are helpful to categorize each observed behavioral component based on rigid criteria by describing the criteria in computer languages. Long-term behavioral analysis has the merit of using a computational approach since computers can perform a repetitive analysis an almost infinite number of times. Statistical analysis based on automatically acquired abundant data may yield a subtle difference in the properties that are usually hidden in the noise of observed measurements. For the analysis of *C. elegans* behavior, several tracking systems have been developed in different labs (Husson et al., 2013a).

Hoshi and Shingai (2006) developed a tracking system for the automated analysis of the locomotion of *C. elegans*. Their system identifies the locomotory state (forward movement, backward movement, rest, and curl) of worms on agar plates using several hours of data. The heads and tails of tracked worm are also identified from acquired images using their algorithm (Hoshi and Shingai, 2006). Using this system, Wakabayashi et al. (2004) identified distinct behavioral states during forward locomotion. The addition of the laser ablation technique further allowed the quantification of the relationship between the behavioral state and related neurons (Wakabayashi et al., 2004). Visualizing locomotory behavior with computational measurements itself is also useful for discriminating behavioral phenotypes. Miyara et al. (2011) analyzed the role of a novel protein called macoilin with a tracking system by visualizing locomotory undulation of *C. elegans*. Similar methods have been developed by several labs and this approach is becoming popular to describe the locomotory undulation of *C. elegans* (Korta et al., 2007; Pierce-Shimomura et al., 2008; Stephens et al., 2008; Fang-Yen et al., 2010).

OPTOGENETICS OF NEURAL CIRCUITS

Optogenetic techniques enhance the validity of tracking systems by adding non-invasive operation for neural activities using photoactivation of ion channels or pumps on the target neurons during long-term observation of freely moving animals. The combination of neuronal perturbation and behavioral monitoring is a powerful approach for understanding the mechanisms of behavioral control by neural circuits. A pioneering work that combined a tracking system and optogenetics was done in order to analyze thermotaxic behavior (Kuhara et al., 2011). A yellow light stimulus enabled to weaken the activity of the thermosensory neuron AFD with a transgenic line expressing halorhodopsin coding a light-activated chloride pump. Together with a tracking technique, mutant analysis, and calcium imaging for AFD neurons and the downstream interneurons AIY, Kuhara et al. (2011) showed that the AFD–AIY circuit could regulate the activity of AIY neurons in both excitatory and inhibitory directions, which accounts for thermophilic and cryophilic movements, respectively.

While the laser ablation technique completely disrupts activity of the target neuron, optogenetic methods perturb the target neural circuits quantitatively in a specific time window. Long-term observation of such quantitatively perturbed target animals would be beneficial for uncovering the detailed mechanisms of neural circuits. Studies with powerful new light-driven proton-pumps such as Arch (Chow et al., 2010; Okazaki et al., 2012; Husson et al., 2013b) and as ArchT (Okazaki and Takagi, 2013) in *C. elegans* research has enabled very effective and long-term silencing of neurons, under continuous illumination for up to 1 min, at a minimum. When an Arch mutant (M128A/S151A/A226T), designed to cause a blue shift in the action spectrum, is expressed in *C. elegans* neurons, locomotory arrest can be elicited by blue light, proving that *C. elegans* locomotion can serve as a convenient assay for *in vivo* evaluation of new optogenetic tools (Sudo et al., 2013).

MANIPULATION OF SPATIOTEMPORAL GENE EXPRESSION

A previous report indicated that available cell-specific promoters enable unique expression of transgenes in only 12% of neuronal groups (Chelur and Chalfie, 2007). Since some promoters only drive gene expression relatively weakly, the number of promoters with practical utility for driving transgene expression in unique neuronal types is further limited. Several intersectional approaches utilize a pair of promoters with overlapping specificities to express a target gene in a single neuronal group. Split GFP and split apoptotic factor can function following the intersectional gene expression of each partner fragment, and an FLP-out strategy using *in vivo* recombination systems such as Flp-FRT or Cre-loxP enables expression of a given protein with higher cell-type specificity. However, it is still impossible to express a particular gene in a single targeted neuron, or a combination of multiple targeted neurons.

Inducible promoters are also frequently used for temporal regulation of transgene expression in model organisms. Given the targeting of external stimuli to a defined local region, the use of inducible promoters can enable spatially targeted induction of genes, even at single cell spatial resolution. The use of heat-activated heat shock promoters has been explored, and attempts have been made to deliver heat locally. Lasers with high spatial resolution can target small areas in tissue for local heating, a promising approach for activating transgenes under the control of heat shock promoters. The heat shock response, which is aided by the heat shock promoter, leads to activation of transcription. Since the heat shock response is a physiological defense mechanism inherent in almost all cell types in most organisms, such methods would have broad applicability in biological studies.

Irradiation with a Coumarin 440 dye laser beam under microscopic control is a common technique for cell ablation in *C. elegans* and other organisms. Assuming that heat generated by the laser is the main cause of cell death, attempts have been made to induce the heat shock response in targeted cells without causing cell death, by reducing the laser power level. Pioneering researchers have reported successful laser-mediated heat shock induction in single targeted cells in *C. elegans*, *Drosophila* and zebrafish (Stringham and Candido, 1993; Halfon et al., 1997; Halloran et al., 2000). However, there have been few follow-up studies using this method because it was found to have two major drawbacks: low efficiency of gene induction, and cell damage caused by irradiation (Harris et al., 1996; Kamei et al., 2009). Thus, it appears that the Coumarin 440 dye laser is not a good choice for heating cells.

THE IR-LEGO SYSTEM

The IR-LEGO (infrared laser-evoked gene operator) is a novel recently developed system that uses an infrared (IR) laser radiating at 1480 nm, a wavelength at which the absorption coefficient of water is about 10^5 times higher than that at 440 nm (Kamei et al., 2009; Suzuki et al., 2013). The much higher absorption rate enables efficient heating of water in specimens so that the heat shock response can be effectively induced using relatively low input power, which in turn helps avoid photochemical damage during irradiation. The IR-LEGO system was first applied to *C. elegans*, and the induced gene expression was successfully demonstrated in targeted single cells for multiple cell types, including neurons (Kamei et al., 2009). By choosing an appropriate laser power level, gene expression can be induced at a frequency of around 50% using short irradiation periods (less than 1 s), a much shorter duration than those (75 s to 10 min) reported in gene induction experiments using the Coumarin 440 dye laser. Following irradiation, targeted cells showed no apparent damage; they expressed marker genes, executed cell divisions, and eventually completed differentiation normally. Induction of wild type gene expression in single mutant cells has also confirmed that phenotypic defects such as cell migration or fate determination can be successfully rescued. The IR-LEGO system's induction efficiency, which is sufficient for practical use, and its lack of harmful effects indicate that the problems inherent in earlier laser-mediated gene induction methods have been overcome. The IR-LEGO system can be applied to many transparent organisms, and can be equipped for transgenic technology. To date, it has been used on fish (*Oryzias latipes* and *Danio rerio*) and on a higher plant (*Arabidopsis thaliana*; Deguchi et al., 2009; Kimura et al., 2013). In fish, cells at a depth of 150 μm were induced to express a transgene using the IR-LEGO system.

An *in vitro* study using a polyacrylamide gel tissue model has suggested that temperatures at the irradiation focus change very quickly in response to IR irradiation, and that the area with temperature shifts exceeding 20°C was essentially confined to a vertically extended ellipsoidal area 7 μm along the *x*–*y* axes (Kamei et al., 2009). Although this size is sufficiently small to heat individual cells in most organisms, the original continuous irradiation procedure of the IR-LEGO system sometimes induces gene expression in multiple cells in *C. elegans* when the target lies in a densely packed cell cluster such as a ganglion. This may reflect the more limited dissipation of heat in living organisms compared with that in the *in vitro* model. In order to achieve efficient gene induction in single neurons in ganglion by using the IR-LEGO system, a promising approach is to use pulsed irradiation that minimizes the heating of areas surrounding the focus area by facilitating heat dissipation during interpulse periods. When combined with an FLP-out strategy, the IR-LEGO system can be used for inducing sustained gene expression in single targeted neurons, broadening its potential for future applications.

THEORETICAL APPROACHES

Theoretical approaches promote the understanding of the mechanisms of neural circuits by providing an integrated view of different experiments or bringing new insights into the analyses of the complex data. With this in mind, computational simulations can validate hypothesized rules, especially when several rules are combined.

As described above, *C. elegans* exhibits food and temperature associative learning behavior called thermotaxis, where animals grown at a constant temperature with food migrate to the previous cultivation temperature on a thermal gradient. For the analysis of thermotaxis, several theoretical studies have attempted to explain different results of thermotaxis behavioral assays in different conditions.

Although the original study on this topic reported both cryophilic and thermophilic migration, where the animals migrate toward colder and warmer regions, respectively, some reports have shown the absence of thermophilic migration under certain experimental conditions (Hedgecock and Russell, 1975; Ryu and Samuel, 2002; Yamada and Ohshima, 2003; Kimata et al., 2012).

Based on a biased random walk model for *C. elegans* searching behavior, Matsuoka et al. (2008) examined the inconsistency between the results of population and individual thermotaxis assays used in the different reports. The Monte Carlo approach, which involves random sampling from a numerical model, showed the simulated population dynamics of *C. elegans* thermotaxis based on the migration rules for individual worms. In spite of the lack of thermophilic rules above growth temperatures for hypothetical individual worms, the simulated population dynamics showed a thermophilic tendency. Thus, the simulation results were consistent with the different results in various experimental conditions.

Nakazato and Mochizuki (2009) took another approach to deal with the problems that include inconsistency in thermotaxis assays in the different reports. They constructed a mathematical model based on the differential equations for the population dynamics of *C. elegans* migration during thermotaxis. With hypothetical parameter sets based on the previously published experimental data, they examined the results of thermotaxis assays in the different reports. In spite of the inconsistent results of previous theoretical reports, the proposed model generates consistent results for each experiment with the same parameter set.

In contrast to the above behavioral modeling studies, a detailed computational neural model for dynamic body regulation

elucidates different aspects of the modeling study. Suzuki et al. (2005) constructed a computational model for locomotory regulation of *C. elegans* based on the known anatomical neural wiring map. Even with the complete anatomical neural wiring map of 302 neurons of *C. elegans*, orchestration of each motor neuron for locomotory movements, including the location of the central pattern generator, is still unclear. Simulation approaches allow the reconstruction of the dynamic behavior of a system combining the knowledge of the components of the system. Describing the dynamics of the whole system that consists of multiple components is helpful for understanding the orchestration inside the system; once a model is constructed, a survey of the effects of each component is feasible. Suzuki et al. (2005) modeled the locomotory movement of *C. elegans* with a motor neuronal network and regulated body using a multi-joint rigid link model. Then they reconstructed the movements of wild type animals and *unc-25* mutants that lack GABA inhibitory signals in motor neurons. Such a reconstruction approach of the dynamic system is helpful for understanding the relationship between each component and the whole system.

Another theoretical approach involves observing quantitatively measured experimental data in combination with computational simulations. Ohkubo et al. (2010) analyzed trajectory data of worms during NaCl chemotaxis. Using cumulative distributions of curving rates in a log-log scale, comparison with the Gaussian distribution showed the long-tail behavior of curving rate of the worm trajectories (Ohkubo et al., 2010). The long-tail property of the curving rate implies the multiplicative noise of neural outputs, which inherit noise term by multiplication, although the long-tail behavior is not restricted to the specificity of the multiplicative noise. They constructed mathematical models based on the random walk model, and the simulation results showed the robustness of the long-tail property in several conditions. As shown by Ohkubo et al. (2010), the analysis with the theoretical standpoint would help extract the essence of the system's properties.

Particularly for the complex objects like neural circuits, computational results do not assure the validity of hypothesized model, since biological systems usually include many unknowns. However, theoretical approaches and computational simulations provide logically descriptive tools for dynamic systems to develop working hypotheses. Mutual feedback between experimental and theoretical studies will advance the understanding of complex phenomena such as behavioral regulation by neural circuits.

SUMMARY AND PERSPECTIVE

As we have reviewed above, studies using *C. elegans* have carried neural circuit studies forward. They include studies on the complex functions of nervous systems such as learning and memory. The understanding of the design of behavioral assay captures the essence of complex neural functions; the simple neural circuit of *C. elegans* is well suited for the detailed investigation for the target mechanism. Development and application of novel technologies accelerate the progress of research and also shed light on the hidden aspects of neural mechanisms. The Japanese *C. elegans* research community contributes to advance the neural circuit studies by providing unique behavioral assay frameworks and technological developments. Behavioral and neural circuit studies of *C. elegans* have furnished molecular and mechanical insights into neural operation to the understanding of the human brain. This pioneering role of *C. elegans* for neuroscience is expected to continue to be important for human brain studies. "The Brain Activity Map Project," declared by Barack Obama, President of United States, in April 2013, is a large-scale, 10-year continuous project that finally aims to map the activity of every neuron functional connection in the human brain (Alivisatos et al., 2012, 2013). This large-scale project is equivalent to the "Human Genome Project" in which *C. elegans* genome studies played a pivotal role as a pilot case. The already identified complete connectome (302 neurons and approximately 7,000 connections) and full recording of all neuronal activity in the near future will be an important boost for the brain activity map project. Given this situation, *C. elegans* neuroscience is becoming more valuable than ever.

ACKNOWLEDGMENTS

We thank Hitoshi Okamoto for stimulating discussion, Ichiro Aoki for critical comments on the manuscript, and members of the Mori Lab for discussion. This work was supported by CREST-JST, Strategic Research Program for Brain Sciences, MEXT, and a Grant-in-Aid for Scientific Research on Innovative Area-Neural Diversity and Neocortical Organization from MEXT (to Ikue Mori), and by grants from JSPS KAKENHI (Grant Numbers 25560424, 25291044), MEXT KAKENHI (Grant Number 25111708), the Research Foundation for Opto-Science and Technology, and the Ichihara International Scholarship Foundation (to Shin Takagi).

REFERENCES

Adachi, T., Kunitomo, H., Tomioka, M., Ohno, H., Okochi, Y., Mori, I., et al. (2010). Reversal of salt preference is directed by the insulin/PI3K and Gq/PKC signaling in *Caenorhabditis elegans*. *Genetics* 186, 1309–1319. doi: 10.1534/genetics.110.119768

Akemann, W., Mutoh, H., Perron, A., Rossier, J., and Knöpfel, T. (2010). Imaging brain electric signals with genetically targeted voltage-sensitive fluorescent proteins. *Nat. Methods* 7, 643–649. doi: 10.1038/nmeth.1479

Akerboom, J., Chen, T.-W., Wardill, T. J., Tian, L., Marvin, J. S., Mutlu, S., et al. (2012). Optimization of a GCaMP calcium indicator for neural activity imaging. *J. Neurosci.* 32, 13819–13840. doi: 10.1523/JNEUROSCI.2601-12.2012

Alivisatos, A. P., Chun, M., Church, G. M., Deisseroth, K., Donoghue, J. P., Greenspan, R. J., et al. (2013). Neuroscience. The brain activity map. *Science* 339, 1284–1285. doi: 10.1126/science.1236939

Alivisatos, A. P., Chun, M., Church, G. M., Greenspan, R. J., Roukes, M. L., and Yuste, R. (2012). The brain activity map project and the challenge of functional connectomics. *Neuron* 74, 970–974. doi: 10.1016/j.neuron.2012.06.006

Amano, H., and Maruyama, I. N. (2011). Aversive olfactory learning and associative long-term memory in *Caenorhabditis elegans*. *Learn. Mem.* 18, 654–665. doi: 10.1101/lm.2224411

Ansley, S. J., Badano, J. L., Blacque, O. E., Hill, J., Hoskins, B. E., Leitch, C. C., et al. (2003). Basal body dysfunction is a likely cause of pleiotropic Bardet–Biedl syndrome. *Nature* 425, 628–633. doi: 10.1038/nature02030

Avery, L., and You, Y. J. (2012). *C. elegans* feeding. *WormBook* 1–23. doi: 10.1895/wormbook.1.150.1.

Bargmann, C. I. (1998). Neurobiology of the *Caenorhabditis elegans* genome. *Science* 282, 2028–2033. doi: 10.1126/science.282.5396.2028

Bargmann, C. I. (2006). Chemosensation in *C. elegans*. *WormBook* 1–29. doi/10.1895/wormbook.1.123.1.

Bargmann, C. I., Hartwieg, E., and Horvitz, H. R. (1993). Odorant-selective genes and neurons mediate olfaction in *C. elegans*. *Cell* 74, 515–527. doi: 10.1016/0092-8674(93)80053-H

Bargmann, C. I., and Kaplan, J. M. (1998). Signal transduction in the *Caenorhabditis elegans* nervous system. *Annu. Rev. Neurosci.* 21, 279–308. doi: 10.1146/annurev.neuro.21.1.279

Bargmann, C. I., and Mori, I. (1997). *Chemotaxis and Thermotaxis. C. elegans II.* 2nd Edn, Chap. 25. Cold Spring Harbor: Cold Spring Harbor Laboratory Press, 717–738.

Bauer Huang, S. L., Saheki, Y., VanHoven, M. K., Torayama, I., Ishihara, T., Katsura, I., et al. (2007). Left–right olfactory asymmetry results from antagonistic functions of voltage-activated calcium channels and the Raw repeat protein OLRN-1 in *C. elegans. Neural Dev.* 2, 24. doi: 10.1186/1749-8104-2-24

Beets, I., Janssen, T., Meelkop, E., Temmerman, L., Suetens, N., Rademakers, S., et al. (2012). Vasopressin/oxytocin-related signaling regulates gustatory associative learning in *C. elegans. Science* 338, 543–545. doi: 10.1126/science.1226860

Bendesky, A., Tsunozaki, M., Rockman, M. V., Kruglyak, L., and Bargmann, C. I. (2011). Catecholamine receptor polymorphisms affect decision-making in *C. elegans. Nature* 472, 313–318. doi: 10.1038/nature09821

Blacque, O. E., Reardon, M. J., Li, C., Mccarthy, J., Mahjoub, M. R., Ansley, S. J., et al. (2004). Loss of *C. elegans* BBS-7 and BBS-8 protein function results in cilia defects and compromised intraflagellar transport. *Genes Dev.* 18, 1630–1642. doi: 10.1101/gad.1194004

Bowler, D. E., and Benton, T. G. (2005). Causes and consequences of animal dispersal strategies: relating individual behaviour to spatial dynamics. *Biol. Rev. Camb. Philos. Soc.* 80, 205–225. doi: 10.1017/S1464793104006645

Brenner, S. (1974). The genetics of *Caenorhabditis elegans. Genetics* 77, 71–94.

Brockie, P. J., and Maricq, A. V. (2006). Ionotropic glutamate receptors: genetics, behavior and electrophysiology. *WormBook* 1–16. doi: 10.1895/wormbook.1.61.1.

C. elegans Sequencing Consortium. (1998). Genome sequence of the nematode *C. elegans*: a platform for investigating biology. *Science* 282, 2012–2018. doi: 10.1126/science.282.5396.2012

Chalasani, S. H., Chronis, N., Tsunozaki, M., Gray, J. M., Ramot, D., Goodman, M. B., et al. (2007). Dissecting a circuit for olfactory behaviour in *Caenorhabditis elegans. Nature* 450, 63–70. doi: 10.1038/nature06292

Chalfie, M., and Jorgensen, E. M. (1998). *C. elegans* neuroscience: genetics to genome. *Trends Genet.* 14, 506–512. doi: 10.1016/S0168-9525(98)01623-0

Chase, D. L., and Koelle, M. R. (2007). Biogenic amine neurotransmitters in *C. elegans. WormBook* 1–15. doi: 10.1895/wormbook.1.132.1.

Chelur, D. S., and Chalfie, M. (2007). Targeted cell killing by reconstituted caspases. *Proc. Natl. Acad. Sci. U.S.A.* 104, 2283–2288. doi: 10.1073/pnas.0610877104

Chen, T.-W., Wardill, T. J., Sun, Y., Pulver, S. R., Renninger, S. L., Baohan, A., et al. (2013). Ultrasensitive fluorescent proteins for imaging neuronal activity. *Nature* 499, 295–300. doi: 10.1038/nature12354

Cho, S. W., Cho, J. H., Song, H. O., and Park, C. S. (2005). Identification and characterization of a putative cyclic nucleotide-gated channel, CNG-1, in *C. elegans. Mol. Cells* 19, 149–154.

Chow, B. Y., Han, X., Dobry, A. S., Qian, X., Chuong, A. S., Li, M., et al. (2010). High-performance genetically targetable optical neural silencing by light-driven proton pumps. *Nature* 463, 98–102. doi: 10.1038/nature08652

Choy, R. K., and Thomas, J. H. (1999). Fluoxetine-resistant mutants in *C. elegans* define a novel family of transmembrane proteins. *Mol. Cell.* 4, 143–152. doi: 10.1016/S1097-2765(00)80362-7

Chuang, C. F., and Bargmann, C. I. (2005). A Toll-interleukin 1 repeat protein at the synapse specifies asymmetric odorant receptor expression via ASK1 MAPKKK signaling. *Genes Dev.* 19, 270–281. doi: 10.1101/gad.1276505

Clark, D. A., Biron, D., Sengupta, P., and Samuel, A. D. T. (2006). The AFD sensory neurons encode multiple functions underlying thermotactic behavior in *Caenorhabditis elegans. J. Neurosci.* 26, 7444–7451. doi: 10.1523/JNEUROSCI.1137-06.2006

Colbert, H. A., and Bargmann, C. I. (1995). Odorant-specific adaptation pathways generate olfactory plasticity in *C. elegans. Neuron* 14, 803–812. doi: 10.1016/0896-6273(95)90224-4

Colbert, H. A., and Bargmann, C. I. (1997). Environmental signals modulate olfactory acuity, discrimination, and memory in *Caenorhabditis elegans. Learn. Mem.* 4, 179–191. doi: 10.1101/lm.4.2.179

de Bono, M., and Bargmann, C. I. (1998). Natural variation in a neuropeptide Y receptor homolog modifies social behavior and food response in *C. elegans. Cell* 94, 679–689. doi: 10.1016/S0092-8674(00)81609-8

de Bono, M., and Maricq, A. V. (2005). Neuronal substrates of complex behaviors in *C. elegans. Annu. Rev. Neurosci.* 28, 451–501. doi: 10.1146/annurev.neuro.27.070203.144259

Deguchi, T., Itoh, M., Urawa, H., Matsumoto, T., Nakayama, S., Kawasaki, T., et al. (2009). Infrared laser-mediated local gene induction in medaka, zebrafish and *Arabidopsis thaliana. Dev. Growth Differ.* 51, 769–775. doi: 10.1111/j.1440-169X.2009.01135.x

Fang-Yen, C., Wyart, M., Xie, J., Kawai, R., Kodger, T., Chen, S., et al. (2010). Biomechanical analysis of gait adaptation in the nematode *Caenorhabditis elegans. Proc. Natl. Acad. Sci. U.S.A.* 107, 20323–20328. doi: 10.1073/pnas.1003016107

Garrison, J. L., Macosko, E. Z., Bernstein, S., Pokala, N., Albrecht, D. R., and Bargmann, C. I. (2012). Oxytocin/vasopressin-related peptides have an ancient role in reproductive behavior. *Science* 338, 540–543. doi: 10.1126/science.1226201

Giles, A. C., and Rankin, C. H. (2009). Behavioral and genetic characterization of habituation using *Caenorhabditis elegans. Neurobiol. Learn. Mem.* 92, 139–146. doi: 10.1016/j.nlm.2008.08.004

Giles, A. C., Rose, J. K., and Rankin, C. H. (2006). Investigations of learning and memory in *Caenorhabditis elegans. Int. Rev. Neurobiol.* 69, 37–71. doi: 10.1016/S0074-7742(05)69002-2

Goodman, M. B., Hall, D. H., Avery, L., and Lockery, S. R. (1998). Active currents regulate sensitivity and dynamic range in *C. elegans* neurons. *Neuron* 20, 763–772. doi: 10.1016/S0896-6273(00)81014-4

Gray, J. M., Hill, J. J., and Bargmann, C. I. (2005). A circuit for navigation in *Caenorhabditis elegans. Proc. Natl. Acad. Sci. U.S.A.* 102, 3184–3191. doi: 10.1073/pnas.0409009101

Gray, J. M., Karow, D. S., Lu, H., Chang, A. J., Chang, J. S., Ellis, R. E., et al. (2004). Oxygen sensation and social feeding mediated by a *C. elegans* guanylate cyclase homologue. *Nature* 430, 317–322. doi: 10.1038/nature02714

Gruninger, T. R., Gualberto, D. G., and Garcia, L. R. (2008). Sensory perception of food and insulin-like signals influence seizure susceptibility. *PLoS Genet.* 4:e1000117. doi: 10.1371/journal.pgen.1000117

Halfon, M. S., Kose, H., Chiba, A., and Keshishian, H. (1997). Targeted gene expression without a tissue-specific promoter: creating mosaic embryos using laser-induced single-cell heat shock. *Proc. Natl. Acad. Sci. U.S.A.* 94, 6255–6260. doi: 10.1073/pnas.94.12.6255

Halloran, M. C., Sato-Maeda, M., Warren, J. T., Su, F., Lele, Z., Krone, P. H., et al. (2000). Laser-induced gene expression in specific cells of transgenic zebrafish. *Development* 127, 1953–1960.

Han, X., and Boyden, E. S. (2007). Multiple-color optical activation, silencing, and desynchronization of neural activity, with single-spike temporal resolution. *PLoS ONE* 2:e299. doi: 10.1371/journal.pone.0000299

Harris, J., Honigberg, L., Robinson, N., and Kenyon, C. (1996). Neuronal cell migration in *C. elegans*: regulation of Hox gene expression and cell position. *Development* 122, 3117–3131.

Hart, A. C., and Chao, M. Y. (2010). "From odors to behaviors in *Caenorhabditis elegans*," in *The Neurobiology of Olfaction*, Chap. 1, ed. A. Menini (Boca Raton: CRC Press).

Hawkins, R. D., Kandel, E. R., and Siegelbaum, S. A. (1993). Learning to modulate transmitter release: themes and variations in synaptic plasticity. *Annu. Rev. Neurosci.* 16, 625–665. doi: 10.1146/annurev.ne.16.030193.003205

Hedgecock, E. M., and Russell, R. L. (1975). Normal and mutant thermotaxis in the nematode *Caenorhabditis elegans. Proc. Natl. Acad. Sci. U.S.A.* 72, 4061–4065. doi: 10.1073/pnas.72.10.4061

Hendricks, M., Ha, H., Maffey, N., and Zhang, Y. (2012). Compartmentalized calcium dynamics in a *C. elegans* interneuron encode head movement. *Nature* 487, 99–103.

Hirotsu, T., and Iino, Y. (2005). Neural circuit-dependent odor adaptation in *C. elegans* is regulated by the Ras-MAPK pathway. *Genes Cells* 10, 517–530. doi: 10.1111/j.1365-2443.2005.00856.x

Hobert, O. (2003). Behavioral plasticity in *C. elegans*: paradigms, circuits, genes. *J. Neurobiol.* 54, 203–223. doi: 10.1002/neu.10168

Hobert, O. (2005). Specification of the nervous system. *WormBook* 1–19. doi: 10.1895/wormbook.1.12.1.

Hobert, O., Johnston, R. J. Jr., and Chang, S. (2002). Left–right asymmetry in the nervous system: the *Caenorhabditis elegans* model. *Nat. Rev. Neurosci.* 3, 629–640.

Hobert, O., Mori, I., Yamashita, Y., Honda, H., Ohshima, Y., Liu, Y., et al. (1997). Regulation of interneuron function in the *C. elegans* thermoregulatory pathway

by the ttx-3 LIM homeobox gene. *Neuron* 19, 345–357. doi: 10.1016/S0896-6273(00)80944-7

Hoerndli, F. J., Walser, M., Frohli Hoier, E., de Quervain, D., Papassotiropoulos, A., and Hajnal, A. (2009). A conserved function of *C. elegans* CASY-1 calsyntenin in associative learning. *PLoS ONE* 4:e4880. doi: 10.1371/journal.pone.0004880

Horvitz, H. R., Chalfie, M., Trent, C., Sulston, J. E., and Evans, P. D. (1982). Serotonin and octopamine in the nematode *Caenorhabditis elegans. Science* 216, 1012–1014. doi: 10.1126/science.6805073

Hoshi, K., and Shingai, R. (2006). Computer-driven automatic identification of locomotion states in *Caenorhabditis elegans. J. Neurosci. Methods* 157, 355–363. doi: 10.1016/j.jneumeth.2006.05.002

Hu, P. J. (2007). Dauer. *WormBook* 1–19. doi: 10.1895/wormbook.1.144.1.

Hukema, R. K., Rademakers, S., Dekkers, M. P., Burghoorn, J., and Jansen, G. (2006). Antagonistic sensory cues generate gustatory plasticity in *Caenorhabditis elegans. EMBO J.* 25, 312–322. doi: 10.1038/sj.emboj.7600940

Hukema, R. K., Rademakers, S., and Jansen, G. (2008). Gustatory plasticity in *C. elegans* involves integration of negative cues and NaCl taste mediated by serotonin, dopamine, and glutamate. *Learn. Mem.* 15, 829–836. doi: 10.1101/lm.994408

Husson, S. J., Costa, W. S., Schmitt, C., and Gottschalk, A. (2013a). Keeping track of worm trackers. *WormBook* 1–17. doi: 10.1895/wormbook.1.156.1

Husson, S. J., Gottschalk, A., and Leifer, A. M. (2013b). Optogenetic manipulation of neural activity in *C. elegans*: from synapse to circuits and behaviour. *Biol. Cell* 105, 235–250. doi: 10.1111/boc.201200069

Ikeda, D. D., Duan, Y., Matsuki, M., Kunitomo, H., Hutter, H., Hedgecock, E. M., et al. (2008). CASY-1, an ortholog of calsyntenins/alcadeins, is essential for learning in *Caenorhabditis elegans. Proc. Natl. Acad. Sci. U.S.A.* 105, 5260–5265. doi: 10.1073/pnas.0711894105

Inoue, A., Sawatari, E., Hisamoto, N., Kitazono, T., Teramoto, T., Fujiwara, M., et al. (2013). Forgetting in *C. elegans* is accelerated by neuronal communication via the TIR-1/JNK-1 pathway. *Cell Rep.* 3, 808–819. doi: 10.1016/j.celrep.2013.02.019

Ishihara, T., Iino, Y., Mohri, A., Mori, I., Gengyo-Ando, K., Mitani, S., et al. (2002). HEN-1, a secretory protein with an LDL receptor motif, regulates sensory integration and learning in *Caenorhabditis elegans. Cell* 109, 639–649. doi: 10.1016/S0092-8674(02)00748-1

Jarrell, T. A., Wang, Y., Bloniarz, A. E., Brittin, C. A., Xu, M., Thomson, J. N., et al. (2012). The connectome of a decision-making neural network. *Science* 337, 437–444. doi: 10.1126/science.1221762

Jorgensen, E. M. (2005). GABA. *WormBook* 1–13. doi: 10.1895/wormbook.1.14.1.

Kamei, Y., Suzuki, M., Watanabe, K., Fujimori, K., Kawasaki, T., Deguchi, T., et al. (2009). Infrared laser-mediated gene induction in targeted single cells in vivo. *Nat. Methods* 6, 79–81. doi: 10.1038/nmeth.1278

Kandel, E. R. (2001). The molecular biology of memory storage: a dialogue between genes and synapses. *Science* 294, 1030–1038. doi: 10.1126/science.1067020

Kawazoe, Y., Yawo, H., and Kimura, K. D. (2012). A simple optogenetic system for behavioral analysis of freely moving small animals. *Neurosci. Res.* 75, 65–68. doi: 10.1016/j.neures.2012.04.011

Kerr, R. A. (2006). Imaging the activity of neurons and muscles. *WormBook* 1–13. doi: 10.1895/wormbook.1.113.1

Kimata, T., Sasakura, H., Ohnishi, N., Nishio, N., and Mori, I. (2012). Thermotaxis of *C. elegans* as a model for temperature perception, neural information processing and neural plasticity. *Worm* 1, 31–41. doi: 10.4161/worm.19504

Kimura, E., Deguchi, T., Kamei, Y., Shoji, W., Yuba, S., and Hitomi, J. (2013). Application of infrared laser to the zebrafish vascular system: gene induction, tracing, and ablation of single endothelial cells. *Arterioscler. Thromb. Vasc. Biol.* 33, 1264–1270. doi: 10.1161/ATVBAHA.112.300602

Kimura, K. D., Fujita, K., and Katsura, I. (2010). Enhancement of odor avoidance regulated by dopamine signaling in *Caenorhabditis elegans. J. Neurosci.* 30, 16365–16375. doi: 10.1523/JNEUROSCI.6023-09.2010

Kimura, K. D., Miyawaki, A., Matsumoto, K., and Mori, I. (2004). The *C. elegans* thermosensory neuron AFD responds to warming. *Curr. Biol.* 14, 1291–1295. doi: 10.1016/j.cub.2004.06.060

Kodama, E., Kuhara, A., Mohri-Shiomi, A., Kimura, K. D., Okumura, M., Tomioka, M., et al. (2006). Insulin-like signaling and the neural circuit for integrative behavior in *C. elegans. Genes Dev.* 20, 2955–2960. doi: 10.1101/gad.1479906

Komatsu, H., Mori, I., Rhee, J. S., Akaike, N., and Ohshima, Y. (1996). Mutations in a cyclic nucleotide-gated channel lead to abnormal thermosensation and chemosensation in *C. elegans. Neuron* 17, 707–718. doi: 10.1016/S0896-6273(00)80202-0

Korta, J., Clark, D. A., Gabel, C. V., Mahadevan, L., and Samuel, A. D. T. (2007). Mechanosensation and mechanical load modulate the locomotory gait of swimming *C. elegans. J. Exp. Biol.* 210, 2383–2389. doi: 10.1242/jeb.004572

Kuhara, A., and Mori, I. (2006). Molecular physiology of the neural circuit for calcineurin-dependent associative learning in *Caenorhabditis elegans. J. Neurosci.* 26, 9355–9364. doi: 10.1523/JNEUROSCI.0517-06.2006

Kuhara, A., Ohnishi, N., Shimowada, T., and Mori, I. (2011). Neural coding in a single sensory neuron controlling opposite seeking behaviours in *Caenorhabditis elegans. Nat. Commun.* 2, 355. doi: 10.1038/ncomms1352

Lanjuin, A., VanHoven, M. K., Bargmann, C. I., Thompson, J. K., and Sengupta, P. (2003). Otx/otd homeobox genes specify distinct sensory neuron identities in *C. elegans. Dev. Cell* 5, 621–633. doi: 10.1016/S1534-5807(03)00293-4

Li, C., and Kim, K. (2008). Neuropeptides. *WormBook* 1–36. doi: 10.1895/wormbook.1.142.1

Marrs, W. R., Blankman, J. L., Horne, E. A., Thomazeau, A., Lin, Y. H., Coy, J., et al. (2010). The serine hydrolase ABHD6 controls the accumulation and efficacy of 2-AG at cannabinoid receptors. *Nat. Neurosci.* 13, 951–957. doi: 10.1038/nn.2601

Matsuoka, T., Gomi, S., and Shingai, R. (2008). Simulation of *C. elegans* thermotactic behavior in a linear thermal gradient using a simple phenomenological motility model. *J. Theor. Biol.* 250, 230–243. doi: 10.1016/j.jtbi.2007.10.002

Millan, M. J. (1999). The induction of pain: an integrative review. *Prog. Neurobiol.* 57, 1–164. doi: 10.1016/S0301-0082(98)00048-3

Miyara, A., Ohta, A., Okochi, Y., Tsukada, Y., Kuhara, A., and Mori, I. (2011). Novel and conserved protein macoilin is required for diverse neuronal functions in *Caenorhabditis elegans. PLoS Genet.* 7:e1001384. doi: 10.1371/journal.pgen.1001384

Miyawaki, A., Llopis, J., Heim, R., Mccaffery, J. M., Adams, J. A., Ikurak, M., et al. (1997). Fluorescent indicators for Ca^{2+} based on green fluorescent proteins and calmodulin. *Nature* 388, 882–887. doi: 10.1038/42264

Mohri, A., Kodama, E., Kimura, K. D., Koike, M., Mizuno, T., and Mori, I. (2005). Genetic control of temperature preference in the nematode *Caenorhabditis elegans. Genetics* 169, 1437–1450. doi: 10.1534/genetics.104.036111

Mori, I., and Ohshima, Y. (1995). Neural regulation of thermotaxis in *Caenorhabditis elegans. Nature* 376, 344–348. doi: 10.1038/376344a0

Mori, I., Sasakura, H., and Kuhara, A. (2007). Worm thermotaxis: a model system for analyzing thermosensation and neural plasticity. *Curr. Opin. Neurobiol.* 17, 712–719. doi: 10.1016/j.conb.2007.11.010

Murayama, T., Takayama, J., Fujiwara, M., and Maruyama, I. N. (2013). Environmental alkalinity sensing mediated by the transmembrane guanylyl cyclase GCY-14 in *C. elegans. Curr. Biol.* 23, 1007–1012. doi: 10.1016/j.cub.2013.04.052

Nakai, J., Ohkura, M., and Imoto, K. (2001). A high signal-to-noise Ca(2+) probe composed of a single green fluorescent protein. *Nat. Biotechnol.* 19, 137–141. doi: 10.1038/84397

Nakazato, K., and Mochizuki, A. (2009). Steepness of thermal gradient is essential to obtain a unified view of thermotaxis in *C. elegans. J. Theor. Biol.* 260, 56–65. doi: 10.1016/j.jtbi.2009.05.027

Nishida, Y., Sugi, T., Nonomura, M., and Mori, I. (2011). Identification of the AFD neuron as the site of action of the CREB protein in *Caenorhabditis elegans* thermotaxis. *EMBO Rep.* 12, 855–862. doi: 10.1038/embor.2011.120

Nishio, N., Mohri-Shiomi, A., Nishida, Y., Hiramatsu, N., Kodama-Namba, E., Kimura, K. D., et al. (2012). A novel and conserved protein AHO-3 is required for thermotactic plasticity associated with feeding states in *Caenorhabditis elegans. Genes Cells* 17, 365–386. doi: 10.1111/j.1365-2443.2012.01594.x

Nuttley, W. M., Atkinson-Leadbeater, K. P., and Van Der Kooy, D. (2002). Serotonin mediates food-odor associative learning in the nematode *Caenorhabditis elegans. Proc. Natl. Acad. Sci. U.S.A.* 99, 12449–12454. doi: 10.1073/pnas.192101699

Oda, S., Tomioka, M., and Iino, Y. (2011). Neuronal plasticity regulated by the insulin-like signaling pathway underlies salt chemotaxis learning in *Caenorhabditis elegans. J. Neurophysiol.* 106, 301–308. doi: 10.1152/jn.01029.2010

Ohkubo, J., Yoshida, K., Iino, Y., and Masuda, N. (2010). Long-tail behavior in locomotion of *Caenorhabditis elegans. J. Theor. Biol.* 267, 213–222. doi: 10.1016/j.jtbi.2010.08.020

Okazaki, A., Sudo, Y., and Takagi, S. (2012). Optical silencing of *C. elegans* cells with arch proton pump. *PLoS ONE* 7:e35370. doi: 10.1371/journal.pone.0035370

Okazaki, A., and Takagi, S. (2013). An optogenetic application of proton pump ArchT to *C. elegans* cells. *Neurosci. Res.* 75, 29–34. doi: 10.1016/j.neures.2012.09.002

Okochi, Y., Kimura, K. D., Ohta, A., and Mori, I. (2005). Diverse regulation of sensory signaling by *C. elegans* nPKC-epsilon/eta TTX-4. *EMBO J.* 24, 2127–2137. doi: 10.1038/sj.emboj.7600697

Ortiz, C. O., Faumont, S., Takayama, J., Ahmed, H. K., Goldsmith, A. D., Pocock, R., et al. (2009). Lateralized gustatory behavior of *C. elegans* is controlled by specific receptor-type guanylyl cyclases. *Curr. Biol.* 19, 996–1004. doi: 10.1016/j.cub.2009.05.043

Pierce-Shimomura, J. T., Chen, B. L., Mun, J. J., Ho, R., Sarkis, R., and McIntire, S. L. (2008). Genetic analysis of crawling and swimming locomotory patterns in *C. elegans*. *Proc. Natl. Acad. Sci. U.S.A.* 105, 20982–20987. doi: 10.1073/pnas.0810359105

Pierce-Shimomura, J. T., Faumont, S., Gaston, M. R., Pearson, B. J., and Lockery, S. R. (2001). The homeobox gene lim-6 is required for distinct chemosensory representations in *C. elegans*. *Nature* 410, 694–698. doi: 10.1038/35070575

Quinn, W. G., Harris, W. A., and Benzer, S. (1974). Conditioned behavior in *Drosophila melanogaster*. *Proc. Natl. Acad. Sci. U.S.A.* 71, 708–712. doi: 10.1073/pnas.71.3.708

Raizen, D. M., Zimmerman, J. E., Maycock, M. H., Ta, U. D., You, Y., Sundaram, M. V., et al. (2008). Lethargus is a *Caenorhabditis elegans* sleep-like state. *Nature* 451, 569–572. doi: 10.1038/nature06535

Rand, J. B. (2007). Acetylcholine. *WormBook* 1–21. doi: 10.1895/wormbook.1.131.1

Ranganathan, R., Cannon, S. C., and Horvitz, H. R. (2000). MOD-1 is a serotonin-gated chloride channel that modulates locomotory behaviour in *C. elegans*. *Nature* 408, 470–475. doi: 10.1038/35044083

Ranganathan, R., Sawin, E. R., Trent, C., and Horvitz, H. R. (2001). Mutations in the *Caenorhabditis elegans* serotonin reuptake transporter MOD-5 reveal serotonin-dependent and -independent activities of fluoxetine. *J. Neurosci.* 21, 5871–5884.

Rankin, C. H. (2002). From gene to identified neuron to behaviour in *Caenorhabditis elegans*. *Nat. Rev. Genet.* 3, 622–630.

Rankin, C. H., Beck, C. D., and Chiba, C. M. (1990). *Caenorhabditis elegans*: a new model system for the study of learning and memory. *Behav. Brain Res.* 37, 89–92. doi: 10.1016/0166-4328(90)90074-O

Rogers, C., Reale, V., Kim, K., Chatwin, H., Li, C., Evans, P., et al. (2003). Inhibition of *Caenorhabditis elegans* social feeding by FMRFamide-related peptide activation of NPR-1. *Nat. Neurosci.* 6, 1178–1185. doi: 10.1038/nn1140

Ryu, W. S., and Samuel, A. D. T. (2002). Thermotaxis in *Caenorhabditis elegans* analyzed by measuring responses to defined thermal stimuli. *J. Neurosci.* 22, 5727–5733.

Saeki, S., Yamamoto, M., and Iino, Y. (2001). Plasticity of chemotaxis revealed by paired presentation of a chemoattractant and starvation in the nematode *Caenorhabditis elegans*. *J. Exp. Biol.* 204, 1757–1764.

Sagasti, A., Hisamoto, N., Hyodo, J., Tanaka-Hino, M., Matsumoto, K., and Bargmann, C. I. (2001). The CaMKII UNC-43 activates the MAPKKK NSY-1 to execute a lateral signaling decision required for asymmetric olfactory neuron fates. *Cell* 105, 221–232. doi: 10.1016/S0092-8674(01)00313-0

Sahley, C. L. (1995). What we have learned from the study of learning in the leech. *J. Neurobiol.* 27, 434–445. doi: 10.1002/neu.480270314

Sambongi, Y., Takeda, K., Wakabayashi, T., Ueda, I., Wada, Y., and Futai, M. (2000). *Caenorhabditis elegans* senses protons through amphid chemosensory neurons: proton signals elicit avoidance behavior. *Neuroreport* 11, 2229–2232. doi: 10.1097/00001756-200007140-00033

Sasakura, H., and Mori, I. (2013). Behavioral plasticity, learning, and memory in *C. elegans*. *Curr. Opin. Neurobiol.* 23, 92–99. doi: 10.1016/j.conb.2012.09.005

Sawin, E. R., Ranganathan, R., and Horvitz, H. R. (2000). *C. elegans* locomotory rate is modulated by the environment through a dopaminergic pathway and by experience through a serotonergic pathway. *Neuron* 26, 619–631. doi: 10.1016/S0896-6273(00)81199-X

Schafer, W. R. (2005). Deciphering the neural and molecular mechanisms of *C. elegans* behavior. *Curr. Biol.* 15, R723–R729. doi: 10.1016/j.cub.2005.08.020

Schafer, W. R. (2006). Neurophysiological methods in *C. elegans*: an introduction. *WormBook* 1–4. doi: 10.1895/wormbook.1.111.1

Shidara, H., Kobayashi, J., Tanamoto, R., Hotta, K., and Oka, K. (2013). Odorant-induced membrane potential depolarization of AIY interneuron in *Caenorhabditis elegans*. *Neurosci. Lett.* 541, 199–203. doi: 10.1016/j.neulet.2013.02.016

Shinkai, Y., Yamamoto, Y., Fujiwara, M., Tabata, T., Murayama, T., Hirotsu, T., et al. (2011). Behavioral choice between conflicting alternatives is regulated by a receptor guanylyl cyclase, GCY-28, and a receptor tyrosine kinase, SCD-2, in AIA interneurons of *Caenorhabditis elegans*. *J. Neurosci.* 31, 3007–3015. doi: 10.1523/JNEUROSCI.4691-10.2011

Shivers, R. P., Kooistra, T., Chu, S. W., Pagano, D. J., and Kim, D. H. (2009). Tissue-specific activities of an immune signaling module regulate physiological responses to pathogenic and nutritional bacteria in *C. elegans*. *Cell Host Microbe* 6, 321–330. doi: 10.1016/j.chom.2009.09.001

Sieburth, D., Madison, J. M., and Kaplan, J. M. (2007). PKC-1 regulates secretion of neuropeptides. *Nat. Neurosci.* 10, 49–57. doi: 10.1038/nn1810

Stephens, G. J., Johnson-Kerner, B., Bialek, W., and Ryu, W. S. (2008). Dimensionality and dynamics in the behavior of *C. elegans*. *PLoS Comput. Biol.* 4:e1000028. doi: 10.1371/journal.pcbi.1000028

Stringham, E., and Candido, E. (1993). Targeted single-cell induction of gene products in *Caenorhabditis elegans*: a new tool for developmental studies. *J. Exp. Zool.* 266, 227–233. doi: 10.1002/jez.1402660309

Sudo, Y., Okazaki, A., Ono, H., Yagasaki, J., Sugo, S., Kamiya, M., et al. (2013). A blue-shifted light-driven proton pump for neural silencing. *J. Biol. Chem.* 288, 20624–20632. doi: 10.1074/jbc.M113.475533

Sugi, T., Nishida, Y., and Mori, I. (2011). Regulation of behavioral plasticity by systemic temperature signaling in *Caenorhabditis elegans*. *Nat. Neurosci.* 14, 984–992. doi: 10.1038/nn.2854

Sulston, J. E., Schierenberg, E., White, J. G., and Thomson, J. N. (1983). The embryonic cell lineage of the nematode *Caenorhabditis elegans*. *Dev. Biol.* 100, 64–119. doi: 10.1016/0012-1606(83)90201-4

Suo, S., Culotti, J. G., and Van Tol, H. H. (2009). Dopamine counteracts octopamine signalling in a neural circuit mediating food response in *C. elegans*. *EMBO J.* 28, 2437–2448. doi: 10.1038/emboj.2009.194

Suzuki, H., Thiele, T. R., Faumont, S., Ezcurra, M., Lockery, S. R., and Schafer, W. R. (2008). Functional asymmetry in *Caenorhabditis elegans* taste neurons and its computational role in chemotaxis. *Nature* 454, 114–117. doi: 10.1038/nature06927

Suzuki, M., Goto, T., Tsuji, T., and Ohtake, H. (2005). A dynamic body model of the nematode *C. elegans* with neural oscillators. *J. Robot. Mechatron.* 17, 318–326.

Suzuki, M., Toyoda, N., Shimojou, M., and Takagi, S. (2013). Infrared laser-induced gene expression in targeted single cells of *Caenorhabditis elegans*. *Dev. Growth Differ.* 55, 454–461. doi: 10.1111/dgd.12061

Tanaka-Hino, M., Sagasti, A., Hisamoto, N., Kawasaki, M., Nakano, S., Ninomiya-Tsuji, J., et al. (2002). SEK-1 MAPKK mediates Ca^{2+} signaling to determine neuronal asymmetric development in *Caenorhabditis elegans*. *EMBO Rep.* 3, 56–62. doi: 10.1093/embo-reports/kvf001

Tian, L., Hires, S. A., Mao, T., Huber, D., Chiappe, M. E., Chalasani, S. H., et al. (2009). Imaging neural activity in worms, flies and mice with improved GCaMP calcium indicators. *Nat. Methods* 6, 875–881. doi: 10.1038/nmeth.1398

Tomida, T., Oda, S., Takekawa, M., Iino, Y., and Saito, H. (2012). The temporal pattern of stimulation determines the extent and duration of MAPK activation in a *Caenorhabditis elegans* sensory neuron. *Sci. Signal.* 5, ra76. doi: 10.1126/scisignal.2002983

Tomioka, M., Adachi, T., Suzuki, H., Kunitomo, H., Schafer, W. R., and Iino, Y. (2006). The insulin/PI 3-kinase pathway regulates salt chemotaxis learning in *Caenorhabditis elegans*. *Neuron* 51, 613–625. doi: 10.1016/j.neuron.2006.07.024

Torayama, I., Ishihara, T., and Katsura, I. (2007). *Caenorhabditis elegans* integrates the signals of butanone and food to enhance chemotaxis to butanone. *J. Neurosci.* 27, 741–750. doi: 10.1523/JNEUROSCI.4312-06.2007

Troemel, E. R., Kimmel, B. E., and Bargmann, C. I. (1997). Reprogramming chemotaxis responses: sensory neurons define olfactory preferences in C. *elegans*. *Cell* 91, 161–169. doi: 10.1016/S0092-8674(00)80399-2

Troemel, E. R., Sagasti, A., and Bargmann, C. I. (1999). Lateral signaling mediated by axon contact and calcium entry regulates asymmetric odorant receptor expression in *C. elegans*. *Cell* 99, 387–398. doi: 10.1016/S0092-8674(00)81525-1

Tsunozaki, M., Chalasani, S. H., and Bargmann, C. I. (2008). A behavioral switch: cGMP and PKC signaling in olfactory neurons reverses odor preference in *C. elegans*. *Neuron* 59, 959–971. doi: 10.1016/j.neuron.2008.07.038

Van Buskirk, C., and Sternberg, P. W. (2007). Epidermal growth factor signaling induces behavioral quiescence in *Caenorhabditis elegans*. *Nat. Neurosci.* 10, 1300–1307. doi: 10.1038/nn1981

Vanhoven, M. K., Bauer Huang, S. L., Albin, S. D., and Bargmann, C. I. (2006). The claudin superfamily protein nsy-4 biases lateral signaling to generate left–right asymmetry in *C. elegans* olfactory neurons. *Neuron* 51, 291–302. doi: 10.1016/j.neuron.2006.06.029

Wakabayashi, T., Kitagawa, I., and Shingai, R. (2004). Neurons regulating the duration of forward locomotion in *Caenorhabditis elegans*. *Neurosci. Res.* 50, 103–111. doi: 10.1016/j.neures.2004.06.005

Ward, S., Thomson, N., White, J., and Brenner, S. (1975). Electron microscopical reconstruction of the anterior sensory anatomy of the nematode *Caenorhabditis elegans*. *J. Comp. Neurol.* 160, 313–337. doi: 10.1002/cne.901600305

Ware, R., Clark, D., Crossland, K., and Russell, R. (1975). The nerve ring of the nematode *Caenorhabditis elegans*: sensory input and motor output. *J. Comp. Neurol.* 162, 71–110. doi: 10.1002/cne.901620106

Weiss, J. B., Suyama, K. L., Lee, H. H., and Scott, M. P. (2001). Jelly belly: a *Drosophila* LDL receptor repeat-containing signal required for mesoderm migration and differentiation. *Cell* 107, 387–398. doi: 10.1016/S0092-8674(01)00540-2

Wes, P. D., and Bargmann, C. I. (2001). *C. elegans* odour discrimination requires asymmetric diversity in olfactory neurons. *Nature* 410, 698–701. doi: 10.1038/35070581

White, J. G., Southgate, E., Thomson, J. N., and Brenner, S. (1986). The structure of the nervous system of the nematode *Caenorhabditis elegans*. *Philos. Trans. R. Soc. Lond. B Biol. Sci.* 314, 1–340. doi: 10.1098/rstb.1986.0056

Xu, X., and Kim, S. K. (2011). The early bird catches the worm: new technologies for the *Caenorhabditis elegans* toolkit. *Nat. Rev. Genet.* 12, 793–801. doi: 10.1038/nrg3050

Yamada, K., Hirotsu, T., Matsuki, M., Butcher, R. A., Tomioka, M., Ishihara, T., et al. (2010). Olfactory plasticity is regulated by pheromonal signaling in *Caenorhabditis elegans*. *Science* 329, 1647–1650. doi: 10.1126/science.1192020

Yamada, Y., and Ohshima, Y. (2003). Distribution and movement of *Caenorhabditis elegans* on a thermal gradient. *J. Exp. Biol.* 206, 2581–2593. doi: 10.1242/jeb.00477

Yu, S., Avery, L., Baude, E., and Garbers, D. L. (1997). Guanylyl cyclase expression in specific sensory neurons: a new family of chemosensory receptors. *Proc. Natl. Acad. Sci. U.S.A.* 94, 3384–3387. doi: 10.1073/pnas.94.7.3384

Zhang, F., Aravanis, A. M., Adamantidis, A., de Lecea, L., and Deisseroth, K. (2007). Circuit-breakers: optical technologies for probing neural signals and systems. *Nat. Rev. Neurosci.* 8, 577–581. doi: 10.1038/nrn2192

Zhao, Y., Araki, S., Wu, J., Teramoto, T., Chang, Y.-F., Nakano, M., et al. (2011). An expanded palette of genetically encoded Ca^{2+} indicators. *Science* 333, 1888–1891. doi: 10.1126/science.1208592

Conflict of Interest Statement: The authors declare that the research was conducted in the absence of any commercial or financial relationships that could be construed as a potential conflict of interest.

Received: 04 August 2013; accepted: 03 November 2013; published online: 28 November 2013.

Citation: Sasakura H, Tsukada Y, Takagi S and Mori I (2013) Japanese studies on neural circuits and behavior of Caenorhabditis elegans. Front. Neural Circuits ***7****:187. doi: 10.3389/fncir.2013.00187*

This article was submitted to the journal Frontiers in Neural Circuits.

frontiers in
NEURAL CIRCUITS

REVIEW ARTICLE
published: 03 September 2013
doi: 10.3389/fncir.2013.00140

Elucidating information processing in primate basal ganglia circuitry: a novel technique for pathway-selective ablation mediated by immunotoxin

Masahiko Takada[1]*, Ken-Ichi Inoue[1], Daisuke Koketsu[2], Shigeki Kato[3], Kazuto Kobayashi[3] and Atsushi Nambu[2]

[1] *Systems Neuroscience Section, Primate Research Institute, Kyoto University, Inuyama, Japan*
[2] *Division of System Neurophysiology, Department of Physiological Sciences, National Institute for Physiological Sciences, The Graduate University for Advanced Studies, Okazaki, Japan*
[3] *Department of Molecular Genetics, Institute of Biomedical Sciences, Fukushima Medical University School of Medicine, Fukushima, Japan*

Edited by:
Yasuo Kawaguchi, National Institute for Physiological Sciences, Japan

Reviewed by:
Peter Redgrave, The University of Sheffield, Sheffield, UK
Kaoru Takakusaki, Research center for brain function and medical engineering, Asahikawa Medical University, Japan

****Correspondence:***
Masahiko Takada, Systems Neuroscience Section, Department of Cellular and Molecular Biology, Primate Research Institute, Kyoto University, 41-2 Kanrin, Inuyama, Aichi 484-8506, Japan
e-mail: takada.masahiko.7x@kyoto-u.ac.jp

Employing a neuron-specific retrograde gene-transfer vector (NeuRet vector), we have recently developed a novel technique that achieves pathway-selective ablation in the primate brain. This technique is mediated by immunotoxin (IT) and eliminates a neuronal population that constitutes a particular pathway, leaving other pathways intact. By means of this technique, we have made an attempt to remove the hyperdirect pathway selectively from basal ganglia circuitry. The hyperdirect pathway links the motor cortex to the subthalamic nucleus (STN) directly and plays a crucial role in motor control. After electrical stimulation in the motor cortex, triphasic responses consisting of an early excitation, an inhibition, and a late excitation are usually elicited in the internal pallidal segment (GPi). Several pieces of pharmacophysiological evidence imply that the early excitation may be derived from the hyperdirect pathway. In our experiments, the NeuRet vector expressing human interleukin-2 receptor α-subunit was injected into the STN of macaque monkeys. Then, IT injections were performed into the supplementary motor area (SMA). When single neuron activity in the GPi was recorded in response to the SMA stimulation, it was found that the early excitation was significantly reduced with neither the inhibition nor the late excitation affected. The spontaneous firing rate and pattern of GPi neurons remained to be altered. This clearly indicates that IT-mediated tract targeting successfully eliminated the hyperdirect pathway with spontaneous activity of STN neurons unaffected. The electrophysiological findings were histologically confirmed by retrograde and anterograde neuronal labeling. The overall data define that the motor cortically driven early excitation in GPi neurons is conveyed through the hyperdirect pathway. The IT-mediated pathway-selective ablation technique will provide a powerful tool for elucidating information processing in various neural networks.

Keywords: basal ganglia, hyperdirect pathway, information processing, immunotoxin, lentivirus, vectors, gene transfer, primates

INTRODUCTION

To know about a variety of higher brain functions systematically, it is essential to elucidate the architecture of complex and elaborate neural networks. For clarifying the functional role of a given pathway, it is an effective way to explore behavioral and physiological changes due to ablation of a neuronal population that constitutes the target pathway. Neuronal targeting mediated by immunotoxin (IT) has been established in mice as a genetic method for eliminating a specific neuron group from a certain neural network (Kobayashi et al., 1995; Sano et al., 2003; Yasoshima et al., 2005). Recently, it has been revealed that the use of modified glycoprotein of rabies virus for preparing a pseudotyped lentiviral vector based on human immunodeficiency virus type 1 (HIV-1) can enhance the efficiency of gene transfer through retrograde transport of the vector (Kato et al., 2007, 2011a). This property of the pseudotyped lentiviral vector largely allows for gene transfer into cell bodies of neurons that are located remote from the injection site of the vector. For IT-mediated removal of a particular pathway, the highly efficient retrograde gene-transfer vector was produced to express human interleukin-2 receptor α-subunit (IL-2Rα), a receptor molecule for the recombinant IT, in neuronal cell bodies via retrograde transport of the vector. In mice receiving injection of the IL-2Rα-expressing vector into the striatum, IT injection into the thalamus successfully resulted in selective removal of the thalamostriatal pathway (Kato et al., 2011b).

In our recent work, we have applied the IT-mediated pathway-selective elimination technique to the primate brain, because the use of non-human primates as animal models is critical for investigating higher brain functions. Employing the nigrostriatal dopamine pathway as a test system, we have first established the basic methodology with a neuron-specific retrograde gene-transfer vector (NeuRet vector) that has newly

been developed with improved neuron specificity (Kato et al., 2011c). Next, an attempt has been made to eliminate the cortico–subthalamic "hyperdirect" pathway selectively from basal ganglia circuitry in macaque monkeys (Inoue et al., 2012). The subthalamic nucleus (STN) receives major input from the motor cortex and, in turn, sends output to the internal segment of the globus pallidus (GPi), a main output station of the basal ganglia (Hartmann-von Monakow et al., 1978; Mink and Thach, 1993; Parent and Hazrati, 1995; Mink, 1996; Nambu et al., 1996, 1997, 2002a). It has been demonstrated that electrical stimulation in the motor cortex induces an early, short-latency excitation in GPi neurons, followed by an inhibition and then a late, long-latency excitation (**Figure 1**; Nambu et al., 2000, 2002a; Tachibana et al., 2008). According to several pharmacophysiological data, the early excitation is most likely to be conveyed through the cortico-STN-GPi pathway (**Figure 1**; Nambu et al., 2000, 2002a; Tachibana et al., 2008). However, no direct evidence has as yet been available. By means of IT-mediated pathway-selective ablation, we have successfully proven the contribution of the hyperdirect pathway to the emergence of the early excitation. Here we introduce the detailed data on this issue.

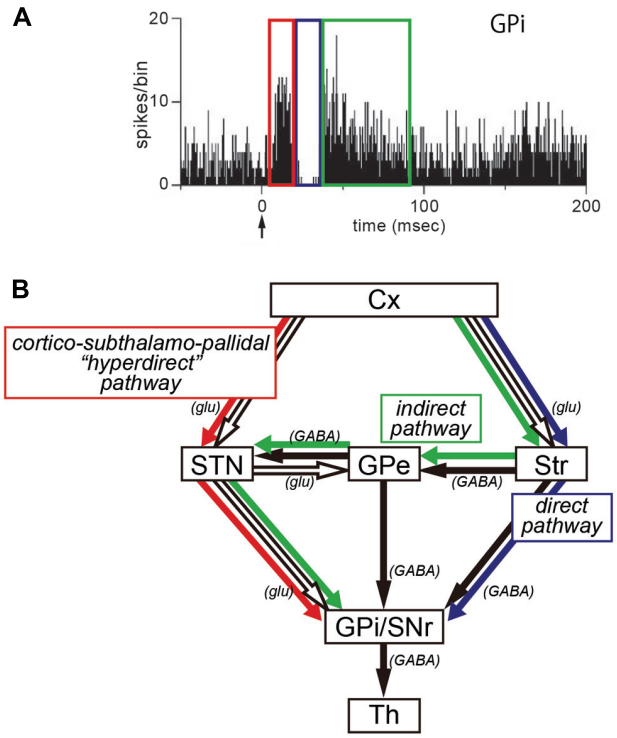

FIGURE 1 | (A) Peri-stimulus time histogram (PSTH; bin width of 1 ms, summed for 100 stimulus trials) showing triphasic responses of a neuron in the internal segment of the globus pallidus (GPi). Electrical stimulation in the motor cortex was given at time = 0 (arrow). Note that an early excitation (red), an inhibition (blue), and a late excitation (green) are derived respectively from the hyperdirect, direct, or indirect pathway depicted in **(B)**. **(B)** Three pathways of the basal ganglia. Cx, cerebral cortex; glu, glutamate; GPe, external segment of the globus pallidus; GPi, internal segment of the globus pallidus; SNr, substantia nigra pars reticulata; STN, subthalamic nucleus; Str, striatum; Th, thalamus.

PREPARATION OF NeuRet VECTOR

We have developed a new vector system that permits NeuRet by pseudotyping the HIV-1-based lentiviral vector with fusion glycoprotein C type (FuG-C) consisting of a hybrid of rabies virus glycoprotein (RV-G) and vesicular stomatitis virus glycoprotein (VSV-G; Kato et al., 2011c). Interestingly, the NeuRet vector exhibits high efficiency of retrograde gene transfer into various populations of neurons, while it markedly reduces gene transduction into dividing cells, including glial and neural stem/progenitor cells, around the vector injection site. The NeuRet vector is composed of the N-terminal segment of the extracellular domain (439 amino acids) of RV-G and the C-terminal segment

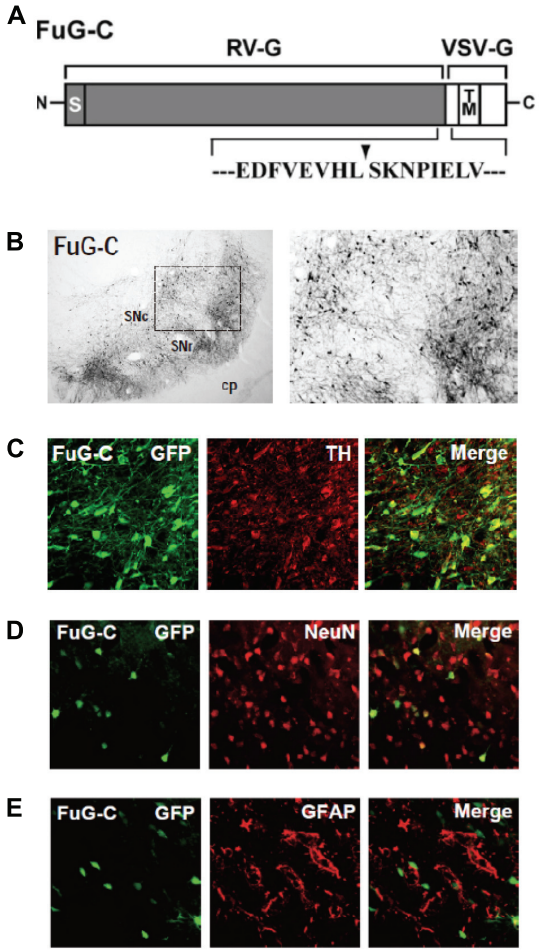

FIGURE 2 | (A) Structure of fusion envelope glycoprotein of a neuron-specific retrograde gene-transfer vector (NeuRet vector). Fusion glycoprotein C type (FuG-C) is composed of the N-terminal segment of the extracellular domain of rabies virus glycoprotein (RV-G) and the C-terminal segment of the extracellular domain and the transmembrane (TM)/cytoplasmic domains of vesicular stomatitis virus glycoprotein (VSV-G). Amino acid sequences around the junction between the RV-G and VSV-G segments are shown. S, signal peptide. **(B)** Green fluorescent protein (GFP) immunostaining in the substantia nigra pars compacta (SNc). cp, cerebral peduncle; SNr, substantia nigra pars reticulata. **(C)** Double immunofluorescence staining for GFP and tyrosine hydroxylase (TH) in the SNc. **(D,E)** Double immunofluorescence staining for GFP/NeuN **(D)** or GFP/glial fibrillary acidic protein (GFAP; **E)** in the striatum.

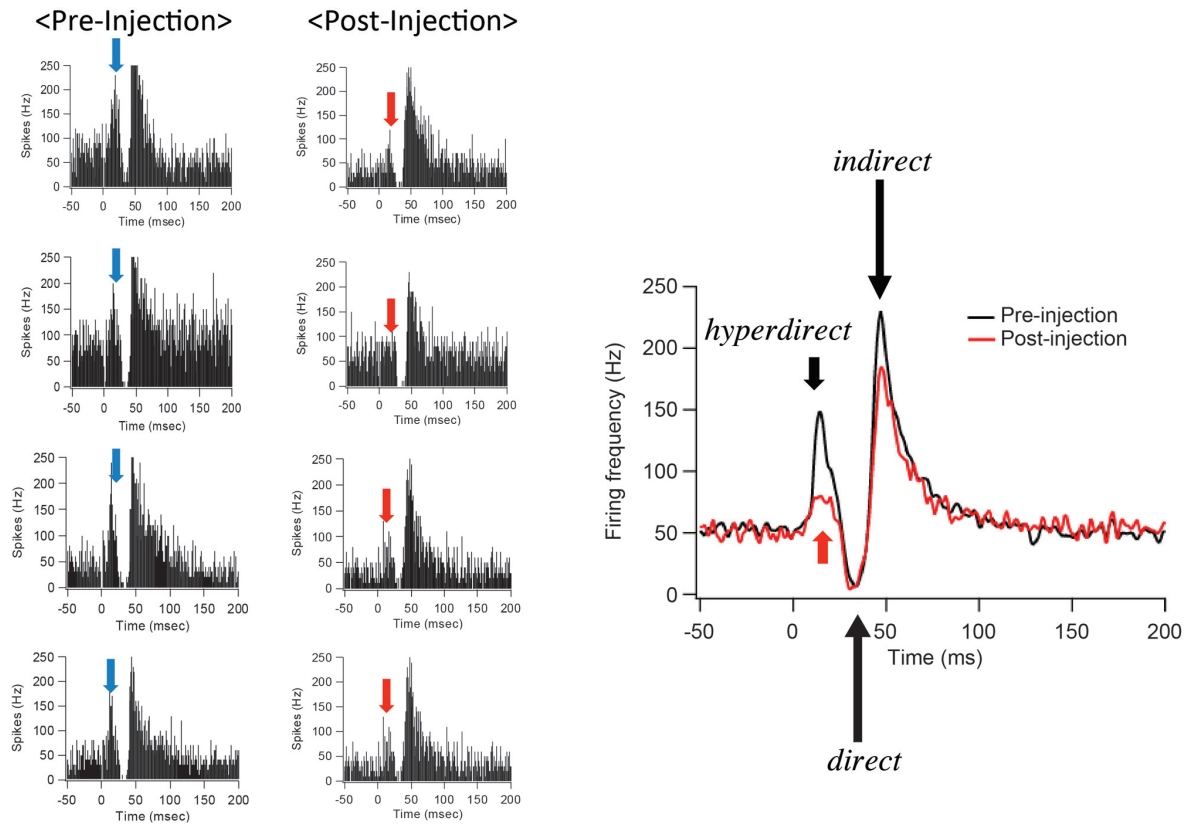

FIGURE 3 | Changes in GPi neuron responses after selective ablation of the hyperdirect pathway. Examples of PSTHs (bin width of 1 ms, summed for 100 stimulus trials) before (Pre-Injection) and after (Post-Injection) immunotoxin (IT) injections into the supplementary motor area (SMA). Electrical stimulation in the SMA was given at time = 0. Note that the early excitation is diminished without either the inhibition or the late excitation affected.

of the extracellular domain (16 amino acids) and transmembrane/cytoplasmic domains of VSV-G (**Figure 2A**). To verify the capability of the NeuRet vector for efficient retrograde gene transfer into the nigrostriatal pathway, we injected the vector encoding the green fluorescent protein (GFP) transgene into the striatum (caudate nucleus and putamen) of crab-eating monkeys. Intrastriatal injection of the NeuRet vector produced a large number of GFP-positive neurons in the nigra (**Figure 2B**). These neurons were immunostained for tyrosine hydroxylase, a key enzyme for dopamine biosynthesis (**Figure 2C**), indicating the transgene expression in the nigrostriatal dopamine neurons. Moreover, we assessed the extent of gene transfer with the NeuRet vector around the injection sites in the monkey striatum. The vector displayed a low level of gene transfer into neuronal cells, and the level of vector transfer into glial cells was also quite low in the striatum (**Figures 2D,E**). Therefore, the NeuRet vector mediates enhanced retrograde gene transfer into neuronal cells, whereas it reduces the efficiency of gene transfer into glial cells around the injection sites.

SELECTIVE ABLATION OF HYPERDIRECT PATHWAY

The NeuRet vector expressing IL-2Rα was injected into electrophysiologically identified sites in the STN of Japanese monkeys. Following the vector injections into the STN, activity of GPi neurons was recorded in response to electrical stimulation in the supplementary motor area (SMA). In most of the GPi neurons in which certain responses were induced, we observed a triphasic response pattern consisting of an early excitation, a subsequent inhibition, and a late excitation, as previously reported in normal monkeys (see **Figure 1**; Nambu et al., 2000; Tachibana et al., 2008). This indicated that the vector injections into the STN did not affect cortically evoked responses of GPi neurons.

After IT injections into the SMA, especially its arm region, neuronal activity in the GPi was recorded in response to the SMA stimulation. Many of the recorded GPi neurons exhibited a biphasic pattern, an inhibition followed by a late excitation without an early excitation (**Figure 3**). Compared with a control condition (before the IT injections), the amplitude of the early excitation was largely (by almost 90% of the control) reduced after the IT injections. On the other hand, the amplitude of the inhibition and the late excitation remained relatively unchanged, although the late excitation slightly decreased with no significant change (**Figure 3**). In addition, virtually no alterations were found in the latency of the inhibition or the late excitation, or the duration of the inhibition or the late excitation. In the control monkey in which no vector injections were made into the STN, the response pattern of GPi neurons on SMA stimulation was essentially the same before and after IT injections into the SMA (**Figure 4**). Thus,

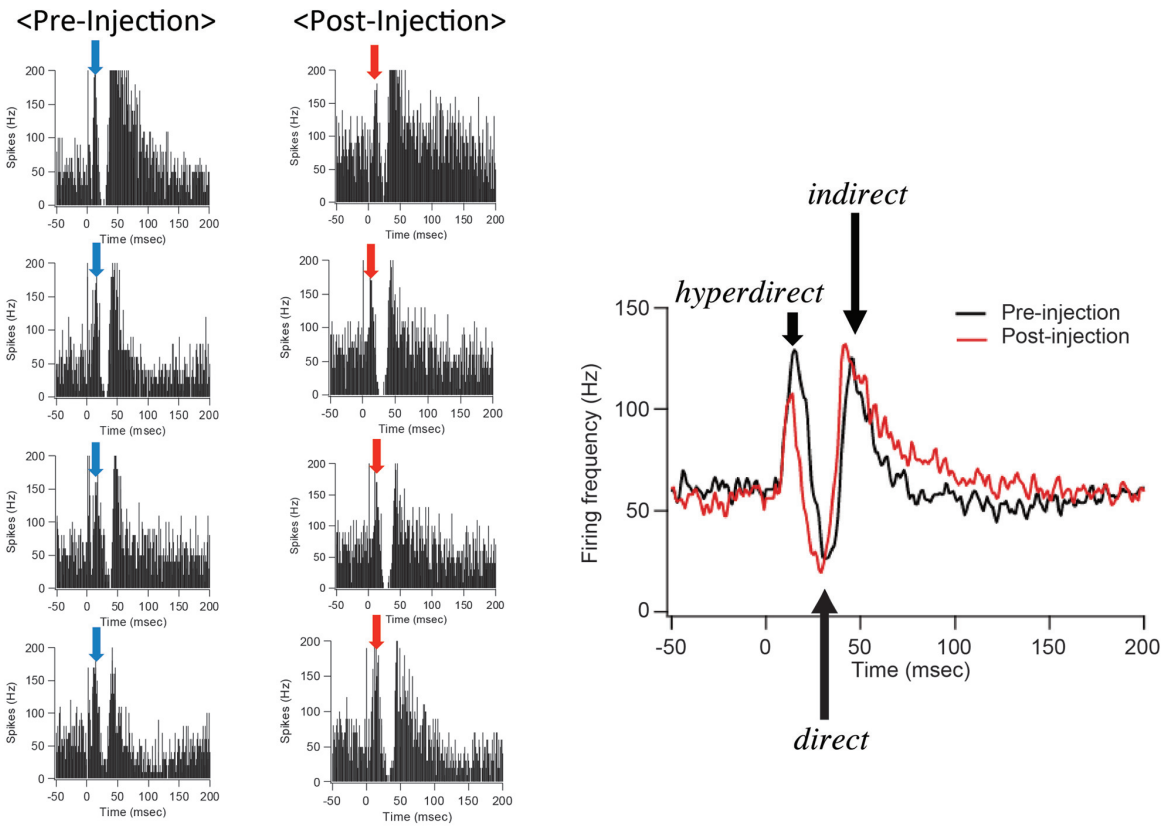

FIGURE 4 | GPi neuron responses to SMA stimulation in the control case in which no vector injections were made into the STN. All conventions are as in **Figure 3**. Note that the response pattern of a GPi neuron is essentially the same before and after IT injections into the SMA.

the IT injections into the SMA combined with the injections of the NeuRet vector expressing IL-2Rα into the STN abolished the cortically evoked early excitation in the GPi without affecting either the inhibition or the late excitation.

Furthermore, the spontaneous firing rate and pattern were compared before and after the IT injections into the SMA. The spontaneous firing rate was left intact (**Figure 5**). Neurons in the GPi fired randomly at high frequency before the IT injections, and no apparent changes were observed after the IT injections (**Figure 5**). These results suggested that the firing rate and pattern of GPi neurons remained unchanged even after the removal of the cortico-STN projection.

In the monkeys subjected to the disappearance of the early excitation responding to the SMA stimulation, we performed retrograde and anterograde neuronal labeling by injecting Fluoro-ruby (FR) into the STN and biotinylated dextran amine (BDA) into the SMA. After the FR injection into the STN, retrogradely labeled neurons in the SMA were much fewer in the arm region where the IT injections were primarily aimed than in the face and leg regions (**Figure 6**). Moreover, immunostaining for NeuN revealed that the IT injections into the SMA caused no marked tissue damage (**Figure 6**). After the BDA injections into the SMA forelimb region, anterogradely labeled axon terminals were so largely decreased in the STN, as compared to the control case (data not shown). In remarkable contrast, dense terminal labeling from the SMA was seen in the striatum, especially the putamen, as in the control case (data not shown). These anatomical data clearly indicated that cortico-STN projection originating from the SMA arm region was selectively eliminated without affecting either the corticostriatal projection or the cortico-STN projections from SMA regions with other representations than the arm.

We did not closely examine behavioral changes to be produced after elimination of the hyperdirect pathway, because our study was primarily designed to develop a new methodological approach to selective removal of a given pathway. As far as our experimental conditions were concerned, no apparent motor abnormalities were observed.

DISCUSSION

Taking advantage of the NeuRet vector that allows for highly efficient retrograde gene-transfer with improved neuron specificity (Kato et al., 2011c), we have established IT-mediated pathway-selective ablation in the primate brain. Here we have applied this technique to the hyperdirect pathway (Inoue et al., 2012). In conjunction with the direct and indirect pathways (for reviews, see Albin et al., 1989; Alexander and Crutcher, 1990), the hyperdirect pathway is known to be among the key pathways of the basal ganglia, being involved in motor information processing in the basal

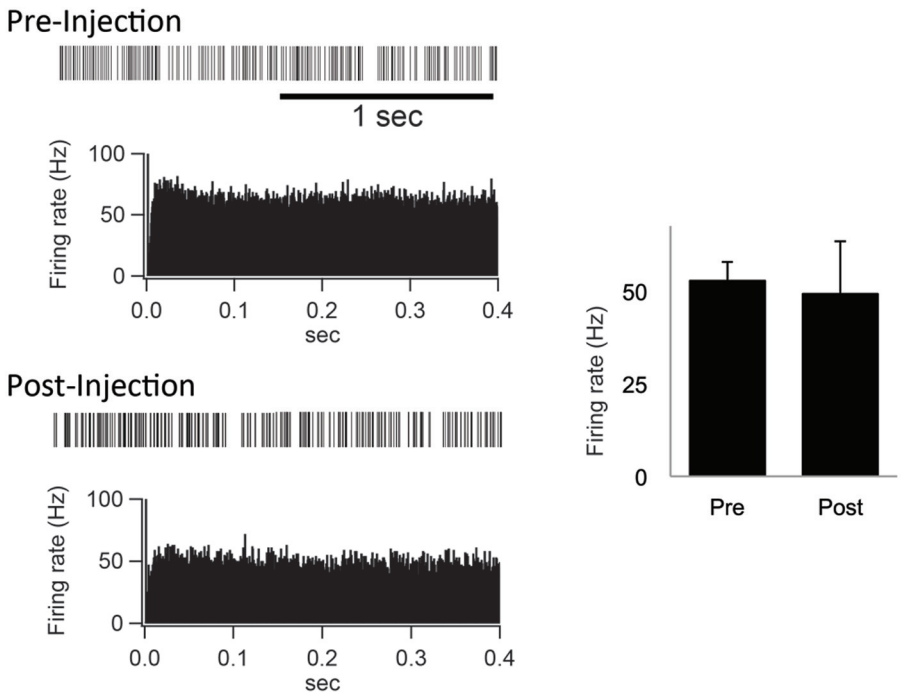

FIGURE 5 | (Left) Examples of spontaneous activities denoted by slow traces of digitized spikes and autocorrelograms (bin width of 0.5 ms) before (Pre-Injection) and after (Post-Injection) IT injections into the SMA. (Right) Firing rates before (Pre) and after (Post) the IT injections.

ganglia (Nambu et al., 1996, 2002a). This pathway connects the motor cortex to the GPi at short latency through the STN without relay at the striatum. When single neuron activity was recorded in the monkey GPi in response to electrical stimulation in the motor cortex, triphasic responses composed of an early (short-latency) excitation, an inhibition, and a late (long-latency) excitation were obtained. Based on the following pharmacophysiological data (see also Nambu et al., 2002a), it has been considered that the early excitation may be derived from the cortico-STN-GPi hyperdirect pathway: (1) Blockade of STN neuron activity by injection of the $GABA_A$ receptor agonist, muscimol, there into abolished the early as well as the late excitation of GPi neurons (Nambu et al., 2000); (2) Blockade of glutamatergic input from the STN to the GPi by local injection of an ionotropic glutamatergic receptor antagonist diminished the early as well as the late excitation of GPi neurons (Tachibana et al., 2008).

For selective removal of the hyperdirect pathway, the NeuRet vector expressing IL-2Rα was injected into the STN, and, subsequently, IT was injected into the SMA in our experimental protocol. Our histological examination clearly indicated that cortical neurons in the arm region of the SMA projecting to the STN were selectively ablated. In such model monkeys, GPi neuron activity was recorded in response to electrical stimulation in the SMA. The SMA stimulation yields selective activation of SMA-recipient zones in the basal ganglia (Nambu et al., 2002b). It was found that out of the triphasic responses, only the early excitation was largely suppressed without either the inhibition or the late excitation affected. This indicates that IT-mediated tract targeting successfully eliminated the hyperdirect pathway selectively from basal ganglia circuitry. Our results define that the cortically driven early excitation of GPi neurons is derived from the cortico-STN projection. It has also been revealed that the firing rate and pattern of GPi neurons remain unchanged even after the removal of the cortico-STN projection. This implies that the cortico-STN projection conveys phasic activity changes from the SMA to the GPi, but does not contribute to maintenance of tonic activity of GPi neurons. In contrast to the early excitation, the inhibition in the GPi was not affected by the elimination of the cortico-STN projection, as it can be considered that the inhibition is mediated through the cortico-striato-GPi direct pathway (Tachibana et al., 2008). On the other hand, the late excitation in the GPi was slightly diminished though not significant. This late excitation is ascribable to the late excitation in the STN and is probably mediated by the cortico-striato-external pallidal segment (GPe)-STN-GPi indirect pathway. However, it has also been suggested that the late excitation in the STN is part of the prolonged excitation induced by the cortico-STN projection, which may explain a slight decrease in the late excitation in the GPi after the elimination of the cortico-STN projection (Tachibana et al., 2008). The SMA neurons giving rise to the cortico-STN projection are likely to issue axon collaterals to cortical and/or subcortical (other than the STN) regions. Thus, it cannot be ruled out that no such possible collateral projections may be affected by IT injected into the SMA.

According to the cortically driven triphasic response pattern elicited in GPi neurons, the hyperdirect pathway conveys excitatory signals from the motor cortex toward the GPi, bypassing the striatum, with shorter conduction time than signals via the striatum that arise from both the direct and the indirect pathways (see

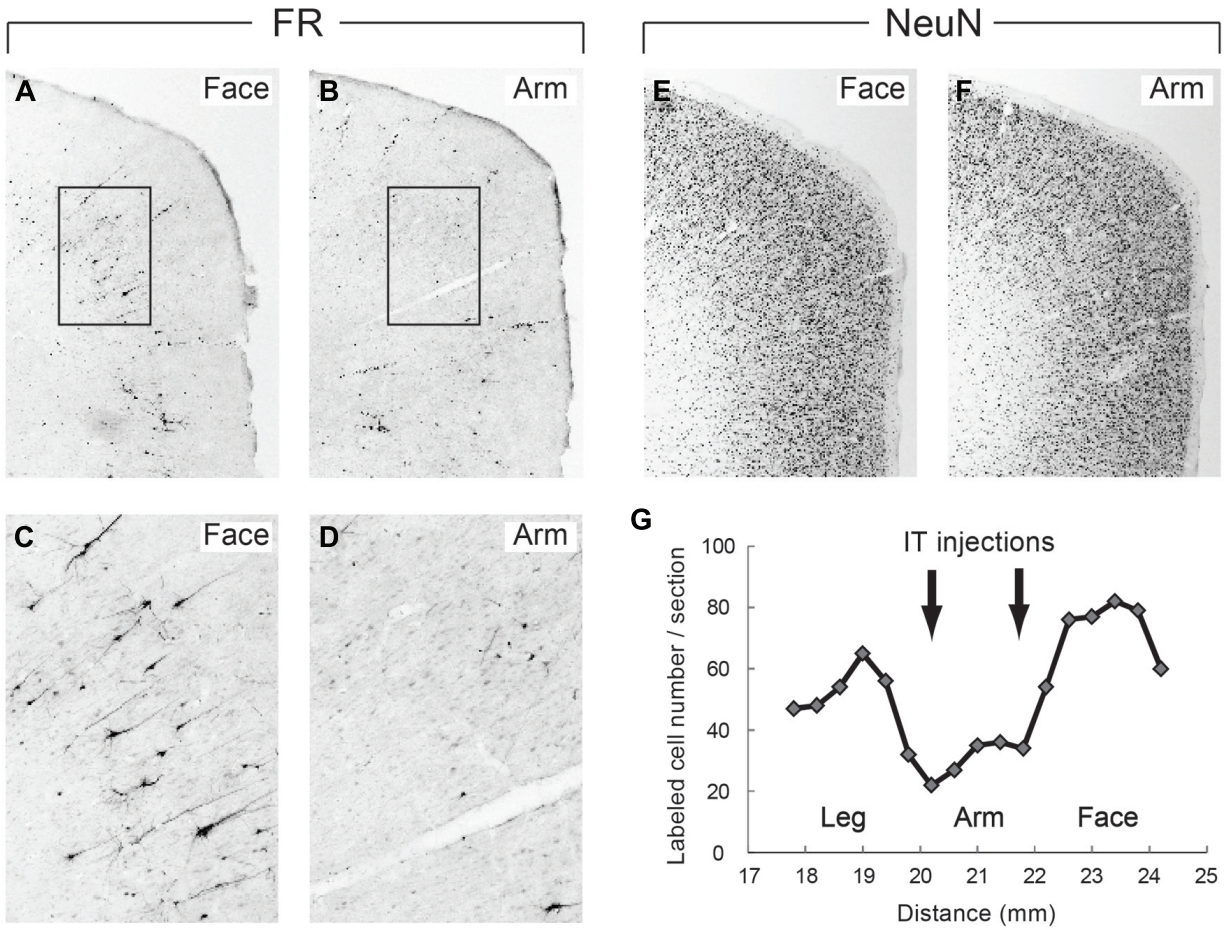

FIGURE 6 | (A,B) Retrograde neuronal labeling in the face and arm regions of the SMA after Fluoro-ruby (FR) injection into the STN. **(C,D)** Higher-power magnifications of the rectangular areas in **(A,B)**. **(E,F)** NeuN immunostaining of the face and arm regions of the SMA. Note that the IT injections cause no marked tissue damage. **(G)** Distribution of FR-positive neurons in the face, arm, and leg regions of the SMA. Note that FR-positive neurons are so few in the arm region where IT injections were made (at two rostrocaudally distinct levels pointed to by arrows), as compared to those in the face and leg regions. Numerals on the abscissa represent the distance from rostrocaudal zero on the stereotaxic frame (equivalent to the interaural line).

Nambu et al., 2000, 2002a). In favor of a dynamic "center-surround model" of basal ganglia function that was first proposed by Mink and Thach (1993), the functional role of the hyperdirect pathway has been implicated in the control of voluntary limb movements (see also Mink, 1996; Hikosaka et al., 2000; Nambu et al., 2002a). When a voluntary movement is about to be initiated by the motor cortical mechanism, a corollary signal conveyed through the cortico-STN-GPi hyperdirect pathway first inhibits large areas of the thalamic and cortical target structures that are related not only to a desired motor program, but also to other competing programs. Then, another corollary signal through the cortico-striato-GPi direct pathway disinhibits part of the thalamic and cortical target areas and releases the desired motor program alone. Finally, the third corollary signal conveyed by way of the cortico-striato-GPe-STN-GPi indirect pathway again inhibits the thalamic and cortical target areas extensively. By virtue of such sequential motor information processing, only the desired motor program is initiated, executed, and terminated at appropriate timings, whereas other competing programs are canceled. Thus, it is most likely that the hyperdirect pathway exerts a powerful excitatory effect on the GPi to suppress involuntary and unnecessary movements prior to the selected motor action. This notion is substantiated by the following issues: (1) Lesions or blockade of STN neuron activity induced involuntary movements, hemiballism (Carpenter et al., 1950; Hamada and DeLong, 1992; Nambu et al., 2000), suggesting that both the hyperdirect and indirect pathways might inhibit unnecessary movements; (2) According to functional magnetic resonance imaging studies using human subjects, the cortico-STN projection conveys stop signals to inhibit motor responses (Aron and Poldrack, 2006; Jahfari et al., 2011); (3) It is also suggested that the cortico-STN projection may inhibit automatic movements and switch to volitionally controlled movement (Isoda and Hikosaka, 2008).

Since no explicit motor abnormalities were seen in our experimental conditions, changes in the activity of GPi neurons in response to the cortical stimulation following a limited amount of elimination of the hyperdirect pathway may not be enough to elicit behavioral alterations. Accordingly, there is a need to

determine the relationship between the extent of the elimination of the selected pathway and the expression of altered behaviors.

The IT-mediated tract targeting achieves selective ablation of a given pathway in primates. This novel technique will provide a potent strategy to explore not only specific functional roles of individual pathways constituting a particular neural network, but also large-scale operative mechanisms underlying the entire network.

ACKNOWLEDGMENT

We are grateful to T. Kuroda for technical assistance.

REFERENCES

Albin, R. L., Young, A. B., and Penney, J. B. (1989). The functional anatomy of basal ganglia disorders. *Trends Neurosci.* 12, 366–375. doi: 10.1016/0166-2236(89)90074-X

Alexander, G. E., and Crutcher, M. D. (1990). Functional architecture of basal ganglia circuits: neural substrates of parallel processing. *Trends Neurosci.* 13, 266–271. doi: 10.1016/0166-2236(90)90107-L

Aron, A. R., and Poldrack, R. A. (2006). Cortical and subcortical contributions to stop signal response inhibition: role of the subthalamic nucleus. *J. Neurosci.* 26, 2424–2433. doi: 10.1523/JNEUROSCI.4682-05.2006

Carpenter, M. B., Whittier, J. R., and Mettler, F. A. (1950). Analysis of choreoid hyperkinesia in the rhesus monkey; surgical and pharmacological analysis of hyperkinesia resulting from lesions in the subthalamic nucleus of Luys. *J. Comp. Neurol.* 92, 293–331. doi: 10.1002/cne.900920303

Hamada, I., and DeLong, M. R. (1992). Excitotoxic acid lesions of the primate subthalamic nucleus result in transient dyskinesias of the contralateral limbs. *J. Neurophysiol.* 68, 1850–1858.

Hartmann-von Monakow, K., Akert, K., and Künzle, H. (1978). Projections of the precentral motor cortex and other cortical areas of the frontal lobe to the subthalamic nucleus in the monkey. *Exp. Brain Res.* 33, 395–403. doi: 10.1007/BF00235561

Hikosaka, O., Takikawa, Y., and Kawagoe, R. (2000). Role of the basal ganglia in the control of purposive saccadic eye movements. *Physiol. Rev.* 80, 953–978.

Inoue, K., Koketsu, D., Kato, S., Kobayashi, K., Nambu, A., and Takada, M. (2012). Immunotoxin-mediated tract targeting in the primate brain: selective elimination of the cortico–subthalamic "hyperdirect" pathway. *PLoS ONE* 7:e39149. doi: 10.1371/journal.pone.0039149

Isoda, M., and Hikosaka, O. (2008). Role for subthalamic nucleus neurons in switching from automatic to controlled eye movement. *J. Neurosci.* 28, 7209–7218. doi: 10.1523/JNEUROSCI.0487-08.2008

Jahfari, S., Waldorp, L., van den Wildenberg, W. P., Scholte, H. S., Ridderinkhof, K. R., and Forstmann, B. U. (2011). Effective connectivity reveals important roles for both the hyperdirect (fronto-subthalamic) and the indirect (fronto-striatal-pallidal) fronto-basal ganglia pathways during response inhibition. *J. Neurosci.* 31, 6891–6899. doi: 10.1523/JNEUROSCI.5253-10.2011

Kato, S., Inoue, K., Kobayashi, K., Yasoshima, Y., Miyachi, S., Inoue, S., et al. (2007). Efficient gene transfer via retrograde transport in rodent and primate brains by an HIV-1-based vector pseudotyped with rabies virus glycoprotein. *Hum. Gene Ther.* 18, 1141–1151. doi: 10.1089/hum.2007.082

Kato, S., Kobayashi, K., Inoue, K., Kuramochi, M., Okada, T., Yaginuma, H., et al. (2011a). A lentiviral strategy for highly efficient retrograde gene transfer by pseudotyping with fusion envelope glycoprotein. *Hum. Gene Ther.* 22, 197–206. doi: 10.1089/hum.2009.179

Kato, S., Kuramochi, M., Kobayashi, K., Fukabori, R., Okada, K., Uchigashima, M., et al. (2011b). Selective neural pathway targeting reveals key roles of thalamostriatal projection in the control of visual discrimination. *J. Neurosci.* 31, 17169–17179. doi: 10.1523/JNEUROSCI.4005-11.2011

Kato, S., Kuramochi, M., Takasumi, K., Kobayashi, K., Inoue, K., Takahara, D., et al. (2011c). Neuron-specific gene transfer through retrograde transport of lentiviral vector pseudotyped with a novel type of fusion envelope glycoprotein. *Hum. Gene Ther.* 22, 1511–1523. doi: 10.1089/hum.2011.111

Kobayashi, K., Morita, S., Sawada, H., Mizuguchi, T., Yamada, K., Nagatsu, I., et al. (1995). Immunotoxin-mediated conditional disruption of specific neurons in transgenic mice. *Proc. Natl. Acad. Sci. U.S.A.* 92, 1132–1136. doi: 10.1073/pnas.92.4.1132

Mink, J. W. (1996). The basal ganglia: focused selection and inhibition of competing motor programs. *Prog. Neurobiol.* 50, 381–425. doi: 10.1016/S0301-0082(96)00042-1

Mink, J. W., and Thach, W. T. (1993). Basal ganglia intrinsic circuits and their role in behavior. *Curr. Opin. Neurobiol.* 3, 950–957. doi: 10.1016/0959-4388(93)90167-W

Nambu, A., Takada, M., Inase, M., and Tokuno, H. (1996). Dual somatotopical representations in the primate subthalamic nucleus: evidence for ordered but reversed body-map transformations from the primary motor cortex and the supplementary motor area. *J. Neurosci.* 16, 2671–2683.

Nambu, A., Tokuno, H., Hamada, I., Kita, H., Imanishi, M., Akazawa, T., et al. (2000). Excitatory cortical inputs to pallidal neurons via the subthalamic nucleus in the monkey. *J. Neurophysiol.* 84, 289–300.

Nambu, A., Tokuno, H., Inase, M., and Takada, M. (1997). Cortico-subthalamic input zones from forelimb representations of the dorsal and ventral divisions of the premotor cortex in the macaque monkey: comparison with the input zones from the primary motor cortex and the supplementary motor area. *Neurosci. Lett.* 239, 13–16. doi: 10.1016/S0304-3940(97)00877-X

Nambu, A., Tokuno, H., and Takada, M. (2002a). Functional significance of the cortico–subthalamo–pallidal 'hyperdirect' pathway. *Neurosci. Res.* 43, 111–117. doi: 10.1016/S0168-0102(02)00027-5

Nambu, A., Kaneda, K., Tokuno, H., and Takada, M. (2002b). Organization of corticostriatal motor inputs in monkey putamen. *J. Neurophysiol.* 88, 1830–1842.

Parent, A., and Hazrati, L.-N. (1995). Functional anatomy of the basal ganglia. II. The place of subthalamic nucleus and external pallidum in basal ganglia circuitry. *Brain Res. Brain Res. Rev.* 20, 128–154. doi: 10.1016/0165-0173(94)00008-D

Sano, H., Yasoshima, Y., Matsushita, N., Kaneko, T., Kohno, K., Pastan, I., et al. (2003). Conditional ablation of striatal neuronal types containing dopamine D2 receptor disturbs coordination of basal ganglia function. *J. Neurosci.* 23, 9078–9088.

Tachibana, Y., Kita, H., Chiken, S., Takada, M., and Nambu, A. (2008). Motor cortical control of internal pallidal activity through glutamatergic and GABAergic inputs in awake monkeys. *Eur. J. Neurosci.* 27, 238–253. doi: 10.1111/j.1460-9568.2007.05990.x

Yasoshima, Y., Kai, N., Yoshida, S., Shiosaka, S., Koyama, Y., Kayama, Y., et al. (2005). Subthalamic neurons coordinate basal ganglia function through differential neural pathways. *J. Neurosci.* 25, 7743–7753. doi: 10.1523/JNEUROSCI.1904-05.2005

Conflict of Interest Statement: The authors declare that the research was conducted in the absence of any commercial or financial relationships that could be construed as a potential conflict of interest.

Received: 29 July 2013; accepted: 19 August 2013; published online: 03 September 2013.

Citation: Takada M, Inoue K-I, Koketsu D, Kato S, Kobayashi K and Nambu A (2013) Elucidating information processing in primate basal ganglia circuitry: a novel technique for pathway-selective ablation mediated by immunotoxin. Front. Neural Circuits 7:140. doi: 10.3389/fncir.2013.00140

This article was submitted to the journal Frontiers in Neural Circuits.

frontiers in
NEURAL CIRCUITS

REVIEW ARTICLE
published: 21 October 2013
doi: 10.3389/fncir.2013.00158

Cortico-basal ganglia networks subserving goal-directed behavior mediated by conditional visuo-goal association

Eiji Hoshi [1,2] *

[1] Frontal Lobe Function Project, Tokyo Metropolitan Institute of Medical Science, Tokyo, Japan
[2] Japan Science and Technology Agency, Core Research for Evolutionary Science and Technology, Tokyo, Japan

Edited by:
Yasuo Kawaguchi, National Institute for Physiological Sciences, Japan

Reviewed by:
Aldo Genovesio, La Sapienza, Italy
Takashi Hanakawa, National Center of Neurology and Psychiatry, Japan

***Correspondence:**
Eiji Hoshi, Frontal Lobe Function Project, Tokyo Metropolitan Institute of Medical Science, Kamikitazawa 2-1-6, Setagaya-ku, Tokyo 156-8506, Japan
e-mail: hoshi-ej@igakuken.or.jp

Action is often executed according to information provided by a visual signal. As this type of behavior integrates two distinct neural representations, perception and action, it has been thought that identification of the neural mechanisms underlying this process will yield deeper insights into the principles underpinning goal-directed behavior. Based on a framework derived from conditional visuomotor association, prior studies have identified neural mechanisms in the dorsal premotor cortex (PMd), dorsolateral prefrontal cortex (dlPFC), ventrolateral prefrontal cortex (vlPFC), and basal ganglia (BG). However, applications resting solely on this conceptualization encounter problems related to generalization and flexibility, essential processes in executive function, because the association mode involves a direct one-to-one mapping of each visual signal onto a particular action. To overcome this problem, we extend this conceptualization and postulate a more general framework, conditional visuo-goal association. According to this new framework, the visual signal identifies an abstract behavioral goal, and an action is subsequently selected and executed to meet this goal. Neuronal activity recorded from the four key areas of the brains of monkeys performing a task involving conditional visuo-goal association revealed three major mechanisms underlying this process. First, visual-object signals are represented primarily in the vlPFC and BG. Second, all four areas are involved in initially determining the goals based on the visual signals, with the PMd and dlPFC playing major roles in maintaining the salience of the goals. Third, the cortical areas play major roles in specifying action, whereas the role of the BG in this process is restrictive. These new lines of evidence reveal that the four areas involved in conditional visuomotor association contribute to goal-directed behavior mediated by conditional visuo-goal association in an area-dependent manner.

Keywords: sensorimotor integration, visuomotor integration, goal, action, globus pallidus, executive function

INTRODUCTION

When we drive a car and arrive at an intersection, we press the brake pedal if we see a red light, or we continue to press the gas pedal if we see a green light. More generally, we often act based on information provided by a visual signal. Because this type of goal-directed behavior integrates two forms of neural representations (i.e., perception and action), it is thought that identification of the neural mechanisms underlying their integration will yield insights into the fundamental principles underpinning goal-directed behavior. Some studies in this domain have used the framework provided by arbitrary visuomotor mapping (Passingham, 1993; Murray et al., 2000; Wise and Murray, 2000). In this paper, we will refer to this framework as conditional visuomotor association because it maintains that the integration of visual and motor signals is guided by behavioral rules (Wallis et al., 2001; Bunge et al., 2005) and because the association areas in the brain are believed to play a central role in this process (Goldman-Rakic, 1988; Miller and Cohen, 2001; Serrien et al., 2007; Fuster, 2008; Tanji and Hoshi, 2008; Passingham and Wise, 2012).

Accurate definitions of the goals and rules are therefore critical. Schall (2001) and Passingham and Wise (2012) presented clear definitions of the links between the goals and decisions and between actions and choices. Based on these studies, we here define the goals as "the objects or locations that an animal chooses as the target for its actions" (p. 71 in Passingham and Wise, 2012). In contrast, Bunge et al. (2005) and Bunge and Wallis (2008) defined the rules as ones that specify the most appropriate response under a given set of circumstances or contexts. In the case of goal-directed behavior, the rules are viewed as being implemented by individual neurons and/or neuronal networks for specifying the most appropriate goal or action under specific circumstances. Studies by White and Wise (1999) and Wallis et al. (2001) revealed that single neurons in the prefrontal cortex represent the rules, whereas studies by Hoshi et al. (2000) and Tanji and Hoshi (2001) suggested that the rules are implemented within networks or populations of neurons in the prefrontal cortex. Finally, Buschman et al. (2012) showed that the rules are implemented via oscillatory synchronization of ensembles of neurons. The multilevel representation of the rules is viewed as essential for cognitive control of goal-directed behavior (Miller, 2000).

The conditional visuomotor association framework posits that neurons or networks directly link a visual signal to a bodily movement (action) in a rule-dependent manner (**Figure 1A**). However, this assumption encounters a problem when generalization and

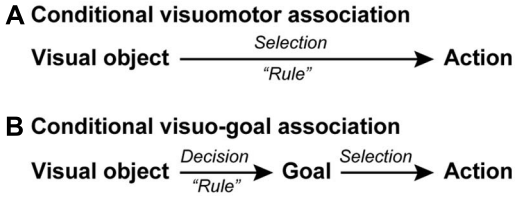

FIGURE 1 | Schematic representations of conditional visuomotor association and conditional visuo-goal association. (A) In conditional visuomotor association, perceptual signals representing visual objects are directly mapped onto the motor signals (actions) in a *rule*-dependent manner to achieve an action selection. **(B)** In conditional visuo-goal association, perceptual signals are first mapped in a *rule*-dependent manner onto signals representing behavioral goals for making a goal decision. The goal-related signals are subsequently transformed into signals representing actions, corresponding to an action selection.

flexibility are required. Because the perceptual and action signals are supposed to be linked on a one-to-one basis, it is necessary to account for every combination of perceptual and action signals. In reality, this requirement is untenable. For example, responding to a red light involves squeezing a brake lever if one is riding a bicycle, pressing a brake pedal if one is driving a car, and stopping one's movement if one is walking. Moreover, many varieties of visual signals and gestures can be the source of the instruction to stop. Actually, coming to a halt in the context of a signal to do so requires that numerous combinations of perceptual and action signals have been the foci of preparation. This requirement involving one-to-one combinations leads to another problem when the information provided by sensory signals changes or when a new motor response is required to execute the action implied by the information. For example, if a red light were to become the signal for proceeding or if the positions of the brake and gas pedals were reversed, we would need to relearn every combination of perceptual and action signals. Thus, neuronal networks that rely solely on computations based on conditional visuomotor associations would face major difficulties when information processing requires generalization or flexibility.

These flaws seem to rule out conditional visuomotor association as the mechanism underlying higher cognitive functions, which are characterized by flexibility and the ability to generalize (Milner, 1963; Luria, 1966). Thus, we must ask if we should discard this framework and seek a new conceptualization of the neural basis of information processing. Here, we would like to answer "no" and propose a new understanding of "goal" that renders the network responsible for conditional visuomotor association suitable as the underpinning of higher cognitive functions. Whereas the conditional visuomotor association framework assumes direct mapping between a visual signal and an actual movement (action), the new view is based on two additional assumptions (**Figure 1B**). First, it assumes that the visual signals provide information about an abstract behavioral goal instead of a concrete action. Second, it assumes that individuals subsequently specify or select an action to achieve that goal. We will refer to this new processing mode as conditional visuo-goal association because the visual signal is linked to a goal rather than to an action. The conditional visuo-goal association framework posits that neurons or networks directly link a visual signal to a behavioral goal in a rule-dependent manner (**Figure 1B**). This framework is considered to provide the goal-directed behavior with the generalization and flexibility. Once the goal is determined the subjects can specify or select an appropriate action to achieve the goal in various conditions, corresponding to the generalization. In addition, if the goal information provided by sensory signals changes, the subjects can address it by updating the association rules between the sensory signals and the goals, corresponding to the flexibility.

We will first review the mechanisms underlying conditional visuomotor association and then attempt to extend them to conditional visuo-goal association to elucidate how this network can serve as a basis of the higher cognitive functions that subserve goal-directed behavior.

INVOLVEMENT OF THE DORSAL PREMOTOR CORTEX IN CONDITIONAL VISUOMOTOR ASSOCIATION

Pioneering studies by Halsband and Passingham (1982, 1985) and Petrides (1982, 1986) investigated the involvement of the premotor cortex (area 6) of monkeys in conditional visuomotor association. Halsband and Passingham (1982, 1985) trained monkeys to turn a handle when a yellow panel was presented and to pull a lever when a blue panel was presented. They found that monkeys with lesions of the bilateral premotor cortex but not of the bilateral frontal eye field failed to relearn the task in 1,000 trials. Petrides (1982) trained monkeys to grip a stick when a green circular bottle top was presented and to place their hand on a button when a blue and yellow toy truck was presented. He found that monkeys with lesions of the bilateral periarcuate areas, including the dorsal premotor cortex (PMd) and the frontal eye field, were severely impaired compared with normal monkeys or with monkeys with lesions around the bilateral principal sulci. Subsequently, Petrides (1986) showed that the periarcuate areas were involved in selecting between GO and NO-GO responses based on visual signals when GO and NO-GO were symmetrically rewarded. Importantly, these studies confirmed that monkeys with lesions centered on the premotor cortex were not impaired in perceiving visual signals or in executing movements. These observations revealed that the premotor cortex and the periarcuate areas are crucially involved in making conditional associations between visual signals and actions and in selecting between actions based on visual signals.

The lesions in these studies were fairly large and spanned multiple areas. In the studies conducted by Petrides (1982, 1986), lesions were made in both banks of the actuate sulcus, impairing the functions of both the frontal eye field and the premotor cortex. Although the lesions in the studies conducted by Halsband and Passingham (1982, 1985) were confined within the premotor cortex, they were made along both the superior and inferior limbs of the arcuate sulcus, leading to lesions of both the dorsal and ventral premotor cortices (Matelli et al., 1985; Rizzolatti and Luppino, 2001). Thus, the cortical areas that were most responsible remained elusive. To identify the responsible sites, Kurata and Hoffman (1994) injected the $GABA_A$ receptor agonist muscimol to temporarily inactivate the PMd or the ventral premotor cortex (PMv). They first identified clusters of task-related neurons in the PMd and PMv while monkeys performed a conditional visuomotor association task that required them to perform a

wrist flexion (extension) movement when a red (green) signal was presented. They next injected muscimol into the cluster in either the PMd or the PMv to reversibly inactivate it. They found that inactivation of the PMd cluster led to directional errors (i.e., impairments in selecting between the flexion and extension movements), whereas inactivation of the PMv cluster led to reduced movement amplitudes and velocities (i.e., impairments in movement execution). These findings provided compelling evidence that the PMd of monkeys is crucially involved in conditional visuomotor association (**Figure 2**).

Working with humans, Halsband and Freund (1990) revealed that patients with lesions that included the premotor cortex had difficulty selecting one of six arm movements according to visual signals, although the patients could execute the six different movements themselves and could perceive the sensory stimuli used as the instructions. Schluter et al. (1998) applied transcranial magnetic stimulation (TMS) to transiently interrupt local neural computations. They found that when TMS was applied over the PMd just after visual-cue presentation, which corresponds to the period of action selection, the selection process was delayed. Grafton et al. (1998) identified an activation focus of regional cerebral blood flow (rCBF) in the PMd while subjects chose between a power grip and a precision grip depending on the color of a LED. In a functional magnetic resonance imaging (fMRI) experiment, Amiez et al. (2006) determined that the PMd of humans was selectively activated when subjects selected one of four buttons in response to the presentation of one of four colors. These studies revealed that the PMd in humans is crucially involved in the selection of actions based on visual signals.

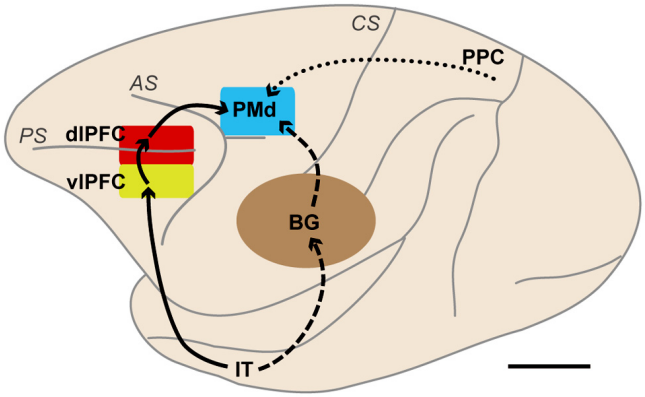

FIGURE 2 | Brain networks centered on the dorsal premotor cortex (PMd) involved in motor behavior based on visual object and visuospatial signals. The solid lines indicate a pathway from the IT to the PMd via the vlPFC and dlPFC. The broken lines indicate pathways from the IT to the PMd. These two types of pathways are thought to be involved in behavior based on visual-object signals, such as those involved in conditional visuomotor association and conditional visuo-goal association. The dotted line indicates a pathway from the PPC to the PMd. This pathway is considered to carry visuospatial information. BG, basal ganglia; dlPFC, dorsolateral prefrontal cortex; IT, inferotemporal cortex; PMd, dorsal premotor cortex; PPC, posterior parietal cortex; vlPFC, ventrolateral prefrontal cortex; *AS*, arcuate sulcus; *CS*, central sulcus; *PS*, principal sulcus. Scale bar, 10 mm.

The PMd of human and non-human primates has been shown to play a crucial role in conditional visuomotor association (**Figure 2**). The specific aspects of information processing in which the PMd participates were revealed by recording neurons while monkeys performed a variety of motor tasks. Godschalk et al. (1981) found that PMd neurons responded to the presentation of visual signals and discharged in relation to the execution of reaching movements. Wise and colleagues recorded neurons while monkeys performed a variety of visuomotor tasks (Weinrich and Wise, 1982; Weinrich et al., 1984). They reported that PMd neurons strongly responded to the appearance of visuospatial signals and began to show sustained, set-related activity reflecting the direction of the forthcoming arm movements after the direction of forelimb movement was specified by visuospatial signals. Moreover, the set-related activity was more intense when a visuospatial information signaled execution of action than when it signaled inhibition of an action (Wise et al., 1983). When the motor plan was changed, the set-related activity also changed in accordance with the monkey's motor intention (Wise and Mauritz, 1985). These observations revealed that the PMd is involved in the preparation and execution of movement based on visual signals.

Wise and colleagues subsequently conducted a series of landmark studies (Kurata and Wise, 1988; Mitz et al., 1991; Chen and Wise, 1995a,b). First, Kurata and Wise (1988) examined whether set-related activity was significantly modulated by type of visual signals. Subjects in their study participated in a conditional visuomotor association task, in which the color of the stimuli (conditional instructional stimuli) indirectly indicated the direction of an arm movement, and a directional task, in which the direction (left or right) of the visuospatial stimuli (directional instruction stimuli) directly indicated the direction of the movement. By examining the set-related activity of PMd neurons, they found that the activity of a great majority (81%) of neurons did not differ under the two task conditions. This observation indicates the relevance of set-related activity to the monkeys' determination of the direction of a forelimb movement based on associated visual stimuli. Subsequently, Mitz et al. (1991) investigated the involvement of the PMd in learning conditional visuomotor association. They examined PMd neurons while monkeys learned new associations between visual images and the directions of handle movement and found that PMd neurons showed learning-dependent activity. Specifically, the visual, set-related, and movement-related activities associated with the same movement direction were more pronounced when the association was established than when it was not, indicating that PMd neurons are involved in the selection or retrieval of arm movements based on learned conditional associations between visual stimuli and movements as well as in the preparation and execution of movement, as discussed above. Chen and Wise (1995a) subsequently revealed that neurons in the supplementary eye field in the pre-PMd were involved in the conditional visuomotor associations for oculomotor behavior (Schlag and Schlag, 1987; Huerta and Kaas, 1990; Picard and Strick, 2001; Luppino et al., 2003). They identified learning-selective activity that was enhanced while monkeys learned new associations between visual signals and the direction of saccadic eye movements, and they specified the learning-dependent activity that was enhanced when such associations were established. They

further found that a subset of neurons shows persistent differences in activity between novel and familiar information when performance is stable (learning-static effects; Chen and Wise, 1995b). These results revealed that the PMd and pre-PMd are involved in associating visual signals with actions with regard to arm and eye movements, respectively. From the perspectives of attention and intention, these observations suggest that the pre-PMd plays a major role in attentional or cognitive control of behavior with the prefrontal cortex, whereas the PMd plays a key role in the intentional control of actions or arm movements (Boussaoud and Wise, 1993a,b; di Pellegrino and Wise, 1993; Boussaoud, 2001; Lebedev and Wise, 2001; Rushworth et al., 2005; Abe and Hanakawa, 2009).

INVOLVEMENT OF THE PMd IN PLANNING REACHING MOVEMENTS VIA CONDITIONAL VISUOMOTOR ASSOCIATION

The subjects in the studies discussed above could specify a forthcoming movement after the instruction cue was presented. However, prior studies also revealed that the PMd stores partial information about the direction or amplitude of movement when such information is provided in a stepwise manner (Riehle and Requin, 1989; Kurata, 1993). This phenomenon raises the intriguing possibility that the PMd may be involved in collecting and integrating diverse sets of information via the operation of conditional visuomotor association. In the case of planning a reaching movement, it is necessary to determine for which target to reach and which arm to use to do so. Thus, three hierarchical levels of information processing are presumably involved in the process of planning and executing a reaching movement (**Figure 3**). At the first level, information regarding which arm to use or for which target to reach is selected. At the second level, these two sets of information (the arm to be used and the location of the target) are collected and integrated to specify a reaching movement. This integration process must incorporate distinct types of information; although the arm is part of the participant's body, the target exists outside of his or her body. After the reaching movement is planned, the neural processes at the third level prepare and execute it.

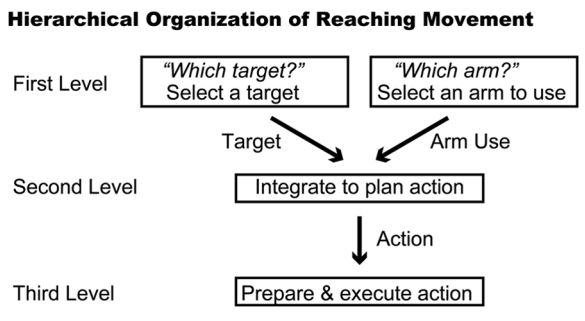

FIGURE 3 | Hierarchical organization of reaching movement. Three levels of information processing are summarized schematically. The first level represents the components of the reaching movement, such as arm use and target location. The second level integrates these components to plan the reaching movement. The third level prepares and executes the planned movement.

A new behavioral task was developed to study the neuronal basis of these processes (Hoshi and Tanji, 2000). This task involves two sequential visual instruction cues separated by a delay (**Figures 4A,B**). One cue signals the location of the target (right or left), and the other cue signals which arm (right or left) to use. These instructions are given in the framework of what is known about conditional visuomotor association in that each compound visual signal is arbitrarily associated with each signal regarding arm use or target location. Therefore, after the first cue, it is necessary to collect and maintain information about the target location (if the first cue signals target location) or arm use (if the first cue signals arm use). After the second cue, monkeys were able to combine the two successive instructions about target location and arm use. Thereafter, the monkeys prepared to reach for the designated target with the designated arm, and they executed the reaching movement once a GO signal appeared (the disappearance of the fixation point). Altogether, the task design allowed us to study the neural mechanisms of the three levels of hierarchical organization underlying the reaching movement. It further allowed us to examine whether PMd neurons retrieve a partial motor instruction given by an arbitrarily associated visual signal.

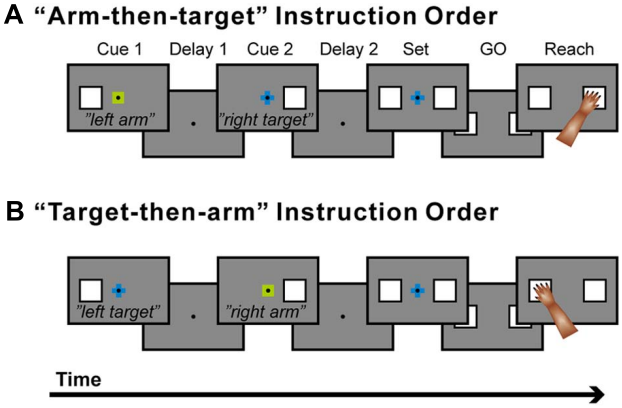

FIGURE 4 | Temporal sequence of behavioral events. (A) The trial in which a signal about arm use ("arm") was followed by a signal about the target to reach for ("target"). **(B)** The trial in which the two signal were given in the reverse order. When a monkey placed one hand on each touch pad and gazed at a fixation point (FP), the first instruction (cue 1; 400 ms in duration), which contained information about either the target location or which arm to use, was presented. A small, colored cue indicated the type of signal (i.e., whether it related to target location or arm use). A green square was used for an arm-use signal, whereas a blue cross was used for a target-location signal. At the same time, a white square appeared to the left or right of the FP and indicated laterality of arm use (for arm-related instructions) or target location (for target-related instructions). After the subsequent delay period (delay 1) that lasted ≥1,200 ms, the second instruction (cue 2: 400 ms) was given to complete the information required for the subsequent action. After the second delay (delay 2: ≥1,200 ms), squares appeared on each side of the fixation point (set cue: ≥1,000 ms), signaling the monkey to prepare to reach for the target when the fixation point disappeared (the GO signal). If the monkey subsequently reached for the appropriate target with the appropriate arm, s/he received a reward. The order of appearance of the target and arm signals was alternated in a block of 20 trials, and laterality was randomized within each block. A series of five 250 Hz tones was presented after a reward signaled a reversal of the order of the instructions.

By recording neurons in the PMd while the monkeys performed the task, three groups of neurons were identified that followed three distinct patterns of activity during the performance of this task (Hoshi and Tanji, 2000, 2006). Two patterns of neuronal activity were observed after the appearance of the first cue. The first group of neurons selectively responded to the appearance of the first cue about which arm to use, and the activity of this group persisted until the second cue was presented. For example, the neuron shown in **Figure 5A** discharged selectively after the appearance of the right-arm (RA) cue. The second group of neurons became active after the appearance of the cue regarding target location. The neuron shown in **Figure 5B** selectively discharged after the right-target (RT) cue was given, and, like those in the first group, its activity persisted until the second cue was presented. These findings revealed that PMd neurons retrieve and store a partial motor instruction, or a building block of action, when this information is embedded in a conditional visuomotor association. These processes correspond to the first level in the hierarchical organization of the reaching movement. When the second cue appeared, the third group of neurons became active. Neurons in this group seemed to represent the specific combination of the two instructions on arm use and target location given by the two cues. For example, the neuron shown in **Figure 5C** responded to the appearance of the second cue only when the combination of the two instructions on arm use and target location signaled the RA and the left target (LT). In other words, the third group of neurons was considered to contribute to the forthcoming reaching movement by integrating the two distinct sets of motor information, on arm use and target location. The existence of the three patterns of activity in the PMd suggests that this area contributes to planning reaching movements by collecting and integrating distinct sets of information on target location and arm use. These processes correspond to the second-level processing in the hierarchical organization and are the cardinal ones involved in action planning. We also found that during the preparation and execution periods of a reaching movement, PMd neurons selectively represented the specific combination of arm and target information (Hoshi and Tanji, 2002), which corresponded to the third level of processing in the hierarchical organization of the reaching movement. Altogether, the variety of activity found in the PMd suggests that this area is involved in all three levels of the processes underlying the generation of reaching movements. In humans, neurovascular activation in subjects performing a task with these demands indicated that the PMd represents the neural processes identified in monkeys (Beurze et al., 2007), revealing that the PMd of both human and non-human primates plays a crucial role in planning reaching movements.

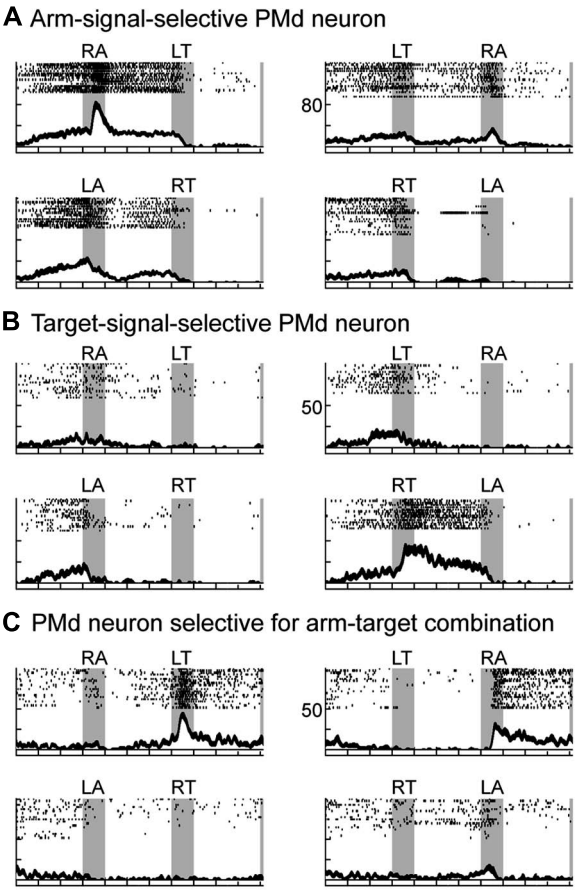

FIGURE 5 | Three types of neuronal activity in the PMd when monkeys planned a forthcoming reaching movement. (A–C) Three examples of PMd neuronal activity presented with raster displays and plots of spike density functions (SDFs). Gray areas (from left to right) represent when the first, second, and set cues were presented. Tick marks on the abscissa are at 400-ms intervals. First and second signals are shown at the top of each panel (RA, right arm; LA, left arm; RT, right target; LT, left target). SDFs (Gaussian kernel, $\sigma = 20$ ms, mean $\pm$ SE) appear below each raster display. Raster plots and SDFs were aligned to the onset of the first and second signal and the onset of the set cue. The ordinate represents the instantaneous firing rate. Of the eight possible sequences of first and second cues (four instructions $\times$ two presentation orders), only four are illustrated. **(A)** Activity of this PMd neuron was greater when cue 1 signaled the use of the right arm (RA). **(B)** Activity of this PMd neuron was greater when cue 1 signaled the right target. **(C)** Activity of this PMd neuron was observed when the combination of the two signals was RA (use of the right arm) and LT (left target). Activity was similar, regardless of the order of the two instructions (adapted from Hoshi and Tanji, 2006).

In the behavioral task described above (Hoshi and Tanji, 2000), an identical instruction was presented with the first and second cues. An aim of this was to assess how each PM neuron responded to the first and second cues. By comparing the selectivity of the response of each neuron to each cue, we found that neurons selective for each instruction given by the first cue were evenly distributed among the three groups of the forthcoming action selectivity (arm use only, target location only, and both arm use and target location; see Figure 13A in Hoshi and Tanji, 2006). This suggests that there are no direct relationships between the selectivity after the first cue and that after the second cue. This indicates that PMd neurons conditionally represent the motor information in a planning-stage-dependent manner. This is consistent with a previous report showing that neuronal selectivity in the dorsomedial frontal cortex, which partly overlaps with the PMd, changed dynamically depending on the task requirements (Mann et al., 1988).

Taken together, the data discussed in this section suggest that the planning process of the PMd in humans and monkeys relies on conditional visuomotor association to retrieve the partial motor

instructions provided by visual signals and integrate them for specific actions (Hoshi and Tanji, 2007).

HOW IS THE PMd INVOLVED IN CONDITIONAL VISUOMOTOR ASSOCIATION?

Although these studies established that the PMd plays a central role in selecting or specifying an action and in representing and integrating the building blocks of action provided by arbitrarily associated visual signals, PMd neurons only rarely represented the visual-object signals themselves (Wallis and Miller, 2003). The absence of object-feature selectivity is consistent with the absence of direct connections with the inferotemporal cortex or the ventrolateral prefrontal cortex (vlPFC; Luppino et al., 2003), where visual features are amply represented (Ungerleider et al., 1982; Wilson et al., 1993; Tanaka, 1996; Orban, 2008). These observations lead to a question: How does the PMd contribute to conditional visuomotor association in the absence of its carrying information about the identity of visual objects?

Kalaska et al. (1998) proposed a theoretical account asserting that visual inputs are used in two different ways. First, the identity of a visual object provided through the ventral "what" visual pathway is used to make decisions about objectives and strategies for action. Second, the spatial visual signals provided through the dorsal "how" visual pathway are used to represent potential motor actions. They further proposed that the action to be executed is chosen through interaction between these two systems. This theoretical account suggests that the PMd may also contribute an abstract representation, such as "objectives and strategies for action," to the process of conditional visuomotor association. Importantly, neurophysiological studies support this hypothesis. Specifically, Cisek and Kalaska (2002, 2005) developed a task in which two potential targets (red and blue) were initially presented, and monkeys chose between them based on the target color. Their findings revealed that PMd neurons initially represent potential reach directions and subsequently represent the direction of the selected reach target. Based on these findings, they proposed that multiple reach options are initially specified and then gradually eliminated in competition for which is to be actually executed. Subsequently, Cisek and Kalaska (2004) showed that PMd neurons carry task-relevant signals when monkeys observe a learned, visuomotor task being performed by others as well as when monkeys perform the task themselves. Bastian et al. (2003) reported that the activity of PMd neurons is modulated by the degree of certainty that the selected object is indeed the correct reach target. Wallis and Miller (2003) found that PMd neurons can represent abstract information that is not directly related to the movement parameters. In that study, monkeys were required to apply a "same" or "different" rule to execute or withhold action in response to two successively presented pictures. They found that neurons in both the PMd and prefrontal cortex represented abstract rules, which are more strongly represented in the PMd than in the prefrontal cortex. In oculomotor behavior, Olson and colleagues revealed that neurons in the supplementary eye field in the pre-PMd represented the relative position of two target objects for saccadic eye movements (Olson and Tremblay, 2000; Tremblay et al., 2002). These crucial observations indicate that PMd neurons reflect abstract representation that is not directly related to the movement in question in advance of the specification of an action.

INVOLVEMENT OF THE PMd IN CONDITIONAL VISUO-GOAL ASSOCIATION

Based on this account, we developed a new behavioral task for monkeys (Nakayama et al., 2008) that includes an abstract representation of behavior; a cue evoking this abstract representation was inserted between a visual object and an action (**Figure 1B**). This design was also based on the notion that a visual signal often indicates an abstract aspect of behavior rather than an actual movement. For instance, a red traffic light instructs us to "stop"; subsequently, we execute an action to "stop" (e.g., squeezing a bicycle brake lever or pressing a car brake pedal). Thus, it can be seen that we first make a decision about a behavioral goal ("stop") based on a sensory signal (a red traffic light) and subsequently choose the appropriate action to achieve the goal. **Figure 6** shows the time sequence of the behavioral task (the symbolic cue task; Nakayama et al., 2008). This task had the following three behavioral phases, which were temporally separated: (1) determining the behavioral goal on the basis of the visual-object cue; (2) specifying or selecting an action based on the information about the behavioral goal and the spatial position of the choice cue; (3) preparing and executing the action. The visual object indicated that either the LT or the RT should be selected later in the task period, but it did not indicate the exact position of the future target. During this phase, the monkeys could determine only the relative position of the reach target (an abstract behavioral goal), but no specific information about the actual reach target was available because the choice cue, consisting of two potential targets, was presented later at various positions on the screen. At this stage, the monkeys could determine, for the first time, where to reach on the screen (an action) by transforming the behavioral goal into an action based on the choice-cue position. After a delay, the color changed from gray to white, which served as the GO signal. In this task, "the relative position of the reach target" corresponds to "the locations that an animal choses as the targets for its actions" (i.e., the goals), but not "the representations specifying which goal is appropriate in a given context" (i.e., the rules; see Introduction for the definitions of goals and rules). Thus, by analyzing the activity of neurons while monkeys performed the task, we were able to examine the information-processing operation from the perception of visual objects to the specification of the action mediated by the abstract behavioral goal.

While monkeys performed this task, we first recorded neurons from the PMd. The activity of PMd neurons initially reflected the behavioral goal, reaching toward the LT or the RT after the choice cue signaled by the visual objects (**Figure 7A**), although it was rarely selective for the visual objects themselves (**Figure 8A**). Subsequently, when a pair of potential targets was presented as the choice cue, information about the spatial position of the choice cue was rapidly combined with information about the behavioral goal (**Figure 8B**), resulting in the development of an action representation (**Figure 7B**), which eventually replaced the behavioral goal representation. Our observations also revealed a subset of PMd neurons that first exhibited activity representing the behavioral goal, which changed into activity representing a mixture of

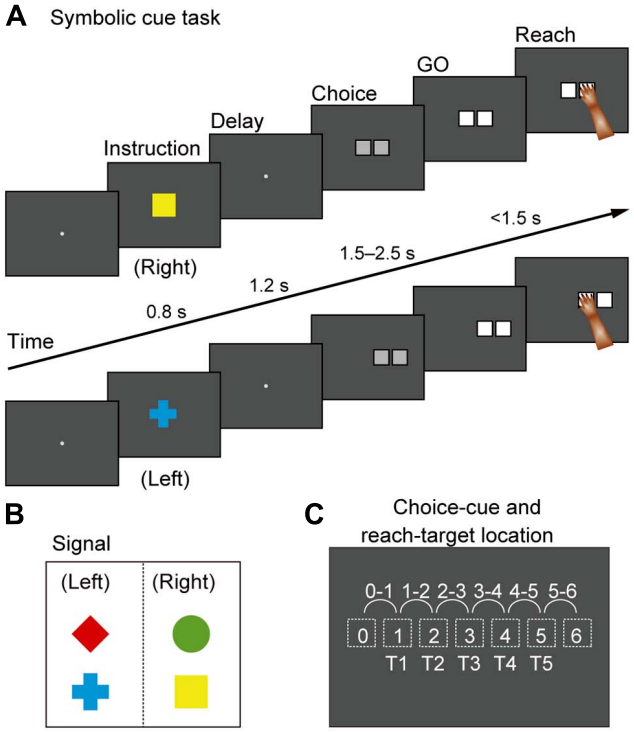

FIGURE 6 | Symbolic cue task. (A) Temporal sequence of behavioral events in the symbolic cue task. If the monkey continued to gaze at the fixation point for 1,200 ms, a cue was randomly presented for 800 ms to signal the animal to select either the right or the left target (i.e., the behavioral goal). A green circle and a yellow square signaled selection of the target on the right, whereas a red diamond and a blue cross indicated that the left target should be selected **(B)**. Because no information about future targets was available at this stage, the monkeys were required to select right or left without specifying a forthcoming action. If the monkey continued to gaze at the fixation point for 1,200 ms during the subsequent delay, a choice cue consisting of two gray squares appeared at one of six different locations on the screen **(C)**. At this point, the animal could specify what to do (i.e., action) for the first time. After 1,500–2,500 ms, the color changed from gray to white (the GO signal). If monkeys reached for the target with their right arm, they received a fruit juice reward 500 ms after touching the correct square. **(B)** Visual signals used to designate selection of left or right in the forthcoming choice cue. **(C)** Locations of the choice cue and target on the screen. For the choice cue, two gray squares appeared at neighboring positions (locations 0–6, depicted with dotted squares). The target position was selected from five potential targets (T1–T5) that were located on the left or the right of the choice cue.

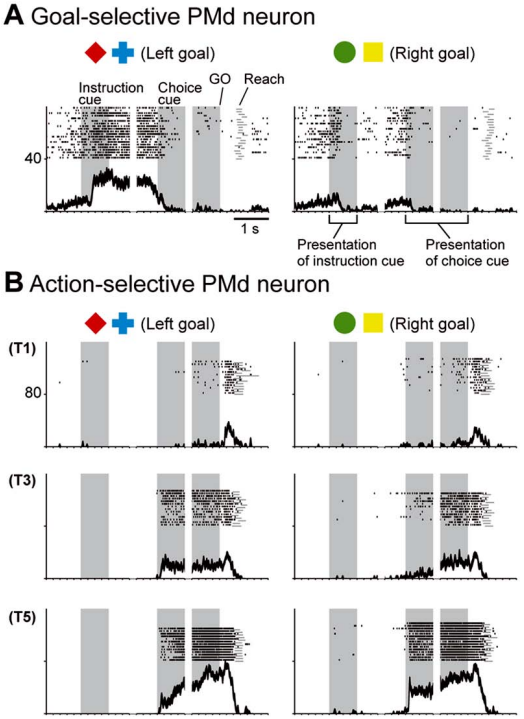

FIGURE 7 | Two examples of neurons in the PMd. (A) Goal-related activity of a PMd neuron. Activity of this PMd neuron increased when either a red diamond or a blue cross was used to specify the left target. **(B)** Action-related activity of a PMd neuron. After choice-cue onset, this PMd neuron exhibited more activity when the correct target was located on the right side of the screen (T5), regardless of the goal. Of the five positions (T1–T5), only three (T1, T3, and T5) are displayed here. **(A,B)** Rasters and spike-density functions (smoothed using a Gaussian kernel; $\sigma = 10$ ms, mean $\pm$ SEM) indicate activity in sorted trials. The ordinate represents the instantaneous firing rate (spikes/s). Neuronal activity was aligned with the onset of the instruction, choice-cue, and GO signals. Gray areas on the left indicate when the instruction was presented, and gray areas in the middle and on the right represent when the choice cue was presented. Tick marks on the horizontal axis are placed at 200-ms intervals (adapted from Nakayama et al., 2008).

the behavioral goal and the choice-cue location after the appearance of the choice cue, suggesting that these neurons directly contributed to the transition between the goal-related and the action-related use of the information. These results suggest that the PMd hosts a neural network involved in integrating the behavioral goals retrieved from visual-object signals with the locations of choice cues to specify forthcoming actions.

As discussed above, prior studies have indicated that the PMd employs abstract representations as a part of an information-processing operation involving partial motor instructions, the rule for linking visual-signal processing to action, the potential reach direction, others' performance of a learned visuomotor task, and the certainty with which a target is selected. Our study revealed that the PMd represents abstract behavioral goals derived from arbitrarily associated visual signals that specify later action. These results provide compelling evidence that the PMd is involved not only in the preparation and execution of action but also in the representation of the abstract information needed to specify an action. In general, the PMd is involved not only in visuomotor association but also in conditional visuo-goal association, which includes an abstract representation of a behavioral goal as a core element. Consistent with this, Hanakawa et al. (2002) showed that the PMd in humans is active during mental-operation tasks, such as mental calculation, that do not involve any immediate overt movement. Based on this finding, they proposed that the PMd plays a major role in motor behavior requiring cognitive manipulation of abstract representations. The goal neurons found by Nakayama et al. (2008) were considered to play an important role in this process; the goal is the abstract representation that does not directly relate to action execution, but goal representation is crucial for specifying the action.

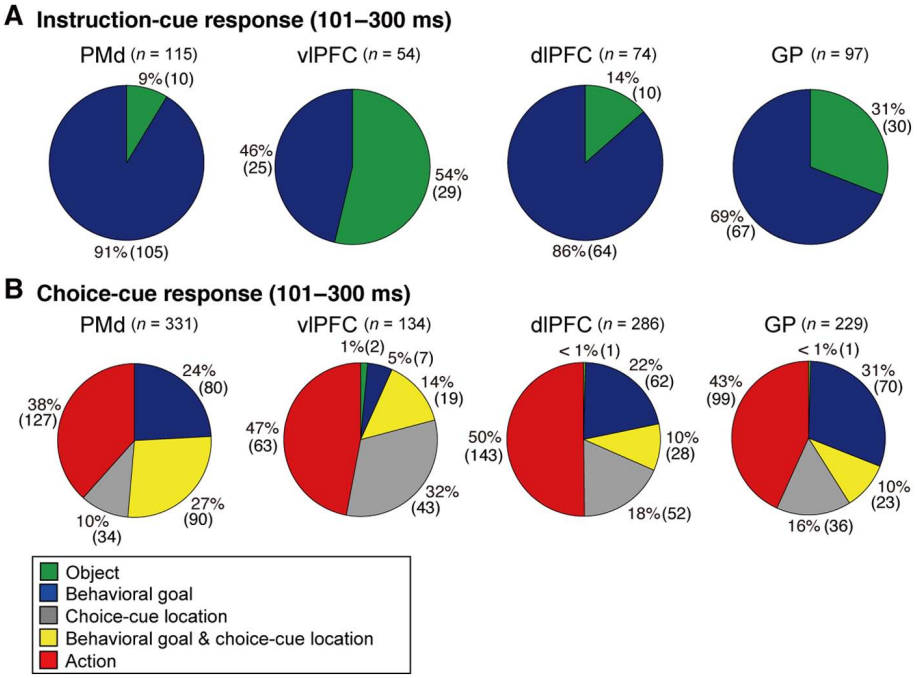

FIGURE 8 | Distribution of selective neurons in the PMd, vlPFC, dlPFC, and GP. Pie charts summarize the proportion of neurons classified into five categories. Two sets of data are shown for 101–300 ms after the onset of instruction cue **(A)** and 101–300 ms after the onset of the choice cue **(B)**. Each category is color coded according to the inset. The parentheses enclose the number of neurons. Green, object neurons; Blue, goal neurons; Gray, neurons selective for choice-cue location; Yellow, neurons selective for both goal and choice-cue location; Red, action neurons (adapted from Arimura et al., 2013).

SOURCES OF PMd INFORMATION ABOUT ABSTRACT GOALS

Nakayama et al. (2008) reported that the PMd retrieves the abstract information derived from a visual-object signal even though it rarely represents that information. This paradox raises an intriguing question: From which areas does the PMd receive such abstract information? To gain insight into this issue, the temporal development of the selection of the behavioral goal was compared with the development of visuospatial selectivity (Yamagata et al., 2009). PMd neurons represented the initial visuospatial signals 90 ms after the presentation of visual stimuli. The rapidity of this process suggests that the PMd receives this signal from the directly interconnected posterior parietal cortex, where visuospatial signals are amply represented (**Figure 2**; Johnson et al., 1993; Galletti et al., 1997; Snyder et al., 1997; Wise et al., 1997; Matelli et al., 1998; Colby and Goldberg, 1999; Pesaran et al., 2008). By contrast, the development of the goal representation was found to take much more time; PMd neurons began to represent the goals 150 ms after the visual object was presented. This 60-ms delay indicates that goal signals reach the PMd via distinct pathways. Based on the following findings, we hypothesized that the basal ganglia (BG) and/or lateral prefrontal cortex mediate these pathways.

The BG and lateral prefrontal cortex play crucial roles in associating visual signals with actions in a goal-oriented and adaptive manner (Graybiel et al., 1994; Wise et al., 1996; Konishi et al., 1998; Rainer et al., 1998; Kim and Shadlen, 1999; Hollerman et al., 2000; Everling et al., 2002; Nieder et al., 2002; Packard and Knowlton, 2002; Takeda and Funahashi, 2002; Barraclough et al., 2004; Genovesio et al., 2005; Saito et al., 2005; Sakagami and Pan, 2007; Sakai, 2008; Buckley et al., 2009; Hussar and Pasternak, 2009; Yoshida and Tanaka, 2009; Cisek and Kalaska, 2010; Goodwin et al., 2012; Meyers et al., 2012; Swaminathan and Freedman, 2012). Substantial structural interactions between the BG and the frontal cortex are considered to provide the structural basis for this process (Alexander et al., 1986; Flaherty and Graybiel, 1994; Inase and Tanji, 1994; Middleton and Strick, 2000; Nambu et al., 2002; Graybiel, 2008). Neurovascular activation in humans performing conditional visuomotor association was observed in the vlPFC and the BG as well as in the PMd (Toni et al., 2001, 2002). Because the BG and vlPFC receive inputs from the inferotemporal cortex, where visual-object signals are amply represented (Saint-Cyr et al., 1990; Webster et al., 1993, 1994; Middleton and Strick, 1994; Schall et al., 1995; Cheng et al., 1997; Petrides and Pandya, 2002), these projections are thought to provide visual-object signals to these areas. Lesion studies of monkeys have revealed that impairments in conditional visuomotor association arise from disruptions in the vlPFC (Wang et al., 2000; Bussey et al., 2001), the interconnection between the vlPFC and the inferotemporal cortex (Eacott and Gaffan, 1992; Bussey et al., 2002), and the interaction between the BG and the PMd (Nixon et al., 2004). From a functional perspective, vlPFC neurons have been shown to integrate the two sets of information about object features and the selected directions of saccades (Asaad et al., 1998). Furthermore, association learning in the BG (the striatum) has been shown to precede that in the lateral PFC (Pasupathy and Miller, 2005). Modulation of the activity of neurons in the globus pallidus (GP)

is enhanced when the stimulus–response association is familiar (Inase et al., 2001). Similarly, the activity of neurons in the striatum is enhanced during learning of visuomotor associations (Hadj-Bouziane and Boussaoud, 2003). Moreover, the learning of associations between visual objects and movements has been shown to progress simultaneously in striatal and PMd neurons (Brasted and Wise, 2004). These observations suggest that the BG and vlPFC are crucially involved in conditional visuomotor association and that the interaction between the PMd and these areas is essential to the successful operation of this process.

However, because the PMd does not receive direct inputs from either area (Barbas and Pandya, 1987; Webster et al., 1994; Luppino et al., 2003), this anatomical connection remains to be proven. To address this issue, the rabies virus was transneuronally traced in macaque monkeys to provide evidence for communication across synapses between the PMd and the vlPFC and BG (Takahara et al., 2012). The rabies virus is transported across synapses from the postsynaptic to presynaptic neurons in a time-dependent manner. This feature allowed the identification of the areas that project across synapses to the PMd after injection of the rabies virus into the PMd.

Initially, the corticocortical pathways from the vlPFC to the PMd were analyzed. Fast Blue (a conventional retrograde tracer) was injected into the PMd to identify the cortical areas that send projection fibers directly to the PMd. Considerable retrograde labeling occurred in the dlPFC, area F7 (pre-PMd), pre-supplementary motor area (pre-SMA), and PMv (Barbas and Pandya, 1987; Lu et al., 1994; Luppino et al., 2003), whereas the vlPFC was virtually devoid of neuronal labeling. Subsequently, the rabies virus was injected into the PMd. Three days after the rabies injections, second-order neurons were newly labeled in the vlPFC, providing evidence that the vlPFC sends disynaptic projections to the PMd. To identify the areas that mediate the pathways from the vlPFC to the PMd, an anterograde/retrograde dual-labeling experiment was conducted in individual monkeys. By examining the distribution of axon terminals labeled from the vlPFC and cell bodies labeled from the PMd, substantial overlap was found in the dlPFC (area 46d), area F7 (pre-PMd), and pre-SMA (**Figure 9**). These results indicate that vlPFC outflow is directed toward the PMd in a multisynaptic fashion through these areas (**Figure 2**).

Subsequently, the multisynaptic projections from the BG to the PMd were analyzed (Saga et al., 2011) after the injection of the

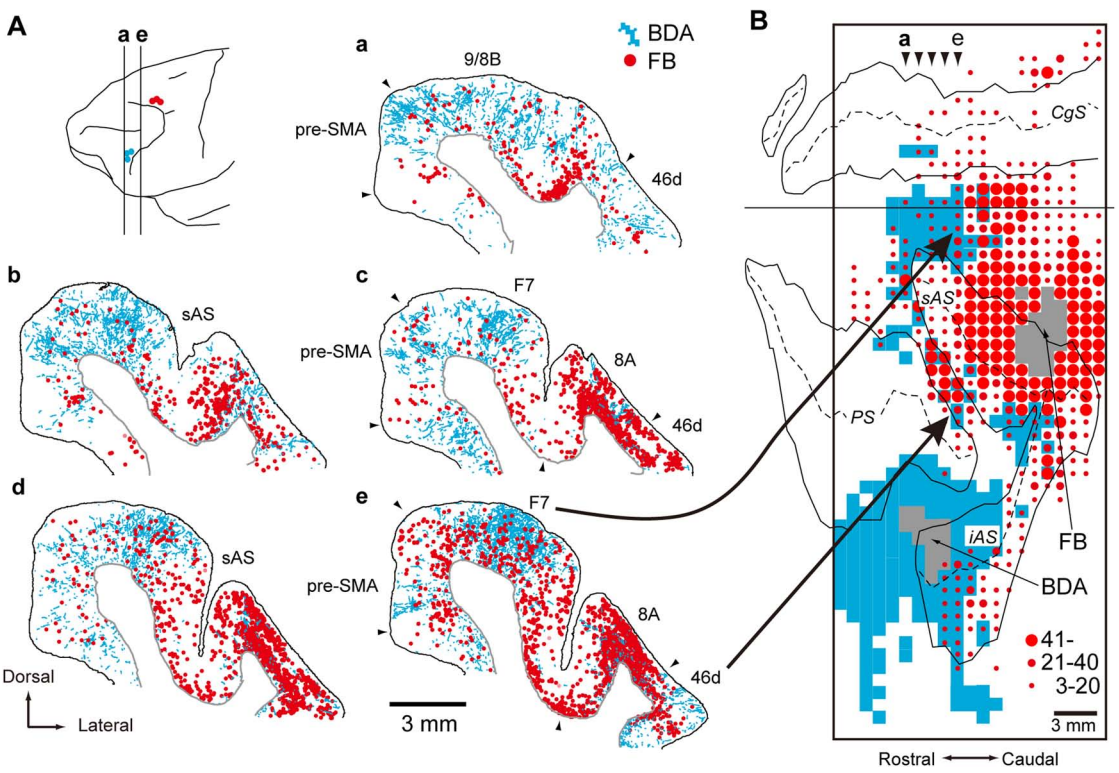

FIGURE 9 | Overlaps of axon terminals arising from the vlPFC and cell bodies projecting to the PMd in the frontal cortex. (A) Five representative coronal sections are arranged rostrocaudally. The approximate rostrocaudal levels of the sections (a–e) are indicated in the lateral view of the brain (with the sites of BDA and FB injections specified by blue and red circles, respectively). Labels in blue represent axon terminals labeled with BDA injected into vlPFC (area 45), and labels in red represent cell bodies labeled with FB injected into PMd. **(B)** A two-dimensional density map showing the distribution patterns of axon terminals labeled with BDA and cell bodies labeled with FB. The bins (900 × 1,000 μm) where the BDA-labeled axon terminals were observed appear in blue. The box encloses the area where BDA terminals were investigated. The gray zone denotes the extent of the FB or BDA injection sites. Three different sizes of filled circles represent the numbers of neurons labeled with FB. Arrowheads (a–e) point to the approximate rostrocaudal levels of coronal sections (a–e) shown in **(A)**. BDA, biotinylated dextran amine; FB, Fast Blue. AS, arcuate sulcus; CgS, cingulate sulcus; F7, area F7 (Luppino et al., 2003); iAS, inferior limb of AS; PS, principal sulcus; sAS, superior limb of AS (adapted from Takahara et al., 2012).

rabies virus into the PMd. Specifically, second-order neurons were identified in the internal segment of the globus pallidus (GPi) and the substantia nigra pars reticulata (SNr). Labeled GPi neurons were found in the dorsal portion at the rostrocaudal middle level and in the caudoventral portion. In the SNr, labeled neurons were widespread in the rostrocaudal direction. Subsequently, third-order neuron labeling was observed in the external segment of the globus pallidus (GPe), the subthalamic nucleus (STN), and the striatum. In the GPe, the labeled neurons were observed over a broad territory centered in the rostral and dorsal portions. In the STN, PMd injection resulted in extensive labeling over the nucleus, especially in the dorsoventral middle and dorsal portions. In the striatum, labeled neurons were widespread in the striatal cell bridge region and neighboring areas, as well as in the ventral striatum. These results provide evidence that the PMd receives substantial inputs across synapses from the BG. Taken together with prior studies revealing the projections from the PMd to the striatum and the STN (Nambu et al., 1997; Takada et al., 1998; Tachibana et al., 2004), it appears that the PMd and BG form loop circuits that subserve multiple aspects of information processing (Alexander et al., 1986; Alexander and Crutcher, 1990a).

These anatomical studies revealed that the PMd receives inputs across synapses from the vlPFC and the BG (**Figure 2**), raising the intriguing possibility that the circuits linking the PMd to the vlPFC and/or the BG may be involved in retrieving the abstract goals from the visual-object signals. To test this hypothesis, the response properties of neurons in the lateral PFC and the BG were compared with those of neurons in the PMd.

INVOLVEMENT OF THE PREFRONTAL CORTEX IN CONDITIONAL VISUO-GOAL ASSOCIATION

These anatomical studies suggest that the PMd receives inputs from the vlPFC partly via the dlPFC, which has been implicated in behavioral planning (Luria, 1966; Shallice, 1982; Funahashi et al., 1989, 1993; Frith et al., 1991; Goel and Grafman, 1995; Rowe et al., 2000; Averbeck et al., 2002, 2003; Hoshi and Tanji, 2004a; Mushiake et al., 2006; Mansouri et al., 2007). Based on these observations, the neuronal activity in the vlPFC and dlPFC was examined while monkeys performed the symbolic cue task involving conditional visuo-goal association (Yamagata et al., 2012).

When the instruction cue was presented, a sizeable number of vlPFC neurons exhibited responses that were selective for visual-object features (**Figure 8A**). For example, the neuron shown in **Figure 10A** strongly responded to the appearance of a yellow square. This object representation is consistent with anatomical reports that the vlPFC receives input from the inferotemporal cortex and with prior studies reporting ample object representations by vlPFC neurons (Wilson et al., 1993; O Scalaidhe et al., 1997, 1999). The existence of object-selective activity suggests that vlPFC neurons participate substantially in encoding visual-object features for subsequent use. We found that the object-feature selectivity in the vlPFC was rapidly replaced with activity that was selective for behavioral goals. In contrast, dlPFC neurons rarely represented visual-object features; instead, they began to represent goals after the instruction cue was presented (**Figure 8A**). For example, the dlPFC neuron shown in **Figure 10B** selectively responded to the appearance of a red diamond and a blue cross

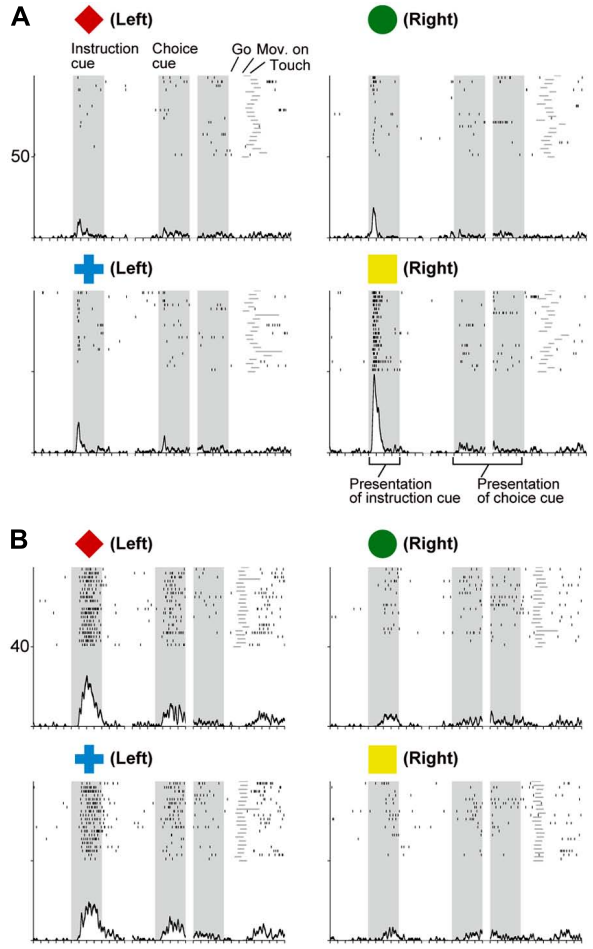

FIGURE 10 | Two examples of neurons in the prefrontal cortex selective for visual objects (A) and behavioral goals (B). (A) Activity of this vlPFC neuron increased when the yellow square was presented. **(B)** Activity of this dlPFC neuron increased when the instruction was presented and either a red diamond or a blue cross was used to specify the left target. The display formats are the same as those used in **Figure 7** (adapted from Yamagata et al., 2012).

signaling the LT. The limited representation of the visual-object signals in the dlPFC is in accord with the paucity of anatomical connectivity between the dlPFC and the inferotemporal cortex (Petrides and Pandya, 1999). These observations indicate that both the vlPFC and dlPFC are involved in retrieving the goals signaled by visual objects. However, the two areas are involved in different ways: the visual-object feature was represented in the vlPFC when the neural representations of the goal developed, whereas the goal representation in the dlPFC developed independently of any encoding of object features. From a perspective of a categorization, Freedman et al. (2001) revealed that lateral PFC neurons categorize visual stimuli as "cats" and "dogs," whereas the observations made by Nakayama et al. (2008) and Yamagata et al. (2012) suggest that lateral PFC and PMd neurons categorize visual stimuli as associated with right and left behavioral goals.

To better understand the flow of information across the vlPFC, dlPFC, and PMd, the timing of the emergence of selectivity was

compared with a measure of population selectivity (Yamagata et al., 2012). In the vlPFC, object selectivity began 130 ms after onset of the instruction cue, whereas goal selectivity began 150 ms after that point, indicating that goal selectivity developed in the vlPFC while object information was represented. In the dlPFC, goal selectivity developed 170 ms after the instruction-cue onset. Based on these findings, we propose the following hypothesis regarding the involvement of the vlPFC and dlPFC in conditional visuo-goal association: Neurons in the vlPFC retrieve goal signals (150 ms after instruction-cue onset) from the visual-object signals that are already represented there (130 ms). Then, the retrieved signals are transferred via cortico-cortical connections to the dlPFC, where they trigger the goal representation (170 ms). If the development of the goal representation in the PMd were later than that in the dlPFC, we could propose the operation of a cortico-cortical pathway from the vlPFC to the PMd via the dlPFC. However, goal representation developed in the PMd 150 ms after the onset of the instruction cue, which was comparable to the timing in the vlPFC (150 ms) and earlier than that in the dlPFC (170 ms). Furthermore, the selectivity developed significantly earlier in the PMd than in the dlPFC for individual neurons representing the behavioral goals (**Figure 11B**, Kolmogorov–Smirnov test, $p = 0.0293$). These observations reveal that goal representation develops almost simultaneously in the PMd and vlPFC, which are indirectly interconnected, whereas goal development in the dlPFC, which is thought to mediate the pathway between these areas, tends to follow that in the PMd and vlPFC. These data did not support the view that the goal signals generated in the vlPFC travel cortico-cortically to the PMd via the dlPFC. Wallis and Miller (2003) showed this kind of non-hierarchal representation between the PFC and the PMd in the representation of an abstract, matching-to-sample, or a non-matching-to-sample rule related to initiating action and revealed that PMd neurons begin to encode the rule information earlier than PFC neurons do.

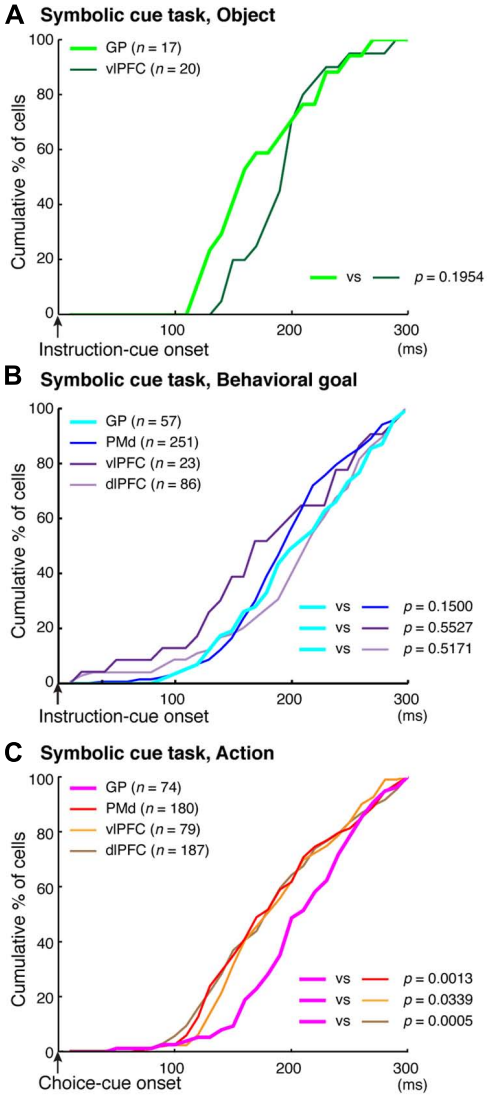

FIGURE 11 | Comparison of the development of selectivity for visual objects, behavioral goals, and actions. (A) Cumulative fractions of selectivity onset for visual objects in the GP (light green) and vlPFC (dark green) after instruction-cue onset in the symbolic cue task. **(B)** Cumulative fractions of selectivity onset for the behavioral goal in the GP (light blue), PMd (dark blue), vlPFC (dark purple), and dlPFC (light purple) after instruction-cue presentation in the symbolic cue task. **(C)** Cumulative fractions of the onset of action selectivity in the GP (pink), PMd (red), vlPFC (orange), and dlPFC (brown) after choice-cue onset in the symbolic cue task. **(A–C)** The *p*-values indicate the results of the statistical analysis (Kolmogorov–Smirnov test) between the GP and the other three areas (adapted from Arimura et al., 2013).

INVOLVEMENT OF THE CORTICO-BG CIRCUITS IN CONDITIONAL VISUO-GOAL ASSOCIATION

In the context of this evidence against the hierarchical organization of goal development, the areas from which the PMd receives goal signals remain unidentified. To address this issue, we examined neurons in the BG while monkeys performed the symbolic cue task. We recorded neurons in the GP of the BG while monkeys performed the task (Arimura et al., 2013). GP neurons were considered to carry signals within the BG at the output stage (the internal segment, GPi) and at the intermediate stage (the external segment, GPe) of a series of information-processing steps. Thus, comparing the neuronal response properties in the GP with those in the PMd and lateral PFC would lead to a better understanding of the involvement of cortico-BG circuits in conditional visuo-goal association. When the instruction cue appeared, a subset of GP neurons started to reflect visual features (**Figure 12A**), and selectivity developed as early as it did in vlPFC neurons (**Figure 11A**). This prompt representation of visual objects by BG neurons is consistent with previous reports (Caan et al., 1984; Brown et al., 1995; Yamamoto et al., 2012, 2013; Yasuda et al., 2012). Subsequently, GP neurons began to reflect goals that were informed by the visual signals (**Figure 12B**), and the timing of selectivity development was no later than it was in the PMd, vlPFC, and dlPFC (**Figure 11B**). These observations indicate that the GP is involved in the early determination of behavioral goals, suggesting that the GP may emit a signal to inform wide cortical areas that a certain object or goal has appeared, serving to trigger subsequent information processing in these

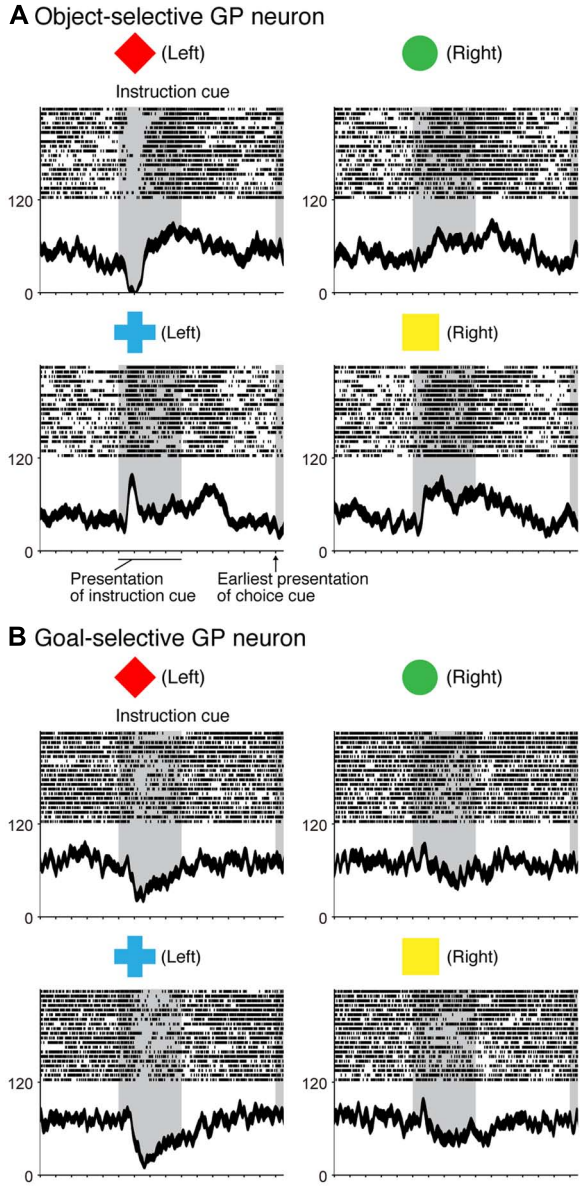

FIGURE 12 | Two examples of neurons in the GP selective for a visual object and a behavioral goal in the symbolic cue task. (A) Activity of this GP neuron decreased when a red diamond was presented as an instruction cue, whereas it increased when a blue cross was presented as an instruction cue. **(B)** Activity of this GP neuron decreased when either a red diamond or a blue cross was presented. Neuronal activity was aligned with the onset of the instruction cue. The gray areas on the left indicate when the instruction was presented, and the gray areas on the right represent the earliest presentation of the choice cue. The tick marks on the horizontal axis are placed at 200-ms intervals. The display formats are the same as those used in **Figure 7** (adapted from Arimura et al., 2013).

areas. The representation of an abstract aspect of motor behavior is consistent with prior reports showing that neurons in the putamen and GP represent a target position or a movement direction as the intended movement direction (Mitchell et al., 1987; Alexander and Crutcher, 1990b,c). Clinical studies have reported that BG dysfunction results in deficits in cognitive processes (Mendez et al., 1989; Dubois and Pillon, 1997; Crucian and Okun, 2003; Uc et al., 2005). The loss of neurons representing abstract aspects of behavior may underlie these deficits.

INVOLVEMENT OF CORTICO-BG CIRCUITS IN SELECTION OF ACTION BASED ON A GOAL

Monkeys participating in the symbolic cue task could specify or select the forthcoming action (the absolute position of a target on the screen) after the appearance of the choice cue. We found that neuronal activity selective for actions developed in the GP as well as in the PMd, dlPFC, and vlPFC. In contrast to the timing of the development of goal selectivity, the timing of the development of action selectivity in the GP differed from that in cortical areas; action representation in the GP emerged 30 ms later than it did in the cortical areas (**Figure 11C**). Furthermore, neurons that integrated representations of goals with choice-cue locations, which are considered to play a crucial role in the transformation from goal to action, were less numerous in the GP than in the PMd (**Figure 8B**). Muhammad et al. (2006) reported that behavioral responses in a visuomotor task employing the GO/NO-GO paradigm tended to begin earlier in the PMd than in the striatum. Antzoulatos and Miller (2011) showed that the lateral PFC plays a major role in the abstract categorization of visual signals for executing saccadic eye movements. Seo et al. (2012) revealed that representation of a selected action occurred earlier in the lateral PFC than in the dorsal striatum. Taken together, these data suggest that an action command determination based on visual signals is initially specified in cortical areas such as the PMd and lateral PFC, and this is followed by representation in the GP. This suggests that the BG do not play a major role in the process by which a behavioral goal is transformed into an action or in specifying an action based on a goal. Rather, the BG may be involved in registering an established action, based on which, competing motor programs are suppressed (Mink, 1996) or subsequent processes for action preparation and execution are initiated.

NEURAL COMPUTATIONS OF CORTICO-BG CIRCUITS

In a series of studies on conditional visuo-goal association (Nakayama et al., 2008; Yamagata et al., 2009, 2012; Arimura et al., 2013), neurons from both the cortical areas (the PMd, vlPFC, and dlPFC) and the BG (GP) were recorded. This provided an opportunity to analyze activity with the aim of gaining insights into the neural computations of cortico-BG circuits. According to Marsden (1982), "the BG might focus attention on a single event in the environment to the exclusion of all others" (p. 512). Additionally, Houk and Wise (1995) proposed that the BG may play a role in contextual pattern recognition. According to this theory, GP neurons transiently decrease or increase activity, giving rise to sustained activity enhancement (context registration) or suppression (context negation) in the thalamus and cerebral cortex. Graybiel (2008) revealed that the BG are involved in representing behavioral boundaries. Consistent with these, we observed that goal and action representations by each GP neuron were transient in nature and much briefer than were those in the PMd and dlPFC (**Figure 13**). In contrast, the duration of goal selectivity of vlPFC neurons was comparable to that of GP neurons, supporting the hypothesis that vlPFC

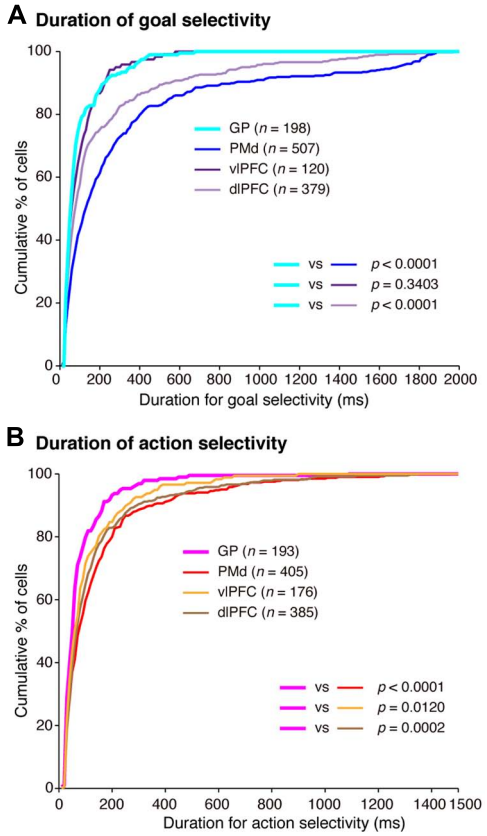

FIGURE 13 | Temporal profiles of neuronal selectivity for behavioral goals and actions in the symbolic cue task. (A) Cumulative fractions of the duration of goal selectivity in the GP (light blue), PMd (dark blue), vlPFC (dark purple), and dlPFC (light purple) after instruction cue-onset in the symbolic cue task. **(B)** Cumulative fractions of the duration of action selectivity in the GP (pink), PMd (red), vlPFC (orange), and dlPFC (brown) after choice-cue presentation in the symbolic cue task. In **(A)** and **(B)**, the parentheses enclose the number of neurons with an onset of selectivity ≤2,000 ms after instruction-cue onset (for goal selectivity, **A**) and ≤1,500 ms after choice-cue onset (for action selectivity, **B**). The *p*-values indicate the results of the statistical analysis (Kolmogorov–Smirnov test) examining differences between neurons in the GP and the three cortical areas (adapted from Arimura et al., 2013).

is not essential for maintaining working memory (Rushworth et al., 1997). Although the duration of the goal and action representations of GP neurons was shorter, the magnitude of the selective responses representing the goal and action were considerable: the mean activity modulation of GP neurons amounted to 16–47 spikes/s. The potency of neuronal responses was further characterized by the promptness of activity modulation, which was revealed by population selectivity, as selectivity peaked shortly (<400 ms) after the onset of the instruction and choice cues. Overall, the GP codes information via highly active neurons with short-lasting selectivity. This type of information coding is known as sparse coding and is thought to constitute a critical mechanism underpinning sensory (Olshausen and Field, 2004) and motor processing (Hahnloser et al., 2002). Taken together, our data suggest that the BG may employ sparse coding in the determination of behavioral goals and the specification of actions, whereas the PMd and dlPFC neurons are involved in maintaining the determined goals and specified actions with sustained responses, as well as in goal determination and action specification.

FUTURE DIRECTIONS

The data and hypotheses discussed in the present study should be expanded in several directions to gain deeper insights into the neural mechanisms underlying conditional visuo-goal association. First, although we focused on the lateral frontal cortex, other cortical areas may also play a role, including the orbitofrontal cortex, the anterior cingulate cortex, the frontal polar cortex, the pre-SMA and the posterior parietal cortex (Matsuzaka et al., 1992; Matsuzaka and Tanji, 1996; Sakai et al., 1999; Hernández et al., 2002; Hoshi and Tanji, 2004b; Stoet and Snyder, 2004; Diedrichsen et al., 2006; Freedman and Assad, 2006; Kamigaki et al., 2009; Tsujimoto et al., 2009, 2010, 2011; Amiez et al., 2012; Luk and Wallis, 2013). Because these areas are interconnected with the networks involving the PMd, lateral PFC, and BG (Selemon and Goldman-Rakic, 1985; Barbas and Pandya, 1989; Luppino et al., 1993; Matelli et al., 1998; Petrides and Pandya, 1999, 2002; Ongur and Price, 2000; Haber et al., 2006; Rozzi et al., 2006; Morecraft et al., 2012; Haynes and Haber, 2013), it is suggested that a large-scale network underlies the goal-directed behavior mediated by conditional visuo-goal association. Second, we here focused on neural representations when the animals were familiar with the association between the visual stimuli and goals. However, it is also necessary to examine the mechanisms at different stages of association or rule learning because each area/network can play a specific role depending on these parameters (Schultz et al., 1997; Hikosaka et al., 1999; Doya, 2000; Samejima et al., 2005; Lee et al., 2012). For example, Amiez et al. (2012) showed in humans that as the learning of conditional visuomotor associations progresses, the areas active in relation to motor selection move from the cognitive networks involving the dlPFC, the caudate nucleus, and the PMd to the motor networks, including the putamen and the PMd. They also showed that that the orbitofrontal cortex and anterior cingulate cortex are active in relation to the evaluation of the consequences of a selected action. Consistent with this, neurons in the orbitofrontal cortex can represent response choices when feedback is provided (Tsujimoto et al., 2009, 2011), and neurons in the anterior cingulate cortex can interactively represent actions and rewards (Matsumoto et al., 2003). Third, we discussed the representation of goals in the spatial domain (spatial-specific goals; i.e., right vs. left). In future studies, goal representations in other domains should be examined. For example, neurons in the prefrontal cortex and the GP can encode object-specific goals, such as shape or color (Hoshi et al., 1998; Genovesio et al., 2012; Saga et al., 2013). Neural mechanisms for making associations between visual objects were identified in the prefrontal cortex (Hasegawa et al., 1998; Rainer et al., 1999) and the inferotemporal cortex (Sakai and Miyashita, 1991; Naya et al., 2001; Hirabayashi et al., 2013a,b). However, it remains unclear whether the same brain areas responsible for motor behavior based on spatial-specific goals support motor behavior based on object-specific goals.

SUMMARY AND CONCLUSION

Previous studies based on a framework derived from conditional visuomotor association (**Figure 1A**) revealed neural mechanisms underlying the specification and planning of actions based on sensory signals. However, applications resting solely on this conceptualization encounter problems related to generalization and flexibility, which are essential processes in executive function. To overcome this problem, we extended this conceptualization and postulated a more general framework, conditional visuo-goal association (**Figure 1B**), in which the visual signal identifies an abstract behavioral goal, and an action is subsequently selected and executed to meet this goal. Neuronal activity recorded from the brain areas of monkeys performing a task involving conditional visuo-goal association revealed that they regulate the task in an area-dependent manner. By comparing the response properties of neurons in the GP, PMd, dlPFC, and vlPFC of monkeys engaging in goal-directed behavior mediated by conditional visuo-goal association, we revealed that these areas are commonly involved in the initial stages of goal determination based on visual signals. Neurons representing an abstract behavioral goal are considered to provide a foundation for executive function. In contrast, we found that GP activity follows the leading activity in the PMd, dlPFC, and vlPFC in specifying an action based on an abstract behavioral goal. Taken together with the finding that a shorter length of time represented goal and action by neurons in the GP compared with neurons in the PMd and dlPFC, these data suggest a unique involvement of the BG and the frontal cortical areas in goal-directed behavior. Increased understanding of the neural mechanisms underlying conditional visuo-goal association will yield deeper insights into the fundamental principles underpinning goal-directed behavior.

ACKNOWLEDGMENT

This work was supported by CREST, JST.

REFERENCES

Abe, M., and Hanakawa, T. (2009). Functional coupling underlying motor and cognitive functions of the dorsal premotor cortex. *Behav. Brain Res.* 198, 13–23. doi: 10.1016/j.bbr.2008.10.046

Alexander, G. E., and Crutcher, M. D. (1990a). Functional architecture of basal ganglia circuits: neural substrates of parallel processing. *Trends Neurosci.* 13, 266–271. doi: 10.1016/0166-2236(90)90107-L

Alexander, G. E., and Crutcher, M. D. (1990b). Neural representations of the target (goal) of visually guided arm movements in three motor areas of the monkey. *J. Neurophysiol.* 64, 164–178.

Alexander, G. E., and Crutcher, M. D. (1990c). Preparation for movement: neural representations of intended direction in three motor areas of the monkey. *J. Neurophysiol.* 64, 133–150.

Alexander, G. E., Delong, M. R., and Strick, P. L. (1986). Parallel organization of functionally segregated circuits linking basal ganglia and cortex. *Annu. Rev. Neurosci.* 9, 357–381. doi: 10.1146/annurev.ne.09.030186.002041

Amiez, C., Hadj-Bouziane, F., and Petrides, M. (2012). Response selection versus feedback analysis in conditional visuo-motor learning. *Neuroimage* 59, 3723–3735. doi: 10.1016/j.neuroimage.2011.10.058

Amiez, C., Kostopoulos, P., Champod, A. S., and Petrides, M. (2006). Local morphology predicts functional organization of the dorsal premotor region in the human brain. *J. Neurosci.* 26, 2724–2731. doi: 10.1523/JNEUROSCI.4739-05.2006

Antzoulatos, E. G., and Miller, E. K. (2011). Differences between neural activity in prefrontal cortex and striatum during learning of novel abstract categories. *Neuron* 71, 243–249. doi: 10.1016/j.neuron.2011.05.040

Arimura, N., Nakayama, Y., Yamagata, T., Tanji, J., and Hoshi, E. (2013). Involvement of the globus pallidus in behavioral goal determination and action specification. *J. Neurosci.* 33, 13639–13653. doi: 10.1523/JNEUROSCI.1620-13.2013

Asaad, W. F., Rainer, G., and Miller, E. K. (1998). Neural activity in the primate prefrontal cortex during associative learning. *Neuron* 21, 1399–1407. doi: 10.1016/S0896-6273(00)80658-3

Averbeck, B. B., Chafee, M. V., Crowe, D. A., and Georgopoulos, A. P. (2002). Parallel processing of serial movements in prefrontal cortex. *Proc. Natl. Acad. Sci. U.S.A.* 99, 13172–13177. doi: 10.1073/pnas.162485599

Averbeck, B. B., Chafee, M. V., Crowe, D. A., and Georgopoulos, A. P. (2003). Neural activity in prefrontal cortex during copying geometrical shapes. I. Single cells encode shape, sequence, and metric parameters. *Exp. Brain Res.* 150, 127–141.

Barbas, H., and Pandya, D. N. (1987). Architecture and frontal cortical connections of the premotor cortex (area 6) in the rhesus monkey. *J. Comp. Neurol.* 256, 211–228. doi: 10.1002/cne.902560203

Barbas, H., and Pandya, D. N. (1989). Architecture and intrinsic connections of the prefrontal cortex in the rhesus monkey. *J. Comp. Neurol.* 286, 353–375. doi: 10.1002/cne.902860306

Barraclough, D. J., Conroy, M. L., and Lee, D. (2004). Prefrontal cortex and decision making in a mixed-strategy game. *Nat. Neurosci.* 7, 404–410. doi: 10.1038/nn1209

Bastian, A., Schoner, G., and Riehle, A. (2003). Preshaping and continuous evolution of motor cortical representations during movement preparation. *Eur. J. Neurosci.* 18, 2047–2058. doi: 10.1046/j.1460-9568.2003.02906.x

Beurze, S. M., De Lange, F. P., Toni, I., and Medendorp, W. P. (2007). Integration of target and effector information in the human brain during reach planning. *J. Neurophysiol.* 97, 188–199. doi: 10.1152/jn.00456.2006

Boussaoud, D. (2001). Attention versus intention in the primate premotor cortex. *Neuroimage* 14, S40–S45. doi: 10.1006/nimg.2001.0816

Boussaoud, D., and Wise, S. P. (1993a). Primate frontal cortex: effects of stimulus and movement. *Exp. Brain Res.* 95, 28–40. doi: 10.1007/BF00229651

Boussaoud, D., and Wise, S. P. (1993b). Primate frontal cortex: neuronal activity following attentional versus intentional cues. *Exp. Brain Res.* 95, 15–27. doi: 10.1007/BF00229650

Brasted, P. J., and Wise, S. P. (2004). Comparison of learning-related neuronal activity in the dorsal premotor cortex and striatum. *Eur. J. Neurosci.* 19, 721–740. doi: 10.1111/j.0953-816X.2003.03181.x

Brown, V. J., Desimone, R., and Mishkin, M. (1995). Responses of cells in the tail of the caudate nucleus during visual discrimination learning. *J. Neurophysiol.* 74, 1083–1094.

Buckley, M. J., Mansouri, F. A., Hoda, H., Mahboubi, M., Browning, P. G., Kwok, S. C., et al. (2009). Dissociable components of rule-guided behavior depend on distinct medial and prefrontal regions. *Science* 325, 52–58. doi: 10.1126/science.1172377

Bunge, S. A., and Wallis, J. D. (2008). *Neuroscience of Rule-Guided Behavior.* New York: Oxford University Press.

Bunge, S. A., Wallis, J. D., Parker, A., Brass, M., Crone, E. A., Hoshi, E., et al. (2005). Neural circuitry underlying rule use in humans and nonhuman primates. *J. Neurosci.* 25, 10347–10350. doi: 10.1523/JNEUROSCI.2937-05.2005

Buschman, T. J., Denovellis, E. L., Diogo, C., Bullock, D., and Miller, E. K. (2012). Synchronous oscillatory neural ensembles for rules in the prefrontal cortex. *Neuron* 76, 838–846. doi: 10.1016/j.neuron.2012.09.029

Bussey, T. J., Wise, S. P., and Murray, E. A. (2001). The role of ventral and orbital prefrontal cortex in conditional visuomotor learning and strategy use in rhesus monkeys (*Macaca mulatta*). *Behav. Neurosci.* 115, 971–982. doi: 10.1037/0735-7044.115.5.971

Bussey, T. J., Wise, S. P., and Murray, E. A. (2002). Interaction of ventral and orbital prefrontal cortex with inferotemporal cortex in conditional visuomotor learning. *Behav. Neurosci.* 116, 703–715. doi: 10.1037/0735-7044.116.4.703

Caan, W., Perrett, D. I., and Rolls, E. T. (1984). Responses of striatal neurons in the behaving monkey. 2. Visual processing in the caudal neostriatum. *Brain Res.* 290, 53–65. doi: 10.1016/0006-8993(84)90735-2

Chen, L. L., and Wise, S. P. (1995a). Neuronal activity in the supplementary eye field during acquisition of conditional oculomotor associations. *J. Neurophysiol.* 73, 1101–1121.

Chen, L. L., and Wise, S. P. (1995b). Supplementary eye field contrasted with the frontal eye field during acquisition of conditional oculomotor associations. *J. Neurophysiol.* 73, 1122–1134.

Cheng, K., Saleem, K. S., and Tanaka, K. (1997). Organization of corticostriatal and corticoamygdalar projections arising from the anterior inferotemporal area TE of the macaque monkey: a *Phaseolus vulgaris* leucoagglutinin study. *J. Neurosci.* 17, 7902–7925.

Cisek, P., and Kalaska, J. F. (2002). Simultaneous encoding of multiple potential reach directions in dorsal premotor cortex. *J. Neurophysiol.* 87, 1149–1154.

Cisek, P., and Kalaska, J. F. (2004). Neural correlates of mental rehearsal in dorsal premotor cortex. *Nature* 431, 993–996. doi: 10.1038/nature03005

Cisek, P., and Kalaska, J. F. (2005). Neural correlates of reaching decisions in dorsal premotor cortex: specification of multiple direction choices and final selection of action. *Neuron* 45, 801–814. doi: 10.1016/j.neuron.2005.01.027

Cisek, P., and Kalaska, J. F. (2010). Neural Mechanisms for Interacting with a world full of action choices. *Annu. Rev. Neurosci.* 33, 269–298. doi: 10.1146/annurev.neuro.051508.135409

Colby, C. L., and Goldberg, M. E. (1999). Space and attention in parietal cortex. *Annu. Rev. Neurosci.* 22, 319–349. doi: 10.1146/annurev.neuro.22.1.319

Crucian, G. P., and Okun, M. S. (2003). Visual-spatial ability in Parkinson's disease. *Front. Biosci.* 8:s992–s997. doi: 10.2741/1171

Diedrichsen, J., Grafton, S., Albert, N., Hazeltine, E., and Ivry, R. B. (2006). Goal-selection and movement-related conflict during bimanual reaching movements. *Cereb. Cortex* 16, 1729–1738. doi: 10.1093/cercor/bhj108

di Pellegrino, G., and Wise, S. P. (1993). Visuospatial versus visuomotor activity in the premotor and prefrontal cortex of a primate. *J. Neurosci.* 13, 1227–1243.

Doya, K. (2000). Complementary roles of basal ganglia and cerebellum in learning and motor control. *Curr. Opin. Neurobiol.* 10, 732–739. doi: 10.1016/S0959-4388(00)00153-7

Dubois, B., and Pillon, B. (1997). Cognitive deficits in Parkinson's disease. *J. Neurol.* 244, 2–8. doi: 10.1007/PL00007725

Eacott, M. J., and Gaffan, D. (1992). Inferotemporal-frontal disconnection: the uncinate fascicle and visual associative learning in monkeys. *Eur. J. Neurosci.* 4, 1320–1332. doi: 10.1111/j.1460-9568.1992.tb00157.x

Everling, S., Tinsley, C. J., Gaffan, D., and Duncan, J. (2002). Filtering of neural signals by focused attention in the monkey prefrontal cortex. *Nat. Neurosci.* 5, 671–676. doi: 10.1038/nn874

Flaherty, A. W., and Graybiel, A. M. (1994). Input–output organization of the sensorimotor striatum in the squirrel monkey. *J. Neurosci.* 14, 599–610.

Freedman, D. J., and Assad, J. A. (2006). Experience-dependent representation of visual categories in parietal cortex. *Nature* 443, 85–88. doi: 10.1038/nature05078

Freedman, D. J., Riesenhuber, M., Poggio, T., and Miller, E. K. (2001). Categorical representation of visual stimuli in the primate prefrontal cortex. *Science* 291, 312–316. doi: 10.1126/science.291.5502.312

Frith, C. D., Friston, K., Liddle, P. F., and Frackowiak, R. S. (1991). Willed action and the prefrontal cortex in man: a study with PET. *Proc. Biol. Sci.* 244, 241–246. doi: 10.1098/rspb.1991.0077

Funahashi, S., Bruce, C. J., and Goldman-Rakic, P. S. (1989). Mnemonic coding of visual space in the monkey's dorsolateral prefrontal cortex. *J. Neurophysiol.* 61, 331–349.

Funahashi, S., Chafee, M. V., and Goldman-Rakic, P. S. (1993). Prefrontal neuronal activity in rhesus monkeys performing a delayed anti-saccade task. *Nature* 365, 753–756. doi: 10.1038/365753a0

Fuster, J. (2008). *The Prefrontal Cortex.* London: Academic Press.

Galletti, C., Fattori, P., Kutz, D. F., and Battaglini, P. P. (1997). Arm movement-related neurons in the visual area V6A of the macaque superior parietal lobule. *Eur. J. Neurosci.* 9, 410–413. doi: 10.1111/j.1460-9568.1997.tb01410.x

Genovesio, A., Brasted, P. J., Mitz, A. R., and Wise, S. P. (2005). Prefrontal cortex activity related to abstract response strategies. *Neuron* 47, 307–320. doi: 10.1016/j.neuron.2005.06.006

Genovesio, A., Tsujimoto, S., and Wise, S. P. (2012). Encoding goals but not abstract magnitude in the primate prefrontal cortex. *Neuron* 74, 656–662. doi: 10.1016/j.neuron.2012.02.023

Godschalk, M., Lemon, R. N., Nijs, H. G., and Kuypers, H. G. (1981). Behaviour of neurons in monkey peri-arcuate and precentral cortex before and during visually guided arm and hand movements. *Exp. Brain Res.* 44, 113–116. doi: 10.1007/BF00238755

Goel, V., and Grafman, J. (1995). Are the frontal lobes implicated in "planning" functions? Interpreting data from the Tower of Hanoi. *Neuropsychologia* 33, 623–642. doi: 10.1016/0028-3932(95)90866-P

Goldman-Rakic, P. S. (1988). Topography of cognition: parallel distributed networks in primate association cortex. *Annu. Rev. Neurosci.* 11, 137–156. doi: 10.1146/annurev.ne.11.030188.001033

Goodwin, S. J., Blackman, R. K., Sakellaridi, S., and Chafee, M. V. (2012). Executive control over cognition: stronger and earlier rule-based modulation of spatial category signals in prefrontal cortex relative to parietal cortex. *J. Neurosci.* 32, 3499–3515. doi: 10.1523/JNEUROSCI.3585-11.2012

Grafton, S. T., Fagg, A. H., and Arbib, M. A. (1998). Dorsal premotor cortex and conditional movement selection: A PET functional mapping study. *J. Neurophysiol.* 79, 1092–1097.

Graybiel, A. M. (2008). Habits, rituals, and the evaluative brain. *Annu. Rev. Neurosci.* 31, 359–387. doi: 10.1146/annurev.neuro.29.051605.112851

Graybiel, A. M., Aosaki, T., Flaherty, A. W., and Kimura, M. (1994). The basal ganglia and adaptive motor control. *Science* 265, 1826–1831. doi: 10.1126/science.8091209

Haber, S., Kim, K.-S., Mailly, P., and Calzavara, R. (2006). Reward-related cortical inputs define a large striatal region in primates that interface with associative cortical connections, providing a substrate for incentive-based learning. *J. Neurosci.* 26, 8368–8376. doi: 10.1523/JNEUROSCI.0271-06.2006

Hadj-Bouziane, F., and Boussaoud, D. (2003). Neuronal activity in the monkey striatum during conditional visuomotor learning. *Exp. Brain Res.* 153, 190–196. doi: 10.1007/s00221-003-1592-4

Hahnloser, R. H., Kozhevnikov, A. A., and Fee, M. S. (2002). An ultra-sparse code underlies the generation of neural sequences in a songbird. *Nature* 419, 65–70. doi: 10.1038/nature00974

Halsband, U., and Freund, H. J. (1990). Premotor cortex and conditional motor learning in man. *Brain* 113(Pt 1), 207–222. doi: 10.1093/brain/113.1.207

Halsband, U., and Passingham, R. E. (1982). The role of premotor and parietal cortex in the direction of action. *Brain Res.* 240, 368–372. doi: 10.1016/0006-8993(82)90239-6

Halsband, U., and Passingham, R. E. (1985). Premotor cortex and the conditions for movement in monkeys (*Macaca fascicularis*). *Behav. Brain Res.* 18, 269–277. doi: 10.1016/0166-4328(85)90035-X

Hanakawa, T., Honda, M., Sawamoto, N., Okada, T., Yonekura, Y., Fukuyama, H., et al. (2002). The role of rostral Brodmann area 6 in mental-operation tasks: an integrative neuroimaging approach. *Cereb. Cortex* 12, 1157–1170. doi: 10.1093/cercor/12.11.1157

Hasegawa, I., Fukushima, T., Ihara, T., and Miyashita, Y. (1998). Callosal window between prefrontal cortices: cognitive interaction to retrieve long-term memory. *Science* 281, 814–818. doi: 10.1126/science.281.5378.814

Haynes, W., and Haber, S. (2013). The organization of prefrontal-subthalamic inputs in primates provides an anatomical substrate for both functional specificity and integration: implications for Basal Ganglia models and deep brain stimulation. *J. Neurosci.* 33, 4804–4814. doi: 10.1523/ JNEUROSCI.4674-12.2013

Hernández, A., Zainos, A., and Romo, R. (2002). Temporal evolution of a decision-making process in medial premotor cortex. *Neuron* 33, 959–972. doi: 10.1016/S0896-6273(02)00613-X

Hikosaka, O., Nakahara, H., Rand, M. K., Sakai, K., Lu, X., Nakamura, K., et al. (1999). Parallel neural networks for learning sequential procedures. *Trends Neurosci.* 22, 464–471. doi: 10.1016/S0166-2236(99)01439-3

Hirabayashi, T., Takeuchi, D., Tamura, K., and Miyashita, Y. (2013a). Functional microcircuit recruited during retrieval of object association memory in monkey perirhinal cortex. *Neuron* 77, 192–203. doi: 10.1016/j.neuron.2012.10.031

Hirabayashi, T., Takeuchi, D., Tamura, K., and Miyashita, Y. (2013b). Microcircuits for hierarchical elaboration of object coding across primate temporal areas. *Science* 341, 191–195. doi: 10.1126/science.1236927

Hollerman, J. R., Tremblay, L., and Schultz, W. (2000). Involvement of basal ganglia and orbitofrontal cortex in goal-directed behavior. *Prog. Brain Res.* 126, 193–215. doi: 10.1016/S0079-6123(00)26015-9

Hoshi, E., Shima, K., and Tanji, J. (1998). Task-dependent selectivity of movement-related neuronal activity in the primate prefrontal cortex. *J. Neurophysiol.* 80, 3392–3397.

Hoshi, E., Shima, K., and Tanji, J. (2000). Neuronal activity in the primate prefrontal cortex in the process of motor selection based on two behavioral rules. *J. Neurophysiol.* 83, 2355–2373.

Hoshi, E., and Tanji, J. (2000). Integration of target and body-part information in the premotor cortex when planning action. *Nature* 408, 466–470. doi: 10.1038/35044075

Hoshi, E., and Tanji, J. (2002). Contrasting neuronal activity in the dorsal and ventral premotor areas during preparation to reach. *J. Neurophysiol.* 87, 1123–1128.

Hoshi, E., and Tanji, J. (2004a). Area-selective neuronal activity in the dorsolateral prefrontal cortex for information retrieval and action planning. *J. Neurophysiol.* 91, 2707–2722. doi: 10.1152/jn.00904.2003

Hoshi, E., and Tanji, J. (2004b). Differential roles of neuronal activity in the supplementary and presupplementary motor areas: from information retrieval to motor planning and execution. *J. Neurophysiol.* 92, 3482–3499. doi: 10.1152/jn.00547.2004

Hoshi, E., and Tanji, J. (2006). Differential involvement of neurons in the dorsal and ventral premotor cortex during processing of visual signals for action planning. *J. Neurophysiol.* 95, 3596–3616. doi: 10.1152/jn.01126.2005

Hoshi, E., and Tanji, J. (2007). Distinctions between dorsal and ventral premotor areas: anatomical connectivity and functional properties. *Curr. Opin. Neurobiol.* 17, 234–242. doi: 10.1016/j.conb.2007.02.003

Houk, J. C., and Wise, S. P. (1995). Distributed modular architectures linking basal ganglia, cerebellum, and cerebral cortex: their role in planning and controlling action. *Cereb. Cortex* 5, 95–110. doi: 10.1093/cercor/5.2.95

Huerta, M. F., and Kaas, J. H. (1990). Supplementary eye field as defined by intracortical microstimulation: connections in macaques. *J. Comp. Neurol.* 293, 299–330. doi: 10.1002/cne.902930211

Hussar, C. R., and Pasternak, T. (2009). Flexibility of sensory representations in prefrontal cortex depends on cell type. *Neuron* 64, 730–743. doi: 10.1016/j.neuron.2009.11.018

Inase, M., Li, B. M., Takashima, I., and Iijima, T. (2001). Pallidal activity is involved in visuomotor association learning in monkeys. *Eur. J. Neurosci.* 14, 897–901. doi: 10.1046/j.0953-816x.2001.01701.x

Inase, M., and Tanji, J. (1994). Projections from the globus pallidus to the thalamic areas projecting to the dorsal area 6 of the macaque monkey: a multiple tracing study. *Neurosci. Lett.* 180, 135–137. doi: 10.1016/0304-3940(94)90505-3

Johnson, P. B., Ferraina, S., and Caminiti, R. (1993). Cortical networks for visual reaching. *Exp. Brain Res.* 97, 361–365. doi: 10.1007/BF00228707

Kalaska, J. F., Sergio, L. E., and Cisek, P. (1998). Cortical control of whole-arm motor tasks. *Novartis Found. Symp.* 218, 176–190.

Kamigaki, T., Fukushima, T., and Miyashita, Y. (2009). Cognitive set reconfiguration signaled by macaque posterior parietal neurons. *Neuron* 61, 941–951. doi: 10.1016/j.neuron.2009.01.028

Kim, J. N., and Shadlen, M. N. (1999). Neural correlates of a decision in the dorsolateral prefrontal cortex of the macaque. *Nat. Neurosci.* 2, 176–185. doi: 10.1038/5739

Konishi, S., Nakajima, K., Uchida, I., Kameyama, M., Nakahara, K., Sekihara, K., et al. (1998). Transient activation of inferior prefrontal cortex during cognitive set shifting. *Nat. Neurosci.* 1, 80–84. doi: 10.1038/283

Kurata, K. (1993). Premotor cortex of monkeys: set- and movement-related activity reflecting amplitude and direction of wrist movements. *J. Neurophysiol.* 69, 187–200.

Kurata, K., and Hoffman, D. S. (1994). Differential effects of muscimol microinjection into dorsal and ventral aspects of the premotor cortex of monkeys. *J. Neurophysiol.* 71, 1151–1164.

Kurata, K., and Wise, S. P. (1988). Premotor cortex of rhesus monkeys: set-related activity during two conditional motor tasks. *Exp. Brain Res.* 69, 327–343. doi: 10.1007/BF00247578

Lebedev, M. A., and Wise, S. P. (2001). Tuning for the orientation of spatial attention in dorsal premotor cortex. *Eur. J. Neurosci.* 13, 1002–1008. doi: 10.1046/j.0953-816x.2001.01457.x

Lee, D., Seo, H., and Jung, M. W. (2012). Neural basis of reinforcement learning and decision making. *Annu. Rev. Neurosci.* 35, 287–308. doi: 10.1146/annurev-neuro-062111-150512

Lu, M. T., Preston, J. B., and Strick, P. L. (1994). Interconnections between the prefrontal cortex and the premotor areas in the frontal lobe. *J. Comp. Neurol.* 341, 375–392. doi: 10.1002/cne.903410308

Luk, C. H., and Wallis, J. D. (2013). Choice coding in frontal cortex during stimulus-guided or action-guided decision-making. *J. Neurosci.* 33, 1864–1871. doi: 10.1523/JNEUROSCI.4920-12.2013

Luppino, G., Matelli, M., Camarda, R., and Rizzolatti, G. (1993). Corticocortical connections of area F3 (SMA-proper) and area F6 (pre-SMA) in the macaque monkey. *J. Comp. Neurol.* 338, 114–140. doi: 10.1002/cne.903380109

Luppino, G., Rozzi, S., Calzavara, R., and Matelli, M. (2003). Prefrontal and agranular cingulate projections to the dorsal premotor areas F2 and F7 in the macaque monkey. *Eur. J. Neurosci.* 17, 559–578. doi: 10.1046/j.1460-9568.2003.02476.x

Luria, A. R. (1966). *Higher Cortical Functions in Man.* New York: Basic Book.

Mann, S. E., Thau, R., and Schiller, P. H. (1988). Conditional task-related responses in monkey dorsomedial frontal cortex. *Exp. Brain Res.* 69, 460–468. doi: 10.1007/BF00247300

Mansouri, F. A., Buckley, M. J., and Tanaka, K. (2007). Mnemonic function of the dorsolateral prefrontal cortex in conflict-induced behavioral adjustment. *Science* 318, 987–990. doi: 10.1126/science.1146384

Marsden, C. D. (1982). The mysterious motor function of the basal ganglia: the Robert Wartenberg Lecture. *Neurology* 32, 514–539. doi: 10.1212/WNL.32.5.514

Matelli, M., Govoni, P., Galletti, C., Kutz, D. F., and Luppino, G. (1998). Superior area 6 afferents from the superior parietal lobule in the macaque monkey. *J. Comp. Neurol.* 402, 327–352. doi: 10.1002/(SICI)1096-9861(19981221)402:3<327::AID-CNE4>3.0.CO;2-Z

Matelli, M., Luppino, G., and Rizzolatti, G. (1985). Patterns of cytochrome oxidase activity in the frontal agranular cortex of the macaque monkey. *Behav. Brain Res.* 18, 125–136. doi: 10.1016/0166-4328(85)90068-3

Matsumoto, K., Suzuki, W., and Tanaka, K. (2003). Neuronal correlates of goal-based motor selection in the prefrontal cortex. *Science* 301, 229–232. doi: 10.1126/science.1084204

Matsuzaka, Y., Aizawa, H., and Tanji, J. (1992). A motor area rostral to the supplementary motor area (presupplementary motor area) in the monkey: neuronal activity during a learned motor task. *J. Neurophysiol.* 68, 653–662.

Matsuzaka, Y., and Tanji, J. (1996). Changing directions of forthcoming arm movements: neuronal activity in the presupplementary and supplementary motor area of monkey cerebral cortex. *J. Neurophysiol.* 76, 2327–2342.

Mendez, M. F., Adams, N. L., and Lewandowski, K. S. (1989). Neurobehavioral changes associated with caudate lesions. *Neurology* 39, 349–354. doi: 10.1212/WNL.39.3.349

Meyers, E. M., Qi, X. L., and Constantinidis, C. (2012). Incorporation of new information into prefrontal cortical activity after learning working memory tasks. *Proc. Natl. Acad. Sci. U.S.A.* 109, 4651–4656. doi: 10.1073/pnas.1201022109

Middleton, F. A., and Strick, P. L. (1994). Anatomical evidence for cerebellar and basal ganglia involvement in higher cognitive function. *Science* 266, 458–461. doi: 10.1126/science.7939688

Middleton, F. A., and Strick, P. L. (2000). Basal ganglia and cerebellar loops: motor and cognitive circuits. *Brain Res. Brain Res. Rev.* 31, 236–250. doi: 10.1016/S0165-0173(99)00040-5

Miller, E. K. (2000). The prefrontal cortex and cognitive control. *Nat. Rev. Neurosci.* 1, 59–65. doi: 10.1038/35036228

Miller, E. K., and Cohen, J. D. (2001). An integrative theory of prefrontal cortex function. *Annu. Rev. Neurosci.* 24, 167–202. doi: 10.1146/annurev.neuro.24.1.167

Milner, B. (1963). Effects of different brain lesions on card sorting. *Arch. Neurol.* 9, 90–100. doi: 10.1001/archneur.1963.00460070100010

Mink, J. W. (1996). The basal ganglia: focused selection and inhibition of competing motor programs. *Prog. Neurobiol.* 50, 381–425. doi: 10.1016/S0301-0082(96)00042-1

Mitchell, S. J., Richardson, R. T., Baker, F. H., and Delong, M. R. (1987). The primate globus pallidus: neuronal activity related to direction of movement. *Exp. Brain Res.* 68, 491–505. doi: 10.1007/BF00249793

Mitz, A. R., Godschalk, M., and Wise, S. P. (1991). Learning-dependent neuronal activity in the premotor cortex: activity during the acquisition of conditional motor associations. *J. Neurosci.* 11, 1855–1872.

Morecraft, R., Stilwell-Morecraft, K., Cipolloni, P., Ge, J., Mcneal, D., and Pandya, D. (2012). Cytoarchitecture and cortical connections of the anterior cingulate and adjacent somatomotor fields in the rhesus monkey. *Brain Res. Bull.* 87, 457–497. doi: 10.1016/j.brainresbull.2011.12.005

Muhammad, R., Wallis, J. D., and Miller, E. K. (2006). A comparison of abstract rules in the prefrontal cortex, premotor cortex, inferior temporal cortex, and striatum.

J. Cogn. Neurosci. 18, 974–989. doi: 10.1162/jocn.2006.18.6.974

Murray, E. A., Bussey, T. J., and Wise, S. P. (2000). Role of prefrontal cortex in a network for arbitrary visuomotor mapping. *Exp. Brain Res.* 133, 114–129. doi: 10.1007/s002210000406

Mushiake, H., Saito, N., Sakamoto, K., Itoyama, Y., and Tanji, J. (2006). Activity in the lateral prefrontal cortex reflects multiple steps of future events in action plans. *Neuron* 50, 631–641. doi: 10.1016/j.neuron.2006.03.045

Nakayama, Y., Yamagata, T., Tanji, J., and Hoshi, E. (2008). Transformation of a virtual action plan into a motor plan in the premotor cortex. *J. Neurosci.* 28, 10287–10297. doi: 10.1523/JNEUROSCI.2372-08.2008

Nambu, A., Tokuno, H., Inase, M., and Takada, M. (1997). Corticosubthalamic input zones from forelimb representations of the dorsal and ventral divisions of the premotor cortex in the macaque monkey: comparison with the input zones from the primary motor cortex and the supplementary motor area. *Neurosci. Lett.* 239, 13–16. doi: 10.1016/S0304-3940(97)00877-X

Nambu, A., Tokuno, H., and Takada, M. (2002). Functional significance of the cortico-subthalamo-pallidal 'hyperdirect' pathway. *Neurosci. Res.* 43, 111–117. doi: 10.1016/S0168-0102(02)00027-5

Naya, Y., Yoshida, M., and Miyashita, Y. (2001). Backward spreading of memory-retrieval signal in the primate temporal cortex. *Science* 291, 661–664. doi: 10.1126/science.291.5504.661

Nieder, A., Freedman, D. J., and Miller, E. K. (2002). Representation of the quantity of visual items in the primate prefrontal cortex. *Science* 297, 1708–1711. doi: 10.1126/science.1072493

Nixon, P. D., Mcdonald, K. R., Gough, P. M., Alexander, I. H., and Passingham, R. E. (2004). Cortico-basal ganglia pathways are essential for the recall of well-established visuomotor associations. *Eur. J. Neurosci.* 20, 3165–3178. doi: 10.1111/j.1460-9568.2004.03788.x

Olshausen, B. A., and Field, D. J. (2004). Sparse coding of sensory inputs. *Curr. Opin. Neurobiol.* 14, 481–487. doi: 10.1016/j.conb.2004.07.007

Olson, C. R., and Tremblay, L. (2000). Macaque supplementary eye field neurons encode object-centered locations relative to both continuous and discontinuous objects. *J. Neurophysiol.* 83, 2392–2411.

Ongur, D., and Price, J. L. (2000). The organization of networks within the orbital and medial prefrontal cortex of rats, monkeys and humans. *Cereb. Cortex* 10, 206–219. doi: 10.1093/cercor/10.3.206

Orban, G. A. (2008). Higher order visual processing in macaque extrastriate cortex. *Physiol. Rev.* 88, 59–89. doi: 10.1152/physrev.00008.2007

O Scalaidhe, S. P., Wilson, F. A., and Goldman-Rakic, P. S. (1997). Areal segregation of face-processing neurons in prefrontal cortex. *Science* 278, 1135–1138. doi: 10.1126/science.278.5340.1135

O Scalaidhe, S. P., Wilson, F. A., and Goldman-Rakic, P. S. (1999). Face-selective neurons during passive viewing and working memory performance of rhesus monkeys: evidence for intrinsic specialization of neuronal coding. *Cereb. Cortex* 9, 459–475. doi: 10.1093/cercor/9.5.459

Packard, M. G., and Knowlton, B. J. (2002). Learning and memory functions of the Basal Ganglia. *Annu. Rev. Neurosci.* 25, 563–593. doi: 10.1146/annurev.neuro.25.112701.142937

Passingham, R., and Wise, S. P. (2012). *The Neurobiology of the Prefrontal Cortex: Anatomy, Evolution, and the Origin of Insight.* Oxford: Oxford University Press.

Passingham, R. E. (1993). *The Frontal Lobes and Voluntary Action.* Oxford: Oxford University Press.

Pasupathy, A., and Miller, E. K. (2005). Different time courses of learning-related activity in the prefrontal cortex and striatum. *Nature* 433, 873–876. doi: 10.1038/nature03287

Pesaran, B., Nelson, M. J., and Andersen, R. A. (2008). Free choice activates a decision circuit between frontal and parietal cortex. *Nature* 453, 406–409. doi: 10.1038/nature06849

Petrides, M. (1982). Motor conditional associative-learning after selective prefrontal lesions in the monkey. *Behav. Brain Res.* 5, 407–413. doi: 10.1016/0166-4328(82)90044-4

Petrides, M. (1986). The effect of periarcuate lesions in the monkey on the performance of symmetrically and asymmetrically reinforced visual and auditory go, no-go tasks. *J. Neurosci.* 6, 2054–2063.

Petrides, M., and Pandya, D. N. (1999). Dorsolateral prefrontal cortex: comparative cytoarchitectonic analysis in the human and the macaque brain and corticocortical connection patterns. *Eur. J. Neurosci.* 11, 1011–1036. doi: 10.1046/j.1460-9568.1999.00518.x

Petrides, M., and Pandya, D. N. (2002). Comparative cytoarchitectonic analysis of the human and the macaque ventrolateral prefrontal cortex and corticocortical connection patterns in the monkey. *Eur. J. Neurosci.* 16, 291–310. doi: 10.1046/j.1460-9568.2001.02090.x

Picard, N., and Strick, P. L. (2001). Imaging the premotor areas. *Curr. Opin. Neurobiol.* 11, 663–672. doi: 10.1016/S0959-4388(01)00266-5

Rainer, G., Asaad, W. F., and Miller, E. K. (1998). Selective representation of relevant information by neurons in the primate prefrontal cortex. *Nature* 393, 577–579. doi: 10.1038/31235

Rainer, G., Rao, S. C., and Miller, E. K. (1999). Prospective coding for objects in primate prefrontal cortex. *J. Neurosci.* 19, 5493–5505.

Riehle, A., and Requin, J. (1989). Monkey primary motor and premotor cortex: single-cell activity related to prior information about direction and extent of an intended movement. *J. Neurophysiol.* 61, 534–549.

Rizzolatti, G., and Luppino, G. (2001). The cortical motor system. *Neuron* 31, 889–901. doi: 10.1016/S0896-6273(01)00423-8

Rowe, J. B., Toni, I., Josephs, O., Frackowiak, R. S., and Passingham, R. E. (2000). The prefrontal cortex: response selection or maintenance within working memory? *Science* 288, 1656–1660. doi: 10.1126/science.288.5471.1656

Rozzi, S., Calzavara, R., Belmalih, A., Borra, E., Gregoriou, G. G., Matelli, M., et al. (2006). Cortical connections of the inferior parietal cortical convexity of the macaque monkey. *Cereb. Cortex* 16, 1389–1417. doi: 10.1093/cercor/bhj076

Rushworth, M. F., Buckley, M. J., Gough, P. M., Alexander, I. H., Kyriazis, D., Mcdonald, K. R., et al. (2005). Attentional selection and action selection in the ventral and orbital prefrontal cortex. *J. Neurosci.* 25, 11628–11636. doi: 10.1523/JNEUROSCI.2765-05.2005

Rushworth, M. F., Nixon, P. D., Eacott, M. J., and Passingham, R. E. (1997). Ventral prefrontal cortex is not essential for working memory. *J. Neurosci.* 17, 4829–4838.

Saga, Y., Hashimoto, M., Tremblay, L., Tanji, J., and Hoshi, E. (2013). Representation of spatial- and object-specific behavioral goals in the dorsal globus pallidus of monkeys during reaching movement. *J. Neurosci.* 33, 16360–16371. doi: 10.1523/JNEUROSCI.1187-13.2013

Saga, Y., Hirata, Y., Takahara, D., Inoue, K., Miyachi, S., Nambu, A., et al. (2011). Origins of multisynaptic projections from the basal ganglia to rostrocaudally distinct sectors of the dorsal premotor area in macaques. *Eur. J. Neurosci.* 33, 285–297. doi: 10.1111/j.1460-9568.2010.07492.x

Saint-Cyr, J. A., Ungerleider, L. G., and Desimone, R. (1990). Organization of visual cortical inputs to the striatum and subsequent outputs to the pallido-nigral complex in the monkey. *J. Comp. Neurol.* 298, 129–156. doi: 10.1002/cne.902980202

Saito, N., Mushiake, H., Sakamoto, K., Itoyama, Y., and Tanji, J. (2005). Representation of immediate and final behavioral goals in the monkey prefrontal cortex during an instructed delay period. *Cereb. Cortex* 15, 1535–1546. doi: 10.1093/cercor/bhi032

Sakagami, M., and Pan, X. (2007). Functional role of the ventrolateral prefrontal cortex in decision making. *Curr. Opin. Neurobiol.* 17, 228–233. doi: 10.1016/j.conb.2007.02.008

Sakai, K. (2008). Task set and prefrontal cortex. *Annu. Rev. Neurosci.* 31, 219–245. doi: 10.1146/annurev.neuro.31.060407.125642

Sakai, K., Hikosaka, O., Miyauchi, S., Sasaki, Y., Fujimaki, N., and Putz, B. (1999). Presupplementary motor area activation during sequence learning reflects visuo-motor association. *J. Neurosci.* 19, RC1.

Sakai, K., and Miyashita, Y. (1991). Neural organization for the long-term memory of paired associates. *Nature* 354, 152–155. doi: 10.1038/354152a0

Samejima, K., Ueda, Y., Doya, K., and Kimura, M. (2005). Representation of action-specific reward values in the striatum. *Science* 310, 1337–1340. doi: 10.1126/science.1115270

Schall, J. D. (2001). Neural basis of deciding, choosing and acting. *Nat. Rev. Neurosci.* 2, 33–42. doi: 10.1038/35049054

Schall, J. D., Morel, A., King, D. J., and Bullier, J. (1995). Topography of visual cortex connections with frontal eye field in macaque: convergence and segregation of processing streams. *J. Neurosci.* 15, 4464–4487.

Schlag, J., and Schlag, R. M. (1987). Evidence for a supplementary eye field. *J. Neurophysiol.* 57, 179–200.

Schluter, N. D., Rushworth, M. F., Passingham, R. E., and Mills, K. R. (1998). Temporary interference in human lateral premotor cortex suggests dominance for the selection of movements. A study using transcranial magnetic stimulation.

Brain 121(Pt 5), 785–799. doi: 10.1093/brain/121.5.785

Schultz, W., Dayan, P., and Montague, P. R. (1997). A neural substrate of prediction and reward. *Science* 275, 1593–1599. doi: 10.1126/science.275.5306.1593

Selemon, L. D., and Goldman-Rakic, P. S. (1985). Longitudinal topography and interdigitation of corticostriatal projections in the rhesus monkey. *J. Neurosci.* 5, 776–794.

Seo, M., Lee, E., and Averbeck, B. B. (2012). Action selection and action value in frontal-striatal circuits. *Neuron* 74, 947–960. doi: 10.1016/j.neuron.2012.03.037

Serrien, D. J., Ivry, R. B., and Swinnen, S. P. (2007). The missing link between action and cognition. *Prog. Neurobiol.* 82, 95–107. doi: 10.1016/j.pneurobio.2007.02.003

Shallice, T. (1982). Specific impairments of planning. *Philos. Trans. R. Soc. Lond. B Biol. Sci.* 298, 199–209. doi: 10.1098/rstb.1982.0082

Snyder, L. H., Batista, A. P., and Andersen, R. A. (1997). Coding of intention in the posterior parietal cortex. *Nature* 386, 167–170. doi: 10.1038/386167a0

Stoet, G., and Snyder, L. H. (2004). Single neurons in posterior parietal cortex of monkeys encode cognitive set. *Neuron* 42, 1003–1012. doi: 10.1016/j.neuron.2004.06.003

Swaminathan, S. K., and Freedman, D. J. (2012). Preferential encoding of visual categories in parietal cortex compared with prefrontal cortex. *Nat. Neurosci.* 15, 315–320. doi: 10.1038/nn.3016

Tachibana, Y., Nambu, A., Hatanaka, N., Miyachi, S., and Takada, M. (2004). Input–output organization of the rostral part of the dorsal premotor cortex, with special reference to its corticostriatal projection. *Neurosci. Res.* 48, 45–57. doi: 10.1016/j.neures.2003.09.006

Takada, M., Tokuno, H., Nambu, A., and Inase, M. (1998). Corticostriatal projections from the somatic motor areas of the frontal cortex in the macaque monkey: segregation versus overlap of input zones from the primary motor cortex, the supplementary motor area, and the premotor cortex. *Exp. Brain Res.* 120, 114–128. doi: 10.1007/s002210050384

Takahara, D., Inoue, K., Hirata, Y., Miyachi, S., Nambu, A., Takada, M., et al. (2012). Multisynaptic projections from the ventrolateral prefrontal cortex to the dorsal premotor cortex in macaques – anatomical substrate for conditional visuomotor behavior. *Eur. J. Neurosci.* 36, 3365–3375. doi: 10.1111/j.1460-9568.2012.08251.x

Takeda, K., and Funahashi, S. (2002). Prefrontal task-related activity representing visual cue location or saccade direction in spatial working memory tasks. *J. Neurophysiol.* 87, 567–588.

Tanaka, K. (1996). Inferotemporal cortex and object vision. *Annu. Rev. Neurosci.* 19, 109–139. doi: 10.1146/annurev.ne.19.030196.000545

Tanji, J., and Hoshi, E. (2001). Behavioral planning in the prefrontal cortex. *Curr. Opin. Neurobiol.* 11, 164–170. doi: 10.1016/S0959-4388(00)00192-6

Tanji, J., and Hoshi, E. (2008). Role of the lateral prefrontal cortex in executive behavioral control. *Physiol. Rev.* 88, 37–57. doi: 10.1152/physrev.00014.2007

Toni, I., Rowe, J., Stephan, K. E., and Passingham, R. E. (2002). Changes of cortico-striatal effective connectivity during visuomotor learning. *Cereb. Cortex* 12, 1040–1047. doi: 10.1093/cercor/12.10.1040

Toni, I., Rushworth, M. F., and Passingham, R. E. (2001). Neural correlates of visuomotor associations. Spatial rules compared with arbitrary rules. *Exp. Brain Res.* 141, 359–369. doi: 10.1007/s002210100877

Tremblay, L., Gettner, S. N., and Olson, C. R. (2002). Neurons with object-centered spatial selectivity in macaque SEF: do they represent locations or rules? *J. Neurophysiol.* 87, 333–350.

Tsujimoto, S., Genovesio, A., and Wise, S. P. (2009). Monkey orbitofrontal cortex encodes response choices near feedback time. *J. Neurosci.* 29, 2569–2574. doi: 10.1523/JNEUROSCI.5777-08.2009

Tsujimoto, S., Genovesio, A., and Wise, S. P. (2010). Evaluating self-generated decisions in frontal pole cortex of monkeys. *Nat. Neurosci.* 13, 120–126. doi: 10.1038/nn.2453

Tsujimoto, S., Genovesio, A., and Wise, S. P. (2011). Comparison of strategy signals in the dorsolateral and orbital prefrontal cortex. *J. Neurosci.* 31, 4583–4592. doi: 10.1523/JNEUROSCI.5816-10.2011

Uc, E. Y., Rizzo, M., Anderson, S. W., Qian, S., Rodnitzky, R. L., and Dawson, J. D. (2005). Visual dysfunction in Parkinson disease without dementia. *Neurology* 65, 1907–1913. doi: 10.1212/01.wnl.0000191565.11065.11

Ungerleider, L. G., Mishkin, M., Ingle, D. J., Goodale, M. A., and Mansfield, R. J. W. (1982). "Two cortical visual systems," in *Analysis of Visual Behavior*, eds D. J. Ingle, M. A. Goodale, and R. J. W. Mansfield (Cambridge: MIT press), 549–586.

Wallis, J. D., Anderson, K. C., and Miller, E. K. (2001). Single neurons in prefrontal cortex encode abstract rules. *Nature* 411, 953–956. doi: 10.1038/35082081

Wallis, J. D., and Miller, E. K. (2003). From rule to response: neuronal processes in the premotor and prefrontal cortex. *J. Neurophysiol.* 90, 1790–1806. doi: 10.1152/jn.00086.2003

Wang, M., Zhang, H., and Li, B. M. (2000). Deficit in conditional visuomotor learning by local infusion of bicuculline into the ventral prefrontal cortex in monkeys. *Eur. J. Neurosci.* 12, 3787–3796. doi: 10.1046/j.1460-9568.2000.00238.x

Webster, M. J., Bachevalier, J., and Ungerleider, L. G. (1993). Subcortical connections of inferior temporal areas TE and TEO in macaque monkeys. *J. Comp. Neurol.* 335, 73–91. doi: 10.1002/cne.903350106

Webster, M. J., Bachevalier, J., and Ungerleider, L. G. (1994). Connections of inferior temporal areas TEO and TE with parietal and frontal cortex in macaque monkeys. *Cereb. Cortex* 4, 470–483. doi: 10.1093/cercor/4.5.470

Weinrich, M., and Wise, S. P. (1982). The premotor cortex of the monkey. *J. Neurosci.* 2, 1329–1345.

Weinrich, M., Wise, S. P., and Mauritz, K. H. (1984). A neurophysiological study of the premotor cortex in the rhesus monkey. *Brain* 107 (Pt 2), 385–414. doi: 10.1093/brain/107.2.385

White, I. M., and Wise, S. P. (1999). Rule-dependent neuronal activity in the prefrontal cortex. *Exp. Brain Res.* 126, 315–335. doi: 10.1007/s002210050740

Wilson, F. A., Scalaidhe, S. P., and Goldman-Rakic, P. S. (1993). Dissociation of object and spatial processing domains in primate prefrontal cortex. *Science* 260, 1955–1958. doi: 10.1126/science.8316836

Wise, S. P., Boussaoud, D., Johnson, P. B., and Caminiti, R. (1997). Premotor and parietal cortex: corticocortical connectivity and combinatorial computations. *Annu. Rev. Neurosci.* 20, 25–42. doi: 10.1146/annurev.neuro.20.1.25

Wise, S. P., and Mauritz, K. H. (1985). Set-related neuronal activity in the premotor cortex of rhesus monkeys: effects of changes in motor set. *Proc. R. Soc. Lond. B Biol. Sci.* 223, 331–354. doi: 10.1098/rspb.1985.0005

Wise, S. P., and Murray, E. A. (2000). Arbitrary associations between antecedents and actions. *Trends Neurosci.* 23, 271–276. doi: 10.1016/S0166-2236(00)01570-8

Wise, S. P., Murray, E. A., and Gerfen, C. R. (1996). The frontal cortex-basal ganglia system in primates. *Crit. Rev. Neurobiol.* 10, 317–356. doi: 10.1615/CritRevNeurobiol.v10.i3-4.30

Wise, S. P., Weinrich, M., and Mauritz, K. H. (1983). Motor aspects of cue-related neuronal activity in premotor cortex of the rhesus monkey. *Brain Res.* 260, 301–305. doi: 10.1016/0006-8993(83)90685-6

Yamagata, T., Nakayama, Y., Tanji, J., and Hoshi, E. (2009). Processing of visual signals for direct specification of motor targets and for conceptual representation of action targets in the dorsal and ventral premotor cortex. *J. Neurophysiol.* 102, 3280–3294. doi: 10.1152/jn.00452.2009

Yamagata, T., Nakayama, Y., Tanji, J., and Hoshi, E. (2012). Distinct information representation and processing for goal-directed behavior in the dorsolateral and ventrolateral prefrontal cortex and the dorsal premotor cortex. *J. Neurosci.* 32, 12934–12949. doi: 10.1523/JNEUROSCI.2398-12.2012

Yamamoto, S., Kim, H. F., and Hikosaka, O. (2013). Reward value-contingent changes of visual responses in the primate caudate tail associated with a visuomotor skill. *J. Neurosci.* 33, 11227–11238. doi: 10.1523/JNEUROSCI.0318-13.2013

Yamamoto, S., Monosov, I. E., Yasuda, M., and Hikosaka, O. (2012). What and where information in the caudate tail guides saccades to visual objects. *J. Neurosci.* 32, 11005–11016. doi: 10.1523/JNEUROSCI.0828-12.2012

Yasuda, M., Yamamoto, S., and Hikosaka, O. (2012). Robust representation of stable object values in the oculomotor Basal Ganglia. *J. Neurosci.* 32, 16917–16932. doi: 10.1523/JNEUROSCI.3438-12.2012

Yoshida, A., and Tanaka, M. (2009). Enhanced modulation of neuronal activity during antisaccades in the primate globus pallidus. *Cereb. Cortex* 19, 206–217. doi: 10.1093/cercor/bhn069

Conflict of Interest Statement: The author declares that the research was conducted in the absence of any commercial or financial relationships that could be construed as a potential conflict of interest.

Received: 15 August 2013; accepted: 17 September 2013; published online: 21 October 2013.
Citation: Hoshi E (2013) Cortico-basal ganglia networks subserving goal-directed behavior mediated by conditional visuo-goal association. Front. Neural Circuits ***7****:158. doi: 10.3389/fncir.2013.00158*
This article was submitted to the journal Frontiers in Neural Circuits.

frontiers in
NEURAL CIRCUITS

ORIGINAL RESEARCH ARTICLE
published: 20 December 2013
doi: 10.3389/fncir.2013.00202

Regulation of thalamocortical axon branching by BDNF and synaptic vesicle cycling

Björn Granseth[1,2†], Yuichi Fukushima[1†], Noriuki Sugo[1], Leon Lagnado[3] and Nobuhiko Yamamoto[1]*

[1] Neuroscience Laboratories, Graduate School of Frontier Biosciences, Osaka University, Suita, Osaka, Japan
[2] Division of Cell Biology, Department of Clinical and Experimental Medicine, Linköping University, Linköping, Sweden
[3] Sussex Neuroscience, School of Life Sciences, University of Sussex, Brighton, UK

Edited by:
Masanobu Kano, The University of Tokyo, Japan

Reviewed by:
Edward S. Ruthazer, McGill University, Canada
Yumiko Yoshimura, National Institute for Physiological Sciences, National Institutes of Natural Sciences, Japan
Kohtaro Takei, Yokohama City University, Japan

***Correspondence:**
Nobuhiko Yamamoto, Neuroscience Laboratories, Graduate School of Frontier Biosciences, Osaka University, 1-3 Yamadaoka, Suita, Osaka 565-0871, Japan
e-mail: nobuhiko@fbs.osaka-u.ac.jp

† Björn Granseth and Yuichi Fukushima have contributed equally to this work.

During development, axons form branches in response to extracellular molecules. Little is known about the underlying molecular mechanisms. Here, we investigate how neurotrophin-induced axon branching is related to synaptic vesicle cycling for thalamocortical axons. The exogenous application of brain-derived neurotrophic factor (BDNF) markedly increased axon branching in thalamocortical co-cultures, while removal of endogenous BDNF reduced branching. Over-expression of a C-terminal fragment of AP180 that inhibits clathrin-mediated endocytosis affected the laminar distribution and the number of branch points. A dominant-negative synaptotagmin mutant that selectively targets synaptic vesicle cycling, strongly suppressed axon branching. Moreover, axons expressing the mutant synaptotagmin were resistant to the branch-promoting effect of BDNF. These results suggest that synaptic vesicle cycling might regulate BDNF induced branching during the development of the axonal arbor.

Keywords: axon, branching, neurotrophin, synapse, endocytosis, thalamus, neocortex, development

INTRODUCTION

During development, axons form elaborate arbors to make synaptic contacts with their target cells. Neurotrophins, such as brain-derived neurotrophic factor (BDNF), have been shown to regulate axon branching in the developing brain (Cohen et al., 1954; Vicario-Abejón et al., 1998; Cohen-Cory, 1999; Marshak et al., 2007). Neurotrophins secreted from cells in a given region of the brain bind Trk or p75 receptors and activate intracellular signaling pathways in neurons projecting to that region (Chao and Hempstead, 1995). Activated Trk receptors can be internalized at the terminals and undergo retrograde trafficking along the axon via signaling endosomes (for a recent review, see Ascano et al., 2012). Growing evidence suggests that activated Trk receptors recruit different signaling pathways after endocytosis compared to when they remain on the cell surface (Grimes et al., 1996; Watson et al., 2001; Zheng et al., 2008).

Experimental evidence suggests that Trk receptor internalization is achieved through clathrin-mediated endocytosis, as Trk receptors co-localize with clathrin in immunohistochemical analyses (Grimes et al., 1996), BDNF induces the translocation of clathrin and clathrin-related proteins to the plasma membrane (Beattie et al., 2000), and RNAi targeting proteins required for clathrin-mediated endocytosis inhibit BDNF-induced retrograde signaling (Zheng et al., 2008). However, a clathrin-independent endocytic pathway has also been identified (Valdez et al., 2005). Synaptic vesicles are normally endocytosed using clathrin (Granseth et al., 2006; Zhu et al., 2009). Interestingly, Trk receptors and synaptic vesicle markers co-localize at synapses and in endosomes in dissociated cultures of neocortical neurons (Gomes et al., 2006). This indicates that clathrin-dependent endocytosis might be important for axon development.

The aim of this work is to determine if BDNF affects axon branching in the thalamocortical projection and to investigate whether synaptic vesicle cycling might influence this component of development. We demonstrate that exogenously applied and endogenously produced BDNF promote axon arbors in a co-culture system containing explants from the thalamus and cortex (Yamamoto et al., 1989). When clathrin function was reduced, the effect on branching was multifaceted; however, there were indications that endocytosis contributes to branching and synapse formation. When synaptic vesicle cycling was inhibited, branching was markedly reduced and was unresponsive to the branch-promoting effect of BDNF. These results suggest that BDNF and synaptic vesicle cycling are involved in thalamocortical axon branching.

MATERIALS AND METHODS

CELL CULTURE

Thalamocortical slice co-cultures were prepared according to Yamamoto et al. (1989, 1992). Cortical slices were dissected from postnatal day (P) 1 Sprague-Dawley rat pups of either sex. Dorsal thalamic blocks were prepared from embryonic day (E) 15 embryos. The thalamic and cortical slices were plated on a membrane filter (Millicell-CM PICMORG50; Millipore) coated with rat-tail collagen. The culture medium is comprised of a 1:1 mixture

of Dulbecco's modified eagle medium (DMEM) and Ham's F-12 (Invitrogen) containing N2 supplement and 5% Fetal Bovine Serum.

Dissociated thalamic cell cultures were prepared as described previously (Maruyama et al., 2008). Thalamic blocks were prepared from E15 rat embryos. After trituration with 0.1% trypsin containing Calcium-, Magnesium-free Hanks' solution, the cells were plated at 5000 cells/cm^2 in 24-well culture dishes. The culture medium comprised a 1:1 mixture of DMEM and Ham's F-12 supplemented with B27 (Invitrogen).

Dissociated hippocampal cell cultures were prepared according to Granseth et al. (2006). Hippocampi were dissected from E18 embryos, and the cells were dissociated using papain (10 U/ml). The cells were plated on 16-mm borosilicate glass coverslips at 15000–20000 cells/cm^2 to obtain low-density neuronal networks on astrocyte monolayers. The culture medium was initially HEPES-buffered minimum essential medium (MEM) without phenol red, supplemented with N2, and 10% horse serum, but was subsequently changed to Neurobasal media without phenol red (Invitrogen), supplemented with L-glutamine and B27 at 10 days *in vitro* (DIV).

The cultures were maintained at 37°C in an environment of humidified 95% air and 5% CO_2. All procedures were performed according to the guidelines of the animal welfare committees of Osaka University (Japan) or the Home Office regulations (UK).

PROTEIN APPLICATION

Brain-derived neurotrophic factor (Alomone Labs) was applied at 200 ng/ml to the culture medium between 7–14 DIV. A recombinant fragment of the ligand-binding domain of the TrkB receptor fused to the Fc region of human IgG (TrkB.Fc, R&D systems) or the Fc region alone was applied at 1 μg/ml to the culture medium between 7 and 14 DIV.

Cy3-BDNF LOADING

To produce Cy3-conjugated BDNF, 20 μl of a 32 μM BDNF (a generous gift from Sumitomo Seiyaku) solution was incubated with 0.2 μl of a 32 mM Cy3 maleimide (Amersham) solution overnight on ice. The reaction was stopped with 1 μl of 100 mM DTT. To remove free-Cy3 maleimide, the solution was passed through a gel filtration column (AutoSeq G-50, Amersham). The eluate containing Cy3-labeled BDNF was collected and confirmed using SDS-PAGE. The labeled BDNF was added to melted agar at 42°C to a final concentration of 500 μM and rapidly cooled to room temperature. Strips approximately 1 mm× 0.5 mm× 0.5 mm in size were cut and placed in the center of the cortical explant after 10 DIV.

REVERSE TRANSCRIPTION PCR

Total RNA was extracted from thalamic explants, and cDNA was synthesized. A DNA fragment (174 bp) of *trkB* (NM_001163168) was amplified by PCR with a pair of primers (5′-TCTCCAGGAGACGAAATCCAGCC-3′ and 5′-CTGCAGGAAATGGTCACAGA-3′). The cycling parameters were 32 cycles at 95°C (30 s), 55°C (20 s), and 72°C (2 min).

PLASMID CONSTRUCTION

The coding region of a fusion protein of the C-terminal fragment of accessory protein 180 (AP180C) and monomeric red fluorescent protein (mRFP) was cloned into a pCAGGS vector (Niwa et al., 1991; Granseth et al., 2006) or the pTRE-Tight response vector of the Tet-On Advanced gene expression system (Clontech). To optimize the Tet-On Advanced plasmid for use in the slice culture system, the coding region for the reverse tetracycline-controlled transactivator protein (rtTA^{2}M2) was cloned into the pCAGGS vector. No mRFP-AP180C production could be detected through fluorescence microscopy in cells double transfected with pCAGGS-rtA^{2}M2 and pTRE-mRFP-AP180C until doxycycline was added to the culture medium at 12 DIV. The control cells expressed enhanced green fluorescent protein (EGFP) from the pCAGGS vector.

To prepare the synaptotagmin expression plasmids, the coding region for wild-type synaptotagmin 1 (Syt1) or mutant Syt1 (mSyt1) was cloned into an expression vector. Total RNA was extracted from P2 rat brain RNA, and was subjected to reverse transcription (Thermoscript RT-PCR system, Invitrogen). To obtain Syt1 cDNA (Genbank: AJ617615), PCR was carried out with a set of primers (5′-ATCCGCAGTCAGATCGGAAG-3′ and 5′-AAGAGCACTATGTGGGCAGA-3′). The obtained cDNA was subcloned into pGEM-T vector (Promega), and the cDNA containing the coding region was further amplified with primers containing *XhoI* site (5′-GCTCGAGATGGTGAGTGCCAGTCATCC-3′ and 5′-CGGATCCTTCTTGACAGCCAGCATGG-3′) to be cloned into a pCAGGS (Niwa et al., 1991) or pCMV plasmid. To generate the mSyt1 expression plasmid, a Ca^{2+}-binding aspartic acid at position 209 was substituted with asparagine (Nishiki and Augustine, 2004). For this, the whole pCAGGS-Syt1 was subjected to PCR with two complementary primers (5′-GTGGGTGGCTTATCTAATCCCTACGTGAAG-3′ and 5′-CTTCACGTAGGGATTAGATAAGCCACCCAC-3′) containing a mutation site (underlined), which produces the amino acid replacement.

TRANSFECTION

To visualize thalamic axons in thalamocortical slice co-cultures, an expression plasmid (pCAGGS) encoding EGFP or enhanced yellow fluorescent protein (EYFP) was transfected into a small number of thalamic neurons at 1 DIV using an electroporation method as thoroughly described in Uesaka et al. (2005, 2008). The plasmid solution was applied through a fire-polished borosilicate glass micropipette (50-μm tip diameter), and electrical pulses (five to seven trains of 200 square pulses of 1 ms duration at 200 Hz, 500–700 μA) were delivered through a second borosilicate micropipette (tip diameter of 200–300 μm). Two to four sites were electroporated on each thalamic explant. The plasmids, pCAGGS-mSyt1 and pCAGGS-Syt1 were co-transfected with either pCAGGS-EGFP or pCAGGS-EYFP. The plasmid concentrations used were 2.0 and 1.0 μg/μl for pCAGGS-mSyt1/Syt1 and pCAGGS-EGFP/EYFP, respectively. Electroporations using the Tet-On system were performed with a plasmid solution containing pCAGGS-rtA^{2}M2, pTRE-mRFP-AP180C, and pCAGGS-EGFP at 2.0, 2.0, and 1.0 μg/μl, respectively.

Transfections in dissociated cell culture were performed using Lipofectamine 2000 (Invitrogen) according to the manufacturer's instruction. The hippocampal cells were transfected at 12 DIV with pCMV-synaptophysin-pHluorin (SypHy) and pCMV-mRFP. The thalamic cells were transfected with pCMV-mSyt1 and pCMV-EGFP immediately before plating the cells.

IMMUNOHISTOCHEMISTRY

After 14 DIV, the slice cultures were fixed with 4% paraformaldehyde in phosphate buffered saline (PBS) on ice for 1 h and pre-incubated in blocking solution containing 20% normal goat serum and 0.3% Triton X-100 in PBS at room temperature for 3 h. The cultures with EGFP or EYFP labeled axons were incubated with rat monoclonal anti-GFP (1:2000; Nacalai Tesque) at 4°C for 24 h followed by an Alexa488-conjugated anti-rat secondary antibody (1:400, Invitrogen) at 4°C for 12 h. For double labeling of EGPF and mRFP, the cultures were incubated for an additional 24 h at 4°C with rabbit polyclonal anti-RFP (1:2000, Medical and Biological Laboratories Co.) followed by Cy3-conjugated anti-rabbit (1:400; Chemicon) at 4°C for 12 h. The slices were mounted on glass slides using a 50% glycerol mounting medium containing 2.3% 1,4-diazobicyclo[2.2.2]octane (DABCO, Sigma Aldrich), cover-slipped and sealed with nail polish.

MICROSCOPY

Alexa488-labeled axons were visualized through confocal microscopy at a >515 nm fluorescence emission excited at 488 nm using an argon-laser scanning microscope (MRC-600; Bio-Rad). Images were obtained using a 10×, 0.30 NA objective and digitized at a depth of 8 bits. For the Alexa488/Cy3 double-labeled cultures, the fluorescence was sequentially detected for two channels using a Zeiss LSM 700 to avoid emission spectral bleed-through. For Alexa488, a 495–544 nm fluorescence emission from 488 nm diode laser excitation was used. For Cy3, a 560-nm longpass fluorescence emission from 555 nm diode laser excitation was used. Confocal stacks were captured using 10×, 0.45 NA and 40×, 1.3 NA Zeiss objective lenses and digitized at a depth of 16 bits. Overlapping image stacks consisting of 2–20 optical sections 1–5 μm apart were collected to completely visualize the entire axon arbor. Individual optical sections were normalized according to average background fluorescence and collapsed to a single plane using the maximum intensity for each pixel. Axons were reconstructed using the NeuronJ plugin for ImageJ (Meijering et al., 2004). An analysis of the axonal tracings was performed using IgorPro (Wavemetrics). Small processes (<5 μm) were excluded from analysis. The axonal fluorescence intensity was calculated by subtracting the background fluorescence measured using an offset version of the axon trace from the average intensity for pixels along the axon.

SYNAPTIC VESICLE IMAGING

Hippocampal cultures were imaged at 14 DIV using a Photometrics Cascade 512B camera mounted on an inverted Nikon Diaphot 200 microscope with a 40×, 1.3 NA, oil immersion objective. Images were captured at a depth of 16 bits. The cells were superfused with a pH 7.4 buffer containing (in mM) 136 NaCl, 2.5 KCl, 10 HEPES, 1.3 $MgCl_2$, 10 glucose, 2 $CaCl_2$, 0.01 CNQX, and 0.05 dl-APV. All chemicals were obtained from Sigma Aldrich, and the receptor antagonists were purchased from Tocris Cookson. A 100 W Xenon arc lamp was used for illumination. To minimize photobleaching, the light was attenuated 4–8 times using neutral density filters. A Uniblitz VMM-D3 shutter was used to restrict illumination to periods when the camera was actively acquiring images. Action potentials were evoked through field stimulation (20 mA, 1 ms pulses) in a custom-built chamber with two parallel platinum wires 5 mm apart (Royle et al., 2008). The image sequences were imported into IgorPro (Wavemetrics) and analyzed using custom-written scripts. Square regions of interest (ROIs) measuring 4.8 μm × 4.8 μm were positioned on synapses identified by the presence of a >2 SD SypHy fluorescence increase to 40 APs at 20 Hz compared with the baseline noise. The SypHy fluorescence was quantified using a 475:40 nm bandpass excitation filter, a 505 nm dichroic mirror, and a 535:45 nm bandpass emission filter (Omega Filters). For mRFP-AP180C, the filterset comprised a 560:35 nm bandpass excitation filter, a 595 nm dichroic mirror, and a 645:75 nm bandpass emission filter. To subtract the local background fluorescence, the intensity of the ROI displaced in the x- or y-direction was used (Royle et al., 2008). A corrected baseline for individual synapses prior to averaging was used to normalize the traces. All traces were visually inspected before averaging.

STATISTICS

The data are presented as the means ± standard error of the mean (SEM). A value of $P < 0.05$ was considered statistically significant using Student's *t*-test unless otherwise indicated. Multiple comparisons were evaluated using analysis of variance (one-way ANOVA) with a significance level 0.05 with *post hoc* Newman–Keuls test. The Kolmogorov–Smirnov test was used to compare cumulative distributions. All analyses were performed using IgorPro.

RESULTS

BDNF PROMOTES THALAMOCORTICAL AXON BRANCHING

Using co-cultures of the thalamus and cortex (Yamamoto et al., 1989) we set out to investigate the effect of BDNF on thalamocortical axon branching. Low numbers of thalamic cells were transfected with EYFP or EGFP encoding plasmids so individual axons could be observed in the neocortical explant (**Figures 1A,B**). As demonstrated previously, thalamocortical axons branched extensively in the neocortical explant after 14 DIV (**Figure 1E**; Yamamoto et al., 1992; Uesaka et al., 2007). The average number of branch points was 11.4 ± 1.6 ($n = 19$; **Figure 1C**), and consistent with previous studies (Yamamoto et al., 1992; Uesaka et al., 2007), the majority of branches were formed in the upper layers of the cortical explant (**Figures 1D,E**).

When BDNF (200 ng/ml) was added to the culture medium at 10 DIV, thalamic axon branching was substantially increased (**Figure 1F**). At 14 DIV, the number of branch points more than doubled to 26.9 ± 6.2 when BDNF was present ($n = 9$, $P < 0.01$; **Figure 1C**). The laminar location of the BDNF-induced branches seemed normal since the cumulative plot of branch point distribution across the cortical layers was not significantly different from control condition (**Figure 1D**; Kolmogorov–Smirnov test). Thus, BDNF promotes axonal branching without disturbing the laminar pattern of branch formation.

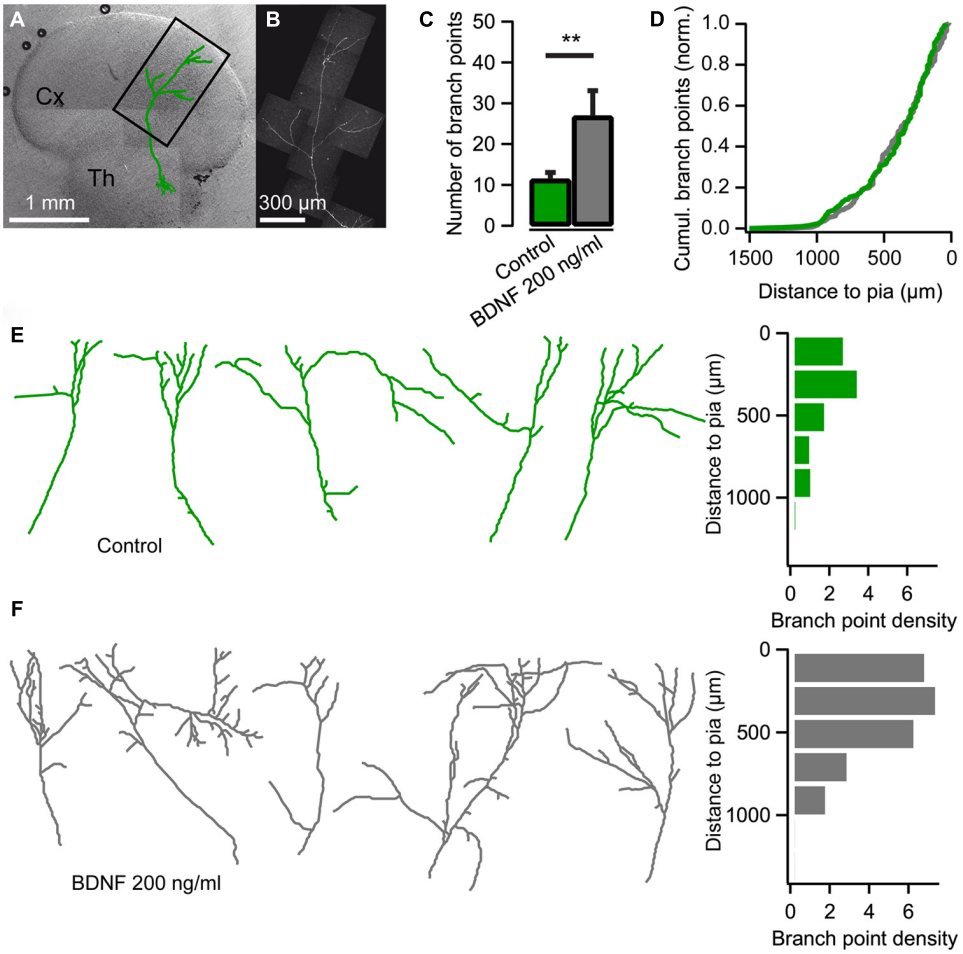

FIGURE 1 | Brain-derived neurotrophic factor (BDNF) promotes axon branching in thalamocortical co-cultures. **(A)** Reconstruction of a thalamic neuron expressing EYFP (green) superimposed on a differential interference contrast-enhanced micrograph of a thalamocortical co-culture. *Cx* cerebral cortex; *Th* thalamus. **(B)** Confocal micrograph of the axon from the neuron reconstructed in A. **(C)** Bar diagram for the average number of axonal branch points (the number of times the axon bifurcates) when BDNF is added to the medium. The error bars represent SEM. $^{**}P < 0.01$. **(D)** Cumulative plot of branch-point location with respect to pial surface for control cultures (green) and cultures treated with BDNF (gray). **(E)** Reconstructions of representative axons from thalamic cells in the neocortical explant and a histogram showing the distribution of axonal branch points with respect to the pial surface. Branch-point density = number of branch points/number of axons. **(F)** Reconstructions of representative axons from thalamic cells in the neocortical explant when BDNF was added to the medium. A histogram plotting the distribution of the axonal branch points with respect to the pial surface is shown on the right.

To investigate the role of endogenous BDNF, TrkB.Fc was added to the culture medium at 10 DIV to sequester the existing neurotrophin. We found that branch formation of thalamocortical axons was inhibited in the presence of TrkB.Fc, whereas axons grew up to the pial surface. The number of axonal branch points at 14 DIV was significantly reduced in the presence of TrkB.Fc (6.23 ± 0.91, $n = 17$, $P < 0.001$; **Figures 2B,C**) compared to the control condition when the Fc without TrkB was used (13.1 ± 1.49, $n = 18$; **Figures 2A,C**). Reverse transcription PCR on thalamic explants revealed that *trkB* was expressed in the cultured thalamic cells (**Figure 2D**), indicating that exogenous and endogenous BDNF can promote thalamocortical axon branching via TrkB receptors.

We further investigated whether exogenous BDNF may be taken up from thalamocortical axon terminals. To present neurotrophin to the thalamic axons at a site remote from the cell bodies and their dendrites, agar strips containing 500 µM of Cy3-tagged BDNF were placed on the neocortical explant side at a distance of >1 mm from the thalamic explant (**Figure 2E**). After a 5-day incubation, Cy3-BDNF fluorescence was present at the soma of thalamic neurons (**Figure 2F**). It appears that the labeled BDNF was taken up by the terminals and transported retrogradely to the thalamus.

CLATHRIN-MEDIATED ENDOCYTOSIS IN THALAMOCORTICAL AXONS

Several studies support clathrin-mediated endocytosis as the mechanism for internalizing BDNF bound to TrkB receptors (Grimes et al., 1996; Beattie et al., 2000; Zheng et al., 2008). Thus, we examined whether a clathrin-dependent endocytic mechanism is important for thalamic axon branching. Clathrin-mediated endocytosis can be inhibited through the over-expression of

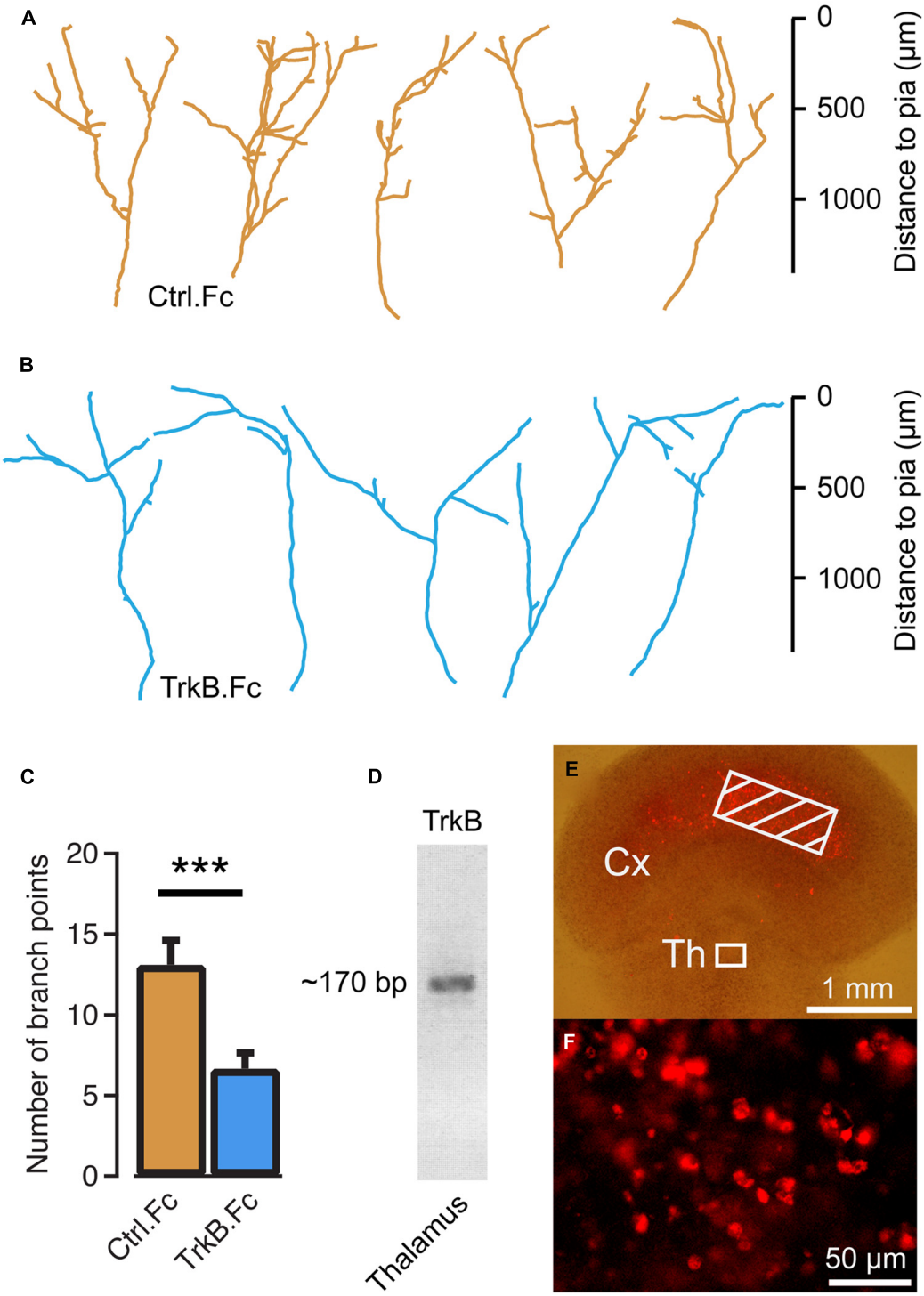

FIGURE 2 | Endogenous brain-derived neurotrophic factor (BDNF) supports thalamocortical axon branching. (A) Reconstructions of representative axons in thalamocortical co-cultures treated with the Fc region of human IgG. Note the similar morphology to untreated controls in **Figure 1E**. **(B)** Reconstructions of representative thalamocortical axons when TrkB.Fc was added to the culture to remove endogenously produced BDNF. **(C)** Bar diagram for average number of branch points for TrkB.Fc treatment and Fc controls. The error bars represent SEM. $***P < 0.001$. **(D)** Reverse transcriptase PCS product from thalamic explants in co-cultures. The ~170 bp PCR product suggests that thalamic cells produce TrkB. **(E)** BDNF tagged with Cy3 was molded in strips of agar and applied to the neocortical explant (hatched region) in thalamocortical co-cultures. **(F)** Neurons in the thalamic explants contained Cy3-BDNF 5 days later. Fluorescence micrograph from the boxed region in E.

AP180C, which contains several clathrin- and adaptor protein 2 (AP2)-binding domains (Ford et al., 2001; Granseth et al., 2006). However, when AP180C was introduced into thalamic cells through electroporation at the second day *in vitro*, the axons did not extend their axons more than halfway into the neocortical explant at 14 DIV (**Figure 3C**). The AP180C transfection seemingly resulted in a defect in initial axonal growth.

To induce the expression at the appropriate point in time when thalamic axons are forming branches after reaching the target layer, an inducible Tet-On expression system was used. For this, thalamocortical neurons were transfected with pCAGGS-rtA^{2}M2, pTRE-mRFP-AP180C and pCAGGS-EGFP (see Materials and Methods) at 1–2 DIV, and doxycycline was added to the culture medium at 12 DIV. When axon branching was examined two days later, the number of branch points (11.8 ± 2.2, $n = 19$) was not significantly different from control axons (12.3 ± 1.4, $n = 19$; **Figures 3A,B,E**). However, the location of branches was affected (**Figure 3D**; $P < 0.05$, Kolmogorov–Smirnov test). More branch points were present in the deeper and the most superficial layer of the cortical explant, and less branch points were found in the appropriate laminae (**Figure 3B**).

The mislocalization of branch points in AP180C-overexpressing thalamic axons could be from defects in clathrin-mediated endocytosis as well as other clathrin-mediated cellular mechanisms. The C-terminal fragment of AP180C contains AP2- and

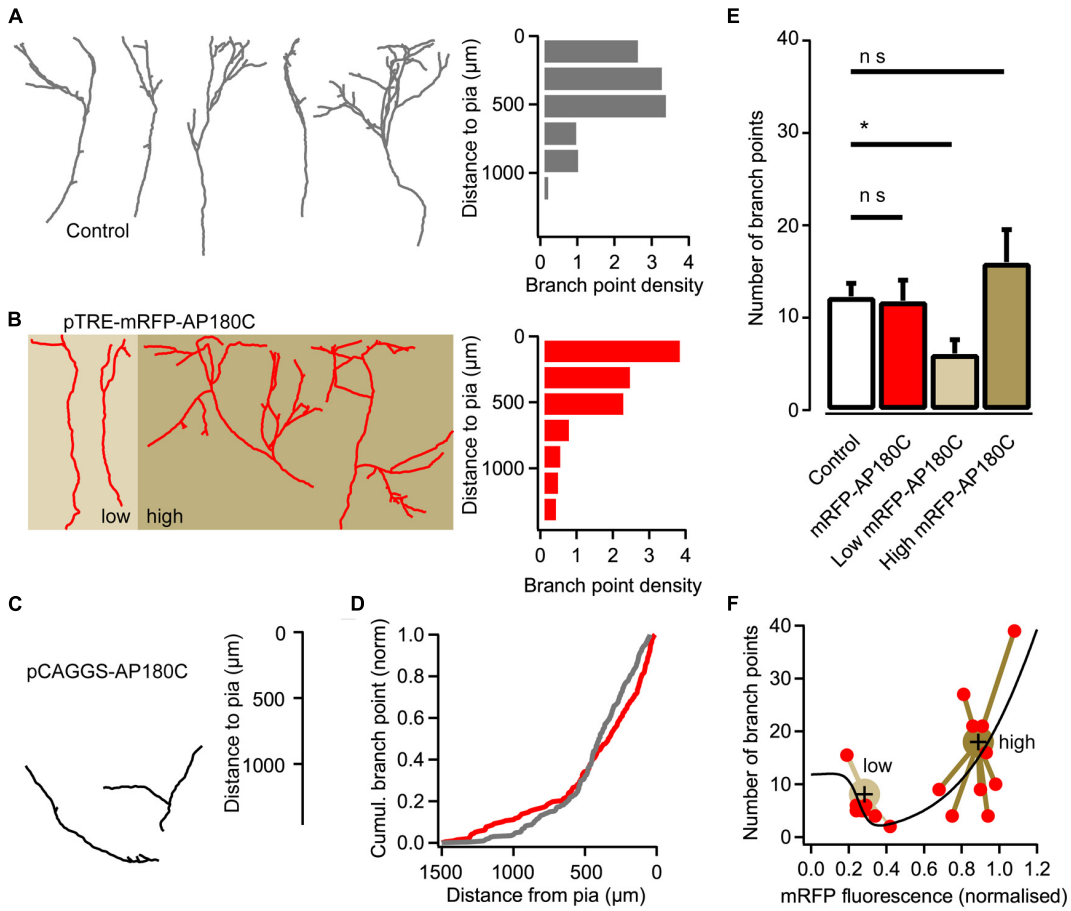

FIGURE 3 | Reducing clathrin-mediated endocytosis with AP180C affects axon branching. **(A)** Reconstructions of representative axons from thalamic cells in the neocortical explant and a histogram showing the distribution of axonal branch points with respect to the pial surface. Control axons exposed to doxycycline for two days. Branch-point density = number of branch points/number of axons. **(B)** Reconstructions of representative axons from thalamic cells where the expression of mRFP-AP180C was induced with doxycycline two days earlier. A histogram showing the distribution of axonal branch points with respect to the pial surface is shown on the right. Axons expressing low amount of mRFP-AP180C are against a light brown background. Axons expressing high amount of the construct are against a dark brown background. **(C)** Reconstructions of representative axons from thalamic cells expressing mRFP-AP180C for 13 days. **(D)** Cumulative plot of the branch-point location with respect to the pial surface for doxycycline-induced mRFP-AP180C-expressing axons (red) and controls (gray). **(E)** Average number of branch points for doxycycline-exposed controls and induced mRFP-AP180C-expressing cells. When mRFP-AP180C-expressing cells were divided into two groups according to a k-means clustering algorithm (see panel **F**), the group with low mRFP-AP180C fluorescence had fewer branch points than the controls. The error bars represent SEM. $^*P < 0.05$ (ANOVA). **(F)** Number of branch points plotted against mRFP-AP180C fluorescence intensity. The black line illustrates opposing effects on branch number from two AP180C-mediated mechanisms using the sum of two sigmoid functions with opposite signs and parameters fit using least sum of squares. Large markers are centroids from a k-means clustering analysis with the relevant data points connected with lines.

clathrin-binding domains but lacks the membrane-binding N-terminal domain (Ford et al., 2001; Zhao et al., 2001). Thus, over-expression could have two molecular consequences: (1) competitive antagonism of endogenous AP180 when clathrin is recruited to AP2 during endocytosis, and (2) clathrin sequestration in the cytosol that diminish the availability of this molecule for endocytosis and other clathrin-mediated cellular processes (Zhao et al., 2001). The first mechanism would be specific for endocytosis, while the second mechanism would affect all clathrin-mediated cellular processes in the neuron. Unassembled clathrin constitutes as much as 0.1% of the total cell-protein mass (Goud et al., 1985); therefore, clathrin-sequestration requires a high concentration of AP180C. Since the AP180C is tagged with mRFP we can get an estimate of intracellular concentration by measuring fluorescence intensity in maximum-intensity z projections of confocal-image stacks. To examine if the two mechanisms have different dose response curves we fitted the sum of two sigmoid curves for branch number as a function of fluorescence intensity (**Figure 3F**). When expression of mRFP-AP180C was low, the number of branches was diminished, and with increasing concentration the number of branch points increased. A k-means clustering algorithm sorted the data into two groups (**Figure 3F**). Neurons with low levels of mRFP-AP180C had fewer branch points than the controls ($P < 0.05$, ANOVA, $n = 8$; **Figure 3E**). The number of branch points in neurons with high expression of mRFP-AP180C was not significantly different to controls (ANOVA, $n = 11$; **Figure 3E**) although branches were often mislocalized ($P < 0.05$, Kolmogorov–Smirnov test). Because of the increased number of mislocalized branches, it seems reasonable to infer that branching in the right cortical laminae might be reduced also in neurons expressing high levels of AP180C.

The sequestration of intracellular clathrin at high concentration of AP180C has been demonstrated using immunohistochemistry (Zhao et al., 2001). An additional mode of action that requires less AP180C, such as the competitive antagonism of endogenous AP180, has not yet been demonstrated in living cells. To investigate if AP180C could act in this way, we investigated if the clathrin-mediated endocytosis of synaptic vesicles was affected when the molecule was present at low concentration. Neurons in hippocampal cultures were double-transfected using vectors for mRFP-AP180C and SypHy (Granseth et al., 2006; Zhu et al., 2009). The cells were incubated for less than 48 h for expression, and the synapses with the lowest mRFP-AP180C fluorescence intensity were selected for separate analysis (20% of the total pool). The speed of clathrin-mediated endocytosis, as measured using the vesicle cycling probe SypHy, was markedly reduced compared with that of the controls (**Figure 4A**). The slowing of the vesicle membrane uptake in the 20% of synapses with the lowest mRFP-AP180C expression was not substantially different from that seen for the entire mRFP-AP180C expressing group in general (**Figure 4A**). Although there was no statistically significant reduction in the total number of synaptic vesicles in synapses with low expression when measured by NH_4 dequenching ($n = 42$), the readily releasable pool of vesicles, that is, the number of vesicles released after 40 action potentials at 20 Hz, was markedly reduced ($P < 0.01$; **Figure 4B**). Thus, clathrin-mediated endocytosis is impaired in the 20% of synapses with mRFP-AP180C levels just above our detection limit for live fluorescence imaging (>2 SEM of background). This result is consistent with the possibility that AP180C acts as an antagonist to endogenous AP180, supporting the interpretation that the reduction of axon branches at low AP180C expression level results from inhibition of clathrin-mediated endocytosis.

Axon branching is closely associated with the formation of synapses (Alsina et al., 2001; Ruthazer et al., 2006; Fukunishi et al., 2011). We examined the varicosities that are the likely locations of synapses along the axons in the hippocampal cultures. SypHy fluorescence responses to NH_4 were usually localized to these varicosities, indicating that they contain large numbers of labeled synaptic vesicles (**Figure 4C**). Axons expressing mRFP-AP180C had fewer of these putative synapses per unit length of axon (0.84 ± 0.07 synapses/10 μm, $n = 8$, **Figure 4D**) compared to controls (1.21 ± 0.10 synapses/10 μm, $n = 9$, $P < 0.01$). The smaller number of putative synapses in AP180C-expressing axons in hippocampal culture is in accordance with the decreased number of axonal branches in thalamocortical co-cultures.

SYNAPTIC VESICLE CYCLING AND BDNF SIGNALING

The AP180C construct potentially slows clathrin-mediated endocytosis of both Trk receptors and synaptic vesicles. To selectively target synaptic vesicle cycling, we over-expressed mSyt1 where a Ca^{2+} binding aspartic acid (209) in the C2B domain was substituted with asparagine (Mackler et al., 2002; Nishiki and Augustine, 2004). This will reduce the exocytosis of synaptic vesicles with an accompanying reduction in endocytic activity at the terminals. The mSyt1 and EYFP expression vectors were co-electroporated into thalamic cells in thalamocortical co-cultures at 2 DIV. At 14 DIV, mSyt1-expressing thalamocortical axons showed less developed axonal arbors (average number of branch points $= 2.7 \pm 0.6$, $n = 19$, $P < 0.001$; **Figures 5A,E**). High-resolution fluorescence microscopy showed that axonal varicosities were less frequent along axons expressing mSyt1 than axons expressing wild-type Syt1 ($P < 0.01$; **Figures 5C,D**). Fewer putative presynaptic boutons per unit length and less extensive axonal arbors suggest that the total number of synaptic connections was severely reduced in neurons with synaptic vesicles carrying the mutant Syt1 protein.

It is unlikely that the small axonal arbors in mSyt1-expressing axons resulted from late-arriving axons having less time to develop branches and synapses. The mSyt1-expressing thalamocortical axons extended well into the upper layers of the neocortical explants (**Figure 5A**), which was different from the obvious growth defect associated with AP180C without the inducible vector (**Figure 3C**). To investigate whether there might be a subtle defect in axon growth when expressing mSyt1, we characterized neurite outgrowth and elongation in dissociated cell culture of E15 thalamic neurons (**Figures 6A,B**). The growth cones were not different from the controls (**Figures 6C,D**), and after 5 days in culture, neurite length of mSyt1-expressing thalamic cells (191 ± 15 μm, $n = 32$) was similar to that of the controls (176 ± 14 μm, $n = 27$). Thus, there is no reason to suspect that the mSyt1 axons arrive in the cortex any later than the controls.

To determine if the reduction in branch number in mSyt1 expressing axons could be related to BDNF signaling, we

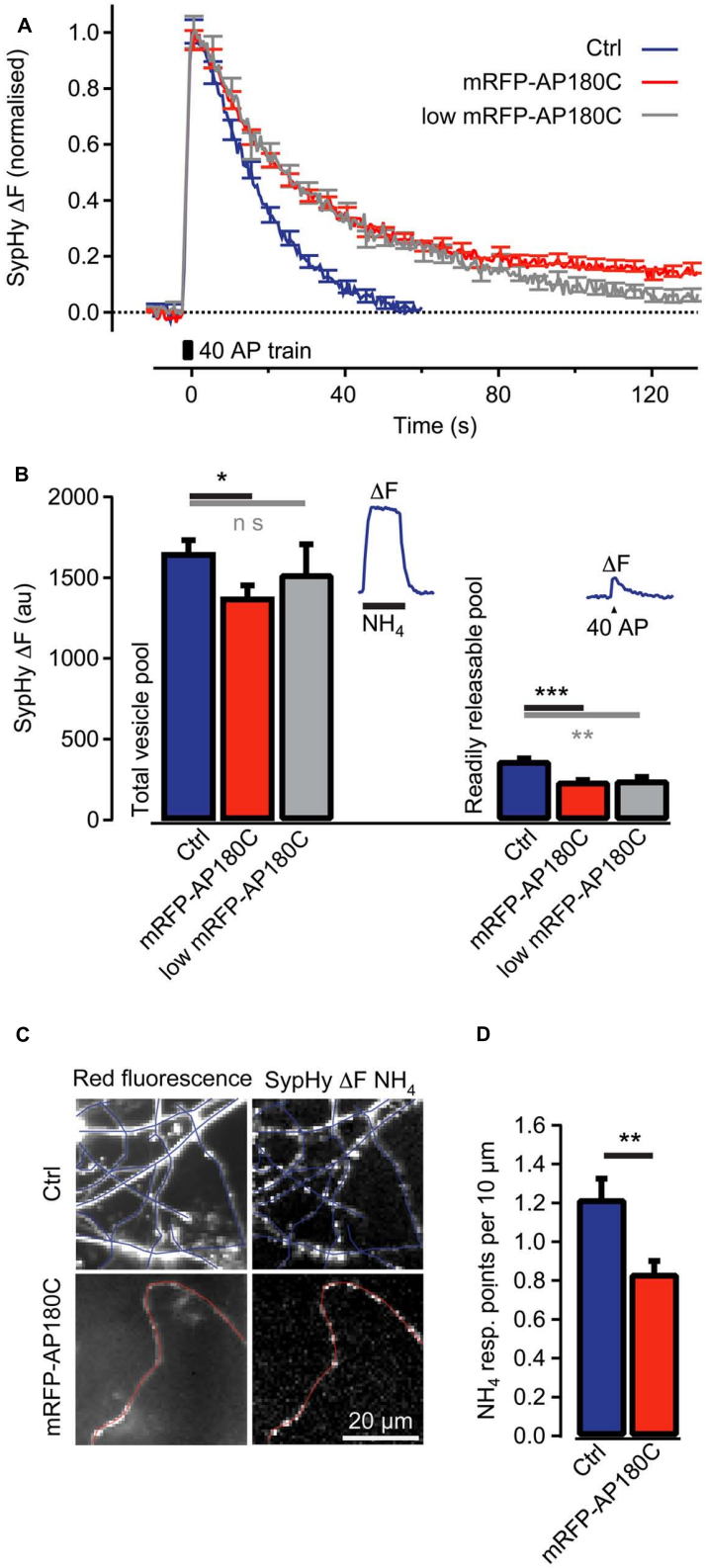

FIGURE 4 | Clathrin-mediated endocytosis of synaptic vesicle membrane is reduced in synapses even when mRFP-AP180C content is low. (A) Change in SypHy fluorescence intensity (normalized to the peak) after 40 action potentials at 20 Hz (40 AP train). During the action potential train, the fluorescence intensity increased from exocytosis of synaptic

(Continued)

FIGURE 4 | Continued
vesicles when SypHy in the acidic lumen of vesicles was exposed to the neutral pH of the extracellular space. After termination of the action potential train, the fluorescence returned to baseline when SypHy was endocytosed with the vesicle membrane and the vesicle lumen re-acidified. The blue trace indicates control synapses with no detectable mRFP-AP180C fluorescence. The red line indicates entire population of synapses containing mRFP-AP180C. The gray trace indicates the 20% of synapses with the least intense mRFP-AP180C fluorescence. **(B)** Total vesicle pool estimated through the fluorescence change from collapsing the pH of all synaptic vesicles using an NH_4-containing buffer at pH 7.4. Readily releasable pool estimated from the fluorescence change after 40 action potentials at 20 Hz. The error bars represent SEM. $*P < 0.05$, $**P < 0.01$, $***P < 0.001$. The inset shows the average response for control synapses in one culture to illustrate the protocol. **(C)** Micrographs of red fluorescence in control axons (Ctrl) expressing mRFP and axons expressing mRFP-AP180C and the increase in green fluorescence (ΔF) from SypHy, induced by NH_4-containing buffer. Blue and red lines are tracings along the axons. **(D)** Average number of points per 10 μm of axon that responds to NH_4-containing buffer. These points where SypHy containing vesicles are accumulated are the locations of putative synapses. The error bars represent SEM. $*P < 0.05$, $**P < 0.01$, $***P < 0.001$.

added recombinant BDNF to the culture medium at the same concentration that induced the marked expansion of axonal branch points in naïve axons (**Figure 1C**). If the effect of synaptic vesicle cycling on axonal branching is unrelated to BDNF signaling, exogenously applied neurotrophin should be efficient at increasing branch numbers. The axons expressing mSyt1 were however unresponsive to the branch-promoting effect of BDNF (**Figures 5B,E**). The average number of branch points was 4.8 ± 1.3 ($n = 12$), which was not significantly different from untreated mSyt1 axons. BDNF-treated mSyt1 neurons remained significantly smaller than untreated wild-type control axons ($P < 0.01$). Thus, inhibiting synaptic vesicle release through mSyt1 desensitizes thalamocortical axons to the branch-promoting effects of BDNF, suggesting that synaptic vesicle cycling might facilitate this aspect of BDNF signaling.

DISCUSSION

The present study demonstrates that BDNF promotes the development of branches in thalamocortical axons. Both exogenously added BDNF and endogenously produced neurotrophin, acting on TrkB receptors in the thalamic neurons, increase axonal branching during development. Although the results from the experiments targeting clathrin function were complex, there were indications that endocytosis supports branching and synapse formation. When synaptic vesicle cycling was inhibited, branching was markedly reduced and was unresponsive to the branch-promoting effect of BDNF. We propose a hypothesis that synaptic vesicle cycling enhaces BDNF signaling via clathrin-dependent endocytosis of activated TrkB receptors.

BRAIN-DERIVED NEUROTROPHIC FACTOR PROMOTES THALAMOCORTICAL AXON BRANCHING

Wiesel and Hubel (1963) showed that the projection from the thalamus will segregate into eye-specific columns in the primary visual cortex after eye-opening. The development of these ocular dominance columns can be inhibited by intracortical injections of BDNF (Cabelli et al., 1995; Galuske et al., 1996) or by removal of endogenous BDNF via TrkB.Fc (Cabelli et al., 1997). Moreover, BDNF is known to be involved in dendritic development of cortical neurons (McAllister et al., 1995, 1997). Until now, the effects of BDNF on thalamocortical axon branching have not been investigated. The present paper demonstrates that BDNF is a potent branch-promoting factor for these axons (**Figures 1** and **2**). BDNF has been known to act both as a retrograde factor (Du and Poo, 2004; Zweifel et al., 2005), and as an anterograde factor (Altar et al., 1997; Conner et al., 1997; Caleo et al., 2000; Kohara et al., 2001; Kojima et al., 2002). Since exogenous BDNF applied only to the cortical portion of the co-culture system can be taken up by thalamic axons and transported to the soma (**Figures 2E,F**), BDNF seems to function as a retrograde signal for the developing thalamocortical neurons.

Recently, Jeanneteau et al. (2010) identified a mechanism by which BDNF promotes branch formation in neocortical pyramidal neurons. BDNF-TrkB activation enhances MAP kinase phosphatase-1 (MKP-1) function by inducing its production and by protecting it from degradation. This phosphatase deactivates c-jun N-terminal kinase (JNK) leading to destabilization of cytoskeletal components and promoting branch formation. Interestingly, selective administration of BDNF to axons robustly induced MKP-1 expression. It is unknown if this retrograde signal might rely on endocytosis and axonal transport of TrkB signaling endosomes.

SYNAPTIC VESICLE CYCLING SUPPORTS AXONAL ARBORIZATIONS

When an action potential reaches the presynaptic bouton, neurotransmitter is released through exocytosis of small synaptic vesicles. The vesicle membrane that has fused with the presynaptic membrane will be recycled to make new vesicles via clathrin-mediated endocytosis (Granseth et al., 2006; Zhu et al., 2009). AP180C slowed down clathrin-mediated endocytosis of synaptic vesicles, but also reduced neurotransmitter release (**Figure 4B**). This is similar to the effect on synaptic vesicle exocytosis seen in the *Drosophila* AP180 knockout (Bao et al., 2005) and when AP2 function is inhibited in the Calyx of Held (Hosoi et al., 2009). While the direct action of mSyt1 was to inhibit neurotransmitter release, it also reduces endocytosis as there is less vesicular membrane to be recycled. In the present study, both manipulations reduced thalamocortical axon branching in the target layer (**Figures 3E** and **5E**), suggesting that synaptic vesicle cycling promotes axon arbor formation.

A recent investigation of thalamocortical axon branching in a SNAP-25 knockout mouse came to a different conclusion (Blakey et al., 2012). Branching was similar in thalamocortical co-cultures when the thalamic explant was prepared from knockouts or from wild-type mice. The conflicting results might be explained by differences in the magnitude and distribution of the induced defects in vesicle cycling. Synchronous synaptic vesicle release is completely absent in the SNAP-25 knockout while mSyt1 and AP180C cause graded reductions of vesicle cycling. All neurons in the thalamic explant from the knockout mouse have the defect in transmitter release while only a small proportion of neurons express mSyt1 or AP180C after electroporation.

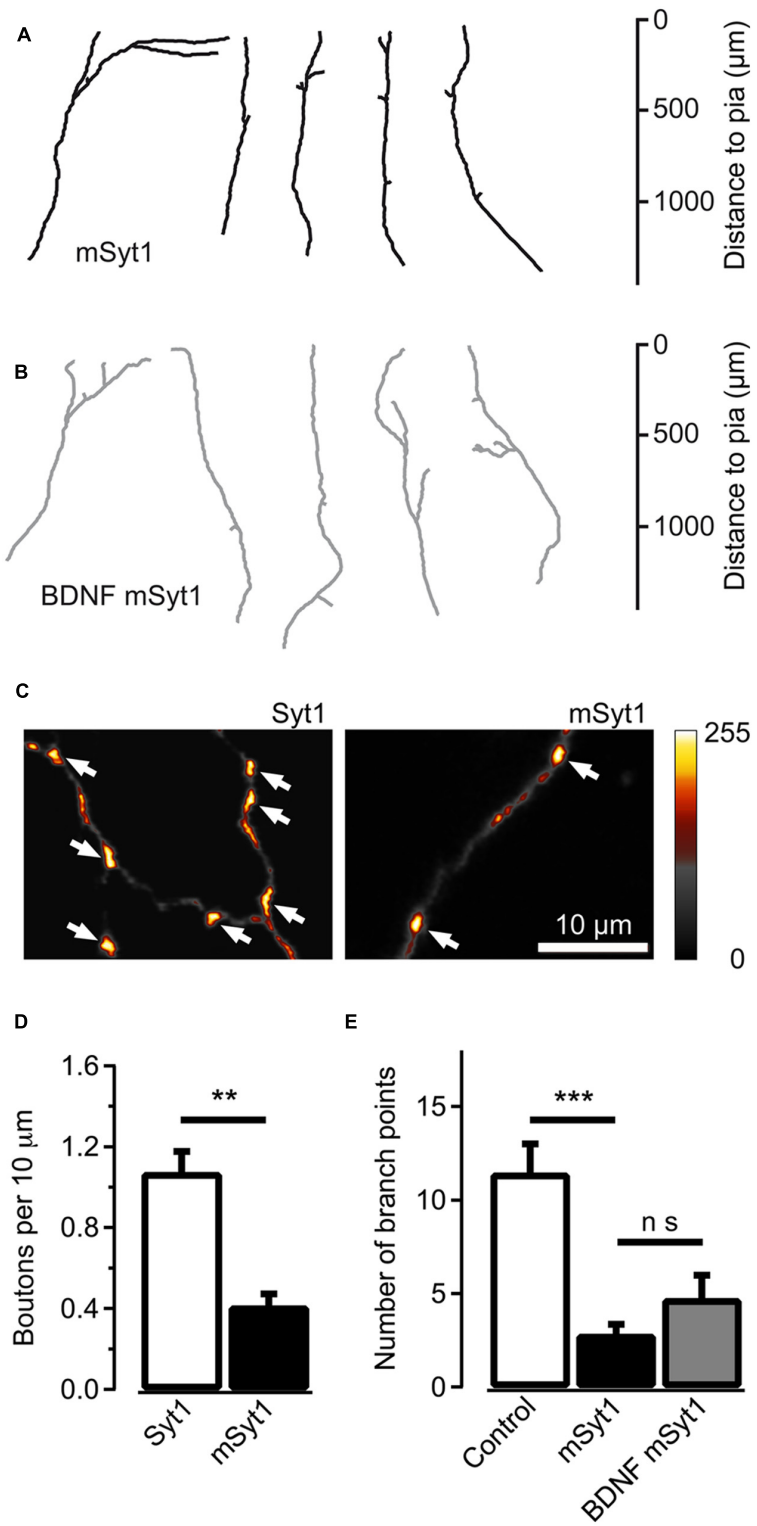

FIGURE 5 | Reducing synaptic vesicle cycling produces less axonal branches. **(A)** Reconstructed axons of thalamic neurons expressing mSyt1. **(B)** Reconstructed axons of mSyt1-expressing neurons supplemented with 200 ng/ml of brain-derived neurotrophic factor (BDNF). Note the similar morphology to the axons without BDNF. **(C)** Pseudocolor micrographs of axons expressing wild type Syt1 or mSyt1. The arrows indicate the locations of varicosities where the EYFP fluorescence accumulates, indicative of presynaptic boutons. **(D)** Average number of fluorescence accumulations per 10 µm of axon in the control cells and neurons expressing mSyt1. **(E)** The average number of branch points is reduced in axons expressing mSyt1 and is not significantly affected by BDNF present in the growth medium. The error bars represent SEM. $^{**}P < 0.01$, $^{***}P < 0.001$.

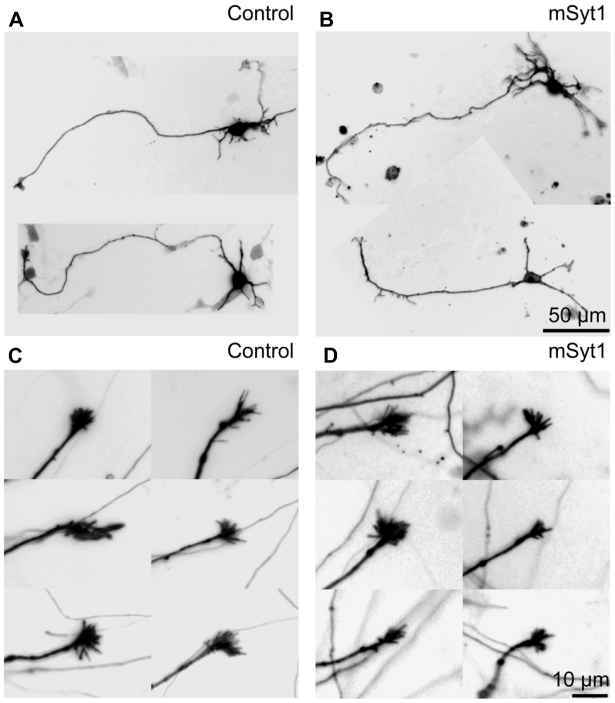

FIGURE 6 | Axon growth is normal in thalamic neurons expressing mutant synaptotagmin. **(A)** Representative fluorescence micrographs of thalamic dissociated neurons in culture. The LUTs are inverted for clarity. **(B)** Representative neurons expressing mSyt1. **(C)** Representative fluorescence micrographs of axonal growth-cones of thalamic neurons in culture. **(D)** The growth cones in the axons of thalamic neurons expressing mSyt1 show a normal morphology.

A HYPOTHESIZED ROLE FOR ENDOCYTOSIS IN ACTIVITY-DEPENDENT AXON COMPETITION

The mechanism that initiates the endocytic uptake of activated Trk receptors is unknown. Since endocytosis of synaptic vesicle membrane and Trk receptors occurs at the same axonal location (Gomes et al., 2006; Granseth et al., 2006), and use the same core components for endocytic internalization (Grimes et al., 1996; Beattie et al., 2000; Granseth et al., 2006; Zheng et al., 2008; Zhu et al., 2009; McMahon and Boucrot, 2011), we would like to propose the hypothesis that Trk receptor endocytosis is enhanced by synaptic vesicle endocytosis following transmitter release. This hypothesis not only explains the experimental findings of the present study, but also provides a mechanism for activity-dependent competition and cooperation between axon arbors during development.

Neuronal activity increases the exocytic secretion of BDNF from neocortical cells (Kolarow et al., 2007; Matsuda et al., 2009). If neighboring axons compete for the supply of this retrograde factor and endocytosis of activated TrkB receptors is enhanced during a time-window defined by synaptic vesicle endocytosis, the thalamic axons that reliably deporarize the target neuron will have a competitive advantage over those that do not. The enhanced survival and growth of stronger axons over weaker axons with disparate action potential firing pattern will lead to a gradual activity-dependent refinement of innervation where relevant axons are kept while unrelated axons retract.

This hypothesis can explain the effects we observed with AP180 and mSyt1. Axons in which vesicle cycling was impaired by mSyt1 would rapidly fail in the competition against normal axons, leading to the markedly reduced axonal arbors we obtained in the present study (**Figure 5E**). Axons with slowed clathrin-mediated endocytosis produced by AP180C would also be at a competitive disadvantage because the mechanism for Trk receptor internalization is impaired. However, since synaptic vesicle endocytosis is slowed-down, the time window during which Trk receptor internalization is enhanced by synaptic activity might be increased. Thus, the effect on branching might be less pronounced, as we observed in the present investigation (**Figure 3E**).

In the proposed hypothesis, AP180C and mSyt1 reduce axon branching through their effects on clathrin-mediated endocytosis. An alternative hypothesis would be that they inhibit branching through their effect on exocytosis. Branching and synapse formation are closely related activities in developing axons (Alsina et al., 2001; Fukunishi et al., 2011). Neurotransmitter release is important for the maturation of synaptic connections (Waites et al., 2005) and is unarguably affected by AP180C and mSyt1 (**Figure 4B**; Mackler et al., 2002; Nishiki and Augustine, 2004,). However, *de novo* formation of synapses does not require neurotransmission (Waites et al., 2005), and it is the appearance of new synapses that seems to be relevant for BDNF induced axon branching (Alsina et al., 2001). So even though exocytosis cannot be excluded, endocytosis appears to be a more likely mechanism.

ACKNOWLEDGMENTS

This study was financially supported through funding from Grants-in-Aid on Innovative Areas "Mesoscopic Neurocircuity" (23115102) from the Japanese Ministry of Education, Culture, Sports, Science, and Technology and For Scientific Research (20300110, 23300118) from the Japan Society for the Promotion of Sciences to Nobuhiko Yamamoto; Wellcome Trust to Leon Lagnado; the Swedish Research Council (3050, 2862), Knut and Alice Wallenberg Foundation and Carl and Axel Molin i Motala minne-foundation to Björn Granseth. Björn Granseth was a Japan Society for the Promotion of Sciences visiting scientist in Osaka. We would like to thank Dr. Harvey McMahon, Dr. Roger Tsien, and Dr. Stephen Royle for providing plasmids used in this study and Dr. Sarah H. Lindstrom for critically reading the manuscript.

REFERENCES

Alsina, B., Vu, T., and Cohen-Cory, S. (2001). Visualizing synapse formation in arborizing optic axons in vivo: dynamics and modulation by BDNF. *Nat. Neurosci.* 4, 1093–1101. doi: 10.1038/nn735

Altar, C. A., Cai, N., Bliven, T., Juhasz, M., Conner, J. M., Acheson, A. L., et al. (1997). Anterograde transport of brain-derived neurotrophic factor and its role in the brain. *Nature* 389, 856–860. doi: 10.1038/39885

Ascano, M., Bodmer, D., and Kuruvilla, R. (2012). Endocytic trafficking of neurotrophins in neural development. *Trends Cell Biol.* 22, 266–273. doi: 10.1016/j.tcb.2012.02.005

Bao, H., Daniels, R. W., Macleod, G. T., Charlton, M. P., Atwood, H. L., and Zhang, B. (2005). AP180 maintains the distribution of synaptic and vesicle proteins in the nerve terminal and indirectly regulates the efficacy of Ca2+-triggered exocytosis. *J. Neurophysiol.* 94, 1888–1903. doi: 10.1152/jn.00080.2005

Beattie, E. C., Howe, C. L., Wilde, A., Brodsky, F. M., and Mobley, W. C. (2000). NGF signals through TrkA to increase clathrin at the plasma membrane and enhance clathrin-mediated membrane trafficking. *J. Neurosci.* 20, 7325–7333.

Blakey, D., Wilson, M. C., and Molnár, Z. (2012). Termination and initial branch formation of SNAP-25-deficient thalamocortical fibres in heterochronic organotypic co-cultures. *Eur. J. Neurosci.* 35, 1586–1594. doi: 10.1111/j.1460-9568.2012.08120.x

Cabelli, R. J., Hohn, A., and Shatz, C. J. (1995). Inhibition of ocular dominance column formation by infusion of NT-4/5 or BDNF. *Science* 267, 1662–1666. doi: 10.1126/science.7886458

Cabelli, R. J., Shelton, D. L., Segal, R. A., and Shatz, C. J. (1997). Blockade of endogenous ligands of TrkB inhibits formation of ocular dominance columns. *Neuron* 19, 63–76. doi: 10.1016/S0896-6273(00)80348-7

Caleo, M., Menna, E., Chierzi, S., Cenni, M. C., and Maffei, L. (2000). Brain-derived neurotrophic factor is an anterograde survival factor in the rat visual system. *Curr. Biol.* 10, 1155–1161. doi: 10.1016/S0960-9822(00)00713-2

Chao, M. V., and Hempstead, B. L. (1995). p75 and Trk: a two-receptor system. *Trends Neurosci.* 18, 321–326. doi: 10.1016/0166-2236(95)93922-K

Cohen, S., Levi-Montalcini, R., and Hamburger, V. (1954). A nerve growth-stimulating factor isolated from sarcomas 37 and 180. *Proc. Natl. Acad. Sci. U.S.A.* 40, 1014–1018. doi: 10.1073/pnas.40.10.1014

Cohen-Cory, S. (1999). BDNF modulates, but does not mediate, activity-dependent branching and remodeling of optic axon arbors in vivo. *J. Neurosci.* 19, 9996–10003.

Conner, J. M., Lauterborn, J. C., Yan, Q., Gall, C. M., and Varon, S. (1997). Distribution of brain-derived neurotrophic factor (BDNF) protein and mRNA in the normal adult rat CNS: evidence for anterograde axonal transport. *J. Neurosci.* 17, 2295–2313.

Du, J. L., and Poo, M. M. (2004). Rapid BDNF-induced retrograde synaptic modification in a developing retinotectal system. *Nature* 429, 878–883. doi: 10.1038/nature02618

Ford, M. G., Pearse, B. M., Higgins, M. K., Vallis, Y., Owen, D. J., Gibson, A., et al. (2001). Simultaneous binding of PtdIns(4,5)P2 and clathrin by AP180 in the nucleation of clathrin lattices on membranes. *Science* 291, 1051–1055. doi: 10.1126/science.291.5506.1051

Fukunishi, A., Maruyama, T., Zhao, H., Tiwari, M., Kang, S., Kumanogoh, A., et al. (2011). The action of Semaphorin7A on thalamocortical axon branching. *J. Neurochem.* 118, 1008–1015. doi: 10.1111/j.1471-4159.2011.07390.x

Galuske, R. A., Kim, D.-S., Castren, E., Thoenen, H., and Singer, W. (1996). Brain-derived neurotrophic factor reverses experience dependent synaptic modifications in kitten visual cortex. *Eur. J. Neurosci.* 8, 1554–1559. doi: 10.1111/j.1460-9568.1996.tb01618.x

Gomes, R. A., Hampton, C., El-Sabeawy, F., Sabo, S. L., and McAllister, A. K. (2006). The dynamic distribution of TrkB receptors before, during, and after synapse formation between cortical neurons. *J. Neurosci.* 26, 11487–11500. doi: 10.1523/JNEUROSCI.2364-06.2006

Goud, B., Huet, C., and Louvard, D. (1985). Assembled and unassembled pools of clathrin: a quantitative study using an enzyme immunoassay. *J. Cell Biol.* 100, 521–527. doi: 10.1083/jcb.100.2.521

Granseth, B., Odermatt, B., Royle, S. J., and Lagnado, L. (2006). Clathrin-mediated endocytosis is the dominant mechanism of vesicle retrieval at hippocampal synapses. *Neuron* 51, 773–786. doi: 10.1016/j.neuron.2006.08.029

Grimes, M., Zhou, J., Beattie, E., Yuen, E., Hall, D., Valletta, J., et al. (1996). Endocytosis of activated TrkA: evidence that nerve growth factor induces formation of signaling endosomes. *J. Neurosci.* 16, 7950–7984.

Hosoi, N., Holt, M., and Sakaba, T. (2009). Calcium dependence of exo- and endocytotic coupling at a glutamatergic synapse. *Neuron* 63, 216–229. doi: 10.1016/j.neuron.2009.06.010

Jeanneteau, F., Deinhardt, K., Miyoshi, G., Bennett, A. M., and Chao, M. V. (2010). The MAP kinase phosphatase MKP-1 regulates BDNF-induced axon branching. *Nat. Neurosci.* 13, 1373–1379. doi: 10.1038/nn.2655

Kohara, K., Kitamura, A., Morishima, M., and Tsumoto, T. (2001). Activity-dependent transfer of brain-derived neurotrophic factor to postsynaptic neurons. *Science* 291, 2419–2423. doi: 10.1126/science. 1057415

Kojima, M., Klein, R. L., and Hatanaka, H. (2002). Pre- and post-synaptic modification by neurotrophins. *Neurosci. Res.* 43, 193–199. doi: 10.1016/S0168-0102(02)00034-2

Kolarow, R., Brigadski, T., and Lessmann, V. (2007). Postsynaptic secretion of BDNF and NT-3 from hippocampal neurons depends on calcium-calmodulin kinase II signaling and proceeds via delayed fusion pore opening. *J. Neurosci.* 27, 10350–10364. doi: 10.1523/JNEUROSCI.0692-07.2007

Mackler, J. M., Drummond, J. A., Loewen, C. A., Robinson, I. M., and Reist, N. E. (2002). The C2B Ca2+-binding motif of synaptotagmin is required for synaptic transmission in vivo. *Nature* 418, 340–344. doi: 10.1038/nature00846

Marshak, S., Nikolakopoulou, A. M., Dirks, R., Martens, G. J., and Cohen-Cory, S. (2007). Cell-autonomous TrkB signaling in presynaptic retinal ganglion cells mediates axon arbor growth and synapse maturation during the establishment of retinotectal synaptic connectivity. *J. Neurosci.* 27, 2444–2456. doi: 10.1523/JNEUROSCI.4434-06.2007

Maruyama, T., Matsuura, M., Suzuki, K., and Yamamoto, N. (2008). Cooperative activity of multiple upper layer proteins for thalamocortical axon growth. *Dev. Neurobiol.* 68, 317–331. doi: 10.1002/dneu.20592

Matsuda, N., Lu, H., Fukata, Y., Noritake, J., Gao, H., Mukherjee, S., et al. (2009). Differential activity-dependent secretion of brain-derived neurotrophic factor from axon and dendrite. *J. Neurosci.* 29, 14185–14198. doi: 10.1523/JNEUROSCI.1863-09.2009

McAllister, A. K., Katz, L. C., and Lo, D. C. (1997). Opposing roles for endogenous BDNF and NT-3 in regulating cortical dendritic growth. *Neuron* 18, 767–778. doi: 10.1016/S0896-6273(00)80316-5

McAllister, A. K., Lo, D. C., and Katz, L. C. (1995). Neurotrophins regulate dendritic growth in developing visual cortex. *Neuron* 15, 791–803. doi: 10.1016/0896-6273(95)90171-X

McMahon, H. T., and Boucrot, E. (2011). Molecular mechanism and physiological functions of clathrin-mediated endocytosis. *Nat. Rev. Mol. Cell Biol.* 12, 517–533. doi: 10.1038/nrm3151

Meijering, E., Jacob, M., Sarria, J. C. F., Steiner, P., Hirling, H., and Unser, M. (2004). Design and validation of a tool for neurite tracing and analysis in fluorescence microscopy images. *Cytometry* 58, 167–176. doi: 10.1002/cyto.a.20022

Nishiki, T., and Augustine, G. J. (2004). Dual roles of the C2B domain of Synaptotagmin I in synchronizing Ca2+-deendent neurotransmitter release. *J. Neurosci.* 24, 8542–8550. doi: 10.1523/JNEUROSCI.2545-04.2004

Niwa, H., Yamamura, K., and Miyazaki, J. (1991). Efficient selection for high-expression transfectants with a novel eukaryotic vector. *Gene* 108, 193–199. doi: 10.1016/0378-1119(91)90434-D

Royle, S. J., Granseth, B., Odermatt, B., Derevier, A., and Lagnado, L. (2008). Imaging phluorin-based probes at hippocampal synapses. *Methods Mol. Biol.* 457, 293–303. doi: 10.1007/978-1-59745-261-8_22

Ruthazer, E. S., Li, J., and Cline, H. T. (2006). Stabilization of axon branch dynamics by synaptic maturation. *J. Neurosci.* 26, 3594–3603. doi: 10.1523/JNEUROSCI.0069-06.2006

Uesaka, N., Hayano, Y., Yamada, A., and Yamamoto, N. (2007). Interplay between laminar specificity and activity-dependent mechanisms of thalamocortical axon branching. *J. Neurosci.* 27, 5215–5223. doi: 10.1523/JNEUROSCI.4685-06.2007

Uesaka, N., Hirai, S., Maruyama, T., Ruthazer, E. S., and Yamamoto, N. (2005). Activity dependence of cortical axon branch formation: a morphological and electrophysiological study using organotypic slice cultures. *J. Neurosci.* 25, 1–9. doi: 10.1523/JNEUROSCI.3855-04.2005

Uesaka, N., Nishiwaki, M., and Yamamoto, N. (2008). Electroporation for axon tracing Single cell electroporation method for axon tracing in cultured slices. *Develop. Growth Differ.* 50, 475–477. doi: 10.1111/j.1440-169X.2008.01024.x

Valdez, G., Akmentin, W., Philippidou, P., Kuruvilla, R., Ginty, D. D., and Halegoua, S. (2005). Pincher-mediated macroendocytosis underlies retrograde signaling by neurotrophin receptors. *J. Neurosci.* 25, 5236–5247. doi: 10.1523/JNEUROSCI.5104-04.2005

Vicario-Abejón, C., Collin, C., McKay, R. D., and Segal, M. (1998). Neurotrophins induce formation of functional excitatory and inhibitory synapses between cultured hippocampal neurons. *J. Neurosci.* 18, 7256–7271.

Waites, C. L., Craig, A. M., and Garner, C. C. (2005). Mechanisms of vertebrate synaptogenesis. *Annu. Rev. Neurosci.* 28, 251–274. doi: 10.1146/annurev.neuro.27.070203.144336

Watson, F. L., Heerssen, H. M., Bhattacharyya, A., Klesse, L., Lin, M. Z., and Segal, R. A. (2001). Neurotrophins use the Erk5 pathway to mediate a retrograde survival response. *Nat. Neurosci.* 10, 981–988. doi: 10.1038/nn720

Wiesel, T. N., and Hubel, D. H. (1963). Single-cell responses in striate cortex of kittens deprived of vision in one eye. *J. Neurophysiol.* 26, 1003–1017.

Yamamoto, N., Kurotani, T., and Toyama, K. (1989). Neural connections between the lateral geniculate nucleus and visual cortex in vitro. *Science* 245, 192–194. doi: 10.1126/science.2749258

Yamamoto, N., Yamada, K., Kurotani, T., and Toyama, K. (1992). Laminar specificity of extrinsic cortical connections studied in co-culture preparations. *Neuron* 9, 217–228. doi: 10.1016/0896-6273(92)90161-6

Zhao, X., Greener, T., Al-Hasani, H., Cushman, S. W., Eisenberg, E., and Greene, L. E. (2001). Expression of auxilin or AP180 inhibits endocytosis by mislocalizing clathrin: evidence for formation of nascent pits containing AP1 or AP2 but not clathrin. *J. Cell Sci.* 114, 353–365.

Zheng, J., Shen, W. H., Lu, T. J., Zhou, Y., Chen, Q., Wang, Z., et al. (2008). Clathrin-dependent endocytosis is required for TrkB-dependent Akt-mediated neuronal protection and dendritic growth. *J. Biol. Chem.* 283, 13280–13288. doi: 10.1074/jbc.M709930200

Zhu, Y., Xu, J., and Heinemann, S. F. (2009). Two pathways of synaptic vesicle retrieval revealed by single-vesicle imaging. *Neuron* 61, 397–411. doi: 10.1016/j.neuron.2008. 12.024

Zweifel, L. S., Kuruvilla, R., and Ginty, D. D. (2005). Functions and mechanisms of retrograde neurotrophin signalling. *Nat. Rev. Neurosci.* 6, 615–625. doi: 10.1038/nrn1727

Conflict of Interest Statement: The authors declare that the research was conducted in the absence of any commercial or financial relationships that could be construed as a potential conflict of interest.

Received: 31 July 2013; accepted: 04 December 2013; published online: 20 December 2013.

Citation: Granseth B, Fukushima Y, Sugo N, Lagnado L and Yamamoto N (2013) Regulation of thalamocortical axon branching by BDNF and synaptic vesicle cycling. Front. Neural Circuits ***7****:202. doi: 10.3389/fncir.2013. 00202*

This article was submitted to the journal Frontiers in Neural Circuits.

frontiers in
NEURAL CIRCUITS

ORIGINAL RESEARCH ARTICLE
published: 10 February 2014
doi: 10.3389/fncir.2014.00008

Parallel neural pathways in higher visual centers of the *Drosophila* brain that mediate wavelength-specific behavior

Hideo Otsuna[1,2], Kazunori Shinomiya[1,3] and Kei Ito[1]*

[1] *Institute of Molecular and Cellular Biosciences (IMCB), University of Tokyo, Tokyo, Japan*
[2] *Department of Neurobiology and Anatomy, University of Utah, Salt Lake City, UT, USA*
[3] *Department of Psychology and Neuroscience, Life Sciences Centre, Dalhousie University, Halifax, NS, Canada*

Edited by:
Masanobu Kano, The University of Tokyo, Japan

Reviewed by:
Bassem Hassan, The Vlaams Instituut voor Biotechnologie (VIB), Belgium
Iris Salecker, MRC National Institute for Medical Research, UK

****Correspondence:***
Kei Ito, Institute of Molecular and Cellular Biosciences (IMCB), University of Tokyo, 1-1-1 Yayoi, Bunkyo-ku, Tokyo 113-0032, Japan
e-mail: itokei@iam.u-tokyo.ac.jp

Compared with connections between the retinae and primary visual centers, relatively less is known in both mammals and insects about the functional segregation of neural pathways connecting primary and higher centers of the visual processing cascade. Here, using the *Drosophila* visual system as a model, we demonstrate two levels of parallel computation in the pathways that connect primary visual centers of the optic lobe to computational circuits embedded within deeper centers in the central brain. We show that a seemingly simple achromatic behavior, namely phototaxis, is under the control of several independent pathways, each of which is responsible for navigation towards unique wavelengths. Silencing just one pathway is enough to disturb phototaxis towards one characteristic monochromatic source, whereas phototactic behavior towards white light is not affected. The response spectrum of each demonstrable pathway is different from that of individual photoreceptors, suggesting subtractive computations. A choice assay between two colors showed that these pathways are responsible for navigation towards, but not for the detection itself of, the monochromatic light. The present study provides novel insights about how visual information is separated and processed in parallel to achieve robust control of an innate behavior.

Keywords: Drosophila, phototaxis, wavelength-dependent, color vision, higher visual center

INTRODUCTION

In animals ranging from insects to mammals, visual information is processed in a highly parallel manner. In certain mammals, segregated retinotopic pathways convey motion and color/contrast signals separately from the eye to the primary visual cortex (Zeki et al., 1991; Van Essen and Gallant, 1994), from where information is sent to multiple higher visual centers distributed in the occipital, parietal and temporal lobes that process different aspects of the information (Zeki et al., 1991; Born, 2001; Nassi and Callaway, 2006). Similarly, in insects, projections from the compound eye to nested neuropils of the optic lobe show clear retinotopic patterns, with each columnar visual cartridge in the optic lobe neuropils having specific projection from the retinal cells oriented to a specific angle of view (**Figure 1A**). These retinotopic projections involve many different morphologically and functionally distinct neurons (Fischbach and Dittrich, 1989; Otsuna and Ito, 2006; Strausfeld et al., 2006; Strausfeld and Okamura, 2007), which encode specific visual information such as figure-ground discrimination, motion detection, spectral information, and stereopsis (Krapp and Hengstenberg, 1996; Wicklein and Strausfeld, 2000; Douglass and Strausfeld, 2003; Strausfeld et al., 2006).

A compound eye of *Drosophila melanogaster* has about 750 ommatidia (*ca*. 730 and 780 in male and female eyes, respectively) (Wolff and Ready, 1993). Each ommatidium consists of eight photoreceptor cells that are called R1-R8. Axons of the R1-R6 cells from neighboring ommatidia, which receive light from the same direction of the visual field, converge into a single visual cartridge in the lamina. Axons of the R7 and R8 cells pass through the lamina cartridge and terminate in specific layers of the corresponding cartridge in the medulla. Relay interneurons connect the cartridges of different neuropils to mediate retinotopic signal transmission (**Figure 1A**).

The R1-R6 cells are essentially identical in that they express Rhodopsin 1 (Rh1) and have relatively broad spectral sensitivity (Salcedo et al., 1999) (**Figure 1B**). The R7 and R8 cells have two subtypes each that are called pale (p type) and yellow (y type) (Chou et al., 1996; Papatsenko et al., 1997; Chou et al., 1999). R7p and R7y cells express Rh3 or Rh4, respectively, and have sensitivity peaks at slightly different wavelengths in the ultraviolet (UV) range. R8p and R8y cells express blue-absorbing Rh5 and green-absorbing Rh6. The UV-, blue-, and green-sensitive R7 and R8 cells are regarded to play important roles in fly color vision (Bausenwein et al., 1992; Anderson and Laughlin, 2000; Strausfeld et al., 2006; Morante and Desplan, 2008; Yamaguchi et al., 2008, 2010), although R1-6 may in part be involved in color discrimination and R7/R8 may also play roles in motion discrimination (Wardill et al., 2012; Zhou et al., 2012).

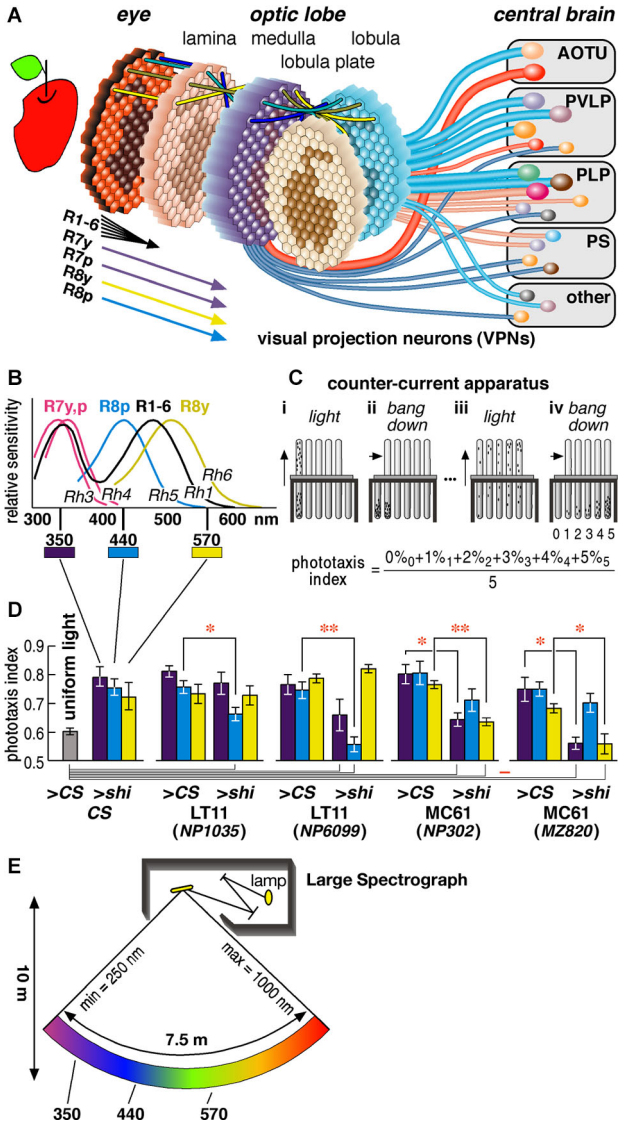

FIGURE 1 | *Drosophila* visual system and phototaxis assay. (A) Schematic diagram of the *Drosophila* visual system. Photoreceptors project from about 750 ommatidia of the retina to as many retinotopic columns (visual cartridges) in the four nested neuropils of the optic lobe. Relay interneurons project each retinotopic level onto the next (indicated by four colored lines on top of each neuropil). Hexagons with the projected images of an apple schematize the distribution of retinotopic visual cartridges and the relayed visual field. Cylindrical lines represent the visual projection neurons (VPNs) that connect the lower visual centers in the optic lobe to higher visual centers in the central brain (Otsuna and Ito, 2006). They terminate in the anterior optic tubercle (AOTU), posterior ventrolateral protocerebrum (PVLP), posterior lateral protocerebrum (PLP), posterior slope (PS) and a few other neuropils. The diameters of the lines reflect the numbers of neurons per pathway. Two red lines represent the pathways we analyzed in this study. **(B)** Sensitivity spectra of the photoreceptors (Salcedo et al., 1999). **(C)** The counter-current apparatus. Flies were put in the first tube and allowed to run towards the light for 30 s (panel i). The flies moved to the opposite tube were transferred to the bottom of the next tubes by tapping (ii) and let run towards light again (iii). After repeating this process five times (iv), flies were distributed to six tubes according to the times they moved towards light (0–5). **(D)** Phototaxis indices of the

(*Continued*)

FIGURE 1 | Continued
wild-type *CS* flies in the apparatus lit completely uniformly with white lamp (as negative control) and of the *CS* flies and GAL4 driver lines crossed with either *CS* (>*CS*, as positive control) or UAS-*shi*^{ts1} (>*shi*) towards specific wavelengths of light (at 30°C). Mean ± SEM of three independent measurements with different sets of flies were shown. Statistical significance of differences by *t*-test is indicated with * ($p < 0.05$) and ** ($p < 0.01$) below the abscissa indicates the cases that were not significantly different from the behavior under uniform light ($p > 0.05$). **(E)** Schematic diagram of the Okazaki Large Spectrograph (OLS).

Compared with connections between the retinae and primary visual centers, relatively less is known in both mammals and insects about the functional segregation of neural pathways connecting primary and higher centers of the visual processing cascade. In the insect nervous system, visual projection neurons (VPNs) connect the lower visual centers in the optic lobe to higher visual centers in the central brain (**Figure 1A**). A minimum of 44 types of VPNs, among which at least 20 are efferent, have been identified (Otsuna and Ito, 2006). Efferent VPNs terminate in the distributed but discrete centers in the central brain. These centers are called the optic glomeruli (Otsuna and Ito, 2006; Strausfeld and Okamura, 2007). Unlike optic lobe neuropils, each optic glomerulus does not have clear columnar arrangement. At this level of the visual system, therefore, simple retinotopic information is transformed to provide higher-level reconstructions about the visual world as in the connections between primary and higher visual cortices of the mammalian brain.

The relationship between the organization of identified neurons within a defined circuit and visual behaviors requiring specific nerve cells has been shown in the primary visual neuropils in the optic lobes (Rister et al., 2007; Yamaguchi et al., 2008; Zhou et al., 2012) and a higher integrative center, the brain's central complex (Liu et al., 2006). Almost nothing, however, is known about the functional roles of neurons connecting these primary and integrative centers except for those mediating information about visual motion (Borst and Haag, 2002). What other functions are supported by these many efferent pathways? To address this question, we examined the roles of specific projection neurons in phototaxis, which is a robust innate behavior. Unlike random-walk phototaxis of unicellular organisms (Häder and Häder, 1988), flies determine the direction of the light source and walk straight towards it (Hotta and Benzer, 1970). Our analysis revealed that visual information required for proper phototaxis is mediated by multiple parallel pathways in a wavelength-specific manner and that phototactic responses towards ambient light and distant light source are handled differently.

MATERIALS AND METHODS

FLY STOCKS

GAL4 enhancer-trap strains with preferential expression in the efferent VPNs (Otsuna and Ito, 2006) were crossed with wild-type *Canton S* (*CS*) or a strain carrying upstream activation sequence (UAS)-*shibire*^{ts1} (Kitamoto, 2001). Flies 4–8 days after eclosion were used for the behavioral assay.

To avoid the effect of UAS-*shibire*^{ts1} during development, flies were reared on standard cornmeal-yeast-agar medium at 19°C (i.e., permissive temperature for *shibire*^{ts1}) under 12/12 h light/dark intervals. Adult flies were collected within 1 day of eclosion and stored in batches of 45–50 flies per vial at 19°C. They were dark-adapted 1–2 h prior to behavioral assay. To avoid the effects of fatigue and possible learning behavior, flies were subjected to the phototaxis assay only once.

WAVELENGTH-SPECIFIC PHOTOTAXIS ASSAY

The Okazaki Large Spectrograph facility (Watanabe et al., 1983) provides evenly dispersed monochromatic light between 250 and 1000 nm (**Figures 1E**, **2A**) with wavelength specificity superior to regular band-pass filters and light-emitting diodes (**Figure 2B**). Counter-current analysis was performed using the original apparatus reported by Benzer (Benzer, 1967; Hotta and Benzer, 1970) (**Figure 1C**). We used polystyrene tubes (Falcon Round-Bottom tube 35-2917, $\phi 17 \times 100$ mm) for visible range of light, and borosilicate tubes (Iwaki PYREX grass TE-32, $\phi 16.5 \times 105$ mm) for ultraviolet light (350 and 380 nm) to avoid autofluorescence of the tubes. The tubes were cleaned thoroughly after each test with an ultrasonic washer in order to remove any remnants of the flies and their secretions.

The wavelength of light was calibrated with digital spectroradiometers USR-40V and USR-40D (Ushio). Because of the width of the counter-current apparatus, the wavelength peaks of the light for the first and sixth tubes were shifted by ±4 nm from that of the mid point (shown as colored rectangles in **Figure 2B**). Light intensity was measured with a digital photometer RMS-101 (Rayon) and adjusted to an equal level by placing neutral-density UV-transparent acrylic filters (Mitsubishi Rayon N083-085, 097, and 099, with 30–80% transmission) in front of the counter-current apparatus (**Figure 2A**). Because flies do not show clear phototaxis if the light is too strong or too weak, we adjusted the light intensity to the same level (3.0×10^{18} photons/m^{2}s, **Figure 2B**) where wild-type flies showed clear phototaxis at all the wavelength ranges examined (**Figure 2D**). Phototaxis towards white light was tested using a 15 w fluorescent lamp driven by a 20,000 Hz inverter and placed 15 cm from the apparatus.

For the negative control experiment under uniform light (**Figure 1D** leftmost column), each tube was covered completely with semi-transparent paper, and the entire apparatus was lit from below and above with a pair of large light boxes.

Experiments with both *CS* and UAS-*shibire*^{ts1} flies were performed at 30°C, i.e., the restrictive temperature of *shibire*^{ts1}. A group of 45–50 flies were subjected to phototaxis assay at one time, and measurements with three independent sets of flies were averaged. All the strains showed normal anti-geotaxis behavior measured by the counter-current apparatus oriented vertically (data not shown).

SELECTION OF GAL4 DRIVER LINES

From the collection of 3,939 NP- and MZ-series GAL4 enhancer-trap strains, we first identified 96 lines that label specific subsets of VPNs but no other neurons in the retina or the optic lobe (Otsuna and Ito, 2006). We chose the strains for phototaxis assay with the following criteria: (1) Efferent pathways, which should convey visual information from the optic lobe to the brain, are labeled; (2) Only a single or maximum two such pathways are labeled; and (3) more than one such strain is available for labeling a particular pathway. We identified 15 such strains for analyzing six efferent pathways, and subjected them to the initial phototaxis experiments towards three wavelengths of monochromatic light (350, 440 and 570 nm). Pathways for which only a subset of the tested strains showed aberrant phenotype were excluded from further analysis.

VISUALIZATION OF GAL4-EXPRESSING CELLS

Confocal serial optical sections of whole-mount brains of the GAL4 strains expressing cytoplasmic UAS-green fluorescence protein (GFP) (S65T) or the combination of synaptic vesicle-targeted UAS-*n-Syb-GFP* and cytoplasmic UAS-*DsRed* were taken with a laser scanning microscope LSM510 (Zeiss) as described before (Otsuna and Ito, 2006). Neuropils were labeled with anti-Bruchpilot monoclonal antibody nc82 (Wagh et al., 2006). Single cells of the MC61 pathway were visualized using the flippase (FLP)-out system (Wong et al., 2002). Obtained serial section datasets were reconstructed using Imaris 2.7 (Bitplane) running on a Silicon Graphics Octane workstation or Fluorender 2.13 (Scientific Computing and Imaging Institute, University of Utah) running on a Windows PC. Definitions of neuropils were according to the systematic nomenclature of the insect brain proposed by the Insect Brain Name Working Group (Ito et al., 2014).

STATISTICAL ANALYSES

Statistical significance of the differences between control and experiment (**Figures 1**, **2**) and between phototaxis and wavelength choice assay (**Figure 4**) were examined using two-tailed *t*-test of the phototaxis indices. We assumed equal variance because of the results of *f*-test. Note, however, that *t*-test sometimes reported significance when both control and experiment data showed clear positive phototaxis but there were certain differences in the distribution of the flies (e.g., 505 and 540 nm of **Figure 3E**, 475 nm of **Figure 3F**, and 540 and 600 nm of **Figure 3H**).

For the phototaxis assay across fly's visual spectrum, we performed 10 experiments for each experimental group (i.e., 350–600 nm and white light; **Figure 2**). Analysis of variance (ANOVA) of these 10 data sets showed no significance ($P > 0.05$) in the control groups (**Figures 2D, I–L**) but clear significance ($P < 0.008$) in all the experimental groups with *shibire* expression (**Figures 2E, H**).

When the counter-current analysis was performed under completely uniform lighting, the phototaxis index was higher than 0.5 (leftmost column of **Figure 1D**), as the distribution of the flies was shifted slightly towards the tubes that were further from the initial tube. This is likely because some flies try to escape from the area of the tube where they experienced shock by the tapping of the apparatus. Taking this effect into account, we determined aberrant phototaxis using the following criteria: (1) phototaxis index is not significantly different from that under uniform lighting ($P > 0.05$, *t*-test); (2) the index is significantly

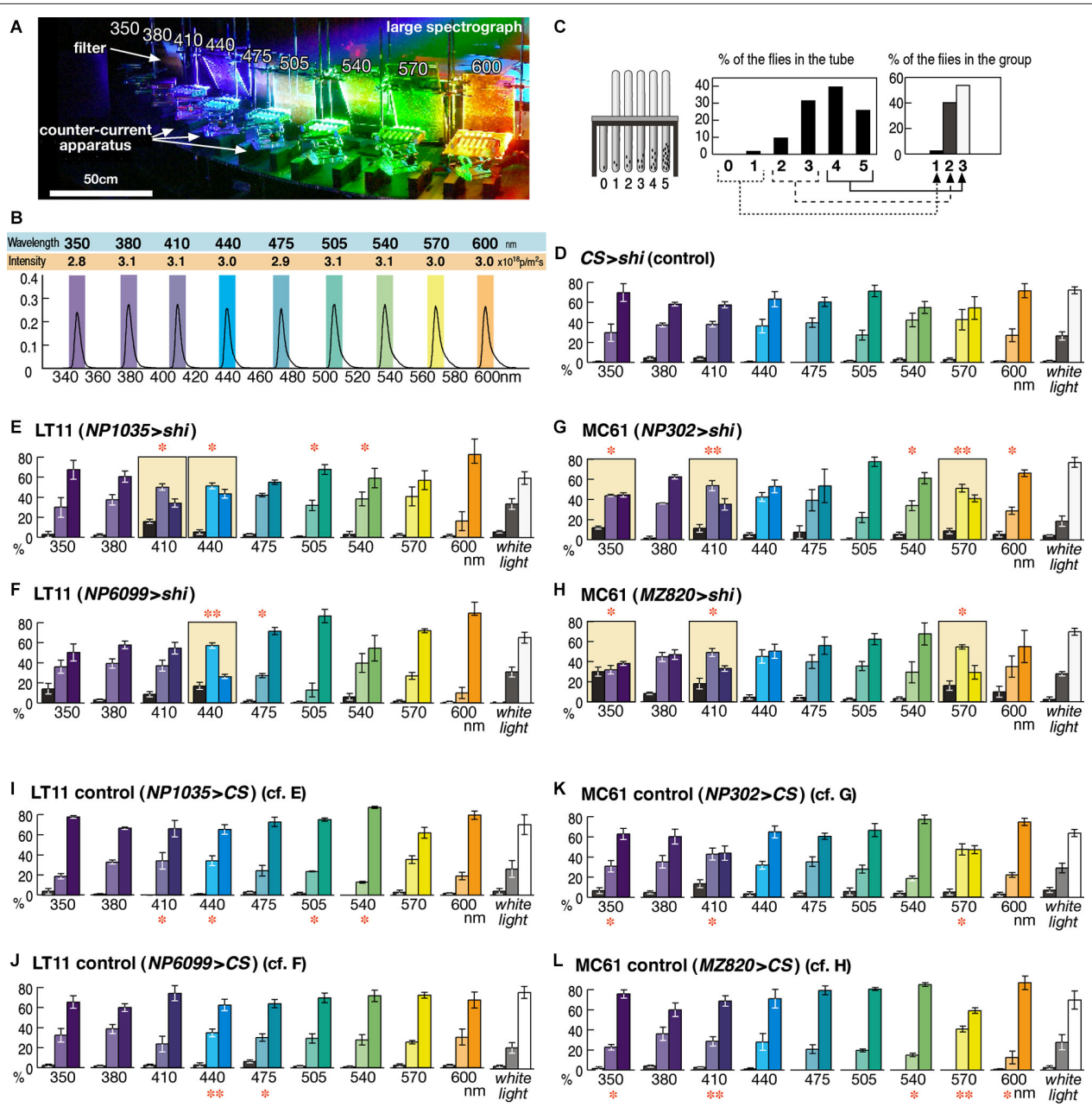

FIGURE 2 | Detailed phototaxis assay across the visual spectrum of the fly eye. (A) Experimental setup of the OLS. Filters are placed in front of the counter-current apparatus to normalize the light intensity. For actual measurement, illumination except for a single apparatus was blocked in order to avoid the effect of stray light. **(B)** Intensity and spectrum of the light used for each experiment, measured at the center of the apparatus. Colored boxes indicate the wavelength range that illuminates each apparatus. **(C)** To minimize minor fluctuation of data, counts of the six tubes (0–5) are merged into three groups, which correspond to the flies that seldom moved towards light (left column, 1), moved or stayed roughly at random (middle, 2), and moved most of the time (right, 3). **(D)** Control experiment of the wild-type *CS* flies crossed with UAS-*shi*^{ts1} (*CS* > *shi*) at 30°C. Mean ± SEM of three independent measurements. **(E–H)** Phenotypes of the GAL4 driver strains crossed with UAS-*shi*^{ts1} at 30°C. Colored background rectangles indicate the cases in which flies showed aberrant phototaxis. The cases that were significantly different from the control **(I–L)** are indicated with ** ($p < 0.01$) and * ($p < 0.05$, *t*-test). **(I–L)** Control phototaxis experiment of **(E–H)**; each GAL4 line was crossed with wild-type *CS*. Phototaxis at 30°C was normal in all the cases.

different from that of the control experiment with the GAL4 strains crossed with *CS* ($P < 0.05$, *t*-test); and (3) the percentage of the flies in the right column of the three-bar graph (i.e., the flies that moved towards light for four or five times out of five trials) is lower than in the middle column (i.e., those that moved two or three times out of five trials), or the right and left columns are about the same level and more than 10% of the flies remain in the left column (i.e., the flies that did not move or moved only once

out of five trials). For example, phototaxis of the NP6099 > *shi* flies towards 350 nm light was considered normal even though the index was not significantly different from negative control (**Figure 1D**), because the index was not significantly different from positive control (NP6099 > *CS*), either (**Figure 2J**).

RESULTS

IDENTIFICATION OF NEURONAL PATHWAYS THAT ARE ASSOCIATED WITH PHOTOTAXIS

Phototaxis can be assayed using the counter-current apparatus (**Figure 1C**) (Benzer, 1967). In this paradigm, flies in a tube are startled, or agitated, by tapping the apparatus, and they are left horizontally for certain period (typically 30 s) to stay in the same end or to run towards the other end of the tube that is facing the light. Flies that moved to the other end are transferred to the next tube, and the same tests are repeated. After five repetitive tests, most wild-type flies end up in the fourth or fifth tubes, showing that they chose to run towards light in 80% or 100% of the trials. The phototaxis index is calculated as the weighted average of the percentage of the flies in each tube. For wild-type flies, the index is above 0.7 if one end of the apparatus is lit by light, and 0.5–0.6 if the apparatus is lit evenly with uniform light (**Figure 1D** leftmost panel).

Mutant flies that show aberrant phototaxis have been screened using such apparatuses, and important mutants that affect development and fate determination of the retinal cells have been identified (Schümperli, 1973; Seiger and Woodruff, 1987; Ballinger and Benzer, 1988). However, such screening was unable to identify mutants that showed defects in the function or structure of the neural circuits deep within the brain. To identify neural pathways that are potentially associated with the phototaxis control, we therefore modified the assay in two respects.

First, instead of looking for gene mutations that are associated with phototaxis, we analyzed the roles of specific subsets of neurons by selectively silencing their functions. We expressed temperature-sensitive synaptic transmission inhibitor UAS-*shibire*^{ts1} (*shi*^{ts1}) (Kitamoto, 2001) with a series of GAL4 enhancer-trap driver strains that label certain VPNs but not retinal cells or intrinsic neurons of the optic lobe (Otsuna and Ito, 2006).

And second, because each ommatidium of the fly compound eye possesses photoreceptor cells with different wavelength sensitivity (**Figure 1B**; Salcedo et al., 1999), we suspected that phototaxis might be controlled in a color-dependent manner via separate neural pathways. We therefore tested phototaxis towards characteristic wavelengths of light that coincide with the sensitivity peak of photopic receptors: UV (350 nm), which correspond to the sensitivity peak (λmax) of the R7y/p photoreceptor cells, blue (440 nm) that is the λmax of R8p, and green (570 nm) that is detected predominantly by the R8y photoreceptors (Feiler et al., 1992; Salcedo et al., 1999).

To minimize the detection of light by other photopic receptors, the wavelength range of the light should be kept narrow. It is difficult to obtain such light with band-pass filters or light emitting diode (LED), which tends to have rather broad half bandwidth. Although a monochromator is ideally suited for this purpose, an ordinary one cannot provide monochromatic light for a broad enough area that covers the size of the counter current apparatus. To overcome this problem, we used the Okazaki Large Spectrograph (OLS) facility (Watanabe et al., 1983), which consists of a 30 kw xenon arc lamp and large interference grating and generates a spectrum from ultraviolet to infrared onto a platform that spans across 7.5 m (**Figure 1E**). By placing the counter current apparatus onto the platform, it is possible to perform phototaxis assay towards specific wavelength of light (**Figures 2A, B**).

Using the OLS, we identified two pairs of GAL4 driver strains that drove expression in the same visual pathways and showed identical phenotypes (**Figure 1D**). Two strains (NP1035 and NP6099) with GAL4 expression in a specific VPN pathway called Lobula Tangential 11 neurons (LT11) showed aberrant phototaxis (i.e., low phototaxis index) towards blue light (440 nm) when crossed with the UAS-*shibire*^{ts1} strain (**Figure 1D** middle panels). The observed phenotype should not be due to general locomotion defects, because the phototaxis of these flies towards UV or green light (350 and 570 nm) was not affected significantly. The other two lines (NP302 and MZ820) had preferential expression in a newly identified neuron type that we named Medulla Columnar 61 neurons (MC61). They showed aberrant phototaxis towards UV and green light, but not towards blue light (**Figure 1D** right panels).

SPECTRAL RESPONSES OF THE PHOTOTAXIS-ASSOCIATED VISUAL PROJECTION NEURONS (VPNs)

Neurons silenced by these GAL4 driver strains are likely to be necessary specifically for phototaxis towards particular wavelength ranges. As shown in **Figure 1D**, the responses of the LT11 and MC61 pathways appear complementary: LT11 for blue and MC61 for UV/green. Possibly, this suggests that the two pathways convey information about primary colors involving a form of color opponency mechanism (Fischbach, 1979). To explore this, we tested the response spectrum of these neurons at higher resolution by subjecting flies to the phototaxis assay at ∼30 nm intervals (**Figure 2**).

When the control flies that carry UAS-*shibire*^{ts1} but without GAL4 driver were subjected to this assay, they showed normal phototaxis behavior not only towards white light but also towards monochromatic light across all the visible ranges from 350 to 600 nm (**Figure 2D**). Functional knockout of LT11 neurons caused aberrant phototaxis specifically at 410- and 440-nm ranges (for NP1035, **Figure 2E**) or at 440 nm (for NP6099, **Figure 2F**). Although these wavelengths correspond to the λmax of the R8p cells (Salcedo et al., 1999), the wavelength dependence appears to be more specific than the sensitivity spectrum of the R8p photoreceptor (**Figure 1B**).

The response to MC61 knockout was even more intriguing (**Figures 2G, H**). Though the MC61-silenced flies showed defective phototaxis at 350 nm, they showed a normal response at a slightly longer UV wavelength (380 nm). They again showed defects towards violet light (410 nm), but behaved normally towards blue (440 nm). Their phototaxis further showed defects in green light (570 nm), but behavior at slightly different wavelengths (470–540 nm and 600 nm) was normal. The characteristic wavelength dependency was identical between the two independent driver strains.

It is important to note that phototaxis towards mixed white light was never affected in all the four strains and that the flies showed normal phototaxis in many wavelength ranges. These indicate that the components of the nervous system that are responsible for locomotion control and for the phototaxis towards these colors of light are kept intact in these flies.

ARCHITECTURE OF THE PHOTOTAXIS-ASSOCIATED VISUAL PROJECTION NEURONS (VPNs)

We next examined the detailed architecture of the LT11 and MC61 pathways. As described earlier, the LT11 pathway consists of a single unique neuron (Otsuna and Ito, 2006), with a cell body in the lateral cell body rind, tree-like arborization in the lobula that spans across the entire relayed visual field, and axon terminals in the posterior ventrolateral protocerebrum (PVLP) of the central brain (**Figures 3A, B**).

The MC61 pathway has not been described before. It is significantly different from LT11 in that it consists not of one neuron but of an ensemble of many isomorphic neurons. They have their cell bodies in the lateral surface of the medulla. These neurons send their neurites in parallel with the medulla visual cartridges and form extensive dendritic arborizations in its middle layers (**Figures 3C, D**). Background labeling with nc82 antibody, which labels neuropils according to the density of the active zone protein Bruchpilot (Wagh et al., 2006), shows two bands that appear darker in the medulla (two arrows in **Figure 3B**). Because of its location that is closely associated with the accessory medulla (AME) at its anterior end, and the relative paucity of synapses because of the massive tangential axon fibers of the serpentine layer that run in this region, the medial band corresponds to the medulla M7 layer. The region just lateral to this layer is labeled densely because of the abundant presynaptic sites of the retinal R7 photoreceptors (Fischbach, 1979) and is called the medulla M6 layer. High-magnification cross section views of this region indicate that the dendrites of the MC61 neurons arborize in these two layers (**Figures 3E, F**).

Axons arising from different optic cartridges of the medulla converge at the second optic chiasmus (OCH2; **Figures 3C, E, F**) but are again get dispersed to pass through the lobula in a mutually parallel manner at various positions (**Figures 3C, D**). The axons again converge at the root of the anterior optic tract and terminate in the lateral zone of the anterior optic tubercle (AOTU).

Interestingly, the two strains label different subsets of isomorphic MC61 neurons (**Figures 3G, H**). NP302 strain labeled *ca*. 120 neurons (111, 120 and 125 cells observed in 3 samples) lying in the dorsal half of the medulla (**Figure 3G**), whereas MZ820 labeled *ca*. 13 neurons (10, 14 and 16 cells observed in three samples) that are scattered more sparsely in the ventral medulla half. Thus, the MC61 neurons labeled in the two strains preferentially process information from the dorsal and ventral halves of the visual field, respectively. In the AOTU, axons labeled in the NP302 strain are spread almost in its entire cross section, whereas those labeled in MZ820 are confined in its dorsal region.

To analyze the dendrites of MC61 neurons in relation to medulla layers, reconstructions viewed from the angles parallel and perpendicular to these layers were examined (**Figures 3I–L**). Because the tangential medulla layer spans obliquely from anterior-medial to posterior-lateral, oblique viewing angles were employed (arrows in **Figure 3C**). The columnar arrangement of the neurites of the MC61 neurons, as well as their dendrites spanning tangentially in specific layers, were apparent when the sample was observed in a view parallel to the layer (**Figure 3I**). When the same sample was viewed at a right angle to the layer, the distribution of the MC61 somata appeared disorganized (**Figure 3J**). Indeed, single-cell labeling showed that tangential dendrites of each neuron arborized in specific subregions of the relayed visual field (**Figures 3K, L**), which is slightly offset compared to the position of the somata. The extent of these dendrites covered about 1% of the tangential cross-section area of the medulla (0.8% and 1.15% in two samples), suggesting that they span roughly across eight out of the total *ca*. 750 medulla visual cartridges.

We then analyzed the distribution of putative input and output sites of these neurons by comparing the labeling patterns of cytoplasmic *GFP* and synaptic vesicle-targeted reporter *n-Syb-GFP* (**Figures 3M, N**). Because the transgenic n-Syb-GFP protein is produced in the cell body and transported to the distal synaptic sites, surplus molecules tend to visualize somata (**Figure 3N**). In spite of this, within the neurites the protein is distributed specifically to the presynaptic sites, while axons and postsynaptic sites-specific regions of dendrites are left unlabeled. The dendrites of LT11 reside in three discrete layers (Lo3, 4 and 5 layers) of the lobula (**Figure 3M**). Presynaptic sites in this neuron were observed not only in its terminals in the PVLP but also in two layers of the lobula (Lo3 and Lo4), suggesting that its distal branches in the lobula outer layers are both receiving and imparting information. Likewise, the MC61 neurons had presynaptic sites both in the distal target in the AOTU and in the proximal dendrites in the medulla (**Figure 3N**). Although MC61 neurons arborized in two layers of medulla (M6 and M7 layers, **Figure 3E**), presynaptic sites were confined only in the M7 layer and the medial half of the M6 layer (M6M; **Figure 3N**).

Thus, for both LT11 and MC61 pathways, one level of their arborizations in, respectively, the lobula Lo5 layer and the lateral half of the medulla M6 layer (M6L) were devoid of presynaptic sites and were therefore exclusively dendritic (**Figures 3M, N**). That efferent neurons also possess discrete levels of presynaptic processes within what looks like a dendritic tree indicates the participation of these neurons also in local computation of the visual signal within the primary visual centers.

As mentioned above, the four strains showed no GAL4 expression in the photoreceptors or intrinsic neurons of the optic lobe. However, some lines label other types of VPNs in addition to the LT11 and MC61: The NP6099 strain labels the horizontal system (HS) cells (**Figure 3B**), whereas MZ820 labels lobula plate tangential 2 (PT2) neurons (**Figures 3D, P**). To ask whether these additionally labeled neurons might affect the observed phenotype, we looked for other GAL4 driver strains that label these neurons. The NP6651 strain labels HS as well as the vertical system (VS) cells, but not the LT11 neuron (**Figures 3Q, R**). Unlike NP1035 and NP6099 strains, phototaxis towards 440 nm light was normal (**Figure 3U**), suggesting that the observed phenotype in NP6099 was not because of the silenced HS cells. Likewise, silencing PT2 as well as LT13 neurons with the NP1582

driver strain (**Figures 3S, T**) caused no aberrant phototaxis (**Figure 3V**).

The four driver lines also labeled a few other neurons or glial cells in the central brain. Because there was no overlap in these central brain neurons that were labeled between NP1035 and NP6099 strains (Otsuna and Ito, 2006) and between NP302 and MZ820 strains (**Figures 3O, P**), these cells were unlikely to be the cause of the observed phenotype that are common within each pair of strains. None of these strains labeled descending motor control neurons projecting from the brain to the thoracico-abdominal ganglia.

ROLE OF THE PHOTOTAXIS-ASSOCIATED VISUAL PROJECTION NEURONS (VPNs) IN COLOR-CHOICE TEST

Why, then, do silencing particular visual neural circuits cause phototactic defects at particular wavelengths? Do the flies become blind to these colors of light? Or, are they able to recognize the source of illumination but unable to navigate towards that direction? To distinguish which of the two is more likely, we performed a choice assay between two wavelengths of light (**Figure 4**).

Wild-type flies prefer shorter wavelength of light (Schümperli, 1973; Fischbach, 1979). Consistent with this, phototaxis of the wild-type flies from dark towards 540 nm green light was lost, if the flies were asked to run from the end of the counter-current apparatus that was lit by blue (440 nm) or UV (350 nm) light towards the end that was lit by green light (**Figure 4B** left panels).

Interestingly, flies with silenced LT11 or MC61 pathways showed the same phenotype (**Figure 4B** middle and right panels). When the flies were placed in the end of the apparatus that was lit by blue or UV light, respectively, and the other end was lit by green light, many flies remained in the blue or UV-lit end and did not run towards green light, even though their phototaxis behavior was normal towards green light but defect towards blue or UV (**Figures 2E, H**).

This apparently contradicting phenotype could be because these flies might have lower sensitivity towards green light than wild-type flies do, causing the misinterpretation that blue or UV light might appear brighter to them. To test whether this would be the case, we increased the intensity of green light tenfold. The phenotype remained essentially the same, however (**Figure 4C**). Thus, these flies were able to determine that blue or UV light is preferable to green light.

We next placed the flies in the end of the tubes that was lit by green light and asked the flies to run towards the end that was lit by blue or UV light. Even though they were able to stay in the end that was lit by shorter wavelengths of light, they failed to run from green-lit towards blue- or UV-lit ends (**Figure 4D**). These data indicate that only navigation towards shorter wavelength of light, but not the detection of ambient light, was impaired by silencing these neural circuits.

DISCUSSION

The current study identified parallel pathways of the visual neural circuits that mediate phototaxis towards highly specific wavelength ranges. The finding is intriguing in three respects.

First, we found that seemingly achromatic behavior such as phototaxis is actually mediated by multiple parallel pathways, each of which responds to only specific colors of light (**Figure 2**). The visual signals conveyed by these neurons are distinct from the spectral sensitivity curves of the photoreceptors. Their spectral responses are so narrowly tuned that animals living in the natural environment would seldom encounter with such monochromatic illumination. Thus, the two pathways should function most of the time in parallel. Such parallel computing is advantageous for the animals, because it should help achieving the robust control of innate behaviors; malfunction of any of these parallel pathways should not affect the fly's response towards mixed light.

Secondly, the pathways we identified are responsible for the navigation towards the light source, but not the detection of the ambient light (**Figure 4**). Phototaxis behavior has been analyzed in two paradigms. In the so-called "slow" phototaxis, animals are put at the center of the tube or the branch point of the T- or Y-maze, and asked to move towards either direction (Fischbach, 1979). In this paradigm the choice of both ends involves navigation through the tubes. On the contrary, in the startled phototaxis such as the counter-current paradigm we used, flies are put in one end of the tube and asked either to stay there or to move towards the other end of the tube. Using the latter paradigm, we were able to distinguish the flies' preference towards specific color of light between the situations when it is presented as an ambient light around where the flies are placed, or when it is presented in the other end of the tube as a distant target. Silencing of the two pathways caused defects only in the latter case. Detection of the colors of the ambient light might be mediated by other, yet unidentified, visual pathways.

The separation of visual processing between ambient color and target color is reminiscent of the motion detection, in which movement of the large background objects and small target objects are handled separately (Kirschfeld, 1994; Fox and Frye, 2013). The fact that the two pathways analyzed here are involved only in the detection of the target light source may infer that they might be involved in the distinction of the colors of distant objects. If this is the case, then the narrowly tuned wavelength responses should be useful for examining the reflection spectra of the target objects.

Thirdly, even though the two pathways seem to function in parallel, they are drastically different in terms of the visual information they convey. The LT11 pathway consists of a single neuron that extends dendrites across the entire relayed visual field. Given its structure, the single neuron cannot convey information about the distribution of light in the visual field (Otsuna and Ito, 2006). The MC61 pathway, on the contrary, consists of more than 100 columnar neurons. Though they are somewhat fewer than the number of the *ca*. 750 visual cartridges, the pathway might be able to transmit retinotopic information albeit at a lower resolution. Their terminals in the AOTU are rather intermingled. Although the terminals of the MC61 neurons arising from the ventral medulla, labeled in the MZ820 strain, are confined in the dorsal region of the AOTU suggesting some sort of retinotopic projection, the terminals labeled in the NP203 strain essentially cover the entire cross section of the AOTU even though these

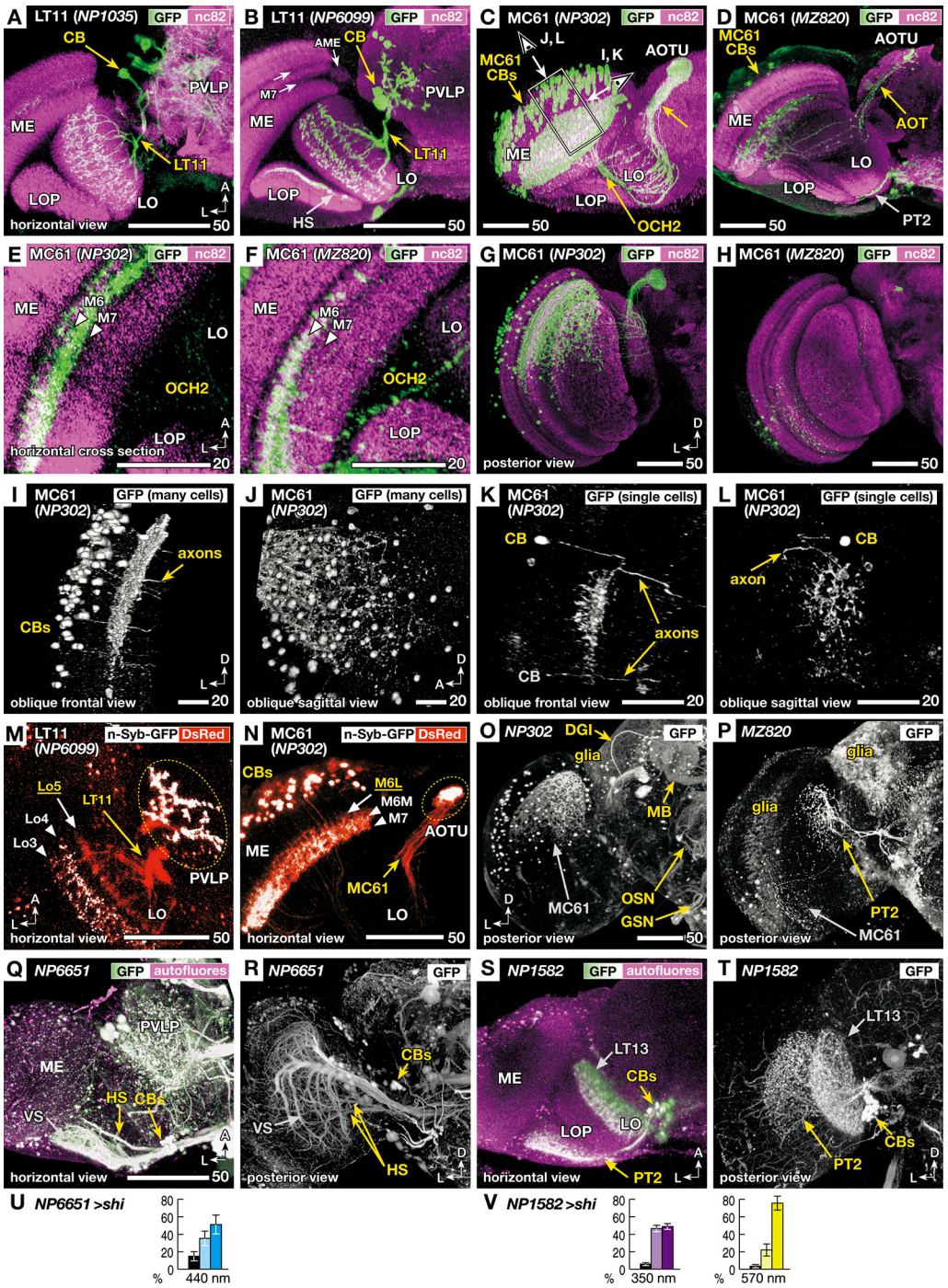

FIGURE 3 | Morphology of the VPNs labeled by the GAL4 lines with aberrant phototaxis. Right-angled arrows on the bottom corners of the panels indicate directions in the images, A: anterior, L: lateral, D: dorsal. Scale bars correspond to either 20 or 50 μm. **(A–D)** Three-dimensional (3D) reconstruction of confocal laser scanning sections (horizontal view). Labeled neurons (green-white, visualized with GAL4-driven UAS-*GFP*) on the background labeling of synaptic neuropils (magenta, with anti-Bruchpilot nc82 antibody). CB indicates labeled cell bodies. In addition to the lobula tangential 11 (LT11) and medulla columnar 61 (MC61) VPNs, NP6099 and MZ820 strains labeled horizontal system (HS) neurons and lobula plate tangential 2 (PT2) neurons, respectively, in the optic lobe. Two arrows in **B** indicate dark-labeled layers in the background neuropil labeling of the medulla. Box and arrows in **C** indicate the region and the direction of oblique frontal views shown in **Figures 3I, L**. ME: medulla, AME: accessory medulla, LO: lobula, LOP: lobula plate, PVLP: posterior ventrolateral protocerebrum, AOT: anterior optic tract, AOTU: anterior optic tubercle, OCH2: second optic chiasmus. **(E, F)** High-magnification view of the horizontal sections of NP302 and MZ820 strains, showing specific arborizations in the medulla M6 and M7 layers (triangles). Note that the dendrites in the 3D reconstruction images of **Figures 3C, D, G, H** appear to extend more medially, because they visualize all the arborizations along the curved surface of the M6 and M7 layers. **(G, H)** Posterior 3D reconstruction of these strains, showing the labeling in different subsets of the MC61 neurons in the dorsal and ventral halves of the medulla. (*Continued*)

FIGURE 3 | Continued
(I, L) 3D reconstruction views of the region shown as a box and arrows in **Figure 3C**, viewed along the axis that is parallel **(I, K)** or perpendicular **(J, L)** to the tangential plane of medulla layers. Entire population of MC61 neurons **(I, J)** and a sample with two FLP-induced (Wong et al., 2002) single-cell clones **(K, L)** are shown. In the latter, one of the cell bodies is out of the region of reconstruction (indicated with gray characters). **(M, N)** Distribution of presynaptic sites (white, visualized with synaptic vesicle-targeting UAS-*n-Syb-GFP*) and all the neural fibers (red, with cytoplasmic UAS-*DsRed*). Stacks of confocal horizontal sections. Lo3-5 and M6L, 6M and 7 indicate the layers of dendrites with (white) and without (yellow) presynaptic cites. Note that some of the cell bodies (CBs) are labeled with surplus amount of n-Syb-GFP. **(O–P)** Labeled cells in the central brain. In addition to the MC61 neurons, NP302 labels glial cells on the surface, dorsal giant interneuron (DGI), mushroom body neurons (MB), terminals of the olfactory sensory neurons (OSN) in the antennal lobe, and putative gustatory and other sensory neurons (GSN) in the gnathal (subesophageal) ganglia. MZ820 labels PT2 neurons as well as extensive glial cells on the surface. See Otsuna and Ito (2006) for the labeling pattern of NP1035 and NP6099. **(Q–V)** Labeling patterns and phototaxis phenotypes of other GAL4 driver strains that label HS and PT2 neurons, which are labeled simultaneously in the NP6099 and MZ820 strains, respectively, but not neurons of the LT11 or MC61 pathway. **Q, R** GAL4 strain NP6651 drives expression in the horizontal system cells (HS). The strain also labels the vertical system cells (VS; Note that in total 8–9 VS cells are observed, not 5–7 cells as previously described Heisenberg et al., 1978). **S, T** GAL4 strain NP1582 drives expression in PT2 neurons. LT13 neurons are also labeled. Reconstruction (horizontal view) of the labeled neurons (green-white, visualized with GAL4-driven UAS-*GFP*) on the background labeling of autofluorescence (magenta) **(Q, S)**, and posterior views without background labeling **(R, T)**. **(U, V)** Phototaxis behavior of NP6651 **(U)** towards 440 nm light and that of NP1582 towards 350- and 570-nm light **(V)**.

axons derive from only the dorsal half of the medulla. It is not yet clear whether precise retinotopic projection is maintained by these neurons.

The two pathways are contrasting also in their target neuropils. Whereas LT11 terminate in the PVLP, MC61 innervate the AOTU. The AOTU is one of the most prominent optic glomeruli, and bundles of neural fibers project from the AOTU towards the region called the bulb, or the lateral triangle, where they contact with the neurons of the ellipsoid body (Ito et al., 2013). Thus, information sent via the MC61 pathway is likely to be transmitted to the central complex, which is known to be important for higher-order visual processing (Liu et al., 2006; Heinze and Homberg, 2007). On the contrary, the PVLP has no direct connection with the bulb or the central complex, although it is connected with various other neuropils (Ito et al., 2013).

The observed phenotypes in terms of a lack of movement towards the light, as opposed to lack of detection *per se*, suggest potential involvement of the downstream neural circuits from visual to motor centers. Because the examined flies showed normal phototaxis towards white as well as towards many specific wavelength ranges of light, and because the four strains we used did not label overlapping neural circuits in the central brain, it is not likely that the downstream neural circuits in the potential higher visual or motor centers were affected in our assay. Further identification of the information pathways arising from the target regions of the LT11 and MZ61 neurons to higher visual/motor centers would be required to understand how wavelength-specific information is utilized for behavior control.

The parallel pathways also differ in the location of their input sites. Whereas LT11 arborizes in the Lo3, 4 and 5 layers of the lobula, MC61 neurons receive information in the M6 and M7 layers of the medulla. The sharp and complex response spectra of LT11 and MC61 neurons should require subtraction of signals deriving from different types of photoreceptors, as has been described for chromatic sensitive ganglion cells in higher mammals (Martin et al., 2001). Indeed, the layers in the medulla and lobula in which these neurons have dendrites receive inputs from neurons relaying information from R7 and R8 photoreceptors (Bausenwein et al., 1992; Gao et al., 2008; Shinomiya et al., 2011).

In spite of their structural differences, the two pathways share one common characteristic: neurons of both pathways can gather information from multiple visual cartridges. The single LT11 neuron arborizes across the entire visual cartridges of the lobula. Even though the MC61 neurons have columnar organization, a single neuron extends its dendrites tangentially across about eight neighboring visual cartridges (**Figures 3K, L**). Considering the existence of extensive pre- and post-synaptic sites in these dendrites (**Figures 3M, N**), it is likely that these dendrites should take part in complex computation to compare light intensity between different parts of relayed visual fields. Not only global comparison of the entire visual field by the LT11 neuron but also local comparison by each of the MC61 neurons will provide information about the gradient of light intensity, which is a decisive cue for determining the direction of light source for phototaxis.

In this study we used two driver strains for assessing the role of each pathway. The observed phenotypes were slightly different between drivers. Concerning the LT11 pathway, NP1035 strain caused defect phototaxis at two wavelength ranges (410 and 440 nm), whereas NP6099 showed defects only at the latter (**Figures 2E, F**). As for the MC61 pathway (**Figures 2G, H**), although the two strains showed aberrant phototaxis at the same sets of wavelengths, defects towards 350- and 570-nm light were slightly weaker with NP302 than with MZ820. (Rightmost bars in the triplet graphs at these wavelengths in **Figure 2G** were higher than the leftmost bar, indicating that slightly more flies ran towards light, whereas the right and left bars in **Figure 2H** had similar heights). Stronger phenotype with MZ820 is interesting, because it drives expression in much fewer number of MC61 neurons compared to NP302.

Recent connectomics analysis has provided highly comprehensive information about the connections of medulla-associated neurons (Takemura et al., 2013). Considering their dendritic arborization patterns, the MC61 neurons should be included in the volume of the electron microscope preparation analyzed in that study, although it is not possible at this state to identify them due to the lack of information about the projection targets outside of the analyzed volume.

Because of the technical difficulty, we were not able to examine the activity of LT11 and MC61 neurons in response to various

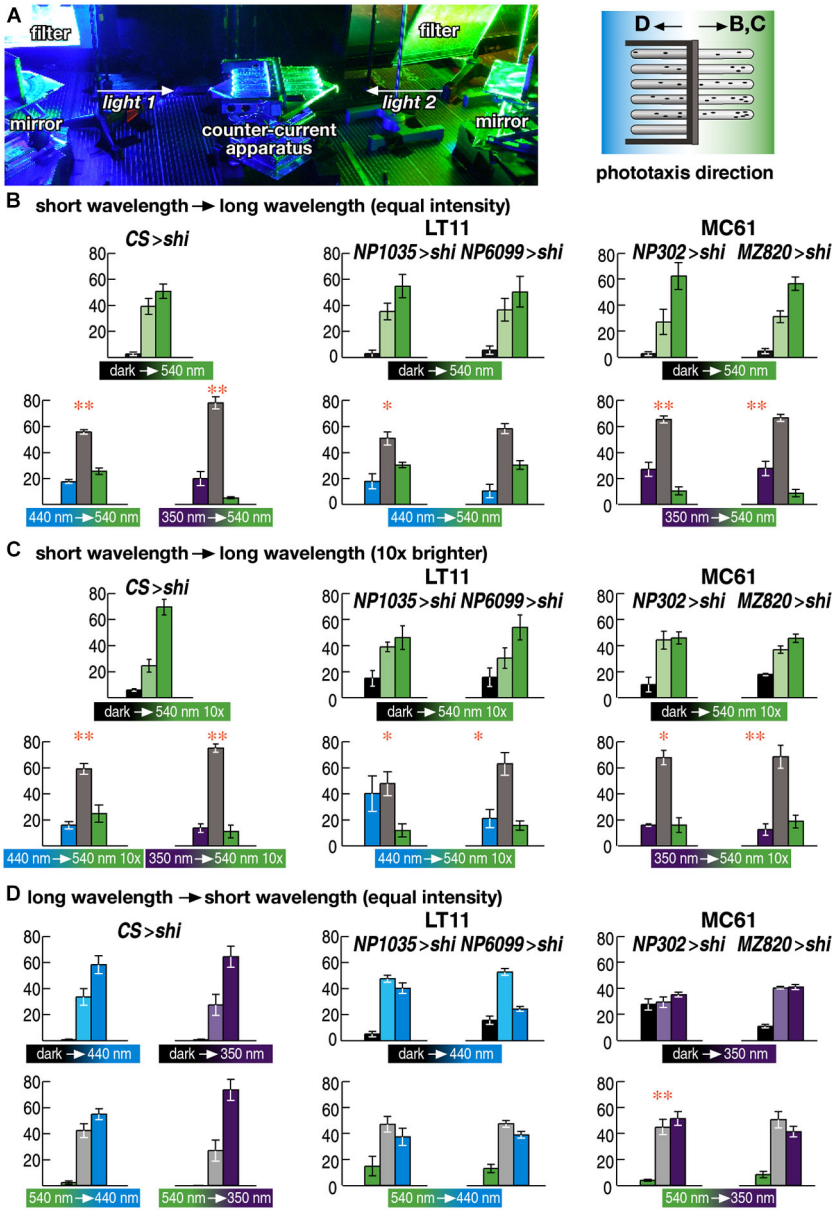

FIGURE 4 | Wavelength choice assay. **(A)** Experimental setup. Two wavelengths of light are redirected using a pair of mirrors and introduced to the counter-current apparatus from both sides. Flies were allowed to run either from shorter to longer wavelength of light **(B, C)** or from longer to shorter wavelength **(D)**. **(B–D)** Choice assay between the wavelengths to which flies showed normal (540 nm) or aberrant phototaxis (440 and 350 nm for LT11 and MC61, respectively). Light intensity was adjusted to the same level as in **Figure 3** (3×10^{18} p/m^{2}s) in **(B, D)** but was set to 10 times brighter (3×10^{19} p/m^{2}s) in **(D)**. Mean ± SEM of three independent measurements. Statistical significance of the differences between phototaxis (above) and choice assay (below) are indicated with ** ($p < 0.01$), * ($p < 0.05$; *t*-test).

wavelengths of light. AOTU of the honeybee brain was recently reported to show spectral responses (Mota et al., 2013). Technical sophistication in the future may reveal wavelength-dependent activity of LT11/MC61 neurons and their possible downstream partners.

Neural mechanisms underlying even a simple behavior like phototaxis have not been well understood. In spite of the recent advances in the understanding of the neural networks involved in color vision, little is yet known about how such information is conveyed to higher centers. Our study has provided a first glimpse into how multiple higher visual centers receive visual signals that encode complex responses to spectra in a complementary manner. Further analyses of the synaptic organization of neural circuits associated with the neurons described above will reveal how such computations are achieved and will shed broader insight into the principles of how the brain reconstructs the visual world.

ACKNOWLEDGMENTS

We thank J. Urban and G. Technau for MZ series enhancer-trap strains; the members of the NP consortium and D. Yamamoto for the NP series strains; B. Dickson, M. Ramaswami, V. V. Verkhusha, T. Kitamoto and G. Struhl for UAS-linked reporter/effecter strains; E. Buchner for antibody; T. Awasaki and N. K. Tanaka for technical discussion and screening of the fly strains; S. Shuto and M. Matsukuma for technical assistance; M. Katsuki and Y. Nishida for their support while in Okazaki; C. Hansen and R. Dorsky for their support while in Utah; C. Ichikawa; Ichikawa, S. Higashi, M. Watanabe, M. Nakamura and N. Ueno for the experiment in the OLS; and Y. Hotta, M. Heisenberg, Y. Hiromi, H. Komatsu and C. Chien for discussion and critical comments on the manuscript. Supported by BIRD and CREST grants by the Japan Science and Technology Agency and Grant-in-Aid for Scientific Research from the Ministry of Education, Culture, Sports, Science and Technology of Japan to Kei ITO. Hideo OTSUNA is supported by NIH grants R01 GM098151-01 to C. Hansen and R01 MH092256-01 to R. Dorsky.

REFERENCES

Anderson, J. C., and Laughlin, S. B. (2000). Photoreceptor performance and the co-ordination of achromatic and chromatic inputs in the fly visual system. *Vision Res.* 40, 13–31. doi: 10.1016/s0042-6989(99)00171-6

Ballinger, D. G., and Benzer, S. (1988). Photophobe (Ppb), a Drosophila mutant with a reversed sign of phototaxis; the mutation shows an allele-specific interaction with sevenless. *Proc. Natl. Acad. Sci. U S A* 85, 3960–3964. doi: 10.1073/pnas.85.11.3960

Bausenwein, B., Dittrich, A. P., and Fischbach, K. F. (1992). The optic lobe of Drosophila melanogaster. II. Sorting of retinotopic pathways in the medulla. *Cell Tissue Res.* 267, 17–28. doi: 10.1007/BF00318687

Benzer, S. (1967). Behavioral mutants of Drosophila isolated by countercurrent distribution. *Proc. Natl. Acad. Sci. U S A* 58, 1112–1119. doi: 10.1073/pnas.58.3.1112

Born, R. T. (2001). Visual processing: parallel-er and parallel-er. *Curr. Biol.* 11, 566–568. doi: 10.1016/s0960-9822(01)00345-1

Borst, A., and Haag, J. (2002). Neural networks in the cockpit of the fly. *J. Comp. Physiol. A Neuroethol. Sens. Neural Behav. Physiol.* 188, 419–437. doi: 10.1007/s00359-002-0316-8

Chou, W. H., Hall, K. J., Wilson, D. B., Wideman, C. L., Townson, S. M., Chadwell, L. V., et al. (1996). Identification of a novel Drosophila opsin reveals specific patterning of the R7 and R8 photoreceptor cells. *Neuron* 17, 1101–1115. doi: 10.1016/s0896-6273(00)80243-3

Chou, W. H., Huber, A., Bentrop, J., Schulz, S., Schwab, K., Chadwell, L. V., et al. (1999). Patterning of the R7 and R8 photoreceptor cells of Drosophila: evidence for induced and default cell-fate specification. *Development* 126, 607–616.

Douglass, J. K., and Strausfeld, N. J. (2003). Retinotopic pathways providing motion-selective information to the lobula from peripheral elementary motion-detecting circuits. *J. Comp. Neurol.* 457, 326–344. doi: 10.1002/cne.10575

Feiler, R., Bjornson, R., Kirschfeld, K., Mismer, D., Rubin, G. M., Smith, D. P., et al. (1992). Ectopic expression of ultraviolet-rhodopsins in the blue photoreceptor cells of Drosophila: visual physiology and photochemistry of transgenic animals. *J. Neurosci.* 12, 3862–3868.

Fischbach, K. F. (1979). Simultaneous and successive colour contrast expressed in "slow" phototactic behaviour of walking Drosophila melanogaster. *J. Comp. Physiol.* 130, 161–171. doi: 10.1007/bf00611050

Fischbach, K. F., and Dittrich, A. P. (1989). The optic lobe of Drosophila melanogaster. I. A Golgi analysis of wild-type structure. *Cell Tissue Res.* 258, 441–475. doi: 10.1007/BF00218858

Fox, J. L., and Frye, M. A. (2013). Figure-ground discrimination behavior in Drosophila. II. Visual influences on head movement. *J. Exp. Biol.* doi: 10.1242/jeb.097220. [Epub ahead of print].

Gao, S., Takemura, S. Y., Ting, C. Y., Huang, S., Lu, Z., Luan, H., et al. (2008). The neural substrate of spectral preference in Drosophila. *Neuron* 60, 328–342. doi: 10.1016/j.neuron.2008.08.010

Häder, D.-P., and Häder, M. A. (1988). Inhibition of motility and phototaxis in the green flagellate, Euglena gracilis, by UV-B radiation. *Arch. Microbiol.* 150, 20–25. doi: 10.1007/bf00409712

Heinze, S., and Homberg, U. (2007). Maplike representation of celestial E-vector orientations in the brain of an insect. *Science* 315, 995–997. doi: 10.1126/science.1135531

Heisenberg, M., Wonneberger, R., and Wolf, R. (1978). Optomotor blind H31 - a Drosophila mutant of the lobula plate giant neurons. *J. Comp. Physiol.* 124, 287–296. doi: 10.1007/BF00661379

Hotta, Y., and Benzer, S. (1970). Genetic dissection of the Drosophila nervous system by means of mosaics. *Proc. Natl. Acad. Sci. U S A* 67, 1156–1163. doi: 10.1073/pnas.67.3.1156

Ito, M., Masuda, N., Shinomiya, K., Endo, K., and Ito, K. (2013). Systematic analysis of neural projections reveals clonal composition of the Drosophila brain. *Curr. Biol.* 23, 644–655. doi: 10.1016/j.cub.2013.03.015

Ito, K., Shinomiya, K., Ito, M., Armstrong, D., Boyan, G., Hartenstein, V., et al. (2014). A systematic nomenclature for the insect brain. *Neuron* in press.

Kirschfeld, K. (1994). Tracking of small objects in front of a textured background by insects and vertebrates: phenomena and neuronal basis. *Biol. Cybern.* 70, 407–415. doi: 10.1007/bf00203233

Kitamoto, T. (2001). Conditional modification of behavior in Drosophila by targeted expression of a temperature-sensitive shibire allele in defined neurons. *J. Neurobiol.* 47, 81–92. doi: 10.1002/neu.1018

Krapp, H. G., and Hengstenberg, R. (1996). Estimation of self-motion by optic flow processing in single visual interneurons. *Nature* 384, 463–466. doi: 10.1038/384463a0

Liu, G., Seiler, H., Wen, A., Zars, T., Ito, K., Wolf, R., et al. (2006). Distinct memory traces for two visual features in the Drosophilabrain. *Nature* 439, 551–556. doi: 10.1038/nature04381

Martin, P. R., Lee, B. B., White, A. J., Solomon, S. G., and Ruttiger, L. (2001). Chromatic sensitivity of ganglion cells in the peripheral primate retina. *Nature* 410, 933–936. doi: 10.1038/35073587

Morante, J., and Desplan, C. (2008). The color-vision circuit in the medulla of Drosophila. *Curr. Biol.* 18, 553–565. doi: 10.1016/j.cub.2008.02.075

Mota, T., Gronenberg, W., Giurfa, M., and Sandoz, J. C. (2013). Chromatic processing in the anterior optic tubercle of the honey bee brain. *J. Neurosci.* 33, 4–16. doi: 10.1523/jneurosci.1412-12.2013

Nassi, J. J., and Callaway, E. M. (2006). Multiple circuits relaying primate parallel visual pathways to the middle temporal area. *J. Neurosci.* 26, 12789–12798. doi: 10.1523/jneurosci.4044-06.2006

Otsuna, H., and Ito, K. (2006). Systematic analysis of the visual projection neurons of Drosophila melanogaster. I. Lobula-specific pathways. *J. Comp. Neurol.* 497, 928–958. doi: 10.1002/cne.21015

Papatsenko, D., Sheng, G., and Desplan, C. (1997). A new rhodopsin in R8 photoreceptors of Drosophila: evidence for coordinate expression with Rh3 in R7 cells. *Development* 124, 1665–1673.

Rister, J., Pauls, D., Schnell, B., Ting, C. Y., Lee, C. H., Sinakevitch, I., et al. (2007). Dissection of the peripheral motion channel in the visual system of Drosophila melanogaster. *Neuron* 56, 155–170. doi: 10.1016/j.neuron.2007.09.014

Salcedo, E., Huber, A., Henrich, S., Chadwell, L. V., Chou, W. H., Paulsen, R., et al. (1999). Blue- and green-absorbing visual pigments of Drosophila: ectopic expression and physiological characterization of the R8 photoreceptor cell-specific Rh5 and Rh6 rhodopsins. *J. Neurosci.* 19, 10716–10726.

Schümperli, R. A. (1973). Evidence for colour vision in Drosophila melanogaster through spontaneous phototactic choice behavior. *J. Comp. Physiol.* 86, 77–94. doi: 10.1007/bf00694480

Seiger, M. B., and Woodruff, D. L. (1987). The effect of relative humidity on photoresponse in sympatric species of Drosophila: long-term exposure to desiccating environments. *J. Insect Physiol.* 8, 529–532. doi: 10.1016/0022-1910(87)90066-7

Shinomiya, K., Matsuda, K., Oishi, T., Otsuna, H., and Ito, K. (2011). Flybrain neuron database: a comprehensive database system of the Drosophila brain neurons. *J. Comp. Neurol.* 519, 807–833. doi: 10.1002/cne.22540

Strausfeld, N. J., and Okamura, J. Y. (2007). Visual system of calliphorid flies: organization of optic glomeruli and their lobula complex efferents. *J. Comp. Neurol.* 500, 166–188. doi: 10.1002/cne.21196

Strausfeld, N. J., Douglass, J. K., Campbell, H., and Higgins, C. M. (2006). "Parallel processing in the optic lobes of flies and the occurrence of motion computing circuits," in *Invertebrate Vision*, eds E. Warrant and D.-E. Nilsson (Cambridge Univ. Press), 349–392.

Takemura, S. Y., Bharioke, A., Lu, Z., Nern, A., Vitaladevuni, S., Rivlin, P. K., et al. (2013). A visual motion detection circuit suggested by Drosophila connectomics. *Nature* 500, 175–181. doi: 10.1038/nature12450

Van Essen, D. C., and Gallant, J. L. (1994). Neural mechanisms of form and motion processing in the primate visual system. *Neuron* 13, 1–10. doi: 10.1016/0896-6273(94)90455-3

Wagh, D. A., Rasse, T. M., Asan, E., Hofbauer, A., Schwenkert, I., Durrbeck, H., et al. (2006). Bruchpilot, a protein with homology to ELKS/CAST, is required for structural integrity and function of synaptic active zones in Drosophila. *Neuron* 49, 833–844. doi: 10.1016/j.neuron.2006.06.022

Wardill, T. J., List, O., Li, X., Dongre, S., Mcculloch, M., Ting, C. Y., et al. (2012). Multiple spectral inputs improve motion discrimination in the Drosophila visual system. *Science* 336, 925–931. doi: 10.1126/science.1215317

Watanabe, M., Furuya, M., Miyoshi, Y., Inoue, Y., and Iwahashi, I. (1983). Design and performance of the Okazaki large spectrograph for photobiological research. *BioScience* 33, 53–54. doi: 10.2307/1309246

Wicklein, M., and Strausfeld, N. J. (2000). Organization and significance of neurons that detect change of visual depth in the hawk moth Manduca sexta. *J. Comp. Neurol.* 424, 356–376. doi: 10.1002/1096-9861(20000821)424:2<356::aid-cne12>3.3.co;2-k

Wolff, T., and Ready, D. F. (1993). "Pattern formation in the Drosophila retina," in *The Development of Drosophila Melanogaster*, eds M. Bate and A. Martinez-Arias (Cold Spring Harbor: Cold Spring Harbor Laboratory Press), 1277–1325.

Wong, A. M., Wang, J. W., and Axel, R. (2002). Spatial representation of the glomerular map in the Drosophila protocerebrum. *Cell* 109, 229–241. doi: 10.1016/s0092-8674(02)00707-9

Yamaguchi, S., Desplan, C., and Heisenberg, M. (2010). Contribution of photoreceptor subtypes to spectral wavelength preference in Drosophila. *Proc. Natl. Acad. Sci. U S A* 107, 5634–5639. doi: 10.1073/pnas.0809398107

Yamaguchi, S., Wolf, R., Desplan, C., and Heisenberg, M. (2008). Motion vision is independent of color in Drosophila. *Proc. Natl. Acad. Sci. U S A* 105, 4910–4915. doi: 10.1073/pnas.0711484105

Zeki, S., Watson, J. D., Lueck, C. J., Friston, K. J., Kennard, C., and Frackowiak, R. S. (1991). A direct demonstration of functional specialization in human visual cortex. *J. Neurosci.* 11, 641–649.

Zhou, Y., Ji, X., Gong, H., Gong, Z., and Liu, L. (2012). Edge detection depends on achromatic channel in Drosophila melanogaster. *J. Exp. Biol.* 215, 3478–3487. doi: 10.1242/jeb.070839

Conflict of Interest Statement: The authors declare that the research was conducted in the absence of any commercial or financial relationships that could be construed as a potential conflict of interest.

Received: 25 August 2013; accepted: 21 January 2014; published online: 10 February 2014.

Citation: Otsuna H, Shinomiya K and Ito K (2014) Parallel neural pathways in higher visual centers of the Drosophila *brain that mediate wavelength-specific behavior. Front. Neural Circuits* ***8****:8. doi: 10.3389/fncir.2014.00008*

This article was submitted to the journal Frontiers in Neural Circuits.

frontiers in
NEURAL CIRCUITS

ORIGINAL RESEARCH ARTICLE
published: 27 November 2013
doi: 10.3389/fncir.2013.00191

Corticosterone rapidly increases thorns of CA3 neurons via synaptic/extranuclear glucocorticoid receptor in rat hippocampus

Miyuki Yoshiya [1,2†], ***Yoshimasa Komatsuzaki*** [1,3†], ***Yasushi Hojo*** [1,2], ***Muneki Ikeda*** [1], ***Hideo Mukai*** [1,2], ***Yusuke Hatanaka*** [1,2], ***Gen Murakami*** [1,2], ***Mitsuhiro Kawata*** [4], ***Tetsuya Kimoto*** [1] ***and Suguru Kawato*** [1,2]***

[1] *Department of Biophysics and Life Sciences, Graduate School of Arts and Sciences, The University of Tokyo, Tokyo, Japan*
[2] *Bioinformatics Project of Japan Science and Technology Agency, The University of Tokyo, Tokyo, Japan*
[3] *Department of Physics, College of Science and Technology, Nihon University, Chiyoda, Tokyo, Japan*
[4] *Department of Anatomy and Neurobiology, Kyoto Prefectural University of Medicine, Kamigyo, Kyoto, Japan*

Edited by:
Yasuo Kawaguchi, National Institute for Physiological Sciences, Japan

Reviewed by:
Yuji Ikegaya, The University of Tokyo, Japan
Janine Prange-Kiel, University of Texas Southwestern Medical Center, USA

***Correspondence:**
Suguru Kawato, Department of Biophysics and Life Sciences, Graduate School of Arts and Sciences, The University of Tokyo, Komaba 3-8-1, Meguro, Tokyo 153, Japan
e-mail: kawato@bio.c.u-tokyo.ac.jp

† *Miyuki Yoshiya and Yoshimasa Komatsuzaki have contributed equally to this work.*

Modulation of synapses under acute stress is attracting much attention. Exposure to acute stress induces corticosterone (CORT) secretion from the adrenal cortex, resulting in rapid increase of CORT levels in plasma and the hippocampus. We tried to test whether rapid CORT effects involve activation of essential kinases as non-genomic processes. We demonstrated rapid effects (∼1 h) of CORT on the density of thorns, by imaging Lucifer Yellow-injected neurons in adult male rat hippocampal slices. Thorns of thorny excrescences of CA3 hippocampal neurons are post-synaptic regions whose presynaptic partners are mossy fiber terminals. The application of CORT at 100, 500, and 1000 nM induced a rapid increase in the density of thorns in the stratum lucidum of CA3 pyramidal neurons. Co-administration of RU486, an antagonist of glucocorticoid receptor (GR), abolished the effect of CORT. Blocking a single kinase, including MAPK, PKA, or PKC, suppressed CORT-induced enhancement of thorn-genesis. On the other hand, GSK-3β was not involved in the signaling of thorn-genesis. Blocking AMPA receptors suppressed the CORT effect. Expression of CA3 synaptic/extranuclear GR was demonstrated by immunogold electron microscopic analysis. From these results, stress levels of CORT (100–1000 nM) might drive the rapid thorn-genesis via synaptic/extranuclear GR and multiple kinase pathways, although a role of nuclear GRs cannot be completely excluded.

Keywords: corticosterone, hippocampus, kinase, thorn, stress, spine

INTRODUCTION

Functions and architectures of mammalian hippocampus are altered or modulated under the stressful conditions. At least in part, the influences of stress are elicited by corticosterone (CORT), produced in adrenal cortex in response to stress. The hippocampus, center for learning and memory, is particularly sensitive to CORT (Woolley et al., 1990b; Watanabe et al., 1992; Reagan and McEwen, 1997), because glucocorticoid receptors (GR) are abundantly expressed in the hippocampus (Morimoto et al., 1996). The chronic stress-induced increase in CORT slowly produces neuronal cell damage in the hippocampus. Rats exposed to restraint stress for 3 weeks have exhibited neuronal atrophy and decreases of dendritic branches similar to that seen in rats treated with a high dose of CORT for 3 weeks (Woolley et al., 1990b; Watanabe et al., 1992).

The CA3 is considered as a region where controls associative memory (Morris et al., 1982; McNaughton and Morris, 1987). In the stratum lucidum of the CA3, pyramidal neurons have huge and complex post-synaptic structures, named thorny excrescences. One thorny excrescence consists of multiple heads named thorns with one neck along a dendritic branch (Amaral and Dent, 1981; Chicurel and Harris, 1992). One mossy fiber terminal of dentate granule cells contacts multiple thorns of thorny excrescences of CA3 neuron. Thorny excrescences may play essential roles in hippocampal function. Chronic restraint stress has induced retraction of thorny excrescences, which has subsequently been reversed after water maze training. On the other hand, water maze training alone has increased the volume of thorny excrescence as well as the number of thorns per thorny excrescence (Stewart et al., 2005). These slow steroid effects may be mediated by nuclear receptors. Upon binding of steroids to nuclear GR, GR forms dimer and bind to the glucocorticoid response element of genes, resulting in modulation of protein synthesis.

The neuronal response to acute stress (within a few hours) may be very different from that of chronic stress (Sorrells et al., 2009). CORT modulates rapidly (within 2 h) the neuronal activity, which may occur independently of the regulation of the gene expression (Lupien and McEwen, 1997). Stress levels (500–1000 nM) of CORT have been demonstrated to rapidly suppress within 0.5 h the long-term potentiation (LTP) induced by primed burst stimulation (Diamond et al., 1992) or tetanic stimulation (Shibuya et al., 2003). A 0.5 h application of 1–10 μM CORT has rapidly suppressed the *N*-methyl D-aspartate (NMDA)-induced Ca^{2+} elevation in the CA1 region of adult hippocampal slices (Sato et al., 2004). In our early study (Komatsuzaki et al., 2012), we demonstrated in CA1 that the application of CORT at 100–1000 nM induces a rapid

(∼1 h) increase in the density of spines of pyramidal neurons. Blocking kinases, including MAPK, PKA, and PKC, suppressed CORT-induced enhancement of spinogenesis. The receptor of this rapid CORT reaction is synaptic GR.

Compared to the CA1 region, little is known about the response of CA3 hippocampal thorns to the acute stress. We perform the investigations in order to examine the hypothesis that CORT may induce activation of synaptic/extranuclear GR, leading to activation of essential kinases, resulting in rapid remodeling of thorns in CA3 neurons.

MATERIALS AND METHODS

ANIMALS

Male Wistar rats were purchased from Saitama Experimental Animal Supply (Japan). All animals were maintained under a 12 h light/12 h dark exposure and free access to food and water. The experimental procedure of this research was approved by the Committee for Animal Research of the University of Tokyo.

CHEMICALS

Corticosterone, actinomycin D, cyano-nitroquinoxaline-dione (CNQX), MK-801, PD98059, RU486, and Lucifer Yellow CH were purchased from Sigma (USA). Chelerythrine and glycogen synthase kinase-3β (GSK-3β) inhibitor VIII (AR-A014418) were purchased from Calbiochem (Germany). H-89 was purchased from Biomol (USA).

SLICE PREPARATION

Twelve weeks male rats were deeply anesthetized and decapitated between 9:00 AM and 10:00 AM when plasma CORT levels are low. Immediately after decapitation, the brain was removed from the skull and placed in ice-cold oxygenated (95% O_2, 5% CO_2) artificial cerebrospinal fluid (ACSF) containing (in mM): 124 NaCl, 5 KCl, 1.25 NaH_2PO_4, 2 $MgSO_4$, 2 $CaCl_2$, 22 $NaHCO_3$, and 10 D-glucose (all from Wako); pH was set at 7.4. Hippocampal slices, 400 μm thick, were prepared with a vibratome (Dosaka, Japan). These slices were "freshly prepared" slices without ACSF incubation. Slices were then incubated for recovery in oxygenated ACSF for 2 h (slice recovery process) in order to obtain conventional "acute slices." These "acute" slices were then incubated at room temperature with CORT or other drugs such as kinase inhibitors. Immediately after drug exposure (for 0.5, 1, or 2 h), slices were prefixed with 4% paraformaldehyde at 4°C for 2–4 h.

CURRENT INJECTION OF LUCIFER YELLOW

Thorn imaging and analysis with confocal microscopy was performed essentially as described previously (Komatsuzaki et al., 2005, 2012; Tsurugizawa et al., 2005; Mukai et al., 2007). Briefly, neurons within slices were visualized by an injection of Lucifer Yellow under a Nikon E600FN microscope (Japan) equipped with a C2400–79H infrared camera (Hamamatsu Photonics, Japan) and with a 40× water immersion lens (Nikon). Dye was injected with a glass electrode whose tip (tip diameter < 1 μm) was filled with 5% Lucifer Yellow under a negative DC current of 10 nA for 15 min, using Axopatch 200B (Axon Instruments, USA). Approximately five neurons within a 100–200 μm depth from the surface of a slice were injected (Duan et al., 2002). After labeling, slices were fixed again with 4% paraformaldehyde at 4°C overnight.

CONFOCAL LASER SCAN MICROSCOPY AND ANALYSIS

The imaging was performed from sequential z-series scans with confocal laser scan microscope (LSM5; Carl Zeiss, Germany) at high zoom (×3.0) with a 63× water immersion lens, NA 1.2. For Lucifer Yellow, the excitation and emission wavelengths were 488 and 515 nm, respectively. Three-dimensional image was reconstructed from approximately 40 sequential z-series sections of every 0.45 μm. The applied zoom factor (×3.0) yielded 23 pixels per 1 μm. The confocal lateral resolution was approximately 0.26 μm. Our resolution limits were regarded to be sufficient to allow the determination of the density of thorns. Confocal images were then deconvoluted using AutoDeblur software (AutoQuant, USA).

In each slice, two to three neurons with more than 100 thorns were analyzed, and at least 90 thorns were counted on each frame. In total, $N = 12$ neurons and $n = 1400$–1800 thorns were analyzed for each drug treatment. The density of thorns was analyzed with Spiso-3D developed by Bioinformatics Project of Kawato's group (Mukai et al., 2011; Komatsuzaki et al., 2012). Results obtained by Spiso-3D are similar to those by Neurolucida (MicroBrightField, USA) within assessment difference of 2%, and Spiso-3D considerably reduces human errors and experimental labor of manual software (Mukai et al., 2011). The apical dendrite in the stratum lucidum has thorns. Such a dendrite (primary or secondary dendrite) is present within 100 μm from the soma. The density of thorns was calculated from the number of thorns along the dendrite having a total length of 30–100 μm. While counting the thorns in reconstructed images, the position and verification of thorns were aided by three-dimensional reconstructions and by observation of the images in consecutive single planes.

POSTEMBEDDING IMMUNOGOLD METHOD FOR ELECTRON MICROSCOPY

Immunoelectroscopic analysis was performed essentially as described elsewhere (Hojo et al., 2004; Mukai et al., 2007; Ooishi et al., 2012b). Rat hippocampus was frozen and sliced coronally. Freeze substitution and low-temperature embedding of the specimens was performed as described previously (Roberson et al., 1999). The samples were immersed in uranyl acetate in anhydrous methanol (−90°C). The samples were infiltrated with Lowicryl HM20 resin (Electron Microscopy Sciences, USA) and polymerization was performed with ultraviolet light. Ultrathin sections were cut using a Reichert-Jung ultramicrotome. For immunolabeling, sections were incubated with primary antibody for GR (Morimoto et al., 1996; diluted to 1/3000) overnight, and incubated with secondary gold-tagged (10 nm) Fab fragment in Tris buffered saline (TBS). Sections were counterstained with 1% uranyl acetate, and viewed on a JEOL 1200EX electron microscope (Japan). Images were captured using a CCD camera (Advanced Microscopy Techniques, USA). The antibody is specific to GR in the hippocampus as shown with Western blot (Komatsuzaki et al., 2005; Ooishi et al., 2012b).

STATISTICAL ANALYSIS

All the data are expressed as means ± SEM. The significance of CORT or drug effect was examined using the Tukey–Kramer *post hoc* multiple comparisons test when one way ANOVA tests yielded $p < 0.05$.

RESULTS

We investigated the effect of CORT on the modulation of the thorn density in the hippocampus CA3 stratum lucidum. Lucifer Yellow-injected neurons in hippocampal slices from 12-week-old male rats were imaged using confocal laser scan microscopy (**Figure 1**). Thorny excrescences were located on apical dendrites within 100 μm from the soma, on which mossy fiber terminals attached.

CORT INCREASED THE DENSITY OF THORNS IN CA3 STRATUM LUCIDUM

Following a 1 h treatment with CORT, treated dendrites had significantly more thorns than control dendrites (i.e., 1 h incubation in ACSF without CORT). Time dependency was examined by treating slices for 0.5, 1, and 2 h with 1 μM CORT. The enhancing effect on the total thorn density was approximately proportional to the incubation time, showing 2.7 (0.5 h), 3.2 (1 h), and 3.2 thorns/μm (2 h) in CORT-treatments (**Figure 2A**). Dose dependency was also examined after a 1 h incubation (**Figure 2B**). In CORT-treatment group, the enhancing effect was significant at 1 μM CORT (3.2 thorns/μm) compared with 10 nM (2.4 thorns/μm), 30 nM (2.9 thorns/μm), 100 nM (3.0 thorns/μm), and 500 nM (3.3 thorns/μm) CORT. Because a 1 h treatment with 1 μM CORT was most effective for thorn-genesis, these incubation time and concentration were used in the following investigations unless specified.

A 1 h treatment with 1 μM CORT was used in the kinase inhibitor investigations unless specified, because 1 μM CORT showed the strongest effects. Blocking of GR by 10 μM RU486 completely abolished the enhancing effect by 1 μM CORT on the thorn density (2.4 thorns/μm; **Figure 3**). It should be noted that rapid CORT effects (within 1 h) did not induce neurodegeneration, as judged from no significant shrinking in dendrite length and atrophy of cell body (data not shown).

EFFECT OF CORT WAS BLOCKED BY SEVERAL KINASE INHIBITORS

Next we investigated kinase signaling pathways involved in the CORT-induced thorn-genesis using specific inhibitors for kinases (**Figure 4**), by examining the total thorn density. We focus on MAPK, PKA, and PKC, since these kinases often play an important role in synaptic plasticity. Blocking of Erk MAPK by application of 20 μM PD98059 (PD; Dudley et al., 1995), abolished the CORT-induced increase in thorn density resulting in 2.6 thorns/μm. Application of 10 μM H-89 (H89), a protein A kinase inhibitor (Chijiwa et al., 1990), prevented the effect by CORT. Application of 10 μM chelerythrine (Chel), an inhibitor of all the PKC species (alpha, delta, and epsilon; Herbert et al., 1990), prevented the effect by CORT. Blocking of glycogen synthase kinase-3β (GSK-3β) by 10 μM Inhibitor VIII (I8; Bhat et al., 2003) did not alter CORT-induced thorn-genesis. Effect of GSK-3β, which is tau protein kinase, was investigated, since phosphorylation of tau protein (that stabilizes microtubules) is necessary for BDNF (brain-derived neurotrophic factor)-induced spinogenesis in the hippocampus (Chen et al., 2012).

Because the concentrations of inhibitors applied are recommended levels (Bhat et al., 2003; Alonso et al., 2004; Birnbaum et al., 2004; Hammond et al., 2008), the observed inhibitory effects are not artifacts due to excess amount of inhibitors. It should be noted that these kinase inhibitors alone did not significantly affect the thorn density within experimental error, indicating that the observed inhibitory effects are not due to simple blocker's non-specific suppressive effects (**Figure 4B**).

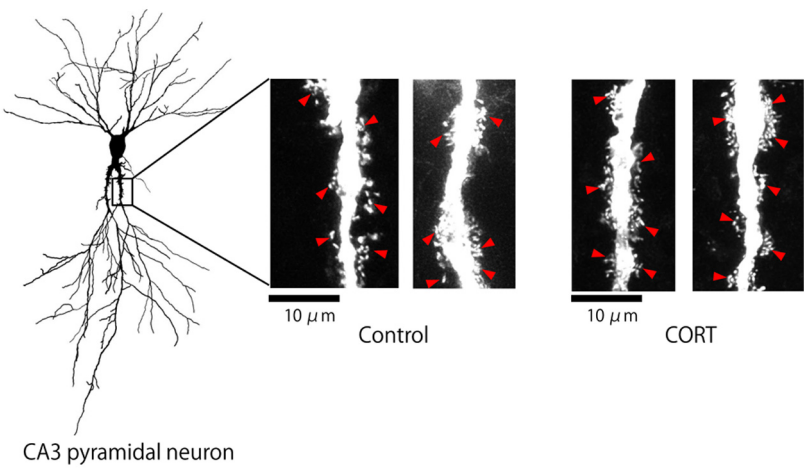

FIGURE 1 | Changes in the density of thorns by CORT in hippocampal slices. Maximal intensity projections onto XY plane from z-series confocal micrographs, showing thorns along the primary dendrites of hippocampal CA3 pyramidal neurons. Left image shows a traced whole image of Lucifer Yellow-injected CA3 neuron. Right images show thorns (red arrowheads) without drug-treatments (Control) or thorns after 1 μM CORT treatments (CORT) for 1 h. Bar 10 μm.

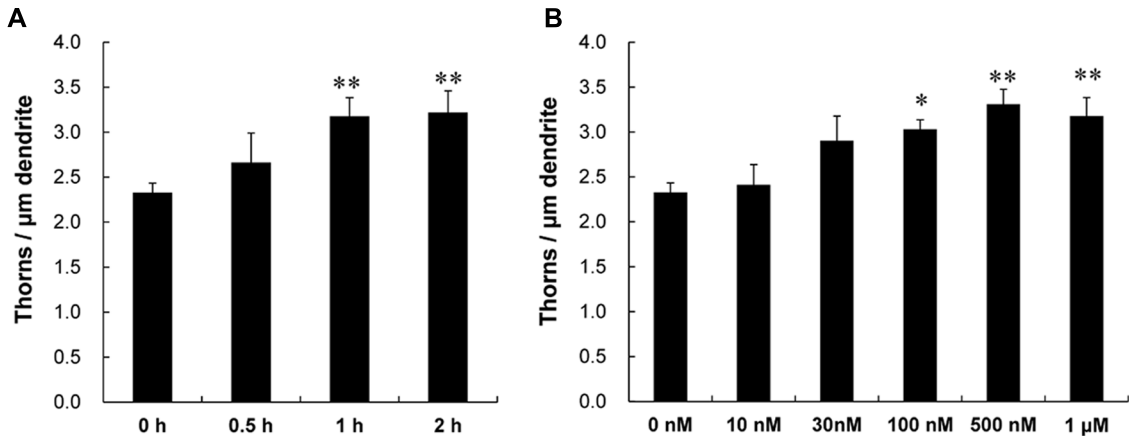

FIGURE 2 | Time dependency and dose dependency of CORT effects on the thorn density of CA3 neurons. Thorns were analyzed along the primary and secondary dendrites of pyramidal neurons in the stratum lucidum of CA3 neurons. **(A)** The time dependency of CORT effects on the thorn density in CA3 neurons, after 0.5 h treatment (0.5 h), 1 h treatment (1 h), and 2 h treatment (2 h) in ACSF with 1 μM CORT. As a control, no treatment with CORT (0 h) is shown. **(B)** Dose dependency of CORT treatments on the thorn density. A 1 h treatment in ACSF without CORT (0 nM), with 10 nM CORT (10 nM), with 30 nM CORT (30 nM), with 100 nM CORT (100 nM), with 500 nM CORT (500 nM), and with 1 μM CORT (1 μM). Vertical axis is the average number of thorns per 1 μm of dendrite. Results are reported as mean ± SEM. The significance of CORT or drug effect was examined using the Tukey–Kramer *post hoc* multiple comparisons test when one way ANOVA tests yielded $P < 0.05$. The significance yielded $^{**}P < 0.01$ $^{*}P < 0.05$, $^{**}P < 0.01$ to 0 h and 0 nM. For each drug treatment, we investigated 3 rats, 6 slices, 12 neurons, 12 dendrites, and 1400–1800 thorns.

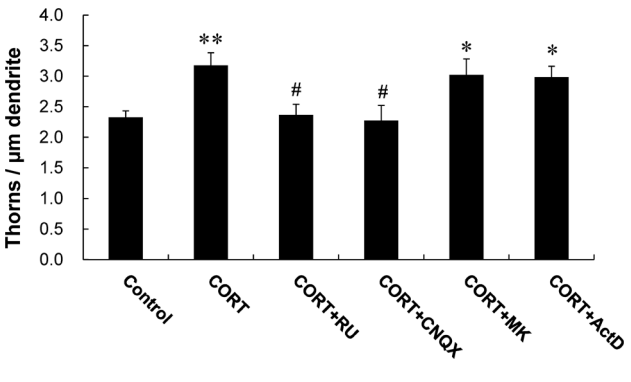

FIGURE 3 | Effects of blockers of receptors on CORT-induced changes in the thorn density. A 1 h treatment in ACSF without drugs (Control), with 1 μM CORT (CORT), with 1 and 10 μM RU486 (CORT + RU), with 1 μM CORT and 20 μM CNQX (CORT + CNQX), and with 1 μM CORT and 50 μM MK-801 (CORT + MK). Vertical axis is the average number of thorns per 1 μm of dendrite. Results are reported as mean ± SEM. The significance of CORT or drug effect was examined using the Tukey–Kramer *post hoc* multiple comparisons test when one way ANOVA tests yielded $P < 0.05$. $^{*}P < 0.05$, $^{**}P < 0.01$ vs. Control. $^{\#}P < 0.05$ vs. CORT. For each drug treatment, we investigated 3 rats, 6 slices, 12 neurons, 12 dendrites, and 1400–1800 thorns.

Blocking of glutamate receptors abolished CORT-induced thorn-genesis

We investigated the importance of Ca^{2+} homeostasis within thorns on CORT effects. Because the Ca^{2+} level may be maintained with spontaneous fluctuation of opening/closing via ionotropic glutamate receptors in thorns, we examined thorn-genesis in the presence of inhibitors of these receptors. 6-cyano-7-nitroquinoxaline-2,3-dione (CNQX), an inhibitor of α-amino-3-hydroxy-5-methyl-4-isoxazolepropionate (AMPA) receptor, significantly suppressed the effect of CORT on the thorn density to 2.3 thorns/μm (**Figure 3**). MK-801, an NMDA receptor blocker, did not abolish the CORT effect.

In additional experiments, Actinomycin D (ActD), an mRNA synthesis inhibitor, did not significantly suppress the CORT-induced increase in the density of thorns (**Figure 3**).

Ultrastructural analysis for synaptic, extranuclear and nuclear localization of GR

To explain the site of rapid thorn-genesis by the activation of GR, a clarification of the subcellular localization (particularly the synaptic or extranuclear localization) of GR in CA3 pyramidal cells is essential. The synaptic, extranuclear and nuclear localization of GR was clarified via ultrastructural investigations using GR IgG (1/3000). An immunoelectron microscopic analysis using post-embedded immunogold was performed to determine the localization of GR-immunoreactivity in the hippocampal CA3 pyramidal cells. GR was localized not only in the nuclei but also in both the axon terminals and thorns of pyramidal cells (**Figure 5A**). At postsynapses, gold particles were distributed within the cytoplasm of the thorn head. Significant labeling along dendrites was also observed (**Figure 5B**). For a search of immunogold-labeled GR proteins, multiple labeling (three or more) of immunogold in the pre- and post-synaptic compartments was confirmed in at least 100 images. Each image contained several synapses among which at least one synapse expressed GR particles. We also observed some synapses in one image that did not express GR particles. Consequently, we observed approximately 10–20% of synapses that expressed GR particles. Preadsorption of the antibody with GR antigen (30 μg/ml) resulted in the disappearance of immunoreactivity.

The antibody used for the current experiments were shown to have specific binding to GR in the hippocampus with Western

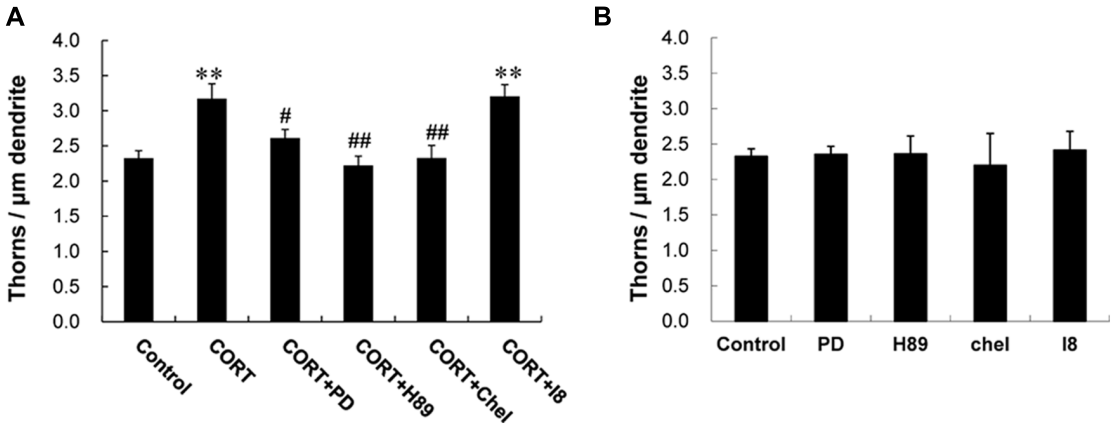

FIGURE 4 | Suppression effects by kinase inhibitors on CORT-induced changes in the density of thorns. (A) A 1 h treatment in ACSF without drugs (Control), with 1 μM CORT (CORT), with 1 μM CORT and 20 μM PD98059 (MAPK inhibitor; CORT + PD), with 1 μM CORT and 10 μM H-89 (PKA inhibitor; CORT + H89), with 1 μM CORT and 10 μM chelerythrine (PKC inhibitor; CORT + Chel), and with 1 μM CORT and 10 μM GSK-3β Inhibitor VIII (CORT + I8). **(B)** No effect of kinase inhibitors alone on the density of thorns in CA3 neurons. Abbreviations are the same as **(A)**. Vertical axis is the average number of thorns per 1 μm of dendrite. Results are reported as mean ± SEM. The significance of CORT or drug effect was examined using the Tukey–Kramer post hoc multiple comparisons test when one way ANOVA tests yielded $P < 0.05$. $^{**}P < 0.01$ vs. Control. $^{\#}P < 0.05$, $^{\#\#}P < 0.01$ vs. CORT. For each drug treatment, we investigated 3 rats, 6 slices, 12 neurons, 12 dendrites, and 1600–1800 thorns.

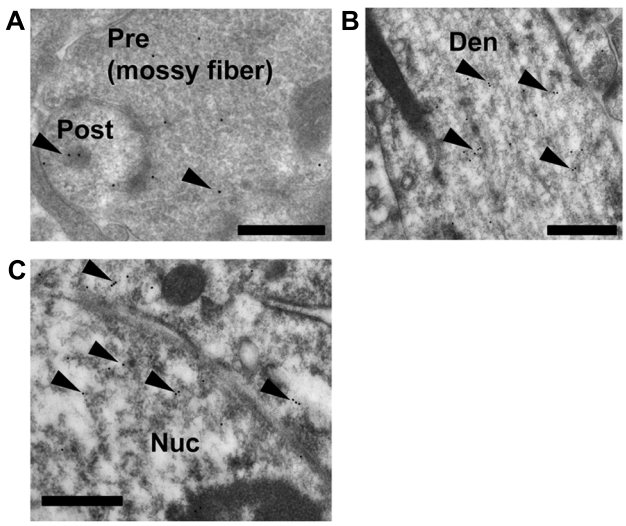

FIGURE 5 | Immunoelectron microscopic analysis of the distribution of GR within the mossy fiber synapses, dendrites in stratum lucidum and nuclei of pyramidal cells in CA3 region. Gold particles (arrowheads), specifically indicating the presence of GR, were localized in the pre- and postsynaptic regions **(A)**. In dendrites, gold particles were often found in the cytoplasmic space **(B)**. Gold particles were also localized in the nuclei **(C)**. A search for immuno-gold labeled GR proteins was performed at least 30 synapses at CA3 region from more than 100 independent images. A 1:3000 dilution of IgG was used to prevent non-specific labeling. Pre, presynaptic region; Post, post synaptic region; Den, dendrite; Nuc, nucleus. Scale bar, 500 nm.

blotting (Komatsuzaki et al., 2005; Ooishi et al., 2012b). As a negative control of GR specificity, no GR immunoreactivity was observed in the magnocellular division of the paraventricular nucleus (Morimoto et al., 1996).

DISCUSSION

The current study demonstrated GR- and kinase-dependent mechanisms of rapid CORT-induced thorn-genesis in CA3 pyramidal neurons of the adult male rat hippocampus. An extremely concentrated distribution of thorny excrescences, as compared with sparse distribution of spines located in other regions, such as CA1, prevented detailed analysis of thorny excrescences by previous studies using Golgi staining methods (Gould et al., 1990; Woolley et al., 1990a). We were able to analyze the number of thorns by the high-resolution image analysis of Lucifer Yellow-injected neurons, using deconvolution, and digital three-dimensional analysis. Mossy fiber terminals originating from granule cells in DG provide excitatory inputs to CA3 neurons via thorny excrescences in the stratum lucidum (Amaral and Dent, 1981; Chicurel and Harris, 1992). Our data imply that CORT may rapidly enhance the excitatory input to CA3 from DG by increasing the density of thorns.

STEROID LEVELS IN "ACUTE" SLICES USED FOR THORN EXPERIMENTS

Following exposure to stress in rat, a high-dose of CORT (about 1 μM) is secreted by the adrenal cortex and readily penetrates into the brain from the blood circulation. The steroid levels in slices used for thorn analysis must be known. From our earlier study (Komatsuzaki et al., 2012), the CORT concentration in the freshly isolated hippocampus was 400–1000 nM as determined by mass-spectrometric analysis (Hojo et al., 2009, 2011; Ooishi et al., 2012a,b), because rats were under decapitation stress which caused penetration of elevated plasma CORT (1-2 μM) into the hippocampus (Pardridge and Mietus, 1979). Note that 1-2 μM CORT is more than the upper limit capacity (400–600 nM) of CORT binding globulin (Breuner and Orchinik, 2002). However, the control "acute" slices, used for the thorn analysis, have very low CORT level of approximaterly 2 nM by recovery incubation of "fresh" slices (with high CORT concentration of 400–1000 nM)

in steroid-free ACSF for 2 h, due to leakage of CORT from slices to ACSF (Hojo et al., 2011; Ooishi et al., 2012a,b). This CORT leakage always occurs in hippocampal slices prepared at different time (morning, afternoon, or evening), therefore control acute slices should have always low CORT. From these reasons, the enhanced thorn-genesis occurred upon increase in CORT level from approximately 2 nM (control) to 100–1000 nM by CORT application.

CONTRIBUTION OF SYNAPTIC/EXTRANUCLEAR GR TO THE RAPID MODULATION

Since the effect of CORT had been blocked by RU486, we confirmed that CORT-effect was directly mediated by GR. The expression of GR in the CA3 region was demonstrated by immunoelectron microscopy, although the GR expression in CA3 was a little bit weak in immunohistochemistry and *in situ* hybridization, in comparison with CA1 (Morimoto et al., 1996). We observed GR localized within the postsynaptic structures via postembedding immunogold staining (**Figure 5**). The current CORT treatment may rapidly activate the synaptic GR. GR was often located in the cytoplasm of thorns (Komatsuzaki et al., 2005; Ooishi et al., 2012b). GR was observed also in dendrites and nuclei (Komatsuzaki et al., 2005; Ooishi et al., 2012b). Our earlier study shows that GR also expressed in purified PSD fraction by Western blot analysis (Komatsuzaki et al., 2005; Ooishi et al., 2012b). These results suggest that the rapid modulation of thorns by CORT may be mediated by postsynaptic or extranuclear GR. The involvement of GR in the CORT effect was also supported by GR antagonist RU486 which blocked CORT-induced thorn-genesis (**Figure 3**). In addition, GR agonist dexamethasone induces rapid spinogenesis in hippocampal CA1 neurons within 1 h (Komatsuzaki et al., 2005). Membrane GR-induced rapid PKA activation (∼1 h) has been demonstrated for inhibitory avoidance behavior via rat basolateral amygdala (Roozendaal et al., 2002), suggesting that synaptic GR may activate kinases.

Since in our "acute" slice CORT level is around 2 nM, all mineral corticoid receptor (MR) may be occupied due to high affinity (Kd ∼ 0.5 nM) to aldosterone or CORT. Therefore the effect of CORT on thorns is mainly mediated by GR but not by MR, in the presence of 1 μM CORT. The 1 h responses may be too rapid for nuclear GR actions which often need more than 5 h due to genetic processes. As an another possibility, these rapid actions may include rapid genomic actions via nuclear GR, which are suggested as a reduction of dendritic length (1–4 h; Alfarez et al., 2009) or an impairment of enhancement of voltage-dependent Ca^{2+} currents in mutated GR (1–4 h; Karst et al., 2000), in hippocampal neurons. However, since ActD did not suppress the CORT-induced thorn-increase (**Figure 3**), rapid transcriptional process probably does not participate in the thorn-genesis. A significant suppression of thorn changes by application of kinase inhibitors (**Figure 4**) may put more weight on GR-kinase pathway rather than DNA binding of GR.

Since RU486 suppresses not only GR but also progesterone receptor (PR) in **Figure 3**, progesterone (PROG) effect should be considered. The treatment of slices with 10 nM PROG for 1 h did not significantly increase the thorn density within experimental error (data not shown), excluding the involvement of PROG and PR in the observed thorn-genesis.

CORT-INDUCED THORN-GENESIS VIA KINASE NETWORKS AND THEIR DOWNSTREAM

There is increasing evidence implying that CORT is capable of driving rapid signaling (around 1h), independent of slow transcriptional signaling (model illustration in **Figure 6**). Rapid MAPK activation (∼2 h) via GR has been demonstrated in the mice hippocampus or pituitary-derived cell-lines AtT20 (Revest et al., 2005). The expression of Raf1, Ras, p-MAPK is elevated rapidly upon application of 10 nM CORT. Fear conditioning of mice is dependent on GR-MAPK pathway. Rapid PKA activation (phosphorylation of PKA; ∼1 h) via membrane located GR has

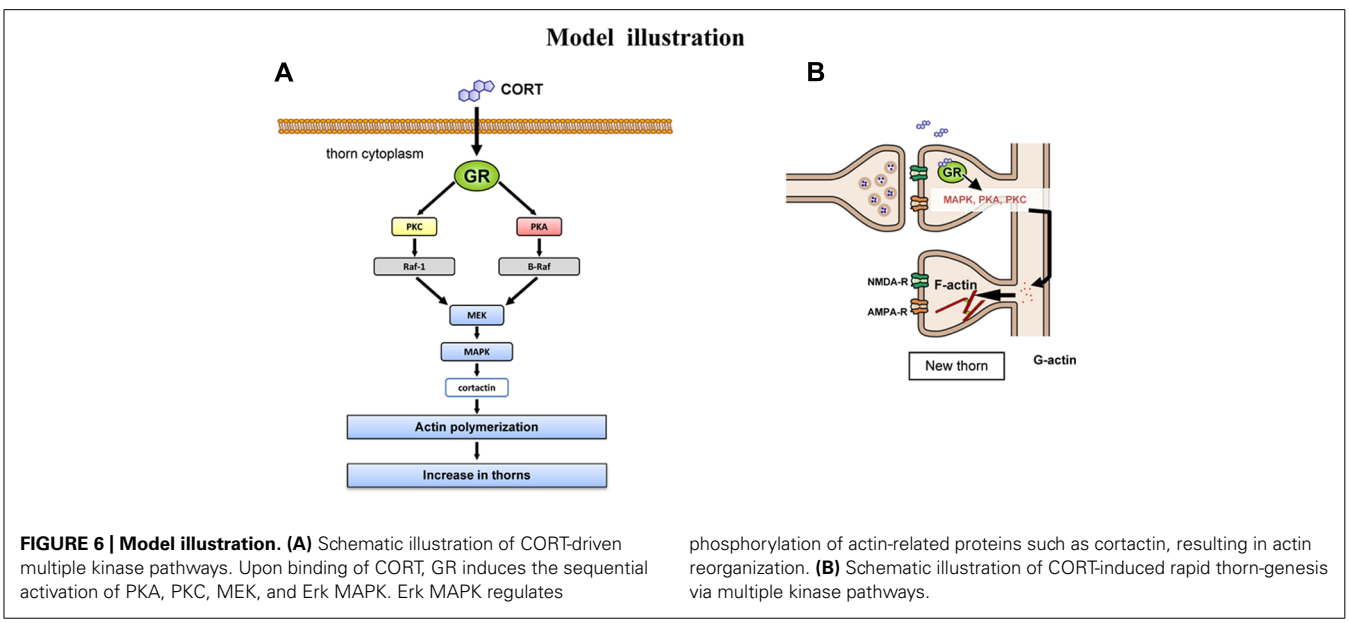

FIGURE 6 | Model illustration. (A) Schematic illustration of CORT-driven multiple kinase pathways. Upon binding of CORT, GR induces the sequential activation of PKA, PKC, MEK, and Erk MAPK. Erk MAPK regulates phosphorylation of actin-related proteins such as cortactin, resulting in actin reorganization. **(B)** Schematic illustration of CORT-induced rapid thorn-genesis via multiple kinase pathways.

been demonstrated in rat basolateral amygdala (Roozendaal et al., 2002).

To consider the molecular mechanisms of kinase signaling in the modulation of CA3 thorn, we temporarily use the model of CA1 region. In this model, MAPK cascade is coupled with PKA and PKC via PKC → Raf1 → MAPK, PKA → B-Raf → MAPK in synaptic modulation (Adams et al., 2000; Komatsuzaki et al., 2012). Taking the knowledge into account, MAPK may be a key kinase responsible for modulation of thorns. The target of Erk MAPK in thorn reorganization is cortactin, since Erk MAPK is known to phosphorylate cortactin, a structural protein associated to actin (MacQueen et al., 2003). Cortactin interacts with both F-actin and actin-related protein (Arp) 2/3 complex as well as scaffold protein Shank in the PSD at the SH3 domain (Weed et al., 1998; Daly, 2004), resulting in promotion of actin fiber remodeling within spines or thorns.

It is thus probable that CORT exerts its effect on thorns via cortactin-actin pathway. Cortactin has multiple phosphorylation sites which are activated by MAPK (Campbell et al., 1999). Phosphorylation of cortactin may promote assembly of actin cytoskeletal matrices, resulting in thorn formation or modulation of thorn morphology (Hering and Sheng, 2003). These sites are putative phosphorylation sites also for other serine/threonine kinase (PKA or PKC) that are activated by CORT.

In the case of *in vivo* hippocampus, the similar rapid CORT-induced modulation of thorns might occur. In response to acute severe stress, elevation of plasma CORT (to 1–2 μM) occurs, resulting in elevation of hippocampal CORT to 0.5–1 μM, due to penetration of CORT into hippocampus after crossing the Blood Brain Barrier (Higo et al., 2011). This increase of CORT level should affect thorn-genesis *in vivo*.

The abolishment of the CORT-induced increase in the density of thorns by CNQX (**Figure 3**) suggests the correlation of the CORT signaling pathway with AMPA receptors. Maintenance of the suitable basal Ca^{2+} level may be important for action of PKC or MAPK on thorn-genesis. CNQX may decrease the basal Ca^{2+} level which is spontaneously formed by ion exchange systems consisting of AMPA receptors plus voltage activated calcium channels. This explanation is deduced from previous study which has shown that the Ca^{2+} influx within thorny excrescences has occurred via AMPA receptor-dependent voltage activated calcium channels during subthreshold activation of CA3 neurons, while NMDA receptors-mediated calcium influx within CA3 thorny excrescences is smaller than that in CA1 spines upon subthreshold activation (Monaghan et al., 1983; Baude et al., 1995; Fritschy et al., 1999; Reid et al., 2001; Reid, 2002).

OTHER EXAMPLES OF KINASE-DEPENDENT THORN-GENESIS OR SPINOGENESIS

The activation of synaptic androgen receptor AR by testosterone or dihydrotestosterone induces a rapid increase of thorns of thorny excrescences in CA3 pyramidal neurons of adult rat hippocampal "acute" slices within 2 h. The rapid synaptic action of androgen is also mediated by activation of many kinases. This thorn-genesis induced by androgen is mediated by Erk MAPK, p38 MAPK, PKC, CaMKII, but not by PKA and PI3K (Hatanaka et al., 2009). The rapid spinogenesis by estradiol in CA3 and CA1 pyramidal neurons of hippocampal "acute" slices is mediated by synaptic ERα → Erk MAPK pathway (Tsurugizawa et al., 2005; Mukai et al., 2007).

Concerning CA3 rapid stress effects, the administration of corticotropin releasing hormone (CRH), rapidly (within 0.5 h) induces loss of CA3 dendritic spines (different from thorns) in stratum radiatum, using Yellow Fluorescence Protein (YFP)-expressing hippocampal neurons (Chen et al., 2008).

One of the physiological significance of GR-induced increase in thorns may be that upon acute stress (for example, stress at examination or oral interview) neurons may be activated and new thorns may appear, resulting in synaptic remodeling. This is very different from chronic stress-induced depression of neural activities via nuclear GR-induced genetic transcription processes.

REFERENCES

Adams, J. P., Roberson, E. D., English, J. D., Selcher, J. C., and Sweatt, J. D. (2000). MAPK regulation of gene expression in the central nervous system. *Acta Neurobiol. Exp. (Wars.)* 60, 377–394.

Alfarez, D. N., De Simoni, A., Velzing, E. H., Bracey, E., Joels, M., Edwards, F. A., et al. (2009). Corticosterone reduces dendritic complexity in developing hippocampal CA1 neurons. *Hippocampus* 19, 828–836. doi: 10.1002/hipo.20566

Alonso, M., Medina, J. H., and Pozzo-Miller, L. (2004). ERK1/2 activation is necessary for BDNF to increase dendritic spine density in hippocampal CA1 pyramidal neurons. *Learn. Mem.* 11, 172–178. doi: 10.1101/lm.67804

Amaral, D. G., and Dent, J. A. (1981). Development of the mossy fibers of the dentate gyrus: I. A light and electron microscopic study of the mossy fibers and their expansions. *J. Comp. Neurol.* 195, 51–86. doi: 10.1002/cne.901950106

Baude, A., Nusser, Z., Molnar, E., Mcilhinney, R. A., and Somogyi, P. (1995). High-resolution immunogold localization of AMPA type glutamate receptor subunits at synaptic and non-synaptic sites in rat hippocampus. *Neuroscience* 69, 1031–1055. doi: 10.1016/0306-4522(95)00350-R

Bhat, R., Xue, Y., Berg, S., Hellberg, S., Ormo, M., Nilsson, Y., et al. (2003). Structural insights and biological effects of glycogen synthase kinase 3-specific inhibitor AR-A014418. *J. Biol. Chem.* 278, 45937–45945. doi: 10.1074/jbc.M306268200

Birnbaum, S. G., Yuan, P. X., Wang, M., Vijayraghavan, S., Bloom, A. K., Davis, D. J., et al. (2004). Protein kinase C overactivity impairs prefrontal cortical regulation of working memory. *Science* 306, 882–884. doi: 10.1126/science.1100021

Breuner, C. W., and Orchinik, M. (2002). Plasma binding proteins as mediators of corticosteroid action in vertebrates. *J. Endocrinol.* 175, 99–112. doi: 10.1677/joe.0.1750099

Campbell, D. H., Sutherland, R. L., and Daly, R. J. (1999). Signaling pathways and structural domains required for phosphorylation of EMS1/cortactin. *Cancer Res.* 59, 5376–5385.

Chen, Y., Dube, C. M., Rice, C. J., and Baram, T. Z. (2008). Rapid loss of dendritic spines after stress involves derangement of spine dynamics by corticotropin-releasing hormone. *J. Neurosci.* 28, 2903–2911. doi: 10.1523/JNEUROSCI.0225-08.2008

Chen, Q., Zhou, Z., Zhang, L., Wang, Y., Zhang, Y. W., Zhong, M., et al. (2012). Tau protein is involved in morphological plasticity in hippocampal neurons in response to BDNF. *Neurochem. Int.* 60, 233–242. doi: 10.1016/j.neuint.2011.12.013

Chicurel, M. E., and Harris, K. M. (1992). Three-dimensional analysis of the structure and composition of CA3 branched dendritic spines and their synaptic relationships with mossy fiber boutons in the rat hippocampus. *J. Comp. Neurol.* 325, 169–182. doi: 10.1002/cne.903250204

Chijiwa, T., Mishima, A., Hagiwara, M., Sano, M., Hayashi, K., Inoue, T., et al. (1990). Inhibition of forskolin-induced neurite outgrowth and protein phosphorylation by a newly synthesized selective inhibitor of cyclic AMP-dependent protein kinase, N-[2-(*p*-bromocinnamylamino)ethyl]-5-isoquinolinesulfonamide (H-89), of PC12D pheochromocytoma cells. *J. Biol. Chem.* 265, 5267–5272.

Daly, R. J. (2004). Cortactin signalling and dynamic actin networks. *Biochem. J.* 382, 13–25. doi: 10.1042/BJ20040737

Diamond, D. M., Bennett, M. C., Fleshner, M., and Rose, G. M. (1992). Inverted-U relationship between the level of peripheral corticosterone and the magnitude

of hippocampal primed burst potentiation. *Hippocampus* 2, 421–430. doi: 10.1002/hipo.450020409

Duan, H., Wearne, S. L., Morrison, J. H., and Hof, P. R. (2002). Quantitative analysis of the dendritic morphology of corticocortical projection neurons in the macaque monkey association cortex. *Neuroscience* 114, 349–359. doi: 10.1016/S0306-4522(02)00305-6

Dudley, D. T., Pang, L., Decker, S. J., Bridges, A. J., and Saltiel, A. R. (1995). A synthetic inhibitor of the mitogen-activated protein kinase cascade. *Proc. Natl. Acad. Sci. U.S.A.* 92, 7686–7689. doi: 10.1073/pnas.92.17.7686

Fritschy, J. M., Meskenaite, V., Weinmann, O., Honer, M., Benke, D., and Mohler, H. (1999). GABAB-receptor splice variants GB1a and GB1b in rat brain: developmental regulation, cellular distribution and extrasynaptic localization. *Eur. J. Neurosci.* 11, 761–768. doi: 10.1046/j.1460-9568.1999.00481.x

Gould, E., Woolley, C. S., Frankfurt, M., and Mcewen, B. S. (1990). Gonadal steroids regulate dendritic spine density in hippocampal pyramidal cells in adulthood. *J. Neurosci.* 10, 1286–1291.

Hammond, R. S., Lin, L., Sidorov, M. S., Wikenheiser, A. M., and Hoffman, D. A. (2008). Protein kinase a mediates activity-dependent Kv4.2 channel trafficking. *J. Neurosci.* 28, 7513–7519. doi: 10.1523/JNEUROSCI.1951-08.2008

Hatanaka, Y., Mukai, H., Mitsuhashi, K., Hojo, Y., Murakami, G., Komatsuzaki, Y., et al. (2009). Androgen rapidly increases dendritic thorns of CA3 neurons in male rat hippocampus. *Biochem. Biophys. Res. Commun.* 381, 728–732. doi: 10.1016/j.bbrc.2009.02.130

Herbert, J. M., Augereau, J. M., Gleye, J., and Maffrand, J. P. (1990). Chelerythrine is a potent and specific inhibitor of protein kinase C. *Biochem. Biophys. Res. Commun.* 172, 993–999. doi: 10.1016/0006-291X(90)91544-3

Hering, H., and Sheng, M. (2003). Activity-dependent redistribution and essential role of cortactin in dendritic spine morphogenesis. *J. Neurosci.* 23, 11759–11769.

Higo, S., Hojo, Y., Ishii, H., Komatsuzaki, Y., Ooishi, Y., Murakami, G., et al. (2011). Endogenous synthesis of corticosteroids in the hippocampus. *PLoS ONE* 6:e21631. doi: 10.1371/journal.pone.0021631

Hojo, Y., Hattori, T. A., Enami, T., Furukawa, A., Suzuki, K., Ishii, H. T., et al. (2004). Adult male rat hippocampus synthesizes estradiol from pregnenolone by cytochromes P45017alpha and P450 aromatase localized in neurons. *Proc. Natl. Acad. Sci. U.S.A.* 101, 865–870. doi: 10.1073/pnas.2630225100

Hojo, Y., Higo, S., Ishii, H., Ooishi, Y., Mukai, H., Murakami, G., et al. (2009). Comparison between hippocampus-synthesized and circulation-derived sex steroids in the hippocampus. *Endocrinology* 150, 5106–5112. doi: 10.1210/en.2009-0305

Hojo, Y., Higo, S., Kawato, S., Hatanaka, Y., Ooishi, Y., Murakami, G., et al. (2011). Hippocampal synthesis of sex steroids and corticosteroids: essential for modulation of synaptic plasticity. *Front. Endocrinol.* 2:43. doi: 10.3389/fendo.2011.00043

Karst, H., Karten, Y. J., Reichardt, H. M., De Kloet, E. R., Schutz, G., and Joels, M. (2000). Corticosteroid actions in hippocampus require DNA binding of glucocorticoid receptor homodimers. *Nat. Neurosci.* 3, 977–978. doi: 10.1038/79910

Komatsuzaki, Y., Hatanaka, Y., Murakami, G., Mukai, H., Hojo, Y., Saito, M., et al. (2012). Corticosterone induces rapid spinogenesis via synaptic glucocorticoid receptors and kinase networks in hippocampus. *PLoS ONE* 7:e34124. doi: 10.1371/journal.pone.0034124

Komatsuzaki, Y., Murakami, G., Tsurugizawa, T., Mukai, H., Tanabe, N., Mitsuhashi, K., et al. (2005). Rapid spinogenesis of pyramidal neurons induced by activation of glucocorticoid receptors in adult male rat hippocampus. *Biochem. Biophys. Res. Commun.* 335, 1002–1007. doi: 10.1016/j.bbrc.2005.07.173

Lupien, S. J., and McEwen, B. S. (1997). The acute effects of corticosteroids on cognition: integration of animal and human model studies. *Brain Res. Brain Res. Rev.* 24, 1–27. doi: 10.1016/S0165-0173(97)00004-0

MacQueen, G. M., Campbell, S., Mcewen, B. S., Macdonald, K., Amano, S., Joffe, R. T., et al. (2003). Course of illness, hippocampal function, and hippocampal volume in major depression. *Proc. Natl. Acad. Sci. U.S.A.* 100, 1387–1392. doi: 10.1073/pnas.0337481100

McNaughton, B. L., and Morris, R. G. M. (1987). Hippocampal synaptic enhancement and information-storage within a distributed memory system. *Trends Neurosci.* 10, 408–415. doi: 10.1016/0166-2236(87)90011-7

Monaghan, D. T., Holets, V. R., Toy, D. W., and Cotman, C. W. (1983). Anatomical distributions of four pharmacologically distinct 3H-L-glutamate binding sites. *Nature* 306, 176–179. doi: 10.1038/306176a0

Morimoto, M., Morita, N., Ozawa, H., Yokoyama, K., and Kawata, M. (1996). Distribution of glucocorticoid receptor immunoreactivity and mRNA in the rat brain: an immunohistochemical and in situ hybridization study. *Neurosci. Res.* 26, 235–269. doi: 10.1016/S0168-0102(96)01105-4

Morris, R. G., Garrud, P., Rawlins, J. N., and O'Keefe, J. (1982). Place navigation impaired in rats with hippocampal lesions. *Nature* 297, 681–683. doi: 10.1038/297681a0

Mukai, H., Hatanaka, Y., Mitsuhashi, K., Hojo, Y., Komatsuzaki, Y., Sato, R., et al. (2011). Automated analysis of spines from confocal laser microscopy images: application to the discrimination of androgen and estrogen effects on spinogenesis. *Cereb. Cortex* 21, 2704–2711. doi: 10.1093/cercor/bhr059

Mukai, H., Tsurugizawa, T., Murakami, G., Kominami, S., Ishii, H., Ogiue-Ikeda, M., et al. (2007). Rapid modulation of long-term depression and spinogenesis via synaptic estrogen receptors in hippocampal principal neurons. *J. Neurochem.* 100, 950–967. doi: 10.1111/j.1471-4159.2006.04264.x

Ooishi, Y., Kawato, S., Hojo, Y., Hatanaka, Y., Higo, S., Mukai, H., et al. (2012a). Modulation of synaptic plasticity in the hippocampus by hippocampus-derived estrogen and androgen. *J. Steroid Biochem. Mol. Biol.* 131, 37–51. doi: 10.1016/j.jsbmb.2011.10.004

Ooishi, Y., Mukai, H., Hojo, Y., Murakami, G., Hasegawa, Y., Shindo, T., et al. (2012b). Estradiol rapidly rescues synaptic transmission from corticosterone-induced suppression via synaptic/extranuclear steroid receptors in the hippocampus. *Cereb. Cortex* 22, 926–936. doi: 10.1093/cercor/bhr164

Pardridge, W. M., and Mietus, L. J. (1979). Transport of steroid hormones through the rat blood-brain barrier. Primary role of albumin-bound hormone. *J. Clin. Invest.* 64, 145–154. doi: 10.1172/JCI109433

Reagan, L. P., and McEwen, B. S. (1997). Controversies surrounding glucocorticoid-mediated cell death in the hippocampus. *J. Chem. Neuroanat.* 13, 149–167. doi: 10.1016/S0891-0618(97)00031-8

Reid, C. A. (2002). The role of dendritic spines: comparing the complex with the simple. *Eur. J. Pharmacol.* 447, 173–176. doi: 10.1016/S0014-2999(02)01841-1

Reid, C. A., Fabian-Fine, R., and Fine, A. (2001). Postsynaptic calcium transients evoked by activation of individual hippocampal mossy fiber synapses. *J. Neurosci.* 21, 2206–2214.

Revest, J. M., Di Blasi, F., Kitchener, P., Rouge-Pont, F., Desmedt, A., Turiault, M., et al. (2005). The MAPK pathway and Egr-1 mediate stress-related behavioral effects of glucocorticoids. *Nat. Neurosci.* 8, 664–672. doi: 10.1038/nn1441

Roberson, E. D., English, J. D., Adams, J. P., Selcher, J. C., Kondratick, C., and Sweatt, J. D. (1999). The mitogen-activated protein kinase cascade couples PKA and PKC to cAMP response element binding protein phosphorylation in area CA1 of hippocampus. *J. Neurosci.* 19, 4337–4348.

Roozendaal, B., Quirarte, G. L., and Mcgaugh, J. L. (2002). Glucocorticoids interact with the basolateral amygdala beta-adrenoceptor – cAMP/cAMP/PKA system in influencing memory consolidation. *Eur. J. Neurosci.* 15, 553–560. doi: 10.1046/j.0953-816x.2001.01876.x

Sato, S., Osanai, H., Monma, T., Harada, T., Hirano, A., Saito, M., et al. (2004). Acute effect of corticosterone on *N*-methyl-D-aspartate receptor-mediated Ca^{2+} elevation in mouse hippocampal slices. *Biochem. Biophys. Res. Commun.* 321, 510–513. doi: 10.1016/j.bbrc.2004.06.168

Shibuya, K., Takata, N., Hojo, Y., Furukawa, A., Yasumatsu, N., Kimoto, T., et al. (2003). Hippocampal cytochrome P450s synthesize brain neurosteroids which are paracrine neuromodulators of synaptic signal transduction. *Biochim. Biophys. Acta* 1619, 301–316. doi: 10.1016/S0304-4165(02)00489-0

Sorrells, S. F., Caso, J. R., Munhoz, C. D., and Sapolsky, R. M. (2009). The stressed CNS: when glucocorticoids aggravate inflammation. *Neuron* 64, 33–39. doi: 10.1016/j.neuron.2009.09.032

Stewart, M. G., Davies, H. A., Sandi, C., Kraev, I. V., Rogachevsky, V. V., Peddie, C. J., et al. (2005). Stress suppresses and learning induces plasticity in CA3 of rat hippocampus: a three-dimensional ultrastructural study of thorny excrescences and their postsynaptic densities. *Neuroscience* 131, 43–54. doi: 10.1016/j.neuroscience.2004.10.031

Tsurugizawa, T., Mukai, H., Tanabe, N., Murakami, G., Hojo, Y., Kominami, S., et al. (2005). Estrogen induces rapid decrease in dendritic thorns of CA3 pyramidal neurons in adult male rat hippocampus. *Biochem. Biophys. Res. Commun.* 337, 1345–1352. doi: 10.1016/j.bbrc.2005.09.188

Watanabe, Y., Gould, E., and Mcewen, B. S. (1992). Stress induces atrophy of apical dendrites of hippocampal CA3 pyramidal neurons. *Brain Res.* 588, 341–345. doi: 10.1016/0006-8993(92)91597-8

Weed, S. A., Du, Y., and Parsons, J. T. (1998). Translocation of cortactin to the cell periphery is mediated by the small GTPase Rac1. *J. Cell Sci.* 111(Pt 16), 2433–2443.

Woolley, C. S., Gould, E., Frankfurt, M., and McEwen, B. S. (1990a). Naturally occurring fluctuation in dendritic spine density on adult hippocampal pyramidal neurons. *J. Neurosci.* 10, 4035–4039.

Woolley, C. S., Gould, E., and McEwen, B. S. (1990b). Exposure to excess glucocorticoids alters dendritic morphology of adult hippocampal pyramidal neurons. *Brain Res.* 531, 225–231. doi: 10.1016/0006-8993(90)90778-A

Conflict of Interest Statement: The authors declare that the research was conducted in the absence of any commercial or financial relationships that could be construed as a potential conflict of interest.

Received: 27 June 2013; accepted: 11 November 2013; published online: 27 November 2013.

Citation: Yoshiya M, Komatsuzaki Y, Hojo Y, Ikeda M, Mukai H, Hatanaka Y, Murakami G, Kawata M, Kimoto T and Kawato S (2013) Corticosterone rapidly increases thorns of CA3 neurons via synaptic/extranuclear glucocorticoid receptor in rat hippocampus. Front. Neural Circuits ***7****:191. doi: 10.3389/fncir.2013.00191*

This article was submitted to the journal Frontiers in Neural Circuits.

frontiers in
NEURAL CIRCUITS

ORIGINAL RESEARCH ARTICLE
published: 21 June 2013
doi: 10.3389/fncir.2013.00112

Multineuronal spike sequences repeat with millisecond precision

Koki Matsumoto*[1], *Tomoe Ishikawa*[1], *Norio Matsuki*[1] *and Yuji Ikegaya*[1,2]

[1] *Graduate School of Pharmaceutical Sciences, The University of Tokyo, Tokyo, Japan*
[2] *Center for Information and Neural Networks, Suita City, Osaka, Japan*

Edited by:
Yoshiyuki Kubota, National Institute for Physiological Sciences, Japan

Reviewed by:
Moshe Abeles, Bar-Ilan University, Israel
Shuzo Sakata, University of Strathclyde, UK

***Correspondence:**
Yuji Ikegaya, Laboratory of Chemical Pharmacology, Graduate School of Pharmaceutical Sciences, The University of Tokyo, 7-3-1 Hongo, Bunkyo-ku, Tokyo 113-0033, Japan
e-mail: ikegaya@mol.f.u-tokyo.ac.jp

Cortical microcircuits are nonrandomly wired by neurons. As a natural consequence, spikes emitted by microcircuits are also nonrandomly patterned in time and space. One of the prominent spike organizations is a repetition of fixed patterns of spike series across multiple neurons. However, several questions remain unsolved, including how precisely spike sequences repeat, how the sequences are spatially organized, how many neurons participate in sequences, and how different sequences are functionally linked. To address these questions, we monitored spontaneous spikes of hippocampal CA3 neurons *ex vivo* using a high-speed functional multineuron calcium imaging (fMCI) technique that allowed us to monitor spikes with millisecond resolution and to record the location of spiking and non-spiking neurons. Multineuronal spike sequences (MSSs) were overrepresented in spontaneous activity compared to the statistical chance level. Approximately 75% of neurons participated in at least one sequence during our observation period. The participants were sparsely dispersed and did not show specific spatial organization. The number of sequences relative to the chance level decreased when larger time frames were used to detect sequences. Thus, sequences were precise at the millisecond level. Sequences often shared common spikes with other sequences; parts of sequences were subsequently relayed by following sequences, generating complex chains of multiple sequences.

Keywords: spontaneous activity, calcium imaging, action potentials, spike sequences, hippocampus, ripple

INTRODUCTION

The brain uses a limited number of neurons to process virtually unlimited patterns of information from external environments. Therefore, individual neurons are unlikely to independently process specific information, and it is more plausible that they cooperatively form subgroups that work as functional units. This idea, called the "cell assembly" hypothesis (Hebb, 1949; Harris, 2005; Buzsaki, 2010), leads to two important predictions about neuronal circuit operation. First, a given neuron can participate in two or more cell assemblies. Second, the synapse weight between two given neurons is modifiable over time. More specifically, the weight is strengthened when the neurons work cooperatively, otherwise it is weakened. This bidirectional synaptic plasticity has been experimentally proven by studies showing that cortical synapses are capable of exhibiting long-term potentiation (LTP) and long-term depression (LTD) of synaptic transmission. These two features suggest that neuronal networks self-organize through reorganization of neuronal connectivity due to ongoing external stimuli and are thereby functionally compartmentalized to form cell assemblies.

Synchronous activity among multiple neurons is regarded as one of the simplest aspects of cell assembly dynamics, not only because it triggers the induction of synaptic plasticity but also because it is realized through synchronization between groups of presynaptic neurons (Takahashi et al., 2010). At a more microscopic level, synchronized activity is often composed of sequential activation of multiple neurons. Indeed, such multineuronal spike sequences (MSSs) are known to exist during sensory-evoked and spontaneous network activity at frequencies greater than chance (Abeles and Gerstein, 1988; Prut et al., 1998; Abeles and Gat, 2001; Ikegaya et al., 2004; Luczak et al., 2007). MSSs are conceptually consistent with the so-called "synfire chains" hypothesis, in which neurons form several layers through which synchronized spikes can stably propagate with temporal precision, therefore generating a chain of spikes across neurons (Abeles, 1991). Although MSSs have been reported in different brain preparations, including the neocortex of monkeys and rodents *in vivo* and *in vitro*, some reports still cast doubt on the existence of MSSs (Oram et al., 1999; Baker and Lemon, 2000; Mokeichev et al., 2007).

We focus the present work on the hippocampus. One of the reasons for this selection is that the hippocampus spontaneously emits sharp waves-ripples (SW-Rs), a transient form of high-frequency field oscillations. SW-Rs primarily occur during slow-wave sleep and quiet awake states (Buzsaki et al., 1983). During SW-Rs, neurons that were previously involved in behavioral exploration, called place cells, increase their firing rates sequentially in the same or opposite order of which those neurons were activated during the behavioral exploration (Lee and Wilson, 2002; Harris et al., 2003; Foster and Wilson, 2006;

O'Neill et al., 2006; Diba and Buzsaki, 2007; Pastalkova et al., 2008; Davidson et al., 2009). Therefore, the hippocampus may be a good model to study MSSs. *In vitro* slices prepared from the hippocampus are also reported to emit spontaneous SW-Rs (Norimoto et al., 2012; Sun et al., 2012), and the slices may produce MSSs. If it were the case, it would be easy to analyze the properties of MSSs because the *in vitro* experimental system is more accessible and manipulatable than the *in vivo* system.

Functional multineuron calcium imaging (fMCI) is an optical technique that monitors spikes of neurons *in situ* through spike-evoked somatic calcium transients. We have optimized the method for hippocampal slice cultures (Takahashi et al., 2007, 2011). In the CA3 region of organotypically cultured slices, the probability of a synaptic connection between randomly selected adjacent pyramidal cells is approximately 25%. This ratio is higher than that reported in acute slice preparations (2–8%) (Miles and Wong, 1983; Smith et al., 1995). In acute hippocampal slices, however, 75–90% of the axons of CA3 pyramidal neurons are cut, even in slices as thick as 500 μm (Gomez-Di Cesare et al., 1997). In contrast, cultured networks self-restore their complexity to a realistic extent. Indeed, levels of spontaneous excitatory or inhibitory postsynaptic currents are similar between *ex vivo* and *in vivo* hippocampal neurons (Takahashi et al., 2010). Moreover, we have demonstrated, by using an optical synapse mapping technique, that in such restored CA3 networks, pyramidal cells are nonrandomly connected to generate diverse repertoires of synchronized activity, like the *in vivo* conditions (Takahashi et al., 2010).

MATERIALS AND METHODS

ANIMAL

Experiments were performed with the approval of the animal experiment ethics committee at the University of Tokyo (approval number: 19-43, P21-6) according to the University of Tokyo guidelines for the care and use of laboratory animals.

SLICE CULTURE PREPARATIONS

Entorhino-hippocampal organotypic slices were prepared from 7-day-old Wistar/ST rats (SLC, Shizuoka, Japan) as previously described (Koyama et al., 2007). Briefly, rat pups were anesthetized by hypothermia and decapitated. The brains were removed and placed in aerated, ice-cold Gey's balanced salt solution supplemented with 25 mM glucose. Horizontal entorhino-hippocampal slices were made at a thickness of 300 μm using a vibratome (DTK-1500, Dosaka, Kyoto, Japan). The slices were placed on Omnipore membrane filters (JHWP02500, Millipore, Bedford, MA, USA) and incubated in 5% CO_2 at 37°C. The culture medium, which was composed of 50% minimal essential medium (Invitrogen, Gaithersburg, MD, USA), 25% Hanks' balanced salt solution, 25% horse serum (Cell Culture Laboratory, Cleveland, OH, USA), and antibiotics, was changed every 3.5 days. Experiments were performed on days 7–11 *in vitro*.

Although slice cultures are known to form abnormal connections that very rarely exist under normal conditions, such as CA1-to-CA1, CA1-to-CA3, and CA3-to-dentate gyrus connections (Gahwiler et al., 1997; De Simoni et al., 2003), there are few of these aberrant connections in our slice culture preparations. Investigation using reverse optical trawling, a synapse mapping technique (Sasaki et al., 2009), demonstrated that these abnormal connections are less than 0.5% of the total connections and that an overwhelming number of connections project to their normal targets. This result is most likely because the entorhinal cortex was not dissected out in our preparations. Lesions of the entorhinal cortex are known to result in abnormal sprouting and reorganization of hippocampal networks *in vivo* and *ex vivo* (Laurberg and Zimmer, 1981; West and Dewey, 1984).

FUNCTIONAL MULTINEURON CALCIUM IMAGING

Slices were incubated with 2 ml of dye solution at 37°C for 1 h (Takahashi et al., 2011). The dye solution was aCSF containing 0.0005% Oregon Green 488 BAPTA-1AM (OGB-1AM), 0.01% Pluronic F-127, and 0.005% Cremophor EL. After a 1-h recovery, a slice was transferred to a recording chamber. Images were acquired at 500 frames/s with a Nipkow-disk confocal unit (CSUX-1, Yokogawa Electric, Tokyo, Japan), a back-illuminated electron-multiplying charge-coupled device (EM-CCD) camera (iXon DV860, Andor, Belfast, Northern Ireland, UK), a water-immersion objective lens (16×, 0.80 NA, Nikon, Tokyo, Japan), and Solis software (Andor). Fluorophores were excited at 488 nm with an argon laser (10–15 mW, 532-BS-AO4, Omnichrome, Chino, CA, USA) and visualized with a 507-nm long-pass emission filter. In each cell body, the fluorescence change ΔF/F was calculated as $(F_t–F_0)/F_0$, where F_t is the fluorescence intensity at frame time t, and F_0 is baseline (**Figure 1A**). Spike timing was defined as the onset of individual calcium transients with an automatic machine-learning algorithm that can accurately detect spike timing within one frame jitter (Sasaki et al., 2008). In some experiments, picrotoxin was bath-applied to prevent fast inhibitory synaptic transmission. Picrotoxin (purchased from Sigma-Aldrich, St. Louis, MO) was dissolved in aCSF at the final concentration of 50 μM and perfused to slices. Imaging was started 30 min after the perfusion onset.

LOCAL FIELD POTENTIAL RECORDINGS AND RIPPLE DETECTION

In a single experiment, CA1 local field potentials (LFP) were recorded during fMCI monitoring of the calcium activity of CA3 neurons. Glass pipettes were filled with 2 M NaCl and placed in CA1 stratum pyramidale. To extract the SW-R activity, the recorded data were band-pass filtered at 150–300 Hz. SW-R-like events were automatically detected based on their oscillatory powers and durations; the root mean square (3-ms window) of the band-passed signal was used to detect SW-Rs of 10 ms duration with a power threshold of 5 standard deviations (SDs).

MSS DETECTION

We used a template-matching algorithm to search for MSSs (Ikegaya et al., 2004). We first selected cells that showed more than one calcium transient. After determining the reference calcium levels of a reference cell ($cell_1$), we designated a vector consisting of a set of cells and relative timings of their calcium events as follows: ($cell_2, \ldots, cell_N, t_2, t_3, \ldots, t_N$), where t_i denotes the delay of the event in $cell_i$ after the reference event. t_i was limited to less

than 500 ms. This vector was used as a template and was slid along the successive events of $cell_1$ throughout the recording session. If more than two elements were identical between any template pairs, we regarded the matched elements as an MSS. Each mismatched spike configuration was used as another template in a subsequent scan. Thus, every event was considered part of a template MSS, and each template occurred at least once. Unless otherwise specified, one frame jitter (2 ms) was allowed so that the total number of MSSs satisfied statistical demands (Kendall et al., 1994).

SURROGATE DATA

To determine whether MSSs or their structures can arise from a stochastic process, we created surrogate raster plots using a Monte Carlo resampling method (Ikegaya et al., 2004). Each calcium event was exchanged between a pair of cells, maintaining their

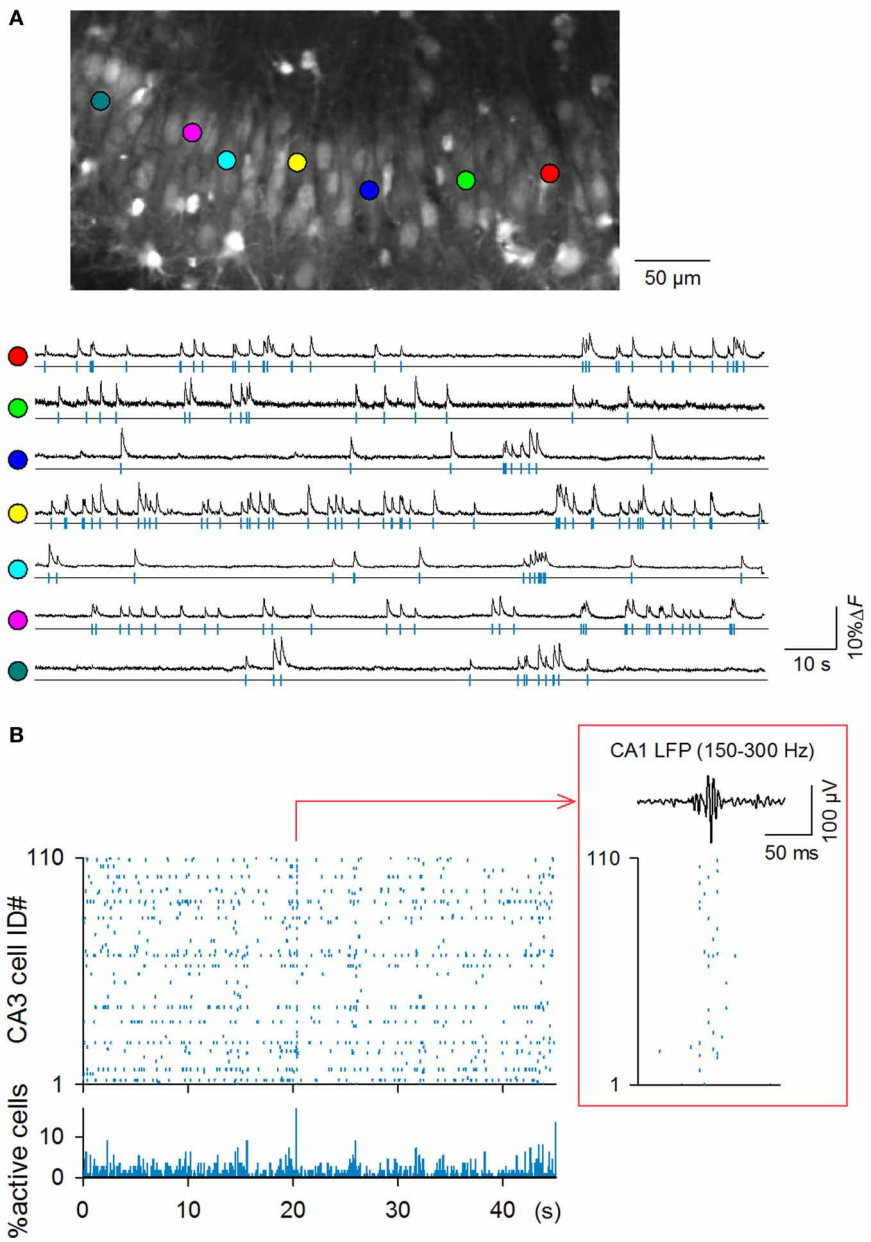

FIGURE 1 | High-speed fMCI of spontaneous CA3 network activity. **(A)** *Top*: representative confocal image of the CA3 stratum pyramidale in an OGB1-loaded hippocampal slice culture. *Bottom*: Time changes in the OGB1 fluorescence intensity in the somata of 7 randomly selected neurons indicated by the colored circles in the top photograph. **(B)** Representative rastergram of all 110 CA3 neurons (top) and time histogram of the percentage of active neurons (bin = 10 ms). A large synchronization is time-expanded in the inset and is displayed together with 150–300 Hz band-passed LFPs simultaneously recorded from the CA1 pyramidal stratum. Synchronization was accompanied by SW-R-like oscillations.

relative timings (**Figure 3A**). This procedure was repeated for all calcium transients in each raster plot. This randomization preserves the event frequencies of individual cells and the population modulation of event timings, such as network synchronization. In each shuffled surrogate, we searched MSSs using the same detection algorithm. Twenty surrogates were generated for each dataset, and the averages across the 20 surrogates were defined as the chance level.

ASYNCHRONY INDEX

The temporal sparseness of network activity during the observation period was captured by a normalized Shannon index, termed asynchrony index (Usami et al., 2008; Mizunuma et al., 2009; Ujita et al., 2011). The Shannon index quantifies the dispersion of components in a histogram and is generally defined as $-\sum_i (k_i/K)\ log_2\ (k_i/K)$, where K is the total number of components, and k_i is the number of components in the i-th bin. This definition of diversity is conceptually equivalent to Shannon's entropy. Because this index is sensitive to K and the bin size, SI has often been normalized with the maximal value and other standard values to compare groups. Here we normalized Shannon index with the maximal (SImax) and minimal values (SImin) that can be taken in the distribution of the same number of spikes in the raster plot. SImax and SImin were obtained through data shuffle with maintaining K and bin; SImax is given when components are as evenly redistributed over the time axis as possible, whereas SImin is given when components are as temporally biased as possible. Then normalized Shannon index is defined as $(SI–SI\text{min})/(SI\text{max}–SI\text{min})$. Thus, it takes a value from 0 to 1, with higher values being more dispersive.

DATA REPRESENTATION

We reported all averaged values as the mean ± SDs.

RESULTS

HIGH-SPEED IMAGING OF SPIKING CA3 NETWORKS *ex vivo*

Hippocampal slice cultures were incubated in OGB1AM, and OGB1-loaded neurons were imaged from the CA3 stratum pyramidale at 500 Hz using a spinning-disk confocal microscope and a high-speed EM-CCD camera (Takahashi et al., 2011). The microscopic field covered an area of approximately 350 × 200 μm (**Figure 1A**) and contained an average of 91.7 ± 26.7 neurons (mean ± SD of 9 videos, ranging from 60 to 137 neurons). Each video was 130 s in length, and a total of 9 videos were recorded from 9 slices ($n = 9$ rat pups borned from 9 mothers).

In all 9 videos, spontaneous activity was evident; among a total of 825 neurons in 9 videos, 757 neurons (91.8%) exhibited at least one spike during the observation period. The mean firing rates of active neurons were 0.25 ± 0.29 Hz ($n = 9$ videos), ranging from 0.008 to 2.33 Hz. Therefore, spontaneous activity was sparse as a whole. Nevertheless, neurons occasionally exhibited synchronization at the population level (**Figure 1B**); synchronization that recruited more than 5% or 10% of the total neurons occurred

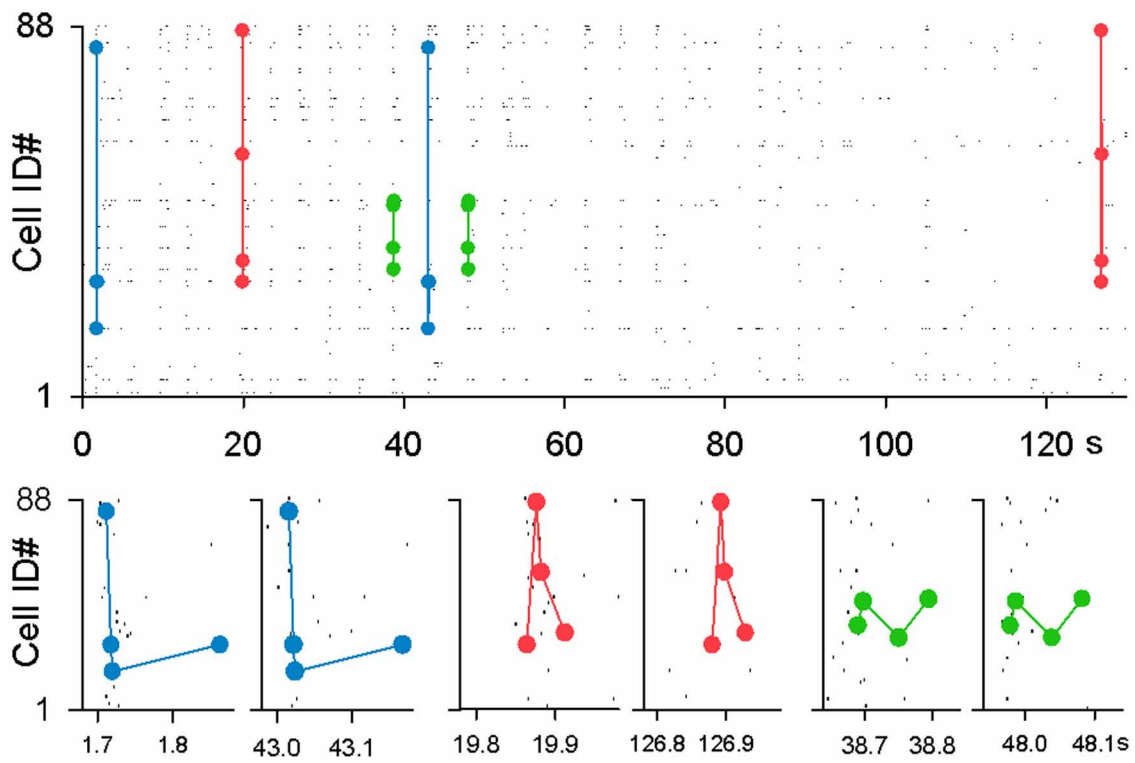

FIGURE 2 | Examples of MSSs. Three representative MSSs are merged in a single rastergram and magnified in time in the bottom panels.

at frequencies of 2.46 ± 3.0 or 0.26 ± 0.52 per min, respectively ($n = 9$ videos, bin = 2 ms = one frame).

We succeeded in simultaneous LFP recording in one single video; note that in general, LFP recording is technically difficult in slice cultures, most likely because neurite reorganization during cultivation slightly alters the fine layer structure of the hippocampus, collapsing the net dipole moment generated by synaptic activity or because cultured networks may be heterogenous from preparation to preparation (e.g., see **Figure 4**). In the single dataset, we found that synchronous activity was always accompanied by SW-R-like high-frequency oscillations (**Figure 1B**, inset).

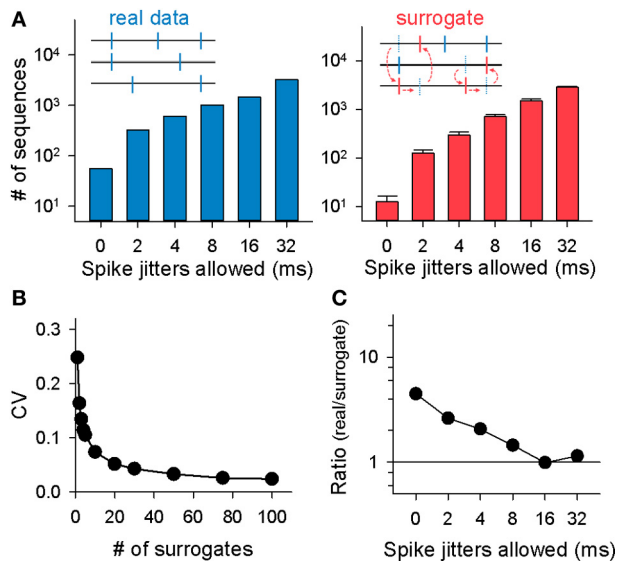

FIGURE 3 | Monte Carlo evaluation for the significance of MSSs. (A) *Left*: the total numbers of MSSs in the rastergram shown in **(A)** are plotted as a function of spike-time jitters allowed for MSS detection. *Right*: MSSs were identified in the same way in spike-shuffled rastergrams. Data are the mean ± SDs of 20 surrogates. **(B)** Relationship between the CVs of the number of MSSs detected in surrogates and the number of surrogates generated. **(C)** Ratios of the numbers of MSSs in the original (real) rastergram to the mean numbers of MSSs in 20 randomized surrogates. Data are the same as **(B)**.

MSSs WITH MILLISECOND PRECISION

We detected MSSs. The maximal length of an MSS, i.e., the time interval between the first spike and the last spike, was set to be 500 ms. Three examples of MSSs found in a raster plot are shown in **Figure 2**. Not surprisingly, the number of MSSs depended on the spike time jitters allowed to detect MSSs (**Figure 3A** left). MSSs increased in number when jitters were increased from 0 ms (0 frame) to 32 ms (16 frames); note that 0-ms jitter (= 0 frames) had a time window of 2 ms due to 500-Hz imaging.

The total number of MSSs varied among videos, probably because the network states fluctuate over time and are not identical among preparations (Sasaki et al., 2007). The total number of MSSs in each video (2-ms jitter allowed) was plotted against the total number of neurons recorded in the corresponding videos (**Figure 4A**), the mean activity frequency of those neurons (**Figure 4B**), and the asynchrony index of the corresponding videos (**Figure 4C**); note that the asynchrony index is a normalized Shannon index for spike dispersion along the time axis (Usami et al., 2008; Mizunuma et al., 2009; Ujita et al., 2011). Thus, we investigated the statistical significance of MSSs by comparing the number of MSSs to its stochastic level. To estimate the stochastic level, we created surrogate raster plots by randomly exchanging spikes across neurons. Specifically, a single spike of a randomly selected neuron was swapped with a spike of another randomly selected neuron without changing their absolute spike timings, and this swapping procedure was repeated until all spikes in the original dataset were exchanged (**Figure 3A** right, inset). This shuffling method preserved both the firing rates of individual neurons and the level and frequency of network synchronization. Therefore, comparing an original dataset with these surrogates makes it possible to examine whether MSSs are actively generated by complex network dynamics or are merely a mathematically natural consequence of the firing rates of individual neurons.

The coefficient of variation (CV) for the number of MSSs detected in surrogates depended on the number of surrogates

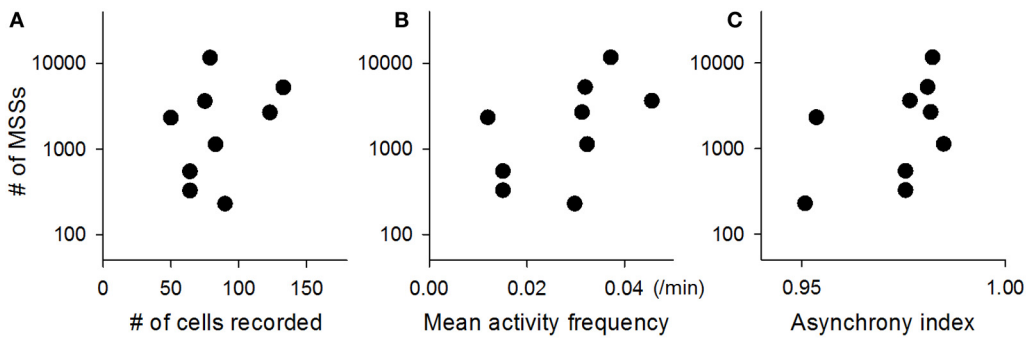

FIGURE 4 | Across-video variations of the number of MSSs. The total number of MSSs varied among datasets and thus is plotted against the total number of neurons recorded in the corresponding videos **(A)**, the mean frequency of activity of those neurons **(B)**, and the synchrony index of the corresponding videos **(C)**. Each dot indicates a single video. $n = 9$ videos.

generated. The CV rapidly decreased as a function of the number of surrogates; it dropped to about 0.05 by 20 surrogates, and thereafter, it was kept almost constant (**Figure 3B**, 2-ms jitter allowed). To reduce computation burden with preserving statistical stability, therefore, we searched MSSs in 20 surrogates generated from each raster plot. MSSs in the surrogates also increased in number with spike jitter timing (**Figure 3A** right). We thus plotted the ratio of the MSS number in the real dataset to that in the surrogates as a function of jitters. The ratio peaked at a jitter of 0 ms and decreased gradually with increasing jitters (**Figure 3C**). We repeated this procedure for all other datasets and found similar results in the pooled data ($n = 9$ videos; **Figure 5**), that is, the mean real-to-surrogate ratio is a simple reduction function of spike jitters. Based on these results, we reached two fundamental conclusions: (1) MSSs emerge more frequently than expected by chance and therefore cannot be explained by a stochastic process, and (2) relative spike times within MSSs are maintained at the millisecond level.

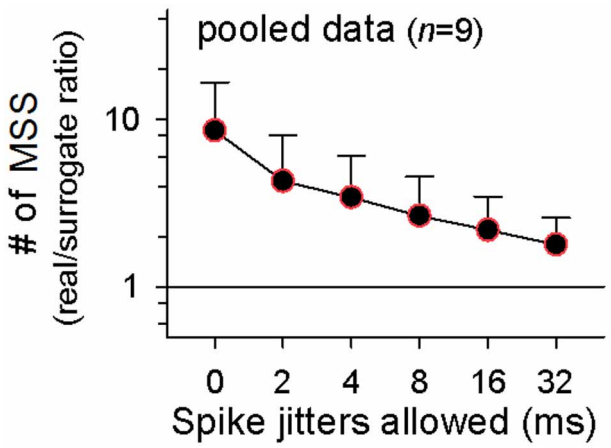

FIGURE 5 | Millisecond precision of MSSs. Summary of 9 videos. Color-edged circles are 5% significant data points between real datasets and surrogates (paired *t*-test). The data are the mean ± SDs.

INTERNAL STRUCTURES OF MSSs

In the following analyses, we used MSSs detected at a spike jitter of 2 ms. Although the real-to-surrogate ratios of MSSs was maximal at a jitter of 0 ms, the absolute number of MSSs detected at 0 ms was substantially smaller than at 2 ms. To enhance statistical accuracy, we selected the 2-ms jitter in this study. Note that the MSS properties described below were fundamentally consistent and exhibited similar tendencies at jitters of 0, 2, 4, and 8 ms (data not shown).

At a jitter of 2 ms, we identified a total of 27,804 MSSs in 9 videos. Among the 825 total neurons, 624 neurons (75.6%) participated in at least one MSS. On average, single MSSs contained 3.4 ± 1.1 neurons, persisted for 107.9 ± 158.6 ms (i.e., the MSS length, defined as the time interval between the first and last spike), and were repeated 2.1 ± 1.1 times during the observation periods. We compared these values to those found in surrogate datasets. The real-to-surrogate ratio of the number of neurons involved in single MSSs was consistently higher than 1 and peaked at 5–8 neurons (**Figure 6A**). As to the MSS length, the real-to-surrogate ratios of the number of MSSs were significantly higher than 1, and roughly in the range of 40–280 ms, peaking at 60 ms (**Figure 6B**). The real-to-surrogate ratios of the number of MSSs were independent of MSS repeat numbers and were consistently higher than 1 (**Figure 6C**).

Two examples of MSSs (**Figure 7A**) are shown in a cell map (**Figure 7B**). We examined whether the neurons involved in each MSS were spatially clustered. For each MSS, we computed the center of gravity for the locations of all neurons that participated in the MSS and calculated the mean distance from these neurons to the center of gravity. If the MSS is spatially clustered, the mean distance will be smaller than chance. The chance values were estimated by 100 surrogates of pseudo-MSSs generated by the same number of neurons randomly selected from the original map. The mean distance from the center of gravity did not differ between real and surrogate MSSs [$t_{(27,\,804)} = 1.08$, $P = 0.28$, paired *t*-test; **Figure 7C**]. Thus, MSS-participating neurons are spatially dispersed at the stochastic level.

Here we returned to the statistical issues about MSS existence. Our spike shuffling method did not consider the spatial

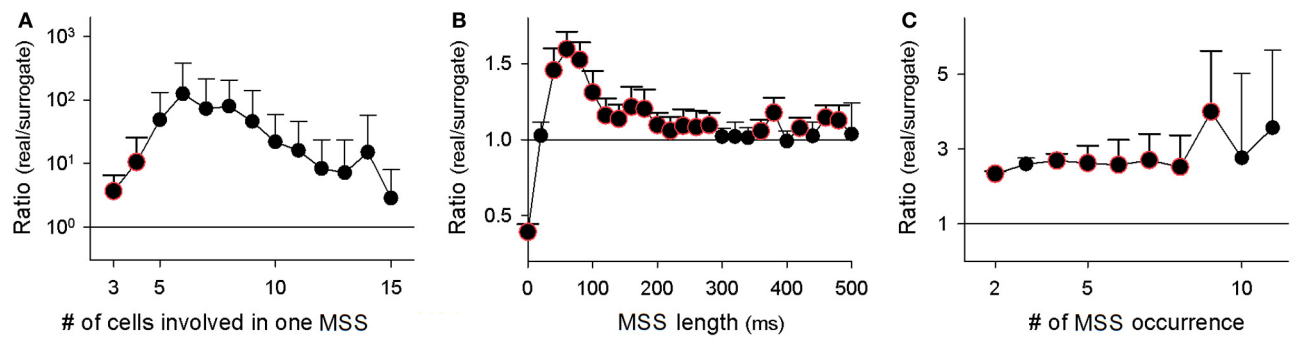

FIGURE 6 | Characterization of MSSs. (A–C) The number of cells that participated in individual MSSs **(A)**, the duration that individual MSS events persisted (i.e., the time intervals between the first and last spikes within MSSs) **(B)**, and the number of repetitions of MSSs **(C)** are shown as ratios of values in real datasets to the mean value of 20 randomized surrogates. Color-edged circles are 5% significant data points between real datasets and surrogates (paired *t*-test). The data are the mean ± SDs of 9 videos.

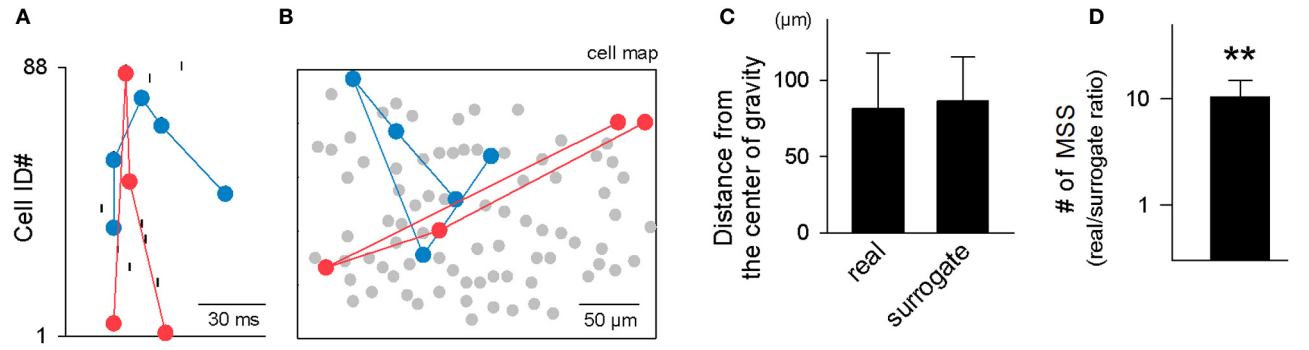

FIGURE 7 | Spatial dispersion of MSSs. (A,B) Two representative MSSs in a rastergram **(A)** and in a cell map **(B)**. **(C)** The mean Euclidean distance from individual cells that participated in a MSS to the center of gravity of all cells that participated in the MSS was compared surrogates in which the same number of cells in the original MSS were selected randomly from the same cell map. This comparison was repeated for 27,804 MSSs in 9 videos, and data are shown as the mean ± SDs. **(D)** The number of MSSs was still overrepresented in surrogates generated by activity shuffling in which spatial configurations were preserved. $^{**}P < 0.01$, paired *t*-test. The data are the mean ± SDs of 9 videos.

organization of cells that participated in MSSs. We thus created surrogates using another shuffling method; for each MSS, spikes were preserved for only one MSS appearance, while the other spikes constituting the MSS were randomly exchanged within the MSS. This procedure did not collapse the spatial organization of cells that exhibited MSSs. Using this shuffling method, we again confirmed that MSSs were overrepresented relative to chance (**Figure 7D**, $n = 9$ videos). However, because these Monte Carlo-shuffling evaluations did not completely abolish statistically innate problems, such as false-negative errors and false-positive errors, we also adopted a completely different approach to validate MSSs without spike shuffling; MSSs are embossed in pairwise correlograms among spike triplets occurring across three distinct cells (Luczak et al., 2007). For each cell trio, one cell was designated the trigger for calculation of the joint distribution of spike times of the other two (**Figure 8A**). A clear dense peak was observed at t_2–$t_1 = -231$ ms and t_3–$t_1 = -12$ ms in this distribution ($n = 180$ triplet spikes), suggesting that a particular sequence occurred preferentially (**Figure 8B**).

We sought to examine the timing of MSS appearance relative to the entire network activity. **Figure 9A** demonstrates the peri-MSS time histogram of the mean firing rates of all neurons in the video. In the peri-MSS time histogram, we aligned the first spikes in individual MSSs at time 0. Data were pooled from 27,804 MSSs in 9 videos. The histogram revealed that the neuronal network transiently increased the global firing rate during MSSs. This transient synchronization persisted for approximately 100 ms, which corresponded to the durations of SW-Rs (Buzsaki et al., 1983).

During SW-Rs, excitatory neurons and inhibitory neurons were both activated at particular phases in a cell type-specific manner (Klausberger et al., 2003). To examine the involvement of GABAergic transmission, we perfused slices with 50 μM picrotoxin, a $GABA_A$ receptor channel inhibitor. Bath application of picrotoxin reduced MSSs, as compared to control solution (**Figure 9B**). Thus, MSSs do not represent simple spike chains via excitatory synapses, but rather, they are more likely to emerge actively from network-coordinated excitatory and inhibitory balance.

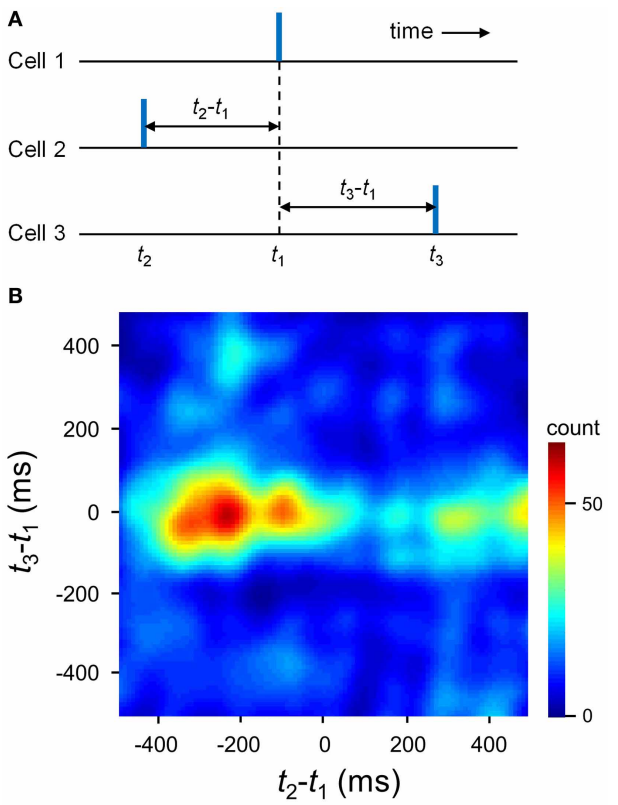

FIGURE 8 | Pairwise correlogram of precisely repeating triplets. (A) For every trio of neurons, a spike triplet is described by two inter-spike intervals (t_2–t_1 and t_3–t_1). **(B)** Count matrix for a representative triplet of neurons, indicating the probability of different inter-spike interval combinations.

BIASED MSS PARTICIPATION OF INDIVIDUAL NEURONS

The same neurons were often recruited in different MSSs. On average, individual cells participated in 81.8 ± 282.2 MSSs; however, the frequency of MSS participation varied among neurons.

The representative cell map shown in **Figure 10A** represents the real-to-surrogate ratios of the number of MSS participations with a pseudo-colored scale, indicating that some neurons frequently participated in MSSs, whereas others did not. In **Figure 10B**, we plotted the Lorenz curve of these frequency ratios ($n = 825$ neurons in 9 videos). The Gini coefficient was 0.44, indicating that neurons are not homogeneous in terms of MSS participation.

To investigate the spatial organization of MSS-participating neurons, we selected neurons that scored in the top 5% of the frequency ratios and computed the mean distance from these cells to their center of gravity (**Figure 10A** bottom). We also calculated the mean distances for the top 5–10, 10–15, 15–20, and 20–25% of the neurons and found that they did not differ among these groups [$P = 0.43$, $F_{(4, 40)} = 0.97$, One-Way ANOVA, **Figure 10A** bottom]. Thus, the spatial distribution of neurons is unlikely to depend on the frequency of MSS participation.

We plotted the frequency of MSS participation against the firing rates of the corresponding neurons (**Figure 10C**). The real-to-surrogate ratios of the MSS participation frequency decreased with the firing rates. These results indicate that frequently firing neurons do not necessarily participate frequently in MSSs, whereas rarely firing neurons seem to contribute more significantly to MSSs.

We then conducted a similar analysis for neuron pairs. Joint participation was defined as when two given neurons simultaneously participated in the same MSS. We counted the number of joint participations for all possible pairs of neurons in each video. **Figure 11A** shows a representative matrix of the real-to-surrogate ratios of the frequency of joint participation of 96 neurons in a single video. Like the behaviors by single neurons, some neuron pairs co-participated frequently in MSSs, whereas other pairs did not. Moreover, the real-to-surrogate ratios of the joint participation frequency decreased with the joint firing rates of the neuron pairs (**Figure 11B**); note that the joint firing rates were defined as $(f_i \times f_j)^{1/2}$, where f_i and f_j are the firing rates of cell$_i$ and cell$_j$.

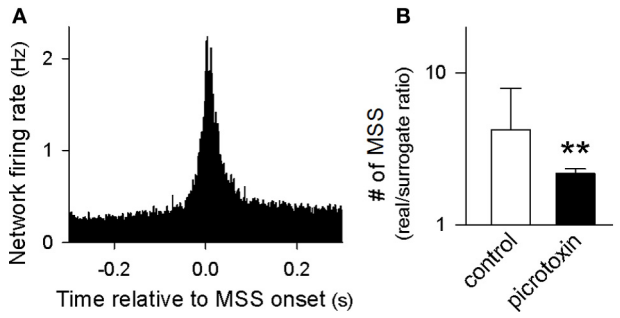

FIGURE 9 | Mechanisms of MSSs. (A) Peri-MSS time histogram of the mean firing rates of all neurons monitored in 9 videos. The firing rates were aligned at the time relative to the onset of 27,804 individual MSSs. **(B)** The number of MSSs relative to chance were decreased by bath application of 50 μM picrotoxin. $^{**}P < 0.01$ versus control, Student's *t*-test. The data are the mean ± SDs of 9 videos.

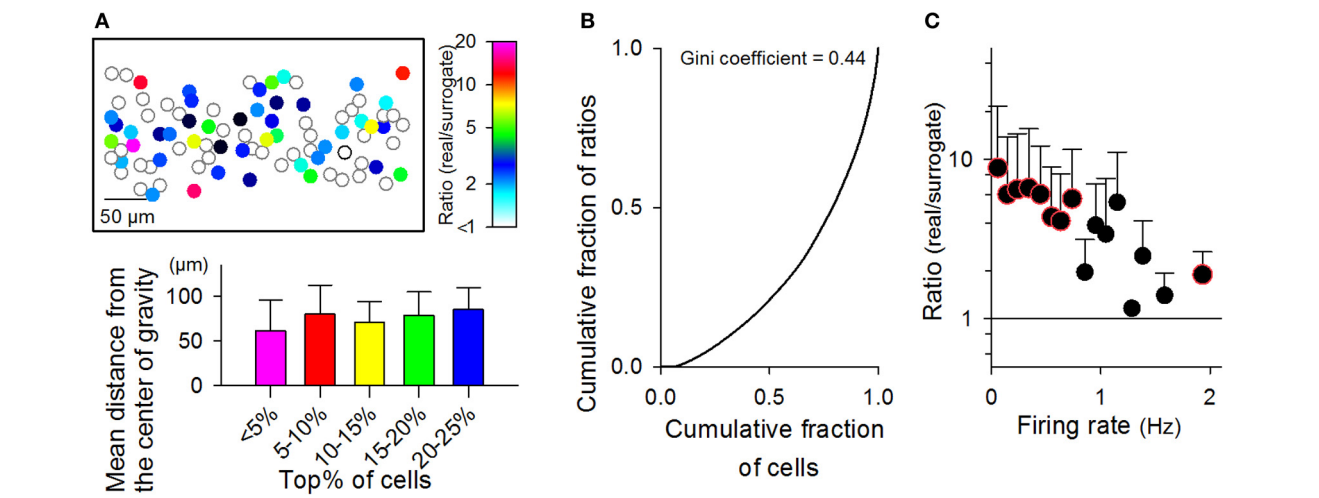

FIGURE 10 | Relationship between the firing rates of neurons and their MSS participations. (A) *Top:* a cell map representing the number of individual cells participating in MSSs during the observation period. Data are shown as the ratio of the real rastergrams to their randomized controls. *Bottom:* The mean Euclidean distance to the center of gravity from individual cells with the highest *x*% of the real-to-surrogate ratio. The ranges of *x* values are indicated in the abscissa. For example, in the case of 5–10%, we selected cells with the real-to-surrogate ratios that ranged from the top 5 to the top 10%, calculated the center of gravity of those selected cells, and measured the mean distance from those cells to their center of gravity. **(B)** A Lorenz curve representing the proportion of real-to-surrogate ratios assumed by the proportion of cells with the lowest ratios. A Lorenz curve is used to show the degree of "inequality" of a distribution defined by two variables (herein, the real-to-surrogate ratio of individual cells *versus* the number of cells with a given real-to-surrogate ratio). The inequality can be represented by a Gini coefficient, a number between 0 and 1, where perfect equality has a Gini coefficient of zero, and absolute inequality yields a Gini coefficient of 1. In this case, the Gini coefficient was 0.44. **(C)** The ratios of the numbers of MSS participations of individual cells in real datasets to the mean values in 20 randomized surrogates are plotted against their mean firing rates. Color-edged circles are 5% significant data points between real datasets and surrogates (paired-*t* test). The data are the mean ± SDs of 9 videos.

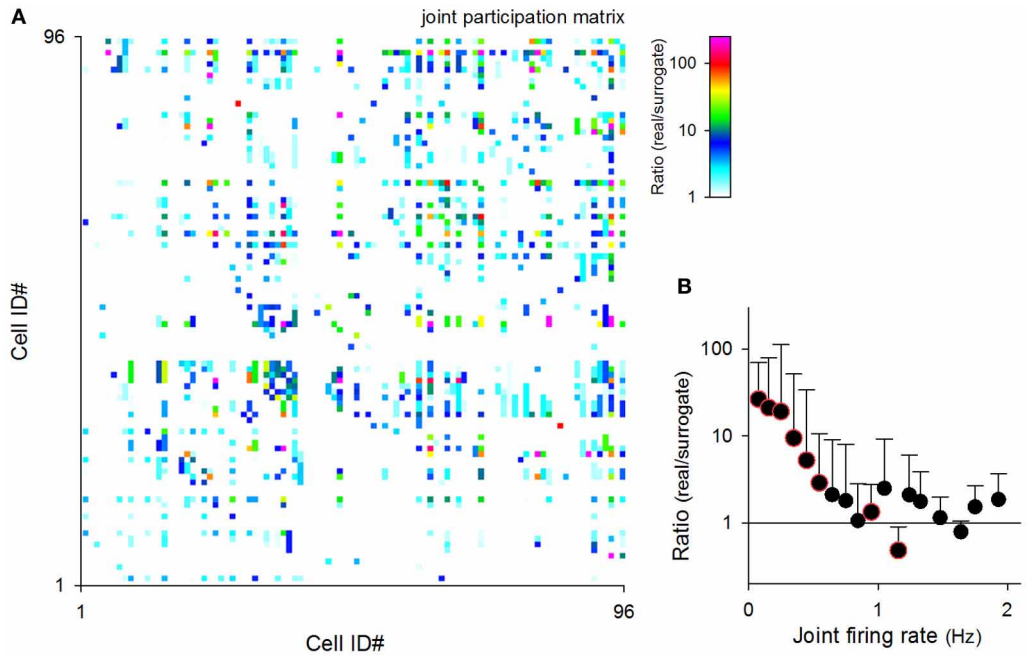

FIGURE 11 | Relationship between the joint firing rates of neuron pairs and their MSS joint participations. (A) A pseudo-colored matrix representing the numbers of joint participations by two given cells. Data are shown as the ratio of the real rastergrams to their randomized controls. **(B)** The ratios of the number of MSS co-participations of cell pairs in real datasets to the mean value of 20 randomized surrogates were plotted against their mean joint firing rates. Color-edged circles are 5% significant data points between real datasets and surrogates (paired-*t* test). The data are the mean ± SDs of 9 videos.

MSS CHAINS

The significant joint participation in MSSs, which was described above, is of importance in understanding MSS dynamics. Given that single neurons were recruited to different MSSs, the joint participation suggests the existence of "core" neuron groups that were shared with different MSSs. Indeed, we often encountered MSS series in which parts of MSSs were replayed by parts of other MSSs (**Figure 12A**).

We thus defined a MSS chain as a sequence of MSSs that shared at least two spikes. Under this definition, a transition from one MSS to another MSS through the shared spikes was referred to herein as 'relay'. We also defined a core pattern as shared spikes at each relay step of a MSS chain. **Figure 12A** shows an example MSS chain in which three MSSs were relayed (from blue to red and from red to green) through two core patterns (indicated by arrows). Of 27,804 MSSs in 9 videos, 22,234 MSSs (80.0%) contained at least one core pattern. Single MSSs contained 1.44 ± 0.85 core patterns, and single core patterns were shared by 4.0 ± 4.2 MSSs ($n = 3264$ core patterns). The mean firing rate of neurons that were involved core patterns was 0.38 ± 0.26 Hz ($n = 401$), which was significantly higher than that of non-core neurons [0.08 ± 0.10 Hz, $n = 427$, $P = 4.6 \times 10^{-8}$, $t_{(826)} = 5.57$]. **Figure 12B** shows the whole dynamics of two representative MSS chains; each circle indicates a single MSS, and each line indicates a relay between two MSSs. Single videos included 26.1 ± 11.6 independent MSS chains ($n = 9$ videos). Single MSS chains consisted of 86.5 ± 284.3 MSSs, contained 53.6 ± 158.1 relay steps, and were 7.9 ± 4.4 s in length ($n = 234$ chains).

Relay steps did not always reflect simple relays between MSSs. The steps often exhibited divergent relays, in which core patterns in one MSS were subsequently used in two or more MSSs, or convergent relays, in which core patterns in two or more MSSs were simultaneously used in a subsequent MSS (see **Figure 12B**). Single chains contained 17.8 ± 56.6 divergent relays and 19.8 ± 61.7 convergent relays ($n = 234$ chains), suggesting that MSS chains constitute MSS subgroups. Therefore, based on core patterns between MSSs, we analyzed MSSs using Ward's method. **Figure 12C** depicts a dendrogram of MSSs in a representative video, indicating that MSSs were clustered into subgroups. Similar MSS cliqueness was observed in the other videos. As a whole, therefore, MSSs are not mere repetitions of precise firing patterns within specific sets of neurons, but they are parts of larger complex and flexible network dynamics.

DISCUSSION

In this work, we used fMCI with 2 ms temporal resolution and monitored CA3 network activity in cultured hippocampal slices. We searched MSSs using a template-matching method and analyzed them by comparing them to surrogates. We generated the surrogates using a spike-exchanging shuffling procedure, a randomization method that is believed to most reliably minimize false-positive errors because it does not collapse the firing rates of individual neurons or population modulation. We demonstrated that the temporal precision of MSSs in the hippocampus is high at the millisecond level. MSSs consisted of heterogeneous neurons

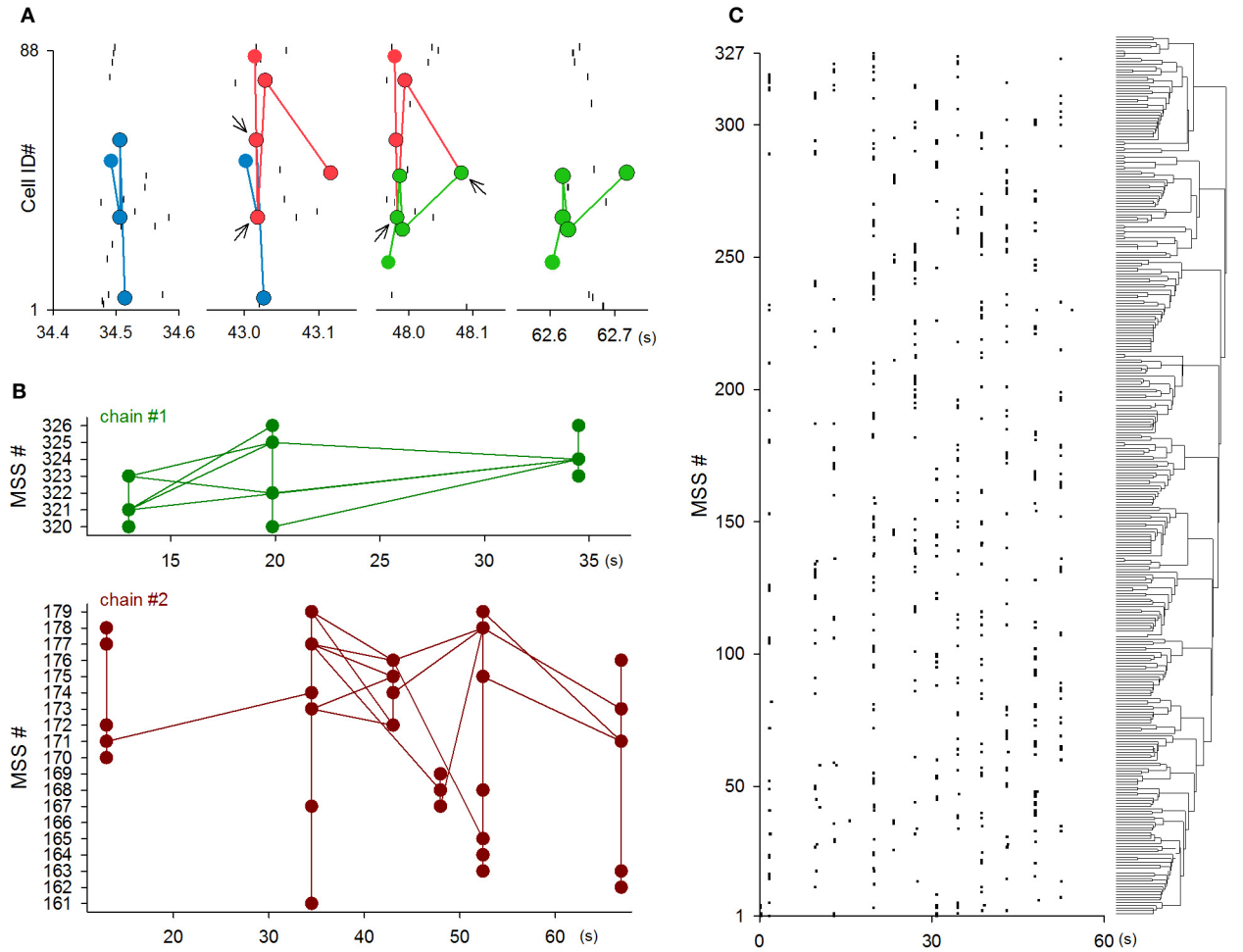

FIGURE 12 | Flexibility and complexity of MSSs. (A) An example of an MSS chain. Spikes that consisted of MSSs were partially shared (i.e., relayed) by other MSSs. Arrows indicate the shared spikes, referred to here as core patterns. **(B)** Two examples of the time evolution of the chains that originated from single MSSs. **(C)** A rastergram of the onset of individual MSSs, the order of which were arranged along the dendrogram clustered by Ward's method.

or neuronal subsets. Moreover, we found core patterns across multiple MSSs, and the core patterns served as hubs through which MSSs are replaced with other MSSs and are sometimes split or joined together with other MSSs.

MSS-like fixed firing patterns have been reported in the neocortex of monkeys and rats (Abeles and Gerstein, 1988; Aertsen et al., 1991; Abeles et al., 1993; Prut et al., 1998; Mao et al., 2001; Cossart et al., 2003; Shmiel et al., 2006; Luczak et al., 2007). They have been thought to be experimental evidence supporting the synfire chain hypothesis, a theoretical framework for efficient spike propagation; however, the statistical significance of MSSs has been questioned by several studies (Oram et al., 1999, 2001; Baker and Lemon, 2000; Mokeichev et al., 2007). In this work, we simultaneously monitored spikes of approximately 100 neurons and confirmed that MSSs occurred in spontaneous activity more than chance. Importantly, the existence of MSSs was most significant at a spike jitter of zero frames. Thus, MSSs were repeated with spike precision of less than 2 ms. However, it is statistically difficult to find the true null hypothesis of temporal structures of spikes (Luczak et al., 2007). Therefore, we also tried to demonstrate the existence of MSSs by examining the properties of MSS-participating neurons. If MSSs are a stochastic product, neurons or neuron pairs with higher firing rates would be expected to participate more frequently in MSSs. Conversely, we found that, in the ratio scale, neurons with lower firing rates contributed more to MSSs. This result implies that MSSs are generated by network dynamics independent of the firing rates of individual neurons. Moreover, the number of neurons involved in single MSSs and the MSS length peaked at 6 neurons and 60 ms. These data also suggest that MSSs reflect organized network dynamics.

The majority of MSSs were generated by specific sets of neurons. Similar heterogeneous participations have been suggested by multi-electrode array recordings from cultures of dissociated mouse neocortical neurons (Sun et al., 2010). In this work, we further identified the core patterns that mediated MSS relays. The core patterns seemed to serve as hubs that generated a wide variety of MSSs that were dynamically associated with each other.

The clustering of MSSs in the dendrogram suggests that single cells participate in different MSSs and that single MSSs are also involved in larger-scale MSS chains. This "MSS-family" concept is consistent with cell assembly dynamics and also with phase sequences of synfire chains, both of which occur together with network synchronization. However, the complexity of MSSs must be interpreted with caution. For instance, the mean number of neurons involved in single MSSs was 3.4. The mean number of total neurons monitored simultaneously was 91.7, whereas approximately 5000 CA3 neurons exist in a hippocampal slice culture (Kimura et al., 2011). This result means that we missed the vast majority of MSSs. Therefore, we underestimate both the true MSS size and the true complexity of MSS dynamics.

Although MSSs are theoretically accepted to be important for stable spike propagation through neuronal microcircuits that consist of weak and stochastic synapses (Abeles, 1991; Diesmann et al., 1999; Reyes, 2003), the physiological roles of MSSs in brain function remain unclear. Our work did not address this fundamental question, but it is intriguing to find that MSSs occurred during SW-Rs. We believe that MSSs underlie memory replay during SW-Rs. Manipulations of MSSs, i.e., artificial controls to increase or decrease MSSs, will help our understanding of the behavioral function of MSSs.

ACKNOWLEDGMENTS

This work was supported by Grants-in-Aid for Science Research on Innovative Areas, "Mesoscopic Neurocircuitry" (No. 22115003), from the Ministry of Education, Culture, Sports, Science and Technology of Japan and by the Funding Program for Next Generation World-Leading Researchers (LS023).

REFERENCES

Abeles, M. (1991). *Corticonics: Neural Circuits of the Cerebral Cortex*. Cambridge, MA: Cambridge University Press. doi: 10.1017/CBO9780511574566

Abeles, M., Bergman, H., Margalit, E., and Vaadia, E. (1993). Spatiotemporal firing patterns in the frontal cortex of behaving monkeys. *J. Neurophysiol.* 70, 1629–1638.

Abeles, M., and Gat, I. (2001). Detecting precise firing sequences in experimental data. *J. Neurosci. Methods* 107, 141–154. doi: 10.1016/S0165-0270(01)00364-8

Abeles, M., and Gerstein, G. L. (1988). Detecting spatiotemporal firing patterns among simultaneously recorded single neurons. *J. Neurophysiol.* 60, 909–924.

Aertsen, A., Vaadia, E., Abeles, M., Ahissar, E., Bergman, H., Karmon, B., et al. (1991). Neural interactions in the frontal cortex of a behaving monkey: signs of dependence on stimulus context and behavioral state. *J. Hirnforsch.* 32, 735–743.

Baker, S. N., and Lemon, R. N. (2000). Precise spatiotemporal repeating patterns in monkey primary and supplementary motor areas occur at chance levels. *J. Neurophysiol.* 84, 1770–1780.

Buzsaki, G. (2010). Neural syntax: cell assemblies, synapsembles, and readers. *Neuron* 68, 362–385. doi: 10.1016/j.neuron.2010.09.023

Buzsaki, G., Leung, L. W., and Vanderwolf, C. H. (1983). Cellular bases of hippocampal EEG in the behaving rat. *Brain Res.* 287, 139–171.

Cossart, R., Aronov, D., and Yuste, R. (2003). Attractor dynamics of network UP states in the neocortex. *Nature* 423, 283–288. doi: 10.1038/nature01614

Davidson, T. J., Kloosterman, F., and Wilson, M. A. (2009). Hippocampal replay of extended experience. *Neuron* 63, 497–507. doi: 10.1016/j.neuron.2009.07.027

De Simoni, A., Griesinger, C. B., and Edwards, F. A. (2003). Development of rat CA1 neurones in acute versus organotypic slices: role of experience in synaptic morphology and activity. *J. Physiol.* 550, 135–147. doi: 10.1113/jphysiol.2003.039099

Diba, K., and Buzsaki, G. (2007). Forward and reverse hippocampal place-cell sequences during ripples. *Nat. Neurosci.* 10, 1241–1242. doi: 10.1038/nn1961

Diesmann, M., Gewaltig, M. O., and Aertsen, A. (1999). Stable propagation of synchronous spiking in cortical neural networks. *Nature* 402, 529–533. doi: 10.1038/990101

Foster, D. J., and Wilson, M. A. (2006). Reverse replay of behavioural sequences in hippocampal place cells during the awake state. *Nature* 440, 680–683. doi: 10.1038/nature04587

Gahwiler, B. H., Capogna, M., Debanne, D., Mckinney, R. A., and Thompson, S. M. (1997). Organotypic slice cultures: a technique has come of age. *Trends Neurosci.* 20, 471–477. doi: 10.1016/S0166-2236(97)01122-3

Gomez-Di Cesare, C. M., Smith, K. L., Rice, F. L., and Swann, J. W. (1997). Axonal remodeling during postnatal maturation of CA3 hippocampal pyramidal neurons. *J. Comp. Neurol.* 384, 165–180. doi: 10.1002/(SICI)1096-9861(19970728)384:2<165::AID-CNE1>3.0.CO;2-#

Harris, K. D. (2005). Neural signatures of cell assembly organization. *Nat. Rev. Neurosci.* 6, 399–407. doi: 10.1038/nrn1669

Harris, K. D., Csicsvari, J., Hirase, H., Dragoi, G., and Buzsaki, G. (2003). Organization of cell assemblies in the hippocampus. *Nature* 424, 552–556. doi: 10.1038/nature01834

Hebb, D. O. (1949). *The Organization of Behavior: A Neuropsychological Theory*. New York, NY: Wiley.

Ikegaya, Y., Aaron, G., Cossart, R., Aronov, D., Lampl, I., Ferster, D., et al. (2004). Synfire chains and cortical songs: temporal modules of cortical activity. *Science* 304, 559–564. doi: 10.1126/science.1093173

Kendall, M. G., Stuart, A., Ord, J. K., Arnold, S. F., and O'Hagan, A. (1994). *Kendall's Advanced Theory of Statistics*. New York, NY: Halsted Press.

Kimura, R., Kang, S., Takahashi, N., Usami, A., Matsuki, N., Fukai, T., et al. (2011). Hippocampal polysynaptic computation. *J. Neurosci.* 31, 13168–13179. doi: 10.1523/JNEUROSCI.1920-11.2011

Klausberger, T., Magill, P. J., Marton, L. F., Roberts, J. D., Cobden, P. M., Buzsaki, G., et al. (2003). Brain-state- and cell-type-specific firing of hippocampal interneurons *in vivo*. *Nature* 421, 844–848. doi: 10.1038/nature01374

Koyama, R., Muramatsu, R., Sasaki, T., Kimura, R., Ueyama, C., Tamura, M., et al. (2007). A low-cost method for brain slice cultures. *J. Pharmacol. Sci.* 104, 191–194. doi: 10.1254/jphs.SC0070119

Laurberg, S., and Zimmer, J. (1981). Lesion-induced sprouting of hippocampal mossy fiber collaterals to the fascia dentata in developing and adult rats. *J. Comp. Neurol.* 200, 433–459. doi: 10.1002/cne.902000310

Lee, A. K., and Wilson, M. A. (2002). Memory of sequential experience in the hippocampus during slow wave sleep. *Neuron* 36, 1183–1194. doi: 10.1016/S0896-6273(02)01096-6

Luczak, A., Bartho, P., Marguet, S. L., Buzsaki, G., and Harris, K. D. (2007). Sequential structure of neocortical spontaneous activity *in vivo*. *Proc. Natl. Acad. Sci. U.S.A.* 104, 347–352. doi: 10.1073/pnas.0605643104

Mao, B. Q., Hamzei-Sichani, F., Aronov, D., Froemke, R. C., and Yuste, R. (2001). Dynamics of spontaneous activity in neocortical slices. *Neuron* 32, 883–898. doi: 10.1016/S0896-6273(01)00518-9

Miles, R., and Wong, R. K. (1983). Single neurones can initiate synchronized population discharge in the hippocampus. *Nature* 306, 371–373. doi: 10.1038/306371a0

Mizunuma, M., Takahashi, N., Usami, A., Matsuki, N., and Ikegaya, Y. (2009). High-temperature, but not high-pressure, conditions alter neuronal activity. *J. Pharmacol. Sci.* 110, 117–121. doi: 10.1254/jphs.09031SC

Mokeichev, A., Okun, M., Barak, O., Katz, Y., Ben-Shahar, O., and Lampl, I. (2007). Stochastic emergence of repeating cortical motifs in spontaneous membrane potential fluctuations *in vivo*. *Neuron* 53, 413–425. doi: 10.1016/j.neuron.2007.01.017

Norimoto, H., Mizunuma, M., Ishikawa, D., Matsuki, N., and Ikegaya, Y. (2012). Muscarinic receptor activation disrupts hippocampal sharp wave-ripples. *Brain Res.* 1461, 1–9. doi: 10.1016/j.brainres.2012.04.037

O'Neill, J., Senior, T., and Csicsvari, J. (2006). Place-selective firing of CA1 pyramidal cells during sharp wave/ripple network patterns in exploratory behavior. *Neuron* 49, 143–155. doi: 10.1016/j.neuron.2005.10.037

Oram, M. W., Hatsopoulos, N. G., Richmond, B. J., and Donoghue, J. P. (2001). Excess synchrony in

motor cortical neurons provides redundant direction information with that from coarse temporal measures. *J. Neurophysiol.* 86, 1700–1716.

Oram, M. W., Wiener, M. C., Lestienne, R., and Richmond, B. J. (1999). Stochastic nature of precisely timed spike patterns in visual system neuronal responses. *J. Neurophysiol.* 81, 3021–3033.

Pastalkova, E., Itskov, V., Amarasingham, A., and Buzsaki, G. (2008). Internally generated cell assembly sequences in the rat hippocampus. *Science* 321, 1322–1327. doi: 10.1126/science.1159775

Prut, Y., Vaadia, E., Bergman, H., Haalman, I., Slovin, H., and Abeles, M. (1998). Spatiotemporal structure of cortical activity: properties and behavioral relevance. *J. Neurophysiol.* 79, 2857–2874.

Reyes, A. D. (2003). Synchrony-dependent propagation of firing rate in iteratively constructed networks *in vitro*. *Nat. Neurosci.* 6, 593–599. doi: 10.1038/nn1056

Sasaki, T., Matsuki, N., and Ikegaya, Y. (2007). Metastability of active CA3 networks. *J. Neurosci.* 27, 517–528. doi: 10.1523/JNEUROSCI.4514-06.2007

Sasaki, T., Minamisawa, G., Takahashi, N., Matsuki, N., and Ikegaya, Y. (2009). Reverse optical trawling for synaptic connections in situ. *J. Neurophysiol.* 102, 636–643. doi: 10.1152/jn.00012.2009

Sasaki, T., Takahashi, N., Matsuki, N., and Ikegaya, Y. (2008). Fast and accurate detection of action potentials from somatic calcium fluctuations. *J. Neurophysiol.* 100, 1668–1676. doi: 10.1152/jn.00084.2008

Shmiel, T., Drori, R., Shmiel, O., Ben-Shaul, Y., Nadasdy, Z., Shemesh, M., et al. (2006). Temporally precise cortical firing patterns are associated with distinct action segments. *J. Neurophysiol.* 96, 2645–2652. doi: 10.1152/jn.00798.2005

Smith, K. L., Szarowski, D. H., Turner, J. N., and Swann, J. W. (1995). Diverse neuronal populations mediate local circuit excitation in area CA3 of developing hippocampus. *J. Neurophysiol.* 74, 650–672.

Sun, J. J., Kilb, W., and Luhmann, H. J. (2010). Self-organization of repetitive spike patterns in developing neuronal networks *in vitro*. *Eur. J. Neurosci.* 32, 1289–1299. doi: 10.1111/j.1460-9568.2010.07383.x

Sun, Y., Norimoto, H., Pu, X. P., Matsuki, N., and Ikegaya, Y. (2012). Cannabinoid receptor activation disrupts the internal structure of hippocampal sharp wave-ripple complexes. *J. Pharmacol. Sci.* 118, 288–294. doi: 10.1254/jphs.11199FP

Takahashi, N., Oba, S., Yukinawa, N., Ujita, S., Mizunuma, M., Matsuki, N., et al. (2011). High-speed multineuron calcium imaging using Nipkow-type confocal microscopy. *Curr. Protoc. Neurosci.* 2, 14. doi: 10.1002/0471142301.ns0214s57

Takahashi, N., Sasaki, T., Matsumoto, W., Matsuki, N., and Ikegaya, Y. (2010). Circuit topology for synchronizing neurons in spontaneously active networks. *Proc. Natl. Acad. Sci. U.S.A.* 107, 10244–10249. doi: 10.1073/pnas.0914594107

Takahashi, N., Sasaki, T., Usami, A., Matsuki, N., and Ikegaya, Y. (2007). Watching neuronal circuit dynamics through functional multineuron calcium imaging (fMCI). *Neurosci. Res.* 58, 219–225. doi: 10.1016/j.neures.2007.03.001

Ujita, S., Mizunuma, M., Matsuki, N., and Ikegaya, Y. (2011). Asynchronously enhanced spiking activity of ischemic neuronal networks. *Biol. Pharmaceut. Bull.* 34, 764–767. doi: 10.1248/bpb.34.764

Usami, A., Matsuki, N., and Ikegaya, Y. (2008). Spontaneous plasticity of multineuronal activity patterns in activated hippocampal networks. *Neural Plast.* 2008:108969. doi: 10.1155/2008/108969

West, J. R., and Dewey, S. L. (1984). Mossy fiber sprouting in the fascia dentata after unilateral entorhinal lesions: quantitative analysis using computer-assisted image processing. *Neuroscience* 13, 377–384. doi: 10.1016/0306-4522(84)90237-9

Conflict of Interest Statement: The authors declare that the research was conducted in the absence of any commercial or financial relationships that could be construed as a potential conflict of interest.

Received: 20 February 2013; accepted: 03 June 2013; published online: 21 June 2013.

Citation: Matsumoto K, Ishikawa T, Matsuki N and Ikegaya Y (2013) Multineuronal spike sequences repeat with millisecond precision. Front. Neural Circuits 7:112. doi: 10.3389/fncir.2013.00112

frontiers in
NEURAL CIRCUITS

ORIGINAL RESEARCH ARTICLE
published: 02 December 2013
doi: 10.3389/fncir.2013.00192

GABAergic neurons in the preoptic area send direct inhibitory projections to orexin neurons

Yuki C. Saito[1], Natsuko Tsujino[1], Emi Hasegawa[1], Kaori Akashi[2], Manabu Abe[2], Michihiro Mieda[1], Kenji Sakimura[2] and Takeshi Sakurai[1]*

[1] *Department of Molecular Neuroscience and Integrative Physiology, Faculty of Medicine, Kanazawa University, Kanazawa, Japan*
[2] *Department of Cellular Neurobiology, Brain Research Institute, Niigata University, Niigata, Japan*

Edited by:
Yasuo Kawaguchi, National Institute for Physiological Sciences, Japan

Reviewed by:
Takatoshi Mochizuki, Beth Israel Deaconess Medical Center, USA
Yoshimasa Koyama, Fukushima University, Japan

****Correspondence:***
Takeshi Sakurai, Department of Molecular Neuroscience and Integrative Physiology, Faculty of Medicine, Kanazawa University, 13-1 Takara-machi, Kanazawa, Ishikawa 920-8640, Japan
e-mail: takeshi.sakurai@gmail.com

Populations of neurons in the hypothalamic preoptic area (POA) fire rapidly during sleep, exhibiting sleep/waking state-dependent firing patterns that are the reciprocal of those observed in the arousal system. The majority of these preoptic "sleep-active" neurons contain the inhibitory neurotransmitter GABA. On the other hand, a population of neurons in the lateral hypothalamic area (LHA) contains orexins, which play an important role in the maintenance of wakefulness, and exhibit an excitatory influence on arousal-related neurons. It is important to know the anatomical and functional interactions between the POA sleep-active neurons and orexin neurons, both of which play important, but opposite roles in regulation of sleep/wakefulness states. In this study, we confirmed that specific pharmacogenetic stimulation of GABAergic neurons in the POA leads to an increase in the amount of non-rapid eye movement (NREM) sleep. We next examined direct connectivity between POA GABAergic neurons and orexin neurons using channelrhodopsin 2 (ChR2) as an anterograde tracer as well as an optogenetic tool. We expressed ChR2-eYFP selectively in GABAergic neurons in the POA by AAV-mediated gene transfer, and examined the projection sites of ChR2-eYFP-expressing axons, and the effect of optogenetic stimulation of ChR2-eYFP on the activity of orexin neurons. We found that these neurons send widespread projections to wakefulness-related areas in the hypothalamus and brain stem, including the LHA where these fibers make close appositions to orexin neurons. Optogenetic stimulation of these fibers resulted in rapid inhibition of orexin neurons. These observations suggest direct connectivity between POA GABAergic neurons and orexin neurons.

Keywords: orexin, preoptic area, GABA, sleep, wakefulness, hypothalamus

INTRODUCTION

The preoptic area (POA) of the hypothalamus has been implicated in a variety of physiological functions, including the regulation of sleep/wakefulness states (Boulant, 1981; McGinty et al., 2001). Especially, this region is thought to play an important role in the initiation and maintenance of sleep. Initially, electrical or chemical stimulation of the lateral POA in animals was shown to promote EEG slow-wave activity and sleep onset (Sterman and Clemente, 1962; Benedek et al., 1982; Ticho and Radulovacki, 1991; Mendelson and Martin, 1992). Consistently, lesions in the POA have been shown to result in profound and persistent sleep loss (John and Kumar, 1998; Lu et al., 2000). However, these studies are not genetically targeted to specific neuron types, and so the cells that are responsible remain to be clarified. In this study, we focused on the GABAergic neurons, as some of them have been shown to provide inputs in particular to the arousal system. We examined the role of the projection from GABAergic neurons in the POA to the orexin neurons in the LHA in inhibiting the latter cells, and the effect of activating this pathway on sleep.

Extracellular recording studies have identified sleep-active neurons in a region extending from the medial through the lateral POA (Kaitin, 1984; Koyama and Hayaishi, 1994), while it was reported that neurons in the rat ventrolateral preoptic area (VLPO) and median preoptic nucleus (MnPN) exhibited Fos expression following consolidated sleep (Gong et al., 2000). The POA was shown to send GABAergic inhibitory projections to monoaminergic regions, including the locus coeruleus (LC), dorsal raphe nucleus (DRN), and tuberomammilary nucleus (TMN) (Sherin et al., 1996, 1998; Steininger et al., 2001; Uschakov et al., 2007). Consistently, firing patterns of monoaminergic neurons in these nuclei across the sleep-waking cycle are the reciprocal of those observed in POA sleep-active neurons. They fire at a rapid rate during wakefulness, slow down during non-rapid eye movement (NREM) sleep, and cease firing during rapid eye movement (REM) sleep (Saper et al., 2001). Electrophysiological studies suggested that VLPO neurons are inhibited by noradrenaline and serotonin (Gallopin et al., 2000), suggesting mutually inhibitory interactions between VLPO and the monoaminergic arousal systems (Saper et al., 2001).

Monoaminergic arousal systems are also thought to be regulated by orexin neuropeptides, which are thought to be a critical regulator of sleep/wake states (Sakurai, 2007). Orexin deficiency causes the sleep disorder narcolepsy in humans and animals (Chemelli et al., 1999; Lin et al., 1999; Peyron et al., 2000;

Thannickal et al., 2000; Hara et al., 2001). Orexin-producing neurons (orexin neurons) in the lateral hypothalamic area (LHA) send dense axonal projections to monoaminergic neurons in the brain stem/hypothalamic regions. Recent studies have suggested the POA also sends projections to orexin neurons in the LHA (Sakurai et al., 2005; Yoshida et al., 2006). However, how the endogenous firing of POA sleep-active neurons affects the activity of orexin neurons has been unknown. Functional studies of this issue are important, because both POA sleep active neurons and orexin neurons play highly important roles in the physiological regulation of sleep.

To examine the electrophysiological impact of activity of endogenous POA neurons, we first confirmed that selective pharmacogenetic stimulation of GABAergic neurons in the POA, using the Designer Receptors Exclusively Activated by Designer Drugs (DREADD) technology, leads to an increase of NREM sleep (Armbruster et al., 2007). We also used channelrhodopsin-2 (ChR2) as an anterograde tracer as well as an optogenetic tool (Bernstein et al., 2012; Yizhar et al., 2011) for selective optical excitation of GABAergic POA neurons and their axons. We examined the axonal projections of ChR2-eYFP-positive fibers and confirmed that POA GABAergic neurons send abundant projections to arousal-related regions, including the LC, DR, TMN, and laterodorsal/pedunculopontine tegmental nucleui (LDT/PPT). Dense projections were also found in the LHA, and these GABAergic fibers made appositions to orexin neurons. We then explored the effects of fast and selective optogenetic stimulation of GABAergic axons on orexin neurons. By combining whole-cell patch-clamp recordings from orexin neurons with optogenetic stimulation of GABAergic axons in acute mouse brain slices, we found that photostimulation of POA GABAergic fibers immediately caused a decrease in the firing rate of orexin neurons through GABA release. These observations suggest that POA GABAergic neurons send direct inhibitory projections to orexin neurons.

MATERIALS AND METHODS

ANIMALS

All experimental procedures involving animals were approved by the Animal Experiment and Use Committee of Kanazawa University (AP-132649), and were thus in accordance with NIH guidelines. *Gad67-Cre* mice, in which the *Cre* gene was knocked-in in the *Gad67* allele were previously described (Wu et al., 2011). The mice were bred with wild type C57BL/6J mice more than ten times and maintained.

AAV PRODUCTION AND PURIFICATION

We used AAV with the FLEX switch system (Atasoy et al., 2008) to specifically express HA-tagged hM3Dq or ChR2 fused with EYFP (ChR2-EYFP) only in Cre recombinase-expressing neurons. We applied this method to heterozygous *Gad67-Cre* mice in which the Cre recombinase gene is specifically expressed in GABAergic neurons (Wu et al., 2011).

pAAV-DIO-HAhM3Dq was provided by Dr. Brian Roth. *pAAV-DIO-hChR2(H134R)-EYFP-WPRE-pA* was provided by Dr. Karl Deisseroth of Stanford University (Kozorovitskiy et al., 2012). We constructed a plasmid, *pAAV-horexin-tdTomato-WPRE-pA*, as follows. A 1.3-kb fragment of the human *prepro-orexin* gene promoter, which has the ability to drive expression in orexin neurons specifically (Moriguchi et al., 2002), was amplified by PCR with a pair of primers 5′-CACGCGTGCATGCTGTAATCCCAGCTAC-3′ and 5′-TGTCGACGGTGTCTGGCGCTCAGGGTG-3′. The PCR product was fully sequenced and digested by MluI and SalI, and ligated to Mlu I and SalI-digested *pAAV-DIO-hChR2(H134R)-EYFP-WPRE-pA*, yielding *pAAV-horexin-hChR2(H134R)-EYFP-WPRE-pA*. The *tdTomato* gene fragment from *ptdTomato* (Clontech) was inserted into the EcoRI and SalI sites of *pAAV-horexin-hChR2(H134R)-EYFP-WPRE-pA*, yielding *pAAV-horexin-tdTomato-WPRE-pA*.

Viruses were produced using a triple-transfection, helper-free method using a modification of a published protocol (Auricchio et al., 2001; Sasaki et al., 2011). The final purified viruses were aliquoted and stored at −80°C. The titers of *AAV-DIO-hChR2(H134R)-EYFP* and *AAV-orexin-tdTomato* were 1.63×10^{12} and 1.03×10^{12} genome copies/ml, respectively.

VIRUS INJECTION

Adenoassociated-virus *AAV-DIO-HAhM3Dq* or *AAV-DIO-hChR2(H134R)-EYFP* was injected into the POA of *Gad67-Cre* mice (Wu et al., 2011). In *in vitro* electrophysiological experiments for recording orexin neurons, *AAV-orexin-tdTomato* was simultaneously injected into the LHA of these mice for identification of orexin neurons (**Figure 4A**). Male mice were anesthetized with isofluorane and placed in a stereotaxic frame (David Kopf Instruments). For injection into the POA, two holes were drilled into the skull of *Gad67-Cre* mice (12–15 weeks of age, weight 25–30 g), at sites +0.3 mm anterior, ±0.65 mm lateral, and −5.72 mm ventral to the bregma under deep anesthesia. For injection into the LHA, four holes were drilled into the skull of each mouse under anesthesia, at sites −1.4 mm posterior, ±0.9 mm lateral, and −5.5 mm ventral; and −1.8 mm posterior, ±0.9 mm lateral, and −5.7 mm ventral to the bregma (four injection sites per mouse).

A Hamilton needle syringe (33-gauge) was placed at each site, and 0.5 μl purified virus was delivered to each site over a 10-min period. After 5 min of rest, the needles were removed. The mice were sacrificed 14 days later, and slice preparations were analyzed by electrophysiological experiments and tissue samples by immunohistochemical staining.

ELECTROPHYSIOLOGY

Acute slices containing the LHA were prepared from the mice 14 days post-AAV injection, as described in our previous studies (Tsujino et al., 2005). The mice were decapitated under deep anesthesia. Brains were isolated in ice-cold cutting solution consisting of (mM): 280 sucrose, 2 KCl, 10 HEPES, 0.5 $CaCl_2$, 10 $MgCl_2$, 10 glucose, pH 7.4, bubbled with 100% O_2. Brains were cut coronally into 300-μm slices with a vibratome (VTA-1200S, Leica, Germany). Slices were transferred to an incubation chamber at room temperature filled with physiological solution containing (mM): 125 NaCl, 2.5 KCl, 1.25 NaH_2PO_4, 2.0 $CaCl_2$, 1.0 $MgSO_4$, 26 $NaHCO_3$, 11 glucose, pH 7.4, bubbled with 95% O_2/5% CO_2. After 1-h incubation in an incubation chamber, the slices were transferred to a recording chamber (RC-27L,

Warner Instrument Corp., CT, USA) at 32℃ on a fluorescence microscope stage (BX51WI, Olympus, Tokyo, Japan). Neurons that showed tdTomato fluorescence were used for patch-clamp recordings. The fluorescence microscope was equipped with an infrared camera (C-3077, Hamamatsu Photonics, Hamamatsu, Japan) for infrared differential interference contrast (IR-DIC) imaging and a CCD camera (JK-TU53H, Olympus) for fluorescent imaging. Each image was displayed separately on a monitor. Recordings were carried out with an Axopatch 200B amplifier (Axon Instruments, Foster City, CA) using a borosilicate pipette (GC150-10, Harvard Apparatus, Holliston, MA) prepared using a micropipette puller (P-97, Sutter Instruments, Pangbourne, UK) and filled with intracellular solution (4–10 MΩ), consisting of (mM): 125 K-gluconate, 5 KCl, 1 $MgCl_2$, 10 HEPES, 1.1 EGTA-Na_3, 5 MgATP, 0.5 Na_2GTP, pH7.3 with KOH. Osmolarity of the solution was checked with a vapor pressure osmometer (model 5520, Wescor, Logan, UT). The osmolarity of the internal and external solutions was 280–290 and 320–330 mOsm/l, respectively. The liquid junction potential of the patch pipette and perfused extracellular solution was estimated to be −16.2 mV and was applied to the data. The recording pipette was under positive pressure while it was advanced toward individual cells in the slice. Tight seals of 0.5–1.0 GΩ were made by applying negative pressure. The membrane patch was then ruptured by suction. The series resistance during recording was 10–25 MΩ and was compensated. The reference electrode was an Ag-AgCl pellet immersed in bath solution. During recordings, cells were superfused with extracellular solution at a rate of 1.0–2.0 ml/min using a peristaltic pump (K.T. Lab, Japan).

Light activation was performed using an LED device (KSL-70; Rapp OptoElectronic, Hamburg, Germany) at a wavelength of 470 nm (maximum: 8 mW/mm^2). Pulse was generated with SEN-3301 stimulator (Nihon Koden, Japan).

CLOZAPINE-N-OXIDE ADMINISTRATION

Clozapine N-oxide (CNO; C0832, Sigma-Aldrich) was dissolved in saline to a concentration of 0.5 mg/ml. Silicon tubes were implanted for remote CNO injection. The tip of a 30 cm-long silicon tube was inserted 1 cm into the peritoneal cavity and sutured to the abdominal wall. The other end of the silicon tube was placed outside the body through an incision in the neck, and all incisions were sutured. All animals were then housed individually for a recovery period of at least 7 days. CNO was administered to each mouse (0.3 ml/30 g body weight) through the silicon tube. Injections were done at 21:00 and at 13:00.

SLEEP RECORDINGS

An electrode for EEG and EMG recording was implanted in the skull of each mouse as decscribed previously (Hara et al., 2001). The three arms of the electrode for EEG recording were placed ∼2 mm anterior and 2 mm to the right, 2 mm posterior and 2 mm to the right, and 2 mm posterior and 2 mm to the left of the bregma. Stainless steel wires for EMG recording were sutured to the neck muscles of each mouse bilaterally, and each electrode was glued solidly to the skull. After the recovery period, animals were moved to a recording cage placed in an electrically shielded and sound attenuated room. A cable for signal output was connected to the implanted electrode and animals were allowed to move freely. Signals were amplified through an amplifier (AB-611J, Nihon Koden, Tokyo) and digitally recorded on a computer using EEG/EMG recording software (Vital recorder, Kissei Comtec). Animals were allowed at least 7 days to adapt to the recording conditions prior to any EEG/EMG recording session. Following the adaptation period, each animal was intraperitoneally administered both CNO and saline on separate experimental days with a 3-day interval. The order of injection was randomized. EEG/EMG data were evaluated and staged for 3 h after administration. Data acquired on the day of saline administration were used as control. We analyzed FFT spectra of NREM period in 1–2 h epoch of saline- or CNO-injected mice ($N = 14$). Power spectral analysis of EEG signals was performed using custom FFT software.

IMMUNOHISTOCHEMISTRY

To confirm GABAergic-specific expression of Cre recombinase activity in the POA of *Gad67-Cre* mice, we crossed them with Rosa26-tdTomato tracer mice (B6; 129S6-Gt(ROSA)26Sortm9(CAG-tdTomato)Hze/J, Jackson Laboratory #007905). Mice at 8 weeks of age were deeply anesthetized with sodium pentobarbital and then fixed by intracardiac perfusion with 4% paraformaldehyde. Then, the brain was post-fixed for 24 h in the same fixative and cryoprotected by immersion in 30% sucrose for 2 days. Cryostat sections (40-μm thick) of the brains were incubated for 1 h in 0.1 M phosphate buffer containing 1% bovine serum albumin and 0.25% Triton-X-100, and incubated overnight at 4°C with rabbit anti-GAD65/67 antibody (Uchigashima et al., 2007) in the same solution. After three washes in the same solution, the sections were incubated with goat anti-rabbit IgG conjugated with Alexa 488 (*Invitrogen*, Carlsbad, CA) for 90 min at room temperature. After three washes in 0.1 M phosphate buffer, the sections were mounted on glass slides and cover-slipped. Slides were examined with a laser-confocal microscope (Olympus FV10i, Olympus, Japan).

To detect monoaminergic and cholinergic neurons, we used mouse anti-tryptophan hydroxylase (TPH) antibody (Sigma, T0648, 1:200), guinea pig anti-histidine decarboxylase (HDC) antibody (PROGEN Biotechnik Gmbh, No.16046, 1:4,000), rabbit anti-tyrosine hydroxylase (TH) antibody (Millipore, AB152, 1:2,000), and goat anti-choline acetyltransferase (ChAT) antibody (Millipore, Ab144D, 1:100). As a second antibody, Alexa Fluor 594-goat anti-mouse IgG (Molecular Probes, 1:800), Alexa Fluor 594-goat anti-guinea pig IgG (Molecular Probes, 1:800) were used.

To detect Fos immunoreactivity in orexin-expressing neurons, coronal sections were incubated overnight with rabbit anti-cFos antibody Ab-5 (Calbiochem, 1:10000) and guenia pig anti-orexin antibody in 0.1 M phosphate buffer containing 1% bovine serum albumin and 0.25% Triton X-100. The primary antibody was localized with the avidin-biotin system (Vector). Bound peroxidase was visualized by incubating sections with 0.01 M imidazole acetate buffer containing 0.05% hydrogen peroxide and 2.5% nickel ammonium sulfate, resulting in a black reaction product in the nuclei. The sections were then incubated with anti-guenia pig IgG and then with the avidin-biotin-peroxidase complex as described above. Nickel sulfate was omitted from the final

incubation, resulting in a golden brown reaction product in the cytoplasm. The numbers of cFos-positive and -negative orexin-containing neurons were counted in coronal sections throughout the hypothalamic region by a single examiner who was blinded to the treatment conditions, using a Keyence BZ-9000 microscope (Keyence, Japan). Cells were counted on both sides of the brain in consecutive 40-μm sections. Orexin neuron activity was scored as the percentage of double-labeled cells per animal.

In situ HYBRIDIZATION

Double *in situ* hybridization was performed according to procedures previously described (Mieda et al., 2006). For double *in situ* hybridization, each combination of two antisense riboprobes labeled with either fluorescein-UTP (Gad1) or digoxygenin-UTP (GFP) was hybridized to sections simultaneously. Following the chromogenic reaction of the first color (blue) obtained with anti-digoxygenin-alkaline phosphatase (AP) Fab fragments, 5-bromo-4-chloro-3-indolyl phosphate (Roche) and nitroblue tetrazolium (Roche), sections were rinsed three times with TBS, treated twice with 0.1M glycine pH 2.2; 0.1% Tween 20 for 5 min, washed, and then incubated with anti-fluorescein-alkaline phosphatase (AP) Fab fragments. For the chromogenic reaction of the second color (orange), 5-bromo-4-chloro-3-indolyl phosphate (Roche) and 2-[4-iodophenyl]-3-[4-nitrophenyl]-5-phenyl-tetrazolium chloride (Roche) were used. Antisense riboprobes were synthesized from plasmids containing GFP and mouse Gad1 (NM_008077, nucleotides 281-821) cDNAs.

STATISTICAL ANALYSIS

Data were expressed as mean ± s.e.m. Two-way analysis of variance (ANOVA) followed by Bonfferoni correction as a *post-hoc* test or Student's *t*-test using IBM SPSS Statistics ver.19 was used for comparison among the various treatment groups. Differences were considered significant at $p < 0.05$.

RESULTS

PHARMACOGENETIC SELECTIVE STIMULATION OF POA GABAergic NEURONS INCREASED NREM SLEEP

Before examining the connectivity between POA GABAergic neurons and orexin neurons, we confirmed whether specific stimulation of GABAergic neurons in the POA affects sleep/wakefulness states in mice. We applied the DREADD technology (Armbruster et al., 2007; Sasaki et al., 2011), to phamacogenetically manipulate the activity of POA GABAergic neurons. To express hM3Dq in GABAergic neurons in the POA, we injected *AAV-DIO-HAhM3Dq* into the POA of *Gad67-Cre* mice, in which GABAergic neurons specifically express Cre recombinase (Wu et al., 2011). GABAergic specific expression of Cre recombinase in the POA of *Gad67-Cre* mice was confirmed by crossing them with *ROSA26-tdTomato* mice (containing *tdTomato* gene preceded by a transcriptional blocker flanked with lox-P sites) (**Figure 1A**). We confirmed virtually all tdTomato-expressing neurons were positive for Gad65/67 immunoreactivity (95.4%). After injection of *AAV-DIO-HAhM3Dq*, we implanted thin silicone tubes into the peritoneal space of *Gad67-Cre* mice so that we could administer clozapine-N-oxide (CNO), the synthetic ligand for hM3Dq, with minimal disturbance. Fourteen days after virus injection, we administered CNO to mice.

Fourteen days after the virus injection, we administered CNO or saline intraperitoneally to *Gad67-Cre* mice expressing hM3Dq at 13:00 (light period) or 21:00 (dark period). The sleep/wakefulness states of these mice were monitored by simultaneous EEG/EMG recording. As a control, we treated the same mice with saline on separate experimental days. Each mouse was administered CNO or vehicle using a randomized crossover design at an interval of 3 days.

After the recording, mice were subjected to immunostaining with anti-HA antibody. We observed expression of HA-immunoreactivity in the POA region of most mice (**Figure 1B**). We injected the virus in 62 mice, and only used data obtained from 14 mice in which the existence of HA-positive cell bodies was limited within the POA. In many cases, we observed expression of HA-positive cells outside the POA, including the basal forebrain regions, such as the horizontal nucleus of the diagonal band. Therefore, we gathered data from 14 mice, in which HA-immunoreactivity was confined in the POA.

After the EEG/EMG recordings, we injected CNO ($n = 8$) or saline ($n = 6$) into *Gad67-Cre* mice expressing hM3Dq at 21:00, sacrificed and fixed them at 23:00. Hypothalamic slices of these mice were examined by double staining with anti-Fos and anti-Gad65/67 antibodies to assess the activity of POA neurons (**Figure 1C**).

We observed an approximately 2.5-fold increase in Fos-positive GABAergic neurons in the whole POA of the CNO-injected group as compared with the vehicle-injected group (29.7 ± 3.7% vs. 76.6 ± 4.3%, $p < 0.001$) (**Figure 1C**). These observations demonstrate that the DREADD system used in this study appropriately stimulates the activity of POA neurons.

EEG/EMG analyses found that the percent of wakefulness during 3 h after CNO administration was significantly shorter (128.3 ± 3.3min vs. 112.7 ± 4.1 min, $p = 0.006$), while NREM time was longer in CNO-treated conditions than in saline-injected control conditions in the dark period (49.9 ± 3.0 min vs. 65.1 ± 3.1 min, $p = 0.004$) (**Figure 2A**). A significant increase of NREM sleep was also observed for 3 h after administration in the light period (13:00). We observed an increase in NREM episode duration when CNO was administered in the light period (**Figure 2B**). Although we also observed similar tendency when CNO was administered in the dark period, the difference was not statistically significant. The power density of EEG of each episode in the CNO-administered group in the dark period showed no difference from that in the vehicle-administered group (**Figure 2C**).

These results suggest that, consistent with previous non-specific electrical and chemical stimulation studies of the POA, specific stimulation of POA GABAergic neurons results in a decrease of wakefulness time, accompanied by increased NREM sleep time. We did not observe a significant difference in REM sleep time between the CNO-injected and control groups (**Figure 2A**).

We next examined the effect of stimulation of POA GABAergic neurons on orexin neuronal activity by Fos-immunostaining. After CNO or saline was injected at 21:00, the brains were fixed

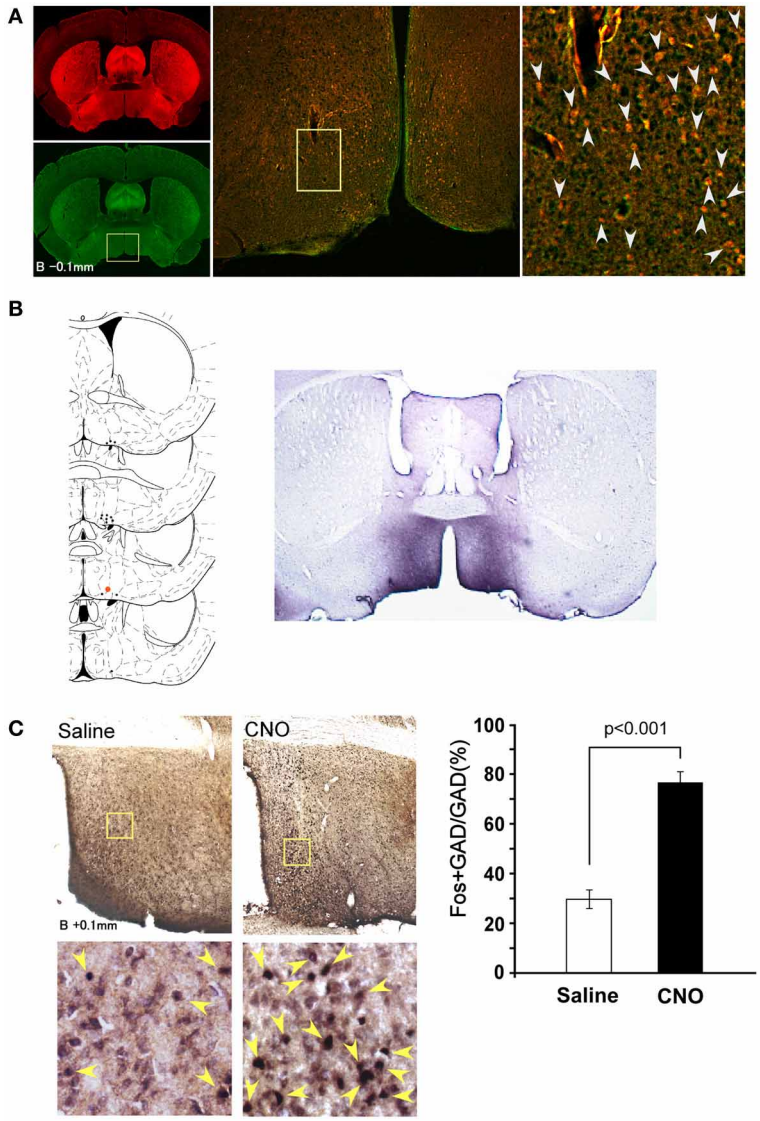

FIGURE 1 | Selective pharmacogenetic stimulation of POA neurons. (A) Gad67-Cre mice were crossed with Rosa26-tdTomato reporter mice (see method) to confirm GABAergic neuron-specific expression of Cre recombinase. A representative image of the POA of the *Gad67-Cre; Rosa26-tdTomato* mice is shown (Bregma-0.1 mm). Left panels, upper, tdTomato fluorescence. Lower, same section stained with Gad65/67 anti-body. Middle panel, merged image of rectangular region in the left panel. Right panel: High power view of rectangular region in central panel. Arrowheads show the colocalization of tdTomato fluorescence and Gad65/67 immunoreactivity. **(B)** Left, Virus injection sites are shown by dots. Injection site for right panel image is shown by a red dot. Right, Representative image of HA-like immunoreactivity observed in POA region of Gad67-Cre mice injected with *AAV-DIO-HAhM3Dq* to express hM3Dq fused with HA tag. **(C)** Activation of POA neurons in Gad67-Cre mice expressing hM3Dq by CNO. Left panels, upper, representative images of double-immunostaining with anti-Fos and anti-Gad 65/67 in the POA region after administration of saline (left) or CNO (right) at 21:00. The brain was fixed at 23:00. Left panels, lower, high power view of the rectangular regions shown in upper panels. Arrowheads show the colocalization of Fos (nuclei) and Gad65/67 (cytoplasm). Right panel, Number of fos-immunoreactive GABAergic neurons in POA after treatment with saline or CNO ($N = 4$ and 4, respectively).

at 23:00, and subjected to double staining with anti-orexin and anti-Fos antibody. We observed decrease in number of double positive cells (45.1 ± 6.5% vs. 27.3 ± 5.3%) (**Figure 2D**), although it was unknown whether the inhibition was directly mediated by POA GABAergic neurons or rather resulted from increased amount of sleep, because orexin neuronal activity was shown to correlate with the amount of wakefulness (Estabrooke et al., 2001).

POA GABAergic NEURONS SEND INNERVATIONS TO REGIONS IMPLICATED IN THE REGULATION OF SLEEP/WAKEFULNESS STATES

We next examined whether POA GABAergic neurons directly innervate orexin neurons. We injected *AAV-DIO-hChR2(H134R)-EYFP* into the POA of *Gad67-Cre* mice, because ChR2 works well as an anterograde tracer (Harris et al., 2012). Because ChR2-eYFP is distributed in axons and dendrites, it is difficult to observe cell bodies of neurons that express

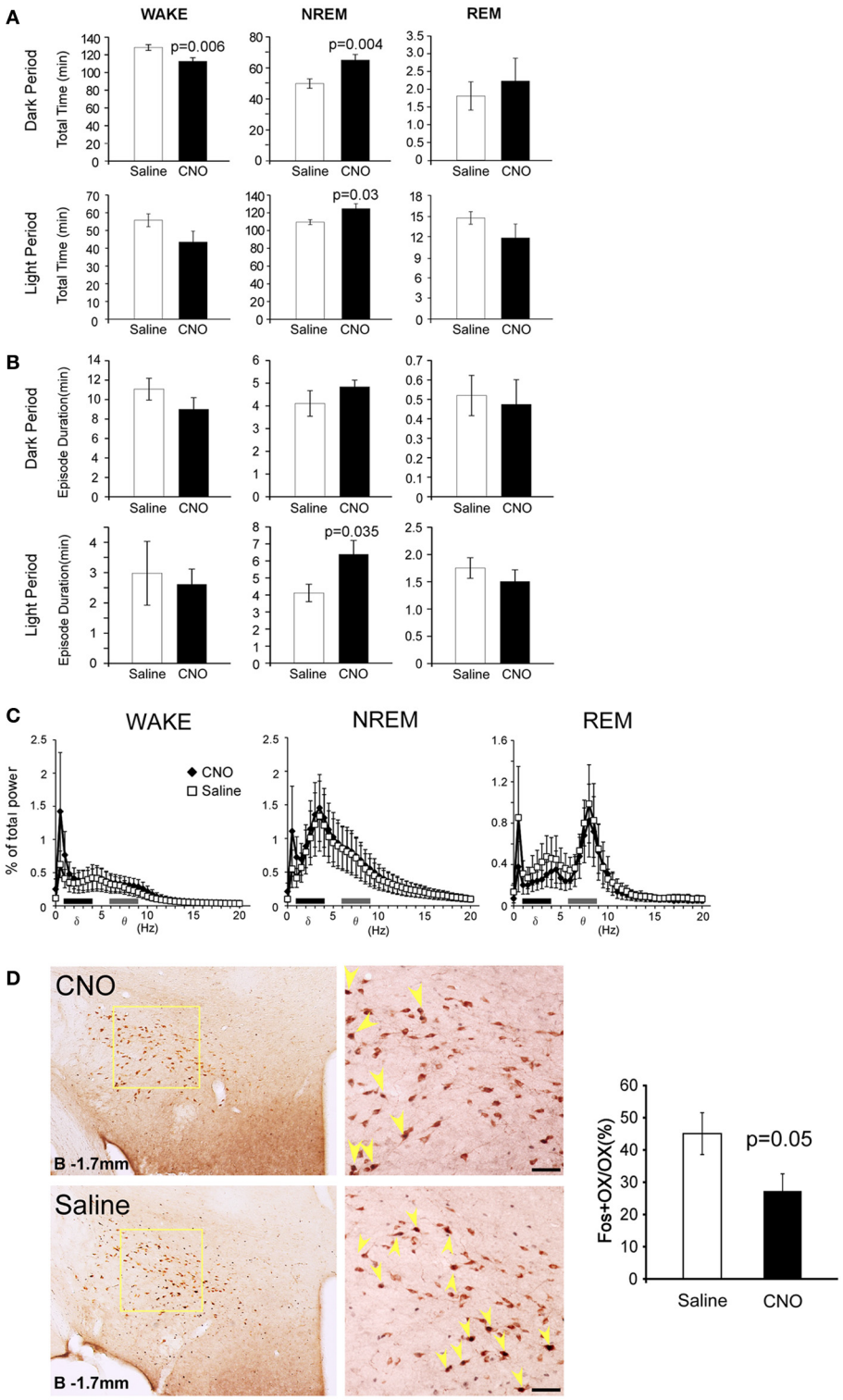

FIGURE 2 | Specific pharmacogenetic stimulation of GABAergic neurons in the POA increased NREM sleep amount. (A) Total time of wakefulness (WAKE), NREM sleep and REM sleep for 3 h after CNO (or saline) administration at 21:00 (upper panels, Saline $n = 14$, CNO $n = 13$) and at 13:00 (lower panels, Saline $n = 7$, CNO $n = 7$). **(B)** Episode duration of WAKE, NREM sleep, and REM sleep for 3 h after CNO (or saline) administration at 21:00 (upper panels, Saline $n = 14$, CNO $n = 13$) and at 13:00 (lower panels, Saline $n = 7$, CNO $n = 7$). **(C)** EEG power density of WAKE, NREM sleep and REM sleep in 1–2 h time window after the administration of CNO or saline at 21:00 (Saline $n = 14$, CNO $n = 13$). EEG power density is shown as the mean percentage of total EEG power ± s.e.m. **(D)** Representative images of fos expression in orexin neurons, as shown by double staining of the LHA of Gad67-Cre mice 2 h after injection of saline ($n = 5$) or CNO ($n = 8$) at 21:00. Scale bars, 50μm. Right panel, ratio of Fos-positive orexin neurons after injections of saline or CNO. Arrowheads show colocalization of Fos (nuclei) and orexin (cytoplasm).

ChR2-eYFP, we examined the expression pattern of *ChR2-eYFP* mRNA in the POA by double label *in situ* hybridization to detect the original cell bodies that expressed *ChR2-eYFP* mRNA and *Gad67* mRNA (**Figure 3A**). *ChR2-eYFP* mRNA-expressing cells were widely spread within the POA. Almost all these *ChR2-eYFP* mRNA-positive neurons also expressed *Gad67* mRNA. We injected the virus into 27 mice, and selected four mice in which *Gad67* mRNA expression was confirmed to be restricted within the POA.

Following the specific expression of ChR2 in GABAergic neurons in the POA of *Gad67-Cre* mice, we observed a network of ChR2-containing axons in the brain by immuostaining the YFP-positive fibers (**Figure 3B**, **Table 1**). We found abundant ChR2-eYFP-positive fibers in many of known arousal-related

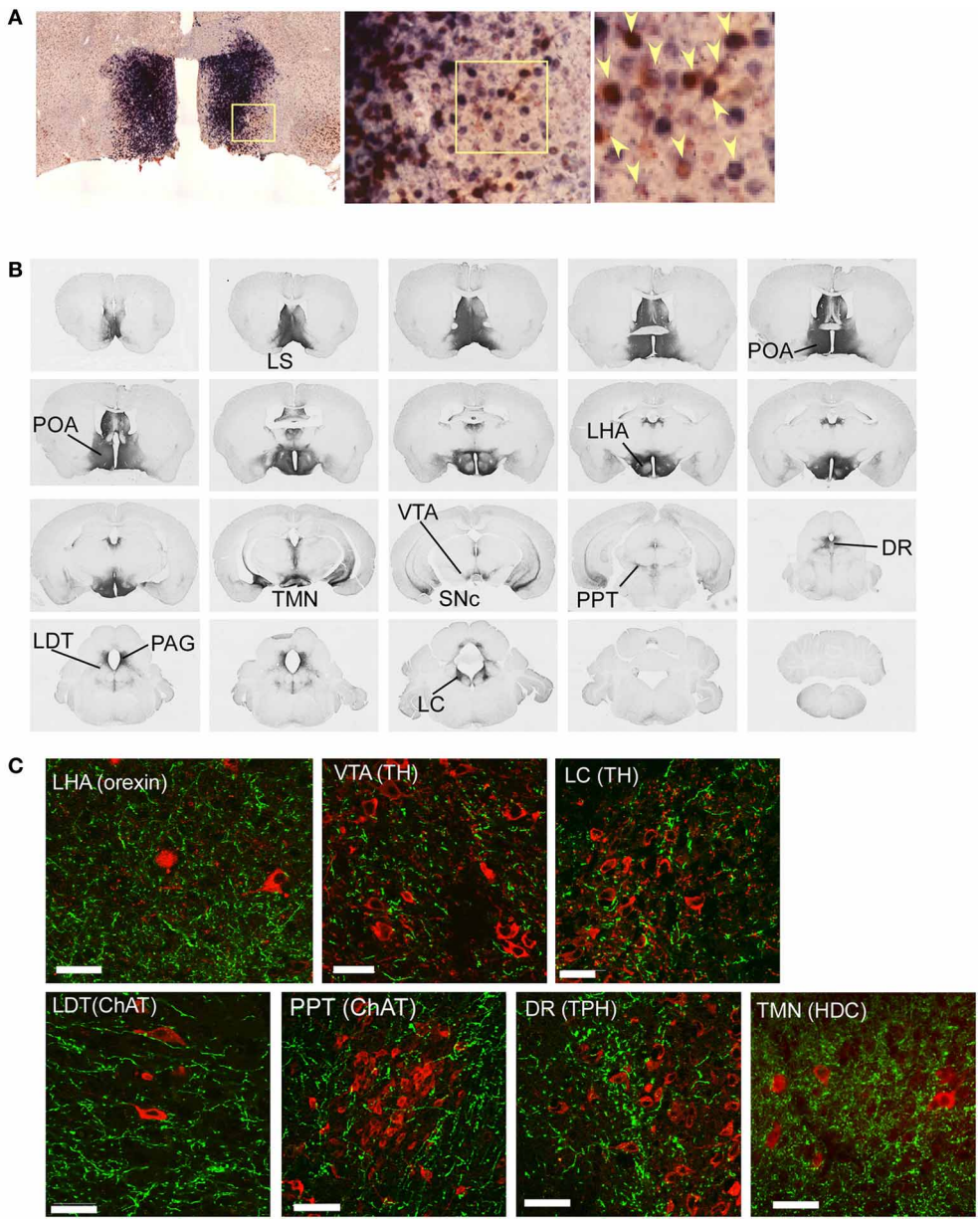

FIGURE 3 | Mapping of projection sites of the POA GABAergic neurons. (A) Expression of *ChR2-eYFP* mRNA (blue) and *Gad67* mRNA (red) in the POA of *Gad67-Cre* mice after bilateral injection of *AAV-DIO-hChR2(H134R)-eYFP* into the POA. Almost all (>95%, $n = 4$) *ChR2-eYFP* mRNA-positive neurons also expressed *Gad67* mRNA. Arrowheads show co-localization of *ChR2-eYFP* mRNA and *Gad67* mRNA. **(B)** After injection of *AAV-DIO-hChR2(H134R)-eYFP* into the POA of *Gad67-Cre* mice, the brain was subjected to histological analysis. Representative images show localization of ChR2-positive fibers from rostral to caudal in Gad67-Cre mouse brain coronal sections revealed by immunohistochemical staining using anti-GFP antiserum. **(C)** Images of single confocal planes showing ChR2-positive axonal fibers observed in the LHA, VTA, LC, LDT, PPT, DR, and TMN. Slices were stained with anti-GFP (green) and designated antibodies (red), including anti-orexin, anti-TH, anti-ChAT, anti-TPH and anti-HDC antibodies. Scale bars: 40 μm.

Table 1 | Projection sites of POA GABAergic neurons.

Cell group	Relative density
I. FOREBRAIN	
A. Isocortex	
I	±
II	±
III	±
IV	±
V	±
VI	±
Claustrum	++
Endoperiform nucleus	++
B. Hippocampal formation	
1. Entorhinal area	+
2. Subculum	+
3. CA1	+
4. CA2	+
5. CA3	+
6. Dentate	±
7. Induseum griseum	−
C. Amygdala	
1. Medial nucleus	++
2. Amygdalohippocampal area	−
3. N. lat. Olfactory tract	−
4. Anterior amygdaloid area	−
5. Central nucleus	−
6. Lateral nucleus	−
7. Basolateral nucleus	+
8. Basomedial nucleus	+
9. Intercalated nuclei	+
10. Cortical nucleus	+
D. Septum	
1. Lateral nucleus	+++
Dorsal part	+++
Intermediate part	+++
Ventral part	+++
2. Medial nucleus	+++
3. Bed n. stria terminalis	+++
Rosteromedial resion	+++
Rosterolateral resion	+++
Posterodorsal resion	+++
Posteroventral resion	+++
4.Septofimbrial nucleus	+++
5. Subfornical organ	+++
6. Bed n. anterior commissure	+++
E. Basal ganglia	
1. Caudoto putamen	−
2. Glabus pallidus	−
3. Substantia nigra, Conpact part	+++
4.Substancia nigra, reticular part	−
5. Subthalamic mucleus	++
F. Thalamus	
1. Medial habenula	+++
2. Lateral habenula	++
3. Anterior group	
Anteroentral n.	+++
Anteromedial n.	++
Anterodorsal n.	++
Interanterolmedial n.	−
Interamediodorsal n.	+
4. Mediodorsal nucleus	
Medial part	+++
Central part	+++
Lateral part	−
5. Lateral groupe	
Lateral dorsal n.	−
Lateral posterior n.	−
6. Midline group	
Paraventricular n.	+++
Paratenial n.	+
Central medial n.	+++
Centrolateral n.	−
Rhomboid n.	−
N. reuniens	−
7. Posterior complex	+
8. Medial geniculate n.	−
9. Lateral geniculate n.	−
10. Intralaminar nuclei	−
11. Reticular nucleus	−
12. Zona incerta	+
13. N.firlds of Forei	±
G. Hypothalamus	
1. Periventricular zone	+++
Median preoptic n.	+++
Anteroventral periventricular n.	+++
Preoptic periventricular nucleus	+++
Suprachiasmatic n.	+++
Supraoptic nucleus	+++
Paraventricular n.	+++
Parvicellular part, post	+++
Magnocellular part	+++
Periventricular nucleus	+++
Arcuate nucleus	+++
Posterior periventricular n.	++
2. Medial zone	
Medial preoptic area	+++
Medial preoptic n.	+++
Anterior hypothalamic n.	+++
Retrochiasmatic area	+++
Ventromedial n.	+++
Dorsomedial n.	+++
Tuberomammillary n.	+++
Supramammillary n.	+++
Lateral mammillary n.	+++
Medial mammillary n.	+++
3. Lateral zone	

(Continued)

Table 1 | Continued

Cell group	Relative density
Lateral preoptic area	+++
Lateral hypothalamic area	+++
Posterior hypothalamic area	+++
II. BRAIN STEM	
A. Sensory	
1. Visual	
Superior colliculus	–
Parabigeminal n.	–
Pretectal resion	
Olivary n.	–
N. optic tract	–
Anterior n.	–
Posterior n.	–
Medial pretectal area	–
N. posterior commissure	–
2. Somatosensory	
Mesencephalic n. (5)	+
Principal sensory, n. (5)	–
Spinal n.	–
Gracile n., dorsal	–
3. Auditory	
Cochlear nuclei	
Dorsal	–
Ventral	–
N. trapezoid body	±
Superior olive	+
N. lateral lemniscus	–
Inferior colliculus	–
Exterminal	–
Dorsal	–
Central	–
N. brachium inf. Coll.	–
4. Vestibular	–
5. Visceral	
N. solitary tract	–
Area postrema	–
Parabranchial n.	
Lateral	+
Medial	+
B. Motor	
1. Eye	
Oculomotor(3)	+
Edinger-westphal nucleus	++
Trochlear(4)	+
Abducens(6)	–
2. Jaw	
Motor n. (5)	–
3. Face	
Facial n. (7)	±
4. Pharynx/larynx	
N. ambiguus	–
5. Tongue	
Hypoglossal. n.(12)	–
6. Viscera	
Dorsal motor n. (10)	+
C. Reticular core (including central gray and raphe)	
1. Periaqueductal gray-assoc. w/PAG	
Interstitial n. of cajal	–
Dorsal tegmental n.	–
Laterodorsal teg. N.	+++
Barrington's n.	+++
Locus coeruleus	+++
2. Raphe	
Interfascicular n.	+++
Rostral linear n.	+++
Dorsal raphe	+++
Median raphe	+++
N. raphe pontis	+++
N. raphe magnus	+++
N. raphe pallidus	+++
3. Interpeduncular n.	
Rostral subnucleus	±
Apical subnucleus	±
Dorsomedial subnucleus	–
Lateral subnucleus	±
Intermediate subnucleus	+
Central subnucleus	+
4. Reticular formation	
Central teg. field	+
Peripeduncular n.	–
Pedunculopontine n.	++
Cuneiform n.	++
Pontine reticular	+
Parvocellular ret. Firld	+
Gigantocellular ret.	+
Lat. paragigantocellular	+
Intermediate ret. field	–
Paramedian reticular n.	–
D. Pre- and postzerebellar	
1. Pontine gray	–
2. Tegmental reticular n.	–
3. Lateral reticular n.	–
4. Red nucleus	–
5. N.Roller	–
6. Prepositus hypoglossal nucleus	–
III. CEREBELLUM	
1. Flocculus	–
2. Other parts	–

We attempt to grade the density of fiber-like structures in the sections into five categories according to Nambu et al. (1999); dense (+++); moderately dense (++); sparse (+); very sparse (–).

regions in the hypothalamus and brain stem, including the LHA, ventral tegmental area (VTA), substantia nigra pars compacta (SNc), TMN, LC, and LDT (**Figure 3B**). The projecting fibers seemed to avoid the main part of the dorsal raphe (DR), and density of the fibers in the PPT was sparser than other arousal-related regions, although we found considerable numbers of YFP-positive fibers in these regions (**Figure 3C**). Double staining studies suggested that these fibers made apposition to LC noradrenergic neurons, PPT cholinergic neurons, DR serotonergic neurons and TMN histaminergic neurons (**Figure 3C**). When we infected *AAV-DIO-hChR2(H134R)-EYFP* into the POA unilaterally, most of (>95%) the axonal projections were found in the ipsilateral side (not shown).

We found prominent projections to the LHA (**Figures 3B,C**), in which orexin neurons are localized. Double staining of LHA slices with anti-GFP and anti-orexin antibodies showed that most orexin neurons in the LHA were densely surrounded by rich ChR2-eYFP fibers (**Figure 3C**). This suggests that POA GABAergic neurons send innervations to orexin neurons in the LHA.

DETECTING SPIKE-MEDIATED GABA RELEASE FROM AXONS OF POA NEURONS ONTO OREXIN NEURONS

To test if stimulation of these axons modulates activity of orexin neurons, we performed whole-cell patch-clamp recordings from orexin neurons during optical stimulation of ChR2-eYFP-containing axons. To make identification of orexin neurons easy, we expressed tdTomato specifically in orexin neurons by AAV-mediated gene transfer (*AAV-horexin-tdTomato*). We used the human *prepro-orexin* promoter (Sakurai et al., 1999) to express tdTomato specifically in orexin neurons (**Figure 4A**). Immunolabeling confirmed that virtually all (>97%, $n = 3$) tdTomato-expressing neurons also contained detectable orexin-like immunoreactivity, suggesting highly specific expression of tdTomato in orexin neurons after injection of AAV (**Figure 4B**), although there were many orexin neurons that were negative for tdTomato fluorescence, suggesting incomplete penetrance of the virus-mediated expression.

To examine the connectivity between POA GABAergic neurons and orexin neurons, we simultaneously injected *AAV-DIO-hChR2(H134R)-EYFP* into the POA and *AAV-horexin-tdTomato* in the LHA of *Gad67-Cre* mice. 14 days after the injection, we prepared acute LHA slices and made patch clamp recordings from red fluoresced cell. We then stimulated axons with light emitting diode (LED) light of 470 nm in a 90-μm diameter window surrounding recorded orexin neurons. When orexin neurons were recorded under current-clamp with zero holding current, the light flashes slowed firing rate (**Figure 4C**). After recording for several minutes without stimuli, we applied 20-ms light stimuli (10 Hz). Since a previous study suggested the firing rates of sleep-active neurons in the POA ranged between about 5 and 20 Hz (Takahashi et al., 2009), we tried stimulation frequencies of 6, 10, and 20 Hz, and found that frequencies above 20 Hz evoked strong inhibition, but this lasted a very short time (for only about 2 s). Because 10 Hz stimulation caused strong and long-lasting inhibition of orexin neurons (data not shown), we used 10 Hz stimulation throughout this study. The inhibition of orexin neuron firing was completely abolished by a specific $GABA_A$ antagonist, bicuculline (**Figure 4C**).

Optical stimulation of ChR2-axons located near orexin neurons produced fast inhibitory post-synaptic currents (IPSCs) in these cells (**Figure 4D**). Orexin neurons from slices prepared from mice without ChR2 expression did not show any membrane responses to the same light flashes ($n = 10$, data not shown), confirming that without ChR2, our optical stimulation does not affect synaptic input to orexin neurons. In ChR2-expressing slices, the delay between flash onset and post-synaptic response was 3.4 ± 1.3 ms (**Figure 4E**). This short delay suggests that it is likely that GABAeric fibers extending from the POA directly inhibit orexin neurons. These observations show that GABAergic axons originating from POA neurons modulate orexin neurons via $GABA_A$ receptor-mediated synaptic transmission.

DISCUSSION

Extracellular recording studies have demonstrated cells in the POA that display elevated firing rates during sleep with attenuated firing during wakefulness (Findlay and Hayward, 1969; Kaitin, 1984). The discharge rate of these "sleep-active" neurons increased several seconds prior to NREM sleep onset as defined by EEG changes. These observations suggest that the POA plays an important role in the initiation and maintenance of sleep. Approximately 80% of sleep-active neurons in the VLPO also contain the neuropeptide galanin, which is highly colocalized with GABA in VLPO neurons (Sherin et al., 1998; Gaus et al., 2002). The number of Fos and GAD-double positive neurons in both the MnPN and the VLPO was shown to be positively correlated with the amount of preceding sleep (Gong et al., 2004).

These POA sleep-regulatory neurons were shown to be activated by adenosine through both direct and indirect actions. Adenosine caused A_1 receptor-mediated suppression of spontaneous IPSPs in rat VLPO neurons recorded *in vitro* (Chamberlin et al., 2003). Moreover, an adenosine A_{2A} receptor agonist evoked direct excitatory effects on a subset of rat VLPO neurons (Gallopin et al., 2005). Furthermore, perfusion of an A_{2A} agonist into the POA in rats promoted sleep (Satoh et al., 1999). These mechanisms have been thought to play an important role in homeostatic regulation of sleep through actions of adenosine.

A recent extracellular recording study suggested widespread distribution of sleep-active neurons within the whole POA (Takahashi et al., 2009), so it is necessary to genetically target the cell types being manipulated. In this study, we expressed hM3Dq or ChR2 broadly in GABAergic neurons in the POA. Firstly, we confirmed that specific stimulation of POA GABAergic neurons leads to an increase of NREM time (**Figure 2**). Sasaki et al. (2011) reported the same or even more NREM induction by hM4D-mediated inhibition of orexin neurons. This was unexpected, because the activation of POA GABA neurons should suppress more wake-active neurons widely throughout the brain. One possible reason why the effects were not so strong in this study is that we activated large numbers of GABAergic neurons in the POA. It is known that only limited number of GABAergic neurons in the POA would become active during sleep. However, in this study, larger numbers of the GABAergic neuorns in the POA, including GABAergic interneurons, might be activated.

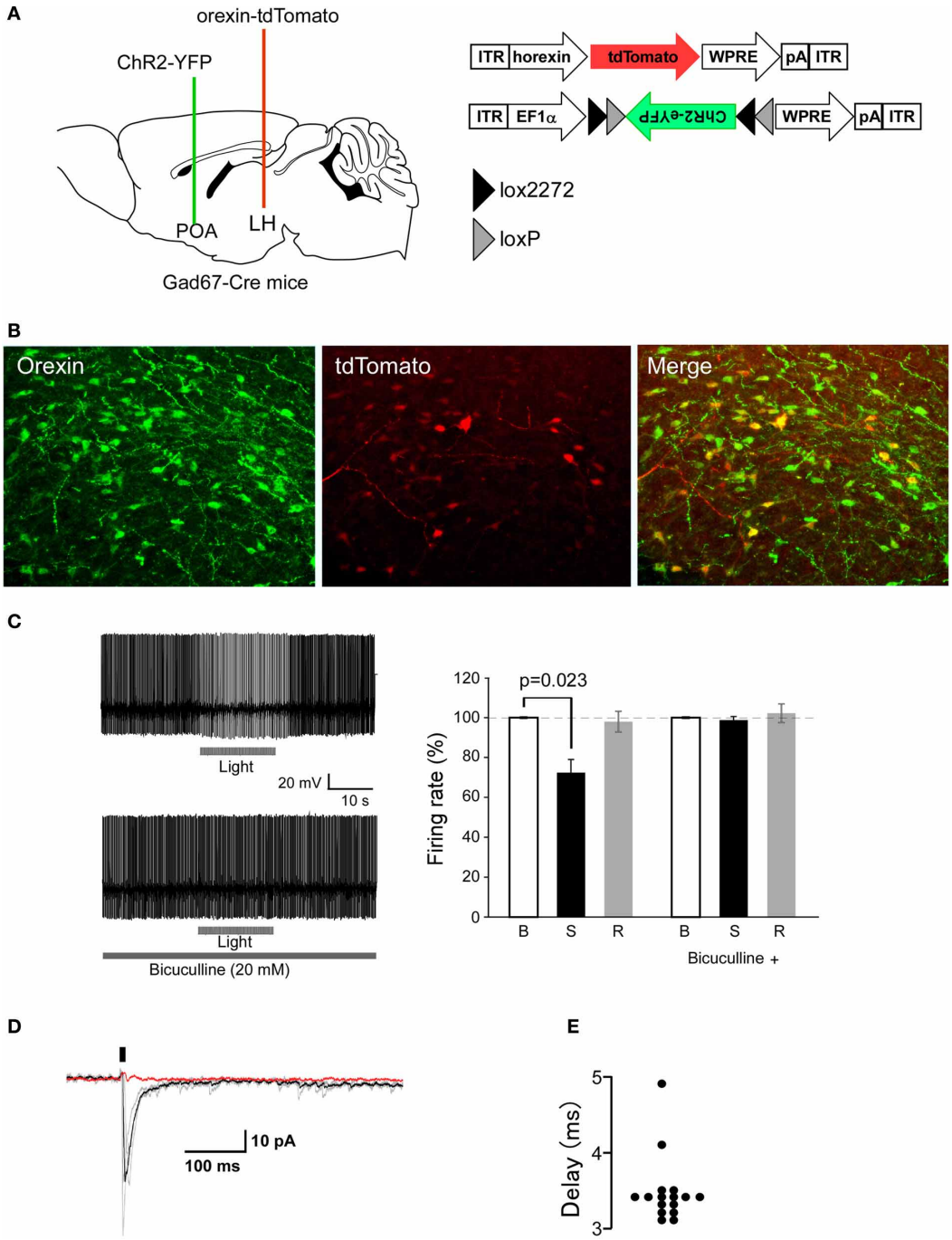

FIGURE 4 | Optogenetic stimulation of POA GABAergic axons rapidly decreases orexin neuron firing. (A) Strategy of this study. We simultaneously injected *AAV-horexin-tdTomato* into the LHA and *AAV-DIO-hChR2(H134R)-eYFP* into the POA. **(B)** Identification of orexin neurons in the LHA by expression of tdTomato in these neurons after injection of *AAV-horexin-tdTomato*. Left: Coronal section at bregma −2.1 mm showing distribution of orexin neurons stained by anti-orexin antiserum (green). Center: Cells with red fluorescence of tdTomato. Right: Merged image **(C)** Typical electrical current-clamp recording of orexin neuron. Left: Example of changes in firing of orexin neurons induced by optical stimulation in the absence (top trace) and presence (bottom trace) of bicuculline (20 μM). We observed similar responses in three out of eight cells. Right: Group data for response and recovery at 10 Hz stimulation, expressed at % change in firing before **(B)**, during (S) and after (R) light stimulation. **(D)** Optogenetically induced IPSCs in orexin neurons with and without bicuculline (20 μM). Holding potential was −60 mV. Black bar indicates light stimulus (5 ms, 1 Hz). Individual responses without bicuculline are shown in gray, average without bicuculline is in black, and average with bicuculline is in red. **(E)** Times after light-on to IPSPs onset are plotted for individual stimulations.

Some population of GABAerigic neurons might rather inhibit sleep-active neurons to counteract direct activation of these cells by CNO.

We also expressed ChR2-eYFP selectively in GABAergic neurons in the POA of *Gad67-Cre* mice. This allowed us to trace axonal fibers of these cells, and perform fast electrical control of action potential firing of these fibers with light (Petreanu et al., 2007). Firstly, we examined the pattern of axonal projections by staining eYFP with an anti-GFP antibody. This revealed that GABAergic neurons in the POA send projections to arousal-regulating regions in the brain stem, including the LC, DR, LDT/PPT, and TMN (**Figures 3B,C**, **Table 1**). Double immunofluorescence study further suggested that these axonal fibers make appositions to orexin neurons in the LHA as well as other arousal-related neurons including TH-positive, noradrenergic cells in the LC, serotonergic cells in the raphe nuclei, cholinergic cells in the LDT, and histaminergic cells in the TMN (**Figure 3C**).

We next examined the effect of optogenetic stimulation of ChR2-positive fibers around orexin neurons in the LHA (**Figure 4**). In the stimulation paradigms used here, blockade of $GABA_A$ receptors completely abolished the post-synaptic effect of GABAergic axon stimulation, suggesting that release of other transmitters, such as galanin, was not sufficient to alter orexin neuron firing.

Previous studies as well as our present findings suggest that POA GABAergic neurons send rich innervations to multiple brain regions, including monoaminergic/cholinergic nuclei in the brain stem, which fire at a rapid rate during wakefulness, slow down during NREM sleep, and cease firing during REM sleep, and are implicated in maintenance of wakefulness (**Figure 3B**). This means it is difficult to speculate on the relative contribution of the inhibitory action on orexin neuronal activity in increasing NREM sleep time. However, because specific pharmacogenetic or optogenetic inhibition of orexin neurons was shown to increase NREM sleep (Sasaki et al., 2011; Tsunematsu et al., 2011), it is possible to speculate that POA GABAergic neuron-mediated NREM sleep promotion might be at least partly through the inhibition of orexin neurons. Further studies, including optogenetic/pharmacogenetic activation/inhibition of POA GABAergic neurons *in vivo* in orexin-deficient animals, will be required to address this.

ACKNOWLEDGMENTS

This study was supported by the Cabinet Office, the Government of Japan through its "Funding Program for Next Generation World-Leading Researchers." The authors thank Dr. Wendy Gray for reading the manuscript. The authors thank Dr. Karl Deisseroth for providing *pAAV-double -floxed-hChR2(H134R)-EYFP-WPRE-pA*, Dr. Brian L. Roth for *pAAV-DIO-HAhM3Dq* and Dr. Masahiko Watanabe for providing anti-Gad65/67 antibody.

REFERENCES

Armbruster, B. N., Li, X., Pausch, M. H., Herlitze, S., and Roth, B. L. (2007). Evolving the lock to fit the key to create a family of G protein-coupled receptors potently activated by an inert ligand. *Proc. Natl. Acad. Sci. U.S.A.* 104, 5163–5168. doi: 10.1073/pnas.0700293104

Atasoy, D., Aponte, Y., Su, H. H., and Sternson, S. M. (2008). A FLEX switch targets Channelrhodopsin-2 to multiple cell types for imaging and long-range circuit mapping. *J. Neurosci.* 28, 7025–7030. doi: 10.1523/JNEUROSCI.1954-08.2008

Auricchio, A., Hildinger, M., O'connor, E., Gao, G. P., and Wilson, J. M. (2001). Isolation of highly infectious and pure adeno-associated virus type 2 vectors with a single-step gravity-flow column. *Hum. Gene Ther.* 12, 71–76. doi: 10.1089/104303401450988

Benedek, G., Obal, F., Jr., Lelkes, Z., and Obal, F. (1982). Thermal and chemical stimulations of the hypothalamic heat detectors: the effects of the EEG. *Acta Physiol. Acad. Sci. Hung.* 60, 27–35.

Bernstein, J. G., Garrity, P. A., and Boyden, E. S. (2012). Optogenetics and thermogenetics: technologies for controlling the activity of targeted cells within intact neural circuits. *Curr. Opin. Neurobiol.* 22, 61–71. doi: 10.1016/j.conb.2011.10.023

Boulant, J. A. (1981). Hypothalamic mechanisms in thermoregulation. *Fed. Proc.* 40, 2843–2850.

Chamberlin, N. L., Arrigoni, E., Chou, T. C., Scammell, T. E., Greene, R. W., and Saper, C. B. (2003). Effects of adenosine on gabaergic synaptic inputs to identified ventrolateral preoptic neurons. *Neuroscience* 119, 913–918. doi: 10.1016/S0306-4522(03)00246-X

Chemelli, R. M., Willie, J. T., Sinton, C. M., Elmquist, J. K., Scammell, T., Lee, C., et al. (1999). Narcolepsy in orexin knockout mice: molecular genetics of sleep regulation. *Cell* 98, 437–451. doi: 10.1016/S0092-8674(00)81973-X

Estabrooke, I. V., McCarthy, M. T., Ko, E., Chou, T. C., Chemelli, R. M., Yanagisawa, M., et al. (2001). Fos expression in orexin neurons varies with behavioral state. *J. Neurosci.* 21, 1656–1662.

Findlay, A. L., and Hayward, J. N. (1969). Spontaneous activity of single neurones in the hypothalamus of rabbits during sleep and waking. *J. Physiol.* 201, 237–258.

Gallopin, T., Fort, P., Eggermann, E., Cauli, B., Luppi, P. H., Rossier, J., et al. (2000). Identification of sleep-promoting neurons *in vitro*. *Nature* 404, 992–995. doi: 10.1038/35010109

Gallopin, T., Luppi, P. H., Cauli, B., Urade, Y., Rossier, J., Hayaishi, O., et al. (2005). The endogenous somnogen adenosine excites a subset of sleep-promoting neurons via A2A receptors in the ventrolateral preoptic nucleus. *Neuroscience* 134, 1377–1390. doi: 10.1016/j.neuroscience.2005.05.045

Gaus, S. E., Strecker, R. E., Tate, B. A., Parker, R. A., and Saper, C. B. (2002). Ventrolateral preoptic nucleus contains sleep-active, galaninergic neurons in multiple mammalian species. *Neuroscience* 115, 285–294. doi: 10.1016/S0306-4522(02)00308-1

Gong, H., McGinty, D., Guzman-Marin, R., Chew, K. T., Stewart, D., and Szymusiak, R. (2004). Activation of c-fos in GABAergic neurones in the preoptic area during sleep and in response to sleep deprivation. *J. Physiol.* 556, 935–946. doi: 10.1113/jphysiol.2003.056622

Gong, H., Szymusiak, R., King, J., Steininger, T., and McGinty, D. (2000). Sleep-related c-Fos protein expression in the preoptic hypothalamus: effects of ambient warming. *Am. J. Physiol. Regul. Integr. Comp. Physiol.* 279, R2079–R2088.

Hara, J., Beuckmann, C. T., Nambu, T., Willie, J. T., Chemelli, R. M., Sinton, C. M., et al. (2001). Genetic ablation of orexin neurons in mice results in narcolepsy, hypophagia, and obesity. *Neuron* 30, 345–354. doi: 10.1016/S0896-6273(01)00293-8

Harris, J. A., Wook Oh, S., and Zeng, H. (2012). Adeno-associated viral vectors for anterograde axonal tracing with fluorescent proteins in nontransgenic and cre driver mice. *Curr. Protoc. Neurosci.* Chapter 1, Unit 1.20 21–18. doi: 10.1002/0471142301.ns0120s59

John, J., and Kumar, V. M. (1998). Effect of NMDA lesion of the medial preoptic neurons on sleep and other functions. *Sleep* 21, 587–598.

Kaitin, K. I. (1984). Preoptic area unit activity during sleep and wakefulness in the cat. *Exp. Neurol.* 83, 347–357.

Koyama, Y., and Hayaishi, O. (1994). Firing of neurons in the preoptic/anterior hypothalamic areas in rat: its possible involvement in slow wave sleep and paradoxical sleep. *Neurosci. Res.* 19, 31–38. doi: 10.1016/0168-0102(94)90005-1

Kozorovitskiy, Y., Saunders, A., Johnson, C. A., Lowell, B. B., and Sabatini, B. L. (2012). Recurrent network activity drives striatal synaptogenesis. *Nature* 485, 646–650. doi: 10.1038/nature11052

Lin, L., Faraco, J., Li, R., Kadotani, H., Rogers, W., Lin, X., et al. (1999). The sleep disorder canine narcolepsy is caused by a mutation in the hypocretin (orexin) receptor 2 gene. *Cell* 98, 365–376. doi: 10.1016/S0092-8674(00)81965-0

Lu, J., Greco, M. A., Shiromani, P., and Saper, C. B. (2000). Effect of lesions of the ventrolateral preoptic nucleus on NREM and REM sleep. *J. Neurosci.* 20, 3830–3842.

McGinty, D., Alam, M. N., Szymusiak, R., Nakao, M., and Yamamoto, M. (2001). Hypothalamic sleep-promoting mechanisms: coupling to thermoregulation. *Arch. Ital. Biol.* 139, 63–75.

Mendelson, W. B., and Martin, J. V. (1992). Characterization of the hypnotic effects of triazolam microinjections into the medial preoptic area. *Life Sci.* 50, 1117–1128. doi: 10.1016/0024-3205(92)90349-T

Mieda, M., Williams, S. C., Richardson, J. A., Tanaka, K., and Yanagisawa, M. (2006). The dorsomedial hypothalamic nucleus as a putative food-entrainable circadian pacemaker. *Proc. Natl. Acad. Sci. U.S.A.* 103, 12150–12155. doi: 10.1073/pnas.0604189103

Moriguchi, T., Sakurai, T., Takahashi, S., Goto, K., and Yamamoto, M. (2002). The human prepro-orexin gene regulatory region that activates gene expression in the lateral region and represses it in the medial regions of the hypothalamus. *J. Biol. Chem.* 277, 16985–16992. doi: 10.1074/jbc.M107962200

Nambu, T., Sakurai, T., Mizukami, K., Hosoya, Y., Yanagisawa, M., and Goto, K. (1999). Distribution of orexin neurons in the adult rat brain. *Brain Res.* 827, 243–260. doi: 10.1016/S0006-8993(99)01336-0

Petreanu, L., Huber, D., Sobczyk, A., and Svoboda, K. (2007). Channelrhodopsin-2-assisted circuit mapping of long-range callosal projections. *Nat. Neurosci.* 10, 663–668. doi: 10.1038/nn1891

Peyron, C., Faraco, J., Rogers, W., Ripley, B., Overeem, S., Charnay, Y., et al. (2000). A mutation in a case of early onset narcolepsy and a generalized absence of hypocretin peptides in human narcoleptic brains. *Nat. Med.* 6, 991–997. doi: 10.1038/79690

Sakurai, T. (2007). The neural circuit of orexin (hypocretin): maintaining sleep and wakefulness. *Nat. Rev. Neurosci.* 8, 171–181. doi: 10.1038/nrn2092

Sakurai, T., Moriguchi, T., Furuya, K., Kajiwara, N., Nakamura, T., Yanagisawa, M., et al. (1999). Structure and function of human prepro-orexin gene. *J. Biol. Chem.* 274, 17771–17776. doi: 10.1074/jbc.274.25.17771

Sakurai, T., Nagata, R., Yamanaka, A., Kawamura, H., Tsujino, N., Muraki, Y., et al. (2005). Input of orexin/hypocretin neurons revealed by a genetically encoded tracer in mice. *Neuron* 46, 297–308. doi: 10.1016/j.neuron.2005.03.010

Saper, C. B., Chou, T. C., and Scammell, T. E. (2001). The sleep switch: hypothalamic control of sleep and wakefulness. *Trends Neurosci.* 24, 726–731. doi: 10.1016/S0166-2236(00)02002-6

Sasaki, K., Suzuki, M., Mieda, M., Tsujino, N., Roth, B., and Sakurai, T. (2011). Pharmacogenetic modulation of orexin neurons alters sleep/wakefulness states in mice. *PLoS ONE* 6:e20360. doi: 10.1371/journal.pone.0020360

Satoh, S., Matsumura, H., Koike, N., Tokunaga, Y., Maeda, T., and Hayaishi, O. (1999). Region-dependent difference in the sleep-promoting potency of an adenosine A2A receptor agonist. *Eur. J. Neurosci.* 11, 1587–1597. doi: 10.1046/j.1460-9568.1999.00569.x

Sherin, J. E., Elmquist, J. K., Torrealba, F., and Saper, C. B. (1998). Innervation of histaminergic tuberomammillary neurons by GABAergic and galaninergic neurons in the ventrolateral preoptic nucleus of the rat. *J. Neurosci.* 18, 4705–4721.

Sherin, J. E., Shiromani, P. J., McCarley, R. W., and Saper, C. B. (1996). Activation of ventrolateral preoptic neurons during sleep. *Science* 271, 216–219. doi: 10.1126/science.271.5246.216

Steininger, T. L., Gong, H., McGinty, D., and Szymusiak, R. (2001). Subregional organization of preoptic area/anterior hypothalamic projections to arousal-related monoaminergic cell groups. *J. Comp. Neurol.* 429, 638–653. doi: 10.1002/1096-9861(20010122)429:4<638::AID-CNE10>3.3.CO;2-P

Sterman, M. B., and Clemente, C. D. (1962). Forebrain inhibitory mechanisms: cortical synchronization induced by basal forebrain stimulation. *Exp. Neurol.* 6, 91–102. doi: 10.1016/0014-4886(62)90080-8

Takahashi, K., Lin, J. S., and Sakai, K. (2009). Characterization and mapping of sleep-waking specific neurons in the basal forebrain and preoptic hypothalamus in mice. *Neuroscience* 161, 269–292. doi: 10.1016/j.neuroscience.2009.02.075

Thannickal, T. C., Moore, R. Y., Nienhuis, R., Ramanathan, L., Gulyani, S., Aldrich, M., et al. (2000). Reduced number of hypocretin neurons in human narcolepsy. *Neuron* 27, 469–474. doi: 10.1016/S0896-6273(00)00058-1

Ticho, S. R., and Radulovacki, M. (1991). Role of adenosine in sleep and temperature regulation in the preoptic area of rats. *Pharmacol. Biochem. Behav.* 40, 33–40. doi: 10.1016/0091-3057(91)90317-U

Tsujino, N., Yamanaka, A., Ichiki, K., Muraki, Y., Kilduff, T. S., Yagami, K., et al. (2005). Cholecystokinin activates orexin/hypocretin neurons through the cholecystokinin A receptor. *J. Neurosci.* 25, 7459–7469. doi: 10.1523/JNEUROSCI.1193-05.2005

Tsunematsu, T., Kilduff, T. S., Boyden, E. S., Takahashi, S., Tominaga, M., and Yamanaka, A. (2011). Acute optogenetic silencing of orexin/hypocretin neurons induces slow-wave sleep in mice. *J. Neurosci.* 31, 10529–10539. doi: 10.1523/JNEUROSCI.0784-11.2011

Uchigashima, M., Fukaya, M., Watanabe, M., and Kamiya, H. (2007). Evidence against GABA release from glutamatergic mossy fiber terminals in the developing hippocampus. *J. Neurosci.* 27, 8088–8100. doi: 10.1523/JNEUROSCI.0702-07.2007

Uschakov, A., Gong, H., McGinty, D., and Szymusiak, R. (2007). Efferent projections from the median preoptic nucleus to sleep- and arousal-regulatory nuclei in the rat brain. *Neuroscience* 150, 104–120. doi: 10.1016/j.neuroscience.2007.05.055

Wu, S., Esumi, S., Watanabe, K., Chen, J., Nakamura, K. C., Nakamura, K., et al. (2011). Tangential migration and proliferation of intermediate progenitors of GABAergic neurons in the mouse telencephalon. *Development* 138, 2499–2509. doi: 10.1242/dev.063032

Yizhar, O., Fenno, L. E., Davidson, T. J., Mogri, M., and Deisseroth, K. (2011). Optogenetics in neural systems. *Neuron* 71, 9–34. doi: 10.1016/j.neuron.2011.06.004

Yoshida, K., McCormack, S., Espana, R. A., Crocker, A., and Scammell, T. E. (2006). Afferents to the orexin neurons of the rat brain. *J. Comp. Neurol.* 494, 845–861. doi: 10.1002/cne.20859

Conflict of Interest Statement: The authors declare that the research was conducted in the absence of any commercial or financial relationships that could be construed as a potential conflict of interest.

Received: 06 August 2013; accepted: 13 November 2013; published online: 02 December 2013.

Citation: Saito YC, Tsujino N, Hasegawa E, Akashi K, Abe M, Mieda M, Sakimura K and Sakurai T (2013) GABAergic neurons in the preoptic area send direct inhibitory projections to orexin neurons. Front. Neural Circuits ***7****:192. doi: 10.3389/fncir.2013.00192*

This article was submitted to the journal Frontiers in Neural Circuits.

frontiers in
NEURAL CIRCUITS

ORIGINAL RESEARCH ARTICLE
published: 11 October 2013
doi: 10.3389/fncir.2013.00164

Direction- and distance-dependent interareal connectivity of pyramidal cell subpopulations in the rat frontal cortex

Yoshifumi Ueta[1,2], Yasuharu Hirai[1,2†], Takeshi Otsuka[1,2,3] and Yasuo Kawaguchi[1,2,3]*

[1] *Division of Cerebral Circuitry, National Institute for Physiological Sciences, Okazaki, Japan*
[2] *Japan Science and Technology Agency, Core Research for Evolutional Science and Technology, Tokyo, Japan*
[3] *Department of Physiological Sciences, Graduate University for Advanced Studies (SOKENDAI), Okazaki, Japan*

Edited by:
Masanobu Kano, The University of Tokyo, Japan

Reviewed by:
Kathleen S. Rockland, Boston University School Medicine, USA
Fumitaka Kimura, Osaka University Graduate School of Medicine, Japan

****Correspondence:***
Yasuo Kawaguchi, Division of Cerebral Circuitry, National Institute for Physiological Sciences, 5-1 Higashiyama, Myodaiji, Okazaki, Aichi 444-8787, Japan
e-mail: yasuo@nips.ac.jp

†Present address:
Yasuharu Hirai, Department of Physiology and Neurobiology, Faculty of Medicine, Kyoto University, Kyoto, Japan

The frontal cortex plays an important role in the initiation and execution of movements via widespread projections to various cortical and subcortical areas. Layer 2/3 (L2/3) pyramidal cells in the frontal cortex send axons mainly to other ipsilateral/contralateral cortical areas. Subpopulations of layer 5 (L5) pyramidal cells that selectively project to the pontine nuclei or to the contralateral cortex [commissural (COM) cells] also target diverse and sometimes overlapping ipsilateral cortical areas. However, little is known about target area-dependent participation in ipsilateral corticocortical (iCC) connections by subclasses of L2/3 and L5 projection neurons. To better understand the functional hierarchy between cortical areas, we compared iCC connectivity between the secondary motor cortex (M2) and adjacent areas, such as the orbitofrontal and primary motor cortices, and distant non-frontal areas, such as the perirhinal and posterior parietal cortices. We particularly assessed the laminar distribution of iCC cells and fibers, and identified the subtypes of pyramidal cells participating in those projections. For connections between M2 and frontal areas, L2/3 and L5 cells in both areas contributed to reciprocal projections, which can be viewed as "bottom-up" or "top-down" on the basis of their differential targeting of cortical lamina. In connections between M2 and non-frontal areas, neurons participating in bottom-up and top-down projections were segregated into the different layers: bottom-up projections arose primarily from L2/3 cells, while top-down projections were dominated by L5 COM cells. These findings suggest that selective participation in iCC connections by pyramidal cell subtypes lead to directional connectivity between M2 and other cortical areas. Based on these findings, we propose a provisional unified framework of interareal hierarchy within the frontal cortex, and discuss the interaction of local circuits with long-range interareal connections.

Keywords: motor cortex, orbitofrontal cortex, posterior parietal cortex, perirhinal cortex, commissural, corticostriatal, corticopontine, corticothalamic

INTRODUCTION

Unlike cortical neurons in primary sensory areas, neurons in the frontal cortex can sustain persistent activity to encode specific information without external inputs, which may be supported by excitatory reverberation of (i) local recurrent connections among pyramidal cells; (ii) thalamocortical loops strongly influenced by the basal ganglia and cerebellum; and (iii) reciprocal interareal loops (Wang, 2001; Arnsten et al., 2012). Therefore, to understand the functional operation of the frontal cortex, it is crucial to reveal the formation rules for its corticocortical connections, as well as the relationships between pyramidal cells sending information to the thalamus, basal ganglia, and cerebellum, and those projecting to various cortical areas (Veinante and Deschênes, 2003).

The rat frontal cortex can be divided into three regions: the motor, orbitofrontal (OFC), and medial prefrontal cortices (Uylings et al., 2003; Gabbott et al., 2005; Hoover and Vertes, 2007). The motor cortex, which sends axons to the spinal cord, is further divided into the rostral secondary motor area (M2) and the caudal primary motor area (M1), which can be distinguished from M2 on the basis of lower stimulation thresholds for movement-evoking intracortical microstimulation and weaker immunolabeling for the neurofilament heavy chain (NF-H) (Brecht et al., 2004; Ueta et al., 2013). We have previously characterized two neuronal subtypes of M2 layer 5 (L5) pyramidal cells based on their long-distance axonal collateralizations to subcortical areas and their intracortical connectivity: corticopontine (CPn) cells that project to ipsilateral pontine nuclei and commissural (COM) cells that project to the contralateral cortex (Morishima and Kawaguchi, 2006; Otsuka and Kawaguchi, 2008, 2011; Morishima et al., 2011; Hirai et al., 2012; Ueta et al., 2013). Furthermore, we recently found that M2 projections preferentially innervate upper layer 1 (L1a), rather than lower L2/3 (layer 2/3) (L2/3b) of M1, whereas M1 efferents preferentially innervate L2/3b rather than L1a of M2 (Ueta et al., 2013). By analogy with the directionality of interareal connection demonstrated between visual cortices, this organization provides an anatomical basis for the "top-down" influence from M2 to M1 and the "bottom-up" influence from M1 to M2 (Coogan and Burkhalter, 1993; Dong et al., 2004).

Areas in the frontal cortex make reciprocal ipsilateral corticocortical (iCC) connections with multiple frontal cortical areas, as well as with distant non-frontal areas (Reep et al., 1990; Condé et al., 1995; Hoover and Vertes, 2007, 2011; Hira et al., 2013). In this study, we examine iCC organization in the fontal cortex and reveal the laminar distribution and subtype specificity of pyramidal cells involved in iCC connections between M2 and its target areas.

We demonstrate that the laminar pattern of iCC projections, and the relative participation of L5 CPn and COM cell subtypes among these projections, are specific to the pair of cortical areas involved as well as the direction of connectivity between the two areas. We outline a unified framework to understand the iCC connections of the frontal cortex with adjacent and distant areas that incorporates differences in top-down and bottom-up connectivity between areas.

MATERIALS AND METHODS

ANIMALS

Wistar rats (Charles River Laboratories Japan, Inc., Tsukuba, Japan) of either sex that were 19–23 days or 4–7 weeks old were used for physiological and histological experiments, respectively. Vesicular gamma-aminobutyric acid (GABA) transporter (VGAT)-Venus transgenic rats, which express the fluorescent protein Venus in GABAergic cells, were used to identify GABAergic cells (Uematsu et al., 2008). VGAT-Venus transgenic rats were generated by Drs. Y. Yanagawa, M. Hirabayashi, and Y. Kawaguchi at the National Institute for Physiological Sciences with pCS2-Venus that was provided by Dr. A. Miyawaki. VGAT-Venus rats are distributed by the National BioResource Project for the Rat in Japan[1]. All experiments were conducted in compliance with the guidelines of the Institutional Animal Care and Use Committee of the National Institutes of Natural Sciences.

IMMUNOHISTOCHEMICAL IDENTIFICATION OF THE LAMINAR STRUCTURE IN FRONTAL CORTEX

Wistar rats were deeply anesthetized with sodium pentobarbital [60 mg/kg, intraperitoneal (i.p.)] and perfused transcardially with a prefixative [250 mM sucrose and 5 mM $MgCl_2$ in 0.02 M phosphate-buffered (PB) saline, pH 7.4] followed by a fixative (4% paraformaldehyde and 0.2% picric acid in 0.1 M PB solution), and post-fixed within 30 min at room temperature. The brain was obliquely cut (Kawaguchi et al., 1989) into 20-μm sections using a vibratome (Leica Microsystems Inc., Buffalo Grove, IL, USA). Sections were incubated overnight at 4°C with a mouse monoclonal antibody against neuronal nuclei (NeuN; MAB377, EMD Millipore Corporation, Billerica, MA, USA; 1:5000) and a rabbit polyclonal antibody against calbindin D-28K (CB-38a, Swant, Marly, Switzerland; 1:2000) in 0.05 M Tris-buffered saline (TBS) containing 10% normal goat serum, 2% bovine serum albumin, and 0.5% Triton X-100. After washing in TBS, the sections were reacted with secondary antibodies conjugated to Alexa Fluor 488 (for NeuN; Life Technologies Corporation, Grand Island, NY, USA; 1:200) and Alexa Fluor 594 (for calbindin; Life Technologies Corporation; 1:200) for 2–3 h at room temperature. Adjacent sections were incubated overnight at 4°C with a guinea pig polyclonal antibody against vesicular glutamate transporter type 2 (VGluT2; AB2251, EMD Millipore Corporation; 1:5000) and a rat monoclonal antibody against chicken ovalbumin upstream promoter transcription factor-interacting protein 2 (Ctip2; ab18465, Abcam plc, Cambridge, UK; 1:500). After washing in TBS, the sections were reacted with secondary antibodies conjugated to Alexa Fluor 594 (for VGluT2) and Alexa Fluor 488 (for Ctip2). The sections were mounted on glass slides, coverslipped with Prolong gold antifade reagent (Life Technologies Corporation), and observed with epifluorescence.

GABAergic CELL IDENTIFICATION AMONG NeuN-POSITIVE CELLS

VGAT-Venus transgenic rats were deeply anesthetized with sodium pentobarbital and perfused transcardially with a prefixative, which was followed by a fixative (4% paraformaldehyde, 0.1% glutaraldehyde, and 0.2% picric acid in 0.1 M PB solution). After post-fixation lasting 2 h at room temperature or overnight at 4°C, the brain was obliquely cut into 8-μm sections on a cryostat (Leica Microsystems Inc.). Sections were incubated overnight at 4°C with a mouse monoclonal antibody against NeuN (1:3000), a chicken polyclonal antibody against GFP/Venus (ab13970, Abcam plc; 1:1000), a guinea pig polyclonal antibody against VGluT2 (1:1500), and a rabbit polyclonal antibody against calbindin D-28K (1:2000) in 0.05 M TBS containing 10% normal goat serum, 2% bovine serum albumin, and 0.2% Triton X-100. After washing in TBS, sections were reacted with secondary antibodies conjugated to Alexa Fluor 594 (for NeuN), Alexa Fluor 488 (for both Venus and VGluT2), and Alexa Fluor 350 (for calbindin) for 2–3 h at room temperature. It was possible to discriminate the staining patterns between Venus (somata) and VGluT2 (fibers) at the same fluorescence.

Ctip2-POSITIVE CELL IDENTIFICATION AMONG NON-GABAergic NEURONS IN L5

VGAT-Venus transgenic rats were deeply anesthetized with sodium pentobarbital and perfused with a prefixative, which was followed by a fixative (4% paraformaldehyde and 0.2% picric acid in 0.1 M PB solution). The brain was obliquely cut into 20-μm sections using a vibratome. Sections were incubated overnight at 4°C with a mouse monoclonal antibody against NeuN (1:1000), a chicken polyclonal antibody against GFP/Venus (1:1000), a guinea pig polyclonal antibody against VGluT2 (1:1500), and a rat monoclonal antibody against Ctip2 (1:500) in 0.05 M TBS containing 10% normal goat serum, 2% bovine serum albumin, and 0.2% Triton X-100. After washing in TBS, sections were reacted with secondary antibodies conjugated to biotin (for NeuN), Alexa Fluor 488 (for Venus), Alexa Fluor 488 (for VGluT2), and Alexa Fluor 594 (for Ctip2) for 2–3 h at room temperature. The NeuN signal was detected by further incubation with Alexa Fluor 350-conjugated streptavidin (Life Technologies Corporation; 1:200). Ctip2-positive and Ctip2-negative cells were counted among the Venus-negative and NeuN-positive cells separately in L5a and the upper and lower halves of L5b.

[1] http://www.anim.med.kyoto-u.ac.jp:80/nbr/default.aspx

RETROGRADE LABELING OF CPn CELL CLASSES

Animals were anesthetized with a mixture of ketamine (40 mg/kg, i.p.) and xylazine (4 mg/kg, i.p.) followed by an injection of glycerol (0.6 g/kg, i.p.) and dexamethasone (1 mg/kg, intramuscular) before being placed in a stereotaxic apparatus. Two tracers were used: Fast Blue (Dr. Illing GmbH and Co. KG, Groß-Umstadt, Hesse, Germany; 2% in distilled water) and Alexa Fluor 555-conjugated cholera toxin subunit B (CTB555; Life Technologies Corporation; 0.2% in distilled water). One or two fluorescent tracers with different excitations were injected into one or two target areas by pressure injection (PV820 Pneumatic PicoPump, World Precision Instruments, Inc., Sarasota, FL, USA) using glass pipettes (tip diameter, 50–100 μm; 100 nL in total).

Pontine nuclei were injected with Fast Blue (5.8–6 mm posterior to bregma, 0.8 mm lateral to the midline, 7.2–7.8 mm depth from the pial surface). The upper cervical cord was injected with Fast Blue or CTB555 (C1–2 segments). Ventral thalamic nuclei were injected with CTB555 (2–2.6 mm posterior to bregma, 1.4–2 mm lateral to the midline, and 5.4–5.8 mm from the surface). For superior colliculus injections, the cerebral cortex just above the superior colliculus was entirely removed by suction; CTB555 was applied vertically at two sites (6.5 mm posterior to bregma, 1.5 and 2 mm lateral to the midline, and 0.6, 0.8, and 1 mm from the surface of the superior colliculus). Because M2-derived anterogradely labeled fibers innervated intermediate and deep, but not superficial, zones of the superior colliculus (data not shown), the tracer was injected at a slightly deeper part of the superior colliculus. In each case, a total tracer volume of 100 nL was injected.

After a survival period of 4–6 days, the animals were deeply anesthetized with sodium pentobarbital and perfused transcardially with a prefixative, followed by a fixative (4% paraformaldehyde and 0.2% picric acid in 0.1 M PB solution). Using a vibratome, the frontal cortex was cut obliquely into 20-μm sections to observe labeled cells, and the brainstem was cut sagittally into 20- or 50-μm sections to confirm the injection sites. Every four serial cortical sections were collected as a set. In each set, the first or third section was used to count labeled cells. The others were used for the determination of cortical areas and layers.

RETROGRADE LABELING OF iCC CELLS

CTB555 was injected into M2, OFC, and the posterior parietal cortex (PPC) by pressure injection (PV820) using glass pipettes (tip diameter, 50–100 μm; 100 nL in total). After a survival period of 4–6 days, the animals were deeply anesthetized with sodium pentobarbital and perfused with a prefixative followed by a fixative (4% paraformaldehyde and 0.2% picric acid in 0.1 M PB solution). After post-fixation ranging from 2 h to overnight (or <30 min when combined with Ctip2 immunostaining), the brain was cut into 20-μm sections. Retrogradely labeled cells were examined in M2 (oblique or sagittal sections) from OFC and PPC, and in OFC (sagittal or coronal sections), PPC (sagittal or coronal sections), and the perirhinal cortex (PRC; coronal sections) from M2. Every four serial sections were collected as a set. The first or third section of each set was used to count labeled cells. The remaining sections were used for the determination of cortical areas and layers.

For area identification, immunostaining for NF-H and NeuN was used. Adjacent sections were incubated overnight at 4°C with a mouse monoclonal antibody against NF-H (N-200 antibody, N0142, Sigma-Aldrich Co. LLC, St. Louis, MO, USA; 1:1000) or a mouse monoclonal antibody against NeuN (1:5000) and a guinea pig polyclonal antibody against VGluT2 (1:5000). After washes with TBS, the sections were incubated with an Alexa Fluor-conjugated secondary antibody (1:200).

To visualize Ctip2 immunoreactivity in retrogradely labeled cells, sections were incubated overnight at 4°C with a rat monoclonal antibody against Ctip2 (1:500) in 0.05 M TBS containing 10% normal goat serum, 2% bovine serum albumin, and 0.5% Triton X-100. After washing in TBS, sections were reacted with an Alexa Fluor 488-conjugated secondary antibody (1:200).

Injection coordinates of M2 were 4–4.5 mm anterior to bregma and 1–2 mm lateral to the midline at four depths (0.2, 0.4, 0.6, and 0.8 mm from the surface, with 25° rostral inclination of pipettes). Injection areas of OFC (including lateral orbital and dorsolateral orbital areas) were 5 mm anterior to bregma, 2–3 mm lateral, and 2–3 mm deep (with a 25° rostral inclination of pipettes), and those for PPC were 3.5 mm posterior to bregma and 2–3 mm lateral at three depths (0.2, 0.4, and 0.6 mm from the surface).

In some cases of CTB555 injection into OFC or M1, Fast Blue was also injected into PRC to examine double-labeling of M2 cells projecting to PRC and those projecting to OFC or M1. The injection approach to the PRC area was described previously (Hirai et al., 2012). In brief, the injection pipette was advanced with a 30° lateral inclination using positions of blood vessels and the rhinal sulcus as a reference.

ANTEROGRADE LABELING OF CC FIBERS

Biotinylated dextran amine (10% w/v in 0.5 M potassium acetate; BDA-10K; Life Technologies Corporation) was injected into L1 to L5 of M2 by pressure injection from glass micropipettes (tip diameter, 50–100 μm). After a survival period of 7–10 days, the animals were deeply anesthetized with sodium pentobarbital and perfused with a prefixative followed by a fixative (4% paraformaldehyde and 0.2% picric acid in 0.1 M PB). The brain was cut into 50-μm coronal sections using a vibratome.

BDA-10K was visualized by incubating sections with avidin–biotin–peroxidase complex (1%; ABC Elite, Vector Laboratories, Inc., Burlingame, CA, USA) in 0.05 M TBS overnight at 4°C. To enhance the signal, sections were reacted for 30 min at room temperature with 2.5 μM biotinylated tyramine, 3 μg/mL glucose oxidase, and 2 mg/mL β-D-glucose in 2% bovine serum albumin, which was dissolved in 0.05 M Tris-buffered (TB) solution. Sections were subsequently incubated with Alexa Fluor 488-conjugated streptavidin (Life Technologies Corporation; 1:200) for 2–3 h at room temperature. Next, the same sections were incubated overnight at 4°C with a guinea pig polyclonal antibody against VGluT2 (1:5000) and a mouse monoclonal antibody against NeuN (1:5000). After washes with TBS, the sections were incubated with secondary antibodies conjugated to Alexa Fluor 594 (for VGluT2) and Alexa Fluor 350 (for NeuN) for 2–3 h at room temperature. For area identification, adjacent sections were incubated with N-200 antibody (1:1000).

To evaluate the laminar distribution of CC innervations from M2, RGB color images were collected using a DP73 microscope camera (Olympus Corporation, Tokyo, Japan), converted

to gray-scale, and analyzed with Image J software. The density of anterogradely labeled fibers was measured in L1 to L5 with a width of 0.1 mm in each target area of M2 to obtain the laminar distribution index, [(fiber density in L1) − (fiber density in L2/3)]/[(fiber density in L1) + (fiber density in L2/3)]. The laminar distributions of anterogradely labeled fibers from M2 were examined in OFC, M1, PRC 36, PPC, and contralateral M2.

IN VITRO ELECTROPHYSIOLOGICAL RECORDINGS OF RETROGRADELY LABELED CELLS

Rats (postnatal days 17–21) were anesthetized with a mixture of ketamine (40 mg/kg, i.p.) and xylazine (4 mg/kg, i.p.) and placed in a stereotaxic apparatus. For simultaneous labeling of COM cells and PRC-projecting cells, green fluorescent Retrobeads (Lumafluor, Inc., Durham, NC, USA) and CTB555 were injected into contralateral M2 and ipsilateral PRC, respectively. To label corticothalamic (CTh) cells, CTB555 was injected into the ipsilateral ventral thalamic nuclei. One or two days after tracer injection (postnatal days 19–23), animals were deeply anesthetized with isoflurane and decapitated. The brain was quickly removed and submerged in ice-cold physiological Ringer's solution. Six 300-μm-thick slices were obtained from M2 ipsilateral to the PRC or thalamic injection site. Slices were immersed in a buffered solution containing 125 mM NaCl, 2.5 mM KCl, 2 mM $CaCl_2$, 1 mM $MgCl_2$, 25 mM $NaHCO_3$, 1.25 mM NaH_2PO_4, 10 mM glucose, and 4 mM lactic acid. This solution was continuously bubbled with a mixture of 95% O_2 and 5% CO_2. Lactic acid was omitted during recordings. In some recordings from CTh cells (13/53 cells), glutamatergic synaptic transmission was blocked by supplemental application of 50 μM D-(−)-2-amino-5-phosphonopentanoic acid (D-AP5; R & D Systems, Inc., Minneapolis, MN, USA) and 20 μM 6-cyano-7-nitro-quinoxaline-2,3-dione (CNQX; Funakoshi, Tokyo, Japan), and $GABA_A$ receptors were blocked with 50 μM picrotoxin (Sigma-Aldrich Co. LLC). The recordings were made in whole-cell mode at 30–31°C. Labeled cells were identified using epifluorescence microscopy (BX50WI, Olympus Corporation) with a 40× water-immersion objective (numerical aperture = 0.8, Olympus Corporation).

The pipette solution for current-clamp recording consisted of 130 mM potassium methylsulfate, 0.5 mM EGTA, 2 mM $MgCl_2$, 2 mM Na_2ATP, 0.2 mM GTP, and 20 mM HEPES, with 0.75% biocytin. The pH of the solution was adjusted to 7.2 using KOH, and the osmolarity was 290 mOsm. The membrane potentials were not corrected for liquid junction potentials. The series resistance of the recording cells was <25 MΩ. The firing responses to depolarizing current pulses were recorded within 5 min from whole-cell break-in. Recordings were amplified with a Multiclamp 700B amplifier (Molecular Devices, LLC, Sunnyvale, CA, USA), digitized at 10 kHz using a Digidata 1440A apparatus (Molecular Devices, LLC), and collected with pClamp 10 software (Molecular Devices, LLC). Data were analyzed with IGOR Pro software (WaveMetrics, Inc., Lake Oswego, OR, USA), including NeuroMatic functions[2].

[2]http://www.neuromatic.thinkrandom.com

CORTICAL AREA IDENTIFICATION

To identify individual cortical areas and to confirm the injection localization to those areas, the following criteria were used.

Frontal areas

N-200 staining of L2/3 to upper L5 in M2 was weaker than that in M1 or that in OFC (Ueta et al., 2013). However, staining in M2 was stronger than that in the anterior cingulate area. Subdivisions of OFC were identified by cytoarchitecture and N-200 staining (Van De Werd and Uylings, 2008). M2 was intimately connected with the lateral part (weaker in N-200 staining) of the lateral orbital and dorsolateral orbital areas in OFC. These laminar structures were determined in a similar manner to M2.

PRC

The areal and laminar structures of area 36 (PRC 36) and area 35 (PRC 35) were identified by immunostaining for N-200 (stronger staining at superficial layers in PRC 36 than PRC 35; Hirai et al., 2012), VGluT2 [stronger staining at layer 4 (L4) or lower at L2/3 in PRC 36 than PRC 35], Ctip2 [positive cells distributed mainly in L5 and layer 6 (L6) of PRC 36, but also in L2/3 of PRC 35], or NeuN (L4 found in PRC 36, but not in PRC 35).

PPC

The PPC area is situated just caudal to the M1 hindlimb area, and rostral to both the secondary visual cortex and retrosplenial cortex. PPC demonstrated stronger NF-H staining than the adjacent caudal cortical areas. The border between L2/3 and L5 was determined by VGluT2 immunoreactivity (stronger in L2/3) and pan-neuronal staining. Localization of retrograde tracer deposition to PPC was confirmed by differences in retrograde labeling among thalamic nuclei: labeled cells were abundant in the LP nucleus after PPC injection, and abundant in the ventral anterior/ventromedial, ventrolateral, and posterior thalamic nuclei upon adjacent M1 injection (Reep et al., 1994). Thalamic nuclei were identified by calbindin expression pattern in addition to pan-neuronal staining, as reported previously (Ushimaru et al., 2012). Abbreviations used in this paper are summarized in **Table 1**.

QUANTITATIVE ANALYSIS OF AXON MORPHOLOGIES

Axon varicosities of biocytin-labeled L5 CTh and PRC-projecting cells (preparations obtained from Hirai et al., 2012) were measured with 100× objective combined with a further 1.25× magnification, using the Neurolucida system (MBF bioscience, Williston, VT, USA) and analyzed quantitatively with NeuroExplorer software (MBF bioscience) and IGOR Pro software. Axon varicosities were defined as darkly stained axonal dilations, typically about 1.5-fold wider than adjoining fibers. Serial images (0.5-μm step depth) of axon varicosities were acquired by the Neurolucida system, and were stacked into Adobe Photoshop software (Adobe Systems, Mountain View, CA, USA).

STATISTICS

Data are presented as the mean ± standard deviation (SD). Pairwise data on the proportion of Ctip2-positive cells among iCC cells were compared with the chi-square test. The ratio of Ctip2-positive and Ctip2-negative cells was compared to an even split (50%) in individual projections with a one-sample *t*-test. The

Table 1 | Abbreviations for brain areas, projection types, and firing types of pyramidal cells.

Abbreviations	Description
Cortical areas	
M1	Primary motor cortex
M2	Secondary motor cortex
OFC	Orbitofrontal cortex
Pir	Piriform cortex
PPC	Posterior parietal cortex
PRC	Perirhinal cortex
Te	Ventral temporal association cortex
Thalamic nuclei	
LP	Lateral posterior nucleus
Po	Posterior nucleus
VA	Ventral anterior nucleus
VL	Ventrolateral nucleus
VM	Ventromedial nucleus
Projection types	
CCS	Crossed corticostriatal
COM	Commissural
CPn	Corticopontine
CSp	Corticospinal
CTc	Corticotectal
CTh	Corticothalamic
CC	Corticocortical
iCC	Ipsilateral corticocortical
Firing types	
FA	Fast adapting
SA	Slow adapting
SA-d	Slow adapting with initial doublet

Mann–Whitney *U*-test was used for two-group comparisons. The difference of axon length and varicosity distributions within L1 and L2/3 was tested by Kolmogorov–Smirnov two-sample test. To assess the difference in anterogradely labeled fiber density between L1 and L2/3, a two-tailed one-sample *t*-test was used to compare the laminar distribution index to a no-difference value (index = 0). The Tukey–Kramer multiple comparisons test was used for statistical comparisons of the L1 sublaminar distribution patterns of anterogradely labeled fibers in OFC, M1, PRC 36, PPC, and contralateral M2. Significance was set at P values <0.05.

RESULTS

MULTIPLE PYRAMIDAL CELL SUBTYPES IN THE RAT FRONTAL CORTEX

The rat frontal cortical layers can be further divided into several sublayers by the size and density of neuronal somata, calbindin expression, thalamic fiber density, and Ctip2 expression (**Figure 1A**; Ueta et al., 2013). In all cortical layers below L1, about 80% of neurons were non-GABAergic, mostly pyramidal cells (**Figures 1B,C**). Among pyramidal cells, those in L5, which provide the major outputs of the cortex to subcortical and subcerebral areas, are highly differentiated in their physiological and morphological characteristics and intralaminar and interlaminar connectivities (Morishima and Kawaguchi, 2006; Hattox and Nelson, 2007; Otsuka and Kawaguchi, 2008, 2011; Brown and Hestrin, 2009; Morishima et al., 2011; Avesar and Gulledge, 2012; Hirai et al., 2012; Ueta et al., 2013).

L5 pyramidal cells consist primarily of Ctip2-positive CPn cells and Ctip2-negative COM cells (Arlotta et al., 2005; Ueta et al., 2013). The proportion of these two major subtypes in the M2 area changed according to depth within L5: both subtypes were abundant in L5a and upper L5b, but in lower L5b, Ctip2-positive cells predominated, suggesting that CPn cells are more prevalent in the lower half of L5b (**Figure 2A**). Furthermore, both CPn and COM cells comprise a variety of subtypes, as described below.

Corticopontine cells innervate additional subcortical and subcerebral targets, including the thalamus, superior colliculus, and spinal cord (**Figure 2B**), relating to their depth within L5. The distribution of corticospinal (CSp) cells is restricted to L5b, whereas CTh cells projecting to ventral thalamic nuclei in L5a are more abundant than those in L5b (Hirai et al., 2012; Ueta et al., 2013). L5b CTh cells send axons to the spinal cord (Ueta et al., 2013). Corticotectal (CTc) cells projecting to intermediate and deep zones of the superior colliculus were commonly found at the border between L5a and L5b, and L5b CTc cells also sent axons to the spinal cord (**Figure 2C**).

Similarly, COM cells are differentiated into two subtypes according to their projections to the striatum (Otsuka and Kawaguchi, 2011). One subtype (COM type I) projects to the contralateral cortex and ipsilateral striatum, while another subtype (COM type II) additionally projects to the contralateral striatum [crossed corticostriatal (CCS) cells; Wilson, 1987; Reiner et al., 2003; Morishima and Kawaguchi, 2006]. These results indicate that L5 of the rat frontal cortex contains multiple CPn and COM cell subtypes that differ in their long-distance axon collateralizations.

IMPLICATION FOR iCC CONNECTIONAL ORGANIZATION FROM THE M2 TO M1 PROJECTION PATTERN

We recently found that iCC projections to M1 preferentially originate from lower L2/3 (L2/3b) and L5a of M2 (**Figure 3**; Ueta et al., 2013). Both CPn cells and two subtypes of COM cells in L5a of M2 send axons to M1. L5a CTh cells in M2 innervate upper L1 (L1a) of M1 (Ueta et al., 2013), similar to their local projections to L1a within M2 (Hirai et al., 2012). Between visual cortical areas, L1 innervation is denser in the direction from higher to lower areas [called "feedback (top-down) connections"] than in the opposite direction ["feedforward (bottom-up) connections"; Coogan and Burkhalter, 1993; Dong et al., 2004]. Analogous to the visual system, we observed that the iCC projection from M2 to M1 forms a top-down type of anatomical connectivity (Ueta et al., 2013). This result gives rise to the hypothesis that the participation of certain pyramidal cell subtypes, especially those of L5, in reciprocal iCC connections correlates with the functional relationship between the two areas.

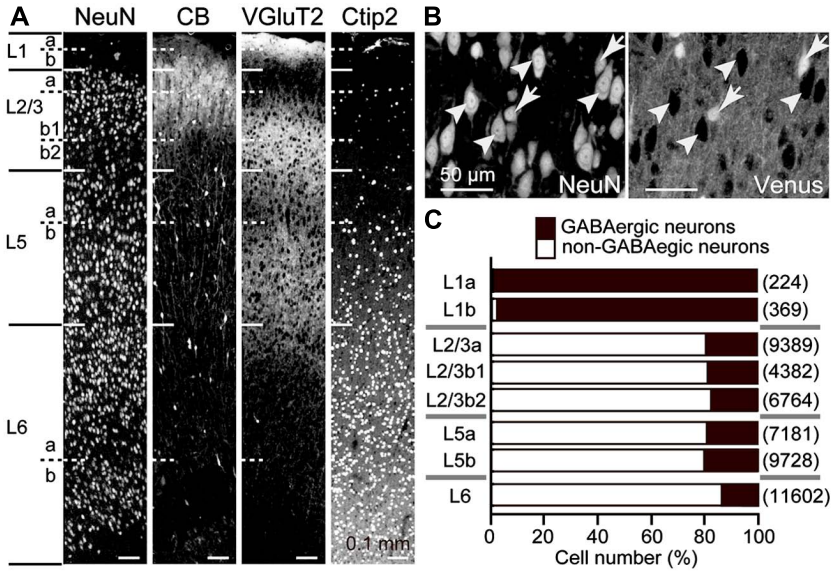

FIGURE 1 | GABAergic and non-GABAergic neuronal populations in M2 sublaminae. (A) Laminar identification of the M2 area by immunofluorescence for NeuN, calbindin (CB), VGluT2, and Ctip2. L1, L2/3, L5, and L6 were identified by cytoarchitecture. L1a demonstrates higher immunoreactivity for VGluT2 than L1b. L2/3a demonstrates weaker immunoreactivity for VGluT2 than L2/3b. L2/3b1 is immunopositive for CB, but L2/3b2 is not. L5 and L6 demonstrate higher immunoreactivity for Ctip2 than superficial layers. L5a demonstrates weaker immunoreactivity for VGluT2 and Ctip2 than L5b. L6a and L6b are divided by an intervening neuron-sparse zone. Oblique section, 20 μm thickness. **(B)** Identification of GABAergic and non-GABAergic neurons. Non-GABAergic neurons were identified by NeuN expression without Venus expression (arrowheads) in the M2 area of VGAT-Venus rats, which express fluorescent protein Venus in GABAergic neurons (arrows). Oblique section, 8 μm thickness. **(C)** The proportion of GABAergic and non-GABAergic neurons in each sublayer. Black bar, GABAergic neurons; white bar, non-GABAergic neurons. (*n*), total number of counted neurons.

M2 projects to various ipsilateral cortices, located proximally or distally. To develop a more generalized organization scheme of M2 iCC connectivity, we compared the iCC connections of M2 with a caudally situated adjacent frontal area (M1), a rostral adjacent area (OFC), a distant polysensory area (PPC), and distant declarative memory-related areas (PRC 36 and PRC 35) by investigating the laminar distributions of iCC cells in the source area, their innervations in the target area, and the composition of L5 pyramidal cell subtypes participating in these iCC projections.

LAMINAR DISTRIBUTIONS OF iCC CELLS IN RECIPROCAL CONNECTIONS OF M2 AND ADJACENT FRONTAL AREAS

We found that the laminar distributions of iCC cells projecting to adjacent frontal areas were more similar between M2 and OFC than between M2 and M1. Both M2 cells projecting to OFC and OFC cells projecting to M2 mainly originated from upper L2/3 and upper L5 (**Figure 4A**; three rats per analysis). By contrast, between M2 and M1, M1 iCC cells were distributed widely from L2/3a to L6b, whereas M2 iCC cells, mainly distributed from L2/3b and L5a, were more restricted in territory (Ueta et al., 2013).

LAMINAR DISTRIBUTIONS OF iCC CELLS CONNECTING M2 AND DISTANT NON-FRONTAL AREAS

We found that the laminar distributions of iCC cells connecting M2 and non-frontal distant areas were strongly related to the combination of source and target areas. PRC 36 cells projecting to M2 were observed in superficial layers (L2/3 and L4) and L6, but rarely in L5 (**Figure 4B**, middle; three rats), whereas M2 cells projecting to PRC 36 were distributed mainly in L5a (Hirai et al., 2012). By contrast, PRC 35 cells projecting to M2 were found exclusively, but in reduced numbers, in L5 (**Figure 4B**, right; three rats), whereas M2 cells projecting to PRC 35 were distributed mainly in L2/3a (Hirai et al., 2012). In PPC, M2-projecting cells were mainly located at the upper and bottom portions of L2/3 and deep L6 (**Figure 4C**, right). In M2, on the other hand, PPC-projecting cells were mainly localized to L5a (**Figure 4C**, middle) and situated in the medial part of M2 (data not shown).

Therefore, between M2 and the adjacent cortical areas, both L2/3 and L5 cells participate in both directions of reciprocal connections (**Figures 4D**, left; **4E**, left), whereas, between M2 and the distant areas, either L2/3 or L5 cells participate in one direction (**Figures 4D**, right; **4E**, right). Additionally, pyramidal cells in M2 L5a projected to all the adjacent and distant cortical areas assessed with the exception of PRC 35 (**Figure 4D**).

PARTICIPATION OF L5 PYRAMIDAL CELL SUBTYPES IN iCC PROJECTIONS IS RELATED TO BOTH THE SOURCE AND TARGET AREAS

Corticopontine and COM cell subtypes in L5 are distinguished by Ctip2 molecular expression (Arlotta et al., 2005; Ueta et al., 2013). We examined the Ctip2 expression pattern in individual iCC projections originating from L5 and found that ratios of Ctip2-positive CPn cells and Ctip2-negative COM cells systematically

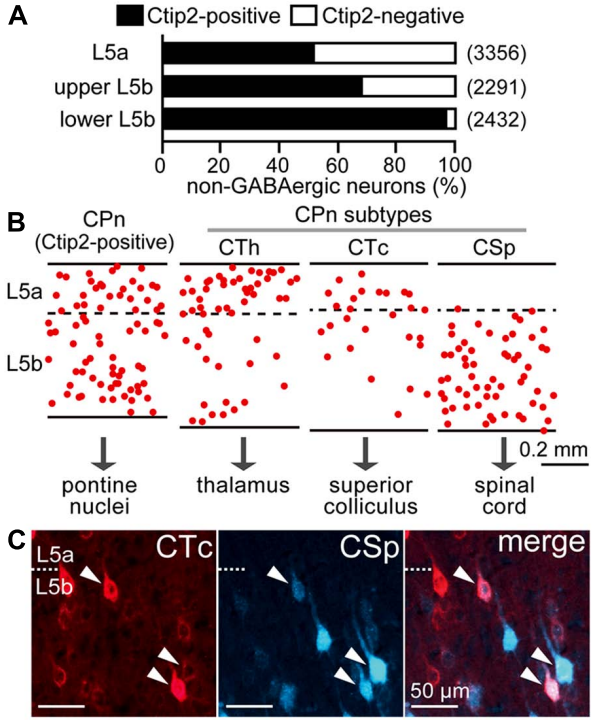

FIGURE 2 | Diversity of pyramidal cell subtypes dependent on L5 depth. (A) The proportions of Ctip2-positive and Ctip2-negative cells dependent on L5 depth. NeuN-positive and Venus-negative populations (corresponding to non-GABAergic neurons) were identified in the M2 area of VGAT-Venus rats. L5b was divided into upper and lower halves. Black bar, Ctip2-positive cells; white bar, Ctip2-negative cells. (*n*), total number of counted neurons. **(B)** Comparative laminar distributions of CPn cell subtypes in M2 L5: corticothalamic (CTh), corticotectal (CTc), and corticospinal (CSp) cells. CPn cells were retrogradely labeled by Fast Blue. Each dot corresponds to a single retrogradely labeled neuron. Oblique section, 20 μm thickness. **(C)** Most L5b CTc cells were also labeled from the spinal cord (arrowheads). CTc and CSp cells were labeled by CTB555 and Fast Blue in the same animal, respectively. Oblique section, 20 μm thickness.

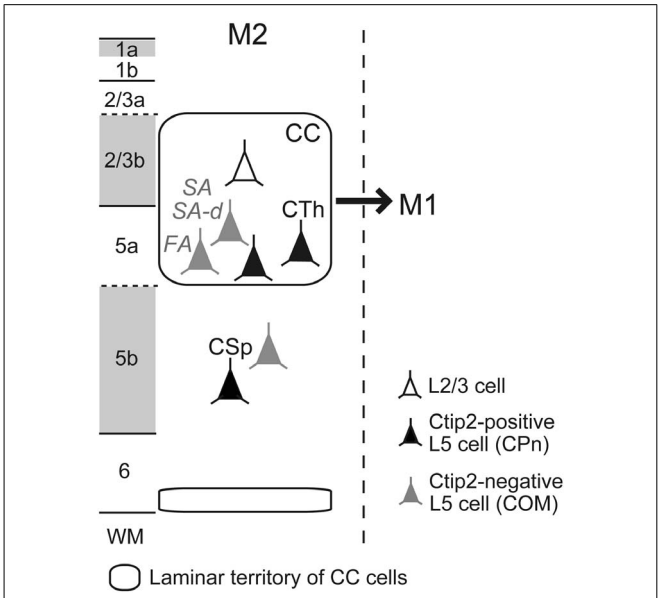

FIGURE 3 | Scheme of ipsilateral corticocortical (iCC) projections from M2 to M1. Multiple L5 CPn (filled-black) and COM (filled-gray) cell subtypes participate in iCC projection from M2 to M1. L1a, L2/3b, and L5b receive dense thalamocortical inputs, labeled by VGluT2 immunoreactivity (gray). FA, fast adapting; SA, slow adapting; SA-d, slow adapting with initial doublet firing; WM, white matter.

differed according to the iCC projection type. The fraction of Ctip2-positive cells in L5 was higher in connections in the direction from OFC to M2 (62.5% in L5; $n = 304$ cells, three rats) than in connections directed from M2 to OFC (**Figure 5A**; 28.4% in L5a; $n = 338$, three rats; $P < 0.01$, chi-square test). As reported previously, the fraction of Ctip2-positive cells in L5a was higher in connections in the direction from M2 to M1 (56.3% in L5a; $n = 679$, four rats) than in connections directed from M1 to M2 (**Figure 5B**; 33.8% in L5a; $n = 225$, three rats; $P < 0.01$, chi-square test; data from Ueta et al., 2013). We found that iCC projections to distant areas that originated from M2 L5a consisted mainly of Ctip2-negative cells (**Figure 5C**; Ctip2-positive cell ratio: M2 to PRC projection, 2.6%, $n = 823$, three rats; M2 to PPC projection, 10.4%, $n = 259$, three rats). Therefore, L5 CPn and COM cells in the source area, especially M2, participate differently in iCC projection based on the target area.

COM cells demonstrate heterogeneous firing patterns as assessed by depolarized somatic current injection: a slow adapting (SA) type, a SA type with an initial doublet firing (SA-d), and a fast adapting (FA) type (**Figure 5D**, whole COM; Otsuka and Kawaguchi, 2008). All three firing types were observed simultaneously among L5 COM cells projecting to M1 (**Figure 5D**, M1-projecting; Ueta et al., 2013), but those projecting to PPC demonstrated more FA-type firing, similar to CCS cells innervating both sides of striatum in addition to the contralateral cortex (**Figure 5D**, CCS and PPC-projecting; Otsuka and Kawaguchi, 2008, 2011). We further investigated the firing subtype composition of COM cells projecting to PRC.

We found that the L5a COM cell population projecting to PRC contained more FA-type cells (**Figure 5D**, PRC-projecting), whereas L5a CTh cells, a CPn subtype in L5a, demonstrated more SA- or SA-d-type cells. We divided retrogradely labeled L5a cells (32 cells simultaneously from PRC and the contralateral M2; 53 cells from the thalamus; 36 cells from contralateral M2 in rats without other injections) into three classes using two firing parameters obtained from interspike intervals (ISIs) during the current pulse injection (recorded with potassium methylsulfate solution; fixed amplitude, 0.5 nA; duration, 1 s): (1) the firing frequencies calculated from the first ISIs (f1) and (2) the ratio of firing frequencies calculated from the seventh and second ISIs (f7/f2; adaptation index). We classified cells with f7/f2 < 0.5 as FA type (81.3% of PRC-projecting COM cells; no FA-type CTh cells; 55.6% of L5a COM cells), cells with f7/f2 > 0.5 as SA type (18.8% of PRC-projecting COM cells; 9.4% of CTh cells; 33.3% of L5a COM cells), and SA cells with f1 > 80 Hz as SA-d type (no SA-d type PRC-projecting COM cells; 90.6% of CTh cells; 11.1% of L5a COM cells). Therefore, COM cell subtypes differentially participate in iCC projection depending on the target area.

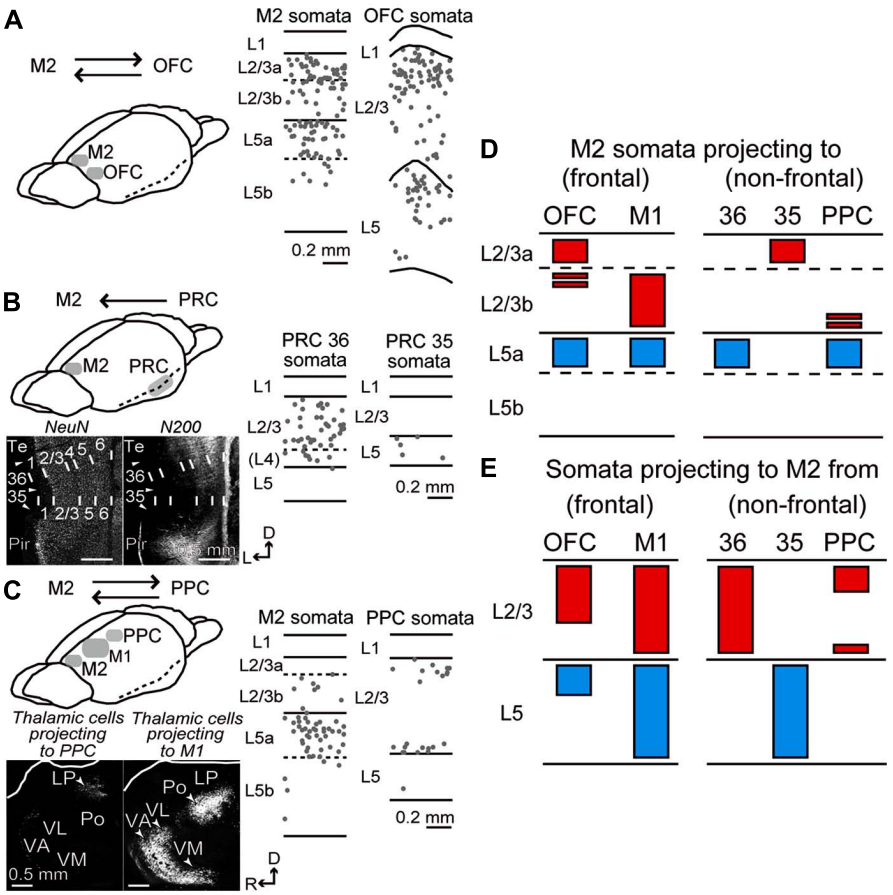

FIGURE 4 | Laminar distributions of iCC cells connecting M2 to OFC, PRC, and PPC. (A) iCC connections between M2 and OFC. Laminar distributions of M2 cells retrogradely labeled by CTB555 from OFC (middle), and OFC cells labeled from M2 (right). In OFC, CTB555 was injected into lateral orbital and dorsolateral orbital areas. iCC cells were mainly distributed in upper L2/3 and upper L5 in both areas. Each dot represents a single retrogradely labeled neuron. Sagittal section, 50 μm thickness. **(B)** iCC connections between M2 and PRC. Bottom left, PRC area identification by immunostaining for NeuN and NF-H (N-200 antibody). Note the N-200 staining differences in the superficial layers among cortical areas. Arrowhead, area border. 35, area 35 of PRC (PRC 35); 36, area 36 of PRC (PRC 36); pir, piriform cortex; Te, ventral temporal association cortex. D, dorsal; L, lateral. Coronal section, 50 μm thickness. Middle and right, laminar distributions of PRC 36 and PRC 35 cells retrogradely labeled by CTB555 from M2. Note iCC cells in L2/3 of PRC 36, but in L5 of PRC 35. **(C)** iCC connections between M2 and PPC. Bottom left, retrograde tracer injection into PPC-labeled thalamic cells in lateral posterior (LP) nucleus, while injection into the rostrally adjacent M1-labeled thalamic cells in ventral anterior/ventromedial (VA/VM), ventrolateral (VL), and posterior (Po) nuclei. Sagittal section, 50 μm thickness. Middle and right, laminar distributions of M2 cells retrogradely labeled by CTB555 from PPC, and PPC cells labeled by CTB555 from M2. PPC-projecting cells were mainly distributed in L5a of M2, whereas M2-projecting cells labeled the superficial and bottom parts of L2/3 of PPC. D, dorsal; R, rostral. **(D)** Laminar patterns of M2 somata projecting to the adjacent frontal areas (OFC and M1) and distant non-frontal areas (PRC 36, PRC 35, and PPC). Red, somata distribution in L2/3; blue, distribution in L5. Based on the present data combined with Hirai et al. (2012) (PRC) and Ueta et al. (2013) (M1). **(E)** Laminar patterns of somata projecting from the adjacent and distant areas to M2. Based on the present data combined with Ueta et al. (2013) (M1).

LAMINAR DISTRIBUTIONS OF FIBERS FROM M2 IN IPSILATERAL CORTICAL AREAS AND CONTRALATERAL M2

To characterize innervation patterns from M2 to target areas, we quantified the relative laminar density of axon fibers in individual areas. First, we confirmed correlation of axonal length and the frequency of their varicosities, most of which correspond to synaptic boutons (**Figures 6A,B**; Kisvárday et al., 1986; Gabbott et al., 1987). Previously we found that L5a CTh cells distribute axon collaterals in the upper part of L1 than PRC-projecting cells (**Figure 6C**; Hirai et al., 2012). Similar to the axon length distributions, we found that axon varicosities of CTh cell were found more in the upper part of L1, whereas those of PRC-projecting cell more in the lower part of L1 (**Figure 6D**). No differences were found between the distributions of axon lengths and varicosities along the depth in both subtypes (Kolmogorov–Smirnov two-sample test). The axon length of individual branches correlated linearly with the number of their axon varicosities in both subtypes (CTh cells, correlation coefficient $= 0.87 \pm 0.05$, six branches of two cells; PRC-projecting cells, correlation coefficient $= 0.83 \pm 0.29$, five branches of two cells).

Next, to examine innervation patterns of M2 in its iCC target areas, we injected the anterograde tracer BDA-10K in M2. We found that the laminar distribution pattern of labeled fibers differed among target areas of M2. To quantify innervation preference

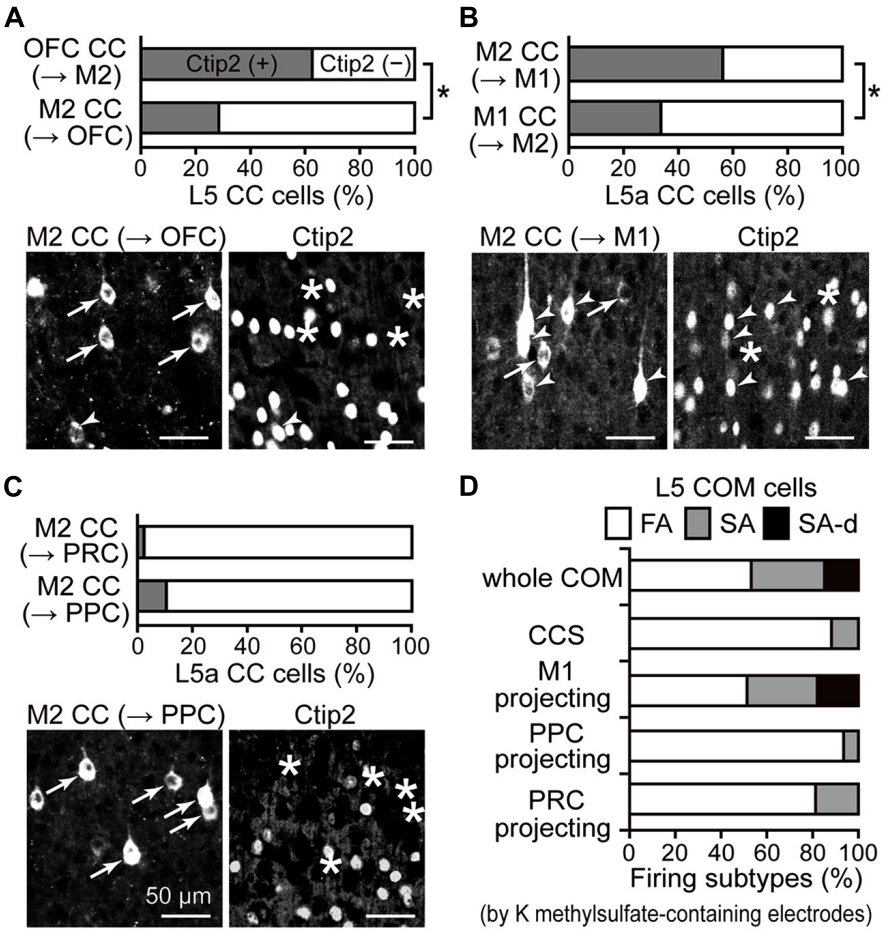

FIGURE 5 | iCC projection-specific participation of Ctip2-positive CPn cells. (A) Ctip2 expression in OFC upper L5 cells projecting to M2 and in M2 L5a cells projecting to OFC. Upper graph, the proportion of Ctip2-positive cells was higher among OFC cells projecting to M2 than M2 cells projecting in the opposite direction ($P < 0.01$, chi-square test). OFC cells projecting to M2 similarly contained Ctip2-positive and Ctip2-negative cells ($P = 0.29$, one-sample *t*-test), but M2 cells projecting to OFC contain more Ctip2-negative cells than Ctip2-positive cells ($P < 0.05$). Lower photograph, M2 cells projecting to OFC (left, labeled by CTB555), which contain cells positive for Ctip2 (arrowheads in left and right) and negative for Ctip2 (arrows in left, asterisks in right). **(B)** Ctip2 expression in M2 L5a cells projecting to M1 and in M1 L5a cells projecting to M2. Upper graph, the proportion of Ctip2-positive cells was higher among M2 cells projecting to M1 than M1 cells projecting in the opposite direction ($P < 0.01$, chi-square test). M2 cells projecting to M1 similarly contained Ctip2-positive and Ctip2-negative cells ($P = 0.68$, one-sample *t*-test), but M1 cells projecting to M2 contain more Ctip2-negative cells than Ctip2-positive cells ($P < 0.01$). Data taken from Ueta et al. (2013). Lower photograph, M2 cells projecting to M1, which contain cells positive for Ctip2 (arrowheads) and negative for Ctip2 (arrows in left, asterisks in right). **(C)** Ctip2 expression in M2 L5a cells projecting to PRC and to PPC. Upper graph, the proportion of Ctip2-positive cells among M2 L5a cells projecting to distant non-frontal areas. M2 L5a cells projecting to PRC and PPC both contain more Ctip2-negative cells than Ctip2-positive cells ($P < 0.01$, respectively, one-sample *t*-test), and demonstrate lower proportion of Ctip2-positive cells than M2 L5a cells projecting to frontal areas (OFC and M1; $P < 0.01$, chi-square test). Lower photograph, M2 cells projecting to PPC negative for Ctip2 (arrows in left, asterisks in right). **(D)** Proportion of firing subtypes among L5 COM cell subtypes in M2, identified by retrograde labeling. COM cells consist of all three firing types (53.1, 32, and 14.8% for FA, SA, and SA-d types; $n = 431$). CCS cells, a type of COM cell, consist mostly of FA-type cells, but contain no SA-d-type cells (88.2, 11.8, and 0% for FA, SA, and SA-d types; $n = 34$). Similar to the entire COM cell population, COM cells projecting to M1 consist of all three firing types (51.3, 30.8, and 17.9%, for FA, SA, and SA-d types; $n = 39$). By contrast, COM cells projecting to PPC (93.5, 6.5, and 0% for FA, SA, and SA-d types; $n = 31$) or to PRC (81.3, 18.8, and 0% for FA, SA, and SA-d types; $n = 32$), like CCS cells, consist mostly of FA-type cells and contain no SA-d-type cells. Data, except for COM cells projecting to PRC, are taken from Otsuka and Kawaguchi (2008, 2011) and Ueta et al. (2013).

for L1 or L2/3 of target areas, we normalized the fiber density to the maximum value (max = 1) in each section and obtained a laminar distribution index from +1 (totally L1) to −1 (totally L2/3), with 0 indicating no difference between L1 and L2/3 (see Materials and Methods). To examine the innervation preference within L1, we divided L1 into four parts (upper and lower halves of L1a and L1b, respectively) and compared the density across L1 subdivisions.

Labeled fibers in OFC were similarly distributed in L1 and L2/3 (**Figure 7A**, left; laminar distribution index, 0.02 ± 0.05, four rats) and localized uniformly within L1 (**Figure 7A**, right; fiber density, 0.37 ± 0.12 in upper L1a, 0.42 ± 0.1 in lower L1a, 0.4 ± 0.09 in upper L1b, and 0.41 ± 0.12 in lower L1b). As reported previously, labeled fibers in M1 were more abundant in L1 than in L2/3 (**Figure 7B**, left; data from Ueta et al., 2013; laminar

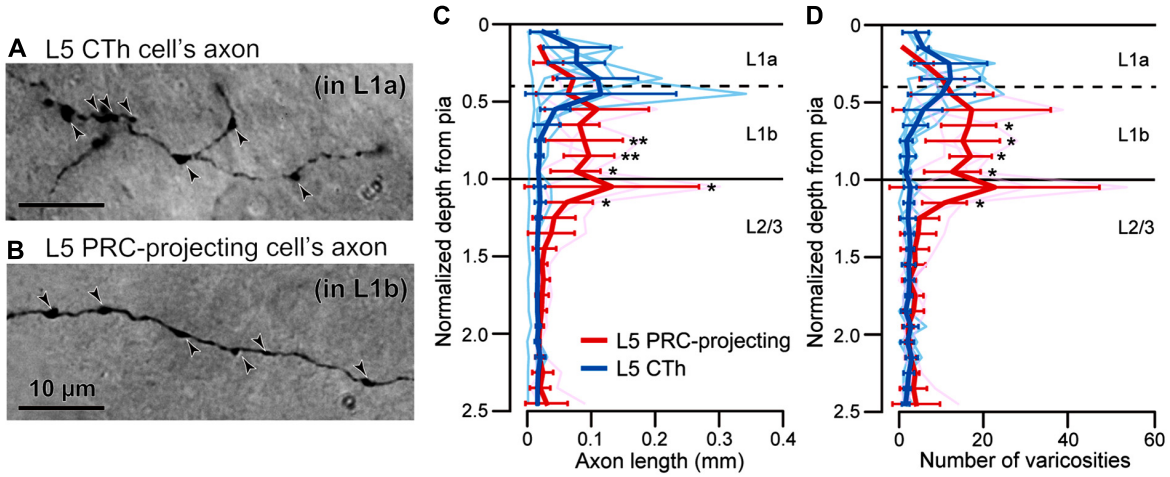

FIGURE 6 | Correlation of axonal length and varicosity number of superficial layer branches from L5 pyramidal cells. (A) L1a axon varicosities (arrowheads) of an L5a CTh cell. **(B)** L1b axon varicosities (arrowheads) of an L5a PRC-projecting cell. **(C)** Axon length distributions of CTh cells (blue, six branches of two cells) and PRC-projecting cells (red, five branches of two cells) within L1 and L2/3. Cortical depth was normalized by L1 thickness: 0, cortical surface; 1, L1/L2 border. Axon length and varicosity number were measured in each depth fraction (fraction length, one-tenth of L1 thickness). Thin lines, individual axon branches; thick lines, mean ± SD. Asterisks indicate significant differences between L5 PRC-projecting and CTh cells in each bin (*$P < 0.05$, **$P < 0.01$; Mann–Whitney *U*-test). **(D)** Axon varicosity distributions of CTh cells (blue) and L5 PRC-projecting cells (red). *$P < 0.05$, Mann—Whitney *U*-test.

distribution index, 0.37 ± 0.03, three rats; $P < 0.05$, two-tailed one-sample *t*-test). Within L1, labeled fibers in L1a were more abundant than those in L1b (**Figure 7B**, right; 0.73 ± 0.05 in upper L1a, 0.78 ± 0.09 in lower L1a, 0.67 ± 0.09 in upper L1b, and 0.49 ± 0.08 in lower L1b; *$P < 0.05$, **$P < 0.01$, Tukey–Kramer multiple comparisons test).

Labeled fibers seemed to demonstrate preference for L1 over L2/3 in the distant areas PRC 36 (**Figure 7C**, left; laminar distribution index, 0.23 ± 0.14, three rats) and PPC (**Figure 7D**, left; laminar distribution index, 0.32 ± 0.24, three rats). The L1 innervation pattern was similar between PRC 36 (**Figure 7C**, right; 0.57 ± 0.06 in upper L1a, 0.61 ± 0.04 in lower L1a, 0.59 ± 0.13 in upper L1b, and 0.42 ± 0.09 in lower L1b) and PPC (**Figure 7D**, right; 0.62 ± 0.07 in upper L1a, 0.6 ± 0.13 in lower L1a, 0.49 ± 0.11 in upper L1b, and 0.43 ± 0.13 in lower L1b).

Callosal fibers issue from COM cells, but not from CPn cells. We found that labeled fibers in contralateral M2 were abundant in both L1 and L2/3 (**Figure 7E**, left; laminar distribution index, −0.04 ± 0.1, four rats). Within L1, however, labeled fibers in L1b were more abundant than those in L1a (**Figure 7E**, right; 0.24 ± 0.07 in upper L1a, 0.44 ± 0.04 in lower L1a, 0.6 ± 0.09 in upper L1b, and 0.61 ± 0.11 in lower L1b; *$P < 0.05$, **$P < 0.01$, Tukey–Kramer multiple comparisons test). Therefore, M2 differentially innervates the superficial layers, especially L1, of other cortical areas depending on the target area.

SUBLAMINAR SEGREGATION OF iCC PROJECTIONS ORIGINATING FROM M2 L2/3 DEPENDS ON THE TARGET AREA

Within L2/3 of M2, pyramidal cells projecting to OFC or PRC 35 were distributed more in L2/3a than in L2/3b, whereas those projecting to M1 were distributed more in L2/3b (**Figure 4**). L2/3 cells retrogradely labeled from PRC partially double-labeled those labeled from OFC (**Figure 8A**; two rats), but were almost entirely distinct from those labeled from M1, with a different sublaminar localization (**Figure 8B**; three rats). By contrast, L5a cells labeled from PRC partially overlapped with those labeled from M1 (data not shown; three rats). Some L2/3a cells projecting to PRC are also retrogradely labeled from the amygdala (Hirai et al., 2012). Therefore, M2 L2/3 sublayers are roughly correlated with different iCC systems: L2/3a projecting to OFC, PRC 35, and amygdala, and L2/3b projecting to M1 (**Figure 8C**).

DISCUSSION

COMPLEMENTARY LAMINAR DISTRIBUTIONS OF iCC CELLS RECIPROCALLY CONNECTING M2 AND NON-FRONTAL AREAS

We found that M2 and the distant non-frontal areas we examined were connected by pyramidal cells in either superficial or deep layers, depending on the direction of connectivity. In visual cortical areas, lower- to higher-order projections [called "forward (bottom-up) connections"] originate either from superficial layers or from both superficial and deep layers, and terminate in middle layers. By contrast, projections in the reverse direction ["backward (top-down) connections"] originate either from deep layers or from both superficial and deep layers and terminate outside middle layers, especially in L1 (Felleman and Van Essen, 1991; Rockland, 1997; Barone et al., 2000; Douglas and Martin, 2004; Shipp, 2007). Similar anatomical differences to the laminar patterns of iCC origins and their innervation sites between visual cortical areas have been found between sensory, motor, and association cortices (Felleman and Van Essen, 1991). Therefore, we assumed the directionality of reciprocal connections between M2 and its target areas by analogy with the directionality demonstrated between visual areas.

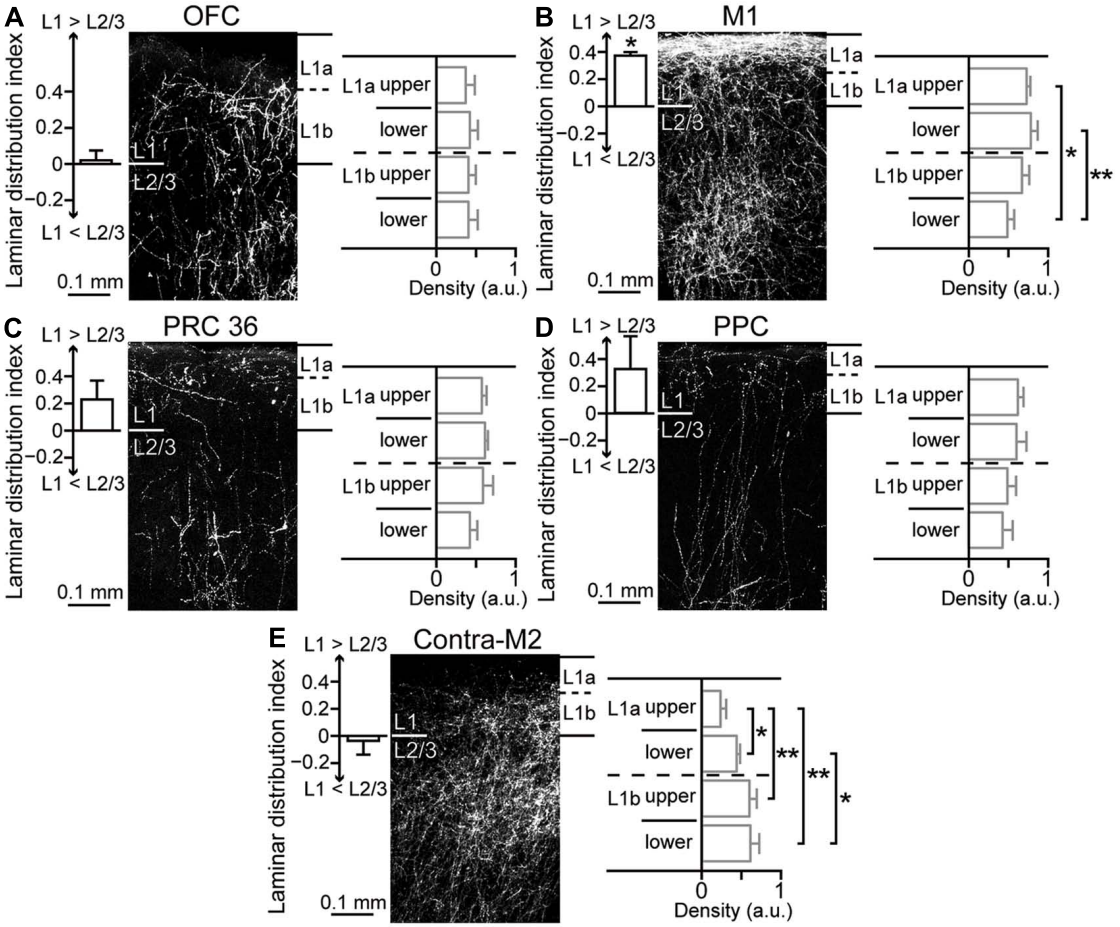

FIGURE 7 | Laminar pattern of fiber terminations arising from M2 to ipsilateral cortical areas and contralateral M2. (A) M2-derived fiber distributions in L1 and L2/3 of ipsilateral OFC, labeled with BDA-10K injections into L1 to L5 of M2. Left graph, uniform fiber distribution between L1 and L2/3 ($P = 0.5$, two-tailed one-sample *t*-test). Laminar distribution index, [(fiber density in L1) − (fiber density in L2/3)]/[(fiber density in L1) + (fiber density in L2/3)], is positive for L1 preference and negative for L2/3 preference. Right graph, uniform fiber distributions along L1, determined by comparing four subdivisions (upper and lower halves of L1a and L1b, respectively). **(B)** M2-derived fiber distributions in ipsilateral M1. Left graph, denser distribution in L1 than in L2/3 ($P < 0.01$). Right graph, denser distribution in L1a than in L1b (*$P < 0.05$, **$P < 0.01$; Tukey–Kramer multiple comparisons test). Data taken from Ueta et al. (2013). **(C)** M2- derived fiber distributions in ipsilateral PRC 36. Left graph, a non-significant trend was observed for denser distribution in L1 than in L2/3 ($P = 0.1$). Right graph, uniform distributions along L1. **(D)** M2-derived fiber distributions in ipsilateral PPC, similar to that in ipsilateral PRC 36 ($P = 0.15$). **(E)** M2-derived fiber distributions in contralateral M2. Left graph, uniform distribution between L1 and L2/3 ($P = 0.53$). Right graph, denser distribution in L1b than in L1a (*$P < 0.05$, **$P < 0.01$; Tukey-Kramer multiple comparisons test).

Between M2 and a distant area, including PRC 35, PRC 36, and PPC, the laminar patterns of iCC cells were highly complementary (**Figures 4D,E**). Between M2 and PPC, the direction from PPC to M2 was considered bottom-up, while that from M2 to PPC was considered top-down (**Figure 9**). The frontal cortex receives visual inputs through the parietal cortex, not directly from the visual cortex, to control visuomotor and attentional performance (Wise et al., 1997; Reep and Corwin, 2009; Corbetta and Shulman, 2011). According to the anatomical connectivity, supposed bottom-up signals from PPC relaying visual information would arrive at M2. By contrast, the anatomical connectivity between M2 and PRC 36 was the reverse of that between M2 and PRC 35. M2-to-PRC 35 and PRC 36-to-M2 projections were considered bottom-up connections (**Figure 9**). Signals from the frontal cortex to the hippocampal formation may initiate active retrieval of declarative memories (Miyashita, 2004). According to the anatomical connectivity, supposed retrieval signals would arrive at PRC 35, with stronger connections with the entorhinal cortex than PRC 36 (Burwell and Amaral, 1998; Agster and Burwell, 2009). Meanwhile, the retrieved memory would be transmitted to the frontal cortex from PRC 36, which is more strongly connected to sensory and temporal cortical areas than PRC 35 (Burwell and Amaral, 1998; Agster and Burwell, 2009).

DIFFERENTIATION OF L5 PYRAMIDAL CELLS ACCORDING TO DIVERSE TELENCEPHALIC AND SUBCEREBRAL PROJECTIONS

L5a pyramidal cells participate in diverse iCC projections from M2 to multiple cortical areas. Based on the projection patterns to subcortical structures and the contralateral cortex, as well as

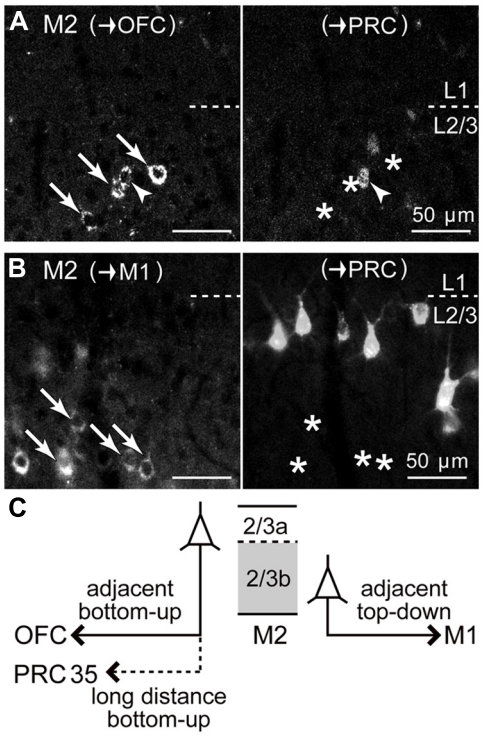

FIGURE 8 | Relation of iCC projections from M2 L2/3 to PRC with those to OFC or to M1. (A) Upper L2/3 distributions of M2 iCC cells projecting to OFC and to PRC, and their partial double-labeling. Left, M2 somata retrogradely labeled from OFC (arrows and arrowhead; labeled by CTB555). Right, M2 somata retrogradely labeled from PRC (labeled by Fast Blue). Arrowhead, double-labeled cell; arrows, OFC-projecting cells not labeled by PRC injection (asterisks). Oblique section, 20 μm thickness. **(B)** Segregation of iCC projections from M2 L2/3 to M1 and to PRC. Left, M2 somata projecting to M1 in lower L2/3 (arrows; labeled by CTB555), not labeled from PRC (asterisks in right). Right, M2 somata projecting to PRC in upper L2/3 (labeled by Fast Blue). **(C)** Schematic summary of M2 L2/3 iCC projections. OFC-projecting cells are more prevalent in L2/3a, some of which also send axon collaterals to PRC. By contrast, M1-projecting cells are abundant in L2/3b.

firing characteristics and Ctip2 molecular expression, L5a pyramidal cells could be divided into at least three subtypes (**Figure 10**). Importantly, these subtypes are also differentially involved in iCC connections.

In addition to their innervation of the pontine nuclei, CPn cells also project to other subcortical targets according to their depth location within L5 of M2: CTh cells without spinal cord innervation in L5a; CTc cells without spinal cord innervation in lower L5a; CSp cells in L5b, some of which innervate the thalamus; and CTc cells with spinal cord innervation in upper L5b. The frontal cortex also sends axon collaterals to the subthalamus (Nambu et al., 2002; Kita and Kita, 2012). The subthalamus-projecting cells are a subtype of L5 CPn cells that also innervate the thalamus and superior colliculus (Kita and Kita, 2012) and are distributed in the middle of L5, consistent with the laminar distribution of CTc cells (**Figure 2B**). This anatomical distribution suggests that CPn cells at a given depth share the same extracortical targets and that CPn cells may differentiate strongly depending on cortical depth. COM cells may be more diverse at a given depth, as the same sublayer contains at least two subtypes of COM cells that differ in physiological, morphological, and projection characteristics (**Figure 10**; Otsuka and Kawaguchi, 2011).

Both CPn and COM cells in L5 participate in iCC projections. In M2, unlike M1, L5 iCC projections originate mainly from L5a (**Figure 4D**; Ueta et al., 2013). L5a CPn cells innervate the adjacent frontal areas, but weakly innervate the distant areas. The involvement of L5a COM cells in iCC connections differs between their subtypes: the SA subtype may participate mainly in adjacent areas, but the FA subtype, including CCS cells, participates in both intrafrontal and distant projections (**Figures 10** and **11**; Otsuka and Kawaguchi, 2008, 2011; Hirai et al., 2012; Ueta et al., 2013). These findings suggest that L5a CPn cells and COM cells with similar firing characteristics to CPn cells share common iCC innervation territory distinct from that of CCS cells, which have a wider area of innervation (**Figures 10** and **11**). For a deeper understanding of the functional interactions of iCC communication with subcortical and COM projections, it would be important to examine their relationships more quantitatively by introducing selective molecular markers for individual neuron subtypes (Molnár and Cheung, 2006; Molyneaux et al., 2007; Fame et al., 2011).

DIRECTION-DEPENDENT INVOLVEMENT OF CPn CELLS IN iCC CONNECTIONS BETWEEN FRONTAL AREAS

Among adjacent frontal areas, M2 is connected not only with M1, but also with OFC (Conte et al., 2008; Reep and Corwin, 2009; Hoover and Vertes, 2011). Since these frontal areas were bidirectionally connected by pyramidal cells in both superficial and deep layers (**Figures 4D,E**), the directional connectivity could not be determined solely based on laminar patterns of iCC origins.

L5 pyramidal cells connecting ipsilateral frontal areas were found in both L5a and L5b, and contained both Ctip2-positive CPn cells and Ctip2-negative COM cells, with their selective sublaminar distribution and Ctip2 expression patterns dependent on the connection direction (**Figures 4D,E** and **5**). M2 innervates L1a of M1 more preferentially than M1 innervates M2 (**Figure 7B**), and the L1a innervation is conveyed by Ctip2-positive cells in M2 L5a, including CTh cells (**Figure 11**; Ueta et al., 2013). Between visual cortical areas, the backward projections innervate upper L1 to a greater degree than the forward projections (Coogan and Burkhalter, 1993; Dong et al., 2004). To understand the CC connections in a unified framework, we assumed that, in reciprocal connectivity between frontal areas, the direction with more involvement of Ctip2-positive L5 cells, from OFC to M2 and from M2 to M1, was defined as top-down (**Figure 9**). Therefore, frontal areas might be directionally connected via L5a CPn cells with more L1 innervation in a rostral-to-caudal, top-down direction. L5a CPn cells are involved in projections to the adjacent ipsilateral cortical areas as well as the ventral thalamic nuclei, whereas L5b CPn cells send specific outputs from individual areas to the thalamus, brainstem, and spinal cord (**Figure 2**).

The framework for iCC connectivity of the frontal cortex proposed here is similar to the idea that descending projections

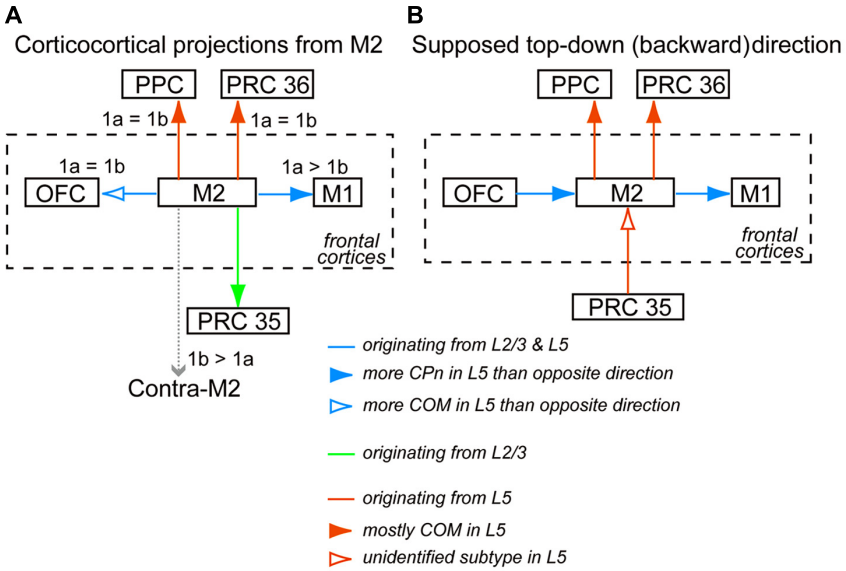

FIGURE 9 | Interareal direction-dependent laminar distributions of iCC cells and involvement of L5 pyramidal cell subtypes. (A) iCC projections from M2 and their L1 innervation in the target area. iCC connections to the adjacent areas are mediated by L2/3 cells as well as L5 cells of both CPn and COM subtypes, but their relative involvement depends on each connection. More fibers from M2 terminate in L1a than in L1b of M1 (1a > 1b), but they terminate in L1a and L1b of OFC at similar levels (1a = 1b). iCC connections to the distant areas are mediated by either L2/3 cells or L5 cells of mostly COM subtypes. Fibers from M2 terminate at comparable levels in L1a and L1b of PRC 36 and PPC. By contrast, more fibers from M2 terminate in L1b than in L1a of contralateral M2 (1b > 1a). **(B)** Supposed top-down (backward) connections, assuming more involvement of L5 cells than L2/3 cells in that direction between M2 and the distant non-frontal areas, and more involvement of L5 CPn cells than COM cells in that direction between M2 and the adjacent areas.

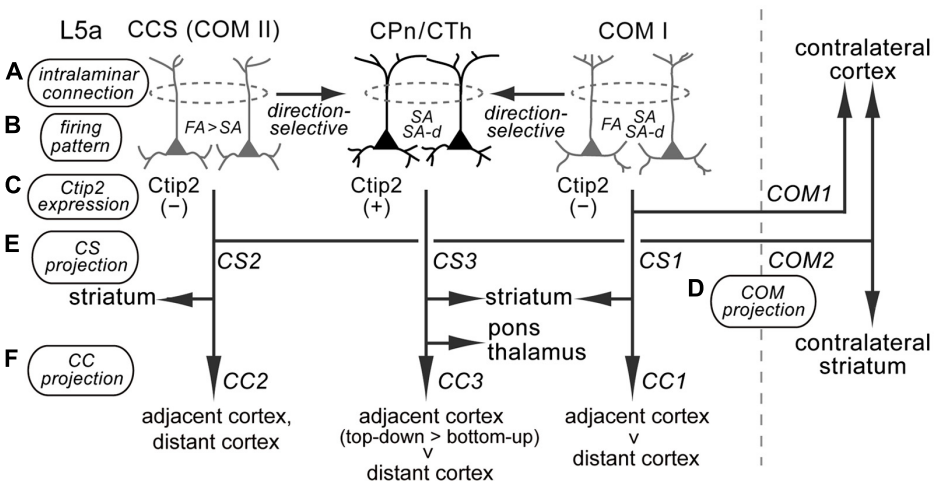

FIGURE 10 | Diversity of supposed relationships among iCC projections, with multiple corticostriatal and COM cell subtypes in M2 L5a. M2 L5a contains CPn/CTh, COM type I, and COM type II/CCS cells that differ in their morphological, physiological, and connectional characteristics, and all of these cells send axon collaterals to the ipsilateral striatum (Morishima and Kawaguchi, 2006; Morishima et al., 2011; Otsuka and Kawaguchi, 2011; Hirai et al., 2012). **(A)** Intralaminar connection pattern: CPn cells innervate other CPn cells, and COM cells form synaptic connections particularly with other COM cells sharing the same firing pattern (Morishima et al., 2011; Otsuka and Kawaguchi, 2011). COM subtypes innervate CPn cells, but CPn cells rarely innervate COM subtypes (Morishima and Kawaguchi, 2006; Kiritani et al., 2012). **(B)** Firing pattern: CPn cells and COM subtypes contain different proportions of FA, SA, and SA-d firing types (Otsuka and Kawaguchi, 2008, 2011; Hirai et al., 2012; the present study). **(C)** Ctip2 expression: CPn/CTh cells specifically express Ctip2, but COM cells do not (Arlotta et al., 2005; Ueta et al., 2013). **(D,E)** Corticostriatal (CS) and COM projection patterns: COM type I cells project to the contralateral cortex (COM1) and ipsilateral striatum (CS1); CCS (COM type II) cells project to the contralateral striatum in addition to the contralateral cortex (COM2) and ipsilateral striatum (CS2); and CPn/CTh cells project to the ipsilateral striatum (CS3), but not to the contralateral hemisphere (Lévesque et al., 1996; Lévesque and Parent, 1998; Otsuka and Kawaguchi, 2011; Hirai et al., 2012; Shepherd, 2013). **(F)** iCC projection pattern: COM type I cells preferentially innervate the adjacent cortex compared to the distant cortex (CC1); COM type II cells project to various adjacent and distant cortices; and CPn/CTh cells preferentially innervate the adjacent cortex (especially in the top-down direction) rather than the distant cortex (the present study).

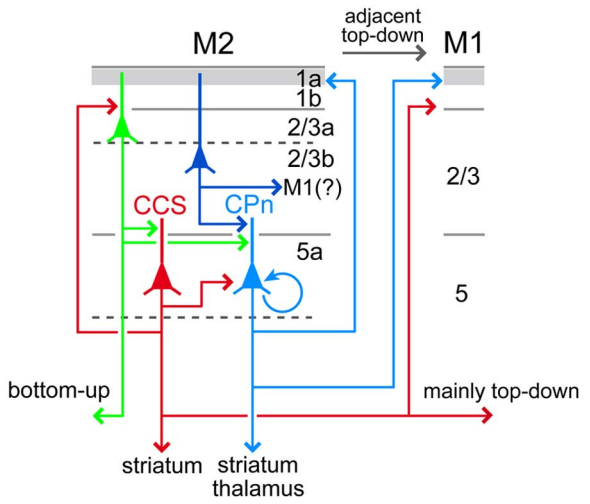

FIGURE 11 | Relationships between local excitation loops involving L5a CCS and CPn cells with iCC projections. L5a CCS cells innervate CPn cells unidirectionally in L5 and may form excitatory loops with L2/3a cells including OFC-projecting (bottom-up projection to an adjacent area) and PRC 35-projecting cells (bottom-up projection to a distant area). L5a CCS cells send axon collaterals to various cortical areas and both sides of striatum, but not to PRC 35. By contrast, CPn cells develop more reciprocal connections with each other than CCS cells, innervate L1a preferentially over L1b/L2/3a in their own area as well as in ipsilateral M1, and receive convergent inputs from L2/3 cells of various depths. L5a CPn cells send outputs to the ipsilateral thalamus as well as striatum. Apical dendrites of L5a CCS and CPn cells extending to L1a are omitted (see **Figure 10**).

from the motor cortex are more like backward connections in the visual cortex than the corresponding forward connections (Shipp, 2005). It is proposed that descending connections of sensory cortices convey predictions of sensory inputs, and by the same token those of frontal cortices send proprioceptive predictions, rather than motor commands (Adams et al., 2013).

DIVERSE LAMINAR INNERVATION PATTERNS BY L5 PYRAMIDAL CELL SUBTYPES IN THE TARGET CORTEX

COM cells in M2 preferentially innervate L1b and L2/3 compared to L1a in contralateral M2 (**Figure 7E**), whereas L5a CPn cells in M2 prefer to send axons to L1a within M2 and in M1 (Hirai et al., 2012; Ueta et al., 2013). Therefore, when both L5a COM and CPn cells in M2 project to another cortical area, two types of M2 L5 activity may be transferred independently into the local circuit of the target cortex. L5a CPn cells in the source area send axon collaterals to L1a in the iCC target area, where they interact with axon collaterals in L1a arising from L5 CPn cells in the target area (Thomson and Bannister, 2003), as well as with thalamocortical innervations relaying basal ganglia outputs that heavily terminate in L1a (Kuramoto et al., 2009, 2011; Rubio-Garrido et al., 2009; Kaneko, 2013). Similarly, axon collaterals of L5a COM cells in the source area would interact with those in the target area at L1b and L2/3. These observations suggest that the activities of L5a CPn and COM cells are separately processed both in their own and iCC target areas.

SUBLAMINAR DISSOCIATION OF L2/3 BOTTOM-UP AND TOP-DOWN iCC PROJECTIONS IN M2

In L2/3 of M2, iCC cells projecting to both OFC and PRC 35 originate mainly from L2/3a, whereas those projecting to M1 originate from L2/3b (**Figure 8**). The former type of projection also sends axon collaterals to the amygdala (Hirai et al., 2012). Therefore, in superficial layers, iCC projections separately originate from the upper and lower L2/3 sublayers according to their targets. Considering the connectivity between M2 and its target cortical areas, the bottom-up projection may originate from L2/3a, whereas the top-down projection may originate from L2/3b.

Both SA and SA-d firing types of L5 pyramidal cells receive strong feedforward excitation from L2/3 pyramidal cells (Thomson and Bannister, 2003; Yu et al., 2008; Petreanu et al., 2009) irrespective of their L2/3 depth (Otsuka and Kawaguchi, 2008), indicating convergent inputs to CPn cells from L2/3 cells. By contrast, FA-type pyramidal cells in upper L5 (probably corresponding to L5a) receive excitation from upper L2/3 (L2/3a) pyramidal cells, whereas those in middle L5 (upper L5b) receive excitatory inputs from middle L2/3 (probably upper L2/3b), indicating that interlaminar connections are topographically organized depending on L5 pyramidal cell subtypes (Otsuka and Kawaguchi, 2008; Anderson et al., 2010; Hirai et al., 2012). Interestingly, this finding suggests that M2 L5 CCS cells can be differentiated into L5a cells receiving excitatory input from L2/3a cells that may carry bottom-up signals, and upper L5b cells receiving excitatory input from L2/3b cells that may carry top-down signals.

L5a CCS cells reciprocally connect with L2/3a pyramidal cells, and their axodendritic contacts are located in L1b and L2/3 (**Figure 11**; Hirai et al., 2012). Therefore, the excitation loop between L2/3a pyramidal cells and L5a CCS cells is important for the integration of the long-distance bottom-up and top-down iCC connections in higher-order frontal motor areas (**Figure 11**). Following the firing of CCS cells, L5a CPn cells would be activated by unidirectional CCS connections and, if sufficiently excited, maintain persistent firing via facilitating reciprocal excitation among CPn cells (**Figure 11**; Morishima and Kawaguchi, 2006; Morishima et al., 2011; Morita et al., 2012). Furthermore, if a sufficient number of CPn cells fired persistently, L2/3 pyramidal cells could begin to fire tonically in response to depolarization evoked by ascending axon collaterals of L5 CPn cells to L1a, targeting distal tufts of L2/3 pyramidal cells. Increased firing of L2/3 pyramidal cells would subsequently facilitate their convergent outputs to L5 CPn cells (**Figure 11**).

We have classified frontal cortical pyramidal cells into several major classes based on their anatomical and physiological properties. It is likely that future studies examining selective expression of molecular markers in these populations may reveal even finer subtype specialization. However, our current work demonstrates a fundamental structural relationship between local circuit elements and long-distance top-down and bottom-up connectivity within the frontal cortex that may reflect a fundamental organizing principle of the cerebral cortex as a whole.

CONCLUSION

We identified individual iCC connections between M2 and other areas as being "top-down" or "bottom-up" by comparing the

laminar distribution of iCC cells and their efferent innervations, COM/subcortical projections of these neurons, and their firing patterns. Based on our results, we proposed a provisional unified framework of interareal hierarchy within the frontal cortex and between the fontal and non-frontal areas. Furthermore, we discussed the functional interaction of the interareal hierarchy with the intraareal local cortical microcircuit.

ACKNOWLEDGMENTS

We thank Noboru Yamaguchi for histological assistance, and Allan T. Gulledge and Fuyuki Karube for comments on the manuscript. This work was supported by the Japan Science and Technology Agency (JST), Core Research for Evolutional Science and Technology (CREST), and Grants-in-Aid for Scientific Research from the Ministry of Education, Culture, Sports, Science, and Technology (MEXT).

REFERENCES

Adams, R. A., Shipp, S., and Friston, K. J. (2013). Predictions not commands: active inference in the motor system. *Brain Struct. Funct.* 218, 611–643. doi: 10.1007/s00429-012-0475-5

Agster, K. L., and Burwell, R. D. (2009). Cortical efferents of the perirhinal, postrhinal, and entorhinal cortices of the rat. *Hippocampus* 19, 1159–1186. doi: 10.1002/hipo.20578

Anderson, C. T., Sheets, P. L., Kiritani, T., and Shepherd, G. M. (2010). Sublayer-specific microcircuits of corticospinal and corticostriatal neurons in motor cortex. *Nat. Neurosci.* 13, 739–744. doi: 10.1038/nn.2538

Arlotta, P., Molyneaux, B. J., Chen, J., Inoue, J., Kominami, R., and Macklis, J. D. (2005). Neuronal subtype-specific genes that control corticospinal motor neuron development in vivo. *Neuron* 45, 207–221. doi: 10.1016/j.neuron.2004.12.036

Arnsten, A. F., Wang, M. J., and Paspalas, C. D. (2012). Neuromodulation of thought: flexibilities and vulnerabilities in prefrontal cortical network synapses. *Neuron* 76, 223–239. doi: 10.1016/j.neuron.2012.08.038

Avesar, D., and Gulledge, A. T. (2012). Selective serotonergic excitation of callosal projection neurons. *Front. Neural Circuits* 6:12. doi: 10.3389/fncir.2012.00012

Barone, P., Batardiere, A., Knoblauch, K., and Kennedy, H. (2000). Laminar distribution of neurons in extrastriate areas projecting to visual areas V1 and V4 correlates with the hierarchical rank and indicates the operation of a distance rule. *J. Neurosci.* 20, 3263–3281.

Brecht, M., Krauss, A., Muhammad, S., Sinai-Esfahani, L., Bellanca, S., and Margrie, T. W. (2004). Organization of rat vibrissa motor cortex and adjacent areas according to cytoarchitectonics, microstimulation, and intracellular stimulation of identified cells. *J. Comp. Neurol.* 479, 360–373. doi: 10.1002/cne.20306

Brown, S. P., and Hestrin, S. (2009). Intracortical circuits of pyramidal neurons reflect their long-range axonal targets. *Nature* 457, 1133–1136. doi: 10.1038/nature07658

Burwell, R. D., and Amaral, D. G. (1998). Cortical afferents of the perirhinal, postrhinal, and entorhinal cortices of the rat. *J. Comp. Neurol.* 398, 179–205. doi: 10.1002/(SICI)1096-9861(19980824)398:2<179::AID-CNE3>3.0.CO;2-Y

Condé, F., Maire-Lepoivre, E., Audinat, E., and Crépel, F. (1995). Afferent connections of the medial frontal cortex of the rat. II. cortical and subcortical afferents. *J. Comp. Neurol.* 352, 567–593. doi: 10.1002/cne.903520407

Conte, W. L., Kamishina, H., Corwin, J. V., and Reep, R. L. (2008). Topography in the projections of lateral posterior thalamus with cingulate and medial agranular cortex in relation to circuitry for directed attention and neglect. *Brain Res.* 1240, 87–95. doi: 10.1016/j.brainres.2008.09.013

Coogan, T. A., and Burkhalter, A. (1993). Hierarchical organization of areas in rat visual cortex. *J. Neurosci.* 13, 3749–3772.

Corbetta, M., and Shulman, G. L. (2011). Spatial neglect and attention networks. *Annu. Rev. Neurosci.* 34, 569–599. doi: 10.1146/annurev-neuro-061010-113731

Dong, H., Wang, Q., Valkova, K., Gonchar, Y., and Burkhalter, A. (2004). Experience-dependent development of feedforward and feedback circuits between lower and higher areas of mouse visual cortex. *Vision Res.* 44, 3389–3400. doi: 10.1016/j.visres.2004.09.007

Douglas, R. J., and Martin, K. A. (2004). Neuronal circuits of the neocortex. *Annu. Rev. Neurosci.* 27, 419–451. doi: 10.1146/annurev.neuro.27.070203.144152

Fame, R. M., MacDonald, J. L., and Macklis, J. D. (2011). Development, specification, and diversity of callosal projection neurons. *Trends Neurosci.* 34, 41–50. doi: 10.1016/j.tins.2010.10.002

Felleman, D. J., and Van Essen, D. C. (1991). Distributed hierarchical processing in the primate cerebral cortex. *Cereb. Cortex* 1, 1–47. doi: 10.1093/cercor/1.1.1

Gabbott, P. L., Warner, T. A., Jays, P. R., Salway, P., and Busby, S. J. (2005). Prefrontal cortex in the rat: projections to subcortical autonomic, motor, and limbic centers. *J. Comp. Neurol.* 492, 145–177. doi: 10.1002/cne.20738

Gabbott, P. L. A., Martin, K. A. C., and Whitteridge, D. (1987). Connections between pyramidal neurons in layer 5 of cat visual cortex (area 17). *J. Comp. Neurol.* 259, 364–381. doi: 10.1002/cne.902590305

Hattox, A. M., and Nelson, S. B. (2007). Layer V neurons in mouse cortex projecting to different targets have distinct physiological properties. *J. Neurophysiol.* 98, 3330–3340. doi: 10.1152/jn.00397.2007

Hira, R., Ohkubo, F., Tanaka, Y. R., Masamizu, Y., Augustine, G. J., Kasai, H., et al. (2013). In vivo optogenetic tracing of functional corticocortical connections between motor forelimb areas. *Front. Neural Circuits* 7:55. doi: 10.3389/fncir.2013.00055

Hirai, Y., Morishima, M., Karube, F., and Kawaguchi, Y. (2012). Specialized cortical subnetworks differentially connect frontal cortex to parahippocampal areas. *J. Neurosci.* 32, 1898–1913. doi: 10.1523/JNEUROSCI.2810-11.2012

Hoover, W. B., and Vertes, R. P. (2007). Anatomical analysis of afferent projections to the medial prefrontal cortex in the rat. *Brain Struct. Funct.* 212, 149–179. doi: 10.1007/s00429-007-0150-4

Hoover, W. B., and Vertes, R. P. (2011). Projections of the medial orbital and ventral orbital cortex in the rat. *J. Comp. Neurol.* 519, 3766–3801. doi: 10.1002/cne.22733

Kaneko, T. (2013). Local connections of excitatory neurons in motor-associated cortical areas of the rat. *Front. Neural Circuits* 7:75. doi: 10.3389/fncir.2013.00075

Kawaguchi, Y., Wilson, C. J., and Emson, P. C. (1989). Intracellular recording of identified neostriatal patch and matrix spiny cells in a slice preparation preserving cortical inputs. *J. Neurophysiol.* 62, 1052–1068.

Kiritani, T., Wickersham, I. R., Seung, H. S., and Shepherd, G. M. (2012). Hierarchical connectivity and connection-specific dynamics in the corticospinal–corticostriatal microcircuit in mouse motor cortex. *J. Neurosci.* 32, 4992–5001. doi: 10.1523/JNEUROSCI.4759-11.2012

Kisvárday, Z. F., Martin, K. A. C., Freund, T. F., Maglóczky, Z., Whitteridge, D., and Somogyi, P. (1986). Synaptic targets of HRP-filled layer III pyramidal cells in the cat striate cortex. *Exp. Brain Res.* 64, 541–552. doi: 10.1007/BF00340492

Kita, T., and Kita, H. (2012). The subthalamic nucleus is one of multiple innervation sites for long-range corticofugal axons: a single-axon tracing study in the rat. *J. Neurosci.* 32, 5990–5999. doi: 10.1523/JNEUROSCI.5717-11.2012

Kuramoto, E., Fujiyama, F., Nakamura, K. C., Tanaka, Y., Hioki, H., and Kaneko, T. (2011). Complementary distribution of glutamatergic cerebellar and GABAergic basal ganglia afferents to the rat motor thalamic nuclei. *Eur. J. Neurosci.* 33, 95–109. doi: 10.1111/j.1460-9568.2010.07481.x

Kuramoto, E., Furuta, T., Nakamura, K. C., Unzai, T., Hioki, H., and Kaneko, T. (2009). Two types of thalamocortical projections from the motor thalamic nuclei of the rat: a single neuron-tracing study using viral vectors. *Cereb. Cortex* 19, 2065–2077. doi: 10.1093/cercor/bhn231

Lévesque, M., Gagnon, S., Parent, A., and Deschênes, M. (1996). Axonal arborizations of corticostriatal and corticothalamic fibers arising from the second somatosensory area in the rat. *Cereb. Cortex* 6, 759–770. doi: 10.1093/cercor/6.6.759

Lévesque, M., and Parent, A. (1998). Axonal arborization of corticostriatal and corticothalamic fibers arising from prelimbic cortex in the

rat. *Cereb. Cortex* 8, 602–613. doi: 10.1093/cercor/8.7.602

Miyashita, Y. (2004). Cognitive memory: cellular and network machineries and their top-down control. *Science* 306, 435–440. doi: 10.1126/science.1101864

Molnár, Z., and Cheung, A. F. (2006). Towards the classification of subpopulations of layer V pyramidal projection neurons. *Neurosci. Res.* 55, 105–115. doi: 10.1016/j.neures.2006.02.008

Molyneaux, B. J., Arlotta, P., Menezes, J. R., and Macklis, J. D. (2007). Neuronal subtype specification in the cerebral cortex. *Nat. Rev. Neurosci.* 8, 427–437. doi: 10.1038/nrn2151

Morishima, M., and Kawaguchi, Y. (2006). Recurrent connection patterns of corticostriatal pyramidal cells in frontal cortex. *J. Neurosci.* 26, 4394–4405. doi: 10.1523/JNEUROSCI.0252-06.2006

Morishima, M., Morita, K., Kubota, Y., and Kawaguchi, Y. (2011). Highly differentiated projection-specific cortical subnetworks. *J. Neurosci.* 31, 10380–10391. doi: 10.1523/JNEUROSCI.0772-11.2011

Morita, K., Morishima, M., Sakai, K., and Kawaguchi, Y. (2012). Reinforcement learning: computing the temporal difference of values via distinct corticostriatal pathways. *Trends Neurosci.* 35, 457–467. doi: 10.1016/j.tins.2012.04.009

Nambu, A., Tokuno, H., and Takada, M. (2002). Functional significance of the cortico-subthalamo-pallidal 'hyperdirect' pathway. *Neurosci. Res.* 43, 111–117. doi: 10.1016/S0168-0102(02)00027-5

Otsuka, T., and Kawaguchi, Y. (2008). Firing-pattern-dependent specificity of cortical excitatory feed-forward subnetworks. *J. Neurosci.* 28, 11186–11195. doi: 10.1523/JNEUROSCI.1921-08.2008

Otsuka, T., and Kawaguchi, Y. (2011). Cell diversity and connection specificity between callosal projection neurons in the frontal cortex. *J. Neurosci.* 31, 3862–3870. doi: 10.1523/JNEUROSCI.5795-10.2011

Petreanu, L., Mao, T., Sternson, S. M., and Svoboda, K. (2009). The subcellular organization of neocortical excitatory connections. *Nature* 457, 1142–1145. doi: 10.1038/nature07709

Reep, R. L., Chandler, H. C., King, V., and Corwin, J. V. (1994). Rat posterior parietal cortex: topography of corticocortical and thalamic connections. *Exp. Brain Res.* 100, 67–84. doi: 10.1007/BF00227280

Reep, R. L., and Corwin, J. V. (2009). Posterior parietal cortex as part of a neural network for directed attention in rats. *Neurobiol. Learn. Mem.* 91, 104–113. doi: 10.1016/j.nlm.2008.08.010

Reep, R. L., Goodwin, G. S., and Corwin, J. V. (1990). Topographic organization in the corticocortical connections of medial agranular cortex in rats. *J. Comp. Neurol.* 294, 262–280. doi: 10.1002/cne.902940210

Reiner, A., Jiao, Y., Del Mar, N., Laverghetta, A. V., and Lei, W. L. (2003). Differential morphology of pyramidal tract-type and intratelencephalically projecting-type corticostriatal neurons and their intrastriatal terminals in rats. *J. Comp. Neurol.* 457, 420–440. doi: 10.1002/cne.10541

Rockland, K. S. (1997). "Elements of cortical architecture: hierarchy revisited," in *Cerebral Cortex*, Vol. 12, *Extrastriate Cortex in Primates*, eds K. S. Rockland, J. H. Kaas, and A. Peters (New York: Plenum Press), 243–293.

Rubio-Garrido, P., Pérez-de-Manzo, F., Porrero, C., Galazo, M. J., and Clascá, F. (2009). Thalamic input to distal apical dendrites in neocortical layer 1 is massive and highly convergent. *Cereb. Cortex* 19, 2380–2395. doi: 10.1093/cercor/bhn259

Shepherd, G. M. (2013). Corticostriatal connectivity and its role in disease. *Nat. Rev. Neurosci.* 14, 278–291. doi: 10.1038/nrn3469

Shipp, S. (2005). The importance of being agranular: a comparative account of visual and motor cortex. *Philos. Trans. R. Soc. Lond. B Biol. Sci.* 360, 797–814. doi: 10.1098/rstb.2005.1630

Shipp, S. (2007). Structure and function of the cerebral cortex. *Curr. Biol.* 17, R443–449. doi: 10.1016/j.cub.2007.03.044

Thomson, A. M., and Bannister, A. P. (2003). Interlaminar connections in the neocortex. *Cereb. Cortex* 13, 5–14. doi: 10.1093/cercor/13.1.5

Uematsu, M., Hirai, Y., Karube, F., Ebihara, S., Kato, M., Abe, K., et al. (2008). Quantitative chemical composition of cortical GABAergic neurons revealed in transgenic Venus-expressing rats. *Cereb. Cortex* 18, 315–330. doi: 10.1093/cercor/bhm056

Ueta, Y., Otsuka, T., Morishima, M., Ushimaru, M., and Kawaguchi, Y. (2013). Multiple layer 5 pyramidal cell subtypes relay cortical feedback from secondary to primary motor areas in rats. *Cereb. Cortex* doi:10.1093/cercor/bht088 [Epub ahead of print].

Ushimaru, M., Ueta, Y., and Kawaguchi, Y. (2012). Differentiated participation of thalamocortical subnetworks in slow/spindle waves and desynchronization. *J. Neurosci.* 32, 1730–1746. doi: 10.1523/JNEUROSCI.4883-11.2012

Uylings, H. B., Groenewegen, H. J., and Kolb, B. (2003). Do rats have a prefrontal cortex? *Behav. Brain Res.* 146, 3–17. doi: 10.1016/j.bbr.2003.09.028

Van De Werd, H. J., and Uylings, H. B. (2008). The rat orbital and agranular insular prefrontal cortical areas: a cytoarchitectonic and chemoarchitectonic study. *Brain Struct. Funct.* 212, 387–401. doi: 10.1007/s00429-007-0164-y

Veinante, P., and Deschênes, M. (2003). Single-cell study of motor cortex projections to the barrel fields in rats. *J. Comp. Neurol.* 464, 98–103. doi: 10.1002/cne.10769

Wang, X. J. (2001). Synaptic reverberation underlying mnemonic persistent activity. *Trends Neurosci.* 24, 455–463. doi: 10.1016/S0166-2236(00)01868-3

Wilson, C. J. (1987). Morphology and synaptic connections of crossed corticostriatal neurons in the rat. *J. Comp. Neurol.* 263, 567–580. doi: 10.1002/cne.902630408

Wise, S. P., Boussaoud, D., Johnson, P. B., and Caminiti, R. (1997). Premotor and parietal cortex: corticocortical connectivity and combinatorial computations. *Annu. Rev. Neurosci.* 20, 25–42. doi: 10.1146/annurev.neuro.20.1.25

Yu, J., Anderson, C. T., Kiritani, T., Sheets, P. L., Wokosin, D. L., Wood, L., et al. (2008). Local-circuit phenotypes of layer 5 neurons in motor-frontal cortex of YFP-H mice. *Front. Neural Circuits* 2:6. doi: 10.3389/neuro.04.006.2008

Conflict of Interest Statement: The authors declare that the research was conducted in the absence of any commercial or financial relationships that could be construed as a potential conflict of interest.

Received: 25 July 2013; paper pending published: 12 August 2013; accepted: 23 September 2013; published online: 11 October 2013.

Citation: Ueta Y, Hirai Y, Otsuka T and Kawaguchi Y (2013) Direction- and distance-dependent interareal connectivity of pyramidal cell subpopulations in the rat frontal cortex. Front. Neural Circuits 7:164. doi: 10.3389/fncir.2013.00164

This article was submitted to the journal Frontiers in Neural Circuits.

frontiers in
NEURAL CIRCUITS

ORIGINAL RESEARCH ARTICLE
published: 20 August 2013
doi: 10.3389/fncir.2013.00130

Disruption of cerebellar microzonal organization in GluD2 (GluRδ2) knockout mouse

Miki Hashizume[1], Taisuke Miyazaki[2], Kenji Sakimura[3,4], Masahiko Watanabe[2,4], Kazuo Kitamura[1,5]* and Masanobu Kano[1]*

[1] *Department of Neurophysiology, Graduate School of Medicine, The University of Tokyo, Tokyo, Japan*
[2] *Department of Anatomy, Graduate School of Medicine, Hokkaido University, Sapporo, Japan*
[3] *Department of Cellular Neurobiology, Brain Research Institute, Niigata University, Niigata, Japan*
[4] *CREST, Japan Science and Technology Agency, Kawaguchi, Japan*
[5] *PRESTO, Japan Science and Technology Agency, Kawaguchi, Japan*

Edited by:
Yasuo Kawaguchi, National Institute for Physiological Sciences, Japan

Reviewed by:
Alanna Watt, McGill University, Canada
Wataru Kakegawa, Keio University School of Medicine, Japan

****Correspondence:***
Kazuo Kitamura and Masanobu Kano, Department of Neurophysiology, Graduate School of Medicine, The University of Tokyo, 7-3-1 Hongo, Bunkyo-ku 113-0033, Tokyo, Japan
e-mail: kkitamura@m.u-tokyo.ac.jp; mkano-tky@m.u-tokyo.ac.jp

Cerebellar cortex has an elaborate rostrocaudal organization comprised of numerous microzones. Purkinje cells (PCs) in the same microzone show synchronous activity of complex spikes (CSs) evoked by excitatory inputs from climbing fibers (CFs) that arise from neurons in the inferior olive (IO). The synchronous CS activity is considered to depend on electrical coupling among IO neurons and anatomical organization of the olivo-cerebellar projection. To determine how the CF–PC wiring contributes to the formation of microzone, we examined the synchronous CS activities between neighboring PCs in the glutamate receptor δ2 knockout (GluD2 KO) mouse in which exuberant surplus CFs make ectopic innervations onto distal dendrites of PCs. We performed *in vivo* two-photon calcium imaging for PC populations to detect CF inputs. Neighboring PCs in GluD2 KO mice showed higher synchrony of calcium transients than those in wild-type (control) mice. Moreover, the synchrony in GluD2 KO mice hardly declined with mediolateral separation between PCs up to ∼200 μm, which was in marked contrast to the falloff of the synchrony in control mice. The enhanced synchrony was only partially affected by the blockade of gap junctional coupling. On the other hand, transverse CF collaterals in GluD2 KO mice extended beyond the border of microzone and formed locally clustered ectopic synapses onto dendrites of neighboring PCs. Furthermore, PCs in GluD2 KO mice exhibited clustered firing (Cf), the characteristic CF response that was not found in PCs of wild-type mice. Importantly, Cf was often associated with localized calcium transients in distal dendrites of PCs, which are likely to contribute to the enhanced synchrony of calcium signals in GluD2 KO mice. Thus, our results indicate that CF signals in GluD2 KO mice propagate across multiple microzones, and that proper formation of longitudinal olivo-cerebellar projection is essential for the spatiotemporal organization of CS activity in the cerebellum.

Keywords: cerebellum, inferior olive, Purkinje cell, climbing fiber, olivo-cerebellar loop, microzone, complex spike

INTRODUCTION

The cerebellum consists of several parasagittal zonal compartments elongated along rostrocaudal direction (designated A, B, C1–3, and D1–2). These compartments are based on the topography of the olivo-cerebellar projection system that constitutes one of the two major afferent systems to the cerebellum (Groenewegen et al., 1979; Voogd and Glickstein, 1998; Sugihara et al., 2001; Sugihara, 2005). These cerebellar zones are thought to be involved in the control of different aspects of posture, movement and motor coordination (Buisseret-Delmas and Angaut, 1993; Horn et al., 2010). Moreover, several physiological studies have revealed that each cerebellar zone is composed of smaller functional units, called microzones (Andersson and Oscarsson, 1978; Lang et al., 1999; Lang, 2002; Apps and Garwicz, 2005). Detailed morphological studies have revealed that axons of neurons in the inferior olive (IO) branch into about 7 climbing fibers (CFs) along rostrocaudal axis of the cerebellum, and each CF innervates a single Purkinje cell (PC) (Sugihara et al., 1999, 2001; Sugihara and Shinoda, 2004). Experiments with a small injection of anterograde tracer into the IO have demonstrated that a small number of adjacent IO neurons project CFs within narrow longitudinal bands of about 200 μm width (Sugihara et al., 2001; Sugihara and Shinoda, 2004), which correspond to physiologically identified microzones (Lang et al., 1999). Because of this anatomical organization and electrical coupling among adjacent IO neurons, CF inputs are synchronized among PCs within a microzone, and the synchrony rapidly falls off as the mediolateral separation between PCs increases (Llinas and Yarom, 1981; Sotelo et al., 1986; Blenkinsop and Lang, 2006; Ozden et al., 2009; Schultz et al., 2009).

A major hypothesis as to the function of the olivo-cerebellar system is that CFs convey error signals to PCs between the intention and the result of movement (Ito, 2011). Defects in the olivo-cerebellar system results in impairment of motor control and coordination (Chen et al., 2010; Horn et al., 2010; Ito, 2011). It has been shown that several mutant mice that are impaired in developmental CF synapse elimination exhibit ataxia (Chen et al., 1995; Kano et al., 1995, 1998; Kashiwabuchi et al., 1995; Offermanns et al., 1997; Hirai et al., 2005b), suggesting that proper wiring of CFs to PCs is important for motor coordination. Among these examples, the mutant mouse deficient in ionotropic glutamate receptor δ2 subtype (GluD2) is best characterized by morphological, electrophysiological, and behavioral studies. GluD2 is richly expressed at dendritic spines of PCs that form synaptic contacts with terminals of parallel fibers (PFs) (Takayama et al., 1995, 1996; Landsend et al., 1997). GluD2 is essential for the formation and stabilization of PF–PC synapses by interacting with Cbln1 that binds to neurexin at PF terminals (Matsuda et al., 2010; Uemura et al., 2010). Thus, the GluD2 knockout (KO) mouse (Kashiwabuchi et al., 1995) has been shown to exhibit various defects in synaptic wiring and neuronal response: (1) the number of PF–PC synapse is reduced to nearly half of that of control mouse, which results in emergence of numerous free spines in PC distal dendrites (Kurihara et al., 1997; Ichikawa et al., 2002; Takeuchi et al., 2005), (2) CFs extend distally along PC dendrites, take over spines from PFs and form ectopic synapses on PC distal dendrites (Ichikawa et al., 2002), (3) transverse collaterals of CFs that run perpendicularly to the plane of PC dendritic tree are markedly elongated and form ectopic synapses on distal dendrites of neighboring PCs along the mediolateral axis (Miyazaki and Watanabe, 2010; Miyazaki et al., 2010), (4) stimulation of the aberrant CFs in cerebellar slices induces atypical excitatory postsynaptic responses with slow rise time and small amplitudes in PCs which are associated with calcium transients localized to distal dendritic arbors (Hashimoto et al., 2001; Miyazaki et al., 2010), and (5) PCs in GluD2 KO mice *in vivo* exhibit atypical "clustered firing (Cf)" (Yoshida et al., 2004), which is considered to be induced by ectopic CF inputs to PC distal dendrites. Thus, GluD2 KO mice provide an excellent model to study how altered CF to PC wiring affects population activity of PCs and functional microzonal organization *in vivo*.

In the present study, we employed *in vivo* two-photon calcium imaging for PC populations (Sullivan et al., 2005; Mukamel et al., 2009; Ozden et al., 2009; Schultz et al., 2009) and examined dendritic calcium signals representing CF inputs. We demonstrated that the degree of synchrony in CF inputs between neighboring PCs was much higher in GluD2 KO mice than in wild-type (control) mice. Moreover, the synchrony of CF inputs in GluD2 KO mice hardly declined with the increase in mediolateral separation between PCs, whereas the synchrony fell off within the separation of ∼200 μm in control mice, which corresponded to the width of a microzone. We also showed that the enhanced synchrony in GluD2 KO mice was mainly ascribed to the aberrant CF to PC wiring, especially to elongated transverse CF collaterals, and also presumably to altered IO firing. Thus, proper formation of CF to PC wiring is a basis for functional microzonal organization in the cerebellum.

MATERIALS AND METHODS

ANIMALS AND SURGERY

We used homozygous Grid2-Cre knock-in mice on pure C57BL/6 genetic background (Yamasaki et al., 2011) as GluD2 knockout (GluD2 KO) mice. The GluD2 KO mice and their wild-type littermates (control) were produced by mating heterozygous animal pairs. All experimental procedures were approved by Animal Experimental Committees of The University of Tokyo and Hokkaido University, and all animal experiments were performed according to the guidelines.

Male or female mice aged 1–3 months were anesthetized by intraperitoneal injection of ketamine (100 mg/kg) and xylazine (10 mg/kg). We confirmed the depth of anesthesia by monitoring the lack of whisker movements and pinch withdrawal reflex, and injected additional dose as needed. Body temperature was kept at 36°C with a heating pad (FHC). The head of the animal was fixed by ear bars and the skull was exposed by removing skins, muscles and connective tissues on it. The occipital bone at the Crus IIa region (centered 4 mm lateral and 2 mm posterior to the occipital bone line) on the left cerebellar hemisphere was drilled to make a small hole (∼2 mm in diameter). The dura matter was removed and the surface of the cerebellar cortex was cleaned with extracellular solution composed of (in mM) 150 NaCl, 2.5 KCl, 2 $CaCl_2$, 1 $MgCl_2$ and 10 HEPES (pH 7.4, adjusted with NaOH). Cortical surface was covered with 1.5% agarose dissolved in the extracellular solution, and a small coverslip was placed on half of the cranial window, in order to reduce motion artifacts caused by respiration and heart beat.

DYE INJECTION AND POPULATION CALCIUM IMAGING

Multi-cell bolus-loading of calcium indicator dye was performed as described (Stosiek et al., 2003; Sullivan et al., 2005; Mukamel et al., 2009; Ozden et al., 2009; Schultz et al., 2009). Oregon Green 488 BAPTA-1 acetoxymethyl ester (OGB-1 AM, ∼200 μM; Invitrogen), was dissolved with 10% w/v Pluronic F-127 (Invitrogen) in DMSO and filled into a glass pipette (5–7 MΩ) together with the extracellular solution containing Alexa 594 fluorescent dye (20 μM; Invitrogen). Dye ejection was performed in the cerebellar molecular layer (50–60 μm from surface) at 5 psi for 3 min by using Picospritzer (General Valve). Successful dye ejection was monitored by two-photon imaging on Alexa channel. More than 30 min after dye ejection, calcium imaging was performed in the molecular layer. To obtain calcium transients from populations of PC dendrites, images were acquired at the resolution of 256 × 64 or 128 × 128 pixels (sampling rate = ∼8 Hz) for ∼2 min. These image stacks were analyzed offline. For detecting local calcium transients in bolus-loaded specimen, line-scan imaging (sampling rate = 500 Hz) was performed on single PC dendrites.

IN VIVO TWO-PHOTON MICROSCOPY

In vivo calcium imaging was performed by using a two-photon microscope (Denk et al., 1990) controlled by PrairieView software (Ultima IV, Prairie technologies), or a custom-built two-photon microscope (Sutter Instruments) controlled by ScanImage software (Pologruto et al., 2003). The cerebellum was illuminated with a pulsed Ti:sapphire laser (MaiTai, 810–840 nm

in wavelength, 80 MHz repetition rate, 100 fsec pulse width; Spectra-Physics). Laser was focused through a 40× water-immersion objective lens (Olympus) onto the tissue. Average laser power was adjusted to be less than 20 mW at the specimen. Fluorescence signals of OGB-1 and Alexa 594 were divided into green and red channels respectively by a dichroic mirror and emission filters (Chroma), and were detected by a pair of photomultiplier tubes (Hamamatsu).

SIMULTANEOUS DENDRITIC CALCIUM IMAGING AND EXTRACELLULAR RECORDING

A glass electrode (5–7 MΩ) filled with the extracellular solution containing Alexa 594 was inserted into the cerebellum and targeted to a PC soma that had been loaded with OGB-1 AM. About 10 min after the establishment of cell-attached configuration, simultaneous extracellular unit recording and dendritic calcium imaging were performed. Electrophysiological data were obtained by Multiclamp 700B (Molecular device). The data were filtered at 10 kHz and digitized at 20 kHz using Digidata 1322A (Axon instruments) controlled by Axograph X software (AxoGraph Scientific). Simple spikes (SSs), complex spikes (CSs), and Cf (Yoshida et al., 2004) were distinguished by their characteristic waveforms. CS showed a prominent spike followed by several spikelets with smaller amplitude. The burst of 2–7 full-amplitude SS-like spikes occurred at >181 Hz (spike train with <5.5 ms of inter-spike interval) was defined as Cf according to the criterion in the previous study (Yoshida et al., 2004). After the recording session, negative current (< −20 nA) was injected into the recorded cell to rupture the membrane and to stain it with Alexa 594, and a morphological image stack for Alexa 594 was obtained to identify the dendrites of the recorded cell among multiple OGB-1 positive PC dendrites in calcium imaging data.

DRUG APPLICATION

Carbenoxolone (120 mg/kg; Sigma), an inhibitor of gap junction, was dissolved in saline (0.8% w/v) and intraperitoneally injected to mouse in which OGB-1 AM had been bolus-loaded. Then, calcium imaging was performed at every 20 min until 120 min after the drug application.

WHOLE-CELL RECORDING AND DENDRITIC CALCIUM IMAGING

For *in vivo* whole-cell current-clamp recording, we used a potassium-based intracellular solution that was composed of (in mM): 133 potassium methanesulfonate, 7.4 KCl, 10 HEPES, 3 Na_2ATP, 0.3 Na_2GTP, 0.3 $MgCl_2$, 0.05 Alexa 594, and 0.2 OGB-1 (285 mmole/kg, pH 7.2 adjusted with KOH). According to the shadowpatching method (Kitamura et al., 2008), PCs were visualized with negative contrast to obtain targeted recordings. A glass electrode (5–9 MΩ) was brought to a PC soma under visual control and a brief suction was applied to form tight gigaohm seal. Cell membrane was then ruptured by short pulses of negative pressure to establish the whole-cell configuration. At least 30 min after break-in, line-scan calcium imaging (500 Hz) on dendrite was performed at ∼100 μm from the soma and the membrane potential was simultaneously recorded.

DATA ANALYSIS

All image analysis was performed offline by using ImageJ software (http://rsb.info.nih.gov/ij/). Regions of interest (ROIs) corresponding to individual PC dendrites were manually identified. Calcium transients were obtained from time-series image stack and expressed as $\Delta F/F = (F - F_0)/(F_0 - F_b)$, where F_0 was baseline fluorescence without calcium transient and F_b was background fluorescence. The distances of mediolateral separation between PC dendrites were measured from a single high-resolution image of the recording field. The detection threshold for calcium transient was defined as 2 SD of $\Delta F/F$ for entire recording time. Cross-correlation coefficients were calculated by the formula below (Lang et al., 1996) using Igor pro software (Wavemetrics).

$$C_{ij}(\tau) = \frac{\sum_{t=0}^{T} X_{i(t)} X_{j(t+\tau)}}{\sqrt{\sum_{t=0}^{T} \{X_{i(t)}\}^2 \sum_{t=0}^{T} \{X_{j(t)}\}^2}}$$

where, X_i and X_j were calcium transient traces of ith and jth dendrites, T was total recording time and τ was lag time between the 2 traces. $C_{ij}(0)$, cross-correlation coefficient at zero lag time, was defined as synchrony. All the averaged data were represented as mean ± s.e.m. Statistical significance of the data was examined by Mann–Whitney U test unless otherwise noted, and all tests were performed using Sigmastat 3.1 (Cranes Software International) or R (http://www.r-project.org/).

ANTEROGRADE TRACER LABELING

Mice at P56 were anesthetized by intraperitoneal injection of chloral hydrate (350 mg/kg) and head-clamped by a stereotaxic instrument (SR-5N; Narishige). A glass pipette filled with 2–3 μl of 10% solution of dextran Alexa 594 (DA-594; Invitrogen) in PBS was inserted into the IO by dorsal approach. The tracer was injected by air pressure at 20 psi with 5 s intervals for 1 min (Pneumatic Picopump; World Precision Instruments). After 4 days of survival, mice were anesthetized by intraperitoneal injection of pentobarbital (100 mg/kg) and transcardially perfused with 4% paraformaldehyde in 0.1 M sodium phosphate buffer (pH 7.4). After excision from the skull, brains were further immersed overnight in the same fixative. Horizontal cerebellar sections with 50 μm thickness were prepared using a microslicer (VT1000S; Leica).

IMMUNOHISTOCHEMISTRY

Horizontal cerebellar sections were obtained from 3 GluD2 KO and 3 control mice. All immunohistochemical incubations were done at room temperature in a free-floating state. At first, cerebellar sections were incubated with 10% normal donkey serum for 20 min. Then, a mixture of primary antibodies, including a guinea pig anti-vesicular glutamate transporter 2 (VGluT2) antibody and a rabbit anti-aldolase C (aldC) antibody, was applied to slices overnight, followed by an incubation with Alexa 488- and Cy5-conjugated species-specific secondary antibodies (Invitrogen; Jackson ImmunoResearch) for 2 h at a

dilution of 1:200. Images of stained molecular layer were taken with a confocal laser scanning microscope (FV1000; Olympus) equipped with digital camera (DP70; Olympus), and analyzed with MetaMorph software (Molecular Devices).

RESULTS

HIGHLY SYNCHRONOUS SPONTANEOUS CALCIUM TRANSIENTS IN NEIGHBORING PCs IN GluD2 KO MICE

In rats and mice, spontaneous calcium transients in PC dendrites *in vivo* have been shown to be attributed to CSs evoked by CF input (Sullivan et al., 2005; Ozden et al., 2008, 2009; Mukamel et al., 2009; Schultz et al., 2009; Kitamura and Häusser, 2011). To compare the spatial pattern of CS firing in PCs of GluD2 KO mice with that of wild-type control mice, OGB-1 AM was bolus-loaded into the molecular layer of the cerebellar cortex (Ozden et al., 2008, 2009; Mukamel et al., 2009; Schultz et al., 2009). About 30 min after dye-loading, OGB-1 was penetrated into various cell types, including PCs, interneurons, and Bergmann glia. In the molecular layer, dendrites of PCs extending along rostrocaudal axis were clearly observed (**Figure 1A**). Spontaneous fluorescence changes induced by calcium influx were observed in individual PC dendrites. In control mice, calcium transients occurred at various timing in each dendrite with occasional highly synchronized transients between neighboring dendrites (**Figure 1B**, upper), which is consistent with the previous results (Sullivan et al., 2005; Ozden et al., 2008, 2009; Mukamel et al., 2009; Schultz et al., 2009). In contrast, almost all calcium transients in GluD2 KO mice occurred at the same timing in all of the dendrites observed (**Figure 1B**, lower). Cross-correlation coefficient was calculated to quantify synchronous activity between neighboring PCs (**Figure 1C**), and the relationship between the synchrony and the distance between the dendrites in mediolateral direction was analyzed for all dendritic pairs in the field of view (**Figure 1D**). As previously reported, synchrony in control mice fell off as the mediolateral separation between PC dendrites increased (Ozden et al., 2009; Schultz et al., 2009). In marked contrast, the synchrony in GluD2 KO mice was almost constant at all the distances of mediolateral separation examined. On average, the synchrony in GluD2 KO mice was significantly higher than that in control mice at all the distances of mediolateral separation (1064 dendrite pairs in 26 GluD2 KO mice and 1009 pairs in 33 control mice, $p < 0.001$ in Two-Way ANOVA) (**Figure 2A**), and the rate of decline in synchrony was smaller in GluD2 KO mice than in control mice (**Figure 2B**). These results indicate that the synchrony of spontaneous CSs among neighboring PCs is greatly enhanced in GluD2 KO mice, and the spatial range of synchrony is extended in mediolateral direction.

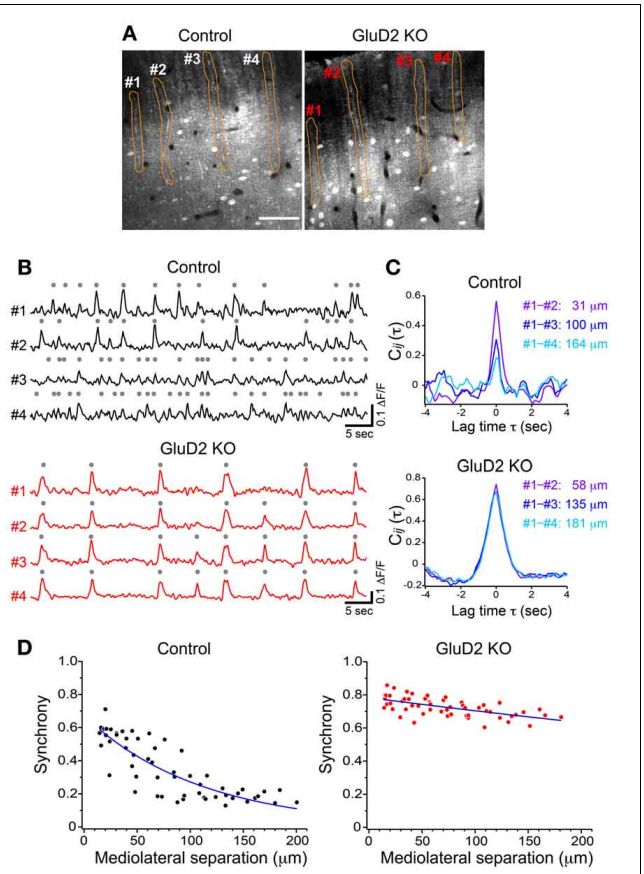

FIGURE 1 | Synchrony of spontaneous calcium transients in control and GluD2 KO mice. (A) Fluorescence images showing the molecular layer of the cerebellar cortex labeled with OGB-1 AM in control and GluD2 KO mice. PC dendrites are seen as gray bands that extend along the rostrocaudal axis and aligned perpendicular to the mediolateral axis. Spontaneous calcium transients were obtained by monitoring fluorescence changes of the specified regions of interest (ROIs; orange). Scale bar, 50 μm. **(B)** Representative traces of calcium transient from 4 dendrites (#1 – #4) that correspond to the ROIs in **(A)**. Gray dots indicate detected calcium transients from the baseline noise. **(C)** Cross-correlation coefficients for the traces in **(B)** were calculated between #1 and the other dendrites, and the distances along the axis (mediolateral separation) between the dendrites were measured. Synchrony (i.e., the cross-correlation at zero lag time, see Materials and Methods) in control mice was the highest at the nearest neighboring pair, and gradually decreased as the mediolateral separation increased. In marked contrast, synchrony in GluD2 KO mice was almost constant regardless of the mediolateral separation. **(D)** Summary graphs for the synchrony between all dendrite pairs plotted against the mediolateral separations from the control and GluD2 KO mice shown in **(A)** (55 dendrite pairs). Blue curves indicate the exponential fit to the data.

RELATIONSHIP BETWEEN CALCIUM TRANSIENT AND CF INPUT IN GluD2 KO MICE

In addition to the enhancement of the synchrony between calcium transients of neighboring PCs, we found that the frequency of calcium transient in GluD2 KO mice was lower than that in control mice (0.15 ± 0.01 Hz and 0.29 ± 0.02 Hz, respectively; 11 mice each, $p < 0.001$) (**Figure 1B**), and the half-width of transients was larger in GluD2 KO mice than in control mice (0.710 ± 0.01 s and 0.517 ± 0.01 s, respectively; 5 mice each, $p < 0.001$), suggesting that the temporal pattern of CS firing is altered in GluD2 KO mice. Therefore, simultaneous dendritic calcium imaging and extracellular recordings were performed on single PCs to clarify the electrophysiological correlates of calcium transients (**Figure 3A**). Cell-attached recordings in both control and GluD2 KO mice showed ongoing SSs and sporadic CSs (**Figure 3B**). The mean firing rates of SS (22.12 ± 5.39 Hz in control and 17.19 ± 2.33 Hz in GluD2 KO mice) and CS

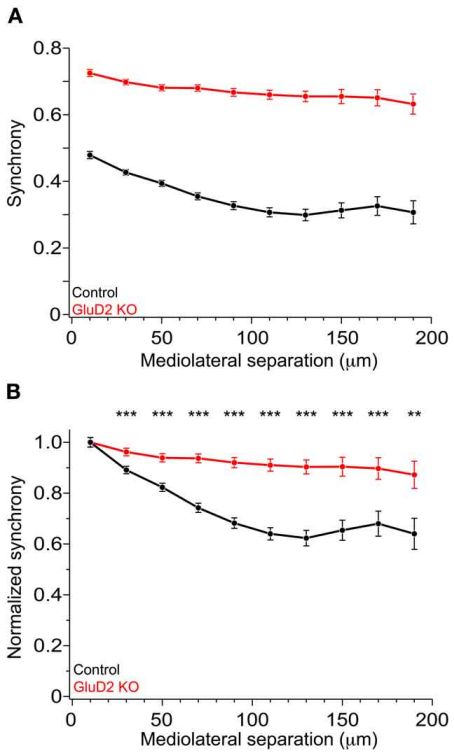

FIGURE 2 | Enhanced synchrony between dendrite pairs of GluD2 KO mice at all the distances of mediolateral separation. (A) Summary graph showing pooled data of synchrony plotted against the mediolateral separation for 1009 dendrite pairs obtained from 33 control mice (black symbols) and for 1064 dendrite pairs from 26 GluD2 KO mice (red symbols). Each data point represents the average of synchrony and error bars indicate SEM. There was significant difference between the two genotypes ($p < 0.001$ by Two-Way ANOVA). **(B)** All values of synchrony were normalized by the mean value of the nearest dendrite pairs within the mediolateral separation of 20 μm. There were significant differences between the two genotypes in all but the nearest pairs (**$p < 0.01$, ***$p < 0.001$ by Two-Way ANOVA and Tukey test), indicating that the degree of decline in synchrony in the mediolateral direction is much smaller in GluD2 KO mice than that in control mice.

(0.32 ± 0.04 Hz in control and 0.40 ± 0.03 Hz in GluD2 KO mice) were not significantly different between the two genotypes (13 mice each; $p > 0.09$ and $p > 0.1$, respectively). Although calcium transients were induced by CS in both genotypes (**Figures 3C,D**), each calcium transient in GluD2 KO mice tended to be associated with multiple successive CSs. The fraction of calcium transients induced by multiple CSs was significantly higher in GluD2 KO mice than in control mice (**Figure 3E**, $p < 0.001$ in χ^2 test). Besides, the histogram of inter-CS interval clearly showed that CSs in GluD2 KO mice were induced in rapid succession with short interval (**Figure 3F**). These results indicate that the lower frequency and longer duration of calcium transients in GluD2 KO mice were attributed to the altered CS firing pattern.

Atypical responses, termed "Cf" (Yoshida et al., 2004), were observed only in GluD2 KO mice at similar frequency to CS firing rate (0.39 ± 0.09 Hz in 11 mice; $p > 0.1$; see Materials and Methods for the definition of Cf). Cf was thought to be induced by aberrant CF input (Yoshida et al., 2004). Cfs showed similar or even shorter inter-Cf intervals than CS (**Figure 3F**). Moreover, most Cfs occurred temporally close to CS (**Figures 3D,G**). These results suggest that the firing pattern of IO neurons is altered in GluD2 KO mice such that bursts of CSs/Cfs frequently occur in PCs.

THE EFFECT OF GAP JUNCTIONAL COUPLING ON ENHANCED SYNCHRONY OF CS ACTIVITY IN GluD2 KO MICE

According to previous reports, altered modulatory inputs in the IO by pharmacological manipulation causes change in rhythmicity and synchrony of CS firing (Llinas and Sasaki, 1989; Lang et al., 1996; Lang, 2002). To examine whether the change in electrical coupling among IO neurons made significant contribution to the enhanced synchrony of CS firing in GluD2 KO mice, carbenoxolone, a non-selective blocker of connexin, was intraperitoneally injected during calcium imaging experiments. Although systemic application of carbenoxolone has been reported to cause various effects on whole mouse body (Rozental et al., 2007), a previous study demonstrates that it has no effects on PC firing (Cheron et al., 2004). About 1 h after drug application, synchronized calcium transients were reduced in both control and GluD2 KO mice (**Figures 4A,B**). As a result, the average synchrony significantly decreased (from 0.48 ± 0.04 to 0.34 ± 0.02 in 8 control, $p = 0.002$ by paired t-test; from 0.73 ± 0.03 to 0.55 ± 0.04 in 5 GluD2 KO mice, $p = 0.003$). The degree of reduction in the synchrony by carbenoxolone injection was not significantly different between the two genotypes (0.14 ± 0.03 in control and 0.18 ± 0.03 in GluD2 KO mice; $p > 0.1$). Therefore, the values of synchrony at all the distances of mediolateral separation in GluD2 KO mice were still larger than those in control mice even though electrical couplings in IO neurons were inhibited (**Figure 4B**; $p < 0.001$ by Two-Way ANOVA). When the synchrony values were normalized to those within 20 μm separation, the rate of decline in the synchrony along the mediolateral axis remained much smaller in GluD2 KO mice than in control mice after carbenoxolone application (**Figure 4C**). While carbenoxolone enhanced the rate of decline in the synchrony along the mediolateral axis to some extent in control mice, it had much smaller effect in GluD2 KO mice (**Figure 4D**). These results indicate that the enhancement of synchrony in the mediolateral direction is likely to be attributable largely to mechanisms other than gap junctional coupling in IO neurons.

MULTI-ZONAL PROJECTION OF TRANSVERSE BRANCHES FROM ASCENDING CF IN GluD2 KO MICE

We hypothesized that the enhanced mediolateral synchrony in GluD2 KO mice was due to disorganized olivo-cerebellar projection by the persistent multiple CF innervation (Kashiwabuchi et al., 1995; Hashimoto et al., 2001; Ichikawa et al., 2002; Miyazaki et al., 2010). Immunohistochemical labeling of CF terminals combined with tracer injection into the IO has revealed that dendrites of PCs in GluD2 KO mice make contact with glutamatergic terminals from ascending CFs as well as from transverse collaterals of neighboring ascending CFs (Ichikawa et al., 2002; Miyazaki et al., 2010). Thus, these aberrant transverse branches were assumed to contribute to the enhanced mediolateral synchrony

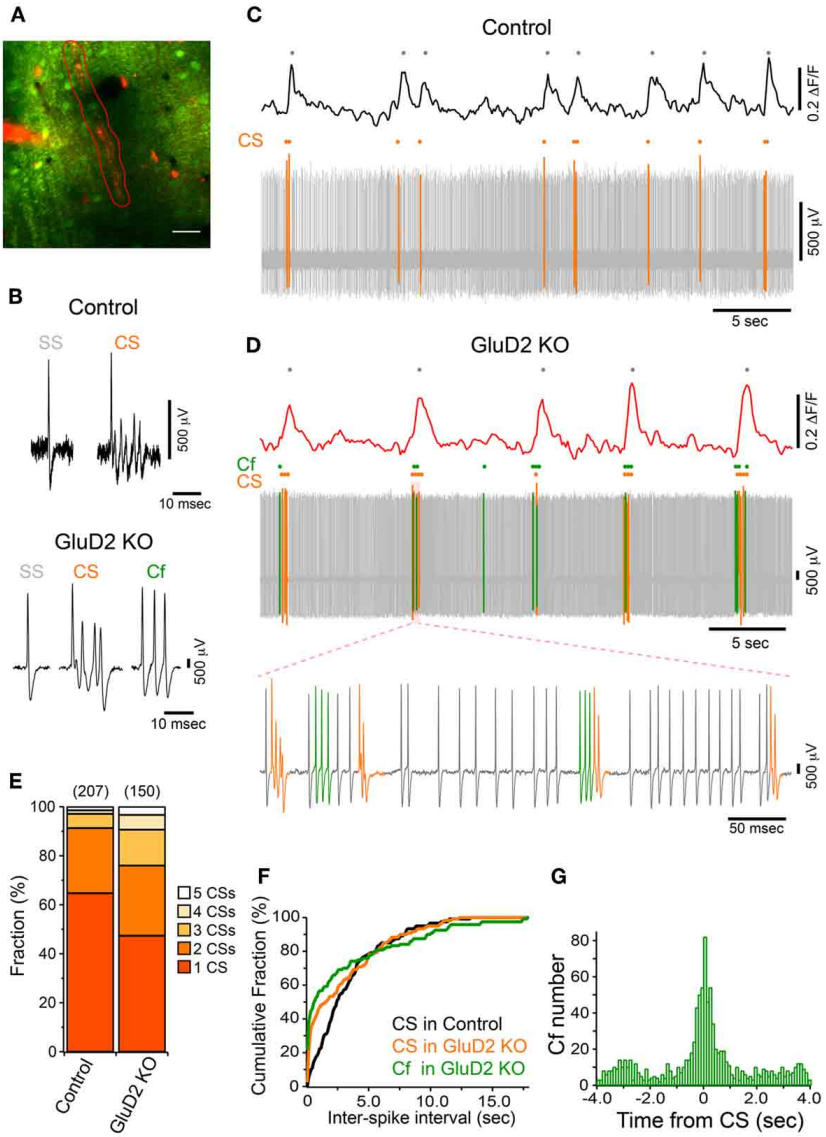

FIGURE 3 | Altered CF activity patterns in GluD2 KO mice. (A) Representative image showing the molecular layer that was loaded with OGB-1 AM in a GluD2 KO mouse. Simultaneous cell-attached recording and dendritic calcium imaging from single PCs were performed. After the recording, Alexa 594 was injected through the patch pipette to the PC from which cell-attached recording was conducted. Spontaneous calcium transients were obtained from the ROI enclosed by red line. Scale bar, 20 μm. **(B)** Sample traces for simple spike (SS), complex spike (CS), and clustered firing (Cf) under cell-attached recordings from control (upper panel) and GluD2 KO (lower panel) mice. Cf was not observed in control mice. **(C)** Simultaneous recording of PC firing and dendritic calcium transients in a control PC. Note that all the calcium transients are associated with CSs. **(D)** Simultaneous recording of PC firing and dendritic calcium transients in the PC shown in **(A)**. SS, CS, and Cf are indicated in gray, orange, and green, respectively. Note that calcium transients are elicited only when CS occurs, or when CS and Cf fire in cluster. The bottom trace shows clustered CS and Cf in an expanded timescale. In this period, a single calcium transient included multiple CSs and Cfs that fired in temporal proximity. **(E)** Bar chart showing the proportion of calcium transient induced by 1–5 CSs. The fraction of each component was significantly different between control and GluD2 KO mice (4 mice for each genotype; $p < 0.001$ by χ^2 test). The numbers in parentheses indicate the number of calcium transients. **(F)** Cumulative probability plot of inter-spike intervals for CS and Cf. Each curve is composed of 120 intervals obtained from 6 mice for each genotype. Curves for CS and Cf in GluD2 KO mice were significantly different from the curve for CS in control mice ($p < 0.001$ by K-S test). Moreover, there was a significant difference between the curve for CS and that for Cf in GluD2 KO mice ($p = 0.004$ by K-S test). Bin width, 100 ms. **(G)** Cross-correlogram of Cf against CS was constructed using the data from 8 GluD2 KO mice. Note that a prominent peak is present at 0 s. Bin width, 25 ms.

beyond the proper range of microzone in GluD2 KO mice. To elucidate whether CFs projecting to a microzone could extend their transverse branches to neighboring microzones in GluD2 KO mice, we examined the relationship between the extension of CF transverse branches and the expression pattern of aldolase C (aldC) in PCs. AldC is expressed in PCs aligned in longitudinal stripes (Hawkes and Leclerc, 1987; Brochu et al., 1990; Sugihara and Quy, 2007), and the tight link between aldC compartments

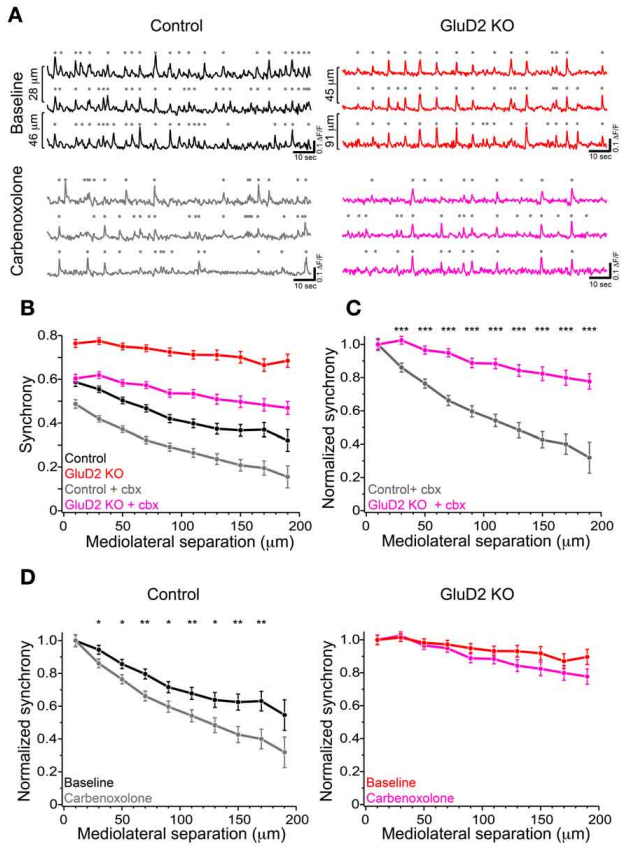

FIGURE 4 | Carbenoxolone reduced the synchrony but little altered the degree of decline along the mediolateral axis in GluD2 KO mice. (A) Three representative traces of calcium transient from neighboring PC dendrites before (baseline) and ∼1 h after carbenoxolone injection (carbenoxolone), obtained from control (left) and GluD2 KO (right) mice. Distances of mediolateral separation between dendrites are indicated on the left of the traces. In both genotypes, synchronous calcium transients were apparently reduced in frequency by carbenoxolone. **(B)** Summary graph showing pooled data of synchrony for 318 dendrite pairs obtained from 8 control mice and for 267 dendrite pairs from 5 GluD2 KO mice. Carbenoxolone (cbx) injection reduced mean values of synchrony in both genotypes. It should be noted that the difference between the genotypes was highly significant after carbenoxolone injection [control + cbx (gray) vs. GluD2 KO + cbx (magenda), $p < 0.001$ by Two-Way ANOVA], as was before drug application (control (black) vs. GluD2 KO (red), $p < 0.001$ by Two-Way ANOVA). **(C)** Normalized synchrony curves of control and GluD2 KO mice after carbenoxolone injection. The rate of decline against the mediolateral separation was significantly smaller in GluD2 KO mice than that in control mice (***$p < 0.001$ by Two-Way ANOVA and Tukey test). **(D)** Normalized synchrony curves before and after carbenoxolone injection plotted for control (left graph) and GluD2 KO (right graph) mice. In control mice, synchrony was significantly decreased by carbenoxolone at all but the nearest and the farthest points of separation, whereas in GluD2 KO mice, significant differences were not detected at all points of mediolateral separation points (*$p < 0.05$, **$p < 0.01$ by Two-Way ANOVA and Tukey test).

and CF projections and CS synchrony have been shown in previous studies (Voogd et al., 2003; Sugihara and Shinoda, 2004; Voogd and Ruigrok, 2004; Pijpers et al., 2005; Sugihara et al., 2007).

A small amount of dextran Alexa 594 (DA594) was injected into a certain subnucleus of the IO in order to visualize the trajectories of subsets of CFs and their innervation patterns. After 4 days of survival, mice were sacrificed, brains were removed and cerebellar sections were prepared. The sections were immunostained for aldC, type 2 vesicular glutamate transporter (VGluT2, a CF terminal marker) and DA594. In control mice, ascending CFs had a few short transverse branches (**Figures 5A2**,**B2**) that had no detectable VGluT2-positive puncta (**Figures 5A1**,**B1**). These short processes ($20.9 \pm 1.2\,\mu m$; 3.6–$107.5\,\mu m$; $n = 188$) originated from an aldC-negative zone and did not reach the neighboring aldC-positive zone (**Figures 5A**,**B**), and vice versa. By contrast, much longer transverse branches (**Figure 5G**; $46.9 \pm 3.0\,\mu m$; 5.3–$176.8\,\mu m$; $n = 135$, $p < 0.001$) containing many VGluT2-positive puncta were observed in GluD2 KO mice (**Figures 5C–F**). These branches bifurcated from ascending CFs located in an aldC-positive (**Figures 5C**,**D**) or -negative (**Figures 5E**,**F**) zone, and elongated toward neighboring zones. Furthermore, they made synaptic connections with multiple PCs aligned in the mediolateral axis beyond the border of aldC compartments (**Figures 5D**,**F**). Notably, 28.1% (38/135) of total transverse branches in GluD2 KO mice had numerous excitatory terminals to broad region of PC dendrites in the neighboring zones (**Figure 5F**; red and yellow arrowheads), whereas no such branch was observed in control mice (0/188) (**Figure 5H**). These morphological data strongly suggest that PCs within a certain microzone receive inputs from ascending CFs in that microzone and from CF transverse collaterals originating from neighboring microzones in GluD2 KO mice.

CALCIUM TRANSIENTS IN DISTAL DENDRITES INDUCED BY ABERRANT CF INPUTS IN GluD2 KO MICE

To examine whether ectopic CF branches, including transverse branches can induce detectable calcium transient *in vivo*, simultaneous somatic whole-cell recordings and calcium imaging at distal dendrite were performed on single PCs in GluD2 KO mice (**Figure 6A**). SS, CS and Cf were detected in current-clamp recordings (**Figure 6B**). High-speed line-scan imaging (2 ms/line) was performed to detect individual calcium transients, because half of the CSs and Cfs occurred with subsecond interspike interval (**Figure 3F**). CSs induced calcium transients over the entire dendritic arbor (**Figures 6C1**,**C2**—orange traces and columns), which was the same as in control mice and in rats (Kitamura and Häusser, 2011). By contrast, Cfs induced calcium transients only at a restricted region of distal dendrites (**Figure 6C**). As exemplified in **Figure 6C**, Cf-evoked transients were consistently observed only in the lower dendritic region (**Figures 6C1**,**C2**—left panel, green trace and column) and virtually no calcium signals were detected in the upper dendritic region (**Figures 6C1**,**C2**—right panel, green trace and column). This result is very similar to that obtained in cerebellar slice preparations from GluD2 KO mice (Hashimoto et al., 2001) in which stimulation of surplus weak CFs induced calcium transients restricted to small regions of distal dendritic arbors of PCs. It should be noted that, although Cf-evoked calcium transients were spatially localized, no significant difference was found between the amplitudes of calcium transients evoked by Cf and

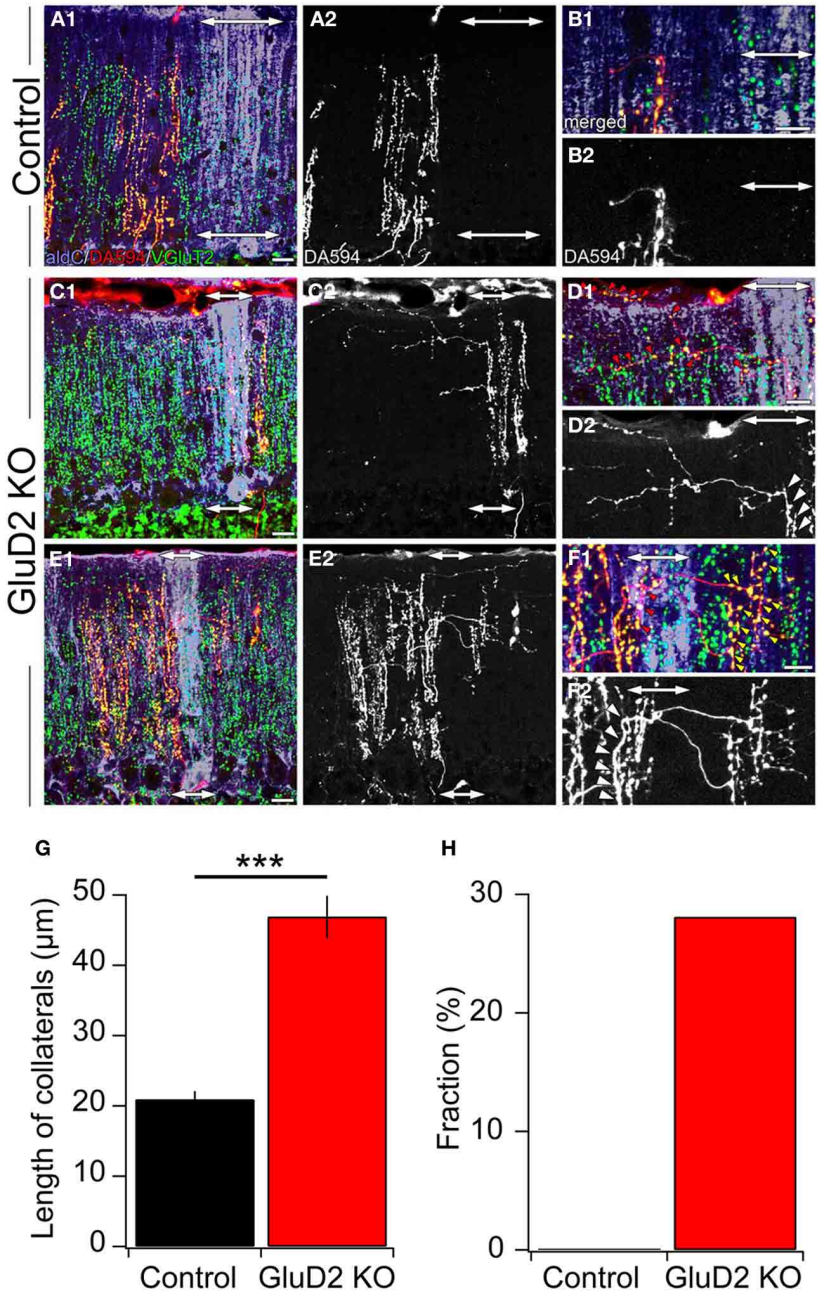

FIGURE 5 | Ectopic CF innervations beyond the zones in GluD2 KO mice. **(A)** Photomicrographs of a horizontal section of cerebellar cortex from a control mouse. In **(A1)**, aldC (purple) and VGluT2 (green) positive structures are present beside CFs labeled with DA594 (red). Double-headed arrows indicate the region in which aldC-positive PCs are localized. In this case, the tracer was taken up by CFs projecting to an aldC-negative zone. **(A2)** is the same section as **(A1)** but shows DA594-labeled CFs only. **(B)** Magnified pictures of the outer molecular layer near the pial surface in **(A1)** and **(A2)**. There are short transverse CF collaterals that lack VGluT2-positive puncta and do not reach the adjacent aldC-positive zone. **(C)** Photomicrographs of a horizontal section of cerebellar cortex from a GluD2 KO mouse. In this case, transverse CF collaterals bifurcate from ascending CFs that project to aldC-positive PCs. Note that transverse CF collaterals extend toward the adjacent aldC-negative zone. **(D)** Magnified pictures of the outer molecular layer near the pial surface in **(C1)** and **(C2)**. Red arrowheads in **(D1)** indicate VGluT2-positive glutamatergic terminals of transverse CF collaterals that form synaptic contacts onto multiple PCs. White arrowheads in **(D2)** indicate the origins of transverse CF collaterals. **(E)** Photomicrographs of a horizontal section of cerebellar cortex in another GluD2 KO mouse. In this case, transverse CF collaterals bifurcate from ascending CFs that innervate aldC-negative PCs and extend toward the next aldC-negative zone beyond the adjacent aldC-positive zone. **(F)** Magnified pictures of the outer molecular layer near the pial surface in **(E1)** and **(E2)**. Red and yellow arrowheads in **(F1)** indicate VGluT2-positive glutamatergic terminals of transverse CF collaterals that form numerous synaptic contacts onto aldC-positive and aldC-negative PCs, respectively. White arrowheads in **(F2)** indicate the origins of transverse CF collaterals. Scale bar, 20 μm in **(A,C,E)**; 10 μm in **(B,D,F)**. **(G)** Length of transverse CF collaterals was significantly longer in GluD2 KO mice than in control mice (***$p < 0.001$). **(H)** Fraction of transverse branches, which had numerous excitatory terminals to broad region of PC dendrites in the neighboring zones.

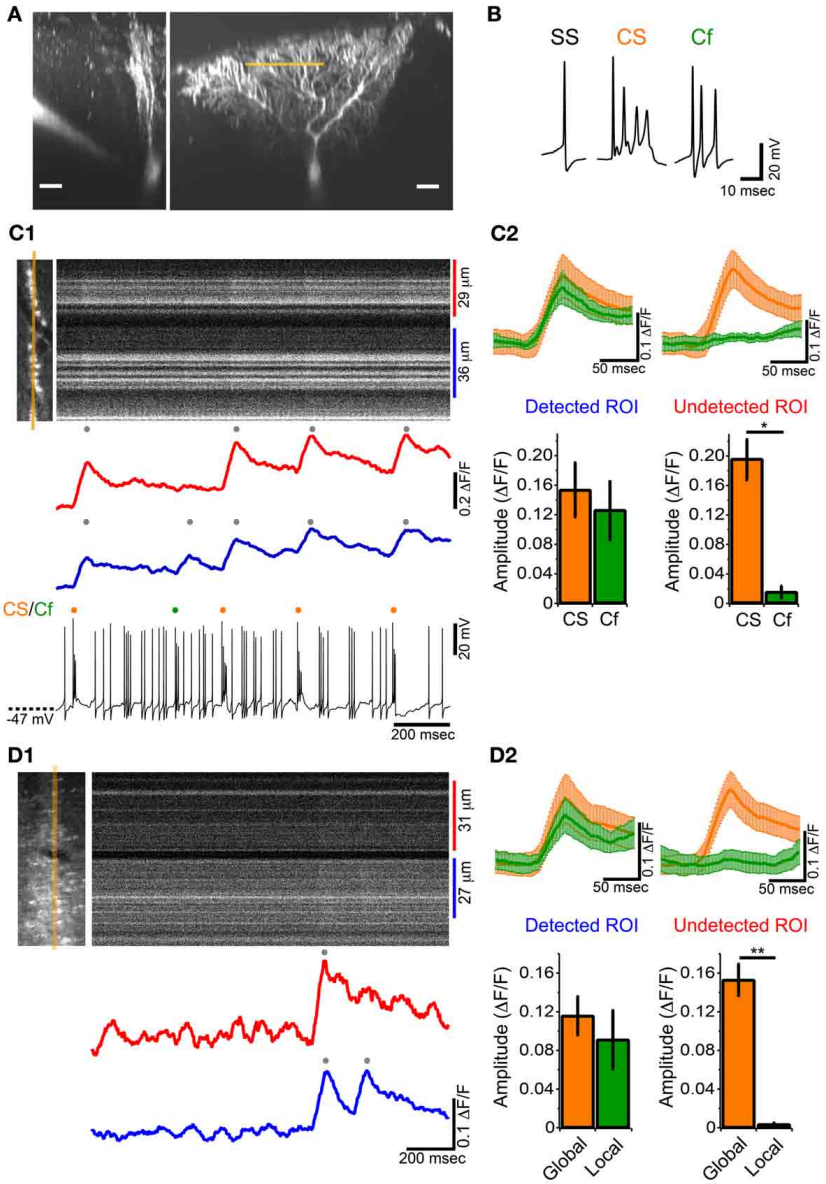

FIGURE 6 | Local calcium transient induced by Cf in GluD2 KO mice. (A) Fluorescence images showing a whole-cell patch-clamped PC of a GluD2 KO mouse in transverse (left) and sagittal (right) views that were taken more than 30 min after filling of OGB-1 and Alexa 594 through the patch pipette. Line-scan calcium imaging was performed at distal dendrite (~100 μm from the soma) indicated by orange line. Scale bar, 20 μm. **(B)** Sample traces of simple spike (SS), complex spike (CS), and clustered firing (Cf) under current-clamp recording from a GluD2 KO mouse. **(C1)** Simultaneous whole-cell recording and line-scan calcium imaging was obtained from the PC shown in **(A)**. Left image indicates the location of line-scan (orange line). ROIs were determined so that local calcium transients could be maximally recorded. The blue trace was obtained from the lower ROI in which local calcium transient was recorded, and the red trace was obtained from the upper ROI in which no local calcium transients were detected for Cf. The onset of local calcium transient coincided with the time when Cf occurred. **(C2)** (upper panels) Average traces of calcium transients induced by CS (orange trace) and by Cf (green trace) in the ROI from which Cf-evoked local calcium transients were detected (Detected ROI) and in the other ROI of the same PC in which Cf-evoked local calcium transients were absent (Undetected ROI). CS- or Cf-evoked calcium transients are shown as mean ± s.e.m from 4 GluD2 KO mice. Note that the magnitude and time course of Cf-evoked calcium transient in the detected ROI was comparable to those of CS-evoked calcium transient (lower panels). Bar graphs showing the magnitudes of calcium transients in the detected ROI (left) and undetected ROI (right). There was no significant difference in magnitude between CS-evoked and Cf-evoked calcium transients in the detected ROI (left, $p > 0.1$). By contrast, there was no detectable fluorescence change in the undetected ROI when Cf occurred (right; $^{*}p = 0.03$). **(D1)** Line-scan imaging on a PC distal dendrite from a GluD2 KO mouse that was stained by bolus-loading of OGB-1 AM. Left picture indicate the location for line-scan (orange line). A local calcium transient was detected in the lower ROI (blue trace) but was absent in the upper ROI (red trace). **(D2)** Average traces of calcium transients (upper panels, from 5 GluD2 KO mice) and bar graphs showing the magnitudes of global and local calcium transients (lower panels) for the ROI from which local calcium transients were recorded (Detected ROI) and for the ROI in which local calcium transients were absent (Undetected ROI). Data are illustrated similarly to **(C2)**. There was no significant difference in magnitude between global and local calcium transients in the detected ROI. There was no detectable fluorescence change in the undetected ROI (right; $^{**}p = 0.008$) at the time when local calcium transients occurred in the detected ROI.

those by CS in the same dendritic regions (**Figure 6C2**, left panel). Importantly, Cfs and localized calcium transients were not detected in control mice (11 mice).

We also found that localized calcium transients could be detected in PC dendrites of GluD2 KO mice that were filled with OGB-1 AM by bolus-loading method (**Figure 6D**). In the case shown in **Figure 6D1** and upper panel of **Figure 6D2**, a calcium transient that was detected in both the upper and lower dendritic regions (**Figure 6D1**, red and blue traces; **Figure 6D2** upper panel, orange traces) was followed by another calcium transient that was confined to the lower dendritic region (**Figure 6D1**, blue trace; **Figure 6D2** upper panel, green traces). The summary data demonstrated that global and localized calcium transients were present in PC dendrites of GluD2 KO mice (**Figure 6D2** lower panel). The global and localized calcium transients of PCs in GluD2 KO mice by bolus-loading of OGB-1 AM (**Figure 6D**) were very similar to CS-evoked and Cf-evoked calcium transients, respectively, in whole-cell recorded PCs in GluD2 KO mice (**Figure 6C**). Since aberrant CF inputs to PCs in GluD2 KO mice are thought to induce Cfs in intact cerebellum (Yoshida et al., 2004) and local calcium transients in cerebellar slices (Hashimoto et al., 2001), these results indicate that the localized calcium transients were induced, at least in part, by aberrant CF inputs from transverse branches. The amplitudes of these localized calcium transients were comparable to those of the global calcium transients (**Figures 6C2**,**D2**). Therefore, the localized calcium transients elicited by CF transverse collaterals are likely to contribute to the enhanced synchrony of PC activity along the mediolateral axis.

DISCUSSION

In the present study, we demonstrated that PCs within a given microzone in GluD2 KO mice showed higher synchrony of CF activities than in control mice, and the synchrony remained high even when the mediolateral separation increased. The enhancement of synchrony in mediolateral direction was ascribed to the local calcium transients evoked by Cfs that frequently occurred in close succession to the global calcium transients evoked by CSs. These local calcium transients were likely to be induced by aberrant CF branches, including transverse collaterals elongated along the mediolateral axis beyond the border of cerebellar zones.

ORIGIN OF THE MEDIOLATERAL ENHANCEMENT OF CS SYNCHRONY IN GluD2 KO MICE

It has been demonstrated that surplus weak CF input can induce localized calcium transients in distal dendrites of PCs in cerebellar slice preparations from GluD2 KO mice (Hashimoto et al., 2001). A recent morphological study also showed that ectopic CF branches in GluD2 KO mice innervate limited areas in the distal dendritic tree of PCs, and that transverse CF collaterals elongating in the outer molecular layer near the pial surface have glutamatergic terminals around dendrites of multiple neighboring PCs (Miyazaki and Watanabe, 2010). These elongated transverse CF collaterals and ectopic synapse formation occur mutually among neighboring PCs (Miyazaki and Watanabe, 2010). Thus, CFs of GluD2 KO mice are considered to activate their main target PCs through ascending main branches and also neighboring PCs through transverse collaterals. Spike discharges of IO neurons in GluD2 KO mice can induce global dendritic calcium transients associated with CSs in their main target PCs, and also induce local dendritic calcium transients associated with Cfs in neighboring PCs (**Figure 6**). Furthermore, we found that Cfs tended to be induced in a rapid succession (**Figure 3F**) in close proximity to the occurrence of CS (**Figure 3G**). At a whole PC level, bursts of Cfs are triggered by several aberrant branches from surrounding CFs and can induce local calcium transients in various dendritic regions of the same PC simultaneously. These clustered "local" calcium signals are closely correlated in time with the CS-evoked "global" calcium signals observed in other neighboring PCs, and thus significantly contribute to the enhanced synchrony in the mediolateral direction.

In contrast to the aberrant CF–PC wiring, the gap junctional coupling between IO neurons seemed less important for the enhanced mediolateral synchrony of CF activity in GluD2 KO mice (**Figures 4C**,**D**). However, the synchrony between adjacent PCs (distance between dendrites $= 20\,\mu m$) of GluD2 KO mice was reduced to the level of control mice by application of a gap junction blocker (**Figure 4B**). This result indicates that the gap junctional coupling among IO neurons contributes significantly to the enhanced synchrony among adjacent PCs in GluD2 KO mice.

CHANGE IN FIRING PATTERNS OF PCs AND ITS POSSIBLE IMPACTS ON ACTIVITIES OF THE OLIVO-CEREBELLAR LOOP IN GluD2 KO MICE

We found that not only spatial pattern but also temporal pattern of CF activity was altered in GluD2 KO mice (**Figure 3**) as reported previously (Yoshida et al., 2004). This alteration in firing pattern was also important for the enhanced synchrony in mediolateral direction. Previous studies demonstrated that firing patterns of IO neurons are modulated by glutamatergic and GABAergic inputs (Lang et al., 1996; Lang, 2002). These inputs are elements of the olivo-cerebellar feedback loop composed of IO, PCs and deep cerebellar nuclei (DCN). IO neurons send their axons to PCs in specific cerebellar zones and their axon collaterals to specific groups of DCN neurons that receive inhibitory inputs from the same PCs to which the same IO neurons project. A part of DCN neurons in turn send inhibitory signals back to the IO (De Zeeuw et al., 1989; Lang et al., 1996; Chen et al., 2010). On the other hand, another population of DCN neurons send excitatory inputs to mesodiencephalic nuclei, such as the red nucleus and the nucleus of Darkschewitsch, which send excitatory signals back to the IO (De Zeeuw et al., 1998). Our results suggest that these excitatory and inhibitory inputs to the IO are likely to be altered by the change in spatial and temporal patterns of CF responses of PCs in GluD2 KO mice. In addition to typical CF response (CS), PCs in GluD2 KO mice showed a characteristic burst of action potentials (Cf), which is most likely due to surplus weak CF inputs arising from aberrant transverse CF collaterals (Yoshida et al., 2004). A Cf is a burst of 2–7 full spikes at a firing rate of >180 Hz, whereas a CS consists of a single full spike followed by several smaller spikelets (**Figure 3B**). As previously shown by simultaneous somatic and axonal recordings from PCs in cerebellar slice preparations, PC axons can transmit SSs with high fidelity at >200 Hz, whereas they cannot faithfully

transmit the secondary spikelets in CS (Khaliq and Raman, 2005; Monsivais et al., 2005). Therefore, weak surplus CF inputs, which induce Cfs, would have significant or even larger impact on the output of PC to DCN, compared with strong main CF inputs that induce typical CSs. Furthermore, CS and Cf in GluD2 KO mice fired in burst (2–16 CS/Cf at 6–12 Hz), even though the mean firing rate was not significantly different from the CS firing rate of control mice. Given the highly convergent nature of connections between PCs and DCN neurons (Palkovits et al., 1977), spatial enhancement of synchrony and temporal clustering of CF activity in PCs would have striking effects on the firings of DCN neurons in GluD2 KO mice. Since synchronized CSs in PCs within a microzone can induce strong hyperpolarization followed by rebound spiking in corresponding DCN neurons (Bengtsson et al., 2011), DCN neurons in GluD2 KO mice are likely to show strong rebound burst firings in response to synchronized CS/Cf clusters. Such burst firings of DCN neurons may generate burst spiking in IO neurons through the excitatory pathway involving mesodiencephalic nuclei, which may eventually be converted to CS bursts in PCs via CFs. On the other hand, burst firings of DCN neurons that send inhibitory inputs directly to the IO are thought to induce large hyperpolarization and rebound excitation in IO neurons (Khosrovani et al., 2007; Choi et al., 2010). Thus, it is expected that highly synchronized PC activation by CS/Cf causes strong modulation of the firing patterns of IO neurons through rebound excitation of DCN neurons in GluD2 KO mice.

HIGHLY SYNCHRONOUS CF ACTIVITY BETWEEN PCs IN GluD2 KO MICE

Previous studies has revealed various cytoarchitectural, electrophysiological and behavioral phenotypes of GluD2 KO mice, including impaired PF–PC synapse formation (Kurihara et al., 1997; Ichikawa et al., 2002; Takeuchi et al., 2005), persistent multiple CF innervation (Hashimoto et al., 2001; Ichikawa et al., 2002; Miyazaki et al., 2010), deficient PF-LTD (Kashiwabuchi et al., 1995; Hirai et al., 2005a), abnormal rhythmic CF firing (Yoshida et al., 2004), ataxic gait (Kashiwabuchi et al., 1995; Hirai et al., 2005a), oscillatory eye movements (Yoshida et al., 2004) and impaired motor learning (Kashiwabuchi et al., 1995; Yoshida et al., 2004; Hirai et al., 2005a). In addition to these deficits, the present study has revealed a novel phenotype of GluD2 KO mice that the synchrony of CF responses among neighboring PCs are greatly enhanced in the mediolateral direction of the cerebellar cortex (**Figures 1**, **2**). Parasagittal longitudinal microzones based on the olivo-cerebellar projection are the functional units of the cerebellar cortex and play a central role in information processing in the cerebellum (Buisseret-Delmas and Angaut, 1993; Sugihara and Shinoda, 2004). Sensory and/or motor information can be robustly encoded in spatial patterns of activated microzones (Welsh et al., 1995; Ozden et al., 2009; Schultz et al., 2009; Ghosh et al., 2011), and the synchrony of CF activities among neighboring PCs in a given microzone can convey sensorimotor information without increasing the firing rates of CFs (Welsh, 2002; Schultz et al., 2009; Bosman et al., 2010). In GluD2 KO mice, the abnormal enhancement of CF synchrony in the mediolateral direction leads to functional broadening of individual microzones and reciprocal reduction in the pattern of activated microzones. This should significantly reduce the quantity of information conveyed by CF inputs, which may result, at least in part, in motor deficits in GluD2 KO mice.

DISRUPTED ZONAL ORGANIZATION BY ABERRANT TRANSVERSE CF COLLATERALS IN GluD2 KO MICE

According to the previous morphological studies, CF terminals of single IO neurons are aligned within single aldC bands, and these compartments are thought to represent functional units ("zones") for motor control of specific body parts (Sugihara and Shinoda, 2004). The rate of decline in synchrony in GluD2 KO mice was smaller than that in control mice (~10% decrease and 35–45% decrease at 190 μm, respectively; **Figures 2B**, **4D**), indicating that PCs in different zones of GluD2 KO mice could be activated simultaneously. In fact, transverse CF collaterals branching from ascending CFs in an aldC-positive band elongated into neighboring aldC-negative bands and vice versa (**Figure 5**). Mean length of transverse branch was 46.9 ± 3.0 μm (maximum length: 176.8 μm) in GluD2 KO mice, but this value is likely to be an underestimate and actual length would be even larger because these branches were often cut during preparation of histological sections. Therefore, anomalously highly synchronous activation of PCs in the mediolateral axis due to aberrant transverse CF collaterals can spread not only over the boundary of microzones but also beyond the border of zones, indicating that the somatotopic organization of cerebellar cortex of GluD2 KO mice might be disrupted.

FUNCTIONAL SIGNIFICANCE

Our findings directly demonstrate the close relationship between anatomical and functional microzonal organization in the cerebellar cortex. Furthermore, it is possible that aberrant transverse wiring affects the firing pattern of IO and DCN neurons through the olivo-cerebellar feedback loop. During postnatal development, only one CF is strengthened, and other surplus CFs are weakened and ultimately eliminated to establish one-to-one relationship between CF and PC (Hashimoto and Kano, 2003, 2005). Results from our on-going reserch suggest that CF-induced calcium transients are highly synchronized among PCs in immature mice and then become desynchronized with development (unpublished data by J.-M. Good, Taisuke Miyazaki, Kenji Sakimura, Masahiko Watanabe, Kazuo Kitamura, Masanobu Kano). Thus, functional differentiation and elimination of redundant CFs during postnatal development are crucial to establish the properly functioning olivo-cerebellar loop.

ACKNOWLEDGMENTS

This work was supported by Grants-in-Aid for Scientific Research (20021011 and 20650047 to Kazuo Kitamura, 17023021, 17100004, 21220006, and 2500015 to Masanobu Kano), the Strategic Research Program for Brain Sciences (Development of biomarker candidates for social behavior) and the Global COE Program (Integrative Life Science Based on the Study of Biosignaling Mechanisms) from MEXT, Japan. We thank to Shinichiro Tsutsumi for technical assistance, and to all member of Kano lab for discussion.

REFERENCES

Andersson, G., and Oscarsson, O. (1978). Climbing fiber microzones in cerebellar vermis and their projection to different groups of cells in the lateral vestibular nucleus. *Exp. Brain Res.* 32, 565–579.

Apps, R., and Garwicz, M. (2005). Anatomical and physiological foundations of cerebellar information processing. *Nat. Rev. Neurosci.* 6, 297–311. doi: 10.1038/nrn1646

Bengtsson, F., Ekerot, C.-F., and Jörntell, H. (2011). *In vivo* analysis of inhibitory synaptic inputs and rebounds in deep cerebellar nuclear neurons. *PLoS ONE* 6:e18822. doi: 10.1371/journal.pone.0018822

Blenkinsop, T. A., and Lang, E. J. (2006). Block of inferior olive gap junctional coupling decreases Purkinje cell complex spike synchrony and rhythmicity. *J. Neurosci.* 26, 1739–1748. doi: 10.1523/JNEUROSCI.3677-05.2006

Bosman, L. W., Koekkoek, S. K., Shapiro, J., Rijken, B. F., Zandstra, F., Van Der Ende, B., et al. (2010). Encoding of whisker input by cerebellar Purkinje cells. *J. Physiol.* 588, 3757–3783. doi: 10.1113/jphysiol.2010.195180

Brochu, G., Maler, L., and Hawkes, R. (1990). Zebrin II: a polypeptide antigen expressed selectively by Purkinje cells reveals compartments in rat and fish cerebellum. *J. Comp. Neurol.* 291, 538–552. doi: 10.1002/cne.902910405

Buisseret-Delmas, C., and Angaut, P. (1993). The cerebellar olivocorticonuclear connections in the rat. *Prog. Neurobiol.* 40, 63–87. doi: 10.1016/0301-008290048-W

Chen, C., Kano, M., Abeliovich, A., Chen, L., Bao, S., Kim, J. J., et al. (1995). Impaired motor coordination correlates with persistent multiple climbing fiber innervation in PKCγ mutant mice. *Cell* 83, 1233–1242. doi: 10.1016/0092-867490148-5

Chen, X., Kovalchuk, Y., Adelsberger, H., Henning, H. A., Sausbier, M., Wietzorrek, G., et al. (2010). Disruption of the olivo-cerebellar circuit by Purkinje neuron-specific ablation of BK channels. *Proc. Natl. Acad. Sci. U S A.* 107, 12323–12328. doi: 10.1073/pnas.1001745107

Cheron, G., Gall, D., Servais, L., Dan, B., Maex, R., and Schiffmann, S. N. (2004). Inactivation of calcium-binding protein genes induces 160 Hz oscillations in the cerebellar cortex of alert mice. *J. Neurosci.* 24, 434–441. doi: 10.1523/JNEUROSCI.3197-03.2004

Choi, S., Yu, E., Kim, D., Urbano, F. J., Makarenko, V., Shin, H. S., et al. (2010). Subthreshold membrane potential oscillations in inferior olive neurons are dynamically regulated by P/Q- and T-type calcium channels: a study in mutant mice. *J. Physiol.* 588, 3031–3043. doi: 10.1113/jphysiol.2009.184705

Denk, W., Strickler, J. H., and Webb, W. W. (1990). Two-photon laser scanning fluorescence microscopy. *Science* 248, 73–76. doi: 10.1126/science.2321027

De Zeeuw, C. I., Holstege, J. C., Ruigrok, T. J., and Voogd, J. (1989). Ultrastructural study of the GABAergic, cerebellar, and mesodiencephalic innervation of the cat medial accessory olive: anterograde tracing combined with immunocytochemistry. *J. Comp. Neurol.* 284, 12–35. doi: 10.1002/cne.902840103

De Zeeuw, C. I., Simpson, J. I., Hoogenraad, C. C., Galjart, N., Koekkoek, S. K., and Ruigrok, T. J. (1998). Microcircuitry and function of the inferior olive. *Trends Neurosci.* 21, 391–400. doi: 10.1016/S0166-223601310-1

Ghosh, K. K., Burns, L. D., Cocker, E. D., Nimmerjahn, A., Ziv, Y., Gamal, A. E., et al. (2011). Miniaturized integration of a fluorescence microscope. *Nat. Methods* 8, 871–878. doi: 10.1038/nmeth.1694

Groenewegen, H. J., Voogd, J., and Freedman, S. L. (1979). The parasagittal zonation within the olivocerebellar projection. II. Climbing fiber distribution in the intermediate and hemispheric parts of cat cerebellum. *J. Comp. Neurol.* 183, 551–601. doi: 10.1002/cne.901830307

Hashimoto, K., Ichikawa, R., Takechi, H., Inoue, Y., Aiba, A., Sakimura, K., et al. (2001). Roles of glutamate receptor δ2 subunit (GluRδ2) and metabotropic glutamate receptor subtype 1 (mGluR1) in climbing fiber synapse elimination during postnatal cerebellar development. *J. Neurosci.* 21, 9701–9712.

Hashimoto, K., and Kano, M. (2003). Functional differentiation of multiple climbing fiber inputs during synapse elimination in the developing cerebellum. *Neuron* 38, 785–796. doi: 10.1016/S0896-627300298-8

Hashimoto, K., and Kano, M. (2005). Postnatal development and synapse elimination of climbing fiber to Purkinje cell projection in the cerebellum. *Neurosci. Res.* 53, 221–228. doi: 10.1016/j.neures.2005.07.007

Hawkes, R., and Leclerc, N. (1987). Antigenic map of the rat cerebellar cortex: the distribution of parasagittal bands as revealed by monoclonal anti-Purkinje cell antibody mabQ113. *J. Comp. Neurol.* 256, 29–41. doi: 10.1002/cne.902560104

Hirai, H., Miyazaki, T., Kakegawa, W., Matsuda, S., Mishina, M., Watanabe, M., et al. (2005a). Rescue of abnormal phenotypes of the δ2 glutamate receptor-null mice by mutant δ2 transgenes. *EMBO Rep.* 6, 90–95.

Hirai, H., Pang, Z., Bao, D., Miyazaki, T., Li, L., Miura, E., et al. (2005b). Cbln1 is essential for synaptic integrity and plasticity in the cerebellum. *Nat. Neurosci.* 8, 1534–1541.

Horn, K. M., Pong, M., and Gibson, A. R. (2010). Functional relations of cerebellar modules of the cat. *J. Neurosci.* 30, 9411–9423. doi: 10.1523/JNEUROSCI.0440-10.2010

Ichikawa, R., Miyazaki, T., Kano, M., Hashikawa, T., Tatsumi, H., Sakimura, K., et al. (2002). Distal extension of climbing fiber territory and multiple innervation caused by aberrant wiring to adjacent spiny branchlets in cerebellar Purkinje cells lacking glutamate receptor δ2. *J. Neurosci.* 22, 8487–8503.

Ito, M. (2011). *The Cerebellum: Brain for an Implicit Self*. New Jersey, NJ: FT Press.

Kano, M., Hashimoto, K., Chen, C., Abeliovich, A., Aiba, A., Kurihara, H., et al. (1995). Impaired synapse elimination during cerebellar development in PKCγ mutant mice. *Cell* 83, 1223–1231. doi: 10.1016/0092-867490147-7

Kano, M., Hashimoto, K., Watanabe, M., Kurihara, H., Offermanns, S., Jiang, H., et al. (1998). Phospholipase cβ4 is specifically involved in climbing fiber synapse elimination in the developing cerebellum. *Proc. Natl. Acad. Sci. U.S.A.* 95, 15724–15729. doi: 10.1073/pnas.95.26.15724

Kashiwabuchi, N., Ikeda, K., Araki, K., Hirano, T., Shibuki, K., Takayama, C., et al. (1995). Impairment of motor coordination, Purkinje cell synapse formation, and cerebellar long-term depression in GluRδ2 mutant mice. *Cell* 81, 245–252. doi: 10.1016/0092-867490334-8

Khaliq, Z. M., and Raman, I. M. (2005). Axonal propagation of simple and complex spikes in cerebellar Purkinje neurons. *J. Neurosci.* 25, 454–463. doi: 10.1523/JNEUROSCI.3045-04.2005

Khosrovani, S., Van Der Giessen, R. S., De Zeeuw, C. I., and De Jeu, M. T. (2007). *In vivo* mouse inferior olive neurons exhibit heterogeneous subthreshold oscillations and spiking patterns. *Proc. Natl. Acad. Sci. U.S.A.* 104, 15911–15916. doi: 10.1073/pnas.0702727104

Kitamura, K., and Häusser, M. (2011). Dendritic calcium signaling triggered by spontaneous and sensory-evoked climbing fiber input to cerebellar Purkinje cells *in vivo*. *J. Neurosci.* 31, 10847–10858. doi: 10.1523/JNEUROSCI.2525-10.2011

Kitamura, K., Judkewitz, B., Kano, M., Denk, W., and Häusser, M. (2008). Targeted patch-clamp recordings and single-cell electroporation of unlabeled neurons *in vivo*. *Nat. Methods* 5, 61–67. doi: 10.1038/nmeth1150

Kurihara, H., Hashimoto, K., Kano, M., Takayama, C., Sakimura, K., Mishina, M., et al. (1997). Impaired parallel fiber Purkinje cell synapse stabilization during cerebellar development of mutant mice lacking the glutamate receptor δ2 subunit. *J. Neurosci.* 17, 9613–9623.

Landsend, A. S., Amiry-Moghaddam, M., Matsubara, A., Bergersen, L., Usami, S., Wenthold, R. J., et al. (1997). Differential localization of δ glutamate receptors in the rat cerebellum: coexpression with AMPA receptors in parallel fiber-spine synapses and absence from climbing fiber-spine synapses. *J. Neurosci.* 17, 834–842.

Lang, E. J. (2002). GABAergic and glutamatergic modulation of spontaneous and motor-cortex-evoked complex spike activity. *J. Neurophysiol.* 87, 1993–2008.

Lang, E. J., Sugihara, I., and Llinas, R. (1996). GABAergic modulation of complex spike activity by the cerebellar nucleoolivary pathway in rat. *J. Neurophysiol.* 76, 255–275.

Lang, E. J., Sugihara, I., Welsh, J. P., and Llinas, R. (1999). Patterns of spontaneous purkinje cell complex spike activity in the awake rat. *J. Neurosci.* 19, 2728–2739.

Llinas, R., and Sasaki, K. (1989). The functional organization of the olivo-cerebellar system as examined by multiple Purkinje cell recordings. *Eur. J. Neurosci.* 1, 587–602. doi: 10.1111/j.1460-9568.1989.tb00365.x

Llinas, R., and Yarom, Y. (1981). Electrophysiology of mammalian inferior olivary neurones *in vitro*. different types of voltage-dependent ionic conductances. *J. Physiol.* 315, 549–567.

Matsuda, K., Miura, E., Miyazaki, T., Kakegawa, W., Emi, K., Narumi, S., et al. (2010). Cbln1 is a ligand for an orphan glutamate receptor

δ2, a bidirectional synapse organizer. *Science* 328, 363–368. doi: 10.1126/science.1185152

Miyazaki, T., and Watanabe, M. (2010). Development of an anatomical technique for visualizing the mode of climbing fiber innervation in Purkinje cells and its application to mutant mice lacking GluRδ2 and Cav2.1. *Anat. Sci. Int.* 86, 10–18. doi: 10.1007/s12565-010-0095-1.

Miyazaki, T., Yamasaki, M., Takeuchi, T., Sakimura, K., Mishina, M., and Watanabe, M. (2010). Ablation of glutamate receptor GluRδ2 in adult Purkinje cells causes multiple innervation of climbing fibers by inducing aberrant invasion to parallel fiber innervation territory. *J. Neurosci.* 30, 15196–15209. doi: 10.1523/JNEUROSCI.0934-10.2010

Monsivais, P., Clark, B. A., Roth, A., and Häusser, M. (2005). Determinants of action potential propagation in cerebellar Purkinje cell axons. *J. Neurosci.* 25, 464–472. doi: 10.1523/JNEUROSCI.3871-04.2005

Mukamel, E. A., Nimmerjahn, A., and Schnitzer, M. J. (2009). Automated analysis of cellular signals from large-scale calcium imaging data. *Neuron* 63, 747–760. doi: 10.1016/j.neuron.2009.08.009

Offermanns, S., Hashimoto, K., Watanabe, M., Sun, W., Kurihara, H., Thompson, R. F., et al. (1997). Impaired motor coordination and persistent multiple climbing fiber innervation of cerebellar Purkinje cells in mice lacking Gαq. *Proc. Natl. Acad. Sci. U.S.A.* 94, 14089–14094. doi: 10.1073/pnas.94.25.14089

Ozden, I., Lee, H. M., Sullivan, M. R., and Wang, S. S. H. (2008). Identification and clustering of event patterns from *in vivo* multiphoton optical recordings of neuronal ensembles. *J. Neurophysiol.* 100, 495–503. doi: 10.1152/jn.01310.2007

Ozden, I., Sullivan, M. R., Lee, H. M., and Wang, S. S. H. (2009). Reliable coding emerges from coactivation of climbing fibers in microbands of cerebellar Purkinje neurons. *J. Neurosci.* 29, 10463–10473. doi: 10.1523/JNEUROSCI.0967-09.2009

Palkovits, M., Mezey, E., Hamori, J., and Szentagothai, J. (1977). Quantitative histological analysis of the cerebellar nuclei in the cat. I. Numerical data on cells and on synapses. *Exp. Brain Res.* 28, 189–209.

Pijpers, A., Voogd, J., and Ruigrok, T. J. (2005). Topography of olivocortico-nuclear modules in the intermediate cerebellum of the rat. *J. Comp. Neurol.* 492, 193–213. doi: 10.1002/cne.20707

Pologruto, T. A., Sabatini, B. L., and Svoboda, K. (2003). Scanimage: flexible software for operating laser scanning microscopes. *Biomed. Eng. Online* 2:13. doi: 10.1186/1475-925X-2-13

Rozental, R., Srinivas, M., and Spray, D. C. (2007). How to close a gap junction channel. *Methods Mol. Biol.* 154, 447–476.

Schultz, S. R., Kitamura, K., Post-Uiterweer, A., Krupic, J., and Häusser, M. (2009). Spatial pattern coding of sensory information by climbing fiber-evoked calcium signals in networks of neighboring cerebellar Purkinje cells. *J. Neurosci.* 29, 8005–8015. doi: 10.1523/JNEUROSCI.4919-08.2009

Sotelo, C., Gotow, T., and Wassef, M. (1986). Localization of glutamic-acid-decarboxylase-immunoreactive axon terminals in the inferior olive of the rat, with special emphasis on anatomical relations between GABAergic synapses and dendrodendritic gap junctions. *J. Comp. Neurol.* 252, 32–50. doi: 10.1002/cne.902520103

Stosiek, C., Garaschuk, O., Holthoff, K., and Konnerth, A. (2003). *In vivo* two-photon calcium imaging of neuronal networks. *Proc. Natl. Acad. Sci. U.S.A.* 100, 7319–7324. doi: 10.1073/pnas.1232232100

Sugihara, I. (2005). Microzonal projection and climbing fiber remodeling in single olivocerebellar axons of newborn rats at postnatal days 4-7. *J. Comp. Neurol.* 487, 93–106. doi: 10.1002/cne.20531

Sugihara, I., Marshall, S. P., and Lang, E. J. (2007). Relationship of complex spike synchrony bands and climbing fiber projection determined by reference to aldolase C compartments in crus IIa of the rat cerebellar cortex. *J. Comp. Neurol.* 501, 13–29. doi: 10.1002/cne.21223

Sugihara, I., and Quy, P. N. (2007). Identification of aldolase C compartments in the mouse cerebellar cortex by olivocerebellar labeling. *J. Comp. Neurol.* 500, 1076–1092. doi: 10.1002/cne.21219

Sugihara, I., and Shinoda, Y. (2004). Molecular, topographic, and functional organization of the cerebellar cortex: a study with combined aldolase C and olivocerebellar labeling. *J. Neurosci.* 24, 8771–8785. doi: 10.1523/JNEUROSCI.1961-04.2004

Sugihara, I., Wu, H., and Shinoda, Y. (1999). Morphology of single olivocerebellar axons labeled with biotinylated dextran amine in the rat. *J. Comp. Neurol.* 414, 131–148.

Sugihara, I., Wu, H. S., and Shinoda, Y. (2001). The entire trajectories of single olivocerebellar axons in the cerebellar cortex and their contribution to cerebellar compartmentalization. *J. Neurosci.* 21, 7715–7723.

Sullivan, M. R., Nimmerjahn, A., Sarkisov, D. V., Helmchen, F., and Wang, S. S. (2005). *In vivo* calcium imaging of circuit activity in cerebellar cortex. *J. Neurophysiol.* 94, 1636–1644. doi: 10.1152/jn.01013.2004

Takayama, C., Nakagawa, S., Watanabe, M., Mishina, M., and Inoue, Y. (1995). Light- and electron-microscopic localization of the glutamate receptor channel δ2 subunit in the mouse Purkinje cell. *Neurosci. Lett.* 188, 89–92. doi: 10.1016/0304-394011403-J

Takayama, C., Nakagawa, S., Watanabe, M., Mishina, M., and Inoue, Y. (1996). Developmental changes in expression and distribution of the glutamate receptor channel δ2 subunit according to the Purkinje cell maturation. *Dev. Brain Res.* 92, 147–155. doi: 10.1016/0165-380600212-X

Takeuchi, T., Miyazaki, T., Watanabe, M., Mori, H., Sakimura, K., and Mishina, M. (2005). Control of synaptic connection by glutamate receptor δ2 in the adult cerebellum. *J. Neurosci.* 25, 2146–2156. doi: 10.1523/JNEUROSCI.4740-04.2005

Uemura, T., Lee, S. J., Yasumura, M., Takeuchi, T., Yoshida, T., Ra, M., et al. (2010). Trans-synaptic interaction of GluRδ2 and Neurexin through Cbln1 mediates synapse formation in the cerebellum. *Cell* 141, 1068–1079. doi: 10.1016/j.cell.2010.04.035

Voogd, J., and Glickstein, M. (1998). The anatomy of the cerebellum. *Trends Neurosci.* 21, 370–375. doi: 10.1016/S0166-223601318-6

Voogd, J., Pardoe, J., Ruigrok, T. J., and Apps, R. (2003). The distribution of climbing and mossy fiber collateral branches from the copula pyramidis and the paramedian lobule: congruence of climbing fiber cortical zones and the pattern of zebrin banding within the rat cerebellum. *J. Neurosci.* 23, 4645–4656

Voogd, J., and Ruigrok, T. J. (2004). The organization of the corticonuclear and olivocerebellar climbing fiber projections to the rat cerebellar vermis: the congruence of projection zones and the zebrin pattern. *J. Neurocytol.* 33, 5–21. doi: 10.1023/B:NEUR.0000029645.72074.2b

Welsh, J. P. (2002). Functional significance of climbing-fiber synchrony: a population coding and behavioral analysis. *Ann. N.Y. Acad. Sci.* 978, 188–204. doi: 10.1111/j.1749-6632.2002.tb07567.x

Welsh, J. P., Lang, E. J., Suglhara, I., and Llinas, R. (1995). Dynamic organization of motor control within the olivocerebellar system. *Nature* 374, 453–457. doi: 10.1038/374453a0

Yamasaki, M., Miyazaki, T., Azechi, H., Abe, M., Natsume, R., Hagiwara, T., et al. (2011). Glutamate receptor δ2 is essential for input pathway-dependent regulation of synaptic AMPAR contents in cerebellar Purkinje cells. *J. Neurosci.* 31, 3362–3374. doi: 10.1523/JNEUROSCI.5601-10.2011

Yoshida, T., Katoh, A., Ohtsuki, G., Mishina, M., and Hirano, T. (2004). Oscillating Purkinje neuron activity causing involuntary eye movement in a mutant mouse deficient in the glutamate receptor δ2 subunit. *J. Neurosci.* 24, 2440–2448. doi: 10.1523/JNEUROSCI.0783-03.2004

Conflict of Interest Statement: The authors declare that the research was conducted in the absence of any commercial or financial relationships that could be construed as a potential conflict of interest.

Received: 17 June 2013; accepted: 18 July 2013; published online: 20 August 2013.
Citation: Hashizume M, Miyazaki T, Sakimura K, Watanabe M, Kitamura K and Kano M (2013) Disruption of cerebellar microzonal organization in GluD2 (GluRδ2) knockout mouse. Front. Neural Circuits 7:130. doi: 10.3389/fncir.2013.00130
This article was submitted to the journal Frontiers in Neural Circuits.

frontiers in
NEURAL CIRCUITS

ORIGINAL RESEARCH ARTICLE
published: 04 October 2013
doi: 10.3389/fncir.2013.00156

IP_3R1 deficiency in the cerebellum/brainstem causes basal ganglia-independent dystonia by triggering tonic Purkinje cell firings in mice

Chihiro Hisatsune[1]*†, Hiroyuki Miyamoto[2,3†], Moritoshi Hirono[4], Naohide Yamaguchi[1], Takeyuki Sugawara[1], Naoko Ogawa[1], Etsuko Ebisui[1], Toshio Ohshima[5], Masahisa Yamada[4], Takao K. Hensch[2], Mitsuharu Hattori[6] and Katsuhiko Mikoshiba[1,7]*

[1] Laboratory for Developmental Neurobiology, RIKEN Brain Science Institute, Wako, Japan
[2] Neuronal Circuit Development, RIKEN Brain Science Institute, Wako, Japan
[3] Precursory Research for Embryonic Science and Technology (PRESTO), Japan Science and Technology Agency (JST), Kawaguchi, Japan
[4] Yamada Research Unit, RIKEN Brain Science Institute, Wako, Japan
[5] Department of Life Science and Medical Bio-Science, Waseda University, Tokyo, Japan
[6] Department of Biomedical Science, Graduate School of Pharmaceutical Sciences, Nagoya City University, Nagoya, Japan
[7] Calcium Oscillation Project, ICORP-SORST, Japan Science and Technology Agency (JST), Kawaguchi, Japan

Edited by:
Masanobu Kano, The University of Tokyo, Japan

Reviewed by:
Taro Ishikawa, Jikei University School of Medicine, Japan
Laurens Bosman, Erasmus MC, Netherlands

***Correspondence:**
Chihiro Hisatsune and Katsuhiko Mikoshiba, Laboratory for Developmental Neurobiology, RIKEN Brain Science Institute, 2-1 Hirosawa, Wako City, Saitama 351-0198, Japan
e-mail: chihiro@brain.riken.jp; mikosiba@brain.riken.jp
† *These authors have contributed equally to this work.*

The type 1 inositol 1,4,5- trisphosphate receptor (IP_3R1) is a Ca^{2+} channel on the endoplasmic reticulum and is a predominant isoform in the brain among the three types of IP_3Rs. Mice lacking IP_3R1 show seizure-like behavior; however the cellular and neural circuit mechanism by which IP_3R1 deletion causes the abnormal movements is unknown. Here, we found that the conditional knockout mice lacking IP_3R1 specifically in the cerebellum and brainstem experience dystonia and show that cerebellar Purkinje cell (PC) firing patterns were coupled to specific dystonic movements. Recordings in freely behaving mice revealed epochs of low and high frequency PC complex spikes linked to body extension and rigidity, respectively. Remarkably, dystonic symptoms were independent of the basal ganglia, and could be rescued by inactivation of the cerebellum, inferior olive or in the absence of PCs. These findings implicate IP_3R1-dependent PC firing patterns in cerebellum in motor coordination and the expression of dystonia through the olivo-cerebellar pathway.

Keywords: dystonia, Purkinje cells, inferior olive, cerebellum, basal ganglia, complex spikes, inositol 1,4,5-trisphosphate, SCA15

INTRODUCTION

The inositol 1,4,5- trisphosphate receptors (IP_3Rs) are intracellular Ca^{2+} channels localized at the endoplasmic reticulum and regulate the spatio-temporal change of intracellular Ca^{2+} concentration, which are important for diverse physiological phenomena including gene expression, development, growth, neural plasticity, and secretion (Berridge et al., 2000). There are three subtypes of IP_3R in mammals and each IP_3R isoform exhibits a distinct expression pattern *in vivo*. Among the three subtypes, the type 1 IP_3 receptor (IP_3R1) is a brain dominant subtype (Foskett et al., 2007; Mikoshiba, 2007). We have previously showed that mice lacking the IP_3R1 receptor ($Itpr1^{-/-}$) exhibit ataxia and seizure-like posture with multiple abnormal movements such as repetitive rigid posture, opisthotonus, tonic contractions of the neck and trunk, and premature death around the third week after birth (Matsumoto et al., 1996). However, since IP_3R1 is expressed in a wide range of brain regions including cerebellum, cerebral cortex, hippocampus, and striatum, the particular neural activities and circuits causing these involuntary movements in the $Itpr1^{-/-}$ mice remain unknown.

Dystonia is a neurological disorder in which sustained muscle contractions induce twisting and repetitive movements or abnormal posturing. Simultaneous abnormal contractions of agonistic and antagonistic muscles (co-contractions) are one of the most distinct features of dystonic movements. Because of various phenotypic and genotypic subtypes in dystonia, its pathogenic mechanisms remain elusive. Traditionally, dystonia has been thought to be a basal ganglia (BG) disorder (Marsden and Quinn, 1990; Lenz et al., 1998; Vitek et al., 1999; Zhuang et al., 2004; Chiken et al., 2008; Nambu et al., 2011). In contrast, recent accumulating evidence has further suggested abnormalities of the cerebellum and brainstem in some dystonic patients (Ceballos-Baumann et al., 1995; Eidelberg et al., 1998; Mazziotta et al., 1998; Odergren et al., 1998; Hutchinson et al., 2000). Several animal models of dystonia also exhibit cerebellar abnormalities (Ledoux and Lorden, 2002; Pizoli et al., 2002; Raike et al., 2005; Walter et al., 2006; Chen et al., 2009; Calderon et al., 2011; Ledoux, 2011; Filip et al., 2013) and aberrant cerebellar activities in dystonic model animals were reported (Ledoux and Lorden, 2002; Walter et al., 2006; Chen et al., 2009), however, little is known about firing patterns of Purkinje cell (PC) activity associated with particular dystonic movements of freely moving mice. At the neural circuit level, it was suggested that cerebellar outputs alter BG activity thereby leading

to dystonic movements (Neychev et al., 2008; Calderon et al., 2011).

In this study, we showed that genetic deletion of IP_3R1 within the cerebellum and brainstem is sufficient to cause dystonia in mice. Although in the previous report we described epileptic-like seizures in *Itpr1*$^{-/-}$ mice, in the current study we concluded that the behavior of *Itpr1*$^{-/-}$ mice is better described as dystonia with severe ataxia because there was no abnormal electroencephalogram activity during the seizure-like posture (**Figure 1A**). In addition, we revealed distinct patterns of PC firing that were tightly coupled to the dystonic movements in freely moving mutant mice. We also showed that pharmacological inactivation of the cerebellum or inferior olive (IO), but not BG, and deletion of PCs ameliorate the dyskinesia. Thus, our mutant mice provide a therapeutic dystonia model solely dependent upon abnormal olivocerebellar pathways and provide a coherent mechanism for a specific type of dystonia.

MATERIALS AND METHODS

MICE

For generation of conditional *Itpr1* knockout mice, the floxed *Itpr1* mice (Sugawara et al., 2013) were crossed with *Wnt1 promoter-Cre* (Danielian et al., 1998), *Emx1-Cre* (Iwasato et al., 2000), and *Gpr88-Cre* transgenic (Tg) mice (Hisatsune et al., 2013). Genotyping of *Lurcher* mice was performed as previously (Nishiyama et al., 2010). Body size/weight of *Emx1-Cre;Itpr1*$^{flox/flox}$ and *Gpr88-Cre;Itpr1*$^{flox/flox}$ was indistinguishable from that of control mice. The conditional mice lacking IP_3R1 in the cerebellum/brainstem (*Wnt1-Cre;Itpr1*$^{flox/flox}$ mice) were severely dystonic and could not take in enough food to survive, so

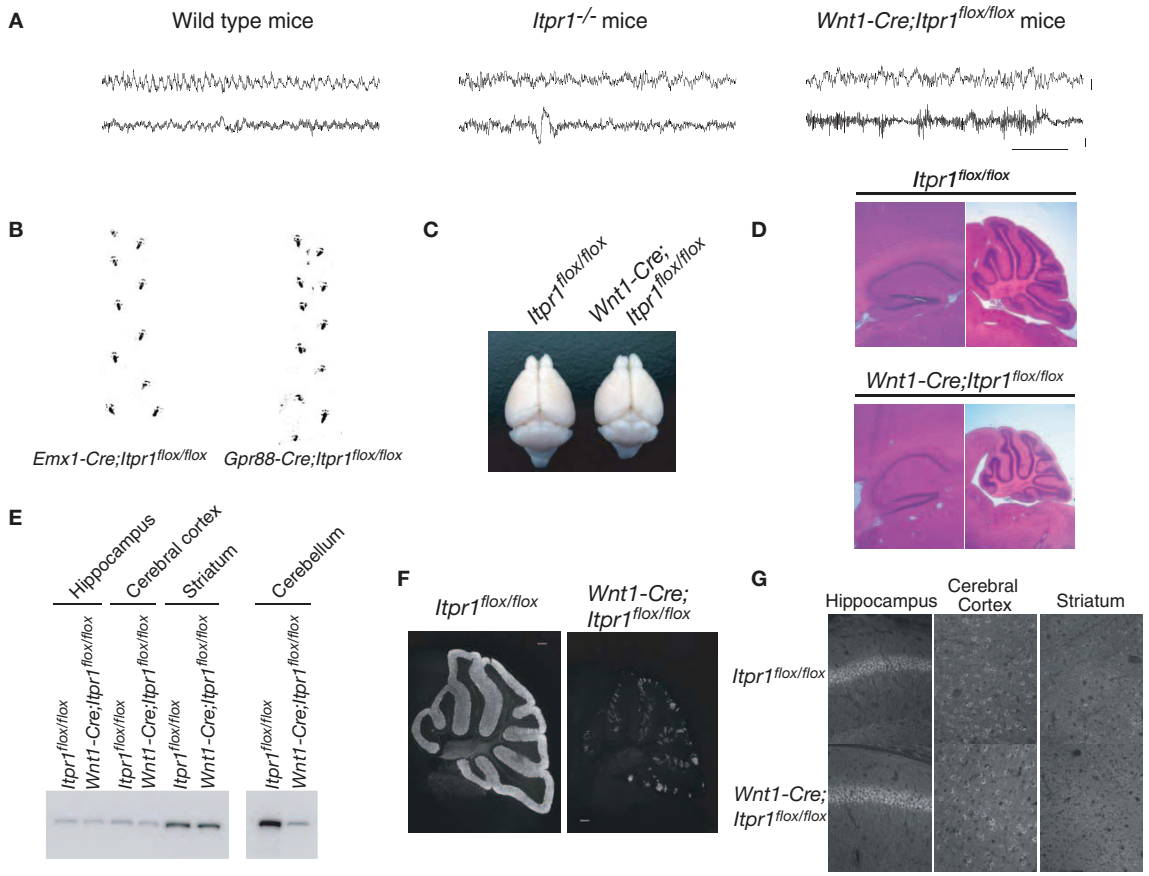

FIGURE 1 | Cerebellum/brainstem specific IP3R1 deficient mice exhibit dystonia. (A) Electroencephalogram of total *Itpr1*$^{-/-}$ and *Wnt1-Cre;Itpr1*$^{flox/flox}$ mice during seizure-like posture. Upper panel showed EEG (bar: 0.1 mV). Lower panel showed EMG (bar: 0.2 mV). Horizontal bar indicates 1.0 s. **(B)** Footprints of *Emx1-Cre;Itpr1*$^{flox/flox}$ and *Gpr88-Cre; Itpr1*$^{flox/flox}$ mice at 8 weeks. **(C)** Gross appearance of the brain from *Wnt1-Cre;Itpr1*$^{flox/flox}$ mice at 8 weeks. **(D)** Hematoxylin and Eosin (HE) staining of the hippocampus and the cerebellum in *Wnt1-Cre;Itpr1*$^{flox/flox}$ mice. Note overall size decrease of cerebellum in *Wnt1-Cre;Itpr1*$^{flox/flox}$ mice, whereas size of the hippocampus was comparable to *Itpr1*$^{flox/flox}$ mice. **(E)** Expression level of IP_3R1 in various parts of the brain at 8 weeks. **(F)** Immunohistochemical analysis of IP_3R1 expression in the cerebellum from *Wnt1-Cre;Itpr1*$^{flox/flox}$ mice at 8 weeks. **(G)** Immunohistochemistry of the IP_3R1 expression in the hippocampus, the cerebral cortex, and the striatum from *Itpr1*$^{flox/flox}$ (upper panels) and *Wnt1-Cre;Itpr1*$^{flox/flox}$ mice (lower panels) at 8 weeks. At least three mice were used for each analysis, and the representative data were shown.

they were hand-fed a nutritionally complete soft diet, DietGel76A (ClearH_2O), for their entire lives after weaning. All animals were ethically treated according to the guideline of Animal Experiments Committee of RIKEN Brain Science Institute.

HISTOLOGY AND *IN-SITU* HYBRIDIZATION

The mice brains (18- to 20-day-old *Itpr1*$^{-/-}$ and littermate *Itpr1*$^{+/+}$ mice; 8-week-old *Wnt1-Cre;Itpr1*$^{flox/flox}$ and *Itpr1*$^{flox/flox}$ mice; and 23-day-old mice for *Lurcher* experiments) were transcardially perfused with 4% PFA in PBS. The fixed brains were immersed in 30% sucrose in PBS for O/N at 4°C. The brains were quickly frozen in Tissue-Tek compound (SAKURA, Japan), and cryostat sections (12 μm in thick) were made.

For immunohistochemistry, the sections were permeablized with 0.25% Triton/PBS for 5 min and immersed with boiled acetate buffer (10 mM, pH = 6.0) for 10 min. After blocked, the sections were probed with the indicated primary antibodies [anti-IP_3R1 antibodies (18A10, 5.0 μg/ml), rabbit anti-Tyrosine hydroxylase (TH) antibodies (1.0 μg/ml), rabbit anti-Homer 3 S120 antibody, and guinea pig anti-Homer 3 antibodies] for ON at 4°C. After washed with PBS, the sections were probed with Alexa 594-conjugated goat anti-rabbit IgG, Alexa 488-conjugated anti-guinea pig IgG, and Alexa 488-conjugated goat anti-rat IgG (Invitrogen) for 1 h at RT. The coverslips were mounted with Vectashield (Vector Laboratories) and observed under fluorescence microscopy E600 (Nikon).

For *in-situ* hybridization, frozen (12 μm thick) or paraffin-embedded (5 μm thick) sections of 18- to 20-day-old *Itpr1*$^{-/-}$ and *Itpr1*$^{+/+}$ mice or 8-week-old and 19-day-old *Wnt1-Cre;Itpr1*$^{flox/flox}$ and *Itpr1*$^{flox/flox}$ mice were treated with proteinase K (1 μg/ml, Wako) for 10 min at RT. The sections were blocked and probed with sense and antisense *cfos* probes for ON at 68°C. The *cfos* fragment was amplified with primers, sense primer: 5′-CCGAATTCATGATGTTCTCGGGTT TCAACG-3′, anti-sense primer: 5′-CCAAGCTTTCACAGGGC CAGCAGCGTGG-3′. The underlines indicate *Eco*RI and *Hind*III sites for cloning the amplified *cfos* fragment to the Bluescript II vector.

IMMUNOBLOTTING

To analyze the expression of IP_3R1 and TH, various parts of the 8-week-old brain were excised and were sonicated in a Sucrose buffer [0.32 M sucrose, 5 mM Hepes-NaOH (pH = 7.5)] containing the 1x proteinase inhibitors (Roshe). The protein concentrations were measured, and 100 μg of the samples were lysed with the sample buffer [125 mM Tris-HCl (pH = 6.8), 20% glycerol, 4.0% SDS, 10% 2-mercaptoethanol, 0.1% bromphenol blue], and separated by 7.5% SDS-polyacrylamide gel electrophoresis and transferred to a polyvinyldene difluoride membrane. For c-Fos detection, the striatum of the 4-week-old mice were excised and homogenized with 0.32 M Sucrose buffer, and the nuclear fraction after centrifugation at 2000 rpm was lysed with sample buffer and used for western blotting. Antibodies were rabbit polyclonal anti-TH antibody (1.0 μg/ml, Chemicon), mouse monoclonal anti-β-actin antibody (1.0 μg/ml Sigma), rat monoclonal anti-IP_3R1 antibody (18A10: 1.0 μg/ml), and rabbit anti-cFos antibody (1.0 μg/ml, Santa cruz).

CYTOCHROME OXIDASE (CO) STAINING

Frozen 4%PFA-fixed 8-week-old brain sections (100 μm thick) were incubated in 0.1 M phosphate buffer containing 4 g sucrose, 50 mg of cytochrome C, and 50 mg of diaminobenzidine per 100 ml of buffer at 37°C for 1–2 h. To compare the CO staining intensities among different genotypes of mice, brains were fixed, cut, and reacted with the same solutions, and the digital photographs were taken on a same day.

ADMINISTRATION OF DRUGS INTO THE MOUSE BRAIN (CEREBELLUM, INFERIOR OLIVE, AND BASAL GANGLIA)

Mice (∼2 month-old) were anesthetized with 1.5% halothane anesthesia with N_2O:O_2 (3:2) ventilation. A guide cannula (C313, inner diameter: 0.39 mm, outer diameter: 0.71 mm, Plastics One) was implanted at the middle of vermis of cerebellum (1.1 mm in depth). After 3 days of recovery, an internal cannula (1.0 mm projection length from the guide cannula) was replaced with the dummy cannula and PBS or CNQX (5 mM in PBS, Tocris) were infused into the cerebellum at the speed of 0.5 μl/min for 20 min. The same guide cannula system was used for lidocaine (4.0% in PBS, MP Biomedicals) injection into the IO (the tip of the cannula was targeted to just above the medial nuclei) and bilateral BG (entopeduncular nucleus, 1.3 mm posterior to the Bregma, lateral to 2.2, 4.5 mm depth).

ELECTROPHYSIOLOGICAL RECORDINGS USING ACUTE CEREBELLAR SLICE

Cerebellar slices were prepared from *Itpr1*$^{+/+}$ and *Itpr1*$^{-/-}$ mice (P17-20). Parasagittal slices (230 μm thick) of the cerebellar vermis were cut using a vibrating microtome (VT1000S, Leica, Nussloch, Germany) in an ice-cold extracellular solution containing (in mM) 252 sucrose, 3.35 KCl, 21 $NaHCO_3$, 0.6 NaH_2PO_4, 9.9 glucose, 1 $CaCl_2$, and 3 $MgCl_2$ and gassed with a mixture of 95% O_2 and 5% CO_2 (pH 7.4). The slices were maintained at RT for at least 1 hr in a holding chamber, where they were submerged in artificial cerebrospinal fluid (ACSF) containing (in mM) 138.6 NaCl, 3.35 KCl, 21 $NaHCO_3$, 0.6 NaH_2PO_4, 9.9 glucose, 2 $CaCl_2$, and 1 $MgCl_2$ (bubbled with 95% O_2 and 5% CO_2 to maintain the pH at 7.4.

PCs were visually identified under Nomarski optics using a water immersion microscope (BX51WI, Olympus, Japan). For loose cell-attached recording, the pipette was gently placed in contact with a cell body of PC, and slight suction was applied. The pipette (2–4 MΩ) containing ACSF was maintained at 0 mV. The membrane currents were recorded using an amplifier, MultiClamp 700B (Molecular Devices, Foster City, CA, USA) and pCLAMP9.2 software (Molecular Devices), digitized, and stored on a computer disk for off-line analysis. All signals were filtered at 2 kHz and sampled at 5–10 kHz. All experiments were performed at 31–32°C. Action potential frequencies were analyzed using the Mini analysis program, version 6 (Synaptosoft, Decatur, GA, USA) and Kyplot 5.0 (Kyence, Tokyo, Japan).

EXTRACELLULAR RECORDING IN ANESTHETIZED MICE

Recordings were performed in anesthetized mice (1–2 months old) after an intraperitoneal injection of 50 mg/kg Nembutal

using 1.5% halothane anesthesia with N_2O:O_2 (3:2) ventilation. Additional doses of 0.15–0.25 mg were given if necessary to maintain anesthetic level. A sedative, chlorprothixene (0.2 mg, i.m.), was administered to supplement of the Nembutal. Atropine (0.3 mg, s.c.) and dexamethasone (0.05 mg, s.c.) were injected subcutaneously (Gordon and Stryker, 1996). The animal's temperature was maintained at 38°C. The heart rate was monitored continuously.

A small hole (1.0 mm) was drilled in the occipital bone above the cerebellar vermis of lobule IV (midline, 4.5 mm caudal from lambda), and the dura was exposed and covered with warm agarose (2.8% in saline). The microelectrode tip (epoxy-coated tungsten microelectrodes, 9–12 MΩ impedance; FHC, ME) was positioned above the small hole and advanced into the cerebellar lobule IV vermis using a stepping motor controlled micromanipulator. Raw signals from the electrodes were amplified, filtered (0.3–5 kHz), digitized at 25 kHz and stored (LabVIEW, National Instrument, Austin, TX). Single and multiunit PC activities (peak heights above the 6 sigma noise level) were isolated by off-line spike sorting (Offline sorter, Plexon, Dallas, TX). Simple spikes (SSs) and complex spikes (CSs) were identified based on their characteristic waveforms.

EEG, EMG RECORDING

A stainless screw electrode for EEG recording was secured over the cerebellar cortex (2.0 mm posterior to the lambda, on the midline) and a reference screw electrode was placed over the somatosensory (1.5 mm lateral to the midline, 1.0 mm posterior to the bregma) or frontal cortex (1.0 mm lateral to the midline, 2.0 mm anterior to the bregma) (Miyamoto et al., 2012). A stainless wire was inserted in the neck muscle for EMG recording. Polygraphic signals (band-pass filtered at 0.7–170 Hz) were amplified by telemetry system (Data Sciences International, St. Paul, MN) and sampled at 500 Hz (SleepSign, KISSEI COMTEC, Japan). Based on polygraph and infra-red camera monitoring, sleep/waking behavioral state and epileptic EEG pattern was explored.

EXTRACELLULAR RECORDING FROM BEHAVING MICE

The tetrodes of four nichrome wires (13 μm) were stereotaxically implanted into the cerebellar vermis of the lobule IV (6.25 mm posterior to the Bregma, on the midline). Signals from each electrode were band-pass filtered (1–6 kHz) and digitized at 25 kHz sampling frequency (Plexon, Dallas, TX). A reference electrode was chosen from electrodes which did not show neuronal activity. Neuronal spike data (firing rate, autocorrelogram, interspike interval) was analyzed by NeuroExplorer (Nex Technologies, Littleton, MA).

Similar to the recording of cerebellar PCs, tetrodes were implanted to monitor neuronal activity in the BG (caudate putamen and globus pallidus, 0.5 mm posterior to the Bregma, 2.0–3.0 mm lateral to the midline, 2.0–4.0 mm depth from the surface) during dystonic movements. Multi-unit neuronal activity data were sampled with a minimal interval of 200 μm by slowly advancing the tetrodes. For behavior analyses, we defined rigid posture as the duration in which mice hunched their backs and extended their paws to maintain the posture. In addition, we defined opisthotonus as an abnormal posture in which the mouse's neck was completely held at the bridging position (i.e., bent fully toward the upper back). We judged the beginning of opisthotonus when the neck was held at the maximal bridging position, and defined the ending as its complete return to the normal (horizontal/unbent) position.

Footprint analysis

The hindpaws of 8-week-old *Emx1-Cre;Itpr1*$^{flox/flox}$ and *Gpr88-Cre;Itpr1*$^{flox/flox}$ mice, or of 19-day-old mice for *Lurcher* experiments, were dipped in non-toxic water-based black paint, and allowed to walk down an enclosed runway lined with white paper, to determine their gait characteristics.

STATISTICAL ANALYSES

The significance of differences between groups was analyzed using Student's *t*-test, paired Student's *t*-test, Mann-Whitney *U*-test, Dunnett's test, or ANOVA followed by the Bonferroni's test as appropriate. A value of $P < 0.05$ is reported as significant.

RESULTS

ENHANCED PC ACTIVITY IN IP_3R1 DEFICIENT MICE

To examine the neural activities and circuits causing the dyskinetic movements of *Itrp1*$^{-/-}$ mice in detail, we generated several brain-specific IP_3R1 conditional knockout mice: restricted to the dorsal telencephalon (*Emx1-Cre;Itpr1*$^{flox/flox}$), the cerebellum/brainstem (*Wnt1-Cre;Itpr1*$^{flox/flox}$ mice), and to the BG (*Gpr88-Cre;Itpr1*$^{flox/flox}$). Neither *Emx1-Cre;Itpr1*$^{flox/flox}$ mice, lacking IP_3R1 in excitatory neurons and glial cells of the cerebral cortex and hippocampus, nor *Gpr88-Cre;Itpr1*$^{flox/flox}$ mice, lacking IP_3R1 in striatal neurons, exhibited apparent dyskinesia like total *Itpr1*$^{-/-}$ mice (**Figure 1B**). The *Emx1-Cre;Itpr1*$^{flox/flox}$ and *Gpr88-Cre;Itpr1*$^{flox/flox}$ mice were born normally and showed normal growth patterns through adulthood. In striking contrast, *Wnt1-Cre;Itpr1*$^{flox/flox}$ mice began to show ataxia around postnatal day 9 (P9), and exhibited dyskinesia including opisthotonus, repetitive rigid posture, and tonic contractions of the neck and trunk as they grew beyond 2 weeks (**Movie S1**, and the footprint analyses shown in **Figure 6B**, left panel).

Unlike the premature death in *Itpr1*$^{-/-}$ mice, *Wnt1-Cre;Itpr1*$^{flox/flox}$ mice grew to adulthood by hand-feeding. Body weight of *Wnt1-Cre;Itpr1*$^{flox/flox}$ mice was about 45% of *Itpr1*$^{flox/flox}$ mice at 5 weeks. Cerebellar size of *Wnt1-Cre;Itpr1*$^{flox/flox}$ mice at 8 weeks was significantly smaller than that of *Itpr1*$^{flox/flox}$ mice, whereas cerebral cortex size was comparable (**Figures 1C,D**). The apparent morphological constituents of the cerebellum, such as granular layer, PC layer, and molecular layer seemed normal and no apparent cell death occurred as judged by DAPI staining for nuclear condensation. The expression level of IP_3R1 in the cerebellum of 8 week-old *Wnt1-Cre;Itpr1*$^{flox/flox}$ mice was significantly lower than that of *Itpr1*$^{flox/flox}$ mice, whereas expression in the hippocampus, striatum, and cerebral cortex of *Wnt1-Cre;Itpr1*$^{flox/flox}$ mice was equivalent to that of *Itpr1*$^{flox/flox}$ mice (**Figures 1E–G**). Residual IP_3R1 expression in the cerebellum of the 8-week-old *Wnt1-Cre;Itpr1*$^{flox/flox}$ mice was attributed at least partly to PCs still expressing IP_3R1 protein after

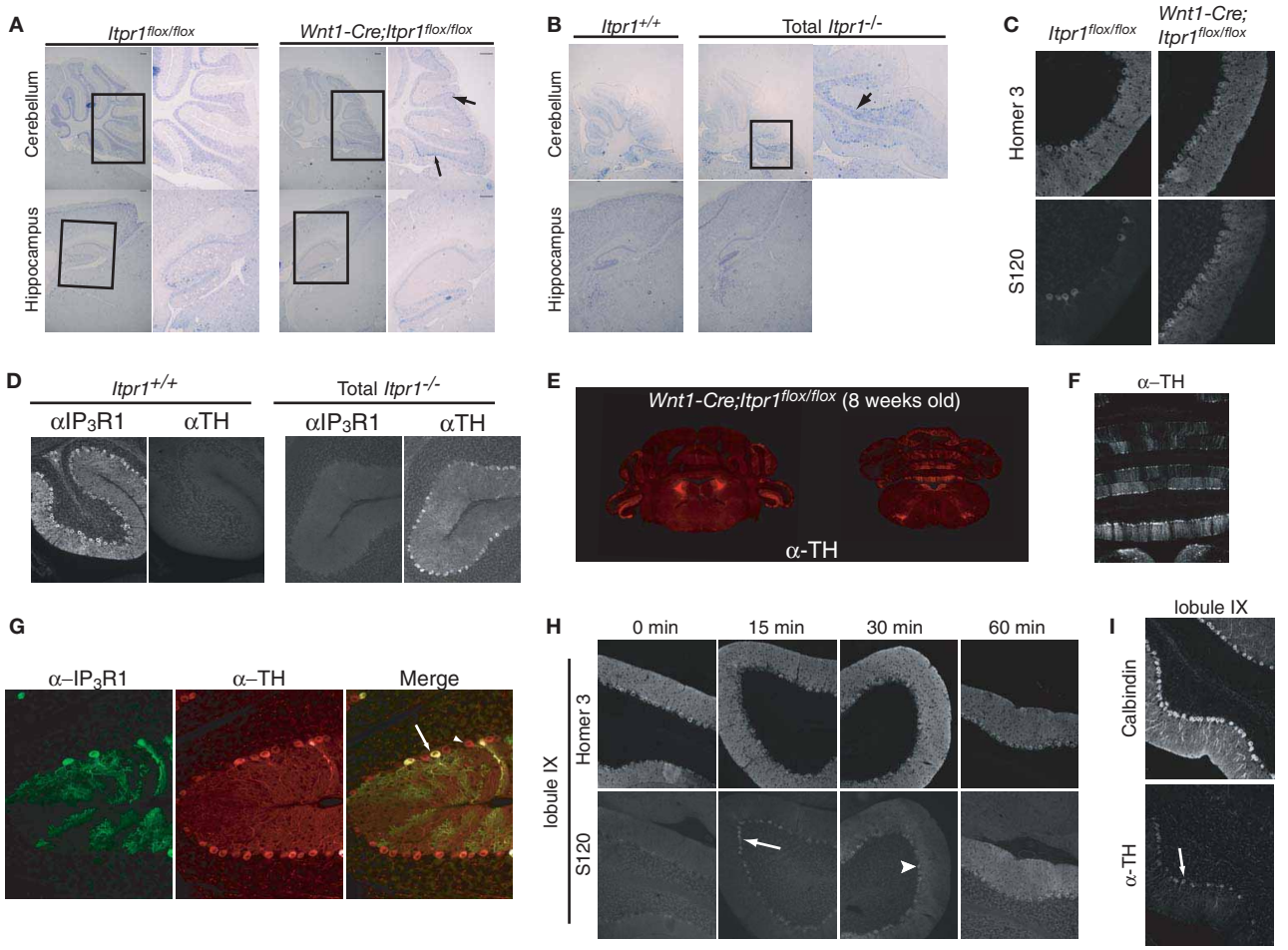

FIGURE 2 | Abnormal PC activities in the cerebellum of both *Itpr1*$^{-/-}$ and *Wnt1-Cre;Itpr1*$^{flox/flox}$ mice. **(A** and **B)** The *cfos* mRNA expression in the PCs and the hippocampus of 8-week-old *Wnt1-Cre;Itpr1*$^{flox/flox}$ **(A)** and 19-day-old *Itpr1*$^{-/-}$ mice **(B)**. Right panel shows magnified inset. Arrow indicates *cfos*-positive soma of PCs. **(C)** Increased phosphorylation level of Homer 3 (S120) in the soma and proximal dendrites of PCs of 8-week-old *Wnt1-Cre;Itpr1*$^{flox/flox}$ mice. **(D)** Ectopic expression of tyrosine hydroxylase (TH) in PCs of 19-day-old *Itpr1*$^{-/-}$ mice. **(E)** The TH expression in coronal sections of the *Wnt1-Cre;Itpr1*$^{flox/flox}$ cerebellum at 8 weeks. **(F)** Banded patterns of TH expressing PC in the *Wnt1-Cre;Itpr1*$^{flox/flox}$ cerebellum at 8 weeks. **(G)** TH expression was not dependent on the IP$_3$R1 expression of PCs in *Wnt1-Cre;Itpr1*$^{flox/flox}$ mice. **(H)** Intrapenitoneal injection of harmaline (30 mg/kg) increased the signals for the Homer 3 phosphorylation of PCs of 8-week-old wild-type mice in a time dependent manner. **(I)** Intrapenitoneal injection of harmaline increased the TH expression of PCs of wild-type mice after 24 h. All experiments were performed at least three times, and the representative data were shown.

incomplete Cre/flox recombination in the PCs of the *Wnt1-Cre* Tg mice (**Figures 1F**, **2G**).

To further delineate the neurons responsible for the expression of dystonia in *Itpr1*$^{-/-}$ and *Wnt1-Cre;Itpr1*$^{flox/flox}$ mice, we investigated the expression of *cfos* mRNA, a neural activity marker (Morgan et al., 1987). Interestingly, we found strong *c-fos* mRNA expression in PCs localized to the caudal parts of the cerebellum in both *Itpr1*$^{-/-}$ and *Wnt1-Cre;Itpr1*$^{flox/flox}$ mice, but not in that of *Itpr1*$^{+/+}$ or *Itpr1*$^{flox/flox}$ mice (**Figures 2A,B**, upper panels). No apparent elevation of *cfos* mRNA was observed in the hippocampus and cortex in either *Itpr1*$^{-/-}$ or *Wnt1-Cre;Itpr1*$^{flox/flox}$ mice (**Figures 2A,B**, lower panels). We also examined CaM kinase II-mediated phosphorylation levels of Homer 3 as a marker of PC depolarization (Mizutani et al., 2008). Only weak Homer 3 phosphorylation (S120) signals were observed in the soma and proximal dendrites of PCs in 8-week-old *Itpr1*$^{flox/flox}$ mice (**Figure 2C**), as reported previously (Mizutani et al., 2008). In 8-week-old *Wnt1-Cre;Itpr1*$^{flox/flox}$ mice, however, intense Homer 3 phosphorylation was observed at the soma and proximal dendrites, including the apical dendrites of PCs in caudal lobules 9 and 10 (**Figure 2C**, right).

In addition, we found aberrant tyrosine hydroxylase (TH) expression which is induced by cFos (Nagamoto-Combs et al., 1997) in the *Itpr1*$^{-/-}$ (**Figure 2D**) and *Wnt1-Cre;Itpr1*$^{flox/flox}$ PCs (**Figure 2E**). The TH-positive PCs were mainly observed in the vermis and flocculus of the *Wnt1-Cre;Itpr1*$^{flox/flox}$ and *Itpr1*$^{-/-}$ cerebellum (**Figure 2E**) and were localized in a banded pattern (**Figure 2F**). In the wild-type cerebellum, we detected some TH-positive PCs as reported previously (Hess and Wilson, 1991). However, TH expression levels were relatively weak, and the

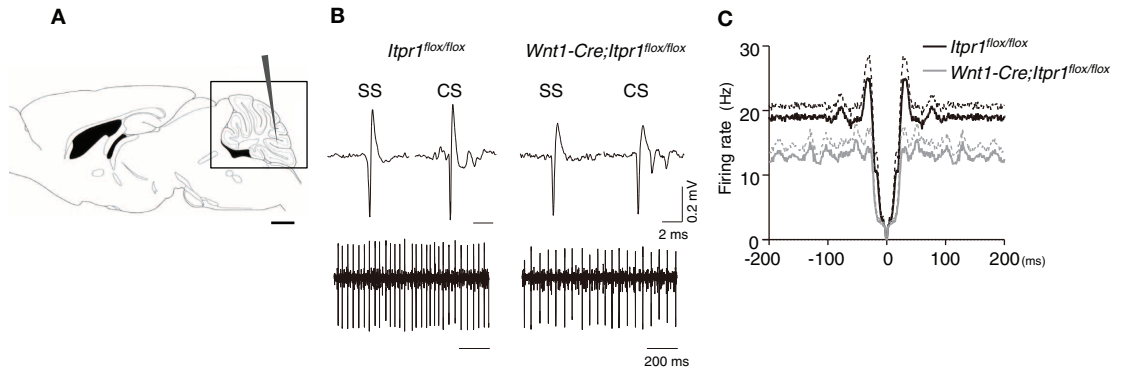

FIGURE 3 | PC firing in anesthetized *Wnt1-Cre;Itpr1$^{flox/flox}$* mice. **(A)** Diagram of *in vivo* recording from PCs of the cerebellum. **(B)** Upper panels: representative SSs and CSs of PCs in the *Itpr1$^{flox/flox}$* (left) and *Wnt1-Cre;Itpr1$^{flox/flox}$* (right) mice under anesthesia. Lower panels: recordings of PC spike trains from anesthetized mice. **(C)** Averaged auto-correlograms of PC spikes in the *Wnt1-Cre;Itpr1$^{flox/flox}$* (gray) and *Itpr1$^{flox/flox}$* (black) mice under anesthesia.

regions expressing TH in a banded manner were both fewer and smaller in size in the *Itpr1*$^{+/+}$ and *Itpr1$^{flox/flox}$* mice than in the *Itpr1* mutant mice (Figure S1). Although PCs normally express a large amount of IP$_3$R1 in the brain, the abnormal TH expression in the *Wnt1-Cre;Itpr1$^{flox/flox}$* cerebellum was observed in PCs regardless of IP$_3$R1 expression (**Figure 2G**), suggesting that altered neural inputs onto PCs may trigger the aberrant TH expression.

Since climbing fibers (CF) innervate PCs localized within banded patterns (Oscarsson, 1979), olivocerebellar inputs may be the cause of abnormal involuntary movements in the *Wnt1-Cre;Itpr1$^{flox/flox}$* mice. Harmaline evokes synchronous firing across large populations of PCs via the olivocellebelar pathway by electrical coupling of IO neurons, resulting in the expression of tremor in mice (Llinas and Sasaki, 1989). We intraperitoneally injected harmaline into wild-type mice and examined Homer 3 phosphorylation and TH expression in PCs. We found that IO activation rapidly increased the phosphorylation levels of Homer 3 in the soma and dendrites of PCs in a time dependent manner (**Figure 2H**). Intense phosphorylation signals were first observed in the soma of PCs within 15 min after injection (**Figure 2H**, arrow), then progressed into proximal and apical dendrites as time passed (**Figure 2H**, arrowhead). Furthermore, we observed elevation of TH signals in PCs at the caudal region of the cerebellum, especially lobules XI and X at 24 h after injection (**Figure 2I**). These results closely resembled those observed in the *Wnt1-Cre;Itpr1$^{flox/flox}$* mice. Therefore, we hypothesized that abnormal PC firing caused by excessive olivocerebellar input is the cause of involuntary movements in the *Itpr1*$^{-/-}$ and *Wnt1-Cre;Itpr1$^{flox/flox}$* mice.

PC ACTIVITY CORRELATES WITH DYSTONIC MOVEMENTS OF MICE

To reveal the nature of abnormal PC firing underlying the expression of dystonia in the *Itpr1*$^{-/-}$ mice, we first measured spontaneous PC activities by loose cell-attached recording using acute cerebellar slices, in which neuronal inputs from climbing and mossy fibers were severed. Because the PCs highly expressing TH were mainly observed in caudal parts of the cerebellar vermis of *Itpr1*$^{-/-}$ mice (**Figure 2E**), we measured spontaneous activities of PCs mainly from those areas. However, we found no apparent difference in spike frequency and coefficient of variation (CV) between PCs from wild-type and total *Itpr1*$^{-/-}$ mice under these conditions (Frequency: *Itpr1*$^{+/+}$: 25.89 ± 2.89 (Means $\pm$ sem), $n = 22$ cells from 3 mice; *Itpr1*$^{-/-}$: 28.86 ± 3.41, $n = 26$ from 3 mice, Student's t-test $P = 0.51$. CV: *Itpr1*$^{+/+}$: 0.23 ± 0.03, $n = 22$; *Itpr1*$^{-/-}$: 0.22 ± 0.02, $n = 26$, Student's t-test $P = 0.72$).

Since the cerebellar slice is devoid of neuronal inputs arising from other brain structures, we next asked whether spontaneous PC activities are altered in anesthetized mice. We performed extracellular recording of PC activities from caudal lobules in the cerebellar vermis (**Figure 3A**), which is responsible for the coordination of body trunk movement. We observed high amplitude PC spiking in both total *Itpr1*$^{-/-}$ and *Wnt1-Cre;Itpr1$^{flox/flox}$* mice as well as in wild-type mice (**Figure 3B**). Typical SSs and CSs were seen in both total *Itpr1*$^{-/-}$ and *Wnt1-Cre;Itpr1$^{flox/flox}$* mice and were used as an indication of PC activity *in vivo* (**Figure 3B**). Spontaneous firing rates of *Wnt1-Cre;Itpr1$^{flox/flox}$* mice were decreased compared to *Itpr1$^{flox/flox}$* mice (*Itpr1$^{flox/flox}$*: 17.12 ± 1.61 ($N = 5$ mice, $n = 37$ cells); *Wnt1-Cre;Itpr1$^{flox/flox}$*: 12.84 ± 1.59 ($N = 4$, $n = 55$). Mann-Whitney U-test: $^{*}P = 0.015$.), and this tendency was also observed in total *Itpr1*$^{-/-}$ mice, although this was not significant [*Itpr1*$^{+/+}$: 26.01 ± 3.42 ($N = 3$, $n = 28$); *Itpr1*$^{-/-}$: 19.95 ± 2.52 ($N = 4$, $n = 25$), Student's t-test $P = 0.169$]. The CVs were not significantly different between the groups [*Itpr1$^{flox/flox}$*: $1.43 + 0.18$ ($n = 37$), *Wnt1-Cre;Itpr1$^{flox/flox}$*: $1.07 + 0.08$ ($n = 55$), Mann-Whitney U-test: $P = 0.083$, *Itpr1*$^{+/+}$: $1.30 + 0.07$ ($n = 28$), *Itpr1*$^{-/-}$: $1.57 + 0.26$ ($n = 25$), Mann-Whitney U-test: $P = 0.91$].

We also found that averaged auto-correlograms of PC activity in *Wnt1-Cre;Itpr1$^{flox/flox}$* mice lacked a peak around 0-100 ms compared to *Itpr1$^{flox/flox}$* mice (**Figure 3C**). The peak height (25-35 ms) was significantly lower than that of *Itpr1$^{flox/flox}$* (*Itpr1$^{flox/flox}$*: $n = 37$ from 5 animals; *Wnt1-Cre;Itpr1$^{flox/flox}$* mice: $n = 55$ from 4 animals, Student's t-test $P < 0.01$, **Figure 3C**), suggesting an alteration of PC activity patterns caused by IP$_3$R1 deletion. Given that the spontaneous activity pattern was little

affected in isolated cerebellar slices, these results suggest that neural inputs to PCs, such as parallel fiber or CF inputs, were changed by IP_3R1 deletion *in vivo*.

Anesthetics influence synaptic neurotransmission or cellular communication (Keane and Biziere, 1987) and suppress animal behavior and movement. To gain more insight into the possible link between PC firing and the expression of dystonia, we recorded multiple unit activity of PCs from freely moving mice (**Figure 4A**). High amplitude putative PC spiking and low amplitude background activity were alternately recorded as the electrode advanced (400–800 μm). Multiple spiking and increased background activity of awake animals sometimes made discrimination between SSs and CSs difficult. In *Itpr1*$^{flox/flox}$ mice, putative PC activity showed regular tonic firing similar to the firing pattern of anesthetized mice (**Figure 4A**, upper panel). We did not see a drastic change of firing rate associated with particular movements or behaviors in the caudal part of the vermis. Likewise, sleep-wake state associated changes of PC firing rate were not evident.

In contrast, a sharp increase of firing rates was observed intermittently (about once/10 s) in *Wnt1-Cre;Itpr1*$^{flox/flox}$ mice and was tightly coupled to body movement related to paroxysmal dyskinesia (**Figure 4A**). Typically, *Wnt1-Cre;Itpr1*$^{flox/flox}$ mice gradually increased rigidity during the low firing period (indicated by the orange bar in **Figure 4A**, lower right panel). Then, they abruptly extended their trunk and limbs simultaneously (**Figure 4A**, lower left panel) during the high frequency period (indicated by the blue bar). This sequence of high and low frequency firing recurred while the animal was awake, but not during stiff ambulation. Though clear isolation of CSs was difficult, CS activity prevailed during the rigid posture (the orange bar), while SS activity became dominant with high frequency firing during the body-extension (the blue bar) (**Figure 4A**, lower panels).

Interestingly, the intraperitoneal injection of harmaline (30 mg/kg) in awake wild-type mice reduced SS, and caused CS-dominant spike patterns in PCs (**Figure 4B**) reminiscent of their firing patterns in the *Wnt1-Cre;Itpr1*$^{flox/flox}$ mice during rigid posture. When *Wnt1-Cre;Itpr1*$^{flox/flox}$ mice fell asleep, these particular patterns of PC activity diminished. The frequency of CSs was significantly increased in behaving *Wnt1-Cre;Itpr1*$^{flox/flox}$ mice as compared to *Itpr1*$^{flox/flox}$ mice, whereas the difference was not evident under anesthetized condition (**Figure 4C**). An increase of multiunit activity corresponded to the body-extension phase (high firing rate period, blue arrowhead) as judged by an independent observer (**Figure 4D**). Multiunit firing peaks in several recordings from lobules in caudal portions of the vermis were averaged ($N = 4$, 20 MUA recordings), and we confirmed distinct cerebellar activity changes associated with rigid and extended postures (**Figure 4E**).

TEMPORAL INACTIVATION OF THE CEREBELLUM AMELIORATES DYSTONIA

To confirm the involvement of cerebellar activity in the dystonic movements of *Wnt1-Cre;Itpr1*$^{flox/flox}$ mice, we inhibited cerebellar activity by α-amino-3-hydroxy-5-methyl-4-isoxazolepropionic acid (AMPA) receptor antagonist (CNQX) infusion. Inactivation of the cerebellum was confirmed by ataxia of CNQX-infused wild-type mice (**Figure 5A**), including abnormal footprints with shorter step length and wider gait after 2 h of infusion that recovered by 5 h (**Figure 5A**). Cerebellum specific infusion of the drug was confirmed by Fluo Ruby (**Figure 5B**). No ataxic gait was observed in wild-type mice infused with saline. Strikingly, CNQX infusion into the cerebellum of *Wnt1-Cre;Itpr1*$^{flox/flox}$ mice improved their voluntary movement significantly: dyskinesia such as opisthotonus, rigid posture, and tremor was abolished (**Figures 5C,D**). Although the mutant mice still showed ataxia, they exhibited partially restored gait within 2 h (**Figures 5E,F**; **Movie S2**). After 5 h, dystonic movements of *Wnt1-Cre;Itpr1*$^{flox/flox}$ mice appeared.

GENETIC DELETION OF PCs RESCUES DYSTONIA OF *Wnt1-Cre;Itpr1*$^{flox/flox}$ MICE

To further explore the influence of cerebellar output from PCs on dystonic movements, we also genetically deleted PCs from the cerebellum of *Wnt1-Cre;Itpr1*$^{flox/flox}$ mice by mating them with *Lurcher* mice (*GluD2*$^{LC/+}$) in which most of PCs die due to a mutation of the delta 2 glutamate receptor (*GluD2*) during the second postnatal week (Barmack and Yakhnitsa, 2003). Interestingly, we found that dystonic movements in *Wnt1-Cre;Itpr1*$^{flox/flox}$ mice were completely abolished in *GluD2*$^{LC/+}$*;Wnt1-Cre;Itpr1*$^{flox/flox}$ mice. The *GluD2*$^{LC/+}$*;Wnt1-Cre;Itpr1*$^{flox/flox}$ mice greatly improved their gait to a level similar to those of *GluD2*$^{LC/+}$ mice [**Figures 6A,B**, and **Movie S3**, $N = 4$. Stride length: *GluD2*$^{LC/+}$: 1.48 ± 0.053 and *GluD2*$^{LC/+}$*;Wnt1-Cre;Itpr1*$^{flox/flox}$: 1.60 ± 0.03 (Mean ± sem, Student's *t*-test $P = 0.06$, $n = 18$ from 3 mice), base width: *GluD2*$^{LC/+}$: 1.03 ± 0.014 and *GluD2*$^{LC/+}$*;Wnt1-Cre;Itpr1*$^{flox/flox}$: 0.83 ± 0.043 (Mean ± sem, Student's *t*-test $P < 0.001$, $n = 12$ from 3 mice)]. Loss of most of PCs were confirmed in the cerebellum of *GluD2*$^{LC/+}$*;Wnt1-Cre;Itpr1*$^{flox/flox}$ mice (**Figures 6C,D**). These results strongly suggested that abnormal cerebellar output from PCs produces dystonia in mice lacking IP_3R1.

OLIVO-CEREBELLAR PATHWAY, BUT NOT BG, IS INVOLVED IN THE EXPRESSION OF DYSTONIA

Because predominant CS activities prevailed during dystonic posture (**Figure 4**), we checked activities of IO neurons, which send CFs to PCs, by a cytochrome oxidase (CO) assay. We found that the CO-staining intensities in the IO of *Wnt1-Cre;Itpr1*$^{flox/flox}$ mice were increased as compared with those of *Itpr1*$^{flox/flox}$ mice (**Figure 7A**, Relative CO activity. Principal nuclei (IOPr), *Itpr1*$^{flox/flox}$: 0.97 ± 0.03, *Wnt1-Cre;Itpr1*$^{flox/flox}$: 1.17 ± 0.05, $P < 0.05$; medial inferior olive (IOM), *Itpr1*$^{flox/flox}$: 0.68 ± 0.02. *Wnt1-Cre;Itpr1*$^{flox/flox}$: 1.64 ± 0.1, $P < 0.0001$; and dorsal accessory inferior olive (IOD), *Itpr1*$^{flox/flox}$: 0.64 ± 0.02, *Wnt1-Cre;Itpr1*$^{flox/flox}$: 0.95 ± 0.06, Means ± sem, Student's *t*-test $P < 0.01$, $n = 6$ from 3 mice). Inferior olive IP_3R1 expression was below the threshold of immunohistochemical detection even in wild-type mice, most likely because of its significantly lower expression relative to hippocampal, striatal, and cerebral cortical neurons. In contrast, we did not detect a significant difference in the CO staining intensities of the BG between *Wnt1-Cre;Itpr1*$^{flox/flox}$ and *Itpr1*$^{flox/flox}$ mice (Relative CO

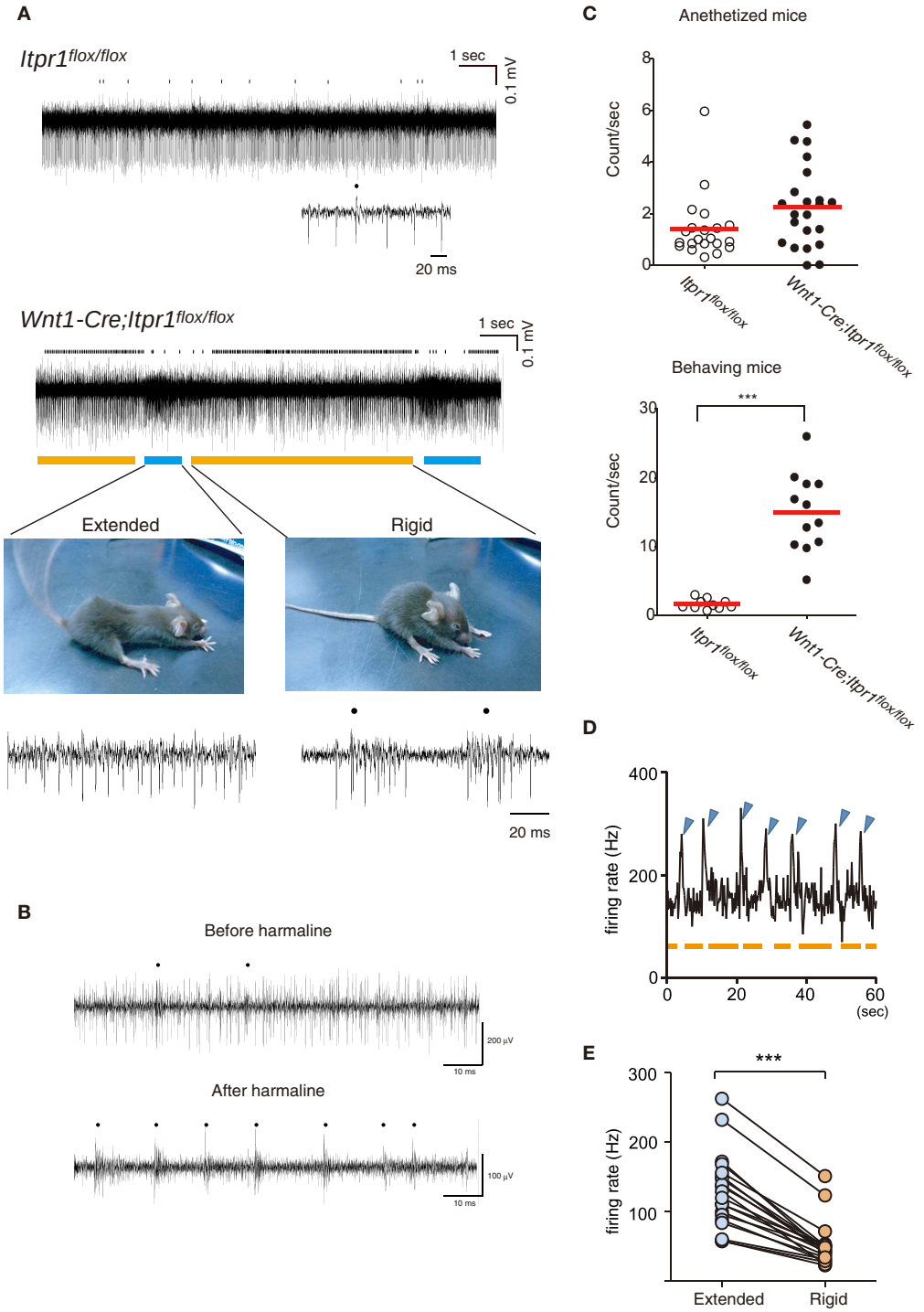

FIGURE 4 | Correlation of abnormal PC firing with the expression of Dystonia in freely moving *Wnt1-Cre;Itpr1*$^{flox/flox}$ mice. (A) Representative recording of PC spiking in freely moving *Itpr1*$^{flox/flox}$ and *Wnt1-Cre;Itpr1*$^{flox/flox}$ mice. Distinct involuntary movements of *Wnt1-Cre;Itpr1*$^{flox/flox}$ mice were highly correlated with change in multi-unit activities of PCs. Bottom picture, representative dyskinetic postures during underlined PC firing periods. Blue line: extension; orange line: compression with rigidity. Dots represent CSs. **(B)** PC spike patterns in wild-type mice before (upper panel) and after (lower panel) intraperitoneal harmaline injection. Dots represent CSs. **(C)** Frequency of CSs in anesthetized (upper panel) and behaving (lower panel) *Itpr1*$^{flox/flox}$ and *Wnt1-Cre;Itpr1*$^{flox/flox}$ mice. Anesthetized mice, *Itpr1*$^{flox/flox}$: 1.41 ± 0.27 count/s (Mean $\pm$ sem. 21 recording sites from 5 animals); *Wnt1-Cre;Itpr1*$^{flox/flox}$: 2.24 ± 0.33 count/s (22 recording sites from 4 animals), $P = 0.053$, Mann-Whitney *U*-test. Behaving mice, *Itpr1*$^{flox/flox}$: 1.61 ± 0.23 (10 recording sites from 4 animals); *Wnt1-Cre;Itpr1*$^{flox/flox}$: 14.96 ± 1.64 (12 recordings form 4 animals), $P < 0.0001$, Mann-Whitney *U*-test. **(D)** Relationship between firing rate and two postures. Blue arrowhead: extension; orange: shrinkage with rigidity. **(E)** Population firing data. ($N = 4$ mice, $n = 20$ recording sites, paired Student's *t*-test $***P < 0.0001$).

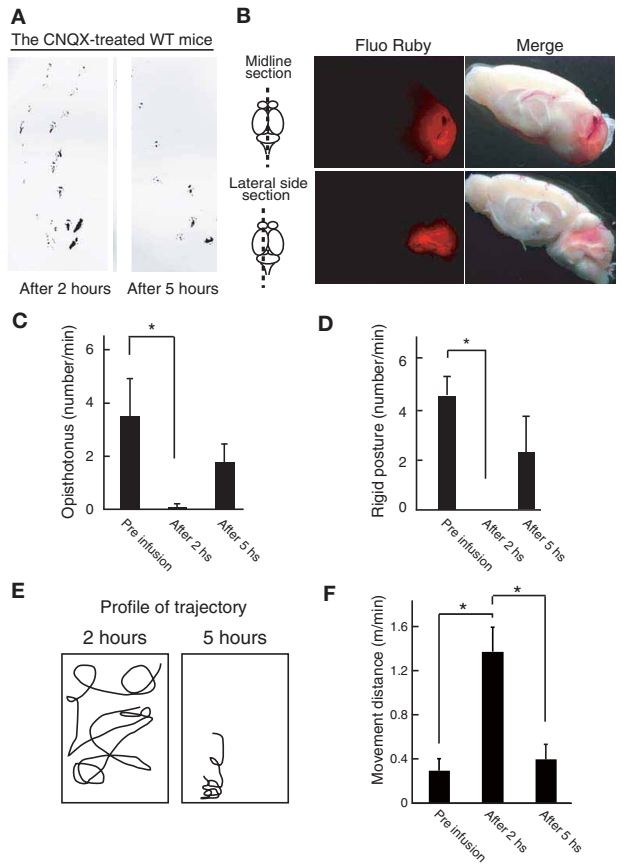

FIGURE 5 | Inhibition of cerebellum activity ameliorates the dystonic movements of *Wnt1-Cre;Itpr1$^{flox/flox}$* mice. **(A)** Footprint of wild-type mice at 2 and 5 h after the CNQX infusion into the cerebellum. The mice hind paws were visualized with non-toxic ink. Note that gait abnormality at 2 h later after infusion. **(B)** Gross appearance of the brain infused with Fluo Ruby after 2 h of infusion. Strong Fluo Ruby signals at cerebellum were detected in the midline and lateral side sections. **(C–F)** Cerebellar AMPA receptor blockade (CNQX infusion) improved voluntary movement of *Wnt1-Cre;Itpr1$^{flox/flox}$* mice. Incidence of abnormal postures **(C**: Opistothonus, **D**: Rigid posture with freezing as shown in **Figure 4A**) were scored. Means ± sem. Opistothonus, pre-infusion: 3.57 ± 1.21; after 2 h: 0.10 ± 0.10, after 5 h: 1.80 ± 0.64, Dunnett's test $^*P < 0.05$; Rigid posture, pre-infusion: 4.50 ± 0.76; after 2 h: 0, after 5 h: 2.23 ± 1.50, Dunnett's test $^*P < 0.05$ ($N = 3$). **(E)** Representative trajectory over 2 min. Box represents 34 × 38 cm square. **(F)** locomotor distance. Means ± sem. Pre infusion: 0.30 ± 0.11; after 2 h: 1.37 ± 0.01; after 5 h: 0.40 ± 0.016. $^*P < 0.05$. ANOVA, followed by Bonferroni's test. ($N = 3$).

activity. *Itpr1$^{flox/flox}$*: 1.02 ± 0.02; *Wnt1-Cre;Itpr1$^{flox/flox}$*: 0.98 ± 0.03, Student's *t*-test $P = 0.20$, $n = 6$ from 3 mice) (**Figure 7B**). In addition, contrary to the PC activity patterns, we did not observe distinct correlations between BG spiking activity and dystonic movement and activity patterns were essentially indistinguishable (**Figure 7C**). Activity levels of neurons in the *Wnt1-Cre;Itpr1$^{flox/flox}$* BG were also similar to those of *Itpr1$^{flox/flox}$* BG (firing rate of the BG neurons, single-unit activity [*Itpr1$^{flox/flox}$*: 8.523 ± 1.669 ($n = 20$). *Wnt1-Cre;Itpr1$^{flox/flox}$*: 15.05 ± 4.398 ($n = 22$). Mean ± sem. Student's *t*-test $P = 0.19$.]. In addition, the expression levels of *cfos* mRNA and cFos in the striatum were comparable between *Itpr1$^{flox/flox}$* and *Wnt1-Cre;Itpr1$^{flox/flox}$* mice (**Figures 7D,E**).

To examine whether altered IO activity was associated with dystonia in the *Wnt1-Cre;Itpr1$^{flox/flox}$* mice, we pharmacologically inhibited IO activities. We found that lidocaine injection into IO decreased opisthotonus of *Wnt1-Cre;Itpr1$^{flox/flox}$* mice (**Figure 7F**), although tremor of limbs and ataxia were still observed (**Movie S4**). In contrast, pharmacological inhibition of bilateral BG (entopeduncular nucleus) activity by lidocaine injection did not significantly affect frequency of opisthotonus in *Wnt1-Cre;Itpr1$^{flox/flox}$* mice (**Figure 7G**; **Movie S5**). These results suggested that altered activities of olivocerebellar tracts cause dystonia in *Wnt1-Cre;Itpr1$^{flox/flox}$* mice in a BG-independent manner.

DISCUSSION

In this study, we demonstrated that genetic deletion of IP$_3$R1 within cerebellum and brainstem is sufficient to cause dystonia in mice, and that further pharmacological inactivation of the cerebellum or the IO and deletion of PCs ameliorate the dyskinesia. Thus, our data suggested that dystonia is a gain of function rather than loss of function of olivocerebellar pathways, which is in line with the previous findings (Campbell et al., 1999; Pizoli et al., 2002). Moreover, using electrophysiological recordings of PC activity from freely behaving dystonic mice, we have also demonstrated the relationship between temporal changes of PC spike activity possibly triggered by altered IO activation and the expression of dystonia. Although altered PC activity was found in the movement-restricted dystonic rat (Ledoux and Lorden, 2002), how the temporal changes of PC firing patterns are related to ongoing dystonic movements were unknown. We revealed a distinct pattern of PC firing in freely moving *Wnt1-Cre;Itpr1$^{flox/flox}$* mice during distinct dystonic postures, which could not be observed in neither the anesthetized preparation nor the cerebellar slices. During dystonic movements, PC activities exhibiting repetitive CS patterns were predominant. Since CSs are thought to be important for voluntary movements (Welsh et al., 1995; Kitazawa et al., 1998; Welsh, 2002), the repetitive abnormal synchronized CSs with high frequency during rigid posture may in part underlie dystonia.

Chen et al. recently reported the low-frequency oscillations of flavoprotein autofluorescence in the cerebellar cortex of tottering mice (Chen et al., 2009), and showed that the oscillation was accentuated during dystonia. However, the cellular types and mechanisms that contribute to the enhancement of the oscillation in the mutant mice were unknown. By measuring the PC activities from behaving *Wnt1-Cre;Itpr1$^{flox/flox}$* mice, here we found a precise temporal association between CS-dominant PC firings and distinct dystonic movements. Thus, increase of CF frequency through IO activation may underlie the expression of dystonia in *Wnt1-Cre;Itpr1$^{flox/flox}$* mice. This hypothesis is in line with our finding that infusion of AMPAR blocker in the cerebellum ameliorates dystonia in *Wnt1-Cre;Itpr1$^{flox/flox}$* mice, because AMPA receptor blocker inhibits CF-PC synapse transmission. Although we don't know the relationship between the CS-dominant PC firings in the present study and the low-frequency oscillations in cerebellar cortex shown in the Chen's paper, the CS-dominant PC firings is most likely to be independent of the cerebellar

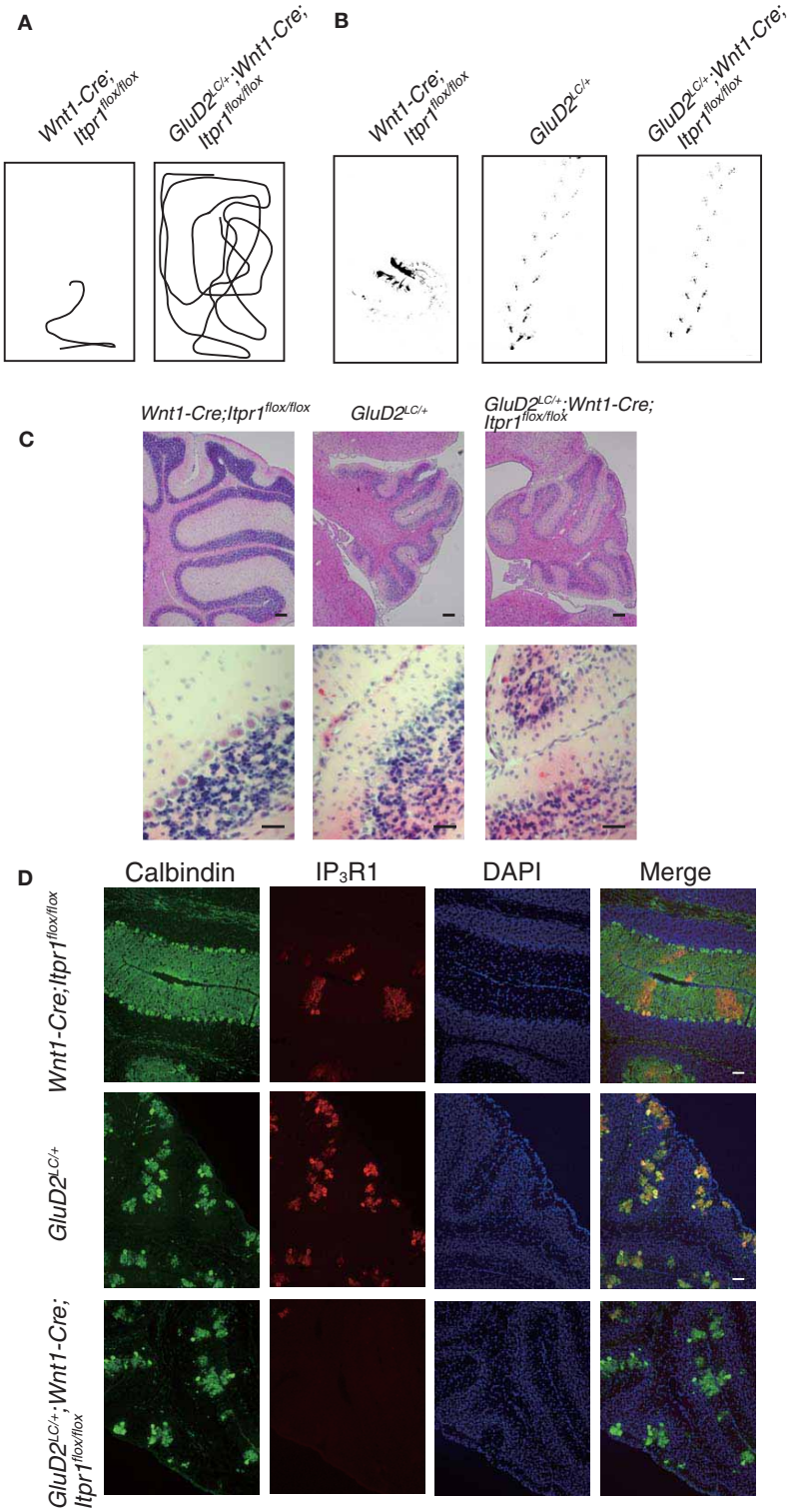

FIGURE 6 | Genetic deletion of PC rescues dystonia of *Wnt1-Cre;Itpr1*$^{flox/flox}$ mice. (A) Representative trajectories over 2 min of *Wnt1-Cre;Itpr1*$^{flox/flox}$ and *GluD2*$^{LC/+}$*;Wnt1-Cre;Itpr1*$^{flox/flox}$ mice at postnatal 19 days after birth. Box represents 17 × 26 cm square. **(B)** Representative footprints of *Wnt1-Cre;Itpr1*$^{flox/flox}$, *GluD2*$^{LC/+}$, and *GluD2*$^{LC/+}$*;Wnt1-Cre;Itpr1*$^{flox/flox}$ mice at 19 days old. Animal's hind paw prints were visualized with non-toxic ink. **(C)** Morphological assessment of cerebellar PC deletion by HE staining at 23 days old. **(D)** Immunohistochemistry of the IP_3R1 and Calbindin expression in the cerebellum from *Wnt1 – Cre*; *Itpr1*$^{flox/flox}$, *GluD2*$^{LC/+}$, and *GluD2*$^{LC/+}$*;Wnt1-Cre;Itpr1*$^{flox/flox}$ mice at 23 days old.

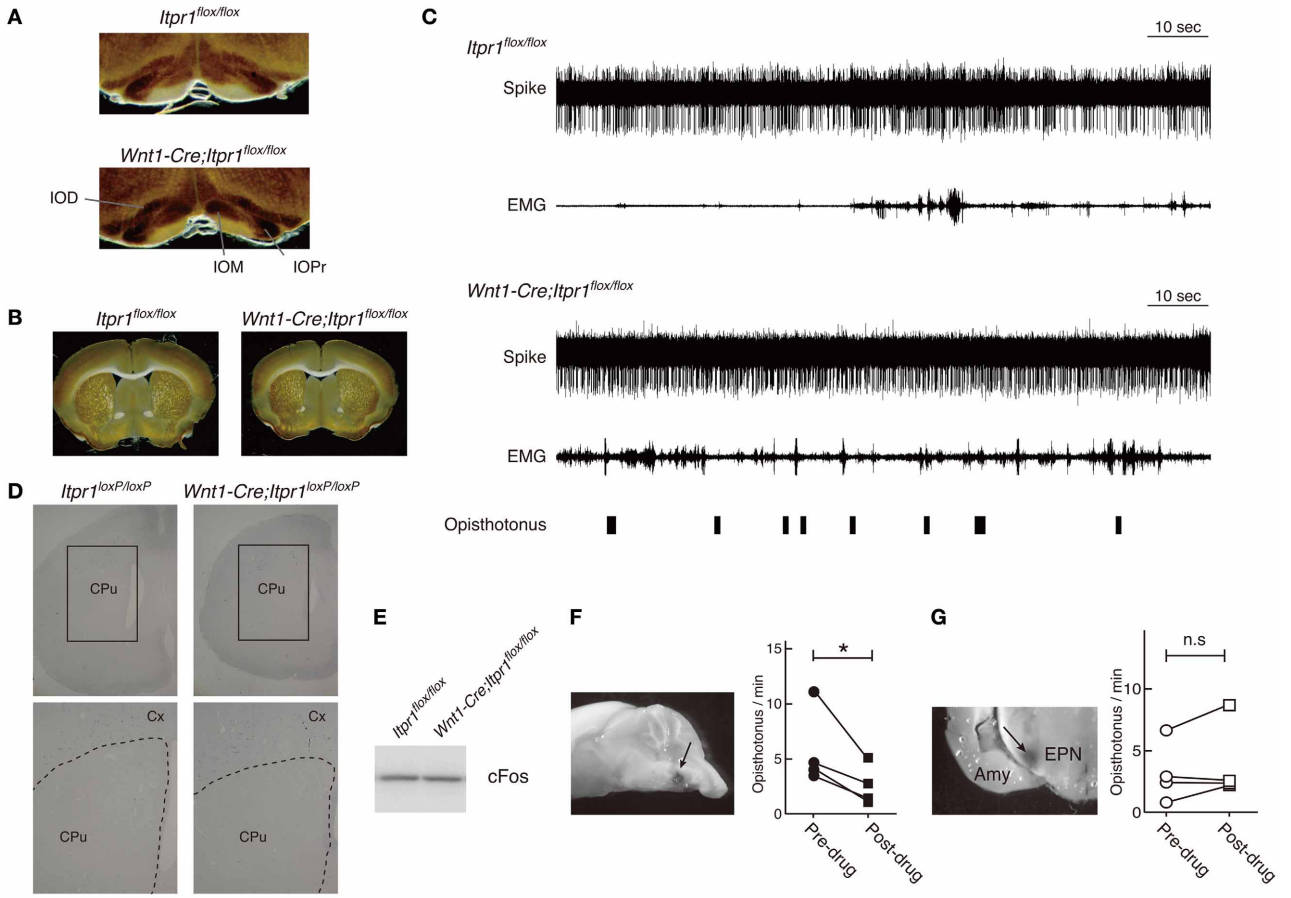

FIGURE 7 | Inhibition of IO but not BG activity ameliorates the dystonic movements of *Wnt1-Cre;Itpr1*$^{flox/flox}$ mice. (A and **B)** CO staining of IO **(A)** and BG **(B)** of 8 week-old *Itpr1*$^{flox/flox}$ and *Wnt1-Cre;Itpr1*$^{flox/flox}$ mice. **(C)** BG spiking activity and EMG in *Itpr1*$^{flox/flox}$ and *Wnt1-Cre;Itpr1*$^{flox/flox}$ mice. Single-unit activity (SUA). *Itpr1*$^{flox/flox}$: 8.523 ± 1.669 ($n = 20$). *Wnt1-Cre;Itpr1*$^{flox/flox}$: 15.05 ± 4.398 ($n = 22$). Mean $\pm$ sem. Student's *t*-test $P = 0.19$. For *Wnt1-Cre;Itpr1*$^{flox/flox}$ mice, opisthotonus was presented by a hand swich. **(D)** The expression level of *cfos* mRNA in the striatum of 19-day-old *Itpr1*$^{flox/flox}$ and *Wnt1-Cre;Itpr1*$^{flox/flox}$ mice. CPu: caudate putamen. Cx, cerebral cortex. $N = 3$. The representative data was shown. **(E)** The expression level of cFos in the striatum of *Itpr1*$^{flox/flox}$ and *Wnt1-Cre;Itpr1*$^{flox/flox}$ mice at 4 weeks old. Fifty μg of proteins were loaded for each lane. The representative data was shown ($n = 3$). **(F)** Effect of lidocaine infusion into IO on the opisthotonus of *Wnt1-Cre;Itpr1*$^{flox/flox}$ mice. Left panels show the infusion site visualized with methylene blue. Right panels show the number of opisthotonus before and after lidocaine infusion ($N = 4$). *Paired Student's *t*-test $P < 0.05$. **(G)** Effect of lidocaine infusion into bilateral BG (entopeduncular nucleus) on opisthotonus number of *Wnt1-Cre;Itpr1*$^{flox/flox}$ mice ($N = 4$). Amy, amygdala; EPN, entopeduncular nucleus; n.s, not significant determined by paired Student's *t*-test.

oscillation, since the oscillation was reported to be intrinsic to the cerebellar cortex and the cerebellar blockade by AMPA receptor or by electrical stimulation of PFs did not affect the oscillation (Chen et al., 2009).

Our results also suggest a previously unknown pathogenesis of dystonia induced by abnormal cerebellar activity in mice, namely BG-independent dystonia, based on the following facts; no apparent motor abnormality of BG-specific IP_3R1 conditional mice, no difference in CO staining intensity in *Itpr1*$^{flox/flox}$ and *Wnt1-Cre;Itpr1*$^{flox/flox}$ mouse's BG, little correlations of BG activity and dystonic movement, and the ineffectiveness of pharmaceutical BG inactivation on dystonia of *Wnt1-Cre;Itpr1*$^{flox/flox}$ mice. Thus, we propose that altered cerebellar activity causes dystonia by a mechanism, which does not involve BG activity in *Wnt1-Cre;Itpr1*$^{flox/flox}$ mice. It is possible that the abnormal cerebellar outputs generated by IO might be directly sent to spinal cords via red nucleus or reticular formation. It is also worth mentioning that the distinctive CSs appeared only in awake *Wnt1-Cre;Itpr1*$^{flox/flox}$ mice, and that altered activation of IO itself was not sufficient for generation of dystonia, since harmaline, which evokes similar CS dominant spike patterns of PCs, does not cause dystonia. Therefore, uncoordinated timings between voluntary corticospinal signals and the involuntary cerebellar-reticulospinal signals generated by IO activation with spinocerebellar (somatosensory) inputs may cause simultaneous activation of agonist- and antagonist muscles, leading to dystonia in the *Wnt1-Cre;Itpr1*$^{flox/flox}$ mice.

In sum, our study suggests that BG-independent dystonia is triggered by abnormal cerebellar outputs in mice. *Wnt1-Cre;Itpr1*$^{flox/flox}$ mice may provide a therapeutic dystonia model solely dependent upon abnormal neural activities within the cerebellum and brainstem. Recently, it was reported that a deletion

of the *Itpr1* gene is associated with involuntary movements in patients of spinocerebellar ataxia type 15 (Di Gregorio et al., 2010; Marelli et al., 2011), which has been thought to be pure cerebellar ataxia (Hara et al., 2008). The above involuntary movements may be dystonia-related, given that dystonia can be a prominent symptom in SCAs, including some cases with exclusively cerebellar pathology (Manto, 2005). However, since spinocerebellar ataxia type 15 is a slow progressive autosomal dominant disease exhibiting cerebellar atrophy with PC death (Knight et al., 2003; Gardner et al., 2005), severe dystonia would not happen in human. Nevertheless, IP_3R is known to interact with Na-K ATPase, a causal gene for DYT12 dystonia, and a Na-K ATPase inhibitor, ouabain, causes aberrant Ca^{2+} release from the IP_3Rs (Zhang et al., 2006). Thus, it is possible that dysfunction of IP_3R1 could be associated with dystonia in human. Further studies on the mechanism by which disturbed Ca^{2+} signals from IP_3R1 lead to the repetitive synchronized CSs in our mutant mice, such as potential Ca^{2+}-dependent regulation of gap junction among IO neurons, may contribute to the understanding of pathogenesis and the development of new therapies for dystonia.

AUTHOR CONTRIBUTIONS

Chihiro Hisatsune designed the project, performed experiments, and wrote the manuscript. Katsuhiko Mikoshiba wrote the manuscript. Hiroyuki Miyamoto, Moritoshi Hirono, Takao K. Hensch, and Masahisa Yamada. performed the electrophysiological experiments and wrote the manuscript. Naoko Ogawa, Etsuko Ebisui, and Takeyuki Sugawara performed the experiments. Naohide Yamaguchi, and Mitsuharu Hattori generated the $Itpr1^{flox/+}$ mice. Toshio Ohshima helped to establish mutant mice.

ACKNOWLEDGMENTS

This study was supported by the Moritani Scholarship Foundation (Chihiro Hisatsune), Takeda Science Foundation (Chihiro Hisatsune), JSPS KAKENHI Grant Numbers, 20500301 (Chihiro Hisatsune), and 20220007 (Katsuhiko Mikoshiba), the JST PRESTO program (Hiroyuki Miyamoto), and the Japan Science and Technology Agency (Katsuhiko Mikoshiba). We thank Dr. S. Itohara and Dr. T. Iwasato for providing us *Lurcher* and *Emx1-Cre* knock-in mice, and Dr. C. Yokoyama and Dr. A. V. Terashima for critical reading and comments. We also thank all members of our laboratories for valuable experimental advice, especially Dr. A. Mizutani for anti-Homer 3 antibodies. We are also grateful to the support of all staff at Research Resources Center, RIKEN Brain Science Institute.

SUPPLEMENTARY MATERIAL

The Supplementary Material for this article can be found online at: http://www.frontiersin.org/Neural_Circuits/10.3389/fncir.2013.00156/abstract

Movie S1 | Behavior of *Wnt1-Cre;Itpr1$^{flox/flox}$* mice.

Movie S2 | Behavior of *Wnt1-Cre;Itpr1$^{flox/flox}$* mice before and 2 h after CNQX infusion.

Movie S3 | Behavior of *GluD2$^{LC/+}$;Wnt1-Cre; Itpr1$^{flox/flox}$* mice.

Movie S4 | Behavior of *Wnt1-Cre;Itpr1$^{flox/flox}$* mice before and after lidocaine injection into the inferior olive.

Movie S5 | Behavior of *Wnt1-Cre;Itpr1 $^{flox/flox}$* mice before and after lidocaine injection into the BG.

REFERENCES

Barmack, N. H., and Yakhnitsa, V. (2003). Cerebellar climbing fibers modulate simple spikes in Purkinje cells. *J Neurosci* 23, 7904–7916.

Berridge, M. J., Lipp, P., and Bootman, M. D. (2000). The versatility and universality of calcium signalling. *Nat. Rev. Mol. Cell Biol.* 1, 11–21. doi: 10.1038/35036035

Calderon, D. P., Fremont, R., Kraenzlin, F., and Khodakhah, K. (2011). The neural substrates of rapid-onset Dystonia-Parkinsonism. *Nat. Neurosci.* 14, 357–365. doi: 10.1038/nn.2753

Campbell, D. B., North, J. B., and Hess, E. J. (1999). Tottering mouse motor dysfunction is abolished on the Purkinje cell degeneration (pcd) mutant background. *Exp. Neurol.* 160, 268–278. doi: 10.1006/exnr.1999.7171

Ceballos-Baumann, A. O., Passingham, R. E., Marsden, C. D., and Brooks, D. J. (1995). Motor reorganization in acquired hemidystonia. *Ann. Neurol.* 37, 746–757. doi: 10.1002/ana.410370608

Chen, G., Popa, L. S., Wang, X., Gao, W., Barnes, J., Hendrix, C. M., et al. (2009). Low-frequency oscillations in the cerebellar cortex of the tottering mouse. *J. Neurophysiol.* 101, 234–245. doi: 10.1152/jn.90829.2008

Chiken, S., Shashidharan, P., and Nambu, A. (2008). Cortically evoked long-lasting inhibition of pallidal neurons in a transgenic mouse model of dystonia. *J. Neurosci.* 28, 13967–13977. doi: 10.1523/JNEUROSCI.3834-08.2008

Danielian, P. S., Muccino, D., Rowitch, D. H., Michael, S. K., and Mcmahon, A. P. (1998). Modification of gene activity in mouse embryos *in utero* by a tamoxifen-inducible form of Cre recombinase. *Curr. Biol.* 8, 1323–1326. doi: 10.1016/S0960-9822(07)00562-3

Di Gregorio, E., Orsi, L., Godani, M., Vaula, G., Jensen, S., Salmon, E., et al. (2010). Two Italian families with ITPR1 gene deletion presenting a broader phenotype of SCA15. *Cerebellum* 9, 115–123. doi: 10.1007/s12311-009-0154-0

Eidelberg, D., Moeller, J. R., Antonini, A., Kazumata, K., Nakamura, T., Dhawan, V., et al. (1998). Functional brain networks in DYT1 dystonia. *Ann. Neurol.* 44, 303–312. doi: 10.1002/ana.410440304

Filip, P., Lungu, O. V., and Bares, M. (2013). Dystonia and the cerebellum: a new field of interest in movement disorders? *Clin. Neurophysiol.* 124, 1269–1276. doi: 10.1016/j.clinph.2013.01.003

Foskett, J. K., White, C., Cheung, K. H., and Mak, D. O. (2007). Inositol trisphosphate receptor Ca^{2+} release channels. *Physiol. Rev.* 87, 593–658. doi: 10.1152/physrev.00035.2006

Gardner, R. J., Knight, M. A., Hara, K., Tsuji, S., Forrest, S. M., and Storey, E. (2005). Spinocerebellar ataxia type 15. *Cerebellum* 4, 47–50. doi: 10.1080/14734220410019029

Gordon, J. A., and Stryker, M. P. (1996). Experience-dependent plasticity of binocular responses in the primary visual cortex of the mouse. *J. Neurosci.* 16, 3274–3286.

Hara, K., Shiga, A., Nozaki, H., Mitsui, J., Takahashi, Y., Ishiguro, H., et al. (2008). Total deletion and a missense mutation of ITPR1 in Japanese SCA15 families. *Neurology* 71, 547–551. doi: 10.1212/01.wnl.0000311277.71046.a0

Hess, E. J., and Wilson, M. C. (1991). Tottering and leaner mutations perturb transient developmental expression of tyrosine hydroxylase in embryologically distinct Purkinje cells. *Neuron* 6, 123–132. doi: 10.1016/0896-6273(91)90127-L

Hisatsune, C., Ogawa, N., and Mikoshiba, K. (2013). Striatum-specific expression of Cre recombinase using the Gpr88 promoter in mice. *Transgenic Res.* doi: 10.1007/s11248-013-9711-x. [Epub ahead of print].

Hutchinson, M., Nakamura, T., Moeller, J. R., Antonini, A., Belakhlef, A., Dhawan, V., et al. (2000). The metabolic topography of essential blepharospasm: a focal dystonia with general implications. *Neurology* 55, 673–677. doi: 10.1212/WNL.55.5.673

Iwasato, T., Datwani, A., Wolf, A. M., Nishiyama, H., Taguchi, Y., Tonegawa, S., et al. (2000). Cortex-restricted disruption of NMDAR1

impairs neuronal patterns in the barrel cortex. *Nature* 406, 726–731. doi: 10.1038/35021059

Keane, P. E., and Biziere, K. (1987). The effects of general anaesthetics on GABAergic synaptic transmission. *Life Sci.* 41, 1437–1448. doi: 10.1016/0024-3205(87)90708-9

Kitazawa, S., Kimura, T., and Yin, P. B. (1998). Cerebellar complex spikes encode both destinations and errors in arm movements. *Nature* 392, 494–497. doi: 10.1038/33141

Knight, M. A., Kennerson, M. L., Anney, R. J., Matsuura, T., Nicholson, G. A., Salimi-Tari, P., et al. (2003). Spinocerebellar ataxia type 15 (sca15) maps to 3p24.2-3pter: exclusion of the ITPR1 gene, the human orthologue of an ataxic mouse mutant. *Neurobiol. Dis.* 13, 147–157. doi: 10.1016/S0969-9961(03)00029-9

Ledoux, M. S. (2011). Animal models of dystonia: lessons from a mutant rat. *Neurobiol. Dis.* 42, 152–161. doi: 10.1016/j.nbd.2010.11.006

Ledoux, M. S., and Lorden, J. F. (2002). Abnormal spontaneous and harmaline-stimulated Purkinje cell activity in the awake genetically dystonic rat. *Exp. Brain Res.* 145, 457–467. doi: 10.1007/s00221-002-1127-4

Lenz, F. A., Suarez, J. I., Metman, L. V., Reich, S. G., Karp, B. I., Hallett, M., et al. (1998). Pallidal activity during dystonia: somatosensory reorganisation and changes with severity. *J. Neurol. Neurosurg. Psychiatr.* 65, 767–770. doi: 10.1136/jnnp.65.5.767

Llinas, R., and Sasaki, K. (1989). The functional organization of the olivo-cerebellar system as examined by multiple Purkinje cell recordings. *Eur. J. Neurosci.* 1, 587–602. doi: 10.1111/j.1460-9568.1989.tb00365.x

Manto, M. U. (2005). The wide spectrum of spinocerebellar ataxias (SCAs). *Cerebellum* 4, 2–6. doi: 10.1080/14734220510007914

Marelli, C., Van De Leemput, J., Johnson, J. O., Tison, F., Thauvin-Robinet, C., Picard, F., et al. (2011). SCA15 due to large ITPR1 deletions in a cohort of 333 white families with dominant ataxia. *Arch. Neurol.* 68, 637–643. doi: 10.1001/archneurol.2011.81

Marsden, C. D., and Quinn, N. P. (1990). The dystonias. *BMJ* 300, 139–144. doi: 10.1136/bmj.300.6718.139

Matsumoto, M., Nakagawa, T., Inoue, T., Nagata, E., Tanaka, K., Takano, H., et al. (1996). Ataxia and epileptic seizures in mice lacking type 1 inositol 1,4,5-trisphosphate receptor. *Nature* 379, 168–171. doi: 10.1038/379168a0

Mazziotta, J. C., Hutchinson, M., Fife, T. D., and Woods, R. (1998). Advanced neuroimaging methods in the study of movement disorders: dystonia and blepharospasm. *Adv. Neurol.* 78, 153–160.

Mikoshiba, K. (2007). The IP3 receptor/Ca2+ channel and its cellular function. *Biochem. Soc. Symp.* 74, 9–22. doi: 10.1042/BSS0740009

Miyamoto, H., Nakamaru-Ogiso, E., Hamada, K., and Hensch, T. K. (2012). Serotonergic integration of circadian clock and ultradian sleep-wake cycles. *J. Neurosci.* 32, 14794–14803. doi: 10.1523/JNEUROSCI.0793-12.2012

Mizutani, A., Kuroda, Y., Futatsugi, A., Furuichi, T., and Mikoshiba, K. (2008). Phosphorylation of Homer3 by calcium/calmodulin-dependent kinase II regulates a coupling state of its target molecules in Purkinje cells. *J. Neurosci.* 28, 5369–5382. doi: 10.1523/JNEUROSCI.4738-07.2008

Morgan, J. I., Cohen, D. R., Hempstead, J. L., and Curran, T. (1987). Mapping patterns of c-fos expression in the central nervous system after seizure. *Science* 237, 192–197. doi: 10.1126/science.3037702

Nagamoto-Combs, K., Piech, K. M., Best, J. A., Sun, B., and Tank, A. W. (1997). Tyrosine hydroxylase gene promoter activity is regulated by both cyclic AMP-responsive element and AP1 sites following calcium influx. Evidence for cyclic amp-responsive element binding protein-independent regulation. *J. Biol. Chem.* 272, 6051–6058. doi: 10.1074/jbc.272.9.6051

Nambu, A., Chiken, S., Shashidharan, P., Nishibayashi, H., Ogura, M., Kakishita, K., et al. (2011). Reduced pallidal output causes dystonia. *Front. Syst. Neurosci.* 5:89. doi: 10.3389/fnsys.2011.00089

Neychev, V. K., Fan, X., Mitev, V. I., Hess, E. J., and Jinnah, H. A. (2008). The basal ganglia and cerebellum interact in the expression of dystonic movement. *Brain* 131, 2499–2509. doi: 10.1093/brain/awn168

Nishiyama, J., Matsuda, K., Kakegawa, W., Yamada, N., Motohashi, J., Mizushima, N., et al. (2010). Reevaluation of neurodegeneration in lurcher mice: constitutive ion fluxes cause cell death with, not by, autophagy. *J. Neurosci.* 30, 2177–2187. doi: 10.1523/JNEUROSCI.6030-09.2010

Odergren, T., Stone-Elander, S., and Ingvar, M. (1998). Cerebral and cerebellar activation in correlation to the action-induced dystonia in writer's cramp. *Mov. Disord.* 13, 497–508. doi: 10.1002/mds.870130321

Oscarsson, O. (1979). Functional units of the cerebellum - sagittal zones and microzones. *Trends Neurosci.* 2, 143–145. doi: 10.1016/0166-2236(79)90057-2

Pizoli, C. E., Jinnah, H. A., Billingsley, M. L., and Hess, E. J. (2002). Abnormal cerebellar signaling induces dystonia in mice. *J. Neurosci.* 22, 7825–7833.

Raike, R. S., Jinnah, H. A., and Hess, E. J. (2005). Animal models of generalized dystonia. *NeuroRx* 2, 504–512. doi: 10.1602/neurorx.2.3.504

Sugawara, T., Hisatsune, C., Le, T. D., Hashikawa, T., Hirono, M., Hattori, M., et al. (2013). Type 1 inositol trisphosphate receptor regulates cerebellar circuits by maintaining the spine morphology of purkinje cells in adult mice. *J. Neurosci.* 33, 12186–12196. doi: 10.1523/JNEUROSCI.0545-13.2013

Vitek, J. L., Chockkan, V., Zhang, J. Y., Kaneoke, Y., Evatt, M., Delong, M. R., et al. (1999). Neuronal activity in the basal ganglia in patients with generalized dystonia and hemiballismus. *Ann. Neurol.* 46, 22–35. doi: 10.1002/1531-8249(199907)46:1<22::AID-ANA6>3.0.CO;2-Z

Walter, J. T., Alvina, K., Womack, M. D., Chevez, C., and Khodakhah, K. (2006). Decreases in the precision of Purkinje cell pacemaking cause cerebellar dysfunction and ataxia. *Nat. Neurosci.* 9, 389–397. doi: 10.1038/nn1648

Welsh, J. P. (2002). Functional significance of climbing-fiber synchrony: a population coding and behavioral analysis. *Ann. N.Y. Acad. Sci.* 978, 188–204. doi: 10.1111/j.1749-6632.2002.tb07567.x

Welsh, J. P., Lang, E. J., Suglhara, I., and Llinas, R. (1995). Dynamic organization of motor control within the olivocerebellar system. *Nature* 374, 453–457. doi: 10.1038/374453a0

Zhang, S., Malmersjo, S., Li, J., Ando, H., Aizman, O., Uhlen, P., et al. (2006). Distinct role of the N-terminal tail of the Na,K-ATPase catalytic subunit as a signal transducer. *J. Biol. Chem.* 281, 21954–21962. doi: 10.1074/jbc.M601578200

Zhuang, P., Li, Y., and Hallett, M. (2004). Neuronal activity in the basal ganglia and thalamus in patients with dystonia. *Clin. Neurophysiol.* 115, 2542–2557. doi: 10.1016/j.clinph.2004.06.006

Conflict of Interest Statement: The authors declare that the research was conducted in the absence of any commercial or financial relationships that could be construed as a potential conflict of interest.

Received: 18 July 2013; accepted: 14 September 2013; published online: 04 October 2013.

Citation: Hisatsune C, Miyamoto H, Hirono M, Yamaguchi N, Sugawara T, Ogawa N, Ebisui E, Ohshima T, Yamada M, Hensch TK, Hattori M and Mikoshiba K (2013) IP_3R1 deficiency in the cerebellum/brainstem causes basal ganglia-independent dystonia by triggering tonic Purkinje cell firings in mice. Front. Neural Circuits 7:156. doi: 10.3389/fncir.2013.00156

This article was submitted to the journal Frontiers in Neural Circuits.

frontiers in
NEURAL CIRCUITS

ORIGINAL RESEARCH ARTICLE
published: 15 November 2013
doi: 10.3389/fncir.2013.00180

Reevaluation of the role of parallel fiber synapses in delay eyeblink conditioning in mice using Cbln1 as a tool

Kyoichi Emi*[1,2], *Wataru Kakegawa*[1,2], *Eriko Miura*[1,2], *Aya Ito-Ishida*[1,2], *Kazuhisa Kohda*[1,2] and *Michisuke Yuzaki*[1,2]

[1] *Department of Physiology, School of Medicine, Keio University, Shinjuku-ku, Tokyo, Japan*
[2] *Core Research for Evolutional Science and Technology, Japan Science and Technology Corporation, Kawaguchi, Saitama, Japan*

Edited by:
Masanobu Kano, The University of Tokyo, Japan

Reviewed by:
G. J. Augustine, Korea Institute of Science and Technology, South Korea
Germund Hesslow, Lund University, Sweden
Shigenori Kawahara, University of Toyama, Japan

****Correspondence:***
Michisuke Yuzaki, Department of Physiology, School of Medicine, Keio University, 35 Shinanomachi, Shinjuku-ku, Tokyo 160-8582, Japan
e-mail: myuzaki@a5.keio.jp

The delay eyeblink conditioning (EBC) is a cerebellum-dependent type of associative motor learning. However, the exact roles played by the various cerebellar synapses, as well as the underlying molecular mechanisms, remain to be determined. It is also unclear whether long-term potentiation (LTP) or long-term depression (LTD) at parallel fiber (PF)–Purkinje cell (PC) synapses is involved in EBC. In this study, to clarify the role of PF synapses in the delay EBC, we used mice in which a gene encoding Cbln1 was disrupted (*cbln1*$^{-/-}$ mice), which display severe reduction of PF–PC synapses. We showed that delay EBC was impaired in *cbln1*$^{-/-}$ mice. Although PF-LTD was impaired, PF-LTP was normally induced in *cbln1*$^{-/-}$ mice. A single recombinant Cbln1 injection to the cerebellar cortex *in vivo* completely, though transiently, restored the morphology and function of PF–PC synapses and delay EBC in *cbln1*$^{-/-}$ mice. Interestingly, the *cbln1*$^{-/-}$ mice retained the memory for at least 30 days, after the Cbln1 injection's effect on PF synapses had abated. Furthermore, delay EBC memory could be extinguished even after the Cbln1 injection's effect were lost. These results indicate that intact PF–PC synapses and PF-LTD, not PF-LTP, are necessary to acquire delay EBC in mice. In contrast, extracerebellar structures or remaining PF–PC synapses in *cbln1*$^{-/-}$ mice may be sufficient for the expression, maintenance, and extinction of its memory trace.

Keywords: mouse, motor learning, cerebellum, long-term depression, Purkinje cell

INTRODUCTION

The cerebellum is one of brain regions in which learning at the behavioral level could be directly associated with changes in neural networks at synaptic levels. The delay eyeblink conditioning (EBC) is a cerebellum-dependent type of associative motor learning extensively studied in rabbits as well as cats, ferrets, and rats (**Figure 1A**; Hesslow and Yeo, 2002; Christian and Thompson, 2003). An unconditioned stimulus (US), e.g., an air puff or weak periorbital electric shock, is applied just before the end of a conditioned stimulus (CS), such as a tone or light (**Figure 1B**). After repeated exposure to paired CS–US presentations, the animal begins to blink its eyes before the US arrives: this is the conditioned response (CR). The CS is thought to be conveyed to the cerebellum via the pontine nuclei and their mossy fiber axons, which innervate granule cells, leading to activation of Purkinje cells (PCs) via parallel fibers (PF; axons of granule cells). Some mossy fibers (MF) may also innervate deep cerebellar nuclei (DCN; Kleim et al., 2002). The US is conveyed as increased activities of climbing fibers (CFs), which originate from the inferior olive of the medulla and innervate PCs. According to the Marr–Albus–Ito theory, the neural activities of CFs convey teacher signals that induce long-term depression (LTD) of PF–PC synaptic transmission (PF-LTD), which serves as a memory trace during acquisition of EBC. In addition, mossy fiber–DCN synapses may also be involved in EBC, depending on the time course or particular aspects of memory (van Alphen and De Zeeuw, 2002; Blazquez et al., 2004; Boyden et al., 2004; Shutoh et al., 2006). The exact roles played by the various cerebellar synapses, as well as the underlying molecular mechanisms, remain to be determined at different learning phases (e.g., acquisition, expression, extinction, and saving) of delay EBC.

Recent advent of genetically modified mice has opened up the possibility to further clarify molecular mechanisms responsible for EBC. Most mutant mice, in which molecules required for PF-LTD induction are modified, display impaired EBC, supporting the notion that PF-LTD is responsible for motor learning *in vivo* (Yuzaki, 2012). Recently, however, three lines of genetically modified mice (Schonewille et al., 2011), in which PF-LTD was abolished, were reported to display normal EBC (Schonewille et al., 2011). Conversely, PC–specific calcineurin knockout mice, which had a normal LTD but impaired long-term potentiation (LTP at PF–PC synapses, showed impaired EBC (Schonewille et al., 2010). Thus, instead of PF-LTD, PF-LTP is proposed as an alternative substrate for motor learning (Porrill and Dean, 2008; Schonewille et al., 2010). However, in most genetically engineered mice where molecules required for PF-LTD induction were modified, PF-LTP has not yet been systemically investigated (Yuzaki, 2012). In addition, compensatory pathways could easily kick in when specific genes are knocked out or expressed throughout life. For example, while PF-LTD is normal in cerebellar slices prepared from PC–specific calcineurin knockout mice (Schonewille et al., 2010), inclusion of calcineurin inhibitory peptides in the patch pipette completely blocks LTD induction in wild-type (WT) cerebellar slices (Fujiwara et al., 2007;

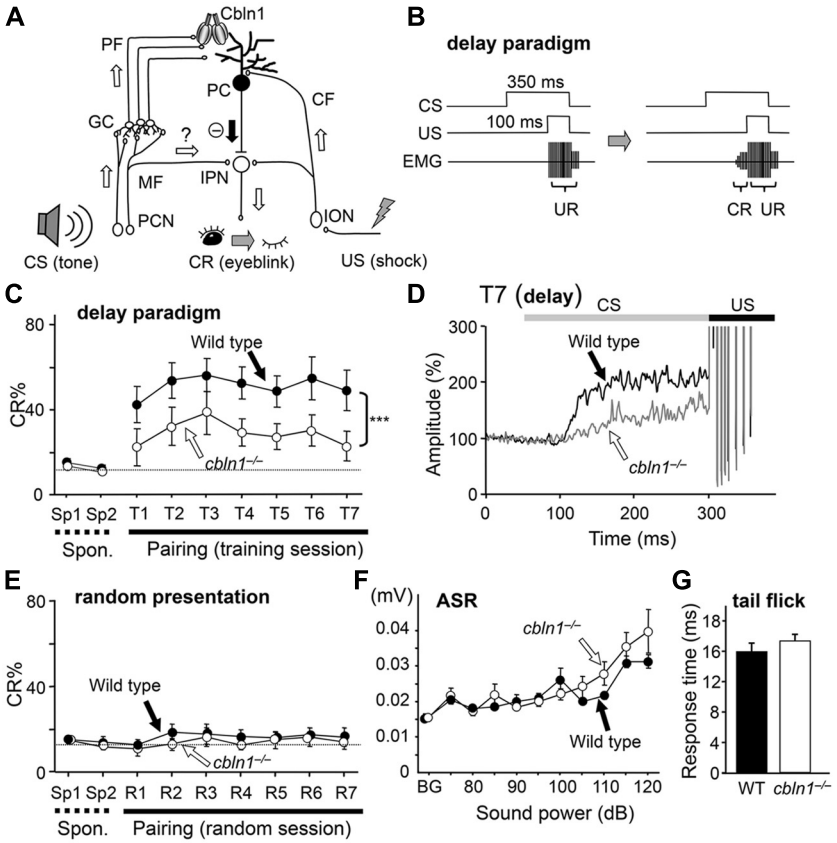

FIGURE 1 | Delay eyeblink conditioning (EBC) is impaired in *cbln1*$^{-/-}$ mice. (**A**) A diagram showing the cerebellar circuits responsible for delay EBC. A conditioned stimulus (CS) tone increases the activities of precerebellar nuclei (PCN), which send MF to granule cells (GCs). Some MFs may also innervate the interpositus nucleus (IPN). Parallel fibers (PFs), which are GC axons, secrete Cbln1, which regulates the integrity and plasticity of PF–Purkinje cell (PC) synapses. An unconditioned stimulus (US) is mediated by the activities of the inferior olivary nuclei (ION), which send climbing fibers (CFs) to the IPN and PCs. **(B)** A diagram showing the delay EBC paradigm. A CS tone (350 ms) precedes and co-terminates with a US (100 ms). Mice were trained for one session per day for 7 days. Associative learning was established when conditioned response (CR), detected by electromyogram (EMG), was observed before the unconditioned eyeblink response (UR). **(C)** Impaired delay EBC in *cbln1*$^{-/-}$ mice. The CR% was significantly smaller for *cbln1*$^{-/-}$ than wild-type mice ($p < 0.01$, two-way repeated measures ANOVA, $n = 8$ mice for each group). T1–T7, training sessions; Sp1 and Sp2, spontaneous eyeblink responses before training. The *Y*-axis gives the percentage of trials showing positive CR. **(D)** Averaged EMG amplitude on the last day of training (T7). The EMG amplitudes were normalized to those during the initial 30 ms of CS. $n = 8$ for each group. **(E)** CRs by pseudo-random test. CS and US stimuli were randomly presented to wild-type and *cbln1*$^{-/-}$ mice. There was no significant difference in CR% between two groups ($p > 0.1$). **(F)** Acoustic startle response (ASR) test. There was no significant difference in the amplitude between wild-type and *cbln1*$^{-/-}$ mice ($p > 0.5$, by two-way repeated measures ANOVA, $n = 8$ for each group). **(G)** A tail-flick test. No significant difference was found in response time to nociceptive stimuli between wild-type and *cbln1*$^{-/-}$ mice ($p > 0.5$, by Mann–Whitney's *U* test, $n = 8$ for each group). The dotted lines in C and E correspond to the percentage of CR-like activities on Sp2 to indicate the baseline for learned responses.

Nomura et al., 2012). Furthermore, the same gene product is often shared by different synapses in the targeted neuron. For example, since protein kinase C (PKC) is ubiquitous in PCs, PF–, CF–, and interneuron–PC synapses may all be affected in L7-PKCI transgenic mice (De Zeeuw et al., 1998). Therefore, temporally specific ablation or expression of gene products at specific synapses will be required to clarify the role of PF-LTD in motor learning.

Cerebellin precursor protein 1 (Cbln1) is a C1q family protein, which is produced and secreted from cerebellar granule cells (Hirai et al., 2005). Cbln1 binds to its postsynaptic receptor, glutamate receptor delta 2 (GluD2), expressed in PCs, and its presynaptic receptor, neurexin (Matsuda et al., 2010; Uemura et al., 2010; Matsuda and Yuzaki, 2011). Mice in which a gene encoding Cbln1 is disrupted (*cbln1*$^{-/-}$ mice) exhibit ∼80% reduction of PF–PC synapses (Hirai et al., 2005). Abnormalities are also found at CF–PC synapses; redundant CFs are gradually eliminated until a one-to-one relation-ship is established by the end of the third postnatal week (PW) In WT PCs, whereas supernumerary CFs remain to innervate *cbln1*$^{-/-}$ PCs even in adulthood (Hirai et al., 2005). A single injection of recombinant Cbln1 into the subarachnoid space over the cerebellum rapidly (in ∼48 h) restores PF synapses in adult *cbln1*$^{-/-}$ mice without affecting CF synapses (Ito-Ishida et al., 2008). Nevertheless, ataxic phenotype of *cbln1*$^{-/-}$ mice is completely but transiently rescued, indicating that Cbln1 is necessary and sufficient for the formation of PF–PC synapses and gross motor performance *in vivo*. Interestingly, PF-LTD is also

impaired in the *cbln1*$^{-/-}$ cerebellum, indicating that Cbln1 is not only required for formation and maintenance of PF synapses, but also for regulation of synaptic plasticity in the remaining PF synapses (Hirai et al., 2005). However, it has been untested whether delay EBC and PF-LTP could be normally induced in *cbln1*$^{-/-}$ mice, and whether Cbln1 injection could modulate these phenomena *in vivo*.

In this study, to clarify the role of PF synapses at different learning phases, we examined the delay EBC in *cbln1*$^{-/-}$ mice after injection of recombinant Cbln1 at different time points. We showed that delay EBC, but not trace EBC (Kishimoto et al., 2001b; Brown et al., 2010), was impaired in *cbln1*$^{-/-}$ mice. Although PF-LTD was impaired, PF-LTP was normally induced in *cbln1*$^{-/-}$ mice. A single recombinant Cbln1 injection completely, though transiently, restored PF-LTD and delay EBC in *cbln1*$^{-/-}$ mice. Interestingly, the *cbln1*$^{-/-}$ mice retained the CR for at least 30 d, after the Cbln1 injection's effect on PF synapses and PF-LTD induction had abated. Furthermore, delay EBC extinction by exposure to the unpaired CS succeeded, even after the Cbln1 injection's effect were lost. These results indicate that intact PF–PC synapses and PF-LTD, not PF-LTP, are necessary to acquire delay EBC in mice. In contrast, extracerebellar structures or remaining PF–PC synapses in *cbln1*$^{-/-}$ mice may be sufficient for the expression, maintenance, and extinction of its memory trace.

MATERIALS AND METHODS

MICE

This study used *cbln1*$^{-/-}$ mice on a C57BL6/J genetic background and their WT littermates. The mice were housed individually on a 12-h light/dark cycle, and given ad-lib access to food and water. All experiments were performed in accordance with the guidelines established by the Institutional Animal Investigation Committee at the Keio University School of Medicine. All efforts were made to minimize the use of animals and to optimize their comfort.

PREPARATION OF RECOMBINANT HA-CBLN1

Recombinant hemagglutinin-conjugated Cbln1 (HA-Cbln1) was prepared as described previously (Ito-Ishida et al., 2008). Briefly, pCAGGS-HA-Cbln1 was transfected into human embryonic kidney 293 (HEK293) cells using a calcium phosphate method (CellPhect, GE Healthcare Inc., USA). After 12 h, the culture medium was replaced with chemically defined 293 medium (Invitrogen Inc., USA). Two days later, the medium was collected and concentrated using centrifugal filtering devices (Centriplus YM-10 and Microcon YM-100, Millipore Inc., USA). The concentrated medium was washed twice with 500 μl phosphate-buffered saline (PBS) and the final volume of the medium was adjusted to 50 μl. Protein was measured using a BCA protein assay kit (Thermo Fischer Scientific, USA). The control solution was prepared from the medium of non-transfected HEK293 cells.

HA-CBLN1 INJECTION

Male *cbln1*$^{-/-}$ mice at PW 7–10 were anesthetized with an intraperitoneal injection of ketamine [80 mg/kg body weight (BW)] and xylazine 20 mg/kg BW (Sigma-Aldrich Inc., USA). A subarachnoid injection of HA-Cbln1 was given as described previously (Ito-Ishida et al., 2008; Matsuda et al., 2010). In brief, a small hole in the occipital bone was made with a dental drill, and the dura mater was ablated. A 33-gage microsyringe needle was inserted onto the surface of the simplex lobules (hemispheric lobule VI, HVI) of the cerebellum. HA-Cbln1 (1 μg/g BW) was injected into the subarachnoid space bilaterally, at a rate of 40 μl/h for 15 min. To prevent the infused solution from leaking, the injection site was sealed with a silicone elastomer (Kwik-Sil; World Precision Instruments, USA).

SURGICAL PROCEDURES FOR EYEBLINK CONDITIONING

Four Teflon-coated stainless steel wires (A-M Systems, Inc. Carlsborg, WA, USA) were implanted into the left eyelid of the mouse under deep anesthesia. Two wires were used to record electromyograms (EMG), and the remaining two to deliver weak electric shocks. The wires were soldered to connector pins, which were secured to small stainless steel screws fixed on the skull with dental acrylic resin. After surgery, the animals were returned to their home cages to recover for 2 days.

EYEBLINK CONDITIONING

Mice were subjected to EBC training as described previously (Kishimoto et al., 2001a; Kakegawa et al., 2008). Each mouse was put in a cylindrical Plexiglas container (10 cm in diameter and 25 cm in height) in a sound- and light-attenuating chamber. The connector pins fixed to the mouse's skull were connected to a flexible cable, which allowed the mouse to move freely during the conditioning trials. EMG activity was recorded through a band-pass filtered amplifier (0.15 and 1.0 kHz, MEG-5200, Nihonkoden, Japan) and fed into a computer at a sampling rate of 10 kHz. A 100-Hz periorbital electrical shock (100 ms) and a 1-kHz tone (85 dB, 350 ms) were used as unconditioned (US) and conditioned stimuli (CS), respectively. We employed this relatively high intensity CS condition (Boele et al., 2010) since WT mice showed stable learning throughout the training sessions (Sakamoto and Endo, 2010). Spontaneous eyeblink activities were recorded without applying US or CS on days 1 and 2.

In the delay paradigm, the CS tone preceded and co-terminated with the US shock. Each training session consisted of 90 CS–US paired trials and 10 CS-only trials that were presented every tenth trial. There was one training session per day, on days 3–9. The trials were separated by randomized inter-trial intervals from 20 to 40 s duration. The US intensity was adjusted daily to elicit an eyeblink/head turn response to obtain a constant amplitude of unconditioned response (UR). In the trace paradigm study, the US started 0, 250, or 500 ms after the CS ended. The trace conditioning experiment also involved 7 days of training sessions (Kishimoto et al., 2001b).

Electromyogram signals were analyzed offline by custom software (Microsoft Visual Basic 2003; Kakegawa et al., 2008). The EMG wave analysis algorithm has been described previously (Kishimoto et al., 2001a). Briefly, the maximum amplitude of EMG signals in each 1-ms bin represented the EMG amplitude during that time window. We calculated the average and the standard deviation (SD) of EMG amplitude during the 300 ms before CS onset in 100 trials. The averaged EMG amplitude plus 1 SD was

defined as a "threshold value." In each trial, the "baseline value" was calculated by averaging EMG amplitude that exceeded the threshold value during the 300 ms prior to the CS onset. In addition, we calculated the "startle value" by averaging EMG amplitude that exceeded the threshold value during the 30 ms after the CS. If the baseline and the startle values were less than 10% and 30% of the threshold value, respectively, the trial was considered valid. In the valid trial, the CR value was calculated by averaging EMG amplitude 200 ms before the US. In CS-only trials, the CR values were obtained by averaging the EMG amplitude over the period from 200 ms before to 100 ms after the expected US onset. If the CR value exceeded 1% of the threshold and was more than twice the baseline value, we regarded the trial as CR positive. The CR% was calculated for each mouse as the percentage of CR-positive trials among the valid trials in each training session. The CR% values for the individual mice were averaged to obtain the group CR% for each training session. In addition, before training session was started, the CR% values were similarly calculated in 100 trials without applying CS or US to estimate CR-like activities in each mouse.

To test retention and extinction of the delay EBC, we first chose mice showing CR% greater than 60%. Each mouse was left undisturbed for 30 days in its home cage after acquisition training and then tested for retention of the conditioned memory. For the retention test, the mice were given a 1-day trial session consisting of 90 CS–US paired trials and 10 CS-only trials (presented every 10th trial) for 1 day. For the extinction test, mice were given 100 CS-only trials for 4 days (Kishimoto et al., 2001b; Thompson and Steinmetz, 2009). The conditioning experiments were all carried out during the light phase of the light/dark cycle. The EBC training, memory testing, and extinction were performed by an experimenter blinded to each mouse's genotype.

ACOUSTIC STARTLE REFLEX TEST

The acoustic startle reflex test was performed as described previously (Emi et al., 2011). Each mouse was placed in the acoustic startle device (SRLAB, San Diego Instruments, USA) consisted of a Plexiglas cylinder (5-cm in outer diameter) in a sound-attenuated box (approximately 20-cm^2) with a high frequency loudspeaker (28 cm above the cylinder) that produced both a continuous background noise (70 dB) and the acoustic stimuli (bursts of white noise between 4 and 14 kHz). Movements of the mouse in the cylinder were transduced by a piezoelectric accelerometer attached to the bottom of the platform, and digitized. The maximal peak-to-peak amplitude from the piezoelectric sensor was used to determine the magnitude of the acoustic startle response (ASR). The session was initiated with a 5-min acclimation period followed by four different sound stimuli (75, 80, 85, 90 dB) presented in a random order with random inter-trial intervals (10–20 s; 15 s on average). All trials were repeated 10 times.

TALE FLICK TEST

Standard nocifensive reflex test (tail flick test) was performed on mice using a radiant heat apparatus (IITC, Woodland Hills, CA, USA). Mice were restrained in a Plexiglas tube and allowed to acclimate for 5–10 min before testing. Ten successive trials (60 s apart) with each mouse were averaged to obtain a mean value for each mouse.

IMMUNOBLOTTING AND IMMUNOHISTOCHEMISTRY

Two days after the HA-Cbln1 injection, the whole cerebellum of a *cbln1*$^{-/-}$ mouse was homogenized in a buffer containing 10 mM Tris-HCl, 1 mM EDTA, and 0.32 M sucrose (pH 7.5), and was centrifuged at 800 × *g* for 10 min at 4°C. The supernatant was centrifuged at 12,000 × *g* for 20 min at 4°C, and the pellet (P2 fraction) was solubilized in 2× SDS sample buffer. The protein concentration was measured using a BCA protein assay kit. Equal protein amounts were subjected to SDS–polyacrylamide gel electrophoresis (PAGE) and blotted onto a PVDF membrane (Hybond-P, GE Healthcare, USA). HA-Cbln1 was detected with an enhanced chemiluminescence system (Immobilon Western, Millipore Inc., USA) and quantified using an LAS-3000 CCD Imaging System (Fujifilm Co Ltd., Japan).

For immunohistochemical analysis, mice were fixed under deep anesthesia by cardiac perfusion with 0.1 M sodium phosphate buffer (PB), pH 7.4, containing 4% paraformaldehyde (4% PFA/PB); the cerebellum was then removed and soaked in 4% PFA/PB for 4 h. After rinsing the specimens with PBS, parasagittal slices (100 μm) were prepared using a microslicer (DTK-2000; Dosaka, Japan) and were permeabilized with 0.2% Triton X-100 in PBS with 2% normal goat serum and 2% bovine serum albumin for 6 h at 4°C. Immunohistochemical staining was performed using anti-HA antibody (1:1000; Covance Research Products), followed by incubation with Alexa546-conjugated secondary antibodies (1:1000; Invitrogen) and fluorescent Nissl stains (Neurotrace; 1:300, Invitrogen). The stained slices were viewed using a confocal laser-scanning microscope (Fluoview; Olympus).

ELECTROPHYSIOLOGY

Parasagittal cerebellar slices (200 μm thick) were prepared from adult *cbln1*$^{-/-}$ mice at 2 or 30 days after the recombinant HA-Cbln1 injection, as described previously (Kakegawa et al., 2008). Briefly, whole-cell patch-clamp recordings were made from visually identified PC s using a 60× water-immersion objective attached to an upright microscope (BX51WI; Olympus Optical, Tokyo, Japan) at room temperature. The patch pipette resistance was 3–5 MΩ when filled with the following intracellular solution (in millimoles): 65 Cs-methanesulfonate, 65 K-gluconate, 20 HEPES, 10 KCl, 1 $MgCl_2$, 4 Na_2ATP, 1 Na_2GTP, 5 sucrose, and 0.4 EGTA, pH 7.25 (295 mOsm/kg) for LTD experiment and 130 K-gluconate, 10 KCl, 10 HEPES 1 $MgCl_2$, 4 Na_2ATP, 1 Na_2GTP and 16 sucrose, pH 7.25 (295 mOsm/kg) for LTP experiment. The solution used for slice storage and recording contained (in millimoles) 125 NaCl, 2.5 KCl, 2 $CaCl_2$, 1 $MgCl_2$, 1.25 NaH_2PO_4, 26 $NaHCO_3$, and 10 D-glucose, bubbled continuously with a mixture of 95% O_2 and 5% CO_2. To block inhibitory synaptic transmission, 100 μM picrotoxin (P1675, Sigma-Aldrich Inc., MI, USA) was always added to the saline.

To induce synaptic plasticity at PF–PC synapses, PF–evoked excitatory postsynaptic currents (PF–EPSCs) were first recorded successively at a frequency of 0.1 Hz from PCs clamped at –80 mV.

After stable PF–EPSCs were observed for at least 10 min, a conjunctive stimulation (CJ-stim) composed of 30 single PF stimuli together with 200-ms depolarizing pulses from a holding potential of –60 to +20 mV was applied to induce LTD (Kakegawa et al., 2008). For induction of postsynaptic LTP, 300 times of PF stimuli were applied at a frequency of 1 Hz in the current-clamp mode (Lev-Ram et al., 2002). Access resistances were monitored every 10 s by measuring the peak currents in response to 2-mV, 50-ms hyperpolarizing steps throughout the experiments; the measurements were discarded if the resistance changed by more than 20% of its original value. EPSCs were recorded using an Axopatch 200B amplifier (Molecular Devices Inc., USA), and pClamp software (version 9.2, Molecular Devices Inc., USA) was used for data acquisition and analysis. The signals were filtered at 1 kHz and digitized at 4 kHz.

ELECTRON MICROSCOPIC STUDIES

Samples for electron microscopic studies were prepared as previously described (Ito-Ishida et al., 2008). Mice under deep pentobarbital anesthesia were perfused transcardially with 2% paraformaldehyde/2% glutaraldehyde in 0.1 M PB (pH 7.2). Parasagittal sections (300 μm thick) of the simplex lobule of the cerebellum were postfixed and stained for 2 h with 1% OsO_4 in 0.1 M PB. The sections were block-stained in 1% aqueous uranyl acetate solution, dehydrated with graded alcohols, and embedded in Epon 812. Ultrathin sections (70 nm thick) were made with an ultramicrotome (Leica Microsystems Co Ltd., Germany) and stained with 2% uranyl acetate for 5 min, followed by mixed lead solution for 2 min. Electron micrographs of the molecular layer were taken (H7100, Hitachi Co Ltd., Japan) at 4,000× and printed at 16,000×. The numbers of normal and free PC spines (which contained postsynaptic density-like condensations but lacked presynaptic contact) were counted using 10 micrographs per mouse, taken randomly (Hirai et al., 2005).

Statistical analysis

All data are presented as mean ± SEM. Statistical significance was determined by Mann–Whitney's *U* test, the Fisher's exact test, or an ANOVA, followed by the Bonferroni's test for multiple comparisons, using the SPSS program (Ver.15, SPSS Co Ltd., Japan). The difference was considered as significant when the *p*-value was less than 0.05.

RESULTS

DELAY, BUT NOT TRACE, EYEBLINK CONDITIONING WAS IMPAIRED IN *CBLN1*$^{-/-}$ MICE

To examine motor learning in *cbln1*$^{-/-}$ mice, we employed an EBC delay paradigm, in which a CS tone preceded and co-terminated with a US shock (**Figures 1A,B**). Although both *cbln1*$^{-/-}$ and WT mice showed increased occurrence of conditioned responses (CRs) after several training sessions, there were significant differences in acquisition of CRs between *cbln1*$^{-/-}$ and WT mice during the 7-day training period ($p < 0.01$ for genotype, a two-way repeated-measures ANOVA; **Figure 1C**). Similarly, in the delay EBC paradigm, the average CR% saturates at 20–40% in mice with various cerebellar mutations (Chen et al., 1996; Qiao et al., 1998; Kishimoto et al., 2001b; Wada et al., 2007; Emi et al., 2011), although it can reach 50–70% in WT mice. As reported previously for EBC in mice (Boele et al., 2010), eyeblink responses consist of short-latency responses (SLRs), which are likely mediated by amygdala, and a later responses mediated by the cerebellum (Sakamoto and Endo, 2010). Indeed, the averaged EMG amplitudes before the US in the seventh training sessions show SLRs in both *cbln1*$^{-/-}$ and WT mice (**Figure 1D**), indicating that the remaining learning may be mediated by extracerebellar structures. Nevertheless, the averaged EMG amplitudes before the US were significantly lower in *cbln1*$^{-/-}$ mice than in WT mice, suggesting that Cbln1, which is mostly expressed in cerebellar granule cells but not in amygdala (Miura et al., 2006), may be involved in the delay EBC.

To rule out the possibility that mice acquired conditioned responses by nonassociative learning, we next performed random presentation protocol. When the CS and US were randomly presented, the WT nor the *cbln1*$^{-/-}$ mice acquired conditioned responses ($p > 0.1$, a two-way repeated measures ANOVA; **Figure 1E**), excluding the possibility of non-associative learning. There were no differences in ASRs ($p > 0.5$, a two-way repeated measures ANOVA, **Figure 1F**) or tail-flick responses to heat ($p > 0.1$, Mann–Whitney's *U* test; **Figure 1G**) between the two genotypes. The US intensities required to elicit an eyeblink during conditioning did not differ between two genotypes (data not shown), indicating that the *cbln1*$^{-/-}$ mice had no gross sensory system defects. Thus, the delay EBC paradigm, a form of associative motor learning, was likely impaired in the *cbln1*$^{-/-}$ mice.

The trace EBC paradigm, in which a stimulus-free interval intervenes between the CS and the US (**Figure 2A**), requires extracerebellar structures and less depends on the cerebellar cortex in mice (Kishimoto et al., 2001b; Brown et al., 2010). Thus, we examined whether *cbln1*$^{-/-}$ mice could acquire associative memory by the EBC trace paradigm. First, the animals were given a CS, followed by a US 500 ms after the end of the CS, 100 times per day, for 7 days. In both WT and *cbln1*$^{-/-}$ mice, the CR% gradually increased, with no significant differences between the genotypes ($p > 0.1$, a two-way repeated measures ANOVA; **Figure 2B**). Similarly, the averaged EMG amplitudes between the CS and US in the seventh training session were similar between the two genotypes (**Figure 2C**). We also used shorter interstimulus intervals between the CS and US and found that WT and *cbln1*$^{-/-}$ mice showed a similar CR% at the end of the seventh training session ($p > 0.1$ for both 0- and 250-ms intervals, two-way repeated measures ANOVA followed by Bonferroni's correction; **Figure 2D**). Thus, that *cbln1*$^{-/-}$ mice are able to acquire conditioned responses in EBC depending on the training protocol. These results are consistent with an earlier report that mice lacking GluD2, a receptor for Cbln1, showed normal trace EBC (Kishimoto et al., 2001a,b). Together, the delay EBC paradigm was specifically impaired in *cbln1*$^{-/-}$ mice.

INJECTED CBLN1 TRANSIENTLY RESTORED EYEBLINK CONDITIONING IN *CBLN1*$^{-/-}$ MICE

Although Cbln1 is mostly expressed in cerebellar granule cells, it is also expressed in the DCN and extracerebellar structures, such as

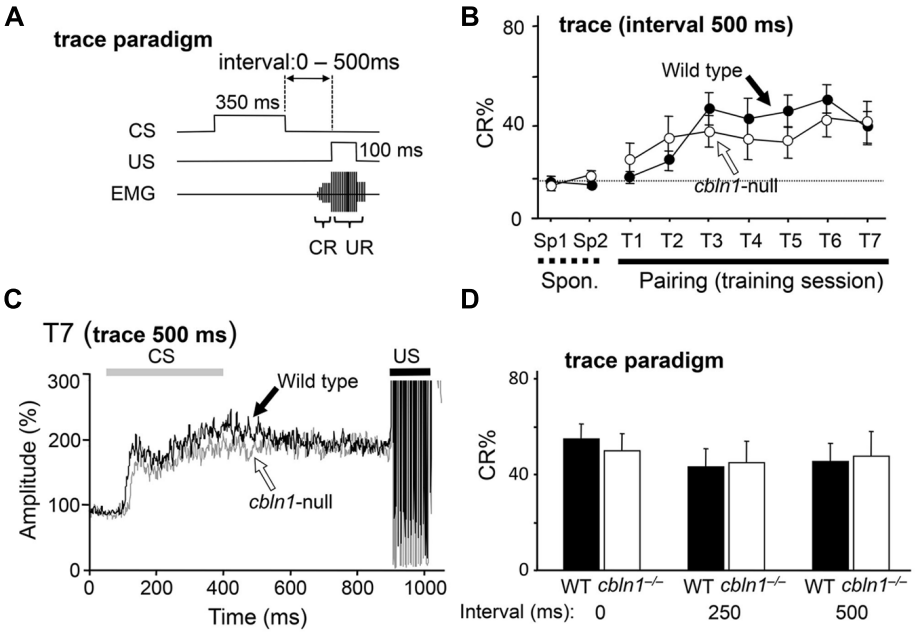

FIGURE 2 | Trace eyeblink conditioning (EBC) is intact in *cbln1*$^{-/-}$ mice. (A) Diagram showing trace EBC. An unconditioned stimulus (US, 100 ms) was applied 500 ms after the end of the conditioned stimulus (CS, 350 ms) tone. Mice were trained for 7 days, one session per day. Associative learning was established when conditioned responses (CR), detected by electromyogram (EMG) were observed before unconditioned eyeblink responses (UR). **(B)** Intact trace EBC in *cbln1*$^{-/-}$ mice. No significant difference in CR% was observed between wild-type and *cbln1*$^{-/-}$ mice ($p > 0.1$, a two-way repeated measures ANOVA, $n = 10$ mice for each group). T1–T7, training sessions; Sp1 and Sp2, spontaneous eyeblink responses before training. The *Y*-axis indicates the percentage of trials showing CR. The dotted line corresponds to the percentage of CR-like activities on Sp2 to indicate the baselin e for learned responses. **(C)** Averaged EMG amplitude on the last day of training (T7). The EMG amplitudes were normalized to those during the initial 30 ms of CS; $n = 10$ for each group. No significant differences were observed between the two groups. **(D)** The effect of different time intervals on trace EBC. The interval between the end of the CS and the beginning of the US was shortened from 500 ms to 250 or 0 ms. The CR% on the last day of training (T7) is shown for each genotype. No significant CR% difference was observed for 500, 250, and 0 ms intervals between wild-type and *cbln1*$^{-/-}$ mice ($p > 0.1$, two-way repeated measures ANOVA followed by Bonferroni's correction, $n = 8$ for each genotype).

the olfactory bulb, entorhinal cortex, and thalamus (Miura et al., 2006). To rule out the involvement of these structures in the delay EBC, we examined whether the delay EBC defect in the *cbln1*$^{-/-}$ mice could be rescued by applying Cbln1 to PF–PC synapses. We previously showed that a single injection of recombinant Cbln1 into the subarachnoid space over the vermis rapidly but transiently restored PF–PC synapses and motor coordination in *cbln1*$^{-/-}$ mice, as measured by the rotor-rod test (Ito-Ishida et al., 2008). Since delay EBC is likely mediated by the bilateral HVI (Miller et al., 2003; Plakke et al., 2007; Sun, 2012), we performed bilateral injections of Cbln1 (a total of 1 μg/g body weight) into the subarachnoid spaces over each HVI (**Figure 3A**) of 7- to 10-week-old *cbln1*$^{-/-}$ mice. We detected recombinant Cbln1 in the membrane fraction of the whole cerebellum by immunoblot analysis at 2 days, but not 10 days, after the injection (**Figure 3B**). Immunohistochemical analysis of coronal cerebellar sections from *cbln1*$^{-/-}$ mice taken 2 days after the Cbln1 injection found recombinant Cbln1 throughout the cerebellar cortex including HVI, but not in the DCN region (**Figure 3C**). When *cbln1*$^{-/-}$ mice were subjected to delay EBC starting 2 days after a Cbln1 injection, they show significantly better CR% than *cbln1*$^{-/-}$ mice that did not receive the injection ($p < 0.01$ for genotype, a two-way repeated measures ANOVA; **Figure 3D**) and comparable to that achieved by WT mice (**Figure 1C**), indicating that the local Cbln1 injection was able to rapidly restore motor learning defects in the *cbln1*$^{-/-}$ mice.

To examine whether Cbln1's effect on delay EBC was as transient as its effect on motor performance (Ito-Ishida et al., 2008), we next subjected *cbln1*$^{-/-}$ mice to delay EBC 30 days after the injection, when the injected Cbln1 was no longer detectable (**Figure 3B**). There were no significant differences in CR% between *cbln1*$^{-/-}$ mice that did or did not receive Cbln1 ($p > 0.1$, a two-way repeated measures ANOVA; **Figure 3D**), showing that the effect of the injected Cbln1 on the impaired EBC in *cbln1*$^{-/-}$ mice was indeed transient. Together, these results indicate that the lack of Cbln1 in the cerebellum was responsible for the defective delay EBC in the *cbln1*$^{-/-}$ mice and that this phenotype was rapidly but transiently rescued by the recombinant Cbln1 injection.

CBLN1 RESTORED PF– BUT NOT CF–PURKINJE CELL SYNAPSES IN *CBLN1*$^{-/-}$ MICE

We used electron microscopy to examine whether the bilateral Cbln1 injection also rescued morphological abnormalities observed at *cbln1*$^{-/-}$ PF–PC synapses with a similar time-course as its rescue of delay EBC. We found that PF–PC synapse anatomical abnormalities in *cbln1*$^{-/-}$ mice were significantly

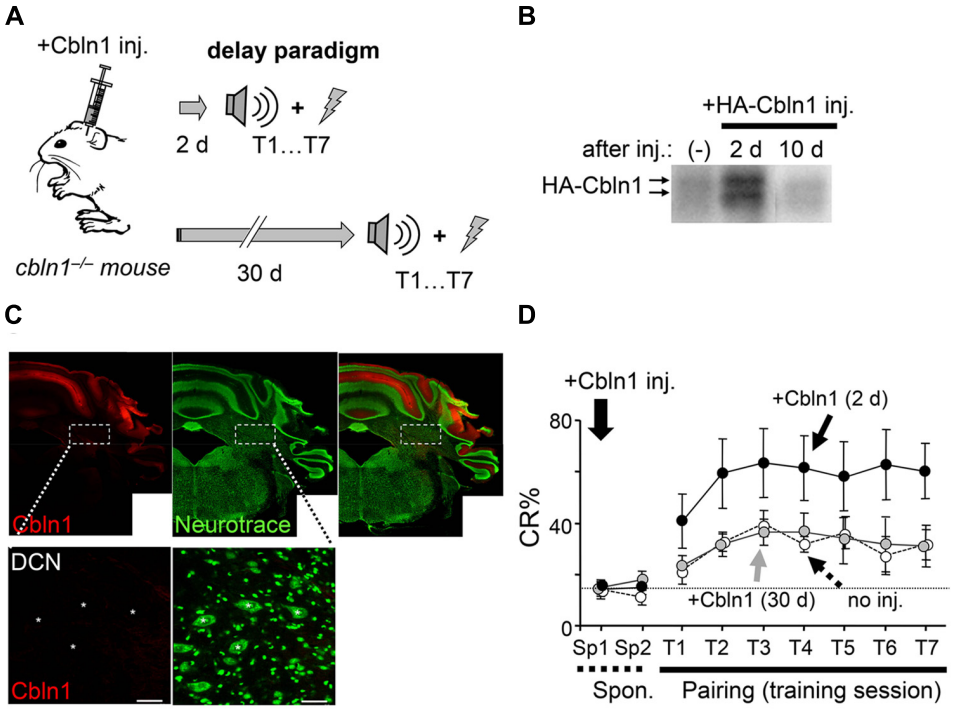

FIGURE 3 | Delay eyeblink conditioning (EBC) in adult *cbln1*$^{-/-}$ mice improves after a cerebellar subarachnoid Cbln1 injection. **(A)** A diagram showing a sequence of experiments. HA-Cbln1 (1 μg/g body weight) was injected into the subarachnoid spaces over the bilateral HVI lobes of 7- to 10-week-old *cbln1*$^{-/-}$ mice. The mice were trained using the delay EBC paradigm beginning 2 or 30 days after the injection. **(B)** HA-Cbln1 disappears from the cerebellum by 10 d after injection. Immunoblotting with an antibody against HA was used to detect injected HA-Cbln1 in the P2 fraction of the whole cerebellum before (–), 2 days, and 10 days after the injection. Arrows indicate bands corresponding to HA-Cbln1. The blot represents results from $n = 3$ mice. **(C)** Distribution of injected Cbln1. Cerebellar slices were stained with anti-HA antibody (red) to detect HA-Cbln1 24 h after the injection. Neurons visualized with fluorescent Nissl stains (Neurotrace; green). The injected Cbln1 was localized to the cerebellar cortex. Asterisks in the enlarged images indicate the deep cerebellar nucleus (DCN). Scale bars, 20 μm. **(D)** Cbln1 transiently rescued the impaired delay EBC in *cbln1*$^{-/-}$ mice. The CR% increased significantly in *cbln1*$^{-/-}$ mice trained 2 days after a Cbln1 injection [+Cbln1 (2d)] compared to those trained 30 days after [+Cbln1 (30 days)] the injection or those not treated with Cbln1 (no inj; $p < 0.01$, a two-way repeated measures ANOVA, $n = 8$ for each group). T1–T7, training sessions; Sp1 and Sp2, spontaneous eyeblink responses before training. The dotted line corresponds to the average percentage of CR-like activities on Sp2 to indicate the baseline for learned responses.

improved 2 days after bilateral Cbln1 injections ($p < 0.001$ vs. non-injected *cbln1*$^{-/-}$ control, Mann–Whitney's U test; **Figures 4A,B**): approximately 90% of the spines formed normal asymmetrical synapses with presynaptic terminals. In contrast, only 20–25% of synapses showed normal morphology in the *cbln1*$^{-/-}$ cerebellum 30 days after the Cbln1 injection, similar to the untreated *cbln1*$^{-/-}$ cerebellum (**Figures 4A,B**), and confirming that Cbln1 transiently rescued PF synapse morphological abnormalities.

Unlike WT PC s, *cbln1*$^{-/-}$ PC s remain innervated by supernumerary CFs even during adulthood (Hirai et al., 2005). Since Cbln1 and its receptor GluD2 are not expressed at CF–PC synapses (Yuzaki, 2009), this defect is likely to be indirectly caused by the loss of PF–PC synapses in *cbln1*$^{-/-}$ mice. Thus, to examine whether bilateral injection of Cbln1 restored normal CF innervation patterns in *cbln1*$^{-/-}$ PCs, we measured the threshold to elicit CF–EPSCs in each PC, since a single CF has a single threshold for excitation. As reported previously (Hirai et al., 2005), single EPSCs were elicited in ∼95% of WT PC s at postnatal day 46 (P46)–P52 ($n = 60$ out of 63 cells from 5 mice), whereas only ∼50% of age-matched *cbln1*$^{-/-}$ PC s that were injected with Cbln1-free control solutions showed a one-to-one relationship with CFs ($n = 34$ out of 68 cells from 5 mice, $p < 0.00001$ vs. WT, Fisher's exact test; **Figure 4C**). In contrast, 2 days after the Cbln1 injection, the percentage of PC s showing single EPSCs increased slightly but not significantly (∼65%, $n = 46$ out of 71 cells from 5 mice, $p < 0.05$ vs. *cbln1*$^{-/-}$ PCs injected with the control solution, Fisher's exact test; **Figure 4C**). No further significant increase in the percentage of PC s with single EPSCs was seen 4 d after the Cbln1 injection (∼60%, $n = 24$ out of 40 cells from 3 mice, $p > 0.1$ vs. *cbln1*$^{-/-}$ PCs at 2 days after Cbln1 injection, $n = 40$ cells from 3 mice, Fisher's exact test; **Figure 4C**). Thus, the CF innervation pattern was only partially rescued by a single Cbln1 injection. Similarly, although transient GluD2 expression restored PF–PC synapses in GluD2$^{-/-}$ mice, it failed to correct the sustained innervation of PC s by multiple CFs (Kohda et al., 2007; Kakegawa et al., 2009), suggesting that rescuing the mature CF innervation pattern may require more time than rescuing PF synapses in both *cbln1*$^{-/-}$ and GluD2$^{-/-}$ mice. These results indicate that acquisition of

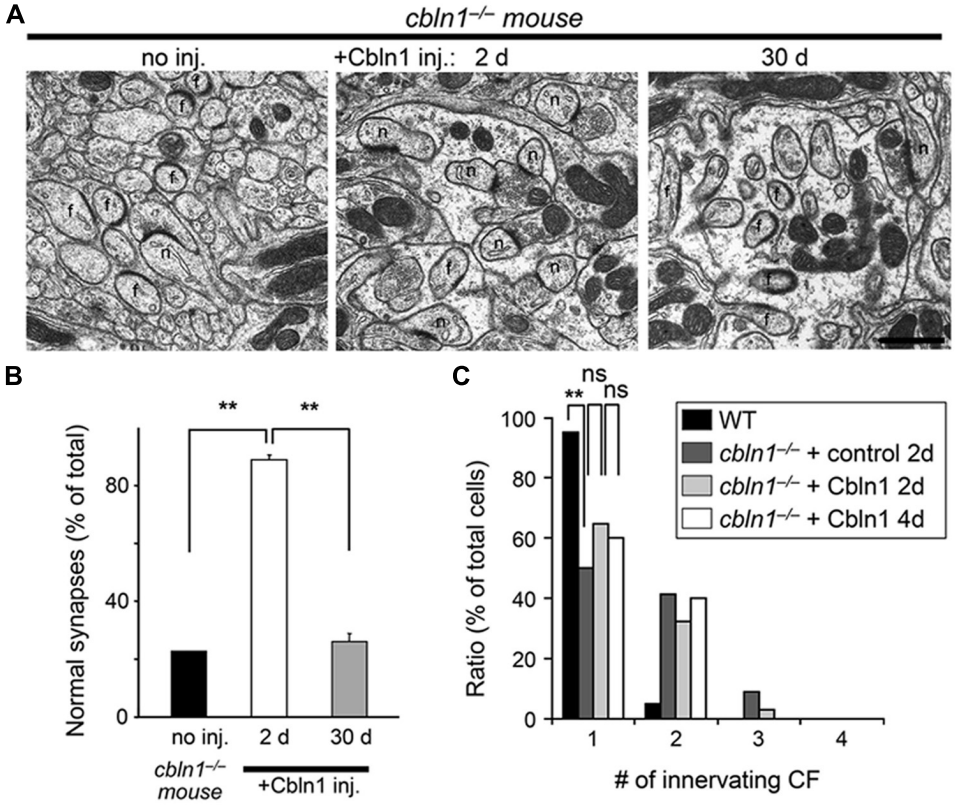

FIGURE 4 | Subarachnoidal Cbln1 injection transiently restores PF–Purkinje cell synapse structure in *cbln1*$^{-/-}$ mice. (A) Electron micrographs of the molecular layer in *cbln1*$^{-/-}$ mice aged P42–P54 without Cbln1 injection (no inj) and at 2 or 30 days after Cbln1 injection. f, free spines without innervation by presynaptic structures; n, normal spines. Scale bar, 500 nm. **(B)** The percentage of normal synapses in *cbln1*$^{-/-}$ mice with no injection (no inj), or 2 or 30 d after a Cbln1 injection. Significant recovery of normal synapses was observed 2 days after a Cbln1 injection, compared with no injection or their state 30 days after the injection (**$p < 0.001$, Mann–Whitney's U test, $n = 3$ for each group). **(C)** Cbln1 injection transiently rescued the multiple CF innervation pattern in a single Purkinje cell from a *cbln1*$^{-/-}$ mouse. The number of CF–EPSCs induced by different stimulus thresholds (0–200 μA) was counted. The percentage of Purkinje cells innervated by single CFs in wild-type (WT) mice was significantly higher than that in *cbln1*$^{-/-}$ mice 2 days after the injection of a control solution (+control 2 days; **$p < 0.00001$, Fisher's exact test). There were no significant (ns) difference between control solution and Cbln1 at 2 days after the injection (+Cbln1 2 days; $p > 0.1$, Fisher's exact test). Similarly, there were no significant difference between 2 and 4 days after a Cbln1 injection (+Cbln1 4 days; $p > 0.1$, Fisher's exact test).

delay EBC may not require mature CF innervation patterns in the cerebellum.

PF-LTD, BUT NOT PF-LTP, IS IMPAIRED IN *CBLN1*$^{-/-}$ MICE AND RESCUED BY CBLN1 INJECTION

Recently, PF-LTP was proposed as a substrate for motor learning in the cerebellum (Schonewille et al., 2010). Thus, we next examined whether PF-LTP could be induced in *cbln1*$^{-/-}$ PC s in acute slice preparations. As reported previously (Lev-Ram et al., 2002; Kakegawa and Yuzaki, 2005), 300 single stimulations of the PF at a frequency of 1 Hz in the current-clamp mode induced postsynaptic PF-LTP in WT PCs (**Figure 5**). Similarly, PF-LTP was normally induced in *cbln1*$^{-/-}$ mice.

In contrast, LTD is impaired at PF–PC synapses in *cbln1*$^{-/-}$ mice (Hirai et al., 2005). To clarify whether this impairment can be rescued by injecting Cbln1, we next prepared cerebellar slices from *cbln1*$^{-/-}$ mice injected with Cbln1. As reported previously, an injection of recombinant Cbln1 rapidly restored PF–PC synaptic transmission (Ito-Ishida et al., 2008). Furthermore, a conjunctive stimulation, which consisted of 30 single stimulations of the PF together with a 200-ms depolarization of the PCs, successfully induced PF-LTD in the *cbln1*$^{-/-}$ PC s 2 days after the Cbln1 injection treatment, but failed to induce PF-LTD in *cbln1*$^{-/-}$ PCs after the injection of the control solution (**Figure 6A**). The PF-EPSC amplitude 25- to 30-min after the combined stimulation was 81 ± 5% ($n = 6$ from five mice) of the control responses in PCs 2 days after a Cbln1 injection, whereas that of cells from mice injected with the control solution was 106 ± 7% ($p < 0.05$, Mann–Whitney's U test, $n = 5$ from 5 mice). In contrast, the conjunctive stimulation failed to induce PF-LTD either in control *cbln1*$^{-/-}$ PCs (injected with the control solution) or in *cbln1*$^{-/-}$ PCs 30 d after Cbln1 treatment (**Figure 6B**). The amplitude of PF-EPSCs 25- to 30 min after stimulation was 105 ± 12% ($n = 6$ from 6 mice) of the control responses in PC s at 30 days after the Cbln1 injection, whereas that of cells treated with the control solution was 105 ± 4% ($p > 0.5$, Mann–Whitney's U test, $n = 5$ from 5 mice). These findings indicate that Cbln1 injection rapidly but transiently restored PF-LTD in *cbln1*$^{-/-}$cerebellum.

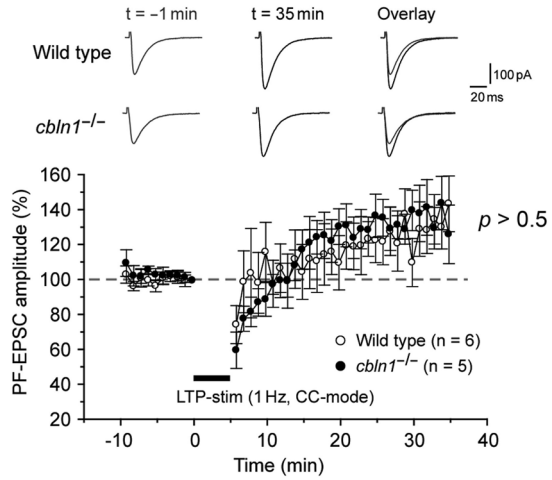

FIGURE 5 | LTP at PF–Purkinje cell synapses is normally induced in *cbln1*$^{-/-}$ mice. A summary of LTP sessions in cerebellar slices prepared from wild-type and *cbln1*$^{-/-}$ mice. The averaged amplitudes of the PF-EPSC over 1 min were normalized to the baseline value, which was the average of the 1 min responses (six traces) that occurred just before an LTP-inducing stimulation (300 times of single PF stimuli at a frequency of 1 Hz in the current-clamp mode). Inset traces show the PF-EPSCs just before ($t = -1$ min) or 35 min ($t = 35$ min) after the LTP stimulation, and their superimposition (overlay). No differences were observed in PF-EPSC amplitudes after the LTP stimulation between wild-type and *cbln1*$^{-/-}$ mice ($p > 0.5$, wild type vs. *cbln1*$^{-/-}$ mice, Mann–Whitney's U test, $n = 6$ for wild type, $n = 5$ for *cbln1*$^{-/-}$ mice).

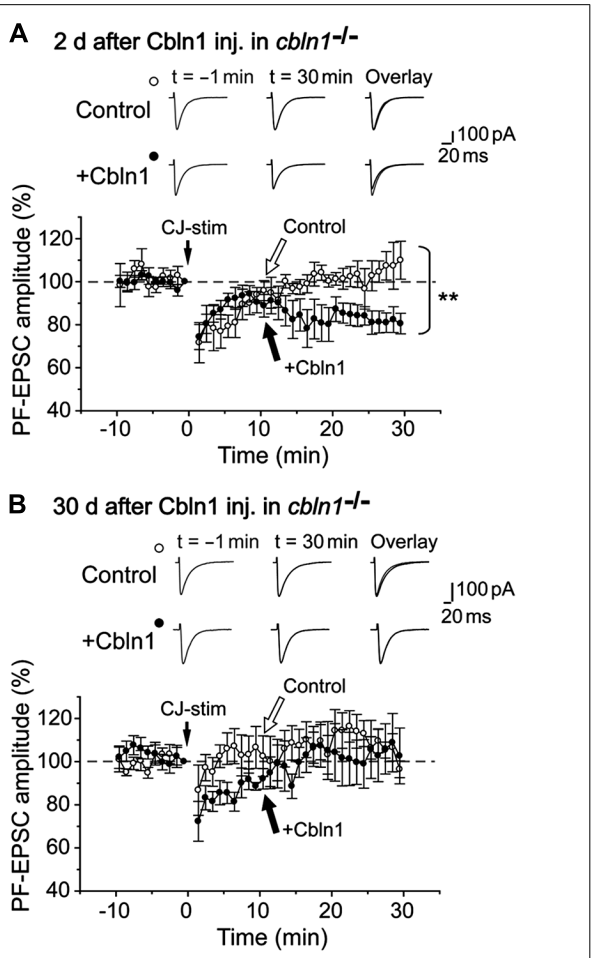

FIGURE 6 | Subarachnoidal Cbln1 injection transiently restores LTD at *cbln1*$^{-/-}$ mouse PF–Purkinje cell synapses. A summary of LTD sessions in cerebellar slices prepared from *cbln1*$^{-/-}$ mice at 2 days **(A)** and 30 days **(B)** after injection of Cbln1 (+Cbln1), or control solution that did not contain Cbln1 (Control). The averaged amplitudes of the PF–EPSC over 1 min were normalized to the baseline value, which was the average of the 1 min responses (six traces) that occurred just before a conjunctive stimulation (CJ-stim) composed of 30 single PF stimuli together with 200-ms depolarizing pulses from a holding potential of –60 to +20 mV. Inset traces show the PF–EPSCs just before ($t = -1$ min) or 30 min ($t = 30$ min) after the CJ-stim, and their superimposition (overlay). Note that LTD was significantly restored in *cbln1*$^{-/-}$ mice at 2 days after Cbln1 injection (**$p < 0.05$, control vs. Cbln1, Mann–Whitney's U test, $n = 5$ for control, $n = 6$ for Cbln1), but not at 30 d after injection ($p > 0.5$, control vs. Cbln1, Mann–Whitney's U test, $n = 5$ for control, $n = 6$ for Cbln1).

Furthermore, PF-LTD, but not PF-LTP, was likely to be directly involved in the acquisition of delay EBC in *cbln1*$^{-/-}$ mice.

CONDITIONED EYEBLINK RESPONSES ARE MAINTAINED AND EXPRESSED IN *CBLN1*$^{-/-}$ MICE

The precise role of PF–PC synapses in delay EBC has been unclear (Christian and Thompson, 2003; Boyden et al., 2004). Taking advantage of Cbln1's ability to rapidly and transiently restore morphological (**Figure 4**) and functional (**Figure 6**; Ito-Ishida et al., 2008) PF synapses, we next examined the roles of PF synapses at various stages of delay EBC. First, we injected Cbln1 into *cbln1*$^{-/-}$ mice and performed delay EBC training 2 days later. After these mice acquired motor learning, as judged by a CR% greater than 60% in the seventh training session (CR% at the seventh session, 63.1 ± 0.1% for wild type vs. 64.2 ± 0.2% for injected *cbln1*$^{-/-}$ mice, $p > 0.1$, Mann–Whitney's U test, $n = 8$ for each group; **Figures 7A,B**), they were kept in their home cages without any further training until the eighth session, 30 days later. Interestingly, *cbln1*$^{-/-}$ mice that received training 2 days after the Cbln1 injection showed high CR% levels at the eighth session, on day 40; these levels were comparable to those of WT mice in the same session (CR% at the eighth session, 58.1 ± 0.2% for WT vs. 60.2 ± 0.1% for injected *cbln1*$^{-/-}$ mice, $p > 0.1$, Mann–Whitney's U test, $n = 8$ for each group; **Figures 7B,C**). In addition, the CR% was similar between the seventh and eighth sessions ($p > 0.1$, Mann–Whitney's U test) in both WT and in *cbln1*$^{-/-}$ mice treated with Cbln1 (**Figures 7B,C**), indicating that Cbln1 was unnecessary for the maintenance and expression of memory traces. However, as shown above, 30 days after the Cbln1 injection, PF–PC synapses had returned to their morphologically (**Figure 4**) and functionally (**Figure 6**) impaired state in *cbln1*$^{-/-}$ mice. In addition, *cbln1*$^{-/-}$ mice that were given a Cbln1 injection but did not receive any training for 30 days failed to acquire associative learning (**Figure 3C**). Together, these results suggest that although intact PF synapses are necessary for acquiring delay EBC, they may be dispensable for its expression and maintenance of previously acquired memory.

EXTINCTION OF CONDITIONED EYEBLINK RESPONSES DOES NOT REQUIRE CBLN1

The memory trace in EBC is known to be rapidly extinguished by repeated exposure to CS-only presentations, but the underlying mechanisms are not completely clear. Thus, using the Cbln1 transient rescue method, we examined PF–PC synapse roles during extinction sessions (**Figure 8A**). We first injected Cbln1 into *cbln1*$^{-/-}$ mice, and performed delay EBC training 2 d later. After these mice acquired motor learning, as judged by a CR% larger than 60% in the seventh training session (CR% at the seventh session, 61.1 ± 0.2% for wild type vs. 62.1 ± 0.1% for injected *cbln1*$^{-/-}$ mice, $p > 0.5$, Mann–Whitney's U test, $n = 7$ for each group; **Figures 8A,B**), they were returned to their home cages and did not receive further training for 30 d, after which they were subjected to 4-day extinction sessions in which only a CS tone was given to the animals 100 times per day. The CR% of both WT and *cbln1*$^{-/-}$ mice was gradually reduced to levels comparable to those prior to training (CR% at the fourth extinction session, 14.0 ± 0.2% for WT vs. to 13 ± 0.1% for injected *cbln1*$^{-/-}$ mice, $p > 0.5$, Mann–Whitney's U test, $n = 7$ for each group; **Figures 8B,C**). These results indicate that the presence of Cbln1 and intact PF–PC synapses may both be dispensable for the extinction of memory traces acquired by delay EBC.

DISCUSSION

Cbln1 is a recently identified synaptic organizer regulating the morphological and functional integrity of PF–PC synapses in the cerebellum (Yuzaki, 2011). Although *cbln1*$^{-/-}$ mice show motor dyscoordination and an ataxic gait, Cbln1's role, if any, in learning tasks *in vivo* has not been studied previously. Here, we showed that the delay EBC paradigm, a form of associative motor learning, was impaired in *cbln1*$^{-/-}$ mice (**Figure 1**). Importantly, a single recombinant Cbln1 injection into the subarachnoid space over the *cbln1*$^{-/-}$ cerebellum rapidly restored delay EBC acquisition (**Figure 3**). Immunohistochemical analysis of the whole brain revealed that the injected Cbln1 was restricted to the cerebellum (Ito-Ishida et al., 2008) and its molecular layer (**Figure 3C**). These findings indicate that, although Cbln1 is expressed in extracerebellar structures, such as the olfactory bulb, entorhinal cortex, and thalamus (Miura et al., 2006), the Cbln1 expressed in the cerebellum probably plays an essential role in acquisition of associative motor memory, as measured by the delay EBC protocol.

Recent studies based on genetically modified mice has challenged a widely held assumptions that PF-LTD is the main mechanism underlying motor learning in the cerebellum, such as EBC (Schonewille et al., 2010, 2011). As an alternative hypothesis, PF-LTP was proposed as a substrate for motor learning (Porrill and Dean, 2008; Schonewille et al., 2010). However, we showed that PF-LTP was normally induced (**Figure 5**), while PF-LTD was impaired in *cbln1*$^{-/-}$ mice (**Figure 6**). Furthermore, impaired PF-LTD was rescued by injection of recombinant Cbln1 (**Figure 6**). These results indicate that although it remains unclear whether and how PF-LTD serves as a memory trace (Hesslow et al., 2013), PF-LTP is dispensable for acquisition of delay EBC at least in *cbln1*$^{-/-}$ mice.

CBLN1 AS A TOOL TO STUDY PF–PURKINJE CELL SYNAPSE ROLES IN MOTOR LEARNING

The mechanisms underlying delay EBC has been characterized has been extensively studied in rabbits as well as cats, ferrets and rats by lesioning or pharmacological methods (Hesslow and Yeo, 2002; Christian and Thompson, 2003). Nevertheless, the exact role played by the various cerebellar synapses at different learning phases has not been completely clear, partly due to the difficulty of manipulating specific synapses by lesioning or pharmacological methods (Christian and Thompson, 2003; Boyden et al., 2004). Although gene targeting in mice has clarified the involvement of specific genes in delay EBC (Aiba et al., 1994; Kishimoto et al., 2001a; Miyata et al., 2001; Koekkoek et al., 2003, 2005), the location of the synapses responsible for storing the associative memory has remained unclear, because the same gene product is often used by different synapses in the targeted neuron. As discussed in the Section "Introduction," many molecules, such as PKC, metabotropic glutamate receptor 1, and calcineurin, are not specifically expressed at PF–PC synapses (Yuzaki, 2012). Thus, temporally and spatially controlled gene ablation or expression is particularly important to prevent compensation by backup pathways. Reversible neurotransmission blocking (RNB) techniques using transiently expressed tetanus toxin light chain in cerebellar granule cells can precisely target specific presynaptic terminals in the cerebellar circuits (Wada et al., 2007). However, like pharmacological AMPA receptor blockers, RNB blocks excitatory neurotransmission at PF–interneuron synapses as well as at PF–PC synapses. In addition, since the effect of RNB was assessed by spontaneous simple spikes under general anesthesia, it is unclear whether or to what extent synaptic transmission is inhibited in PC s during EBC. In contrast, we showed here that injected Cbln1 likely regulates synaptic transmission and plasticity specifically at PF–PC synapses. Although Cbln1 is also expressed in the DCN, recombinant Cbln1 injected into the subarachnoid space does not reach the DCN in *cbln1*$^{-/-}$ mice (**Figure 3C**; Ito-Ishida et al., 2008). In addition, GluD2, a postsynaptic receptor for Cbln1 (Matsuda et al., 2010), is not expressed in PC axons (Matsuda et al., 2008) or by other neurons innervating the DCN. Furthermore, although GluD2 is expressed at very low levels in cerebellar interneurons, synaptic transmission at the PF–interneuron synapses is not affected in *GluD2*$^{-/-}$ mice (Yamasaki et al., 2011). Therefore, although EBC in mice has certain limitations (Boele et al., 2010), a rescue approach using a single injection of recombinant Cbln1 serves as a unique and powerful tool to study the specific roles of PF–PC synapses at different learning phases *in vivo*.

CBLN1 IS REQUIRED FOR THE ACQUISITION, BUT NOT MAINTENANCE OR EXTINCTION OF DELAY EBC

A single injection of recombinant Cbln1 into the *cbln1*$^{-/-}$ cerebellum transiently restored the ability to acquire delay EBC (**Figure 3**). Similarly, a single injection of Cbln1 only transiently morphologically (**Figure 4**) and functionally (**Figure 5**) restored normal PF–PC synapses in *cbln1*$^{-/-}$ mice. These results are consistent with earlier lesion and inactivation experiments targeting the cerebellar cortex in rabbits (Attwell et al., 2002; Christian and Thompson, 2003), suggesting that cerebellar cortical circuits are

crucial for acquiring certain CRs. Interestingly, the impaired delay EBC was rescued in *cbln1*$^{-/-}$ mice even when PC s were innervated by multiple CFs (**Figure 4C**). Similarly, we previously showed that ataxic gait and motor dyscoordination (as measured using the rotor-rod test) were significantly rescued by transiently expressed GluD2 in GluD2$^{-/-}$ mice, which maintained multiple-CF innervations of PC s (Kakegawa et al., 2009). Together, these findings indicate that the CF innervation pattern may not play a major role, but intact PF–PC synapses are indispensable for acquisition of memory in the delay EBC paradigm.

Interestingly, we found that *cbln1*$^{-/-}$ mice that received training that began 2 days after a Cbln1 injection retained normal delay EBC responses, even when their PF–PC synapses became morphologically and functionally impaired by Cbln1 loss (**Figure 7**). This finding could be explained by the two-region memory hypothesis (Thompson and Krupa, 1994; Medina et al., 2001): a memory trace is initially formed at PF–PC synapses in *cbln1*$^{-/-}$ mice when training starts, 2 days after the Cbln1 injection. The memory trace is then transferred to the DCN or other regions over time. Similarly, inactivating the cerebellar cortex by a cooling probe impairs CR acquisition, but does not disrupt CR expression in well-trained animals (Clark et al., 1997). Although plastic changes at DCN synapses reportedly encode trained response amplitudes (Garcia and Mauk, 1998; Koekkoek et al., 2003), it is difficult to evaluate this aspect in the present study using EMG recordings.

Alternatively, since approximately 20% of PF–PC synapses were morphologically normal in *cbln1*$^{-/-}$ mice at 30 d after the Cbln1 injection (**Figure 4**), this finding could be explained by the one-region cortical memory hypothesis (Attwell et al., 2002; Kalmbach et al., 2010) in which a memory trace, probably formed as LTD at the PF–PC synapses in *cbln1*$^{-/-}$ mice, when training begins 2 days after the Cbln1 injection, and 30 days after the injection the remaining PF synapses may retain enough information to express CRs. In either case, our findings indicate that the presence of Cbln1 and a large majority of the PF–PC synapses (and CF synapses) are unnecessary for maintaining and expressing delay EBC memory traces.

The normal extinction of the EBC that was acquired by *cbln1*$^{-/-}$ mice after the Cbln1 injection, even though they had few normal PF–PC synapses remaining (**Figure 8**), is consistent with the one-region cortical memory hypothesis, because inhibition of CF activities is shown to serve as a teaching signal for extinction by reversing LTD in the cerebellar cortex (Medina et al., 2002). In this scenario, the memory trace was formed at PF– PC synapses in *cbln1*$^{-/-}$ mice, as training began 2 days after the Cbln1 injection, maintained in the remaining synapses at 30 days, and removed by reduced CF activity during extinction training. However, the alternative hypothesis that the memory trace is actually stored in regions outside of the cerebellar cortex and is removed during extinction training cannot be ruled out. Although further studies are required to clarify the extinction mechanisms, it is clear that the presence of

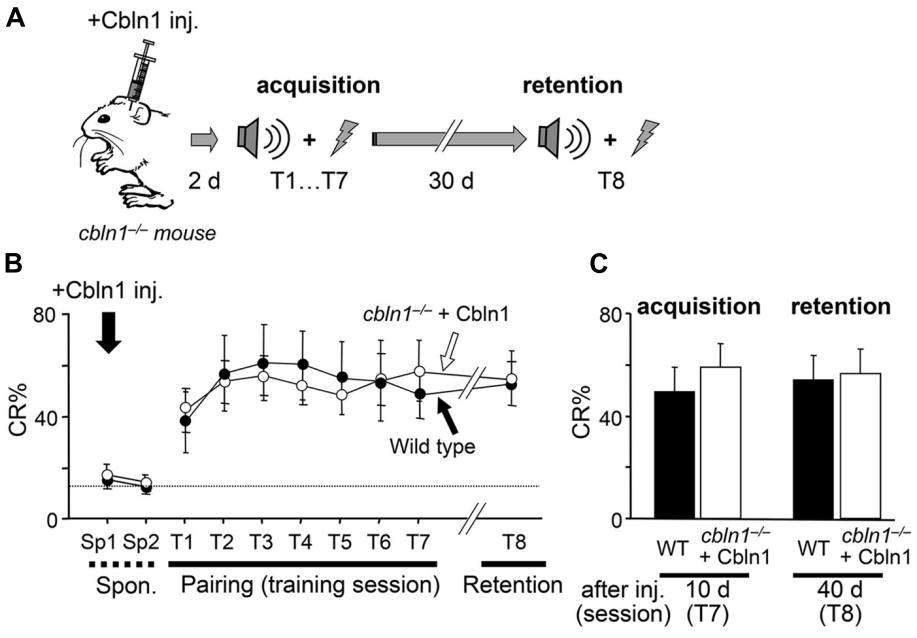

FIGURE 7 | Intact retention and expression of EBC in *cbln1*$^{-/-}$ mice. **(A)** A diagram showing a sequence of experiments: *cbln1*$^{-/-}$ mice were injected with Cbln1 as described in **Figure 3** and subjected to delay eyeblink conditioning (EBC) from 2 (T1–T7) and at 40 days (T8, 30-days interval between T7 and T8) after the injection to examine the retention of learned responses. **(B)** Intact retention and expression of EBC in *cbln1*$^{-/-}$ mice. During training (T1–T7) and retention (T8) sessions, no difference in CR% was observed between wild-type mice and *cbln1*$^{-/-}$ mice injected with Cbln1 ($p > 0.1$, a two-way repeated measures ANOVA, $n = 8$ for each group). The dotted line corresponds to the percentage of CR-like activities on Sp2 to indicate the baseline for learned responses. **(C)** The level of CR% was similar between wild-type and *cbln1*$^{-/-}$ mice injected with Cbln1 at T8 as well as at T7 ($p > 0.1$, by Mann–Whitney's *U* test, $n = 8$ for each group).

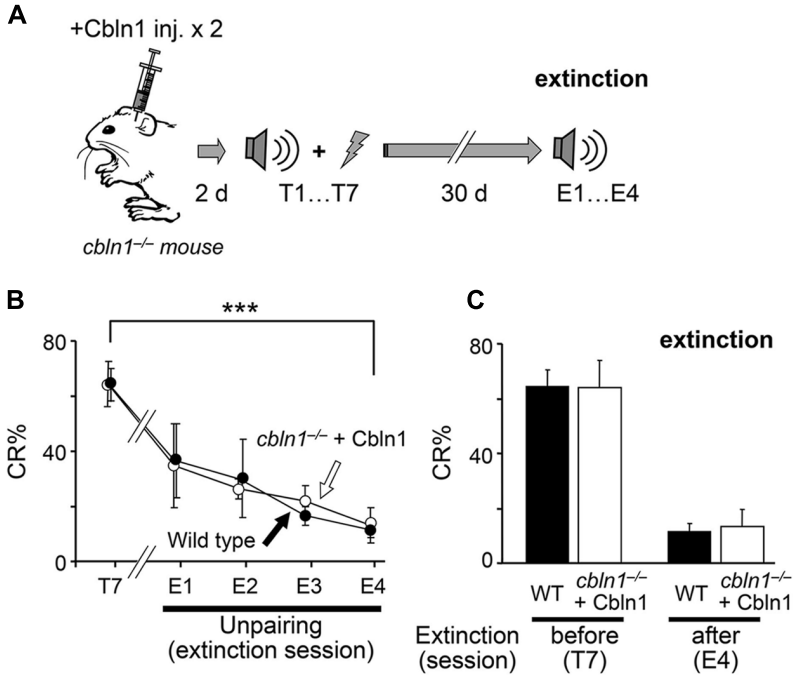

FIGURE 8 | Conditioned eyeblink responses (CRs) are extinguished in *cbln1*$^{-/-}$ mice. (A) A diagram showing a sequence of experiments: *cbln1*$^{-/-}$ mice were injected with Cbln1 as described in **Figure 3** and trained for delay EBC (T1–T7) beginning 2 days after the Cbln1 injection. From day 40 (30 days after T7), mice were given extinction sessions (E1–E4), in which only a CS tone was given, 100 times per day, to examine the extinction of learned responses. **(B)** Intact extinction of conditioned eyeblink responses in *cbln1*$^{-/-}$ mice. The CR% dramatically decreased in both wild-type mice ($n = 7$) and *cbln1*$^{-/-}$ mice injected with Cbln1 ($n = 7$; $^{***}p < 0.01$, T7 vs. E4 in each group, by Mann–Whitney's U test). During extinction sessions (E1–E4), no difference in CR% was observed between wild-type mice and *cbln1*$^{-/-}$ mice injected with Cbln1 ($p > 0.1$, a two-way repeated measures ANOVA, $n = 7$ for each group). **(C)** The CR% was similar between wild-type mice and *cbln1*$^{-/-}$ mice injected with Cbln1 at E4 as well as at T7 ($p > 0.1$, by Mann–Whitney's U test, $n = 8$ for each group).

Cbln1 and intact PF–PC synapses are not likely to be necessary for it.

Inactivating specific synapses could cause imbalances in the overall performance of cerebellar networks, leading to non-specific impairment in motor learning (Bracha et al., 2009). However, our findings that the PF–PC synapses played different roles in acquiring, maintaining, and expressing delay EBC indicate that PF–PC synapses are indeed involved in specific aspects of EBC. This study also establishes the use of a single injection of recombinant Cbln1 as a tool for studying the roles of PF–PC synapses in different stages and paradigms of motor learning. Finally, since LTD and delay EBC become impaired in aged mice (Woodruff-Pak et al., 2010), and these functions were improved in this study by injecting recombinant Cbln1 into the cerebellar subarachnoid space, this molecule may have potential as a therapeutic agent for improving motor performance in elderly people.

AUTHORS CONTRIBUTION

Kyoichi Emi, Wataru Kakegawa, Kazuhisa Kohda, and Michisuke Yuzaki designed the experiments. Kyoichi Emi and Kazuhisa Kohda performed behavioral studies. Wataru Kakegawa performed electrophysiological experiments. Aya Ito-Ishida prepared recombinant HA-Cbln1. Eri Miura performed electron microscopic analyses. Kyoichi Emi, Wataru Kakegawa, Kazuhisa Kohda, and Michisuke Yuzaki wrote the paper.

ACKNOWLEDGMENTS

We thank Sakae Narumi for providing technical assistance. This work was supported by the Core Research for Evolutional Science and Technology from the Japanese Science and Technology Agency (Michisuke Yuzaki), the Grant-in-Aid for the Ministry of Education, Culture, Sports, Science and Technology of Japan (Wataru Kakegawa, Michisuke Yuzaki), and the Takeda Science Foundation (Michisuke Yuzaki, Wataru Kakegawa).

REFERENCES

Aiba, A., Kano, M., Chen, C., Stanton, M. E., Fox, G. D., Herrup, K., et al. (1994). Deficient cerebellar long-term depression and impaired motor learning in mGluR1 mutant mice. *Cell* 79, 377–388. doi: 10.1016/0092-8674(94)90205-4

Attwell, P. J., Cooke, S. F., and Yeo, C. H. (2002). Cerebellar function in consolidation of a motor memory. *Neuron* 34, 1011–1020. doi: 10.1016/S0896-6273(02)00719-5

Blazquez, P. M., Hirata, Y., and Highstein, S. M. (2004). The vestibulo-ocular reflex as a model system for motor learning: what is the role of the cerebellum? *Cerebellum* 3, 188–192. doi: 10.1080/14734220410018120

Boele, H. J., Koekkoek, S. K., and De Zeeuw, C. I. (2010). Cerebellar and extracerebellar involvement in mouse eyeblink conditioning: the ACDC model. *Front. Cell. Neurosci.* 3:19. doi: 10.3389/neuro.03.019.2009

Boyden, E. S., Katoh, A., and Raymond, J. L. (2004). Cerebellum-dependent learning: the role of multiple plasticity mechanisms. *Annu. Rev. Neurosci.* 27, 581–609. doi: 10.1146/annurev.neuro.27.070203.144238

Bracha, V., Zbarska, S., Parker, K., Carrel, A., Zenitsky, G., and Bloedel, J. R. (2009). The cerebellum and eye-blink conditioning: learning versus network performance

hypotheses. *Neuroscience* 162, 787–796. doi: 10.1016/j.neuroscience.2008.12.042

Brown, K. L., Agelan, A., and Woodruff-Pak, D. S. (2010). Unimpaired trace classical eyeblink conditioning in Purkinje cell degeneration (pcd) mutant mice. *Neurobiol. Learn. Mem.* 93, 303–311. doi: 10.1016/j.nlm.2009.11.004

Chen, L., Bao, S., Lockard, J. M., Kim, J. K., and Thompson, R. F. (1996). Impaired classical eyeblink conditioning in cerebellar-lesioned and Purkinje cell degeneration (pcd) mutant mice. *J. Neurosci.* 16, 2829–2838.

Christian, K. M., and Thompson, R. F. (2003). Neural substrates of eyeblink conditioning: acquisition and retention. *Learn. Mem.* 10, 427–455. doi: 10.1101/lm.59603

Clark, R. E., Zhang, A. A., and Lavond, D. G. (1997). The importance of cerebellar cortex and facial nucleus in acquisition and retention of eyeblink/NM conditioning: evidence for critical unilateral regulation of the conditioned response. *Neurobiol. Learn. Mem.* 67, 96–111. doi: 10.1006/nlme.1996.3740

De Zeeuw, C. I., Hansel, C., Bian, F., Koekkoek, S. K., Van Alphen, A. M., Linden, D. J., et al. (1998). Expression of a protein kinase C inhibitor in Purkinje cells blocks cerebellar LTD and adaptation of the vestibulo-ocular reflex. *Neuron* 20, 495–508. doi: 10.1016/S0896-6273(00)80990-3

Emi, K., Kohda, K., Kakegawa, W., Narumi, S., and Yuzaki, M. (2011). A new rapid protocol for eyeblink conditioning to assess cerebellar motor learning. *Neurochem. Res.* 36, 1314–1322. doi: 10.1007/s11064-010-0392-z

Fujiwara, A., Kakizawa, S., and Iino, M. (2007). Induction of cerebellar long-term depression requires activation of calcineurin in Purkinje cells. *Neuropharmacology* 52, 1663–1670. doi: 10.1016/j.neuropharm.2007.03.011

Garcia, K. S., and Mauk, M. D. (1998). Pharmacological analysis of cerebellar contributions to the timing and expression of conditioned eyelid responses. *Neuropharmacology* 37, 471–480. doi: 10.1016/S0028-3908(98)00055-0

Hesslow, G., Jirenhed, D. A., Rasmussen, A., and Johansson, F. (2013). Classical conditioning of motor responses: what is the learning mechanism? *Neural Netw.* 47, 81–87. doi: 10.1016/j.neunet.2013.03.013

Hesslow, G., and Yeo, C. H. (2002). "The functional anatomy of skeletal conditioning," in *A Neuroscientist's Guide to Classical Conditioning*, ed. J. W. Moore (New York: Springer-Verlag), 86–146.

Hirai, H., Pang, Z., Bao, D., Miyazaki, T., Li, L., Miura, E., et al. (2005). Cbln1 is essential for synaptic integrity and plasticity in the cerebellum. *Nat. Neurosci.* 8, 1534–1541. doi: 10.1038/nn1576

Ito-Ishida, A., Miura, E., Emi, K., Matsuda, K., Iijima, T., Kondo, T., et al. (2008). Cbln1 regulates rapid formation and maintenance of excitatory synapses in mature cerebellar Purkinje cells in vitro and in vivo. *J. Neurosci.* 28, 5920–5930. doi: 10.1523/JNEUROSCI.1030-08.2008

Kakegawa, W., Miyazaki, T., Emi, K., Matsuda, K., Kohda, K., Motohashi, J., et al. (2008). Differential regulation of synaptic plasticity and cerebellar motor learning by the C-terminal PDZ-binding motif of GluRdelta2. *J. Neurosci.* 28, 1460–1468. doi: 10.1523/JNEUROSCI.2553-07.2008

Kakegawa, W., Miyazaki, T., Kohda, K., Matsuda, K., Emi, K., Motohashi, J., et al. (2009). The N-terminal domain of GluD2 (GluRdelta2) recruits presynaptic terminals and regulates synaptogenesis in the cerebellum in vivo. *J. Neurosci.* 29, 5738–5748. doi: 10.1523/JNEUROSCI.6013-08.2009

Kakegawa, W., and Yuzaki, M. (2005). A mechanism underlying AMPA receptor trafficking during cerebellar long-term potentiation. *Proc. Natl. Acad. Sci. U.S.A.* 102, 17846–17851. doi: 10.1073/pnas.0508910102

Kalmbach, B. E., Davis, T., Ohyama, T., Riusech, F., Nores, W. L., and Mauk, M. D. (2010). Cerebellar cortex contributions to the expression and timing of conditioned eyelid responses. *J. Neurophysiol.* 103, 2039–2049. doi: 10.1152/jn.00033.2010

Kishimoto, Y., Kawahara, S., Fujimichi, R., Mori, H., Mishina, M., and Kirino, Y. (2001a). Impairment of eyeblink conditioning in GluRdelta2-mutant mice depends on the temporal overlap between conditioned and unconditioned stimuli. *Eur. J. Neurosci.* 14, 1515–1521. doi: 10.1046/j.0953-816x.2001.01772.x

Kishimoto, Y., Kawahara, S., Suzuki, M., Mori, H., Mishina, M., and Kirino, Y. (2001b). Classical eyeblink conditioning in glutamate receptor subunit delta 2 mutant mice is impaired in the delay paradigm but not in the trace paradigm. *Eur. J. Neurosci.* 13, 1249–1253. doi: 10.1046/j.0953-816x.2001.01488.x

Kleim, J. A., Freeman, J. H., Jr., Bruneau, R., Nolan, B. C., Cooper, N. R., Zook, A., et al. (2002). Synapse formation is associated with memory storage in the cerebellum. *Proc. Natl. Acad. Sci. U.S.A.* 99, 13228–13231. doi: 10.1073/pnas.202483399

Koekkoek, S. K., Hulscher, H. C., Dortland, B. R., Hensbroek, R. A., Elgersma, Y., Ruigrok, T. J., et al. (2003). Cerebellar LTD and learning-dependent timing of conditioned eyelid responses. *Science* 301, 1736–1739. doi: 10.1126/science.1088383

Koekkoek, S. K., Yamaguchi, K., Milojkovic, B. A., Dortland, B. R., Ruigrok, T. J., Maex, R., et al. (2005). Deletion of FMR1 in Purkinje cells enhances parallel fiber LTD, enlarges spines, and attenuates cerebellar eyelid conditioning in Fragile X syndrome. *Neuron* 47, 339–352. doi: 10.1016/j.neuron.2005.07.005

Kohda, K., Kakegawa, W., Matsuda, S., Nakagami, R., Kakiya, N., and Yuzaki, M. (2007). The extreme C-terminus of GluRdelta2 is essential for induction of long-term depression in cerebellar slices. *Eur. J. Neurosci.* 25, 1357–1362. doi: 10.1111/j.1460-9568.2007.05412.x

Lev-Ram, V., Wong, S. T., Storm, D. R., and Tsien, R. Y. (2002). A new form of cerebellar long-term potentiation is postsynaptic and depends on nitric oxide but not cAMP. *Proc. Natl. Acad. Sci. U.S.A.* 99, 8389–8393. doi: 10.1073/pnas.122206399

Matsuda, K., Miura, E., Miyazaki, T., Kakegawa, W., Emi, K., Narumi, S., et al. (2010). Cbln1 is a ligand for an orphan glutamate receptor delta2, a bidirectional synapse organizer. *Science* 328, 363–368. doi: 10.1126/science.1185152

Matsuda, K., and Yuzaki, M. (2011). Cbln family proteins promote synapse formation by regulating distinct neurexin signaling pathways in various brain regions. *Eur. J. Neurosci.* 33, 1447–1461. doi: 10.1111/j.1460-9568.2011.07638.x

Matsuda, S., Miura, E., Matsuda, K., Kakegawa, W., Kohda, K., Watanabe, M., et al. (2008). Accumulation of AMPA receptors in autophagosomes in neuronal axons lacking adaptor protein AP-4. *Neuron* 57, 730–745. doi: 10.1016/j.neuron.2008.02.012

Medina, J. F., Garcia, K. S., and Mauk, M. D. (2001). A mechanism for savings in the cerebellum. *J. Neurosci.* 21, 4081–4089.

Medina, J. F., Nores, W. L., and Mauk, M. D. (2002). Inhibition of climbing fibres is a signal for the extinction of conditioned eyelid responses. *Nature* 416, 330–333. doi: 10.1038/416330a

Miller, M. J., Chen, N. K., Li, L., Tom, B., Weiss, C., Disterhoft, J. F., et al. (2003). fMRI of the conscious rabbit during unilateral classical eyeblink conditioning reveals bilateral cerebellar activation. *J. Neurosci.* 23, 11753–11758.

Miura, E., Iijima, T., Yuzaki, M., and Watanabe, M. (2006). Distinct expression of Cbln family mRNAs in developing and adult mouse brains. *Eur. J. Neurosci.* 24, 750–760. doi: 10.1111/j.1460-9568.2006.04950.x

Miyata, M., Kim, H. T., Hashimoto, K., Lee, T. K., Cho, S. Y., Jiang, H., et al. (2001). Deficient long-term synaptic depression in the rostral cerebellum correlated with impaired motor learning in phospholipase C beta4 mutant mice. *Eur. J. Neurosci.* 13, 1945–1954. doi: 10.1046/j.0953-816x.2001.01570.x

Nomura, T., Kakegawa, W., Matsuda, S., Kohda, K., Nishiyama, J., Takahashi, T., et al. (2012). Cerebellar long-term depression requires dephosphorylation of TARP in Purkinje cells. *Eur. J. Neurosci.* 35, 402–410. doi: 10.1111/j.1460-9568.2011.07963.x

Plakke, B., Freeman, J. H., and Poremba, A. (2007). Metabolic mapping of the rat cerebellum during delay and trace eyeblink conditioning. *Neurobiol. Learn. Mem.* 88, 11–18. doi: 10.1016/j.nlm.2007.03.008

Porrill, J., and Dean, P. (2008). Silent synapses, LTP, and the indirect parallel-fibre pathway: computational consequences of optimal cerebellar noise-processing. *PLoS Comput. Biol.* 4:e1000085. doi: 10.1371/journal.pcbi.1000085

Qiao, X., Chen, L., Gao, H., Bao, S., Hefti, F., Thompson, R. F., et al. (1998). Cerebellar brain-derived neurotrophic factor-TrkB defect associated with impairment of eyeblink conditioning in Stargazer mutant mice. *J. Neurosci.* 18, 6990–6999.

Sakamoto, T., and Endo, S. (2010). Amygdala, deep cerebellar nuclei and red nucleus contribute to delay eyeblink conditioning in C57BL /6 mice. *Eur. J. Neurosci.* 32, 1537–1551. doi: 10.1111/j.1460-9568.2010.07406.x

Schonewille, M., Belmeguenai, A., Koekkoek, S. K., Houtman, S. H., Boele, H. J., Van Beugen, B. J., et al. (2010). Purkinje cell-specific knockout of the protein phosphatase PP2B impairs potentiation and cerebellar motor learning. *Neuron* 67, 618–628. doi: 10.1016/j.neuron.2010.07.009

Schonewille, M., Gao, Z., Boele, H. J., Veloz, M. F., Amerika, W. E., Simek, A. A., et al. (2011). Reevaluating the role of LTD in cerebellar motor learning. *Neuron* 70, 43–50. doi: 10.1016/j.neuron.2011.02.044

Shutoh, F., Ohki, M., Kitazawa, H., Itohara, S., and Nagao, S. (2006). Memory trace of motor learning shifts transsynaptically from cerebellar cortex to nuclei for consolidation. *Neuroscience* 139, 767–777. doi: 10.1016/j.neuroscience.2005.12.035

Sun, L. W. (2012). Transsynaptic tracing of conditioned eyeblink circuits in the mouse cerebellum. *Neuroscience* 203, 122–134. doi: 10.1016/j.neuroscience.2011.12.017

Thompson, R. F., and Krupa, D. J. (1994). Organization of memory traces in the mammalian brain. *Annu. Rev. Neurosci.* 17, 519–549. doi: 10.1146/annurev.ne.17.030194.002511

Thompson, R. F., and Steinmetz, J. E. (2009). The role of the cerebellum in classical conditioning of discrete behavioral responses. *Neuroscience* 162, 732–755. doi: 10.1016/j.neuroscience.2009.01.041

Uemura, T., Lee, S. J., Yasumura, M., Takeuchi, T., Yoshida, T., Ra, M., et al. (2010). Trans-synaptic interaction of GluRdelta2 and Neurexin through Cbln1 mediates synapse formation in the cerebellum. *Cell* 141, 1068–1079. doi: 10.1016/j.cell.2010.04.035

van Alphen, A. M., and De Zeeuw, C. I. (2002). Cerebellar LTD facilitates but is not essential for long-term adaptation of the vestibulo-ocular reflex. *Eur. J. Neurosci.* 16, 486–490. doi: 10.1046/j.1460-9568.2002.02094.x

Wada, N., Kishimoto, Y., Watanabe, D., Kano, M., Hirano, T., Funabiki, K., et al. (2007). Conditioned eyeblink learning is formed and stored without cerebellar granule cell transmission. *Proc. Natl. Acad. Sci. U.S.A.* 104, 16690–16695. doi: 10.1073/pnas.0708165104

Woodruff-Pak, D. S., Foy, M. R., Akopian, G. G., Lee, K. H., Zach, J., Nguyen, K. P., et al. (2010). Differential effects and rates of normal aging in cerebellum and hippocampus. *Proc. Natl. Acad. Sci. U.S.A.* 107, 1624–1629. doi: 10.1073/pnas.0914207107

Yamasaki, M., Miyazaki, T., Azechi, H., Abe, M., Natsume, R., Hagiwara, T., et al. (2011). Glutamate receptor delta2 is essential for input pathway-dependent regulation of synaptic AMPAR contents in cerebellar Purkinje cells. *J. Neurosci.* 31, 3362–3374. doi: 10.1523/JNEUROSCI.5601-10.2011

Yuzaki, M. (2009). New (but old) molecules regulating synapse integrity and plasticity: Cbln1 and the delta2 glutamate receptor. *Neuroscience* 162, 633–643. doi: 10.1016/j.neuroscience.2008.12.002

Yuzaki, M. (2011). Cbln1 and its family proteins in synapse formation and maintenance. *Curr. Opin. Neurobiol.* 21, 215–220. doi: 10.1016/j.conb.2011.01.010

Yuzaki, M. (2012). Cerebellar LTD vs. motor learning-Lessons learned from studying GluD2. *Neural Netw.* 47, 36–41.doi: 10.1016/j.neunet.2012.07.001

Conflict of Interest Statement: The authors declare that the research was conducted in the absence of any commercial or financial relationships that could be construed as a potential conflict of interest.

Received: 10 August 2013; accepted: 24 October 2013; published online: 15 November 2013.

*Citation: Emi K, Kakegawa W, Miura E, Ito-Ishida A, Kohda K and Yuzaki M (2013) Reevaluation of the role of parallel fiber synapses in delay eyeblink conditioning in mice using Cbln1 as a tool. Front. Neural Circuits **7**:180. doi: 10.3389/fncir.2013.00180*

This article was submitted to the journal Frontiers in Neural Circuits.

frontiers in
NEURAL CIRCUITS

ORIGINAL RESEARCH ARTICLE
published: 11 October 2013
doi: 10.3389/fncir.2013.00162

Viral vector-mediated selective and reversible blockade of the pathway for visual orienting in mice

Thongchai Sooksawate[1,2]*, Kaoru Isa[1], Ryosuke Matsui[3], Shigeki Kato[4], Masaharu Kinoshita[1†], Kenta Kobayashi[5,6], Dai Watanabe[3], Kazuto Kobayashi[4] and Tadashi Isa[1,5,6]*

[1] Department of Developmental Physiology, National Institute for Physiological Sciences, Okazaki, Japan
[2] Department of Pharmacology and Physiology, Faculty of Pharmaceutical Sciences, Chulalongkorn University, Bangkok, Thailand
[3] Department of Molecular and Systems Biology, Graduate School of Biostudies, Kyoto University, Kyoto, Japan
[4] Department of Molecular Genetics, Institute of Biomedical Sciences, Fukushima Medical University School of Medicine, Fukushima, Japan
[5] Section of Viral Vector Development, National Institute for Physiological Sciences, Okazaki, Japan
[6] Department of Life Sciences, The Graduate University for Advanced Studies (SOKENDAI), Hayama, Japan

Edited by:
Yasuo Kawaguchi, National Institute for Physiological Sciences, Japan

Reviewed by:
Paul J. May, University of Mississippi Medical Center, USA
Masahiko Takada, Kyoto University, Japan

***Correspondence:**
Thongchai Sooksawate, Department of Pharmacology and Physiology, Faculty of Pharmaceutical Sciences, Chulalongkorn University, Phayathai Road, Patumwan, Bangkok 10330, Thailand
e-mail: sthongch@chula.ac.th;
Tadashi Isa, Department of Developmental Physiology, National Institute for Physiological Sciences, Myodaiji, Okazaki 444-8585, Japan
e-mail: tisa@nips.ac.jp

† Present address:
Masaharu Kinoshita, Department of Physiology, Hirosaki University School of Medicine, Hirosaki, Japan

Recently, by using a combination of two viral vectors, we developed a technique for pathway-selective and reversible synaptic transmission blockade, and successfully induced a behavioral deficit of dexterous hand movements in macaque monkeys by affecting a population of spinal interneurons. To explore the capacity of this technique to work in other pathways and species, and to obtain fundamental methodological information, we tried to block the crossed tecto-reticular pathway, which is known to control orienting responses to visual targets, in mice. A neuron-specific retrograde gene transfer vector with the gene encoding enhanced tetanus neurotoxin (eTeNT) tagged with enhanced green fluorescent protein (EGFP) under the control of a tetracycline responsive element was injected into the left medial pontine reticular formation. 7–17 days later, an adeno-associated viral vector with a highly efficient Tet-ON sequence, rtTAV16, was injected into the right superior colliculus. 5–9 weeks later, the daily administration of doxycycline (Dox) was initiated. Visual orienting responses toward the left side were impaired 1–4 days after Dox administration. Anti-GFP immunohistochemistry revealed that a number of neurons in the intermediate and deep layers of the right superior colliculus were positively stained, indicating eTeNT expression. After the termination of Dox administration, the anti-GFP staining returned to the baseline level within 28 days. A second round of Dox administration, starting from 28 days after the termination of the first Dox administration, resulted in the reappearance of the behavioral impairment. These findings showed that pathway-selective and reversible blockade of synaptic transmission also causes behavioral effects in rodents, and that the crossed tecto-reticular pathway clearly controls visual orienting behaviors.

Keywords: superior colliculus, pontine reticular formation, orienting behavior, viral vector, Tet-ON, tetanus neurotoxin, mouse

INTRODUCTION

To study structure-function relationships within neural circuits, it is necessary to manipulate the activity of an "identified" population of neuronal elements in these circuits. Recent advances in molecular genetic techniques enabled such targeted manipulation by making transgenic animals with cell-specific promoters (Kobayashi et al., 1995; Watanabe et al., 1998). However, such techniques have generally been constrained to those animals in which the transgenic manipulation of gene expression is possible (i.e., mouse, nematode, *Drosophila*, etc.) and to neuron types whose cell-specific promoter has been identified. An alternative possibility is to use viral vectors to introduce particular genes. To enable pathway specificity, lentivirus vectors pseudotyped with rabies virus glycoprotein (RVG) were developed as vectors specific for retrograde transport (Kato et al., 2007). However, such vectors were not sufficiently efficient to affect enough of a specific neuron population to induce behavioral effects, especially in larger animals such as non-human primates. To overcome such difficulties, Kobayashi and colleagues recently enhanced the retrograde transport efficiency of lentivirus vectors by pseudotyping with a chimera of rabies virus and vesicular stomatitis virus glycoprotein (VSVG) [highly efficient retrograde gene transfer (HiRet) vector; Kato et al., 2011a]. We incorporated a tetracycline responsive element (TRE) and enhanced tetanus neurotoxin (eTeNT) tagged with enhanced green fluorescent protein (EGFP) into this retrograde vector (HiRet-TRE-EGFP.eTeNT). We also incorporated the newly developed efficient Tet-ON sequence rtTAV16 into an adeno-associated type 2 virus vector (AAV-2) with a cytomegalovirus promoter (CMV) (AAV2-CMV-rtTAV16) (Kinoshita et al., 2012) as a switch to regulate the first construct. To study the function of a subpopulation of propriospinal neurons (PNs) whose cell bodies are located in the mid-cervical segments and project to hand/arm motor neurons in macaque monkeys, we injected HiRet-TRE-EGFP.eTeNT into the ventral horn of the C6–Th1 segments; one week later, we injected AAV2-CMV-rtTAV16 into the intermediate zone of the C2–C5 segments

where the PN cell bodies are located. 1–2 months later, we initiated the administration of doxycycline (Dox). We could observe deficits in reach and grasp movements. Acute electrophysiological experiments clarified that approximately 90% of the transmission through the PNs was blocked. Theoretically, this method should be available for universal use in the various pathways of the central nervous system without the need to identify cell-specific promoters or develop genetically modified animals.

At the current stage, we still need to know the fundamental properties of this technique and how to optimize it. For this purpose, however, non-human primates are not the best animal species because the number of available animals is limited, and behavioral and histological analyses are time consuming. Therefore, we decided to use mice to establish the fundamental protocol of this technique. Moreover, we wished to select a pathway whose function is easy to investigate using behavioral observations. We chose the crossed tectoreticular pathway (cTRNs), which originates from the intermediate and deep layers of the midbrain superior colliculus (SC) and terminates in the medial pontomedullary reticular formation contralateral to the SC (Grantyn and Berthoz, 1987; Redgrave et al., 1990; Isa and Sasaki, 2002; Sooksawate et al., 2005, 2008). This pathway is known to control the orienting response of the eyes, head, and body to visual targets (Wurtz and Albano, 1980; Sparks, 1986; Dean et al., 1989; Isa and Sasaki, 2002; Isa and Hall, 2009), which is an innate behavior that does not require training. In this study, we focused on the time course of the effect of pathway blockade through behavioral and histological examinations after starting Dox administration and after its offset. We also tested the reversibility of the effects by halting and repeating Dox administration. This technique proved very feasible in mice, suggesting that it could be used universally as a relatively convenient method for the pathway-specific manipulation of neural activity and gene expression.

MATERIALS AND METHODS

The animal experimental procedures in this study were conducted in accordance with the Guidelines of the National Institutes of Health and the Ministry of Education, Culture, Sports, Science, and Technology of Japan, and were approved by the Institutional Animal Care and Use Committee of the National Institutes of Natural Sciences. All attempts were made to minimize the suffering and number of animals used in this study. The methods and time schedule of the present experiments are summarized in **Figure 1**.

PREPARATION OF VIRAL VECTORS

Vector preparation was described by Kinoshita et al. (2012). However, a major difference was that we used a neuron-specific highly efficient retrograde gene transfer lentivirus (NeuRet) vector (Kato et al., 2011b) instead of the HiRet vector, because the NeuRet vector is specifically taken up by axons at the injection site.

NeuRet-TRE-EGFP.eTeNT

The NeuRet vector is a pseudotype of a human immunodeficiency virus type 1-based lentiviral vector with fusion glycoprotein type C. In previous studies, it has been shown that pseudotyping the lentiviral vector with the RVG changed the property of the vector specific for retrograde gene transfer (Kato et al., 2007). However, the efficiency of the gene transfer was not enough to affect the majority of neurons projecting to the injection site. Later, it was found that replacing RVG with a chimeric protein of RVG and VSVG domains greatly enhanced the efficiency of retrograde gene transfer (highly efficient retrograde gene transfer vector or HiRet vector) (Kato et al., 2011a). Then, the use of a different chimeric protein composing RVG and VSVG (fusion glycoprotein type C) switched the properties to neuron-specific infection (NeuRet) (**Figure 1A**; Kato et al., 2011b). In the present study, the envelope plasmid encoding fusion glycoprotein type C, which was under the control of the cytomegalovirus (CMV) enhancer/chicken β-actin promoter, was used for vector production. Chimeric EGFP.eTeNT.PEST was generated by fusing the human codon-optimized tetanus neurotoxin light chain (eTeNT) with the EGFP derived from pEGFP-N1 vector (Clontech, Mountain View, CA, USA) and the PEST sequence of ornithine decarboxylase, as reported previously (Kinoshita et al., 2012). The transfer plasmid pLV-TRE-EGFP.eTeNT.PEST was based on pFUGW (a gift from D. Baltimore, California Institute of Technology, Pasadena, CA, USA), and constructed by swapping the ubiquitin promoter-EGFP sequence with the TRE/CMV promoter of the pTRE-Tight vector (Clontech, Mountain View, CA, USA) and EGFP.eTeNT.PEST. The NeuRet vector encoding EGFP.eTeNT was placed downstream of the TRE promoter (termed NeuRet-TRE-EGFP.eTeNT) and was prepared as described previously (Inoue et al., 2012).

AAV2-CMV-rtTAV16

The rtTA variant rtTAV16 was generated by introducing the V9I, G12S, F67S, F86Y, R171K, and A209T mutations into rtTA2S-M2 of the pTet-ON advanced vector (Clontech, Mountain View, CA, USA), as reported previously (Kinoshita et al., 2012). Plasmid pAAV2-CMV-rtTAV16 (**Figure 1A**) is based on pAAV-MCS (Agilent Technologies, Inc., Santa Clare, CA, USA), and was constructed by inserting the CMV promoter sequence of the pTet-On advanced vector rtTAV16, the woodchuck hepatitis virus posttranscriptional regulatory element WPRE sequence of pFUGW, and the SV40 polyadenylation signal (SV40pA) of the pCMV-script vector (Agilent Technologies, Tokyo, Japan) into a multiple cloning site. The AAV vector for *in vivo* injection was produced as described previously (Kaneda et al., 2011).

INJECTIONS OF NeuRet-TRE-EGFP.eTeNT AND AAV2-CMV-rtTAV16

We anesthetized 6–10-week-old male C57BL/6 mice with an intraperitoneal injection of a mixture of ketamine (60 mg/kg body weight) and xylazine (10 mg/kg body weight). In addition, dexamethasone (5.5 mg/kg body weight) was injected intramuscularly as premedication. The head of the mouse was fixed to the stereotaxic apparatus (Narishige, Tokyo, Japan) and injections of the vectors were made from the dorsal approach. NeuRet-TRE-EGFP.eTeNT (0.8–1.2 μL); titer, 3.3–12.1 × 10^{11} copies/mL) was injected into the medial pontine reticular formation (MPRF) on the left side (**Figures 1B,C**) using a thin glass micropipette (tip diameter, 50–70 μm) inclined by 45°caudally to the vertical

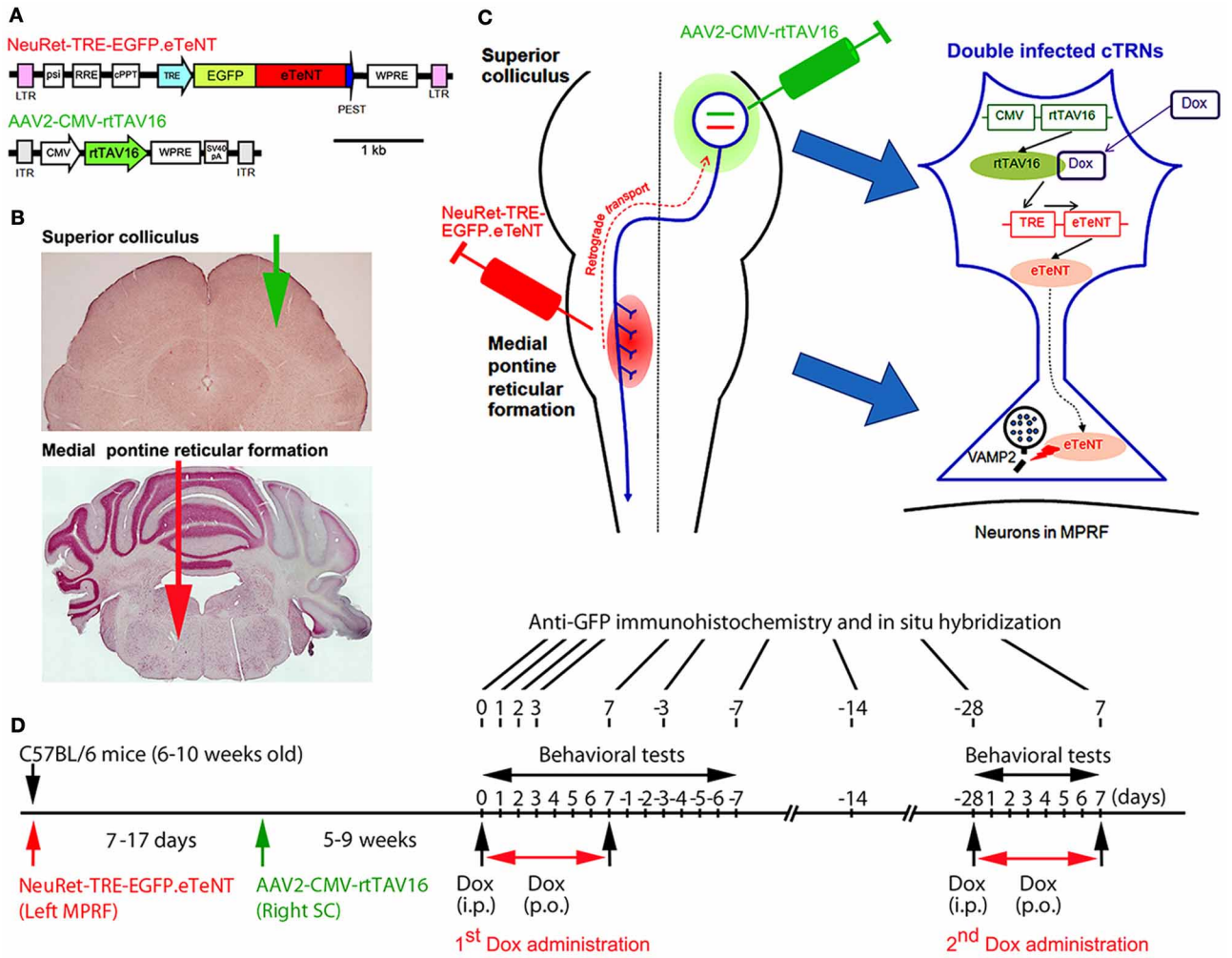

FIGURE 1 | Experimental protocols for the selective blockade of the crossed tectoreticular pathway by double infection with the NeuRet lentiviral vector (carrying EGFP.eTeNT) and the AAV2 vector (carrying the Tet-ON sequence, CMV-rtTAV16). (A) The design of the two viral vectors. **(B)** Photomicrographs of the superior colliculus (SC) and medial pontine reticular formation (MPRF) showing the viral vector injection targets. **(C)** Diagram for the double injection of the viral vectors into the MPRF and SC, and the interaction of NeuRet-TRE-EGFPeTeNT and AAV2-CMV-rtTAV16 in the double infected crossed tectoreticular neurons (cTRNs). **(D)** The experimental schedule of this study.

axis of the stereotaxic coordinates (Franklin and Paxinos, 2008), −8.3 mm from the bregma, 0.7 mm lateral to the midline, and at 3.6 and 4.4 mm from the presumed dorsal surface of the cerebellar cortex (0.4–0.6 μL/point of injection). 7–17 days after the NeuRet-TRE-EGFP.eTeNT injection, AAV2-CMV-rtTAV16 (0.8–1.0 μL; titer, 1.96×10^{13} particles/mL) was injected into the SC on the right side (**Figures 1B,C**). A small hole was made in the skull over the occipital cortex and a thin glass micropipette (tip diameter; 50–70 μm) was inserted vertically into the right SC, −4.0 to −4.2 mm from the bregma, 1.1–1.2 mm lateral to the midline, and at 1.1–1.6 and 1.4–2.3 mm from the presumed dorsal surface of the cerebral cortex (0.4–0.5 μL/point of injection). We used a syringe pump (ESP-32; Eicom, Kyoto, Japan) for the injection; the injection rate was 0.1 μL/min. Before removing the glass micropipette from the injection site, we waited for 5 min.

The transfer plasmid pLV-TRE-EGFP.eTeNT.PEST is switched on to produce the tetanus neurotoxin only when the rtTAV16 sequence provided by the AAV2-CMV-rtTAV16 vector is expressed in the same neuron and activated by Dox (**Figure 1C**). The tetanus neurotoxin blocks the transmitter release by cleaving VAMP-2 at the nerve terminals, but does not kill the cell (for review see Montecucco and Schiavo, 1994).

DOX ADMINISTRATION

5–9 weeks after the injection of AAV2-CMV-rtTAV16, the daily administration of Dox was initiated by a single intraperitoneal injection (10 μg/g body weight) of Dox in a 0.9% NaCl solution, followed by the continuous oral administration of Dox in the drinking water (3 mg/mL in a 5% sucrose solution) for 7 days (**Figure 1D**). In some animals, the second

period of Dox administration (2nd Dox administration) was conducted from 28 days after the offset of the first period of Dox administration (1st Dox administration). One group of mice received Dox continually for 21 days for histological analysis.

BEHAVIORAL TESTS FOR VISUAL ORIENTING AND TURNING BEHAVIOR

We utilized three tests to assess visual orienting and turning behaviors: (1) the visual placing response, (2) the visual orienting response, and (3) a turning behavior test (**Figure 1D**). The behavioral tests began on the day before Dox administration, continued during Dox administration for 7 days, and after Dox administration for 7 days. All tests were performed between 6.00 AM and 3.00 PM.

Visual placing response

A modified visual placing response test was used to evaluate visual orienting behavior toward the affected and unaffected sides of the tested mouse. This test was modified from Metz and Schwab (2004) and Pinto and Enroth-Cugell (2000). In this test, the mouse was suspended by holding its tail and then lowered toward a plastic plate either on the left or right side of the head without any contact to the vibrissae. Normally, when the head of a mouse was lowered to near the edge of the plastic plate, it turned its head and trunk, and extended its forelimbs to place them on the plate (see **Figure 2A**). The procedure was conducted bilaterally (10 trials per side each day). The number of times the mouse successfully placed its forelimbs on the plate was counted.

Visual orienting response

A visual orienting response test was used to evaluate visual orienting behavior toward a visual target presented either on the affected or unaffected side of the tested mouse. The mouse was placed inside a small glass cylinder (15 cm height, 14 cm inner diameter), and a stimulus (a small long-handle stainless steel chemical spoon) was quickly moved into the visual field of the mouse from behind, in the same horizontal plane as its eyes, until the stimulus was located between its eyes (Smith et al., 1998). Normally, when the stimulus entered its visual field, the mouse turned its head toward the stimulus (**Figure 3A**). The procedure was conducted bilaterally in a pseudorandom sequence (10 trials

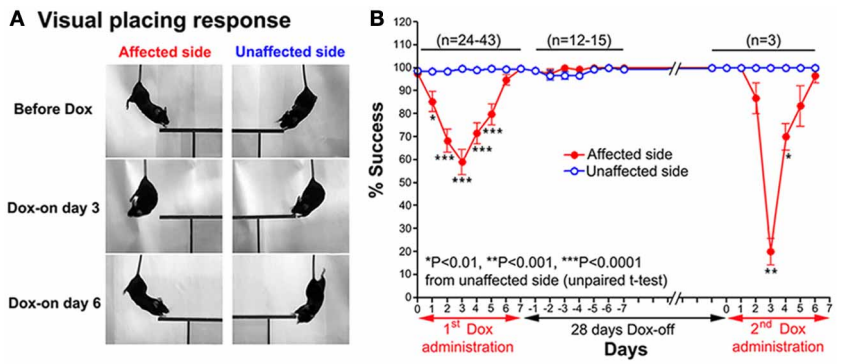

FIGURE 2 | (A) Series of photographs showing the effect of the Tet-induced tetanus neurotoxin-expressing system on the visual placing response toward the affected side (Dox-on day 3) and disappearance of the effect (Dox-on day 6), compared with the unaffected side. **(B)** Effect of the Tet-induced tetanus neurotoxin-expressing system on the visual placing response toward the affected side after the 1st Dox administration for 7 days, termination of Dox administration for 28 days, and the 2nd Dox administration for 7 days.

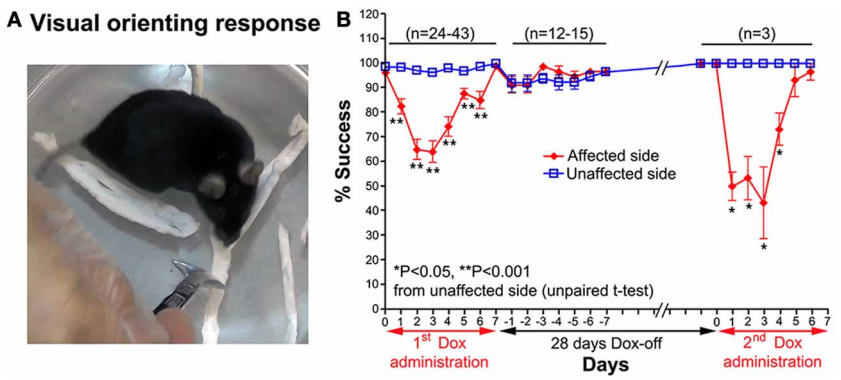

FIGURE 3 | (A) A photograph showing the visual orienting response of a mouse toward the unaffected side. **(B)** Effect of the Tet-induced tetanus neurotoxin-expressing system on the visual orienting response of the affected side after the 1st Dox administration for 7 days, termination of Dox administration for 28 days, and the 2nd Dox administration for 7 days.

per side each day). The number of times the mouse successfully oriented itself to the stimulus was counted.

Turning behavior

A turning behavior test was used to evaluate the effect of the Tet-induced tetanus neurotoxin-expressing system on the preferred side of turning of the tested mouse after Dox administration. The mouse was placed into a small glass cylinder (15 cm height, 14 cm inner diameter), which forced it to turn left or right inside the cylinder (**Figure 4A**). The number of complete turns (360°) to each side was recorded for 10 min each day.

IMMUNOHISTOCHEMICAL ASSESSMENTS

At the end of the experiments, the mice were deeply anesthetized with an intraperitoneal injection of sodium pentobarbital (80 mg/kg body weight) (Hospira Inc., Lake Forest, IL, USA) and transcardially perfused with 0.05 M phosphate-buffered saline and then 4% paraformaldehyde in a 0.1 M phosphate buffer (pH 7.4). The brainstem and spinal cord were cryoprotected and sectioned at a thickness of 40 μm using a sliding microtome (HM 450; Microm, Walldorf, Germany). To obtain a clearer image of the cell bodies, dendrites and axons of the double infected neurons, we adopted permanent visualization of EGFP-positive cells with anti-GFP immunohistochemistry. In particular, the permanent visualization technique made the axon tracing much easier. Moreover, the distribution of neurons infected by AAV2-CMV-rtTAV16 was assessed with *in situ* hybridization to detect the rtTA sequence (the antisense probe for the tetracycline transactivator, tTA, was a gift from T. Yamamori, National Institute for Basic Biology, Okazaki, Japan). The technical details of the anti-GFP immunohistochemistry and *in situ* hybridization against the rtTAV16 sequence were described previously (Kinoshita et al., 2012) and are available on the web (http://www.nibb.ac.jp/brish/indexE.html), respectively. The number of GFP-positive neurons and tracings of the axons originating from their cell bodies to their target areas were counted and drawn using a camera lucida attached to a light microscope (BX51; Olympus, Tokyo, Japan). Photomicrographs of the histological slices were taken using light microscopes (Axioplan2; Zeiss, Göttingen, Germany and BZ-9000; Keyence, Elmwood Park, NJ, USA).

DATA ANALYSIS

Data are expressed as the mean ± standard error of the mean. Significance was tested by Student's *t*-test, and a *P* value of less than 0.05 was considered to be significant.

RESULTS

A total of 61 C57BL/6 mice were used in this study; the two viral vectors were injected into 56 mice. As controls, some mice received an injection of NeuRet-TRE-EGFP.eTeNT without Dox administration ($n = 2$), NeuRet-TRE-EGFP.eTeNT and AAV2-CMV-rtTAV16 without Dox administration ($n = 2$), or NeuRet-TRE-EGFP.eTeNT with Dox administration ($n = 3$), and one group of mice was not injected ($n = 5$). No clear behavioral effects could be observed in any of these control groups. Specifically, the % success rate for the visual placing response on the side contralateral to the collicular injection ranged from 95.00 ± 5.00 to 100.0 ± 0.00%, which was not significantly different from the side ipsilateral to the collicular injection (100.0 ± 0.00%). The % success rate for the visual orienting responses on the side contralateral to the collicular injection ranged from 95.00 ± 5.00 to 100.0 ± 0.00%, which was also not significantly different from the side ipsilateral to the collicular injection that ranged from 95.00 ± 5.00 to 100.0 ± 0.00%. Moreover, the % turning rate to the side contralateral to the collicular injection was not significantly different from the side ipsilateral to the collicular injection on any of the testing days (Dox-on day 0 to Dox-on day 7). It ranged from 44.60 ± 5.63 to 50.40 ± 3.15%.

BEHAVIORAL OBSERVATIONS

Visual placing response

After Dox administration, the visual placing response toward the affected side (left side) of the double infected mice was impaired from Dox-on day 1 to day 5, with the maximal impairment on Dox-on day 3 compared with the unaffected side (right side). The mice failed to turn their head and trunk and place their forelimbs onto the plastic plate when they were lowered with the plastic plate on the affected side (**Figure 2A**). The % success rate for placing toward the affected side was reduced to 58.95 ± 5.41%, compared with 99.47 ± 0.3671% for the unaffected side

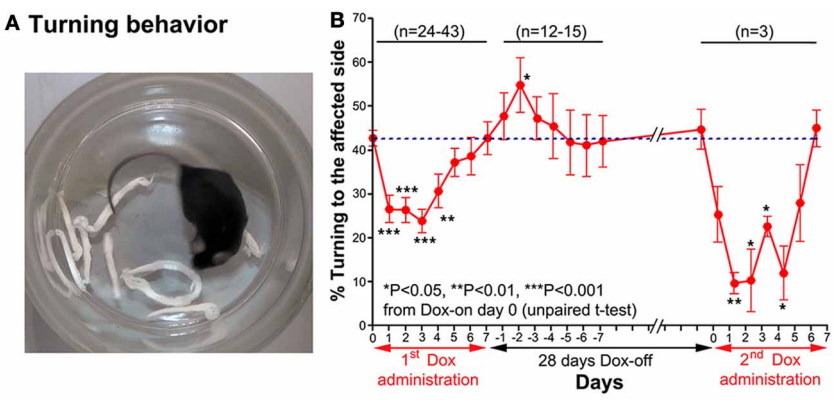

FIGURE 4 | (A) A photograph showing the turning behavior of a mouse to the unaffected side (right). **(B)** Effect of the Tet-induced tetanus neurotoxin-expressing system on turning behavior after the 1st Dox administration for 7 days, termination of Dox administration for 28 days, and the 2nd Dox administration for 7 days.

($P < 0.0001$, $n = 38$, unpaired t-test; **Figure 2B**). However, this behavioral effect was gradually reduced from Dox-on day 4 and completely disappeared on Dox-on days 6–7. After the termination of Dox administration, no behavioral effect could be seen on the affected and unaffected sides for 7 days (Dox-off days −1 to −7).

Visual orienting response

Impairment of the orienting response could also be found in the visual orienting response test. After Dox administration, the visual orienting response toward the affected side (left side) was impaired from days 1–6, while it was not impaired toward the unaffected side (right side) (**Figure 3A**). The % success rate of the affected side was reduced to $64.21 \pm 4.473\%$, compared to the $96.32 \pm 0.793\%$ of the unaffected side ($P < 0.001$, $n = 38$, unpaired t-test; **Figure 3B**). The behavioral effect was gradually reduced from Dox-on day 4, and completely disappeared by Dox-on day 7. After the termination of Dox administration, no behavioral effect could be seen on the affected and unaffected sides for 7 days (Dox-off days −1 to −7).

Turning behavior

Before Dox administration and in the control groups, the mice almost equally preferred to turn toward the left and right. However, after Dox administration, the mice preferred to turn to the unaffected side (right) (**Figure 4A**). The % turning to the affected side (left side) was reduced from Dox-on days 1 to 4, with the maximal reduction on day 3 (**Figure 4B**). The % turning to the affected side was reduced to $23.92 \pm 2.721\%$ from the $42.77 \pm 1.824\%$ of the controls on day 0 ($P < 0.001$, $n = 38$, unpaired t-test). Then, the % turning to the affected side gradually returned to the same level as before Dox administration by Dox-on day 7. It is noteworthy that after the termination of Dox administration, % turning to the affected side (left side) increased to its highest level on Dox-off day −2 ($P < 0.05$, $n = 15$, unpaired t-test), before returning to the same level as before Dox administration on Dox-off days −5 to −7.

REVERSIBILITY OF THE DOX-ON EFFECTS

28 days after the termination of the 1st Dox administration (for 7 days), the 2nd Dox administration was started for another 7 days. All of the behavioral tests for visual orienting were found to be impaired after the 2nd Dox administration. The pattern and time course of the impairments were almost the same as for the 1st Dox administration. The % success rates for the visual placing response (**Figure 2B**) and visual orienting response (**Figure 3B**) and % turning (**Figure 4B**) toward the affected side were reduced on Dox-on days 1–2 to days 4–5 and, then, gradually increased to the same levels as before Dox administration on days 6–7. Although, the maximal effects of the 2nd Dox administration on all behavioral tests appeared to be greater, they were not significantly different from the 1st Dox administration (visual placing response, $P = 0.0531$; visual orienting response, $P = 0.2123$; turning behavior, $P = 0.1544$, unpaired t-test). These results indicate that the selective blockade of the crossed tectoreticular pathway by double infection with NeuRet-TRE-EGFP.eTeNT and AAV2-CMV-rtTAV16 can be performed repeatedly with an interval of 28 days.

HISTOLOGICAL ANALYSIS

The number of GFP-positive crossed tectoreticular neurons (cTRNs) in the intermediate and deep layers of the SC of the double infected mice increased sharply after the start of Dox administration for 1 day and reached its maximum on Dox-on day 3 (**Figures 5A,C**). The maximum number of GFP-positive cTRNs was 458.8 ± 141.4 neurons ($n = 6$). After Dox administration was terminated, the number of GFP-positive cTRNs was gradually reduced on Dox-off days −3 to −14, and had returned to the baseline level by Dox-off day −28. To confirm the injection site of AAV2 in the right SC, *in situ* hybridization of rtTAV16 was performed. The injection sites were found to be located in the intermediate to deep layers of the right SC (**Figure 5B**). To demonstrate the reversibility of the Dox-on effects in these doubled infected mice, the 2nd Dox administration was started after a 28-day Dox-off period. The number of GFP-positive cTRNs in the intermediate and deep layers of the right SC increased again to 400.0 ± 218.3 ($n = 3$; **Figure 5C**). The histological results paralleled the impairment of visual orienting behavior after the 2nd Dox treatment in this group (**Figures 2B**, **3B**, **4B**).

In another group of mice ($n = 3$), the period of Dox administration was extended to 21 days, which resulted in strong staining of the cTRNs with anti-GFP immunohistochemistry that filled their distal dendrites. The axons from their cell bodies in the intermediate and deep layers of the right SC (**Figure 6A**) were labeled all the way to their target areas. Such tracing was difficult to perform in the mice with Dox administration for 7 days. The axons and terminals (**Figures 6B,C**) of these GFP-positive cTRNs could be found in the right mesodiencephalic junction [e.g., fields of Forel (FF), zona incerta (ZID, ZIV)] (**Figure 6Ca**), mesencephalic reticular formation (mRt) (**Figure 6C**b), nucleus reticularis tegmenti pontis (RtTg) (**Figures 6Cc,d**), pontine reticular formation (PRF; including the injection site of NeuRet-TRE-EGFP.eTeNT) (**Figures 6Cc,d,e**), gigantocellular reticular nucleus (Gi) (**Figure 6Ce**), inferior olivary nuclei (IO) (**Figure 6Cf**), etc. Thus, in addition to the injection site of the NeuRet vector, positive axons and terminals were found in many other target areas of collaterals that originated from the cTRNs (see Discussion).

TIME COURSE OF THE DOX-ON AND DOX-OFF PERIODS

To compare the time course of the behavioral effects and the appearance of anti-GFP immunoreactivity in cTRNs for the Dox-on and Dox-off periods, the results of the three behavioral tests were normalized to the maximal impairment and averaged. Then, the normalized values were compared to the normalized number of GFP-positive cTRNs during the Dox-on and Dox-off periods (**Figure 7**). The number of GFP-positive cTRNs increased sharply after the administration of Dox for 1 day, reached its maximum on Dox-on day 3, and was maintained until the end of Dox administration on day 7. Although behavioral impairment was also found from Dox-on day 1, it increased slower than the appearance of GFP-positive cTRNs. In contrast to the number of GFP-positive cTRNs, the behavioral impairment, after reaching its maximal effect on Dox-on day 3, was reduced to near the baseline level on Dox-on days 6–7. After Dox administration was terminated on day 7, the number of GFP-positive cTRNs was

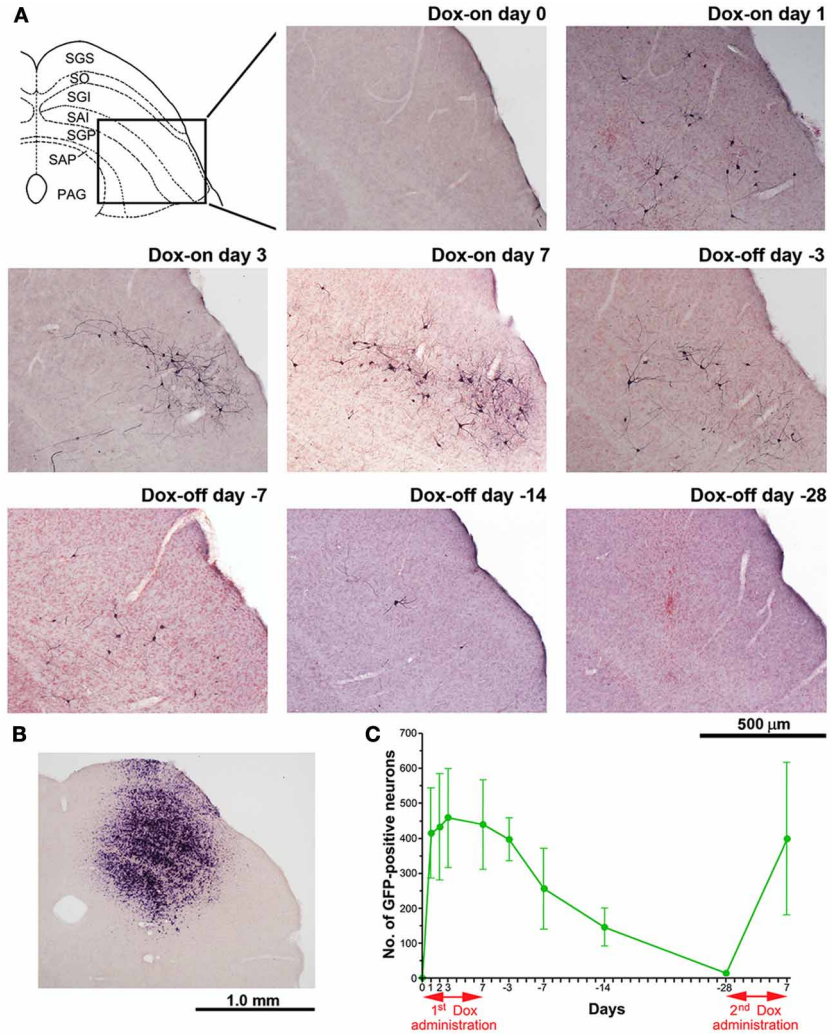

FIGURE 5 | Photomicrographs of GFP-positive cTRNs and *in situ* hybridization to visualize rtTAV16 in the superior colliculus (SC) of double infected mice. (A) Schematic diagram of the laminar structure of the mouse SC (frontal plane) and photomicrographs of the SC slices processed with anti-GFP immunohistochemistry (frontal section, inset area in the SC diagram), before Dox administration (Dox-on day 0), Dox administration for 1 day (Dox-on day 1), 3 days (Dox-on day 3), 7 days (Dox-on day 7), and after the termination of Dox administration for 3 days (Dox-off day −3), 7 days (Dox-off day −7), 14 days (Dox-off day −14), and 28 days (Dox-off day −28). **(B)** *In situ* hybridization against the tTA sequence in an SC slice indicating the cells infected by AAV2. **(C)** Average number of GFP-positive neurons in the SC after the 1st Dox administration for 7 days, termination of Dox administration for 28 days, and after the 2nd Dox treatment for 7 days ($n = 3$). Abbreviations: SGS, superficial gray layer; SO, optic layer; SGI, intermediate gray layer; SAI, intermediate white layer; SGP, deep gray layer; SAP, deep white layer; PAG, periaqueductal gray.

gradually reduced and reached the baseline level on Dox-off day −28.

DISCUSSION

The crossed tectoreticular pathway has been suggested to be involved in the control of orienting responses based on the following evidence: (1) repetitive electrical stimulation of the SC induces contraversive orienting responses (Cowie and Robinson, 1994; Corneil et al., 2002) and that of the medial pontomedullary reticular formation induces ipsiversive orienting responses (Cowie and Robinson, 1994); (2) lesion or reversible inactivation of the SC (Rosenquist et al., 1996; Quaia et al., 1998) or medial pontomedullary reticular formation (Isa and Sasaki, 1988) impairs orienting responses; (3) single unit recordings either from the SC (Sparks, 1975, 1978) or the medial pontomedullary reticular formation (Grantyn and Berthoz, 1987; Isa and Naito, 1995; Isa and Sasaki, 2002) reveal the existence of neurons that show increased firing preceding the orienting response; and (4) anatomically, the medial pontomedullary reticular formation receives massive inputs from the intermediate and deep layers of the contralateral SC (Kawamura and Brodal, 1973; Huerta and Harting, 1982). Thus, there is overwhelming evidence that the tectoreticular pathway plays a major role in the control of orienting responses (Sparks, 1986; Isa and Sasaki, 2002). However, the specific role of cTRNs in gaze has been difficult to resolve. In fact, this difficulty in precisely attributing function

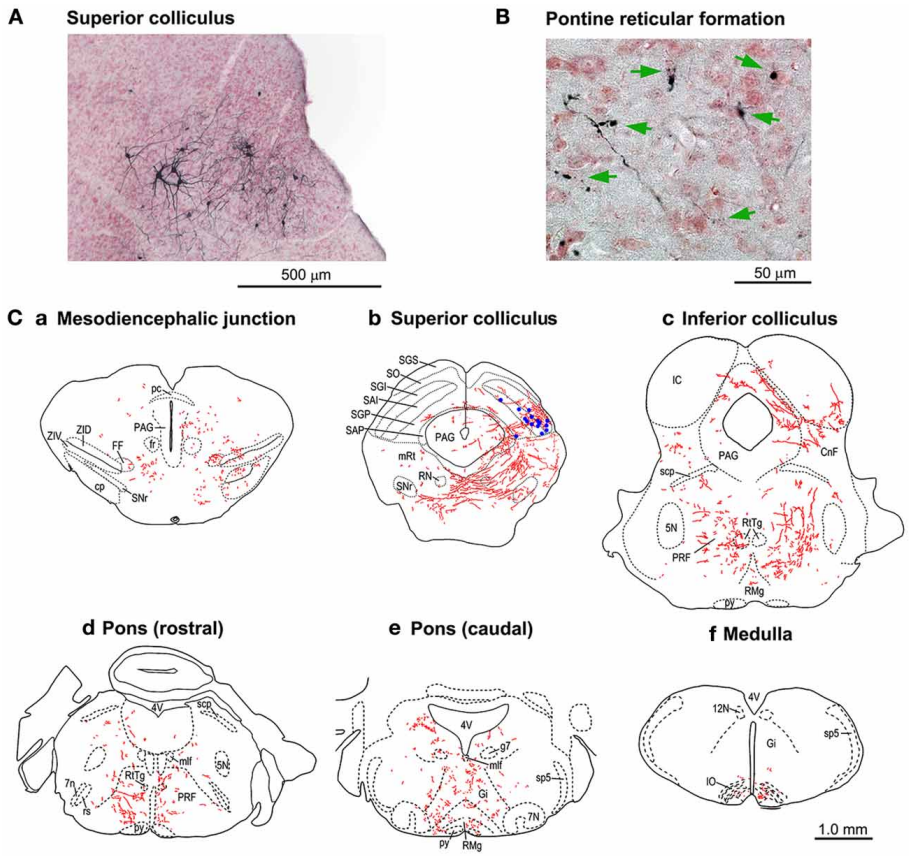

FIGURE 6 | Tracings of the axonal trajectories of the GFP-positive cTRNs in the superior colliculus (SC) in the mice with Dox treatment for 21 days. (A) GFP-positive cTRNs in the right SC. **(B)** Axon terminals (arrows) in the left pontine reticular formation. **(C)** Tracings of the axons and their terminals in the brainstem: a. Pretectum; b. Midbrain (SC level); c. Midbrain (inferior colliculus level); d. Pons (rostral part); e. Pons (caudal part); f. Medulla. GFP-positive cell bodies are indicated as blue dots in Cb. Abbreviations: 5N, trigeminal nucleus; 7N, facial nucleus; 7n, facial nerve; 12N, hypoglossal nucleus; CnF, cuneiform nucleus; cp, cerebral peduncle; FF, fields of Forel; fr, fasciculus retroflexus; g7, genu of the facial nerve; Gi, gigantocellular reticular nucleus; IC, inferior colliculus; IO, inferior olive; mlf, medial longitudinal fasciculus; mRt, mesencephalic reticular formation; PAG, periaqueductal gray; pc, posterior commissure; PRF, pontine reticular formation; py, pyramidal tract; RMg, raphe magnus nucleus; RN, red nucleus; rs, rubrospinal tract; RtTg, nucleus reticularis tegmenti pontis; SAI, intermediate white layer; SAP, deep white layer; scp, superior cerebellar peduncle; SGI, intermediate gray layer; SGP, deep gray layer; SGS, superficial gray layer; SO, optic layer; SNr, substantia nigra pars reticulata; sp5, spinal trigeminal tract; ZID, zona incerta, dorsal part; ZIV, zona incerta, ventral part.

to a specific cell population exists for many of the neural systems in the brain. In this regard, the present study, for the first time, showed that pathway-specific and reversible blockade of synaptic transmission worked as efficiently to cause behavioral deficits in mice, as it has in non-human primates (Kinoshita et al., 2012). Moreover, it specifically provides clear evidence that the direct crossed tectoreticular pathway is essential for the execution of orienting responses. Previous pharmacological techniques were not able to dissect this pathway from other tectal output pathways, such as the thalamic projection from the superficial layer, which might be involved in the higher visual processing (May, 2006), and from the uncrossed tecto-reticular pathway, which has been reported to control the avoidance behaviors (Sahibzada et al., 1986; Dean et al., 1989). However, the present method will enable us to pin down the functions of these individual components of the output pathways from the SC in near future.

Finally, we analyzed the methodological details of this technique, especially the time course of the effects of Dox-on and Dox-off with this relatively simple behavioral system. These experiments made use of a fair number of mice, which would be difficult to perform in non-human primates.

TIME COURSE AFTER DOX-ON

In this study, the behavioral effects of Dox administration could be partially observed as early as 24 h after initiation. This is earlier than observed in our previous study on macaque monkeys, in which the effects appeared on the 2nd day. This may be partly because we used an intraperitoneal injection on the first day to facilitate the quick onset of the effects (Perl et al., 2002). However, a species-related difference cannot be excluded. The effects became maximal on the 2nd and 3rd days after initiation, but gradually became smaller and had mostly disappeared by the 6th day. It is clear that this is not due to the disappearance of

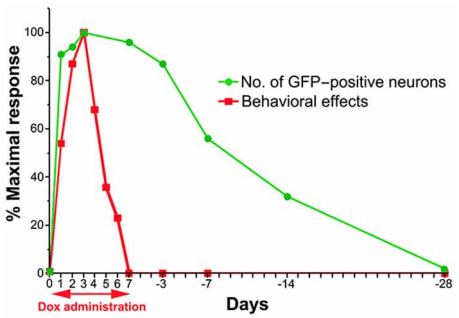

FIGURE 7 | Schematic drawing of the time course for the emergence and disappearance of blocking effects as measured by the behavioral effects and detectability of anti-GFP immunoreactivity after the onset and offset of Dox administration.

the Dox effects on the tetanus toxin production in the doubly infected neurons because the number of GFP-positive cells did not parallel the disappearance of the behavioral effects rather it persisted, as long as Dox was administered continuously. Such a disappearance of the behavioral effects must instead be caused by a compensatory mechanism in the residual pathways. This assumption is partly supported by the observation of a contralateral postural deviation in the turning response at 2 days after Dox-off (**Figure 4**). It is not clear which neural systems were responsible for such compensation, but it is likely due either to cTRNs, which were spared from double infection by vectors, or to direct corticoreticular pathways or to other unknown pathways involved in the control of visual orienting responses. A combination of these must have taken over the function of the blocked neurons.

TIME COURSE AFTER DOX-OFF

In this study, the behavioral changes were mostly not observed after Dox-offset following 7 days of Dox administration. We noticed a postural deviation to the right side at 2 days after Dox-off, which might be due to a compensatory mechanism established during the Dox-on period. Histological analysis showed that the number of GFP-positive cells gradually decreased after Dox-off, and returned to the baseline level on the 28th day after Dox-off. Furthermore, the 2nd Dox application on the 28th day after Dox-off caused as potent behavioral effects as during the 1st Dox administration. At least a one-month interval was necessary to observe the reversibility of the Dox effect. Since the functional compensation for the loss of transmission through a population of cTRNs may be caused by other compensatory neural circuits, this reversibility suggests that the mouse brain reused the cTRNs that had been blocked, once their transmission was restarted.

BLOCKADE OF TRANSMISSION THROUGH OTHER COLLATERALS OF THE cTRNs

Our previous study in macaque monkeys (Kinoshita et al., 2012) showed that anti-GFP immunohistochemistry clarified not only the location of the cell bodies of the PNs that expressed EGFP, but also their axonal trajectories. Similarly, a close examination of histological samples after anti-GFP immunohistochemistry revealed that although the number was small, the axons of the cTRNs could be traced from the cell bodies in the intermediate/deep layers of the right SC to their target areas. Axons and terminals could be observed not only in the left medial pontine reticular formation, the injection site of the NeuRet-TRE-EGFP.eTeNT, but also in several nuclei in the mesodiencephalic junction, pons, and medulla, which are targets of the ascending and descending collaterals of tectoreticular neurons (Grantyn and Grantyn, 1982; Huerta and Harting, 1982) (**Figure 6**). The possibility cannot be excluded that NeuRet-TRE-EGFP.eTeNT had diffused to the right side of the pontine reticular formation from the injection site, and some of these axons and terminals belonged to ipsilaterally projecting tectoreticular neurons. However, this should be a minor occurrence. In fact, the GFP-positive neurons were found exclusively in the caudal and lateral SC, where the cTRNs are located (**Figure 5A**), despite the fact that injection of AAV2-CMV-rtTAV16 included more medial parts of the SC (**Figure 5B**). If NeuRet-TRE-EGFP.eTeNT diffused to the right side, the GFP-positive cells should have been found also in more medial and rostral part of the SC where the uncrossed tectoreticular neurons are primarily located (Redgrave et al., 1990), Furthermore, the behavioral effects were clearly those expected from the impairment of cTRNs. In the previous reports (Grantyn and Grantyn, 1982; Isa and Sasaki, 2002), the pontine projection of the cTRNs was described as almost exclusively contralateral. The present report suggests there may be species differences in this regard between rodents and carnivores. As eTeNT was fused with EGFP, it should be transported to the axon terminals in these areas. These results indicate that synaptic transmission to these targets was also blocked, and that the behavioral effects cannot always be ascribed only to the blockade of transmission from the SC to the medial pontine reticular formation, but also to the blockade of signal transmission to all of the target nuclei. To conclude which connection was critical for the observed behavioral effects, another technique, such as optogenetic blockade of synaptic transmission at the nerve terminal (Kaneda et al., 2011), will need to be combined with our approach.

OTHER POSSIBLE USES OF THIS TECHNIQUE

The present results showed that the successful blockade of a particular central pathway with the double viral vector technique could result in behavioral effects in mice. Using a similar highly efficient retrograde gene transfer vector, some of the authors of this article have produced the permanent ablation of a central pathway by using it in combination with an immunotoxin (Inoue et al., 2012). This may represent a good approach for creating animal disease models. However, one of the major advantages of the present technique is its reversibility. Basically, this technique could be applicable to any pathway in the brain. However, when we apply the current technique to other pathways in the brain, it might be necessary to use other serotypes of AAV, because efficiency of transfection of each serotype could vary depending on the target cell types (Blits et al., 2010; Jakovcevski et al., 2010;

Markakis et al., 2010). The success of the current method was primarily based on the following factors: (1) development of highly efficient retrograde gene transfer using NeuRet; (2) very efficient amplification of gene expression by the recently developed Tet-ON sequence rtTAV16; and (3) very effective expression of the humanized tetanus neurotoxin eTeNT. Replacing eTeNT with other functional proteins, such as light-sensitive opsins for optogenetic control of neural activity (for reviews see Yizhar et al., 2011; Tye and Disseroth, 2012), may open up a novel direction for neural circuit analysis.

ACKNOWLEDGMENTS

This study is the result of "Highly Creative Animal Model Development for Brain Sciences" carried out under the Strategic Research Program for Brain Sciences (to Dai Watanabe, Kazuto Kobayashi, and Tadashi Isa) and a Grant-in-Aid for Scientific Research on Innovative Areas "Mesoscopic Neurocircuitry" (No. 25115731 to Tadashi Isa) by the Ministry of Education, Culture, Sports, Science, and Technology of Japan. We thank Kotomi Shimizu for assistance with immunohistochemistry and *in situ* hybridization.

REFERENCES

Blits, B., Derks, S., Twisk, J., Ehlert, E., Prins, J., and Verhaagen, J. (2010). Adeno-associated viral vector (AAV)-mediated gene transfer in the red nucleus of the adult rat brain: comparative analysis of the transduction properties of seven AAV serotypes and lentiviral vectors. *J. Neurosci. Methods* 185, 257–263. doi: 10.1016/j.jneumeth.2009.10.009

Corneil, B. D., Olivier, E., and Munoz, D. P. (2002). Neck muscle responses to stimulation of monkey superior colliculus. I. Topography and manipulation of stimulation parameters. *J. Neurophysiol.* 88, 1980–1999.

Cowie, R. J., and Robinson, D. L. (1994). Subcortical contributions to head movements in macaques. I. Contrasting effects of electrical stimulation of a medial pontomedullary region and the superior colliculus. *J. Neurophysiol.* 72, 2648–2664.

Dean, P., Redgrave, P., and Westby, G. W. (1989). Event or emergency? Two response systems in the mammalian superior colliculus. *Trends Neurosci.* 12, 137–147. doi: 10.1016/0166-2236(89)90052-0

Franklin, K. B. J., and Paxinos, G. (2008). *The Mouse Brain: in Stereotaxic Coordinates*. 3rd Edn. New York, NY: Academic Press.

Grantyn, A., and Berthoz, A. (1987). Reticulo-spinal neurons participating in the control of synergic eye and head movements during orienting in the cat. I. Behavioral properties. *Exp. Brain Res.* 66, 339–354. doi: 10.1007/BF00243309

Grantyn, A., and Grantyn, R. (1982). Axonal patterns and sites of termination of cat superior colliculus neurons projecting in the tecto-bulbo-spinal tract. *Exp. Brain Res.* 46, 243–256. doi: 10.1007/BF00237182

Huerta, M. F., and Harting, J. K. (1982). Tectal control of spinal cord activity: neuroanatomical demonstration of pathways connecting the superior colliculus with the cervical spinal cord grey. *Prog. Brain Res.* 57, 293–328. doi: 10.1016/S0079-6123(08)64135-7

Inoue, K., Koketsu, D., Kato, S., Kobayashi, K., Nambu, A., and Takada, M. (2012). Immunotoxin-mediated tract targeting in the primate brain: selective elimination of the cortico-subthalamic"hyperdirect" pathway. *PLoS ONE* 7:e39149. doi: 10.1371/journal.pone.0039149

Isa, T., and Hall, W. C. (2009). Exploring the superior colliculus *in vitro*. *J. Neurophysiol.* 102, 2581–2593. doi: 10.1152/jn.00498.2009

Isa, T., and Naito, K. (1995). Activity of neurons in the medial pontomedullary reticular formation during orienting movements in alert head-free cats. *J. Neurophysiol.* 74, 73–95.

Isa, T., and Sasaki, S. (1988). Effects of lesion of paramedian pontomedullary reticular formation by kainic acid injection on the visually triggered horizontal orienting movements in the cat. *Neurosci. Lett.* 87, 233–239. doi: 10.1016/0304-3940(88)90454-5

Isa, T., and Sasaki, S. (2002). Brainstem control of head movements during orienting; organization of the premotor circuits. *Prog. Neurobiol.* 66, 205–241. doi: 10.1016/S0301-0082(02)00006-0

Jakovcevski, M., Guo, Y., Su, Q., Gao, G., and Akbarian, S. (2010). rAAV9–a human-derived adeno-associated virus vector for efficient transgene expression in mouse cingulate cortex. *Cold Spring Harb. Protoc.* 4, pdb.prot5417. doi: 10.1101/pdb.prot5417

Kaneda, K., Kasahara, H., Matsui, R., Katoh, T., Mizukami, H., Ozawa, K., et al. (2011). Selective optical control of synaptic transmission in the subcortical visual pathway by activation of viral vector-expressed halorhodopsin. *PLoS ONE* 6:e18452. doi: 10.1371/journal.pone.0018452

Kato, S., Inoue, K., Kobayashi, K., Yasoshima, Y., Miyachi, S., Inoue, S., et al. (2007). Efficient gene transfer via retrograde transport in rodent and primate brains using a human immunodeficiency virus type 1-based vector pseudotyped with rabies virus glycoprotein. *Hum. Gene. Ther.* 18, 1141–1151. doi: 10.1089/hum.2007.082

Kato, S., Kobayashi, K., Inoue, K., Kuramochi, M., Okada, T., Yaginuma, H., et al. (2011a). A lentiviral strategy for highly efficient retrograde gene transfer by pseudotyping with fusion envelope glycoprotein. *Hum. Gene Ther.* 22, 197–206. doi: 10.1089/hum.2009.179

Kato, S., Kuramochi, M., Takasumi, K., Kobayashi, K., Inoue, K., Takahara, D., et al. (2011b). Neuron-specific gene transfer through retrograde transport of lentiviral vector pseudotyped with a novel type of fusion envelope glycoprotein. *Hum. Gene Ther.* 22, 1511–1523. doi: 10.1089/hum.2011.111

Kawamura, K., and Brodal, A. (1973). The tectopontine projection in the cat: an experimental anatomical study with comments on pathways for teleceptive impulses to the cerebellum. *J. Comp. Neurol.* 149, 371–390. doi: 10.1002/cne.901490306

Kinoshita, M., Matsui, R., Kato, S., Hasegawa, T., Kasahara, H., Isa, K., et al. (2012). Genetic dissection of the circuit for hand dexterity in primate. *Nature* 487, 235–238. doi: 10.1038/nature11206

Kobayashi, K., Morita, S., Sawada, H., Mizuguchi, T., Yamada, K., Nagatsu, I., et al. (1995). Immunotoxin-mediated conditional disruption of specific neurons in transgenic mice. *Proc. Natl. Acad. Sci. U.S.A.* 92, 1132–1136. doi: 10.1073/pnas.92.4.1132

Markakis, E. A., Vives, K. P., Bober, J., Leichtle, S., Leranth, C., Beecham, J., et al. (2010). Comparative transduction efficiency of AAV vector serotypes 1-6 in the substantia nigra and striatum of the primate brain. *Mol. Ther.* 18, 588–593. doi: 10.1038/mt.2009.286

May, P. J. (2006). The mammalian superior colliculus: laminar structure and connections. *Prog. Brain Res.* 151, 321–378. doi: 10.1016/S0079-6123(05)51011-2

Metz, G. A., and Schwab, M. E. (2004). Behavioral characterization in a comprehensive mouse test battery reveals motor and sensory impairments in growth-associated protein-43 null mutant mice. *Neuroscience.* 129, 563–574. doi: 10.1016/j.neuroscience.2004.07.053

Montecucco, C., and Schiavo, G. (1994). Mechanism of action of tetanus and botulinum neurotoxins. *Mol. Microbiol.* 13, 1–8. doi: 10.1111/j.1365-2958.1994.tb00396.x

Perl, A.-K. T., Tichelaar, J. W., and Whitsett, J. A. (2002). Condition gene expression in the respiratory epithelium of mouse. *Transgenic Res.* 11, 21–29. doi: 10.1023/A:1013986627504

Pinto, L. H., and Enroth-Cugell, C. (2000). Tests of the mouse visual system. *Mamm. Genome.* 11, 531–536. doi: 10.1007/s003350010102

Quaia, C., Aizawa, H., Optican, L. M., and Wurtz, R. H. (1998). Reversible inactivation of monkey superior colliculus. II. Maps of saccadic deficits. *J. Neurophysiol.* 79, 2097–2110.

Redgrave, P., Dean, P., and Westby, G. W. (1990). Organization of the crossed tecto-reticulo-spinal projection in rat - I. Anatomical evidence for separate output channels to the periabducens area and caudal medulla. *Neuroscience* 37, 571–584. doi: 10.1016/0306-4522(90)90092-I

Rosenquist, A. C., Ciaramitaro, V. M., Durmer, J. S., Wallace, S. F., and Todd, W. E. (1996). Ibotenic acid lesions of the superior colliculus produce longer lasting deficits in visual orienting behavior than aspiration lesions in the cat. *Prog.*

Brain Res. 112, 117–130. doi: 10.1016/S0079-6123(08)63324-5

Sahibzada, N., Dean, P., and Redgrave, P. (1986). Movements resembling orientation or avoidance elicited by electrical stimulation of the superior colliculus in rats. *J. Neurosci.* 6, 723–733.

Smith, D. R., Striplin, C. D., Geller, A. M., Mailman, R. B., Drago, J., Lawler, C. P., et al. (1998). Behavioural assessment of mice lacking D1A dopamine receptors. *Neuroscience* 86, 135–146. doi: 10.1016/S0306-4522(97)00608-8

Sooksawate, T., Isa, K., and Isa, T. (2008). Cholinergic responses in crossed tecto-reticular neurons of rat superior colliculus. *J. Neurophysiol.* 100, 2702–2711. doi: 10.1152/jn.90723.2008

Sooksawate, T., Saito, Y., and Isa, T. (2005). Electrophysiological and morphological properties of identified cross tecto-reticular neurons in the rat superior colliculus. *Neurosci. Res.* 52, 174–184. doi: 10.1152/jn.90723.2008

Sparks, D. L. (1975). Response properties of eye movement-related neurons in the monkey superior colliculus. *Brain Res.* 90, 147–152. doi: 10.1016/0006-8993(75)90690-3

Sparks, D. L. (1978). Functional properties of neurons in the monkey superior colliculus: coupling of neuronal activity and saccade onset. *Brain Res.* 156, 1–16. doi: 10.1016/0006-8993(78)90075-6

Sparks, D. L. (1986). Translation of sensory signals into commands for control of saccadic eye movements: role of primate superior colliculus. *Physiol. Rev.* 66, 118–171.

Tye, K. M., and Disseroth, K. (2012). Optogenetic investigation of neural circuits underlying brain disease in animal models. *Nat. Rev. Neurosci.* 13, 251–266. doi: 10.1038/nrn3171

Watanabe, D., Inokawa, H., Hashimoto, K., Suzuki, N., Kano, M., Shigemoto, R., et al. (1998). Ablation of cerebellar Golgi cells disrupts synaptic integration involving GABA inhibition and NMDA receptor activation in motor coordination. *Cell* 95, 17–27. doi: 10.1016/S0092-8674(00)81779-1

Wurtz, R. H., and Albano, J. E. (1980). Visual-motor function of the primate superior colliculus. *Annu. Rev. Neurosci.* 3, 189–226. doi: 10.1146/annurev.ne.03.030180.001201

Yizhar, O., Fenno, L. E., Davidson, T. J., Mogri, M., and Deisseroth, K. (2011). Optogenetics in neural systems. *Neuron* 71, 9–34. doi: 10.1016/j.neuron.2011.06.004

Conflict of Interest Statement: The authors declare that the research was conducted in the absence of any commercial or financial relationships that could be construed as a potential conflict of interest.

Received: 01 July 2013; accepted: 21 September 2013; published online: 11 October 2013.

Citation: Sooksawate T, Isa K, Matsui R, Kato S, Kinoshita M, Kobayashi K, Watanabe D, Kobayashi K and Isa T (2013) Viral vector-mediated selective and reversible blockade of the pathway for visual orienting in mice. Front. Neural Circuits ***7****:162. doi: 10.3389/fncir.2013.00162*

This article was submitted to the journal Frontiers in Neural Circuits.

frontiers in
NEURAL CIRCUITS

ORIGINAL RESEARCH ARTICLE
published: 23 September 2013
doi: 10.3389/fncir.2013.00143

Target dependence of orientation and direction selectivity of corticocortical projection neurons in the mouse V1

Teppei Matsui*[1] *and* ***Kenichi Ohki*[1,2]***

[1] *Department of Molecular Physiology, Graduate School of Medical Sciences, Kyushu University, Fukuoka, Japan*
[2] *CREST, Japan Science and Technology Agency, Tokyo, Japan*

Edited by:
Yasuo Kawaguchi, National Institute for Physiological Sciences, Japan

Reviewed by:
David Fitzpatrick, Max Planck Florida Institute for Neuroscience, USA
Yumiko Yoshimura, National Institutes of Natural Sciences, National Institute for Physiological Sciences, Japan

***Correspondence:**
Teppei Matsui and Kenichi Ohki, Department of Molecular Physiology, Graduate School of Medical Sciences, Kyushu University, Building A of Basic Sciences, 3-1-1 Maidashi, Higashi-ku, Fukuoka 812-8582, Japan
e-mail: tematsui@med.kyushu-u.ac.jp; kohki@med.kyushu-u.ac.jp

Higher order visual areas that receive input from the primary visual cortex (V1) are specialized for the processing of distinct features of visual information. However, it is still incompletely understood how this functional specialization is acquired. Here we used *in vivo* two photon calcium imaging in the mouse visual cortex to investigate whether this functional distinction exists at as early as the level of projections from V1 to two higher order visual areas, AL and LM. Specifically, we examined whether sharpness of orientation and direction selectivity and optimal spatial and temporal frequency of projection neurons from V1 to higher order visual areas match with that of target areas. We found that the V1 input to higher order visual areas were indeed functionally distinct: AL preferentially received inputs from V1 that were more orientation and direction selective and tuned for lower spatial frequency compared to projection of V1 to LM, consistent with functional differences between AL and LM. The present findings suggest that selective projections from V1 to higher order visual areas initiates parallel processing of sensory information in the visual cortical network.

Keywords: visual cortex, mouse, corticocortical connection, *in vivo* two photon imaging, axon

INTRODUCTION

The cerebral cortex is a hierarchically organized network that processes information in a parallel and distributed manner (Felleman and Van Essen, 1991). In the visual cortical network, information arrived at the primary visual cortex (V1) is passed to two functionally distinct cortical pathways: The dorsal pathway that consists of extrastriate cortical areas specialized for the processing visual information important for object recognition, and the ventral pathway that consists of cortical areas specialized for the processing of visual information important for spatial navigation, in primates (Ungerleider and Mishkin, 1982) and carnivores (Payne, 1993; Toyama et al., 1994). Neurons in the dorsal pathway have sharper direction selectivity and are tuned to higher temporal frequency stimuli compared to neurons in the ventral pathway that have sharper orientation selectivity and are tuned to higher spatial frequency stimuli (Maunsell and Van Essen, 1983; Albright, 1984; Desimone and Schein, 1987; Toyama et al., 1994; Pollen et al., 2002; Priebe et al., 2003). Analogous functionally distinct cortical pathways have also been found in auditory cortical pathways (Tian et al., 2001; Lomber and Malhotra, 2008).

As in primates, mouse visual cortex consists of V1 and extrastriate visual cortices that receive direct projection from V1 (**Figure 1A**; Wang and Burkhalter, 2007). Based on anatomical connectivity, Wang and Burkhalter suggested that these extrastriate cortices could be grouped into dorsal and ventral pathways analogous to dorsal and ventral pathways in primates and carnivores (Wang et al., 2011, 2012). In particular, two extrastriate areas, namely AL and LM, were identified as the first stage after V1 for the dorsal and ventral pathways, respectively. In line with this idea, recent *in vivo* imaging studies revealed functional distinction between visual response properties of neurons in the extrastriate areas: Neurons in AL have higher orientation/direction selectivity and are tuned to lower spatial frequency information than neurons in LM (Marshel et al., 2011). It was also reported that neurons in AL are tuned response to lower spatial frequency and higher speed stimuli than neurons in another extrastriate area PM (Andermann et al., 2011).

In the primate V1, neurons responding to distinct visual features are spatially segregated into distinct anatomical modules [e.g., cortical layers or columns; Livingstone and Hubel, 1988; but see Nassi and Callaway (2009) for existence of crosstalk between modules] each of which is connected to specific higher order visual areas to form distinct functional pathways [Livingstone and Hubel, 1988; but see Sincich and Horton (2005) for existence of crosstalk between pathways]. However, since distinct visual features are represented in a spatially intermingled manner in rodents, it is unlikely that specific connection between laminar and/or columnar modules are used to selectively route information about visual feature to different higher order visual areas. One potential mechanism to create functional specialization of extrastriate visual areas in rodents is that distinct information intermingled in V1 is selectively routed to relevant pathways with cellular level specificity. Another possibility is that information fed by V1 is not different across two pathways but is processed differently by local neuronal circuit

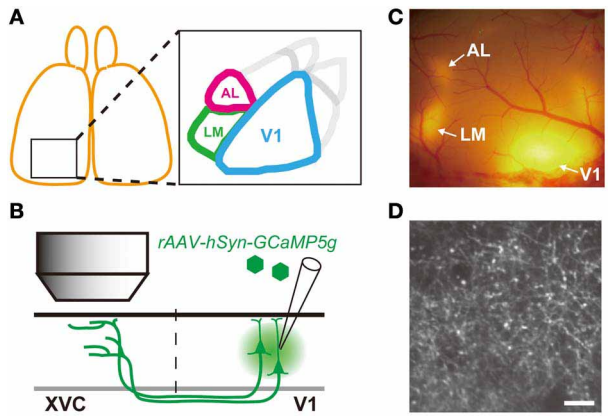

FIGURE 1 | Experimental Strategy. (A) Schematic drawing of visual area map in the mouse visual cortex. AL and LM are the two extrastriate visual areas targeted in this study. **(B)** Schematic drawing of experimental approach. AAV containing GCaMP5g was injected into V1. Axon terminals of V1 neurons projecting to the extrastriate visual cortex (XVC) were imaged by *in vivo* two photon microscopy. **(C)** Epifluorescence TurboRFP signal observed *in vivo* through the cranial window. Patches of red fluorescence are observed in V1 (injected area) as well as in XVC as smaller patches of fluorescence. **(D)** Representative image of axon terminals expressing GCaMP5g observed *in vivo* by two photon microscopy in area LM indicated in **(C)**. Individual axonal boutons can be clearly resolved as bright varicosities. Scale bar, 10 μm.

in the target extrastriate areas to extract different features of visual information. It has been difficult to distinguish between these two possibilities due to a technical difficulty of identifying projection targets of neurons whose activity has been recorded.

Recently, genetically encoded calcium indicators have been greatly improved (Tian et al., 2009; Horikawa et al., 2010; Akerboom et al., 2012) enabling *in vivo* recording of activity from fine neuronal processes such as dendrites and axons (Petreanu et al., 2012; Xu et al., 2012). A recent study took advantage of this technology to record activity of axon terminals projecting from the mouse V1 to higher order visual areas and found difference in the optimal spatial and temporal frequencies between axon terminals projecting to AL, LM (Glickfeld et al., 2013). Since sharpness of orientation and direction selectivity also differs between neurons in AL and LM (Marshel et al., 2011), it is of great interest whether functional property of axonal projections from V1 to AL and LM differs in these two features.

In the present study, we used genetically encoded calcium indicator to observe axonal calcium activity of corticocortical projection neurons in the mouse V1 (Petreanu et al., 2012; Glickfeld et al., 2013). We infected neurons in the mouse V1 by injecting recombinant adeno-associated-virus (rAAV) carrying genetically encoded calcium indicator (GCaMP5g; Akerboom et al., 2012). We then imaged calcium activity of the axon terminals of infected V1 neurons at their projection target (**Figure 1B**). We found that sharpness of orientation and direction selectivity as well as optimal spatial frequency of axon terminals projecting from V1 to AL and LM were distinct and match with the functional characteristics of the neurons in the target areas.

MATERIALS AND METHODS

ANIMALS AND VIRAL INJECTION

Wild type C57/BL6 mice around two to three months of age were prepared for viral injection. Mice were anesthetized with an intraperitoneal injection of chloral hydrate (4 mg/g) and an intramuscular injection of xylazine (2 μg/g). After opening the scalp, a small craniotomy (∼1 mm diameter) was made over the left V1 (∼3 mm lateral from the midline and ∼1.5 mm posterior from the lambda). A glass pipette (tip diameter, 50 μm) containing rAAV-*hSyn-GCaMP5g* mixed with rAAV-*CB7-TurboRFP* (mixed at 10:1; purchased from the University of Pennsylvania Human Gene Therapy Vector Core) were inserted to the cortex at a depth of ∼400 μm. Then a small amount of virus solution (0.1–0.5 μl) was pressure injected at a rate of 0.05 μl/min using a syringe pump (SP101I, World Precision Instruments, Sarasota, FL). Imaging experiments commenced around three weeks after the injection. All experimental procedures used in this study were approved by the Animal Care and Use Committee of Kyushu University.

In vivo TWO PHOTON IMAGING

Detailed procedure for the preparation of *in vivo* two photon imaging is described elsewhere (Ohki and Reid, 2011). Briefly, anesthesia was induced with isoflurane (3%) and maintained with isoflurane (1–2% in surgery, 0.5–1% during imaging). After opening the scalp, the location and the extent of RFP expression was examined through the skull with green LED light. A custom made metal headplate was attached to the skull using dental cement (SunMediacal, Shiga, Japan), and a craniotomy (∼5 mm) was made to expose the cortical surface expressing RFP. After the craniotomy, the dura was removed and exposed cortex was covered by a circular glass window (6.5 mm diameter). We often found a large patch of RFP expression in V1 surrounded by several smaller patches of RFP at the extrastriate areas (**Figure 1C**). This pattern of RFP expression was used to select location for calcium imaging.

In vivo imaging of axonal calcium activity was performed using a two photon microscope (A1RMP, Nikon, Tokyo, Japan) equipped with a X25 water immersion objective (NA1.1, Nikon). GCaMP5g was excited at 920 nm wavelength by a Ti:Sapphire laser (Mai Tai HP DeepSee, Spectra Physics). A square region of cortex 64 μm on each side (512 × 512 pixels) was imaged at 30 Hz. Depth of the imaged plane was carefully adjusted manually every 5–10 min. Image planes from the same cortical location were separated at least by 10 μm in the depth direction to avoid imaging the same axonal boutons twice. During the imaging, the level of anesthesia was adjusted by monitoring the heart rate continuously by electrocardiogram. Body temperature was maintained at 37°C by a feedback-controlled heat-pad. Silicon oil was used to prevent eyes from drying.

For each imaged region its location was identified by matching the spatial pattern of blood vessels on the cortical surface in the two-photon images and that in a macroscopic picture of RFP expression pattern. Subsequently, corresponding extrastriate visual area was assigned to each imaged region based on the pattern of RFP expression and/or retinotopic map obtained with intrinsic signal optical imaging.

INTRINSIC SIGNAL OPTICAL IMAGING

Mapping of cortical retinotopy by optical imaging of intrinsic signal was performed according to the method described in previous studies (Kalatsky and Stryker, 2003; Marshel et al., 2011). Briefly, prior to the optical imaging experiment, mice had either thinned skull or an implanted glass window over the left visual cortex. Throughout the imaging, mice were anesthetized by isoflurane (0.6–1.2%), and 700 nm LED light source was used to illuminate the brain. Data was collected at a frame rate of 5 Hz using a CCD camera (1000-m, Adimec, Boston, MA) controlled by an Imager3001 system (Optical Imaging Ltd., Rehovot, Israel). Obtained signal was Fourier transformed to extract the phase at the stimulus frequency (one cycle in 20 s), which can then be converted to the position in the visual space.

VISUAL STIMULATION

Visual stimuli were presented on a LCD display using a desktop computer running PsychoPy (Peirce, 2009) or a custom made software written in Visual Basic (Microsoft). For mapping of orientation and direction preferences, a drifting square-wave grating [100% contrast; 0.04 cycles per degree (cpd); 2 Hz] tilted at one of four orientations in 45° steps moving in one of two directions orthogonal to the orientation (yielding total of eight directions of motion in 45° steps) was presented. Each stimulus started with a blank period of uniform gray (4 s) followed by the same period of visual stimulation. Each condition was repeated 10–20 times. For mapping of spatial frequency (SF) and temporal frequency (TF) tunings, drifting sine-wave gratings (100% contrast) were used. For SF mapping experiments, sine-wave gratings having six SF between 0.01 and 0.4 cpd and drifting at 2 Hz were used. For TF mapping experiments, sine-wave gratings having 0.04 cpd and drifting at 5 different TF between 0.5 and 8 Hz were used. Each stimulus started with a blank period of uniform gray (4 s) followed by the same period of visual stimulation during vertical and horizontal gratings were presented for 1 s for each of four directions (0°, 180°, 90°, and 270° in order). Each condition was presented 10–20 times in pseudorandom orders. In SF and TF mapping experiments, both SF and TF stimuli were tested at each imaged plane. Stimuli for mapping retinotopy by intrinsic signal optical imaging were adapted from a previous study (Kalatsky and Stryker, 2003). A thin flashing white bar on a black screen was continuously moved in a horizontal or vertical direction at a constant speed of 20 s/cycle. Each run lasted 320 s (16 cycles).

ANALYSIS OF TWO PHOTON CALCIUM IMAGING DATA

All the analyses were performed using custom software written in Matlab (MathWorks, Natick, MA). Acquired images were first realigned by maximizing the correlation across frames. Axon terminals were automatically identified by template matching with a circular template using time averaged image. Time courses of individual axon terminals (boutons) were extracted by summing pixel values within the contours of axonal boutons. Slow drift of the baseline signal over minutes was removed by a low-cut filter (Gaussian, cutoff, 1.6 min) and high-frequency noise was removed by a high-cut filter (first-order Butterworth, cutoff, 1.6 s). Visually responsive axonal boutons were defined by $\Delta F/F > 0.15$ and by one way analysis of variance ($p < 0.01$) across blanks and stimulus periods. The response to each orientation was defined as the mean of the responses to two drifting gratings

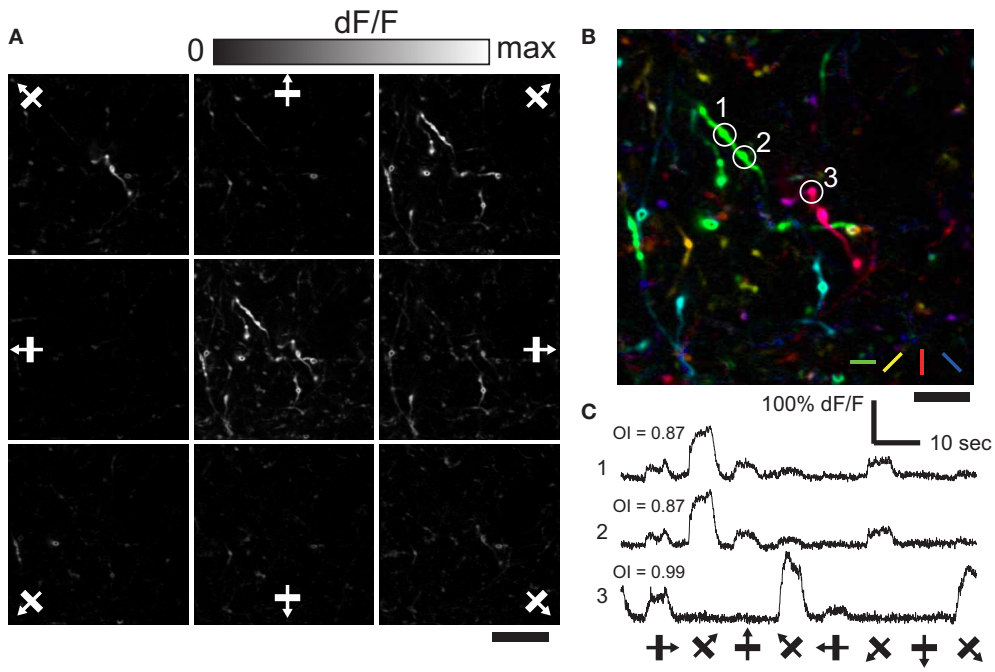

FIGURE 2 | Orientation and direction selective response of axonal boutons in LM. (A) Representative single condition ΔF/F maps for eight directions. Center panel shows max ΔF/F. Scale bar, 20 μm. **(B)** Color-coded map created from **(A)**. Scale bar, 10 μm. **(C)** Representative time courses (average of 10 trials) of three axonal boutons in **(B)**. Note that boutons belonging to the same axon fiber (1 and 2), show very similar time courses.

moving at opposing directions orthogonal to the orientation (e.g., response to 0° orientation was obtained by averaging responses to two gratings moving orthogonal to the 0° orientation, i.e., 90° and 270° directions). Of these boutons, boutons selectively responding to stimulus conditions were defined by one way analysis of variance ($p < 0.01$) across stimulus conditions (four orientations for orientation mapping experiments, and six SF and five TF for SF and TF mapping experiments, respectively). Preferred direction for pixel based direction map (**Figure 2B**) was calculated by vector averaging (Swindale et al., 1987). For the orientation and direction preference analyses Orientation Index (OI) was calculated by the formula: $OI = 1 - R_{ortho} / R_{pref}$, where R_{pref} is the response to the preferred orientation and the R_{ortho} is the response to the orientation orthogonal to the preferred orientation. Direction Index (DI) was calculated by the formula: $DI = 1 - R_{null} / R_{pref}$ (Mikami et al., 1986), where R_{pref} is the response to the preferred direction and the R_{null} is the response to the direction opposite to the preferred direction. For the SF and TF analyses, difference of Gaussian (DOG) was fitted to each axonal bouton's response (Hawken and Parker, 1987). Preferred SF (or TF) for each axonal bouton was then defined by SF (or TF) at the maximum of the fitted DOG. The preferred SF (or TF) was rounded to the maximum or the minimum value of the tested stimulus parameter, when it fell outside of these values. All statistical testing was performed using Statistics Toolbox of Matlab (MathWorks).

RESULTS

In vivo IMAGING OF AXONAL ACTIVITY OF V1 PROJECTION NEURONS

Mice were injected with a mixture of rAAV encoding GCaMP5g and rAAV encoding TurboRFP into V1 resulting in a large patch of red (and green) fluorescence in V1 that was surrounded by smaller patches of fluorescence in the extrastriate areas (**Figure 1C**). Consistent with previous anatomical tracing study, large RFP patches were found in areas AL and LM (Wang and Burkhalter, 2007). At these extrastriate RFP patches, axonal fibers and boutons of V1 projection neurons expressing GCaMP5g (and TurboRFP) could be detected *in vivo* at the cortical depth from ∼20 μm up to ∼500 μm (**Figure 1D**). Large calcium transients in response to visual stimulation could be observed from axonal boutons expressing GCaMP5 (**Supplementary Movie 1**). We first characterized orientation and direction preference of V1 projection neurons by analyzing calcium activity of these axonal boutons.

Many axonal boutons in AL selectively responded to a presentation of particular orientation of drifting square gratings (**Figure 2A**; $n = 108$ visually responsive boutons out of 476 boutons identified. see Materials and Methods). Typically, orientation preference of nearby boutons were different (**Figure 2B**), however boutons belonging to the same axonal fiber showed matched orientation preference as well as closely matched time courses of calcium responses (**Figure 2C**; see Petreanu et al., 2012). Similar spatial organization for orientation preference of axonal boutons was found in LM (data not shown). These results show spatially intermingled pattern of V1 input for orientation information in AL and LM. Moreover, the fact that we could clearly detect the difference in the orientation preference of nearby axonal boutons demonstrates the reliability of our recording from individual axonal boutons.

SHARPNESS OF ORIENTATION AND DIRECTION SELECTIVITY OF V1 AXONS DIFFERS IN AL AND LM

Next we investigated difference in orientation and direction selectivity of axonal boutons in AL and LM. Individual axonal boutons showed highly tuned response to drifting gratings presented at different orientations and directions in both AL and LM (**Figure 3A**). Of all the visually responsive axonal boutons in AL and LM (1250 and 1630 boutons in AL and LM, respectively),

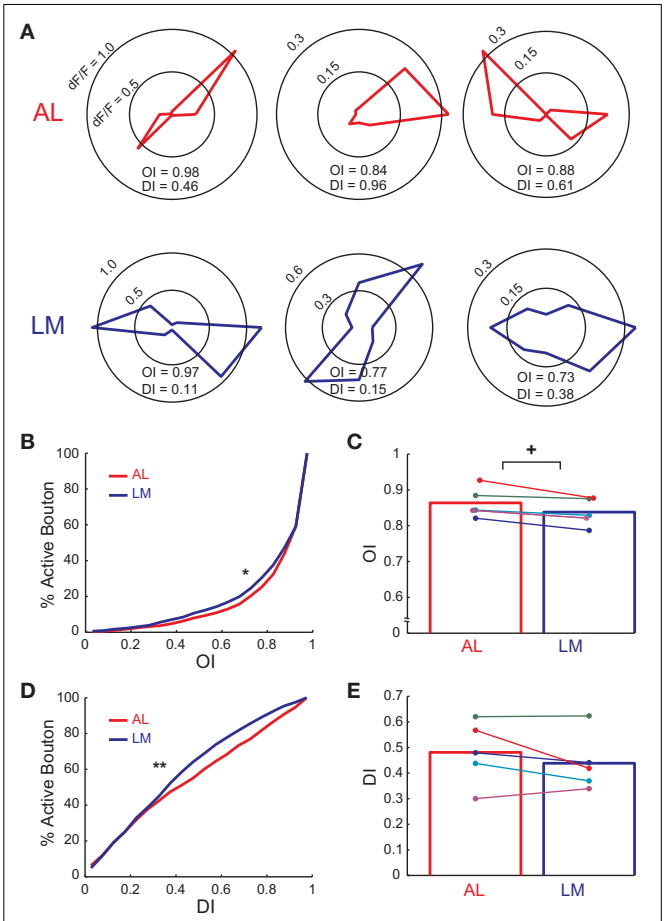

FIGURE 3 | Orientation and direction tuning property of axonal boutons in AL and LM. (A) Polar plots showing responses (ΔF/F) to eight directions for example axonal boutons in AL and LM. **(B)** Cumulative distribution of OI of axonal boutons in AL and LM. Mean OI across all responsive boutons = 0.851 and 0.829 in AL and LM, respectively. *, $P < 0.006$. **(C)** Mean OI in AL and LM for each animal. Mean OI across animals = 0.864 and 0.838 in AL and LM, respectively. Each pair of colored dots indicates data from one animal. Bar graph shows mean of all the animals. $^+$, $P < 0.04$. **(D)** Cumulative distribution of DI of axonal boutons in AL and LM. Mean DI across all boutons = 0.463 and 0.418 for AL and LM, respectively. **, $P < 0.0001$. **(E)** Mean DI in AL and LM for each animal. Each pair of colored dots indicates data from one animal. Mean DI across animals = 0.481 and 0.438 for AL and LM, respectively. Bar graph shows mean of all the animals.

1068 (85%) and 1490 (91%) responded selectively to orientation and direction of drifting gratings in AL and LM, respectively. Cumulative distribution of OI for all visually responsive axonal boutons in AL collected from five mice was significantly shifted toward higher values than that in LM ($P < 0.006$, Kolmogorov-Smirnov test; **Figure 3B**), indicating that V1 neurons projecting to AL were more orientation selective than those projecting to LM. To test for consistency across animals, we also compared mean OI of axonal boutons in AL and LM for each animal. Consistent with the cumulative data, mean OI in each animal was higher in AL than in LM for all the animals and the difference was statistically significant ($P < 0.04$, $n = 6$, sign-rank test; **Figure 3C**).

Next we examined the difference in direction selectivity by calculating DI for the same set of boutons in AL and LM. Cumulative distribution of DI for axonal boutons in AL pooled from all the animals was significantly shifted toward higher values than that in LM ($P < 0.0001$, Kolmogorov-Smirnov test; **Figure 3D**), indicating that V1 neurons projecting to AL were more direction selective than those projecting to LM. Though not statistically significant, the difference in DI across two areas was consistently observed across animals as the mean DI was larger in AL than in LM (**Figure 3E**). When the analysis was restricted to selectively responding boutons, four out of five animals had higher mean DI in AL than in LM (data not shown). Taken together, the functional difference of axonal activity in AL and LM found here closely matches with a previous finding which reported sharper orientation and direction selectivity for neurons in AL than neurons in LM (Marshel et al., 2011).

SPATIAL AND TEMPORAL FREQUENCY PREFERENCE OF V1 AXONS DIFFERS IN AL AND LM

We next conducted mapping of SF and TF tunings of V1 axons in AL and LM (**Figures 4**, **5**). Individual axonal boutons showed variety of SF and TF tuning in both AL and LM (SF, **Figures 4B,E**; TF, **Figures 5B,E**). SF and TF tuning curves obtained for individual axonal boutons were similar to those reported for neurons in the mouse V1 (SF, **Figures 4C,F**; TF, **Figures 5C,F**; Niell and Stryker, 2008). As in the case of orientation and direction preference, visually responsive axonal boutons having various SF and TF tuning were spatially intermingled both in AL and LM without any apparent local clustering according to SF or TF preference.

Of all the visually responsive axonal boutons in AL and LM (835 and 1236 boutons in AL and LM, respectively), 796 (95%) and 1178 (95%) responded selectively to drifting gratings presented at different spatial frequencies in AL and LM, respectively, and were further analyzed. Cumulative distribution of preferred SF (see Materials and Methods for obtaining preferred SF) for population of axonal boutons in LM pooled from seven mice was shifted significantly toward higher SF compared to that in AL ($P < 0.0001$, Kolmogorov-Smirnov test; **Figure 6A**). Consistently, mean value for the preferred SF in LM calculated separately for each animal was significantly higher than that in AL

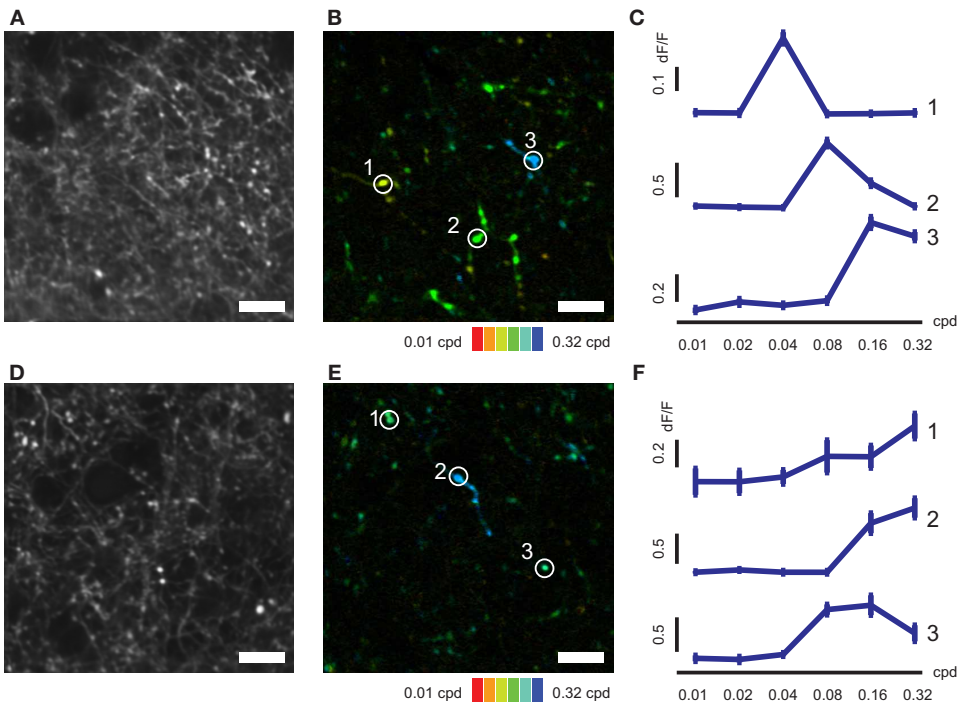

FIGURE 4 | SF-tuned responses of axonal boutons in AL and LM. **(A)** Representative FOV in LM. **(B)** Color-coded map of preferred SF of axonal boutons shown in **(A)**. **(C)** Representative SF tuning curves for three axonal boutons indicated by circles in **(B)**. **(D)** Representative FOV in AL. **(E)** Color-coded map of preferred SF of axonal boutons shown in **(D)**. **(F)** Representative SF tuning curves for three axonal boutons indicated by circles in **(E)**. Error bars indicate s.e.m. Scale bars, 10 μm.

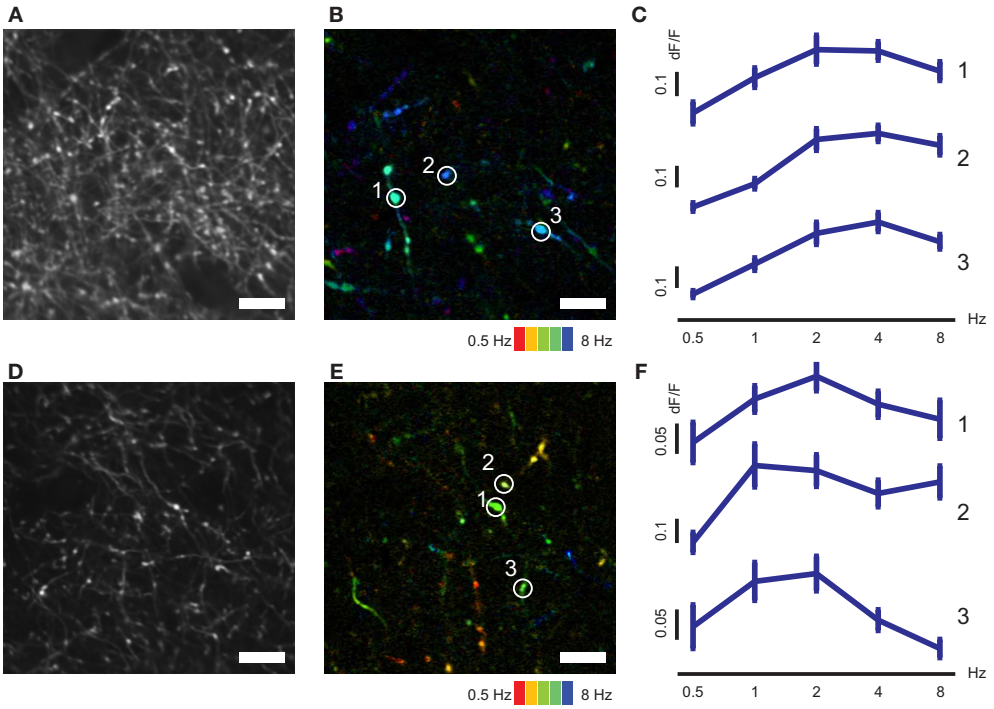

FIGURE 5 | TF–tuned responses of axonal boutons in AL and LM. **(A)** Representative FOV in LM. **(B)** Color-coded map of preferred TF of axonal boutons shown in **(A)**. **(C)** Representative TF tuning curves for three axonal boutons indicated by circles in **(B)**. **(D)** Representative FOV in AL. **(E)** Color-coded map of preferred TF of axonal boutons shown in **(D)**. **(F)** Representative TF tuning curves for three axonal boutons indicated by circles in **(E)**. Error bars indicate s.e.m. Scale bars, 10 μm.

($P < 0.008$, $n = 7$, sign-rank test; **Figure 6B**). Finally, we examined the difference in TF tuning of axonal boutons in AL and LM. Of all the visually responsive axonal boutons in AL and LM (438 and 685 boutons in AL and LM, respectively), 285 (65%) and 444 (65%) responded selectively to drifting gratings presented at different temporal frequencies in AL and LM, respectively, and were further analyzed. The cumulative distribution of the preferred TF pooled from all the animals was larger in AL than in LM ($P < 0.03$, Kolmogorov-Smirnov test; **Figure 6C**). Although not significant, mean preferred TF across animals was also larger in AL than in LM ($P = 0.4$, $n = 7$, sign-rank test; **Figure 6D**). These differences of the axonal boutons in AL and LM found here for SF tuning, and to a weaker extent for TF tuning, are consistent with a recent report (Glickfeld et al., 2013). As in the case for orientation and direction selectivity, the difference in the SF preference of axons in AL and LM matches with that of the reported response properties of neurons in AL and LM (Marshel et al., 2011). Taken together, the present results suggest that the feedforward corticocortical projections from V1 to AL and LM are functionally distinct in a way that matches with the reported functional difference between neurons in AL and LM.

DISCUSSIONS

In the present study, by using *in vivo* two photon calcium imaging of axonal activity, we characterized difference in the visual response properties of corticocortical projection neurons in the mouse V1. Response properties of the corticocortical projection neurons in V1 were significantly different depending on their target extrastriate areas: Axonal boutons of V1 neurons projecting to AL had sharper of orientation and direction selectivity and responded optimally for lower spatial frequency stimuli compared to axonal boutons projecting to LM. These differences in the visual response properties of V1 projection neurons in AL and LM were largely consistent with the reported response properties of the neurons in AL and LM. Therefore, the present results support the notion that functional specialization in the higher order cortical areas is created by selective projections of functionally distinct neurons from the upstream cortical areas.

ADVANTAGES OF AXONAL CALCIUM IMAGING COMPARED TO OTHER TECHNIQUES FOR STUDYING CORTICOCORTICAL PROJECTION NEURONS

Previous electrophysiological studies have used techniques such as antidromic electrical stimulation [Movshon and Newsome (1996) among many others], optogenetic stimulation (Lima et al., 2009) and fluorescent dye filling by electroporation (Igarashi et al., 2012) to identify projection target of neurons whose response properties were characterized electrophysiologically. However, these techniques require significant labor to collect a large number of samples. Indeed, out of 786 neurons recorded in V1, only 12 could be identified as MT projecting neurons by means of antidromic electrical stimulation (Movshon and Newsome, 1996). The present imaging-based approach possesses several advantages compared to these previous approaches. First,

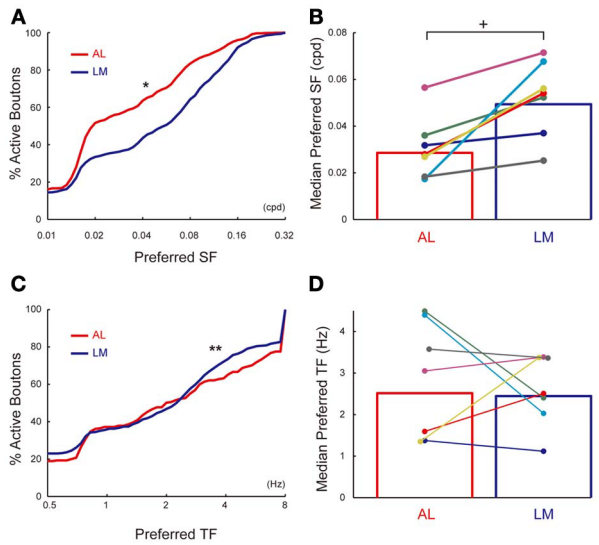

FIGURE 6 | SF and TF tuning properties of axonal boutons in AL and LM. (A) Cumulative distributions of preferred SF in AL and LM. Mean of preferred SF across all boutons = 0.031 and 0.048 cpd for AL and LM, respectively. *, $P < 0.001$. **(B)** Mean preferred SF in AL and LM for each animal. Each pair of colored dots indicates data from one animal. Mean of preferred SF across all animals = 0.029 and 0.049 cpd for AL and LM, respectively. Bar graph shows mean of all the animals. $^{+}$, $P < 0.01$. **(C)** Cumulative distributions of preferred TF in AL and LM [same set of boutons as in **(A)**]. Mean of preferred TF across all boutons = 2.1 and 1.9 Hz for AL and LM, respectively. **, $P < 0.03$. **(D)** Mean preferred TF in AL and LM for each animal. Mean of preferred TF across all animals = 2.5 and 2.4 Hz for AL and LM, respectively. Each pair of colored dots indicates data from one animal. Bar graph shows mean of all the animals.

it is technically straight forward and does not require complicated experimental steps such as identification of antidromically stimulated neurons or single neuron electroporation. Second, and more importantly, the present approach enables collection of many samples of projection neurons from multiple target areas from individual animals. This second advantage was critical in revealing subtle but statistically significant differences between two overlapping distribution of the neuronal response properties.

Several groups have used combination of retrograde neuronal tracing and *in vivo* two photon calcium imaging of labeled neuronal somata to study corticocortical projection neurons (Sato and Svoboda, 2010; Osakada et al., 2011; Jarosiewicks et al., 2012; Chen et al., 2013). Although this approach is promising and complementary to axonal calcium imaging, it is necessary to use multiple colors to label neurons projecting to multiple areas in one animal (Jarosiewicks et al., 2012). Nevertheless, it is of great importance to see whether experiments using retrograde tracers reach the same conclusions as that reached by axonal calcium imaging.

It should be noted that genetically encoded calcium indicator used in the present study (GCaMP5g) is not capable of reporting single action potential reliably (Akerboom et al., 2012). Hence, it is not clear whether large portion of axon terminals that were non-responsive to visual stimulation were indeed non-visually driven V1 neurons (Keller et al., 2012) or their response simply did not reach sensitivity limit of GCaMP5g. In addition, slow time course of GCaMP5g prohibited us from analyzing action potential synchrony of projection neurons which may be important for efficient corticocortical spike transmission (Fries, 2009). Development of more sensitive genetically encoded calcium or voltage indicators with fast kinetics will be critical to resolve these problems (Jin et al., 2012).

COMPARISON WITH PREVIOUS STUDIES

Functional specialization of extrastriate visual areas in the mouse has been reported by previous imaging studies (Andermann et al., 2011; Marshel et al., 2011; Roth et al., 2012). A recent study (Glickfeld et al., 2013) that used similar approach to ours revealed that the difference in the SF and TF tunings among extrastriate areas (AL, LM, and PM) could be accounted for by difference in the SF and TF tuning of V1 neurons projecting to each of these areas. The present study confirms and adds to this result by showing that the difference in the projection neuron can also contribute to the difference in orientation and direction selectivity of neurons in the target area. Since neurons in the dorsal lateral geniculate nucleus are selective for SF and TF (Grubb and Thompson, 2003), target-dependence of the optimal SF and TF of corticocortical projections may be explained by mechanism similar to parallel visual pathways found in primates that relay functionally distinct visual information from subcortical areas (e.g., retina or LGN) to primary and extrastriate visual cortices (Livingstone and Hubel, 1988). Although, unlike primates, neurons preferring various SF and TF are not spatially clustered in mice, parallel functional channels similar to primates may still exist in a spatially intermingled manner (Gao et al., 2010). However, since orientation and direction selectivity are most pronounced in the cortex and rare in LGN (Marshel et al., 2012; Piscopo et al., 2013), similar mechanism based on parallel pathways from subcortical to cortical areas may not be sufficient in these cases. Moreover, SF preference and orientation selectivity are not systematically related in mouse V1 neurons (Gao et al., 2010), hence a mechanism that produce difference in the SF and TF preference of V1 projection neurons cannot explain that of orientation and direction selectivity. Orientation and direction selectivity are related to specifically connected local neuronal circuits in the neocortex (Yoshimura et al., 2005; Yu et al., 2009; Ko et al., 2011). Thus, there may be some common factor that links the specifically connected local neocortical circuit and the target-dependence of orientation and direction selectivity of corticocortical projection neurons.

Differences in the tuning properties of corticocortical projections from V1 to AL and LM are largely consistent with the functional differences of dorsal/ventral pathways expected from the well-studied dorsal/ventral pathways of macaques (Ungerleider and Mishkin, 1982; Maunsell and Van Essen, 1983; Desimone and Schein, 1987; Pollen et al., 2002; Priebe et al., 2003). Axonal boutons in AL that belongs to the putative dorsal pathway in mice had sharper direction selectivity as well as lower optimal SF compared orientation selectivity that was sharper in AL than in LM. Since neurons in AL also have been shown to have sharper orientation tuning compared to neurons in LM (Marshel et al., 2011),

these results may suggest across species difference in the dorsal/ventral pathways of macaques and mice.

Sharpness of orientation and direction selectivity of axon terminals observed in the present study was somewhat higher than that of mouse V1 neurons reported previously (Niell and Stryker, 2008; Andermann et al., 2011; Marshel et al., 2011; Roth et al., 2012). The difference found here may be attributed to inability of GCaMP5g to report single action potentials reliably. For GCaMP3, sensitivity for reporting action potentials in axon terminal (Petreanu et al., 2012) was lower than that in the soma (Tian et al., 2009). Lower sensitivity to action potentials in axon terminals may truncate calcium response to low level spiking activity in the axon terminal but not in the soma, hence resulting in higher orientation and direction selectivity in the axon terminal compared to that in the soma.

OTHER MECHANISMS FOR CREATING FUNCTIONAL SPECIALIZATION IN THE EXTRASTRIATE AREAS

Although several studies including the present one converge to support the presence of selective routing of information between the primary and higher order sensory areas (Sato and Svoboda, 2010; Jarosiewicks et al., 2012; Glickfeld et al., 2013), other mechanisms may also contribute to shape response properties of higher order sensory neurons. Complex dendritic computation is likely to shape response properties of sensory neurons (Jia et al., 2010), and it is unclear whether such intracellular processing works to enhance or attenuate functional differences of V1 projection neurons. It should also be noted that a subset of V1 projections is known to target interneurons in the higher order visual area (Gonchar and Burkhalter, 2003). This feedforward inhibitory circuit could also contribute to shape response properties of excitatory neurons within the extrastriate areas. Nevertheless, while these additional mechanisms may work to fine-tune the response property of neurons within each higher order cortical area, target dependent functional projection from lower cortical area is likely to work as the seed for generating functional specialization in higher order cortical areas.

AUTHOR CONTRIBUTIONS

Teppei Matsui and Kenichi Ohki conceived the study. Teppei Matsui performed experiments, analyses. Teppei Matsui and Kenichi Ohki wrote the manuscript.

ACKNOWLEDGMENTS

We thank Dr. T. Kawashima for the involvement in the initial phase of the experiments, and Drs. S. Kondo and T. Murakami for help with experiments and analysis and other members of the Ohki laboratory for discussion. We thank Drs. L. L. Looger, A. Akerboom, D. S. Kim for providing GCaMP5g. This work was supported by JSPS KAKENHI Grant number 25221001, and grants from CREST-JST, the Takeda-Science Foundation to Kenichi Ohki. Teppei Matsui was supported by JSPS Research Fellowship for Young Scientists (201204982).

SUPPLEMENTARY MATERIAL

The Supplementary Material for this article can be found online at: http://www.frontiersin.org/Neural_Circuits/10.3389/fncir.2013.00143/abstract

Supplementary Movie 1 | Representative axonal calcium activity in response to visual stimulation (x8 speed).

REFERENCES

Akerboom, J., Chen, T. W., Wardill, T. J., Tian, L., Marvin, J. S., Mutlu, S., et al. (2012). Optimization of a GCaMP calcium indicator for neural activity imaging. *J. Neurosci.* 32, 13819–13840. doi: 10.1523/JNEUROSCI.2601-12.2012

Albright, T. D. (1984). Direction and orientation selectivity of neurons in visual area MT of the macaque. *J. Neurophysiol.* 52, 1106–1130.

Andermann, M. L., Kerlin, A. M., Roumis, D. K., Glickfeld, L. L., and Reid, R. C. (2011). Functional specialization of mouse higher visual cortical areas. *Neuron* 72, 1025–1039. doi: 10.1016/j.neuron.2011.11.013

Chen, J. L., Carta, S., Soldado-Magraner, J., Schneider, B. L., and Helmchen, F. (2013). Behavior-dependent recruitment of long-range projection neurons in somatosensory cortex. *Nature* 499, 336–340. doi: 10.1038/nature12236

Desimone, R., and Schein, S. J. (1987). Visual properties of neurons in area V4 of the macaque: sensitivity to stimulus form. *J. Neurophysiol.* 57, 835–868.

Felleman, D. J., and Van Essen, D. C. (1991). Distributed hierarchical processing in the primate cerebral cortex. *Cereb. Cortex* 1, 1–47. doi: 10.1093/cercor/1.1.1

Fries, P. (2009). Neuronal gamma-band synchronization as a fundamental process in cortical computation. *Annu. Rev. Neurosci.* 32, 209–224. doi: 10.1146/annurev.neuro.051508.135603

Gao, E., DeAngelis, D. C., and Burkhalter, A. (2010). Parallel input channels to mouse visual cortex. *J. Neurosci.* 30, 5912–5926. doi: 10.1523/JNEUROSCI.6456-09.2010

Glickfeld, L. L., Andermann, M. L., Bonin, V., and Reid, R. C. (2013). Cortico-cortical projections in mouse visual cortex are functionally target specific. *Nat. Neurosci.* 16, 219–226. doi: 10.1038/nn.3300

Gonchar, Y., and Burkhalter, A. (2003). Distinct GABAergic targets of feedforward and feedback connections between lower and higher areas of rat visual cortex. *J. Neurosci.* 23, 10904–10912.

Grubb, M. S., and Thompson, I. D. (2003). Quantitative characterization of visual response properties in the mouse dorsal lateral geniculate nucleus. *J. Neurophysiol.* 90, 3594–3607. doi: 10.1152/jn.00699.2003

Hawken, M. J., and Parker, A. J. (1987). Spatial properties of neurons in the monkey striate cortex. *Proc. R. Soc. Lond. B Biol. Sci.* 231, 2366–2371. doi: 10.1098/rspb.1987.0044

Horikawa, K., Yamada, Y., Matsuda, T., Kobayashi, K., Hashimoto, M., Matsu-ura, T., et al. (2010). Spontaneous network activity visualized by ultrasensitive Ca(2+) indicators, yellow Cameleon-Nano. *Nat. Methods* 7, 729–732. doi: 10.1038/nmeth.1488

Igarashi, K. M., Ieki, N., An, M., Yamaguchi, Y., Nagayama, S., Kobayakawa, K., et al. (2012). Parallel mitral and tufted cell pathways route distinct odor information to different targets in the olfactory cortex. *J. Neurosci.* 32, 7970–7985. doi: 10.1523/JNEUROSCI.0154-12.2012

Jarosiewicks, B., Schummers, J., Malik, W. Q., Brown, E. N., and Sur, M. (2012). Functional biases in visual cortex neurons with identified projections to higher cortical targets. *Curr. Biol.* 22, 269–277. doi: 10.1016/j.cub.2012.01.011

Jia, H., Rochefort, N. L., Chen, X., and Konnerth, A. (2010). Dendritic organization of sensory input to cortical neurons *in vivo*. *Nature* 464, 1307–1312. doi: 10.1038/nature08947

Jin, L., Han, Z., Platisa, J., Wooltorton, J. R., Cohen, L. B., and Pieribone, V. A. (2012). Single action potentials and subthreshold electrical events imaged in neurons with a fluorescent protein voltage probe. *Neuron* 75, 779–785. doi: 10.1016/j.neuron.2012.06.040

Kalatsky, V. A., and Stryker, M. P. (2003). New paradigm for optical imaging: temporally encoded maps of intrinsic signal. *Neuron* 38, 529–545. doi: 10.1016/S0896-6273(03)00286-1

Keller, G. B., Bonhoeffer, T., and Hubener, M. (2012). Sensorimotor mismatch signals in primary visual cortex of the behaving mouse. *Neuron* 74, 809–815. doi: 10.1016/j.neuron.2012.03.040

Ko, H., Hofer, S. B., Pichler, B., Buchanan, K. A., Sjostrom, P. J., and Mrsic-Flogel, T. D. (2011).

Functional specificity of local synaptic connections in neocortical networks. *Nature* 473, 87–91. doi: 10.1038/nature09880

Lima, S. Q., Hromadka, T., Znamenskly, P., and Zador, A. M. (2009). PINP: a new method of tagging neuronal populations for identification during electrophysiological recording. *PLoS ONE* 4:e6099. doi: 10.1371/journal.pone.0006099

Livingstone, M. S., and Hubel, D. H. (1988). Segregation of form, color, movement and depth: anatomy, physiology and perception. *Science* 240, 740–749. doi: 10.1126/science.3283936

Lomber, S. G., and Malhotra, S. (2008). Double dissociation of 'what' and 'where' processing in auditory cortex. *Nat. Neurosci.* 11, 609–616. doi: 10.1038/nn.2108

Marshel, J. H., Garrett, M. E., Nauhaus, I., and Callaway, E. M. (2011). Functional specialization of seven mouse visual cortical areas. *Neuron* 72, 1040–1054. doi: 10.1016/j.neuron.2011.12.004

Marshel, J. H., Kaye, A. P., Nauhaus, I., and Callaway, E. M. (2012). Anterior-posterior direction opponency in the superficial mouse lateral geniculate nucleus. *Neuron* 76, 713–720. doi: 10.1016/j.neuron.2012.09.021

Maunsell, J. H., and Van Essen, D. C. (1983). Functional properties of neurons in middle temporal visual area of the macaque monkey. I. Selectivity for stimulus direction, speed and orientation. *J. Neurophysiol.* 49, 1127–1247.

Mikami, A., Newsome, W. T., and Wurtz, R. H. (1986). Motion selectivity in macaque visual cortex. I. Mechanisms of direction and speed selectivity in extrastriate area MT. *J. Neurophysiol.* 55, 1308–1327.

Movshon, J. A., and Newsome, W. T. (1996). Visual response properties of striate cortical neurons projecting to area MT in macaque monkeys. *J. Neurosci.* 16, 7733–7741.

Nassi, J. J., and Callaway, E. M. (2009). Parallel processing strategies of the primate visual system. *Nat. Rev. Neurosci.* 10, 360–372. doi: 10.1038/nrn2619

Niell, C. M., and Stryker, M. P. (2008). Highy selective receptive fields in mouse visual cortex. *J. Neurosci.* 28, 7520–7536. doi: 10.1523/JNEUROSCI.0623-08.2008

Ohki, K., and Reid, R. C. (2011). "*In vivo* two-photon calcium imaging in the visual system," in *Imaging in Neuroscience*, eds F. Helmchen, A. Konnerth, and R. Yuste (Cold Spring Harbor, NY: Cold Spring Harbor Laboratory Press), 511–528.

Osakada, F., Mori, T., Cetin, A. H., Marshel, J. H., Virgen, B., and Callaway, E. M. (2011). New rabies virus variants for monitoring and manipulating activity and gene expression in defined neural circuits. *Neuron* 71, 617–631. doi: 10.1016/j.neuron.2011.07.005

Payne, B. R. (1993). Evidence for visual cortical area homologues in cat and macaque monkey. *Cereb. Cortex* 3, 1–25. doi: 10.1093/cercor/3.1.1

Peirce, J. W. (2009). Generating stimuli for neuroscience using PsychoPy. *Front. Neuroinform.* 2, 10. doi: 10.3389/neuro.11.010.2008

Petreanu, L., Gutnisky, D. A., Huber, D., Xu, N. L., O'Connor, D. H., Tian, L., et al. (2012). Activity in motor-sensory projections reveals distributed coding in somatosensation. *Nature* 489, 299–303. doi: 10.1038/nature11321

Piscopo, D. M., El-Danaf, R. N., Hubermann, A. D., and Niell, C. M. (2013). Diverse visual features encoded in mouse lateral geniculate nucleus. *J. Neurosci.* 33, 4642–4656. doi: 10.1523/JNEUROSCI.5187-12.2013

Pollen, D. A., Przsybyszewski, W., Rubin, M. A., and Foote, W. (2002). Spatial receptive field organization of macaque V4 neurons. *Cereb. Cortex* 12, 601–616. doi: 10.1093/cercor/12.6.601

Priebe, N. J., Cassanello, C. R., and Lisberger, S. G. (2003). The neural representation of speed in macaque area MT/V5. *J. Neurosci.* 23, 5650–5661.

Roth, M. M., Helmchen, F., and Kampa, B. M. (2012). Distinct functional properties of primary and posteromedial visual area of mouse neocortex. *J. Neurosci.* 32, 9716–9726. doi: 10.1523/JNEUROSCI.0110-12.2012

Sato, T. R., and Svoboda, K. (2010). The functional properties of barrel cortex neurons projecting to the primary motor cortex. *J. Neurosci.* 30, 4256–4260. doi: 10.1523/JNEUROSCI.3774-09.2010

Sincich, L. C., and Horton, J. C. (2005). The circuitry of V1 and V2: integration of color, form and motion. *Annu. Rev. Neurosci.* 28, 303–326. doi: 10.1146/annurev.neuro.28.061604.135731

Swindale, N. V., Matsubara, J. A., and Cynader, M. S. (1987). Surface organization of orientation and direction selectivity in cat area 18. *J. Neurosci.* 7, 1414–1427.

Tian, B., Reser, D., Durham, A., Kustov, A., and Rauschecker, J. P. (2001). Functional specialization in rhesus monkey auditory cortex. *Science* 292, 290–293. doi: 10.1126/science.1058911

Tian, L., Hires, S. A., Mao, T., Huber, D., Chiappe, M. E., Chalasani, S. H., et al. (2009). Imaging neural activity in worms, flies and mice with improved GCaMP calcium indicators. *Nat. Methods* 6, 875–881. doi: 10.1038/nmeth.1398

Toyama, K., Mizobe, K., Akase, E., and Kaihara, T. (1994). Neuronal responsiveness in areas 19 and 21a, and the posteromedial lateral suprasylvian cortex of the cat. *Exp. Brain Res.* 99, 289–301. doi: 10.1007/BF00239595

Ungerleider, L. G., and Mishkin, M. (1982). "Two cortical visual systems," in *Analysis of Visual Behavior,* eds D. J. Ingel, M. A. Goodale, and R. J. W. Mansfield (Cambridge, MA: Massachusetts Institute of Technology), 549–586.

Wang, Q., and Burkhalter, A. (2007). Area map of mouse visual cortex. *J. Comp. Neurol.* 502, 339–357. doi: 10.1002/cne.21286

Wang, Q., Gao, E., and Burkhalter, A. (2011). Gateways ventral and dorsal streams in mouse visual cortex. *J. Neurosci.* 31, 1905–1918. doi: 10.1523/JNEUROSCI.3488-10.2011

Wang, Q., Sporns, O., and Burkhalter, A. (2012). Network analysis of corticocortical connections reveals ventral and dorsal streams in mouse visual cortex. *J. Neurosci.* 32, 4386–4399. doi: 10.1523/JNEUROSCI.6063-11.2012

Xu, N. L., Harnett, M. T., Williams, S. R., Huber, D., O'Connor, D. H., Svoboda, K., et al. (2012). Nonlinear dendritic integration of sensory and motor input during an active sensing task. *Nature* 492, 247–251. doi: 10.1038/nature11601

Yoshimura, Y., Dantzker, J. L., and Callaway, E. M. (2005). Excitatory cortical neurons form fine-scale functional networks. *Nature* 433, 868–873. doi: 10.1038/nature03252

Yu, Y. C., Bultje, R. S., Wang, X., and Shi, S. H. (2009). Specific synapses develop preferentially among sister excitatory neurons in the neocortex. *Nature* 458, 501–504. doi: 10.1038/nature07722

Conflict of Interest Statement: The authors declare that the research was conducted in the absence of any commercial or financial relationships that could be construed as a potential conflict of interest.

Received: 23 July 2013; accepted: 25 August 2013; published online: 23 September 2013.

Citation: Matsui T and Ohki K (2013) Target dependence of orientation and direction selectivity of corticocortical projection neurons in the mouse V1. Front. Neural Circuits 7:143. doi: 10.3389/fncir.2013.00143

This article was submitted to the journal Frontiers in Neural Circuits.